Simone Luigi Marasso
Matteo Cocuzza *Editors*

High Resolution Manufacturing from 2D to 3D/4D Printing

Applications in Engineering and Medicine

Springer

High Resolution Manufacturing from 2D to 3D/4D Printing

Simone Luigi Marasso • Matteo Cocuzza
Editors

High Resolution Manufacturing from 2D to 3D/4D Printing

Applications in Engineering and Medicine

Springer

Editors
Simone Luigi Marasso
National Research Council (CNR) – Institute of Materials for Electronics and Magnetism (IMEM)
Parma, Italy

Matteo Cocuzza
Department of Applied Science and Technology
Politecnico di Torino
Torino, Italy

ISBN 978-3-031-13778-5 ISBN 978-3-031-13779-2 (eBook)
https://doi.org/10.1007/978-3-031-13779-2

This Springer imprint is published by the registered company Springer Nature Switzerland AG
The registered company address is: Gewerbestrasse 11, 6330 Cham, Switzerland

Preface

Nowadays the design and development of devices requiring microelectronic components as well micro-nano structures are extremely complex and expensive. Moreover, the materials and the facilities involved in the micro- and nano-scale fabrication processes require high investment, proper area and laboratories to be installed and maintained. The recent progresses in the additive manufacturing technologies open new fabrication paradigms that can evolve in the direction of simplifying devices fabrication. This is the main motivation feeding the editing of a book containing the recent development in additive manufacturing, especially in the high-resolution 3D printing techniques, which can represent a useful guide to understand the new achievements already reached in this field, thus providing a different point of view with respect to other editorial works. The collection of techniques and applications reported in this book reinforces our conviction that a new era is coming which is going to reveal the game changer represented by the high-resolution 3D/4D printing of complex devices, often requiring active electrical properties or miniaturization.

About This Book

High-resolution manufacturing has rapidly evolved in the past few years, especially with the advent of innovative additive manufacturing technologies, speeding up the prototyping of novel kind of devices in the micro and nano scale. We are now living an era of transition: A lot has been done in research laboratories, and impacts will be seen in the near future in several fields, from electronics to engineering and medicine. The technologies and the materials behind this revolution are several and this book aims to focus on them. Going from 2D to 3D/4D printing and from millimeters to the nano scale, the book proposes to report not only about the technologies but also about the polymeric materials, the most promising ones concerning composite design and smart objects fabrication. Besides, polymers offer high flexibility and unique cost effectiveness due to the wide range of available compositions. Allowing modification of their structure at a molecular level, the technologies employed to process polymeric materials are no more limited to millimetric feature sizes but can go down to hundreds or tens of nanometers. Therefore, 2D and 3D printing technologies, like Two Photon Polymerization (2PP), represent the last frontier in the field of high-resolution additive manufacturing. Moreover, new polymer composites have been proposed recently, which add active properties to the structural function, and complex devices have been manufactured. This book also provides insights into recent works in different research fields, addressing issues like throughput improvement by volumetric 3D printing and presenting novel applications and case studies. In addition to the strengths of methodology, this book also covers the developments in terms of breakthrough innovations to envisage the future perspective in the field.

Contents

Part I Technologies and Materials

1 Introduction to High-Resolution Manufacturing from 2D to 3D/4D Printing Technology Evolutions and Design Considerations 3
Matteo Parmeggiani, Alberto Ballesio, Matteo Cocuzza, and Simone Luigi Marasso

2 Vat Photopolymerization 17
Roberta Bongiovanni and Alessandra Vitale

3 3D Micro- and Nanostructuring by Two-Photon Polymerization 47
Ayman El-Tamer, Maria Surnina, Ulf Hinze, and Boris N. Chichkov

4 Powder Bed Fusion 81
C. Badini and E. Padovano

5 Direct Writing: Inkjet and Aerosol-Jet Printing 105
Pasquale D'Angelo and Davide Vurro

6 Volumetric 3D Printing 131
Valentina Bertana and Monica Periolatto

Part II Impact on Different Research Fields and Case Studies

7 Biomedical Applications 155
Ignazio Roppolo, Annalisa Chiappone, Alessandro Chiadò, Gianluca Palmara, and Francesca Frascella

8 Electronic Applications 191
Matteo Manachino, Gianluca Melis, Stefano Stassi, Sergio Ferrero, and Luciano Scaltrito

9 Energy Storage Applications 233
Pietro Zaccagnini and Andrea Lamberti

10 Photonic Applications: Impact on "Dielectric Laser Acceleration" and Other Case Studies 269
Costantino De Angelis, Andrea Locatelli, Giorgio S. Mauro, Rita Rizzoli, Gino Sorbello, and Giuseppe Torrisi

11 Future Prospective 293
Alberto Ballesio, Matteo Parmeggiani, Matteo Cocuzza, and Simone Luigi Marasso

Index 299

Part I
Technologies and Materials

Chapter 1
Introduction to High-Resolution Manufacturing from 2D to 3D/4D Printing Technology Evolutions and Design Considerations

Matteo Parmeggiani, Alberto Ballesio, Matteo Cocuzza, and Simone Luigi Marasso

Abstract Additive manufacturing (AM) includes a wide range of technologies that have been specialized to speed up the prototyping, especially in the field of mechanical engineering. In the last years, the use of polymer composites has opened novel opportunities in terms of functionalities to pave the way for a new generation of prototyping. Applications in electronics, medicine, and energy storage are growing and the prototyping of the devices in these fields faces new challenges related to their complexity and functionalities. In parallel, specific resolution capabilities to prototype high-performing devices are needed. For a better understanding of the potentiality and the differences between AM and other manufacturing approaches, a step inside the fundamental principles should be done. One of the main points is the shift from the top-down approach typical of the industry, as, for example, in microelectronics, to a bottom-up approach, which is typical of additive manufacturing and 3D printing. The paradigm change involves first of all the design. The main outcome of the industrial top-down approach is in fact a process flow, while in the AM bottom-up approach, the main outcome is a virtual model. In this scenario, it is of great interest to understand the new approaches introduced not only for the design of the devices, but also the main concepts related to the printability of 3D models and to the post-processing of the final 3D printed object.

Keywords 3D printing · Additive manufacturing · Printability · 3D models · Top-down approach

M. Parmeggiani · A. Ballesio
Department of Applied Science and Technology (DISAT), Politecnico di Torino, Torino, Italy
e-mail: matteo.parmeggiani@polito.it; alberto.ballesio@polito.it

M. Cocuzza · S. L. Marasso (✉)
Department of Applied Science and Technology (DISAT), Politecnico di Torino, Torino, Italy

CNR-IMEM, Parma, Italy
e-mail: matteo.cocuzza@polito.it; simoneluigi.marasso@cnr.it

S. L. Marasso, M. Cocuzza (eds.), *High Resolution Manufacturing from 2D to 3D/4D Printing*, https://doi.org/10.1007/978-3-031-13779-2_1

1.1 Introduction

Three-dimensional printing is quickly developing as a new technology with applications in a growing range of fields, from engineering and medicine to electronics and energy storage. The International Standard Organization (ISO) defined the term 3D printing as the fabrication of objects through the deposition of a material using a print head, nozzle, or another printer technology [1]. The 3D printed objects are fabricated from 3D models by adding layer by layer new materials, in contrast to other typical subtractive and formative manufacturing methodologies; therefore, it is also referred to as additive manufacturing (AM). Rapid prototyping (RP) is also commonly used to identify AM and 3D printing as they are techniques able to rapidly pass from a design to a virtual model and then to the final object [2].

As show in Fig. 1.1a, AM has experienced an exponential growth, and in the last two decades, this technology has steadily entered in our everyday life, changing the manufacturing paradigm of tools used in every field and every place. Moreover, nowadays, high-resolution additive manufacturing is gaining more and more interest, mainly due to its possible applications in electronic, optoelectronics, and biomedical fields.

The development of precise additive manufacturing processes has also led to enormous progress in micro- and nanotechnology, entering in every field of research, but having a stronger impact on engineering and materials science (Fig. 1.1b).

After the first patent in 1984 [3], additive manufacturing has seen a huge differentiation in the several techniques that allow it, from the irradiation of resins in vat photopolymerization to the fusion of powders via laser sintering or other

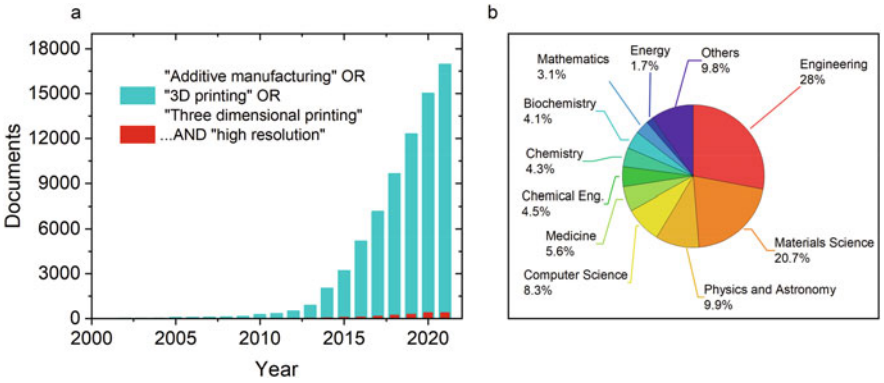

Fig. 1.1 (**a**) Number of publications per year between 2000 and 2021 containing the terms ("Additive manufacturing" or "3D printing" or "Three dimensional printing") (light blue) and ("Additive manufacturing" or "3D printing" or "Three dimensional printing" and "high resolution") (red). (**b**) Distribution of publications between 1970 and 2021 from the query ("Additive manufacturing" or "3D printing" or "Three dimensional printing") in the different application fields. (Source: SCOPUS)

methods in powder bed fusion, from the 3D evolution of printing in inkjet and aerosol jet printing to the fastness of volumetric 3D printing, arriving to one of the most recent and most precise techniques, the two-photon polymerization, which allows the creation of objects with dimensions of a few micrometers [4].

Due to this differentiation and the versatility of this technology, it was able to imbue every critical aspect of the current research state of the art: many biomedical devices have implemented some parts made with additive manufacturing, and in electronics and photonic applications, many problems have been solved with 3D printing [5–7]. Another extremely growing field like energy storage, which in the recent years has become of primary importance due to the need of solutions for the urgent ecological problems, has increasingly benefited from the improvements possible thanks to 3D printed objects [8].

AM and 3D printing are characterized by a bottom-up approach. From this it derives that AM gains strategic advantages with respect to subtractive manufacturing: it enables the production of complex products and small series requiring low energy consumption during production, reduction of waste material, reduced time to market, high versatility for innovation and great potential for customization, and a final product with less weight [9]. The bottom-up approach not only guides the technology itself, but also the design, which is based on the definition of the nominal values in 3D virtual models that are usually translated in a code that works in a Cartesian coordinate system: the two planar 2D dimensions (X and Y) and the Z dimension that makes printing definitively 3D. The generation of three-dimensional models employ different tools [10] involving objects sliced in layers with a specific thickness depending on the selected technology. Since the planar and Z dimensions are generally controlled via very different mechanisms, their resolutions are going to be different and need to be treated separately. For high-resolution 3D printing, it is extremely important to understand which is the nominal limit of the layer thickness which drives the final accuracy of the printed models and then the Z-resolution. Two-photon polymerization (2PP), which allows for feature sizes down to hundreds of nanometers, represents the best technology in terms of resolution in the field, but the high equipment cost and printing time limit its employment for upscaled production. For this reason, this technique is mainly used for research purposes. On the other end, stereolithography (SL) employs a plethora of photocurable resins and finds a huge number of applications. However, these low-cost processes are intrinsically limited by their technology to millimeter and submillimeter resolutions. In this chapter, a better understanding of the new design paradigms is introduced with the aim to explain new terms and concepts as, for example, printability. The latter cannot have a counterpart in a top-down approach, which is typical of the large-scale industry production and that is one of the reasons that decreed the huge success of the clean-room fabrication techniques.

1.2 Short History and State of the Art

The fundamental innovations necessary for the development of additive manufacturing date back to the first half of the twentieth century, with the synthesis of most polymeric materials taking place between the 1920s and 1940s [4]. However, it was only in the last two decades of the century that 3D printing technology emerged. Indeed, the birth of 3D printing is commonly associated with the development of the first stereolithography apparatus (SLA) by C. Hull in 1984 [3]. In the same decade, selective laser sintering (SLS) [11] and fused deposition modelling (FDM) [12] were patented, followed in the 1990s by binder jetting [13], two-photon polymerization [14], and the PolyJet printing process commercialized by Objet. In the early 2000s, the expiration of the earlier patents allowed the widespread diffusion of the technology that became affordable for the general public as well as for an increasing number of researchers. The "beginning of low-cost 3D printing," reported in Fig. 1.2, is indeed reflected by the start of exponential growth in the number of publications per year reported in Fig. 1.1a. Moreover, in the last decade the field of applications of additive manufacturing expanded from research and rapid prototyping to the production of end-use products: in 2010 the first 3D printer (a MakerBot) appeared at the Consumer Electronic Show [15], while in the same year Apple Europe started selling 3D printed iPhone cases [16]. The decreasing cost of 3D printers has been recently accompanied by the appearance of open-source computer-aided design (CAD) software, which have made 3D printing even more affordable.

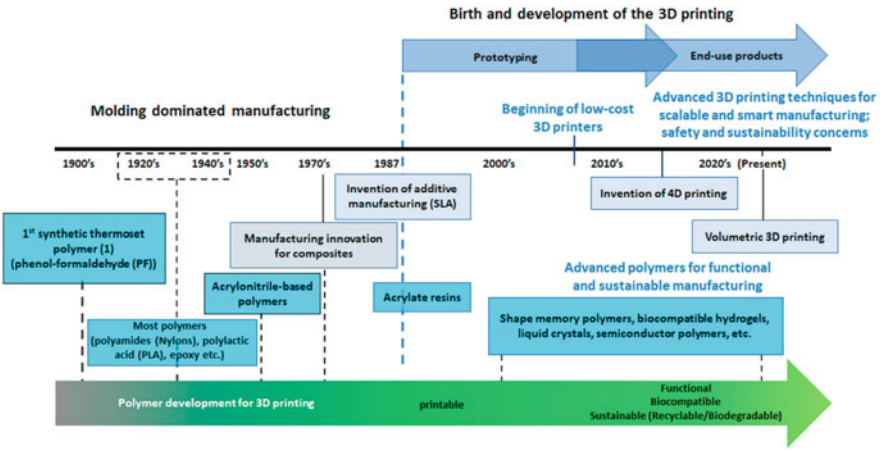

Fig. 1.2 History of 3D printing and polymer development: transition from rapid prototyping to scalable and customizable production. Polymers have evolved from merely meeting the requirements for being printable to being more functional, meeting the requirements for end-use products. (Reprinted with permissions from Ref. [4])

The increasing number of AM applications has been supported by huge improvements concerning both printing resolution, with 2PP able to reach resolutions down to less than 100 nanometers [17], and printing speed, with the Continuous Liquid Interface Production (CLIP) [18] technique reaching growth rates as high as 300 mm h^{-1}.

From the research standpoint, one area in which AM has seen the most promising development is the biomedical field. In the last 25 years, in fact the progresses in this field have been enormous, starting from the 3D printing of the first scaffolds for tissue regeneration in the 1990s to the bioprinting of complex integrated tissues and organs with a single machine in 2016 [6, 19]. Thanks to the advancements in 3D printing of conductive polymers, huge improvements have recently been achieved also concerning the fabrication of bioelectronic devices [5, 20]. Indeed, the development of novel high-performing polymers for 3D printing is a growing research topic, which is not limited to the AM of conductive materials. The printing of shape memory polymers (SMPs) [21], liquid crystal polymers (LCPs) [22] and elastomers (LCEs) [23], and smart hydrogels [24] is nowadays referred to as 4D printing [7, 25, 26].

1.3 The Design for High-Resolution Manufacturing

An industry's large-scale production, as the one used in microelectronics, is based on a top-down approach. It is useful to understand the basic principles of specific high-resolution manufacturing as those related to clean-room technologies, in parallel to the requirements of bottom-up approaches typical of additive manufacturing and 3D printing. In general, the design in AM is based on a 3D virtual model, while the top-down approach is based on a planar design which is replicated several times on a large area. In this scenario, it is of great interest to have a parallel view of these two approaches. For the design of the devices for very large-scale integration, the most important concepts are physical design, process flow, processes and material compatibility, and finally yield. In 3D printing, on the other hand, the main aspects to focus on are printability, 3D models, and the post-processing for 3D printed objects.

1.3.1 Top-Down Approach

1.3.1.1 Physical Design

From the beginning of lithography to its more recent development, there has always been some specific constrain about the design in clean-room processes [27–29]. The process design requires always considering every step and consequently every instrument involved, which may need different software for the device design. At every step some contamination can come into play, and every change between

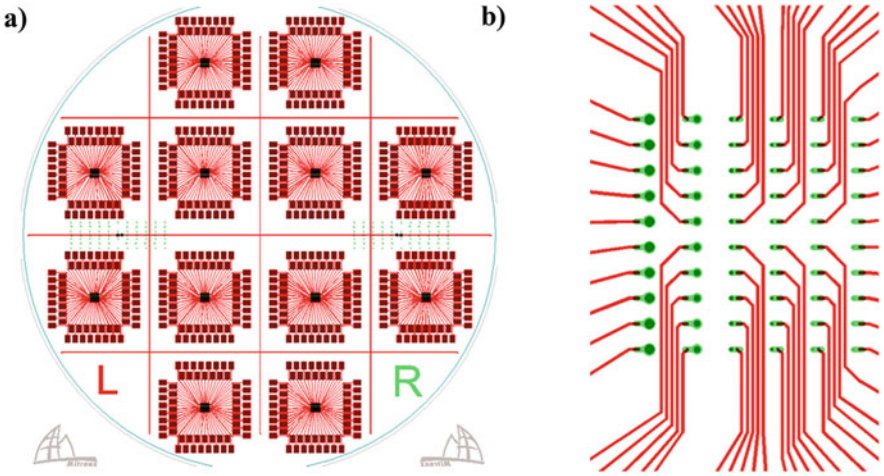

Fig. 1.3 Example of a MEMS design using a layout editor software: (**a**) whole mask layout; (**b**) alignments that are required between two layers containing electrodes (red) and probes (green). (Reprinted with permission from Ref. [32])

instruments increases the likelihood of an error, both human and instrumental. The design needs to have a way to be connected and to retrieve the correct positions and be aligned. A lot of passages of course require different instruments which have a huge economic impact and an important time investment, with a constant interaction with the human operator. For all these reasons, the design should follow highly restrictive rules that usually go under the generic name of "technologies" that are available in a specific fab. In fact every fab can sell fabrication steps correlated to a specific set of available processes that have been already assessed and whose yields are well-known.

The so-called physical design [30] is the step in which the device is translated from the high level to the actual geometries by means of a layout editor software. These are 2D CAD packages that properly work with a hierarchical approach of the layout and with a simple visualization of a filled and transparent area on the virtual draw [31]. Rules in the layout are driven by the technology as, for example, by the alignment between two different photolithographic steps (Fig. 1.3a, b). Finally, design rules should be all verified and checked to be approved for the fabrication step. In the modern layout editor software, this check is automatically executed by algorithms that are linked to the technology library.

1.3.1.2 Process Flow and Material Compatibility

Microelectronics, MEMS, and microsystems are manufactured through the deposition and patterning of multiple layers of semiconductor materials, metals, and dielectrics [33] (Fig. 1.4). The whole process needs to be carefully designed and

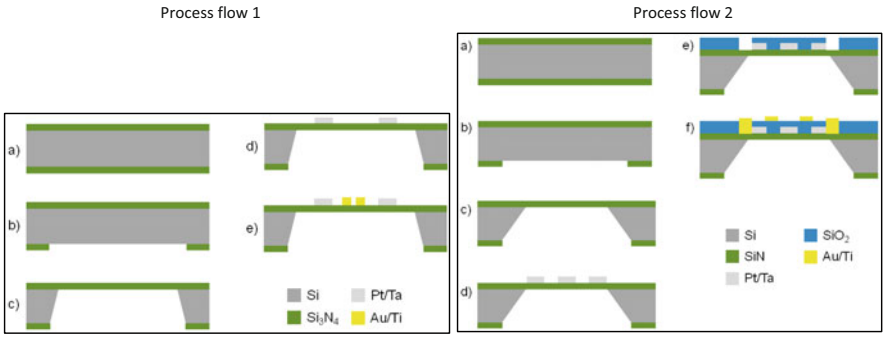

Fig. 1.4 Comparison between two MEMS process flows with increasing complexity (process flow 2 is more complex than process flow 1) to obtain an equivalent MEMS device (a micro-hotplate). (Modified image under Creative Commons Attribution License from Ref. [33])

simulated from the beginning: the masks need to be prepared in advance, and every step requires multiple passages to be performed. The process yield and throughput of the final product can be obtained only at the end of an assessment, after every step has been performed, and the optimization can require the correction of each single step to achieve the wanted result [34, 35].

Each step is fundamental for the whole process flow and they can influence one another, so for the optimization of every single step, a clear overview of the whole procedure is required [36]. A problem in the final device could arise from any step, and sometimes it can be difficult to pinpoint the problem. Most of the time, different tests are required to correctly asses the error and identify the steps that need an optimization to obtain the best result possible.

Compatibility between materials and processes is a key factor in the process flow design. Usually several instruments are required for all the different steps of the process, and every instrument has a specific environment with precise working characteristics like temperature, humidity, vibration, or light. A material suitable for one step of the process may be sensible to one of those characteristics, so every following step needs to remain in the required range of those parameters. For example, two similar SU-8 resists can react differently to pyrolysis and adhere to or detach from a chosen substrate [37, 38]. In addition, the compatibility between materials needs to be correctly addressed since they can affect one another by deteriorating or changing the properties of materials deposited in previous steps. For example, resist solvents may be incompatible with other organic features of the device.

At the same time, even the single process may be detrimental to other materials or limit some following steps. For instance, wet and dry etching need to be carefully designed to affect only the required part of the device, like in graphene processing [39, 40] and MEMS fabrication [41]. Moreover, wet etching, such as bulk micromachining in KOH, and dry etching, such as reactive-ion etching (RIE), can introduce unwanted contaminations in the semiconductors and insulators [42,

43]. Thermal processes, also, can heavily affect the contaminations due to metal diffusion inside the semiconductive, piezoelectric, or insulating layers as well as interdiffusion between metal multilayers [44]. A simple solution can be adopted as, for example, revising the order of the process steps to improve the compatibility.

1.3.2 Bottom-Up Approach

1.3.2.1 3D Models

3D printing is based on the definition of a 3D model which is designed and converted in a standard AM format file. Then, the file is sliced to obtain layers that define sections of the 3D model in the Z-axis stack. The machine used for 3D printing will then receive a code which contains the command lines for the movement and actual printing process [45, 46]. The 3D models can be generated by all major CAD software and a general format that is used for slicing is stereolithography format (.STL). Due to the AM approach, a slicing operation is always needed. Worldwide, the most common solution to perform this operation is by an open-source software called Slic3r. After slicing, a G-code file is commonly generated and then used by the printer to reproduce the objects. After the printing process, other operations can be needed as explained after in this paragraph and depicted in Fig. 1.5.

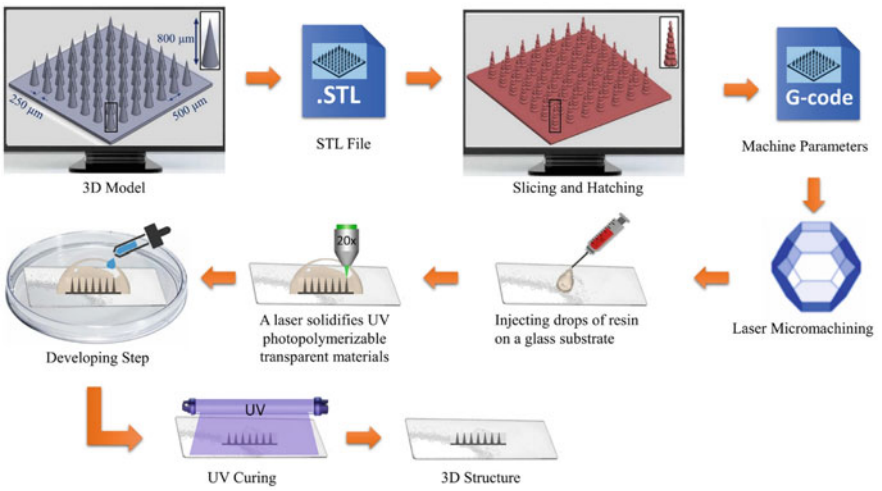

Fig. 1.5 A whole printing process starting from the 3D model. All the printers need to pass from the 3D model to the STL and then to slicing operations and machine-level code as output. Special operations may be required by specific technology as 2PP. (Reprinted with permission from Ref. [47])

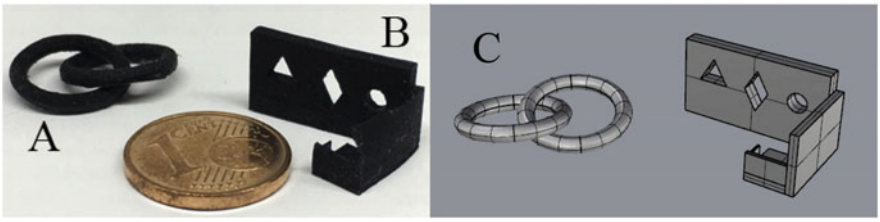

Fig. 1.6 The capability to print a complex object in all its features maintaining the nominal geometries is referred to as printability. (Reprinted with permission from Ref.[49])

1.3.2.2 Printability

Many parameters can affect the capability to print an object as, for example, the materials and the printer parameters. All depend, of course, on the employed technology. In any case, the capability to maintain the nominal geometries described by the 3D model can be used to define the printability of a 3D object. A quantification is obtained by evaluating the agreement of the measured values with respect to the nominal one. From this investigation also the actual best resolution can be obtained. Experiment on printability can be designed by investigating the effects of additives in the materials. For example, in SL, a coloring pigment can affect the dimensional and mechanical characteristics of the same SL resin [48]. In the case of a composite, the printability optimization can be conducted by studying different concentration ratio between the active materials and the photocurable resin [49] (Fig. 1.6).

Other works focus on the fine-tuning of the printed objects by a trial and error approach to finally optimize the printing parameters or, as workaround, go back to the 3D model to operate geometrical compensation to obtain the desired final dimensions and resolutions [50, 51]. Finally, critical elements that should be auto-sustained by the structural material during the printing process should be considered to properly reproduce it without any issue. When necessary, supports made by the same material or by a sacrificial material can be used to obtain a high aspect ratio and undercut structures. A similar concept is the minimum wall thickness that should be adjusted to avoid a collapse of the printed structures [52].

1.3.2.3 Multimaterial Processes

More advanced printers are able to produce parts with materials with different properties as, for example, having different colors or mechanical behavior [53]. This latter can be obtained by varying percentage composition in different parts of a model or by creating a variable porosity by alternating structural materials and void space. A common use of multilateral printing is the alternation between structural material, which constitutes the object, and support material, which will be removed

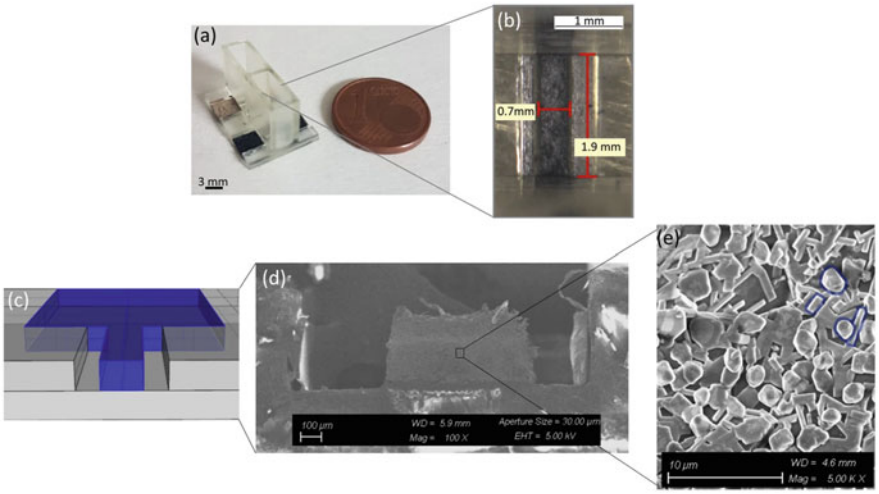

Fig. 1.7 Multimaterial printing allows to attribute to a printed part a specific function and property like conducting or semiconductive behavior with respect to insulating layers. The figure shows how different parts can be printed by changing the composition of the photocurable resin: (**a**) a multimaterials printed device; (**b**) the active part of the device in contact with the electrolyte; (**c**) multimaterials CAD layout; (**d**) SEM image of the semiconductive material; (**e**) material morphology at high magnification. (Reprinted under Creative Commons CC BY from Ref. [20])

at the end of the printing. These multilateral approach for high resolution printing is mainly applied by PolyJet printing technology. In fact this technique is able to reproduce complex multimaterial objects by using specific printing heads for each material [54]. Common rules of printability also apply to multi-materials printing, which are the testing of minimum feature size, support material removal, small feature reproducibility, and the self-supporting angle without any support material.

In the context of multimaterial printing, one of the most challenging improvement is the use of different functional materials, which can act, for example, as a conductive and insulating layer. To this end, a proficient approach is the use of the same base material to be loaded with a filler able to provide the active function only to a part of the object (Fig. 1.7).

1.3.2.4 Post-processing

Most of the additive manufacturing processes require some post-processing steps in order to obtain the best result for the final product. The most common post-processing procedure concerns the techniques that use light for the manufacturing process: in those cases, most of the time it is a necessary step where the final product is exposed for a long time to be sure that all the reactive agents became stable. Such a process is commonly referred to as final curing (Fig. 1.5).

Many times, also a mechanical post-processing procedure is used. For high aspect ratio structures and for undercut structures, some supports are needed for the correct fabrication of the required 3D object. Those supports need then to be removed, and the interfaces with the support material need to be smoothed and cleaned.

Another important step is the cleaning: most of the time devices need to be washed to remove unwanted parts, as unreacted species inside the bulk, and to smooth the surfaces. In some cases, it is even necessary to remove parts of the printed layer, for example, when a first starting layer, different from the following ones, is required for the additive manufacturing technology used.

1.4 Conclusion

The recent advancements in 3D printing and AM technique are changing the paradigm of the object's design. A parallel outline between a top-down and a bottom-up approach has been depicted in this chapter to highlight the distances between the two methodologies. An intuitive freedom in design is correlated to the AM approach with respect to the rigid and 2D way proposed by a standard clean-room process flow. Nevertheless, limitations and challenges arise, since the fabrication of a whole active device by 3D printing cannot be compared with a similar one obtained on the silicon substrate. Moreover, if on one side the fabrication step of AM remains as simple as starting a printing process, all the 3D object complexity is correlated to the materials and their handling by the employed printing technology. This demonstrates that we are still in the infancy age of AM when applied to complex systems as the microelectronics and microsystems are.

References

1. F42 Committee, *ISO/ASTM52900:2021 Additive Manufacturng – General Principles – Terminology*. Internet. https://www.iso.org/obp/ui/#iso:std:iso-astm:52900:ed-2:v1:en (2015)
2. A.E. Alexander et al., A guideline for 3D printing terminology in biomedical research utilizing ISO/ASTM standards. 3D Print. Med. **7**, 4–9 (2021)
3. C. W. Hull, Apparatus for production of three-dimensional objects by stereolithography. Patent 16 (1984)
4. S. Park, W. Shou, L. Makatura, W. Matusik, K. Fu (Kelvin), 3D printing of polymer composites: Materials, processes, and applications. Matter **5**, 43–76 (2022)
5. M. Criado-Gonzalez, A. Dominguez-Alfaro, N. Lopez-Larrea, N. Alegret, D. Mecerreyes, Additive manufacturing of conducting polymers: Recent advances, challenges, and opportunities. ACS Appl. Polym. Mater. **3**, 2865–2883 (2021)
6. W. Jamróz, J. Szafraniec, M. Kurek, R. Jachowicz, 3D printing in pharmaceutical and medical applications. Pharm. Res. **35**, Article 176 (2018)
7. Z.X. Khoo et al., 3D printing of smart materials: A review on recent progresses in 4D printing. Virtual Phys. Prototyp. **10**, 103–122 (2015)

8. F. Zhang et al., 3D printing technologies for electrochemical energy storage. Nano Energy **40**, 418–431 (2017)
9. L.A. Verhoef, B.W. Budde, C. Chockalingam, B. García Nodar, A.J.M. van Wijk, The effect of additive manufacturing on global energy demand: An assessment using a bottom-up approach. Energy Policy **112**, 349–360 (2018)
10. D.M. Nieto, D.M. Sánchez, Design for additive manufacturing: Tool review and a case study. Appl. Sci. **11**, 1–13 (2021)
11. C. Deckard, Us4863538a (1986)
12. S. S. Crump, Apparatus and method for creating a three-dimensional object (1989)
13. E. M. Sachs, J. S. Haggerty, M. J. Cima, P. A. Williams. Three-dimensional printing techniques – United States Patent US5204055 (1993)
14. S. Maruo, S. Kawata, Two-photon-absorbed photopolymerization for three-dimensional microfabrication, in *Proceedings IEEE the Tenth Annual International Workshop on Micro Electro Mechanical Systems. An Investigation of Micro Structures, Sensors, Actuators, Machines and Robots*, (IEEE, 1997), pp. 169–174. https://doi.org/10.1109/MEMSYS.1997.581794
15. https://www.makerbot.com/stories/news/makerbot-reaches-milestone-100000-3d-printers-sold-worldwide/.
16. https://www.3dsystems.com/blog/foc/apple-acquires-exclusivity-for-freshfiber-iphone-cases.
17. A. You, M.A.Y. Be, I. In, Development of functional sub-100 nm structures with 3D two-photon polymerization technique and optical methods for characterization. J. Laser Appl. **24**, 042004 (2015)
18. J.R. Tumbleston et al., Continuous liquid interface production of 3D objects. Science (80-.) **347**, 1349–1352 (2015)
19. H.W. Kang et al., A 3D bioprinting system to produce human-scale tissue constructs with structural integrity. Nat. Biotechnol. **34**, 312–319 (2016)
20. V. Bertana et al., Rapid prototyping of 3D organic electrochemical transistors by composite photocurable resin. Sci. Rep. **10**, 1–11 (2020)
21. H. Wei et al., Direct-write fabrication of 4D active shape-changing structures based on a shape memory polymer and its nanocomposite. ACS Appl. Mater. Interfaces **9**, 876–883 (2017)
22. S. Gantenbein et al., Three-dimensional printing of hierarchical liquid-crystal-polymer structures. Nature **561**, 226–230 (2018)
23. C. Yuan et al., 3D printed reversible shape changing soft actuators assisted by liquid crystal elastomers. Soft Matter **13**, 5558–5568 (2017)
24. J.J. Schwartz, A.J. Boydston, Multimaterial actinic spatial control 3D and 4D printing. Nat. Commun. **10**, 791 (2019)
25. A. Sydney Gladman, E.A. Matsumoto, R.G. Nuzzo, L. Mahadevan, J.A. Lewis, Biomimetic 4D printing. Nat. Mater. **15**, 413–418 (2016)
26. S. Tibbits, 4D printing: Multi-material shape change. Archit. Des. **84**, 116–121 (2014)
27. R. Doering, Y. Nishi, *Handbook of Semiconductor Manufacturing Technology – 2nd Edition. Microelectronics Journal*, vol 32 (CRC Press Taylor/Francis Grouo, 2001)
28. S.A. Rizvi, *Handbook of Photomask Manufacturing Technology* (Taylor & Francis, New York, 2005). https://doi.org/10.1201/9781420028782
29. V. Pavlidis, S. Ioannis, E. Friedman, *Three-Dimensional Integrated Circuit Design – 2nd Edition* (Morgan Kaufmann, 2017)
30. N.A. Sherwani, Via minimization and over-the-cell routing, in *Algorithms for VLSI Physical Design Automation*, (Springer US, 1993), pp. 323–353. https://doi.org/10.1007/978-1-4757-2219-2_8
31. A. Holovatyy, V. Teslyuk, M. Lobur, M. Szermer, C. Maj, Mask layout design of single- and double-arm electrothermal microactuators, in *2016 XII International Conference on Perspective Technologies and Methods in MEMS Design (MEMSTECH)*, (IEEE, 2016), pp. 28–30. https://doi.org/10.1109/MEMSTECH.2016.7507513
32. M. Afshar et al., On-chip nanostructuring and impedance trimming of transparent and flexible ITO electrodes by laser induced coherent sub-20 nm cuts. Appl. Surf. Sci. **360**, 494–501 (2016)

33. A. Tommasi et al., Modeling, fabrication and testing of a customizable micromachined hotplate for sensor applications. Sensors **17**, 62 (2016)
34. N. Wilke, A. Mulcahy, S.-R. Ye, A. Morrissey, Process optimization and characterization of silicon microneedles fabricated by wet etch technology. Microelectron. J. **36**, 650–656 (2005)
35. P.A. Alvi, International Frequency Sensor Association, *MEMS Pressure Sensors: Fabrication and Process Optimization* (International Frequency Sensor Association Publishing, 2012)
36. D.S. Macintyre et al., Nanoimprint lithography process optimization for the fabrication of high electron mobility transistors. J. Vac. Sci. Technol. B Microelectron. Nanom. Struct. **21**, 2783 (2003)
37. O. Pilloni, M. Madou, D. Mendoza, S. Muhl, L. Oropeza-Ramos, Methodology and fabrication of adherent and crack-free SU-8 photoresist-derived carbon MEMS on fused silica transparent substrates. J. Micromech. Microeng. **29**, 027002 (2019)
38. R. Natu, M. Islam, J. Gilmore, R. Martinez-Duarte, Shrinkage of SU-8 microstructures during carbonization. J. Anal. Appl. Pyrolysis **131**, 17–27 (2018)
39. M.C. Prado, D. Jariwala, T.J. Marks, M.C. Hersam, Optimization of graphene dry etching conditions via combined microscopic and spectroscopic analysis. Appl. Phys. Lett. **102**, 193111 (2013)
40. A. Ballesio et al., A novel hot embossing graphene transfer process for flexible electronics. Microelectron. Eng. **209**, 16–19 (2018)
41. A.L. Rickard, M.E. McNie, in *Characterization and Optimization of Deep Dry Etching for MEMS Applications*, ed. by U. F. W. Behringer, D. G. Uttamchandani, (2001), pp. 78–88. https://doi.org/10.1117/12.425287
42. N.N. Alias, K.A. Yaacob, S.N. Yusoh, A.M. Abdullah, Comparison of KOH and TMAH etching on Sinw arrays fabricated via AFM lithography. J. Phys. Conf. Ser. **1082**, 012051 (2018)
43. S.J. Fonash, ChemInform abstract: An overview of dry etching damage and contamination effects. ChemInform **22**(21), 310 (2010)
44. A. Tommasi et al., Process optimisation of a MEMS based PZT actuated microswitch. Microelectron. Eng. **119**, 137–140 (2014)
45. J. Micallef, *Beginning Design for 3D Printing* (Apress, Berkeley, 2015). https://doi.org/10.1007/978-1-4842-0946-2
46. N. van de Werken et al., Design considerations and modeling of fiber reinforced 3D printed parts. Compos. Part B Eng. **160**, 684–692 (2019)
47. S. Mckee et al., Microfabrication of polymer microneedle arrays using two-photon polymerization. J. Photochem. Photobiol. B Biol. **229**, 112424 (2022)
48. V. Bertana et al., 3D printing with the commercial UV-curable standard blend resin: Optimized process parameters towards the fabrication of tiny functional parts. Polymers (Basel). **11**, 292 (2019)
49. G. Scordo et al., A novel highly electrically conductive composite resin for stereolithography. Mater. Today Commun. **19**, 12–17 (2019)
50. F. Barbaresco, M. Cocuzza, C.F. Pirri, S.L. Marasso, Application of a micro free-flow electrophoresis 3D printed lab-on-a-chip for micro-nanoparticles analysis. Nano **10**, 1277 (2020)
51. F. Perrucci et al., Optimization of a suspended two photon polymerized microfluidic filtration system. Microelectron. Eng. **195**, 95–100 (2018)
52. A. Massaccesi et al., Broadband dielectric transmitarray with scanning capabilities, in *13th European Conference on Antennas and Propagation, EuCAP 2019*, (2019), pp. 11–12
53. M.K. Thompson et al., Design for additive manufacturing: Trends, opportunities, considerations, and constraints. CIRP Ann. – Manuf. Technol. **65**, 737–760 (2016)
54. N. Meisel, C. Williams, An investigation of key design for additive manufacturing constraints in multimaterial three-dimensional printing. J. Mech. Des. **137**, 111406 (2015)

Chapter 2
Vat Photopolymerization

Roberta Bongiovanni and Alessandra Vitale

Abstract Vat photopolymerization is an additive manufacturing process to build solid parts by leveraging photoinduced polymerization of liquid resins (i.e., a polymerization reaction triggered by irradiation). The chemical transformation of the monomers, oligomers, and/or prepolymers forming the resin (usually called vat) into polymers is in fact accompanied by a phase change from the liquid to the solid state. Vat photopolymerization includes a wide variety of processes and technologies, such as stereolithography (SLA), digital light processing (DLP), continuous liquid interface production (CLIP), and two-photon lithography (2PP). In all these techniques, the solid part is built layer by layer: the liquid resin fills a tank and its surface is selectively irradiated and cured; then the building platform is raised or lowered of a small increment to allow new liquid to flow forming another layer, which is cured by light and adjoins the previous one. Once the last layer is cured, the printed part is removed from the resin tank. As the polymer chemistry employed in vat photopolymerization is highly versatile, many innovations have been developed, and nowadays, complex multifunctional products with tailored performance can be printed, reaching high resolution and very low feature size, allowing their application in different fields. This chapter reviews vat photopolymerization technology and describes its chemistry, the different techniques (excluding 2PP, which is the focus of Chap. 3), and the materials employed.

Keywords Vat photopolymerization · Photocurable resins · UV curing · Stereolithography · SLA · Digital light processing · DLP · Continuous liquid interface production · CLIP · 3D printing

R. Bongiovanni (✉) · A. Vitale (✉)
Department of Applied Science and Technology, Politecnico di Torino, Torino, Italy

INSTM – Politecnico di Torino Research Unit, Florence, Italy
e-mail: roberta.bongiovanni@polito.it; alessandra.vitale@polito.it

S. L. Marasso, M. Cocuzza (eds.), *High Resolution Manufacturing from 2D to 3D/4D Printing*, https://doi.org/10.1007/978-3-031-13779-2_2

2.1 Introduction

The ISO/ASTM 52900-21 [1] norm standardized the exploding terminology around additive manufacturing. By classifying each of its methods, seven process categories were established, as listed in Fig. 2.1. Each technology differs from another in the manner of the application process, the curing principle, and the initial state of the materials.

Vat photopolymerization allows the building of parts using liquid formulations (usually called vat or resin), which solidify upon irradiation. The radiation triggers a chemical reaction known as photoinduced polymerization (which is described below in details): the transformation of the monomers, oligomers, and/or prepolymers into polymers is accompanied by a phase change of the vat from the liquid state to the solid state, usually showing an amorphous morphology.

In the vat photopolymerization apparatus, the liquid resin fills a tank in which a build platform is submerged. The light is selectively directed across the resin surface with mirrors. Once a layer is cured, the platform is raised or lowered of a small increment to allow new liquid to flow. The next layer is then cured and adjoins the previous one. Once the last layer is cured, the printed part is removed from the resin: although it is fully formed, it can undergo a posttreatment usually consisting of a further curing step either by irradiation or by thermal treatment.

The beginning of vat photopolymerization dates to the 1980s: at that time, H. Kodama of the Nagoya Municipal Industrial Research Institute in Japan described methods for building solids by exposing resins to light either with masks or with optical fibers moved along an x-y plotter [2]. One year later, A. J. Herbert added a lab jack to control the z-direction, discovering that solid polymer patterns could be produced, and thus, he could fabricate a solid 3D part curing one layer over a previous layer [3]. In 1984, two independent patents were filed describing layer-by-layer lithographic fabrication of solids: the French one by J. C. André et al. [4]

Fig. 2.1 Additive manufacturing technology classification according to the ISO/ASTM 52900-21 standard

was abandoned, while C. W. Hull's one [5] laid the groundwork for commercial additive manufacturing by vat photopolymerization. Starting from experimenting with UV-curable resins and exposing them to a scanning laser, like the system adopted in laser printers, he could soon establish a very successful company, 3D Systems Corporation, marketing machines as "rapid prototyping" machines. From his early experiments, he coined the term "stereolithography" (SLA) alluding to the use of a 2D process (i.e., lithography) extending it to the third dimension.

Since then, a wide variety of processes and technologies has been developed where the key chemical process is the photopolymerization, which cures a liquid by irradiation transforming it into a solid. Besides SLA, the most successful vat photopolymerization techniques are digital light processing (DLP), continuous liquid interface production (CLIP), and two-photon lithography (2PP). As the polymer chemistry employed is highly versatile, many innovations have been appearing and vat photopolymerization techniques have attracted special attention from polymer chemists, material scientists, and engineers. From the early works of H. Kodama and C. W. Hull, the progress has been enormous. Nowadays, complex multifunctional products with tailored performance can be printed, reaching high resolution and very low feature size. To this end, vat photopolymerization has entered many fields such as microfluidics, biomedical devices, soft robotics, surgery, tissue engineering, and drug delivery.

This chapter focusses on vat photopolymerization (excluding the two-photon approaches, found in Chap. 3); it first describes its chemistry, then discusses the different techniques, and finally presents a survey on materials for vat photopolymerization.

2.2 Vat Photopolymerization Chemistry

The solidification of the vat used in stereolithography and analogous techniques is due to a polymerization reaction involving light. Independently of the field of application, photopolymerization is advantageous when compared to thermal polymerization, as the solidification formation is fast (in the worst scenario no more than a few minutes, compared to hours requested by thermal processes), and the process is in bulk and therefore is solvent-free and is carried out at room temperature. Moreover, photopolymerization offers features that are crucial for 3D printing, namely, spatial and temporal control: in fact, the reaction occurs nearly exclusively in the illuminated areas and can stop when the light is switched off.

The main component of a vat is the liquid monomer M, which is transformed into a polymer M_n when irradiated by a light of frequency ν. Most photoinduced polymerizations are polyadditions described by Eq. 2.1:

$$n\ M \xrightarrow{h\nu} M_n \tag{2.1}$$

Since most monomers are not photosensitive and/or are unable to produce initiating species with sufficiently high yields under light, a photoinitiator (*PI*) is usually added: it is a chemical compound able to convert photolytic energy and produce the reactive species. The mechanism of the photoinduced polyaddition of Eq. 2.1 is thus composed by different reactions (Eqs. 2.2 and 2.3):

$$\text{Initiation}: PI \overset{h\nu}{\rightarrow} R^* \overset{M}{\rightarrow} RM^* \tag{2.2}$$

$$\text{Propagation}: RM^* \overset{M}{\rightarrow} RMM^* \overset{M}{\rightarrow} RMMM^* \overset{M}{\rightarrow} \overset{M}{\rightarrow} RM_n^* \tag{2.3}$$

In the initiation step (Eq. 2.2), the photoinitiator, which is a photolabile chemical, generates reactive species R^* upon irradiation. R^* is either a radical or an ion, and the symbol * indicates an unpaired electron or a positive/negative charge. The reactive pathways to produce R^* are many; for instance, homolytic photoscission, hydrogen abstraction, and heterolytic cleavage give rise to radicals which trigger radical propagation [6]; redox reactions generate strong acids and promote cationic polyaddition [7].

Radical photoinitiators are usually classified as either Norrish type I or type II. In type I radical photoinitiation, a single molecule, such as a benzyl ketal, cleaves into radical fragments when absorbing light (around 350–360 nm, corresponding to low-energy $n \rightarrow \pi^*$ electronic transitions), as in Scheme 2.1.

Type II radical photoinitiators are two-component systems, made of a light-absorbing molecule (or sensitizer) that typically forms excited triplet states under light and a co-initiator (or synergist); the latter, upon irradiation, donates a hydrogen atom to the excited sensitizer. Alternatively, electron-transfer reactions between the components take place. Most commonly used uncleavable photoinitiators are camphorquinones, benzophenones, and thioxanthones, which are able to undergo hydrogen abstraction in the presence of co-initiators (such as tertiary amines), as in Scheme 2.2.

Thermally stable onium salts (e.g., aryl or diaryl iodonium, triaryl sulfonium salts, having as a counterion nonnucleophilic species such as BF_4^-, PF_6^-, AsF_6^-, SbF_6^-) are common cationic photoinitiators [8]: upon exposure to UV light, they form a mixture of cations, radical cations, and radical intermediates which further react with the monomer or the solvent to give a super acid $HMtX_n$, as in Scheme 2.3.

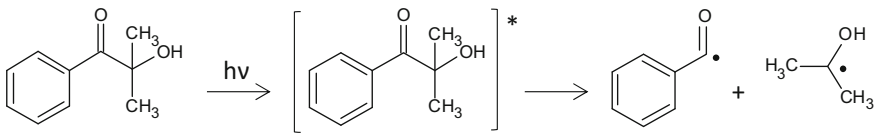

Scheme 2.1 Scheme of the mechanism of formation of radical species of a Norrish type I photoinitiator upon irradiation

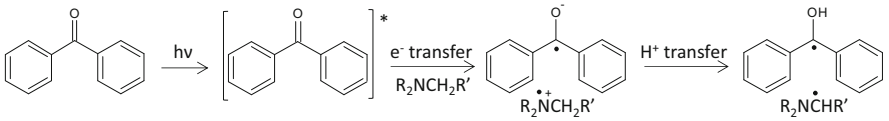

Scheme 2.2 Scheme of the mechanism of formation of radical species of a Norrish type II photoinitiator upon irradiation

$$Ar_2\ I^+\ Mt\ X_n^- \xrightarrow{h\nu} [Ar_2\ I^+\ Mt\ X_n^-]^* \longrightarrow \left\{ \begin{matrix} Ar_2\ I^{\cdot +}\ Mt\ X_n^- + Ar^{\cdot} \\ Ar\ I + Ar^+\ Mt\ X_n^- \end{matrix} \right\} \xrightarrow{\text{monomer}} H\ Mt\ X_n$$

Scheme 2.3 Scheme of the mechanism of formation of the super acid $HMtX_n$ upon irradiation of a cationic photoinitiator

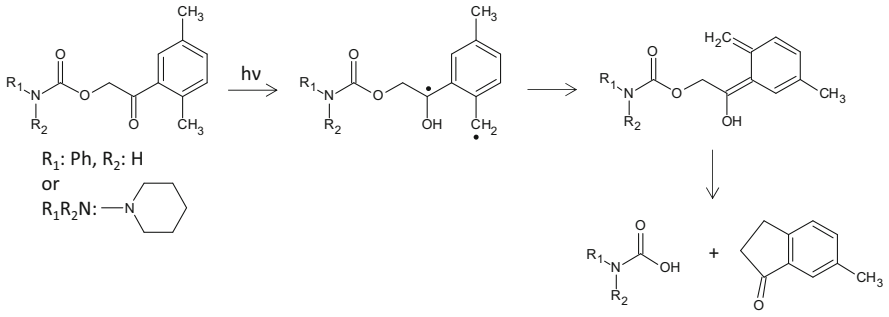

Scheme 2.4 Scheme of the mechanism of photochemically generated bases

$HMtX_n$, depending on its acidity, will protonate the monomer M to start the chain growth propagation of Eq. 2.3. Although not applied in vat polymerization techniques, for completeness of the overview on photoinitiation, we present the initiators for anionic polymerization: they are photochemically generated bases (photolatent bases) able to produce an amine upon UV irradiation, as reported in Scheme 2.4 referring to a carbamate. Besides carbamates, O-acyloximes and ammonium salts have been proposed as photochemically generated bases [9].

Any photoinitiator is developed to assure that the concentration of radicals or ions produced is high and in turn the rate of the initiation reaction is elevated. Typical structures, as those reported in Schemes 2.1, 2.2 and 2.3, have high quantum yield Φ (i.e., number of reactive species obtained per photon absorbed) and high absorption coefficient ε (i.e., absorption of light per unit length in a medium), when irradiated by light with short wavelength, below 400 nm. Thus, UV radiations are mostly used in photopolymerization, which is also often referred as UV curing. It is well known that high-energy UV light is harmful for eyes and skin and promotes the development of ozone when operating in air and eventually the degradation of reactants and products when the exposure is prolonged. Thus, the development of photopolymerization reactions activated under longer irradiation

wavelengths is a relevant research topic for obtaining mild and safe operational conditions. Visible light and near-infrared (NIR)-induced photopolymerizations are rather new strategies [10, 11]. They are safer and benign to living cells as required for biomedical applications and for 3D fabrication technologies involving biological tissues, organs, and cells for medical and biotechnology applications (bioprinting). They also assure a better light penetration, thus allowing the cure of higher layer thicknesses, which is relevant for 3D printing, as discussed later.

After radicals or ions are formed, the propagation step takes place in the form of a polyaddition (while polycondensations are rare). It is a chain reaction (Eq. 2.3) that consumes the monomer at the liquid state and produces a solid polymer very fast. With this mechanism, light affects only the initiation, while the absorption of one photon results in the consumption of many monomers (i.e., the reaction implies a chemical amplification). In this case, IUPAC recommends the term "photoinduced polymerization" as more appropriate than "photopolymerization," which applies to polymerization processes requiring a photon for the propagation step (i.e., one photon for each event leading to chain growth). However, in the different fields of applications and in 3D printing too, it is common to use both photopolymerization and photoinduced polymerization.

In the case of radical reactions, which are the most common reactions employed in vat photopolymerization, there are termination events that stop the reactive species (Eq. 2.4a and 2.4b for termination by coupling and dismutation, respectively):

$$\text{Terminations: } RM_n\bullet + RM_m\bullet \rightarrow RM_{n+m}R \tag{2.4a}$$

$$RM_n\bullet + RM_m\bullet \rightarrow RM_n + RM_m \tag{2.4b}$$

The presence of terminations means that radical polymerizations are not living (i.e., the dead chains $RM_{n+m}R$ or RM_n obtained by termination cannot reinitiate growing). Recently, controlled living radical reactions have been developed: for instance, a living system via photoredox-catalyzed reversible addition−fragmentation chain transfer (RAFT) photopolymerization has been described and also proposed for 3D printing applications [12] with interesting outcomes (see below).

According to the model for chain polymerization, where a pseudo-steady state of the radical concentration is assumed, in the presence of termination reactions, the vat polymerization reaction rate R_p is estimated as in Eq. 2.5:

$$R_P = K_P\,[M]\sqrt{\frac{R_I}{K_T}} \tag{2.5}$$

where $[M]$ is the monomer concentration; K_p and K_T are the rate constants for the propagation and the termination reaction, respectively; and R_I is the initiation rate. R_I depends on the photoinitiator concentration $[PI]$, the initiator absorption

coefficient ε, the incident light intensity I_0, and the quantum yield Φ, as described in Eq. 2.6:

$$R_I = f\ \Phi\varepsilon\,[PI]\,I_0 \tag{2.6}$$

where f is the fraction of radicals starting the propagation (usually below 1, as side reactions may occur).

The reaction rate R_p clearly depends on light intensity; when light penetrates in a sample, it is absorbed and its intensity varies along its optical path (i.e., within the sample thickness). At a certain depth h in the sample, the light intensity I is given by Eq. 2.7:

$$I(h) = \int_{\lambda_1}^{\lambda_2} I_0\, e^{-\alpha_\lambda h}\, d\lambda \tag{2.7}$$

where I_0 is the light intensity at the sample surface ($h = 0$), α_λ is the sample absorption coefficient ($\alpha_\lambda = \varepsilon\,[PI]$), and λ_1 and λ_2 are the wavelengths delimiting the photoinitiator efficiency range. The dependence of the intensity from the thickness h implies that the polymerization rate R_P is different at different h and that rate gradients are formed.

There is a maximum penetration depth $h_{\max}$ of the light corresponding to the zeroing of the light intensity. It is a function of the photoinitiator concentration and its absorption coefficient ε as in Eq. 2.8:

$$\frac{1}{h_{\max}} = 2.3\,\varepsilon\,[PI] \tag{2.8}$$

Therefore, there is a limit for the layer thickness accessible to light and thus to react. In fact, photopolymerization is effective for layers of the order of hundreds μm: this means that 3D printing based on vat polymerization has slow fabrication rates. The molar extinction coefficient of the photoinitiator ε strongly depends on the wavelength λ: as said before, using longer wavelengths than UV can allow reaching a higher penetration depth (layer thickness) and enhancing the photopolymerization rate.

From the simplified kinetic model, photopolymerization processes can be controlled by a wide range of parameters depending on the photoinitiator structure and on the radiation characteristics (e.g., type of light, irradiation intensity). In all practical photopolymerization systems, significant complications of the simple kinetic model proposed arise [13]. In fact, many of the factors influencing R_p change throughout the reaction, especially when the conversion from monomer to polymer becomes high, and the polymer formation is simultaneously associated with dramatic material property change (e.g., viscosity), and thus, mass transfer becomes difficult. Classically, autoacceleration (also referred to as the gel effect or the Trommsdorff effect) plays a significant role in bulk polymerizing systems: when mass transfer becomes more difficult, the termination reaction turns into

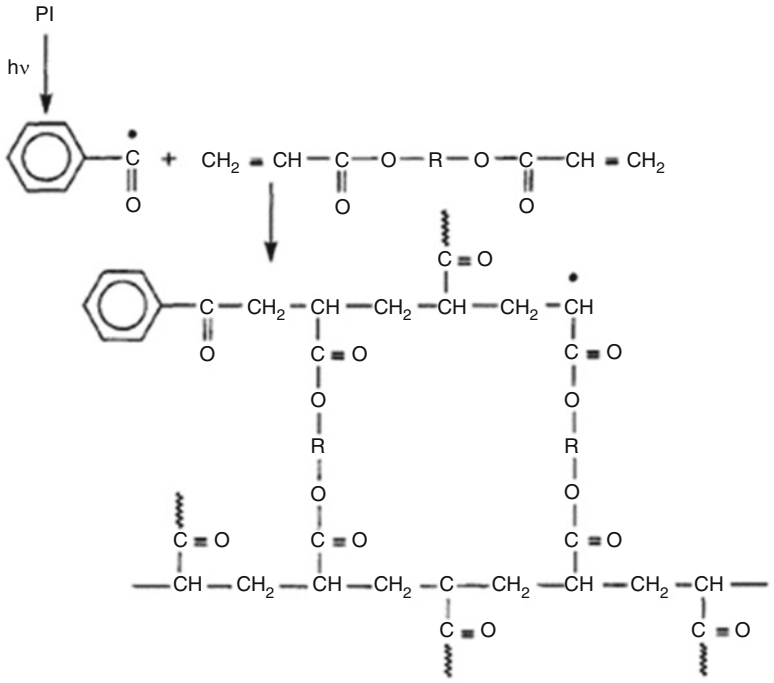

Scheme 2.5 Formation of a cross-linked polymer network by photoinduced polymerization of a diacrylate monomer

being diffusion controlled, the termination kinetic constant diminishes, and the radical concentration increases, sometimes by many orders of magnitude. Thus, the polymerization rate increases (i.e., autoacceleration regime) despite the decreasing of monomer concentration. As the reaction proceeds, diffusion limitations become more important and the propagation rate is reduced: this is known as the autodeceleration regime. Ultimately the reaction stops despite the presence of both radicals and monomers. The rate change is particularly severe when the growing polymer solidifies showing a glassy state and strict diffusional limitations arise: the phenomenon is called vitrification.

Another aspect to be considered is that in most practical applications of photopolymerization, including vat photopolymerization, multifunctional monomers are used; therefore, the reaction forms a network or cross-linked polymer. A radical process for a difunctional system (a diacrylate with two reactive functions, i.e., two double bonds) is sketched in Scheme 2.5.

Due to the architecture of the polymer, phenomena caused by diffusion are even more relevant. Moreover, radicals can be "trapped" in the polymer network and isolated from unreacted functions; thus, they remain present in the polymer for months or years. Also monomers can eventually be found unreacted for the useful lifetime of the polymer, which clearly shows a complex heterogeneity affecting the

Scheme 2.6 Oxygen inhibition on photoinitiation and polymerization reactions

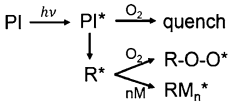

material properties. Important formation–structure–property relationships exist for these reactions: they are particularly relevant as most manipulation and alteration of the material and of the part produced is not possible after vat photopolymerization. In fact, any cross-linked polymer as in Scheme 2.5 is an irreversible network, insoluble gel, as most thermoset materials. This explains the need for a complete comprehension of the polymerization reaction, for a careful molecular design of the vat, and for the study of alternative polymerization mechanisms (e.g., reversible cross-linking).

Another feature of radical polymerization is the sensitivity to oxygen, which has an inhibition effect as in thermal processes when radical species are involved. Oxygen can consume the photoinitiator PI by reacting with initiating radicals; it can also add to the growing polymer radicals *R** competing with the propagation reaction to form peroxy radicals R-O-O*, which are stable and cannot reinitiate the polymerization, according to Scheme 2.6.

The effect of oxygen inhibition results in an induction period, a slowing down of the reaction and a poor double bond conversion, especially in vat photopolymerization that is conducted layer by layer and has a great area in contact with air. Because of the inhibition, the processed layer polymerizes only partially and remains "tacky," due to limited conversion. Therefore, the atmosphere in which the polymerization is conducted is relevant for controlling the reaction rate and conversion. The use of an inert atmosphere is difficult in industrial applications, and thus, usually a greater amount of photoinitiator is the easiest solution; other ways are based on the modification of the reactive formulations as comprehensively reviewed by Ligon et al. [14] Oxygen inhibition can also offer opportunities; for instance, a partially cured tacky layer can easily join with the resin freshly deposited on it: this is the effect enabling the CLIP technology, as will be described below.

Despite the numerous complexities, radical-mediated photopolymerizations are the most facile and capable reactions for vat photopolymerization. The most used monomers in radical photopolymerization are multifunctional acrylates and methacrylates, which are highly reactive, but also sensitive to air and can undergo gelation at low conversion, giving serious shrinkage. This is reported as a major drawback of radical processes and is due to the liquid-to-solid phase change. Especially when gelation happens at very low conversion, the problem is rather severe as the resin is no longer able to flow from the gel point up to the final conversion, and shrinkage stress increases with each newly formed bond. In vat photopolymerization fabrication, this gives rise to a relevant defect, defined curling (the corresponding term used for thermoplastic shrinkage is warping).

Other UV-reactive systems are unsaturated polyesters (usually maleic or fumaric structures located along the polyester backbone) that copolymerize by direct addition with vinyl monomers, such as styrene, thiol−ene systems, vinyl esters,

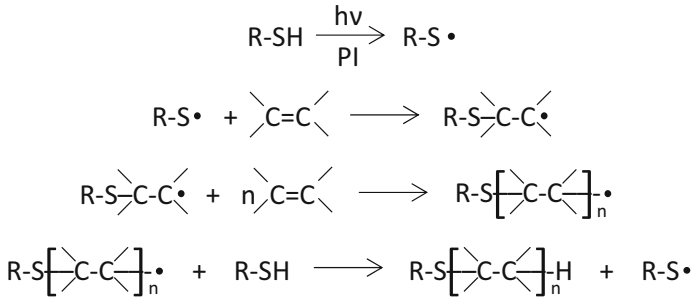

Scheme 2.7 General thiol−ene photopolymerization process

vinyl carbamates, and carbonates. Allyl ethers are used as well: as their reactivity is low, they are preferably employed in copolymerization.

An interesting class of monomers are the thiol−ene systems, which are also proposed as photoinitiator-free systems. Even in the absence of a photoinitiator, they can assure a good reactivity by generating thiyl radicals, thus presenting low sensitivity to oxygen. Interestingly, they polymerize through a step growth mechanism pathway or Michael-addition reactions at a good reaction rate, as in Scheme 2.7. Thiol−ene systems show less polymerization shrinkage and reduced stress compared to acrylates: in fact, they undergo gelation at much higher conversion and produce networks that are more homogeneous than acrylic networks. This difference, due to the step growth reaction mechanism, can be seen in Fig. 2.2 and is deeply discussed by Ligon-Auer et al. [15] Unfortunately, thiol−enes have bad odor and poor shelf life; the polymers obtained are usually soft with low modulus due to the flexible thioeter bonds.

As an alternative to thiols, addition−fragmentation chain transfer (AFCT) reagents are investigated in the curing of acrylates and other photocurable formulations, to control polymer architecture and in turn to tune material properties. AFCT reagents, such as ester-activated β-allyl sulfone, copolymerize in a statistical manner with the unsaturated monomers, typically acrylates; thereby, the gel point is shifted toward higher conversion, and the shrinkage stress is reduced. The reaction rate is lower, but the impact strength of the acrylic networks is improved, without reducing modulus as it happens with thiols [17].

Light-induced cationic polymerization is becoming more popular and displays advantages such as no oxygen inhibition and lower shrinkage, thus translating in the reduction of curling of printed parts. Although involving monomers that are less reactive than radical systems, cationic polymerization permits to use monomers that are inactive toward radical species. Cycloaliphatic epoxides have commercial significance; in particular the monomers containing epoxy-cyclohexane rings are widely employed: their polymerization rate is advantageous due to the ring strain that favors the opening in the presence of the acid produced by the photoinitiator. Besides epoxides, suitable monomers for photoinduced cationic polymerizations are vinyl ethers, propenyl ethers, and oxetanes: unfortunately, not a wide range of such monomers are commercially available. The photoinduced cationic reaction

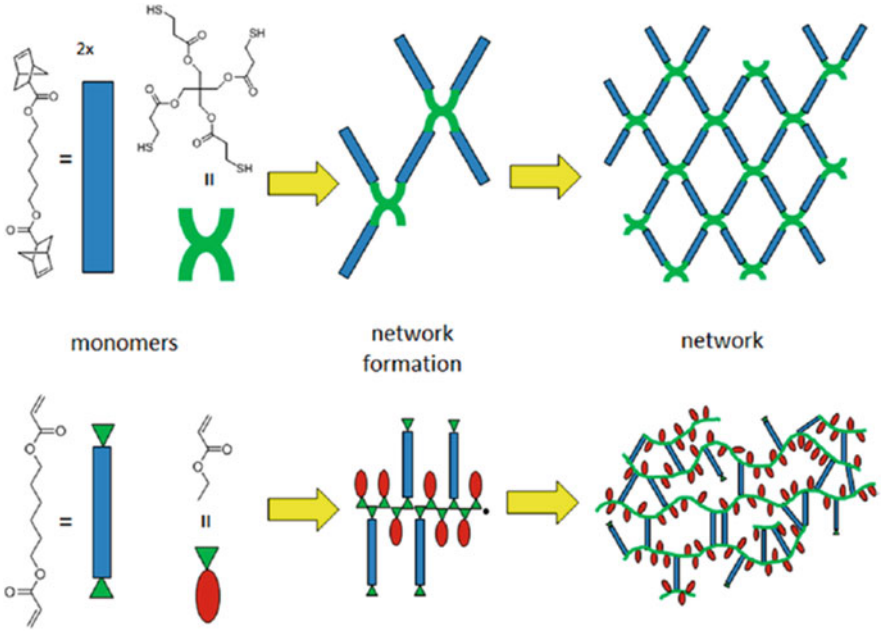

Fig. 2.2 Network formation with thiol−ene monomers (upper reaction) versus network formation with acrylate monomers. (Reprinted under Creative Commons licenses (CC-BY) from [16])

scheme is represented in Scheme 2.8, where the linear photopolymerization of a monofunctional epoxide is shown. Interestingly, with a cationic mechanism, the polymerization has a "living" character, and the oxonium species are essentially nonterminating (i.e., the active centers can stay alive for hours or even days). This means that curing self-sustains even after the light is off: this effect is called post-curing, which can permit to achieve higher conversion (thus to enhance material properties). Reactive species can migrate and may also induce reactions in the nonirradiated areas (shadow curing or dark curing). The livingness of the cationic reaction can pose an issue for the printing resolution in vat photopolymerization. At the same time, it is an opportunity to reinitiate the reaction by addition of further monomers to introduce new chemistries/functionalities/properties in a living manner: this is extremely important in view of designing a living 3D printing process.

Termination of the cationic process can happen either by chain transfers producing inactive species or by reaction with nucleophilic impurities, such as water. Eventually termination can be induced by addition of a base: exposure to ammonia vapor is a common strategy to stop the reaction conversion.

In addition to the mechanism reported in Scheme 2.8, another important cationic polymerization mechanism is the so-called "activated monomer" mechanism, which preferably takes place in the presence of alcohols (Scheme 2.9). By chain transfer reaction, alcohols modify the reaction rate and the network architecture formed.

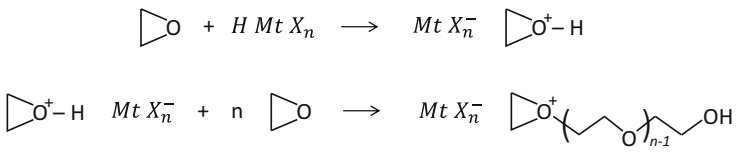

Scheme 2.8 Photopolymerization of a monoepoxide with a cationic photoinitiator $HMtX_n$ producing H^+ species

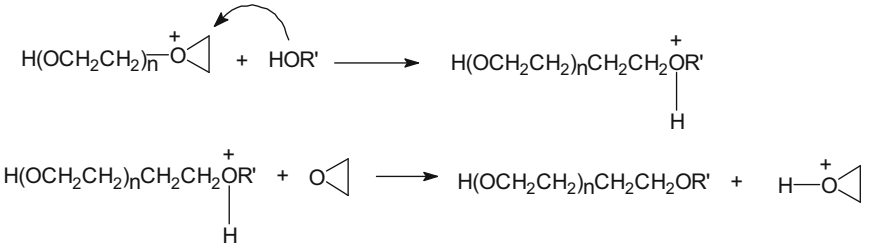

Scheme 2.9 "Activated monomer" mechanism of polymerization of a monoepoxide in the presence of an alcohol

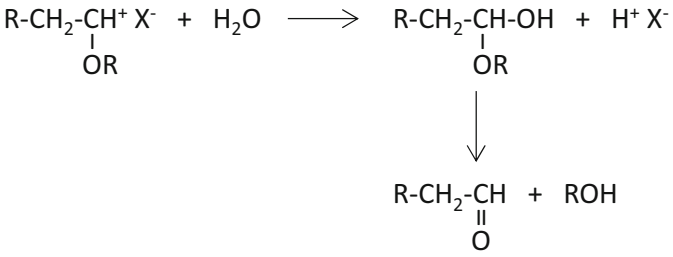

Scheme 2.10 Reaction of water and cationic active centers in vinyl ether polymerization systems without hydroxyl end groups

Used at a low concentration, they lessen the cross-linking density of the networks. A similar reaction can take place with water and can hinder the polymerization, as shown in Scheme 2.10. Therefore, it is reported that cationic polymerization does not proceed in humid conditions.

Reports on photoinduced anionic polymerizations are few compared to radical and cationic systems; as said before, up to now this chemistry is not used in vat photopolymerization additive manufacturing. Anionic photopolymerization implies a photoinitiation reaction releasing a reactive anion, which is added to the monomer, followed by its repetitive addition to the growing anionic chain. Early examples concern the anionic photopolymerization of alkyl cyanoacrylate through the nucleophilic addition of a Lewis photobase onto the monomer or the anionic polymerization of oxirane monomers.

2.3 Vat Photopolymerization Techniques

Vat photopolymerization 3D printing steps are sketched in Fig. 2.3. The 3D printing production process begins with a 3D model that is designed with computer-aided design (CAD) software or 3D scanned from a physical object. In this preprocessing stage, the desired mesh model is formed. Then, the processing stage takes place. As a 3D printed object is fabricated layer by layer, each consecutive layer must be supported by either the platform, the preceding layer, or extra support elements. After designing the correct and optimal orientation of the model and the supports, the model is sliced into layers with a plane parallel to the platform surface (x-y plane). The sliced model is subsequently sent to the printer. Each layer is then built consecutively in the z-direction. The layer thickness depends on the printer, the technology, and the quality requirements of the final printed part. After the printing is finished, the model is extracted from the platform and rinsed in a wash solution to remove the liquid resin. Post-polymerization manipulation is limited because the material is cross-linked (it is a thermoset) and, as explained in the previous section, polymer properties and shape cannot be easily changed. There are however some technical processing procedures to refine the printed object in a stage called post-processing. Typically to complete the curing, thus making the conversion more uniform along the z-direction [18], and enhancing the mechanical properties, the models are subjected to another bulk curing step with light or temperature (post-curing). Post-curing can reduce the anisotropy of the parts produced: eventually the final product can be fully isotropic, unlike with fused deposition modeling (FDM) prints. Fully cured parts can be watertight and airtight: this means that vat photopolymerization is suitable for use in the automotive, aerospace, and healthcare industries. Other post-processes can include support removal, grinding, sealing, gluing, polishing, painting, varnishing, coating, sterilization, inspection, and measurement, depending on the final application of the printed part.

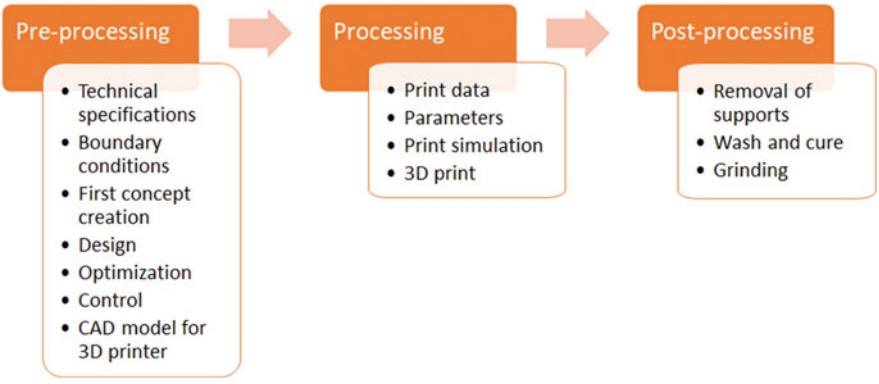

Fig. 2.3 A typical production process by vat photopolymerization 3D printing

Several primary configurations have been developed to exploit vat photopolymerization for the fabrication of printed parts; they differ in the way the liquid vat is illuminated and include the following:

- Vector scan approaches, also known as point-wise approaches.
- Mask projection approaches, also known as layer-wise approaches.
- High-resolution point-by-point approaches, also known as two-photon approaches.
- Line-wise approaches, as used in inkjet printing.

In both the vector scan and the mask projection approach, there is a recoat step, i.e., a new layer of resin must be applied after curing the previous layer: this is done changing the position of the platform inside the vat tank after any layer is solidified. This is the difference with the two-photon polymerization approach (2PP): in the 2PP stereolithography, the part is fabricated below the resin surface and recoating is avoided, and thus, the method allows a faster and less complicated fabrication. In this chapter, only the vat photopolymerization techniques based on a point-wise (i.e., vector scan) and layer-wise (i.e., mask projection) illumination approach are described: SLA, DLP, and related techniques. 2PP is treated in Chap. 3, while line-wise approaches are not included as the products have 2D features.

2.3.1 Stereolithography (SLA)

As shortly mentioned in the introduction, SLA was developed around 40 years ago and is one of the earliest methods of additive manufacturing. SLA adopts a point-wise illumination system, as sketched in Fig. 2.4: a scanning laser beam is used, and the single-point laser traces a thin line along the surface of the resin, filling in the shape of the cross-sectional layer to be solidified. There are two main SLA machine setups: the top-down and the bottom-up orientation (Fig. 2.4). Top-down printers are the most popular in industries: the laser source is above the resin tank, and thus, the part is built facing upwards (Fig. 2.4a). The build platform starts at the very top of the vat and moves downwards after curing each layer. First, the building platform is set in the tank of the liquid photosensitive formulation at a distance of one-layer height from the surface of the liquid. Light exposure is performed sequentially by scanning the laser beam within the plane, on the surface of the vat. The time to produce one slice of the structure depends on the speed of the laser beam and on the irradiated area. The x,y position of the laser is usually controlled by mirrors within a galvanoscanner. After the polymerization of the layer (i.e., the building of the first slice), the platform moves down and a new liquid resin spreads over the cured layer. Once the fresh layer covers the cured one, the beam scanning restarts and the solidification of the individual pattern in each layer of resin is repeated until a 3D part is obtained. The main time-consuming step is the preparation of the liquid layer after the curing of the previous one (here the viscosity of the material plays an important role), while the laser scanning can be fast, depending on the type of laser,

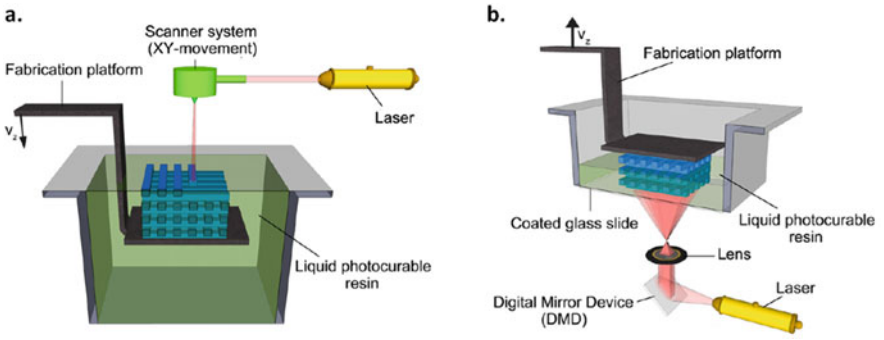

Fig. 2.4 Sketch of a typical SLA vat photopolymerization system for a top-down (**a**) and a bottom-up (**b**) printer. (Figure modified with permission from Ref [19])

intensity, and control of the polymerization rate. As explained above, after printing the part is not fully cured and requires further post-processing: to achieve the best mechanical properties, SLA parts must be post-cured, by placing them under intense UV light and sometimes heating them.

In the bottom-up printers (Fig. 2.4b), mainly used as desktop printers, the laser is under the resin tank and the part is built upside down while the build platform moves upwards: the tank bottom is transparent and has a silicone coating that allows the light to pass through and avoid sticking of the built part to it. With this configuration, printing is less affected by oxygen inhibition than in a top-down printer, where the curing is at the air interface. After curing every layer, the part is detached from the bottom of the tank (peeling step), and the resin flows to make a new liquid layer ready for irradiation. Bottom-up SLA printers are easier to manufacture and operate, but their build size is limited: in fact, the forces applied to the part during the peeling step might cause the print to fail. On the other hand, top-down printers can build large-sized parts with accuracy (and higher cost).

In both configurations, a SLA printing apparatus requires a support structure. Depending on the orientation of the part, the builder chooses the location and the size of support considering that visible surfaces of the part should preferably not be in contact with the support: in fact, it is manually removed after printing and the aspect of the external surface of the part after detachment can be of lower quality than the rest. It is important to notice that bottom-up and top-down SLA printers use support differently: in top-down SLA printers, support should allow to accurately print overhangs and bridges (the critical overhang angle is usually 30°); in bottom-up SLA printers, support requirements can be more complex as minimizing the cross-sectional area of each layer is the most crucial criterion because the forces applied to the part during the peeling step may cause it to detach from the build platform. These forces are proportional to the cross-sectional area of each layer.

As in any additive manufacturing technology, SLA builds a part layer after layer. The slice information is given in the form of a set of coordinates, defining the tilt angle of the two mirrors that control the position of the laser beam along the plane.

Process parameters influencing the x-y resolution include the minimum resolution of the light source employed and the path planning operations: every pixel of the curable layer is irradiated sequentially, and thus, an adjustment of the exposure dose (defined as the product of the light intensity and illuminating time) for each pixel can be possible controlling the laser intensity. This means that SLA could also process grayscale patterns. Vertical resolution (in the z-direction), as described by the minimum obtainable layer thickness, is dependent on the accuracy of the step motor operating the build platform, on the efficiency of the recoating process (which is affected by the viscosity of the resin), and on the light penetration depth h, which is affected by the light intensity and the absorption coefficient of the resin as in Eq. 2.8.

The thickness of a solidified layer is referred to as curing depth C_d (generally expressed in μm). A semiempirical equation (Eq. 2.9) relates C_d to the light irradiation dose E ($E = I \cdot t_{\text{exp}}$, in mJ cm^{-2}):

$$C_d = h \ln \frac{E}{E_c} \tag{2.9}$$

where h is the light penetration depth, and E_c is the critical energy required to reach the gel point and solidify the resin. Therefore, the depth at which the resin is cured increases logarithmically with the applied irradiation dose and depends linearly on the penetration depth.

Although E_c is a crucial value in manufacturing, generally the strength and modulus of a polymer at the gel point are not enough to resist the handling during the printing and development processes. The excess energy (E_x) required to cross-link the polymer to an extent to provide sufficient green strength ("green" refers to the initially formed cured object) is given by Eq. 2.10:

$$E_x = E_c \frac{h}{C_d} \left[\exp\left(\frac{C_d}{h} - 1 \right) - 1 \right] \tag{2.10}$$

As per Eq. 2.8, the penetration depth can be decreased by increasing the photoinitiator concentration or by including a light absorber in the resin (e.g., a dye having a very high absorption coefficient), while the dose can be controlled by the laser scan velocity V_s and the laser power P_L, in accordance with Eq. 2.11:

$$E = \frac{P_L}{h_s V_s} \tag{2.11}$$

where h_s is the scan line spacing of the laser.

As the curing depth depends on the exposure dose, grayscale capability of SLA is not used in practice. In any case SLA has one of the highest manufacturing accuracies: thanks to the high resolution of the light source, the lateral accuracy, related to the diameter of the laser beam at the curing point, namely, the spot size, is of the order of microns; the vertical resolution corresponds to the layer

height, usually ranging between 25 and 150 μm. The layer height is one of the few parameters the user can vary, while all the others are usually set by the producers of the printer. Lower layer heights reproduce curved geometries very accurately but increase the build time and cost. Printed contours can be extremely smooth, even comparable to those obtained by injection molding: this makes SLA suitable for prototyping injection-molded parts, as well as for fabricating highly complex parts. The possibility to print highly fine details with high resolution and tight tolerances allows for consistent repeatability and makes the SLA technology ideal for dental and medical applications and jewelry. However, despite being highly accurate, SLA can be time-consuming: the print speed of standard SLA printers is in the range of 10–20 mm h^{-1} (that is the height of the structure per unit time). In terms of build volumes, they vary a lot between desktop and industrial printers, but are usually smaller than those for other 3D printing technologies such as FDM or powder bed fusion (PBF). The largest build volume is 1500 mm × 750 mm × 550 mm (ProX 950 printer by 3D Systems), keeping the resolution and accuracy comparable to tiny parts of just a few mm in size.

2.3.2 Digital Light Processing (DLP)

DLP technology uses a mask projection illumination approach (Fig. 2.5): a digital light projector is employed to flash a single black and white image of an entire layer all at once. Generally, the light comes from the bottom, as in the bottom-up SLA configuration, and the polymerization reaction is not so much affected by oxygen inhibition. DLP technology differs from SLA solely in the irradiation method: instead of a mirror to reflect a laser source, a digital micromirror device is employed, which is a technology also used in overhead projectors. There are three main types of illumination typically used in DLP projection systems: classical lamps, LEDs, and lasers covering a wavelength range from UV to visible. As said in the introduction, the use of visible light can circumvent the limitations aroused from high-energy UV light exposure, reducing the risks of eye damage and being more benign to living cells, thus preferable for biomedical and dental applications. Moreover, visible LEDs, as compared to UV light lamps, are eco-friendly and do not release ozone while having a low thermal effect with long service lifetimes.

In comparison with SLA technology, the DLP process is faster as each layer is entirely exposed to the curing light projected from the digital screen. While SLA has a processing speed of the order of mm h^{-1}, for DLP it is cm h^{-1}. Since DLP technology utilizes a digital light projector, each layer appears pixelized and the accuracy of the printed part depends greatly on the projector resolution: the lateral resolution is in the range of 10–50 μm depending on the pixels provided by the micromirror and on the optics used to project the pattern. Considering photopolymerization, the printing resolution is always significantly lower than the optical resolution of the system (d) [21], which can be calculated according to the incident wavelength and numerical aperture NA of optics by Eq. 2.12:

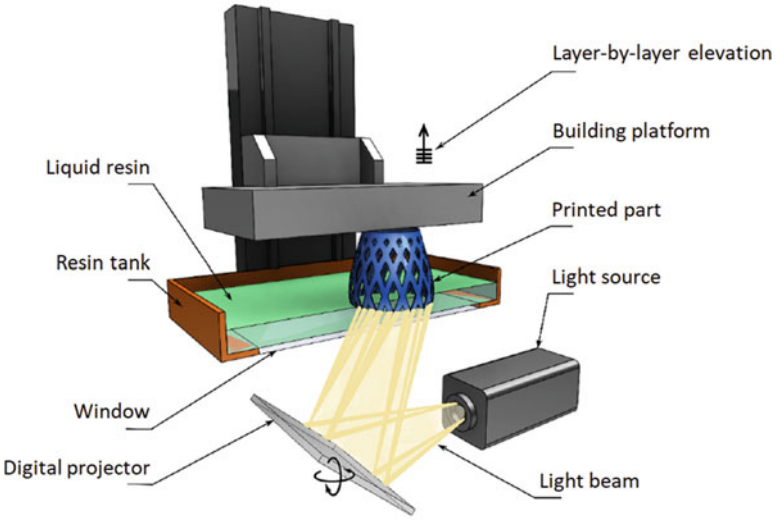

Fig. 2.5 Sketch of a typical DLP vat photopolymerization system. (Figure modified under CC-BY from [20])

$$d = \frac{0.61\,\lambda}{NA} \tag{2.12}$$

A lens with moderate magnification and NA (e.g., 20×, NA = 0.4) can push the optical resolution down to <1 μm, while the best reported printing resolutions with DLP are rarely <5 μm. A major cause could be attributed to the diffusion of reactive species during printing. Free radicals are constantly generated under incident light, and they could migrate a certain distance and induce polymerization in dark regions. The maximum diffusion distance (L) can be calculated according to Fick's laws of diffusion (Eq. 2.13):

$$L = \sqrt{2\,D\,t} \tag{2.13}$$

where D is the diffusivity and t is the free-radical lifetime. The typical radical lifetime has been reported to be ≈10 ms, while the diffusion coefficient of common free radicals is around 10^{-5} cm^{-2} s^{-1} in both polar and nonpolar solvents, corresponding to an L of ≈10 μm. Therefore, printing objects smaller than 10 μm will be extremely challenging, regardless of how good the optics is. In order to eliminate the adverse effect of molecular diffusion, the exposure time in a printing cycle is usually kept on the scale of 10^1–10^2 s. The vertical resolution (in the z-direction), which corresponds to the layer thickness, depends on the light penetration depth into the vat resin, as in Eq. 2.8.

The curing light source and the light-projecting method play key roles in determining the accuracy of the printed parts. For SLA, the footprint of the curing

laser beam on the x-y plane is a spot and the accuracy depends on the spot diameter, whereas in DLP the accuracy is given by the pixel matrix, which is defined by the resolution of the digital projector. In contrast to the flexibility that SLA offers thanks to the free movement of the laser beam, DLP is limited to the network of pixels of the digital screen, which is illuminated wholly one at a time for each layer. As a result, DLP delivers less accurate parts in comparison with SLA, despite its printing speed.

While SLA is characterized by a good scalability, in DLP systems there is a direct trade-off between resolution and build volume. The resolution depends on the projector, which defines the number of pixels/voxels available. If the projector is moved closer to the optical window, the pixels get smaller, which increases the resolution, but limits the available build area. As a result, DLP 3D printers are generally optimized for specific use cases: some have a smaller build volume and offer high resolution to produce small, detailed pieces (e.g., jewelry), while others can produce bigger parts but at a lower resolution.

2.3.3 Continuous Liquid Interphase Production (CLIP)

CLIP technology is an innovation based on DLP technology: it employs digital projection with LEDs and an oxygen-permeable window instead of a normal glass window, allowing the build platform to move in continuous motion [22], as sketched in Fig. 2.6. This allows for even faster build times and smoother contours along the z-axis. The CLIP technology was originally developed by J. M. DeSimone's group and is now proprietary of Carbon®, a 3D printing technology company. In CLIP, curing is conducted above an oxygen-permeable build window, where a continuous liquid interface is enabled by the presence of oxygen: this interface, called dead zone, is a thin uncured liquid layer between the window and the cured part surface. The fabrication proceeds projecting a continuous sequence of images obtained by a DLP unit, through the oxygen-permeable, UV-transparent window below the vat bath. The dead zone created above the window maintains a liquid interface below the advancing cured part, which is drawn out during printing. The process is nonstop and thus is fundamentally different from standard DLP printers, where UV exposure, resin renewal, and part movement must be conducted in discrete steps. The continuous uncured resin flow remarkably increases the resolution of the printed part, as well as decreases the risk of printing failure due to the peeling force. Moreover, as opposed to the layer-by-layer method, CLIP machines are designed with continuous movement of the build platform, thus allowing for undisrupted prototype printing at speeds of several hundred millimeters per hour while maintaining good resolution: resolution in the z-direction can be around 100 μm while keeping a growth rate as high as 300 mm h^{-1}.

Thanks to the continuous printing process, the problem regarding layer connection is eliminated and the visible staircase effect is minimized. Therefore, the

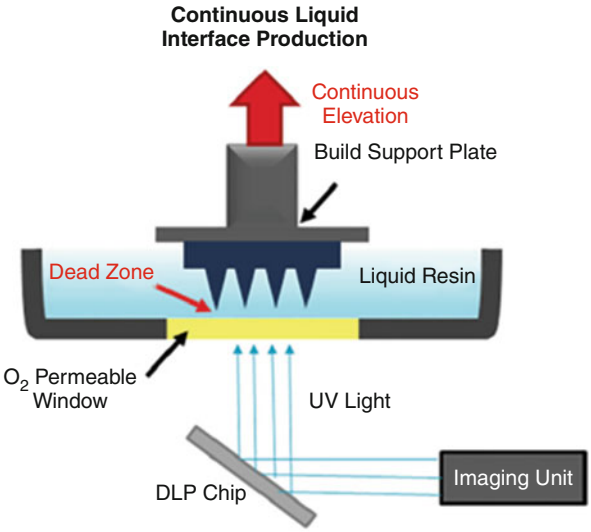

Fig. 2.6 Sketch of the CLIP vat photopolymerization system. (Figure modified under CC-BY from [23])

fabricated parts have isotropic mechanical properties, although they can be expected anisotropic [22].

2.4 Materials for Vat Photopolymerization

Printable precursors are the core of 3D printing, as they determine what materials and devices are produced. Up to now the photopolymerization process behind the solidification is irreversible and takes place on multifunctional systems producing networks (as in Scheme 2.5), which are insoluble and non-reprocessable (differently from thermoplastics as used in FDM). Only in the production of sacrificial mold, formulations are based on monofunctional monomers that form linear polymers and are dissolved after the molding process: an example of vat composition employed for this purpose is a mixture of monofunctional acrylates and methacrylic anhydride. The latter prevents dissolution during the building step by the uncured vat, but cleaves when the part is put in an aqueous alkaline solutions (water-soluble systems) or in amine-containing organic solvents (organo-soluble system) [16].

In vat photopolymerization printing, the most popular monomers are multifunctional acrylates and methacrylates [21, 24]. They are described in the first US patents on SLA resins [25, 26]. The most common (meth)acrylate monomers/oligomers used in vat photopolymerization are poly(ethylene glycol) diacrylate (PEGDA), urethane dimethacrylate (UDMA), triethylene glycol dimethacrylate (TEGDMA), bisphenol A-glycidyl methacrylate (bis-GMA), trimethylolpropane triacrylate (TTA), and bisphenol A ethoxylate diacrylate (bis-EDA) [16, 24]. Their chemical structure is shown in Fig. 2.7.

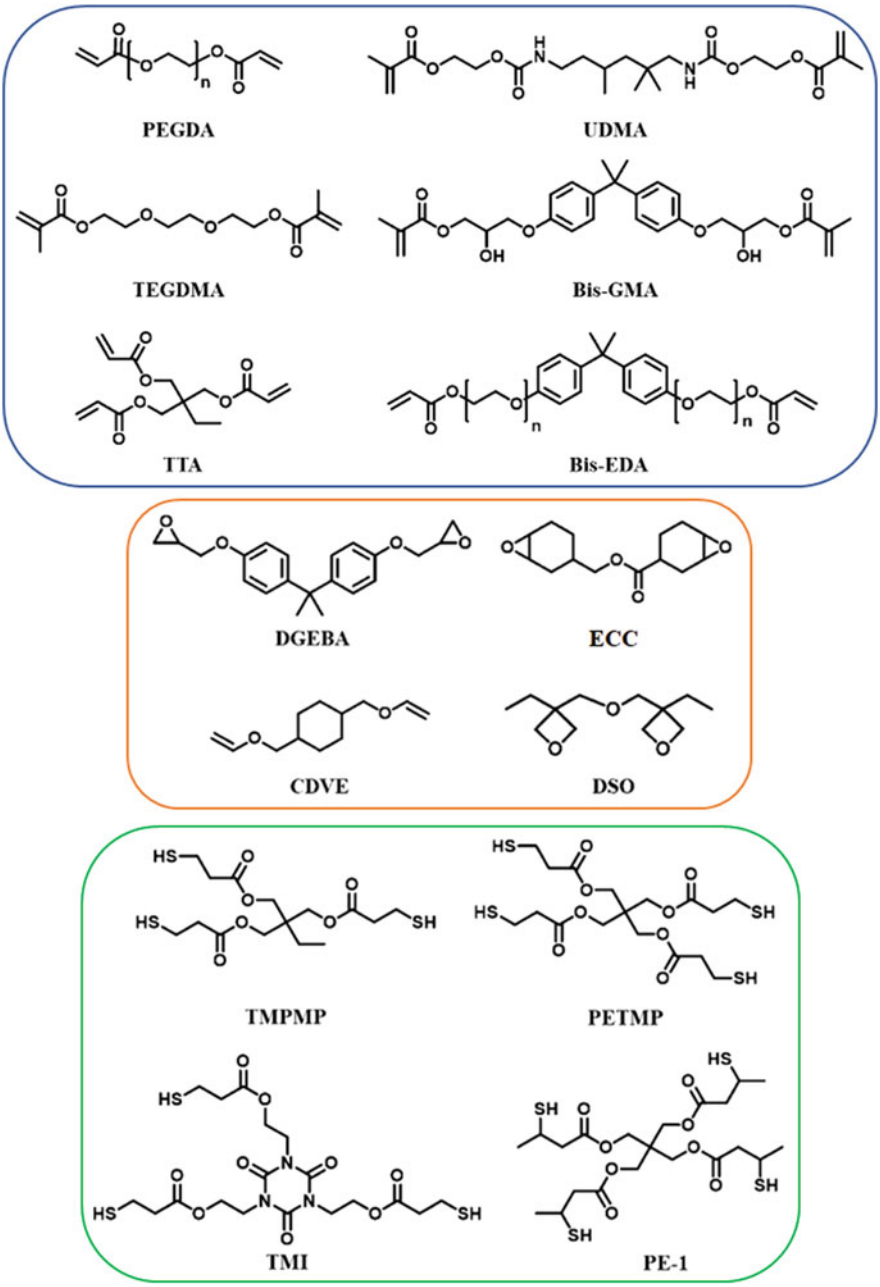

Fig. 2.7 Examples of (meth)acrylate, cationic, and thiol–ene monomers/oligomers typically used in vat photopolymerization 3D printing

Acrylic monomers have high reactivity, so that reaction speed is high, satisfying the constraints of time and cost of manufacturing. However, as explained above, gelation arises early and can stop conversion. Acrylates cannot be used in the biomedical sector, where additive manufacturing is extremely promising, as they are not biocompatible (they are cytotoxic), whereas less reactive methacrylates are generally biocompatible. Both could produce parts with limited accuracy and defects, mainly due to curling and shrinkage. In using (meth)acrylates, oxygen inhibition has to be taken into account. The consequence of the presence of oxygen is the delay of the polymerization, thus the need of using more photoinitiator to have a satisfactory reaction rate. Moreover, when a fresh layer of monomer is put on the previously exposed layer and some radiation pass through, the partially cured layer can react, as it is less susceptible to oxygen inhibition after it had been coated. The advancement of the cross-linking on this layer causes extra shrinkage, and the stress in the layer increases the curling effect. Curling can also take place after the production of the printed object, due to overcuring or exposure of the part to direct sunlight or high temperature. To avoid curling caused by uncontrolled illumination after printing, spray coating with a clear UV acrylic paint before use is sometimes recommended (light has also a detrimental effect in the physical properties and appearance of photocured printed parts).

Shrinkage can be tuned changing the molecular structure of the monomers /oligomers: for instance, cycloaliphatic and aromatic (meth)acrylates giving hydrogen bonds (i.e., assuring a preorganization in the liquid state) shrink less than other monomers. However, it is the ring-opening polymerization through a cationic mechanism that assures the least shrinkage: therefore, resin compositions based on epoxy monomers have been proposed. Among the cationic monomers, epoxide monomers commonly used in vat photopolymerization (Fig. 2.7) are diglycidyl ether derivatives of bisphenol A (DGEBA), 3,4-epoxycyclohexylmethyl-3,4-epoxycyclohexanecarboxylate (ECC), and epoxides of aliphatic alcohols, such as trimethyloyl propane [16, 24]. In using these precursors, curling is often negligible. Moreover, in cationic systems, the photoinitiator concentration is limited with respect to the acrylics, as they do not suffer oxygen inhibition. However, the photocuring speed is low; such slow solidification not only causes an unsatisfactory fabrication speed, but can also give distortions during fabrication and handling of the parts. Another disadvantage of epoxy resins is the sensitivity to humidity, which can inhibit polymerization. Finally, epoxides often produce highly cross-linked and stiff materials, which are fragile, unless chain transfer agents are used as in Scheme 2.9. Vinyl ether (e.g., 1,4-cyclohexane dimethanol divinyl ether, CDVE) and disubstituted oxetanes (DSO) have also been used in vat photopolymerization 3D printing (Fig. 2.7). Oxetanes offer higher reactivity and improved water resistance compared to epoxides, guaranteeing low shrinkage; however, only few structures are available.

Alternatively, in many applications, resins are mixtures, e.g., epoxides and vinyl ether and more often acrylics and epoxides. As the monomers undergo different modes of polymerization and do not react with one another, the material obtained is not a true copolymer, but an interpenetrating polymer network (IPN). Hybrid

resins containing a mixture of epoxides and acrylates offer the advantages of both free-radical and cationic polymerization, thus resulting in materials with high reactivity, high mechanical properties, low shrinkage, and limited oxygen sensitivity. In addition, to avoid the incompatibility of the two different types of monomers, systems containing both epoxide and (meth)acrylate groups (e.g., 3,4-epoxy-cyclohexylmethyl methacrylate) undergoing simultaneously cationic and free-radical photopolymerization can be used.

Indeed, for CLIP 3D printing technology, only photocurable reactive systems that are sensitive to oxygen should be used (i.e., acrylic and methacrylic monomers), as oxygen inhibition is essential to avoid adhesion of the curing part to the bottom of the resin vat.

Thiol−ene systems, adopting a step growth mechanism, are advantageous because they show lower shrinkage and curling than acrylics, thus finding wide applications in many fields, including the biomedical one. Moreover, they are usually less brittle than acrylate networks due to the different polymer architecture. Sometimes, due to the sulfur bridges, thiol−ene parts are even too soft for many applications. However, a strategy to improve the low modulus of the binary thiol−ene systems is the addition of a (meth)acrylate monomer, forming a ternary system. Besides the lower modulus of the final material, other drawbacks of thiol−enes are the limited storage stability (poor shelf life due to an oxidative disulfide bond formation) and the bad odor of resins containing thiols. Common thiol monomers suitable for vat photopolymerization 3D printing are trimethylolpropane tris(3-mercaptopropionate) (TMPMP), pentaerythritol tetra(3-mercaptopropionate) (PETMP), tris[2-(3-mercaptopropionyloxy) ethyl] isocyanurate (TMI), and pentaerythritol tetrakis (3-mercaptopropionate) (PE-1) [16, 24]. Their chemical structure is represented in Fig. 2.7.

Alternatively, AFCT reagents, such as β-allyl sulfones, are being investigated to tune material properties by chain transfer reactions. Such AFCT reagents can be incorporated into (meth)acrylate or thiol−ene systems to modify the radical network formation, leading to more homogeneous networks characterized by a higher toughness and a lower shrinkage stress. However, AFCT-based photopolymerization generally proceeds with limited curing rate, which is not desirable for 3D printing.

Besides reactivity, the viscosity of precursors is a major criterion for choosing the monomers for vat formulations. High viscosity serves to maintain the shape of printed objects at early stages, when they are not fully cured; moreover, it helps to slow down molecular diffusion of unreacted monomers and thus is requested for improving printing resolution. Meanwhile, high viscosity values may also have some negative effects: in the recoating step of SLA and DLP, when the build platform moves, the resin must easily flow over the cured layer; otherwise, as the recoating is the rate-determining step of the printing process, the production rate is reduced. Moreover, viscous resins cannot be refreshed efficiently between printing cycles, which requires the use of additional tools or operations to accelerate the process. Recently, a particular SLA technology called Hot Lithography™ has been developed to process resins and pastes with high viscosity leading to improved toughness for the 3D printed parts [27, 28]. In this technology, the laser is placed

below a heatable, transparent carrier plate so that the resins are cured at operating temperatures of ∼50–150 °C.

Another important component of the photocurable resin formulation is the photoinitiator. In fact, its properties, along with the printing parameters, must be tailored in order to optimize both the polymerization reaction and the process resolution. The choice of the photoinitiator depends on the utilized light source (wavelength and intensity). The light source can be in the form of xenon lamps, mercury arc lamps, LEDs, or lasers. The emission wavelengths can be within UV (190–400 nm), visible (400–700 nm), or IR range (700–1000 nm). Classical benzoyl-based photoinitiators for radical polymerization undergo α-cleavage scission (Norrish I; see Scheme 2.1) and require UVA or UVB light sources to initiate the polymerization. As the SLA lasers of choice are generally He−Cd laser (325 nm) or frequency tripled Nd − YAG sources (355 nm), benzil ketals such as 2-hydroxy-2-methyl-1-phenyl-propan-1-one (Irgacure 1173) and 2,2-dimethoxy-2-phenylacetophenone (Irgacure 651) are suitable photoinitiators for SLA-based processes. With higher wavelength light sources, as in DLP-based systems, phosphine oxide containing photoinitiators are recommended. For instruments based on blue light curing, an appropriate photoinitiator is bisacylgermanium. Mixtures of different types of photoinitiators may also be employed to tune the absorption spectra and the light frequency. Photoinitiating systems are often highly complex mixtures specifically made for any given application. They can also contain photosensitizers, which are used in combination with the photoinitiator to shift the absorption toward longer wavelengths. Pyrene and substituted anthracenes serve as sensitizers, enabling curing with higher wavelength light sources or more accurately lowering the E_c at a particular wavelength (see Eq. 2.9). For polymerization reactions under visible light irradiation (e.g., visible LEDs), visible light-sensitive photoinitiators have been developed, such as bimolecular photoinitiator systems consisting of camphorquinone (CQ) and a tertiary amine, like ethyl 4-dimethylaminobenzoate (DMAB), and titanocene photoinitiators. Photoinitiating systems able to efficiently absorb light at high wavelengths can lead to the achievement of mild and safe conditions of 3D printing, higher penetration depths (layer thickness), and thus enhanced photopolymerization rate, and systems that are benign to living cells for tissue engineering applications. For cationic photopolymerization, photoinitiators of aryl iodonium or sulfonium salts are generally used. In the case of hybrid resins, both radical and cationic photoinitiators are present in the formulation. As radical photoinitiators, Norrish type II species are avoided as they often contain amines which inhibit the cationic polymerization.

There are several other additives present in the vat resin formulations, each one having a specific role either in controlling the reaction or tailoring the final properties of the material and of the part produced.

First, while the main monomers are difunctional chemicals, monofunctional and polyfunctional monomers are also present: they are called reactive diluents, as they also participate in the polymerization reaction and modulate the reactivity of the systems. They are also used to adjust the viscosity of the mixtures, in particular for the recoating step in SLA and DLP printing. Sometimes, to reduce viscosity,

solvents or other rheology modifiers (nonreactive) are used: e.g., block copolymers such as styrene–butadiene–methylmethacrylate, which also increases the impact strength of the printed part.

For radical formulations, the use of additives such as tertiary amines or triphenylphosphine lessens the oxygen inhibition; however, tertiary amines might result in discoloration of the cured material and are not suitable for the commercial resins containing both (meth)acrylate and epoxides due to their inhibition effect on the cationic polymerization.

Light absorbers (LAs) are other important components of most resin formulations. They are mostly dyes and colorants; pyrene, stilbene derivatives, and substituted anthracenes are also described. Their purpose is to reduce the penetration depth h according to Eq. 2.14 (from the modification of Eq. 2.8):

$$\frac{1}{h} = 2.3\,\varepsilon_{PI}\,[PI] + 2.3\,\varepsilon_{LA}\,[LA] \tag{2.14}$$

Thus, the penetration depth of the light source is also dependent on the absorber concentration [LA]: the higher the [LA], the lower the h; thus, by using light absorbers, thinner layers can be cured and better z-resolution is obtained. Overall, more accurate structures as well as in cut structures, otherwise impossible to fabricate, are obtained.

The formulation can also contain fillers to improve the mechanical properties of the product or even to shape composites and fabricate ceramic objects. In the presence of particles, vat photopolymerization is influenced by the way light is scattered, and thus, Eqs. 2.9, 2.10 and 2.11 are no longer valid to model the process. Besides light scattering, which limits the curing depth, vat photopolymerization applied to composite materials poses a few problems, such as the increased viscosity of the resin which can complicate the coating process, the settling of particles resulting in inhomogeneities, air entrapment, and bubble formation [29, 30]. Epoxy composites (e.g., containing glass fiber nonwoven mats) can also be constructed by pausing the fabrication process, manually placing a fiber mat atop each freshly polymerized layer, coating it with the liquid resin and then proceeding with the irradiation. Nanocomposites are particularly relevant in vat photopolymerization. Organic-modified ceramics (ORMOCERs) consist of sol−gel-derived oligomers, typically alkoxysilane monomers, along with monomers (such as acrylates), photoinitiators, and other additives: they are easy to process leveraging on the photopolymerization of the acrylate moieties, while siloxanes cross-link during thermal post-curing. Materials with excellent optical and mechanical properties can be obtained [31].

When slurry of approximately 40–55 wt % ceramic dispersed formulations are used, vat photopolymerization allows to fabricate ceramic objects [32]. The “green” part formed by irradiation undergoes a multistep thermal cure, through thermal ramps (at a slow heating rate to reduce the risk of cracking), which degrades the organic matrix. In particular, the final step is the sintering at a temperature normally above 1000 °C to provide the finished ceramic object.

When formulating a resin for vat photopolymerization, the possible by-products of the selected photochemical reaction should also be considered. For instance, some photocuring reactions generate gaseous by-products, which dramatically scatter light and induce voids in the printed materials.

As the formulations containing monomers and photoinitiators are potentially reactive, they should be stored adequately, without being exposed to light or heat. To prevent premature reaction and gelation of acrylics, low concentrations of radical inhibitors are required, such as butylated hydroxy toluene (BHT) and methoxy hydroquinone (MEHQ) at around 50–200 ppm. When using cationic monomers, the problem of premature cure is not so severe as in radical formulations: in fact, iodonium- and sulfonium-based cationic initiators both have good thermal stability. However, benzyl-N,N′-dimethyl amine (BDMA) as a mild base is often added to neutralize radical cations (concentrations of 5–250 ppm in resins are used when 1 wt % photoacid generator is present).

Nowadays, the range of available formulations for vat photopolymerization is very wide, most of them being proprietary. As in any other printing method, the materials should be tailored to the specific printer to be used. They must also satisfy the request for different application fields, from prototyping to production parts. Depending on the performance of the formulation, vat resins are usually classified as follows: [20]

- Standard resins for general-purpose prototyping.
- High-detail resins.
- Tough or durable resins (ABS-like resins).
- Flexible resins (rubberlike).
- Clear resins.
- High-temperature resins.
- Castable resins with zero ash content after burnout.
- Ceramic-filled resins for very rigid prints.
- Biocompatible resins for medical devices (including dental materials).

A countless number of formulations have already addressed the challenges of diverse application domains, such as bioengineering, aerospace engineering, jewelry, and automotive. It is still desired to broaden the applicability of vat photopolymerization and improve its efficiency in printing functional materials and complex structures. For instance, to make vat photopolymerization a popular manufacturing approach, it is important to further develop resins with optimized performance. Different autonomous systems have been recently proposed to do this without extensive experimental trials and human labor, thus avoiding the testing of an excessive number of samples, which makes also a lot of waste and undesirable environmental impact, while not always finding the most optimal solutions. For example, in a recent work [33], a machine learning approach for the discovery of photocurable materials with optimal trade-offs in mechanical performance is proposed. A multiobjective optimized algorithm that automatically guides the experimental design and proposes how to mix primary formulations, based on acrylic monomers, reactive diluents, a radical photoinitiator, and surfactants, is

developed. The algorithm is coupled with a semiautonomous fabrication platform to reduce the number of experiments and the overall solution time.

New formulations should also respond to other requests such as producing materials that are sustainable, (e.g., environmental benign, able to be recycled, derived from biomass). In fact, at present vat photopolymerization 3D printing processes generally produce nonrecyclable petroleum-based thermosets that are further worsening plastic pollution. Recently, several chemicals derived from biomass have been proposed as renewable feedstock materials for the development of photocurable resins, from lignocellulosic biomass to vegetable oils (e.g., plant-based linseed oils and soybean oils) and animal products (e.g., polyamines, alginate, hyaluronic acid, silk fibroin, globular proteins, gelatin, and keratin) [34]. A prior modification of their chemical structure is often necessary to allow for photo-cross-linking capability: most biobased monomers for SLA and DLP are synthesized from biobased molecules introducing reactive groups such as (meth)acrylates and epoxides. Also waste feedstock materials (e.g., waste cooking oils and carbon dioxide) can be employed for the synthesis of photopolymerizable resins.

Considering the problem of 3D printed part waste, both reprocessing and degradation after end of use are appropriate approaches to be developed. Reversible thermoset and covalent adaptable networks [35] are materials that can be reprocessed and used again in 3D printing or in other processes, such as remolding. Materials that can undergo enzymatic or acid/base hydrolysis of sensitive linkages under an applied stimulus, such as a pH change, assure sustainability by degradation [34].

Eliminating the photoinitiator is another step toward sustainability: in fact, many photoinitiators are toxic; moreover, they can give rise to by-products upon photolysis which can easily migrate without control.

Summarizing, as far as materials are concerned, important objectives are as follows:

- Tuning the physicochemical and mechanical properties of the 3D printed materials [36, 37]
- Improving their biocompatibility [38]
- Assuring sustainability by using waste feedstocks and by recycling parts to recover the monomers [34]
- Shifting the initiation wavelength required to activate the 3D photopolymerization toward longer wavelengths [39].

A transition to an open material model would be a necessary change for further innovation and for increasing the market of vat photopolymerization.

2.5 Conclusion

Besides material innovation, as discussed before, for vat photopolymerization there are other areas and opportunities that are nowadays under exploration. Present

research is also focused on the engineering of the photopolymerization reaction and on the innovation of the printers and of the printing workflow.

In terms of processes, interesting research activities are addressed to the following:

- Development of 4D printing, which refers to the printing of 3D objects able to change their structure because of an external stimulus (e.g., heat, humidity, light, magnetic field among others) [40–42].
- Use of controlled living radical polymerization to design materials with living features in order to modify or functionalize them after printing.
- Development of multimaterial processing [21]; this has the potential to rapidly manufacture in one step devices with a broad range of properties and functionalities, such as mechanical, electrical, chemical, or optical, and addressing a significant bottleneck in present manufacturing approaches, especially for the microfluidics field [43].
- Advancement of bioprinting processes [44].

Coming to the printers, efforts are addressed to increase the build volumes and to improve performance, e.g., changing the peeling step and applying lower forces during the printer movements. Indeed, innovations of the printing processes and machines are foreseen to increase the printing speed, lowering the costs, while maintaining an adequate resolution. Further automatization of the printing process is sought to reduce the labor need and make the fabrication by vat photopolymerization more competitive.

Given the fast growth of vat polymerization forecasted for the next year, in the competitive landscape of the present global market, we can expect that the perspectives listed here will soon be realized and eventually some breakthrough advancement will rise.

References

1. ISO/ASTM52900-15. Standard Terminology for Additive Manufacturing – General Principles – Terminology
2. H. Kodama, Automatic method for fabricating a three-dimensional plastic model with photohardening polymer. Rev. Sci. Instrum. **52**, 1770–1773 (1981)
3. A.J. Herbert, Solid object generation. J. Appl. Photogr. Eng. **8**, 185–188 (1982)
4. J.-C. Andre, A.L. Mehaute, O.D. Witte, Dispositif pour realiser un modele de piece industrielle, FR2567668B1. (1987)
5. Hull, C. W. Apparatus for production of three-dimensional objects by stereolithography, US4575330A. (1986)
6. J.P. Fouassier, X. Allonas, J. Lalevée, C. Dietlin, Photoinitiators for free radical polymerization reactions, in *Photochemistry and Photophysics of Polymer Materials*, (Wiley, 2010), pp. 351–419. https://doi.org/10.1002/9780470594179.ch10
7. J.V. Crivello, The discovery and development of onium salt cationic photoinitiators. J. Polym. Sci. A Polym. Chem. **37**, 4241–4254 (1999)

8. J.V. Crivello, K. Dietliker, *Photoinitiators for Free Radical Cationic & Anionic Photopolymerisation* (Wiley, 1998)
9. K. Suyama, M. Shirai, Photobase generators: Recent progress and application trend in polymer systems. Prog. Polym. Sci. **34**, 194–209 (2009)
10. J. Zhang et al., Structure design of naphthalimide derivatives: Toward versatile photoinitiators for near-UV/visible LEDs, 3D printing, and water-soluble photoinitiating systems. Macromolecules **48**, 2054–2063 (2015)
11. V.V. Rocheva et al., High-resolution 3D photopolymerization assisted by upconversion nanoparticles for rapid prototyping applications. Sci. Rep. **8**, 3663 (2018)
12. M. Chen et al., Living additive manufacturing: Transformation of parent gels into diversely functionalized daughter gels made possible by visible light photoredox catalysis. ACS Cent. Sci. **3**, 124–134 (2017)
13. C.N. Bowman, C.J. Kloxin, Toward an enhanced understanding and implementation of photopolymerization reactions. AICHE J. **54**, 2775–2795 (2008)
14. S.C. Ligon, B. Husár, H. Wutzel, R. Holman, R. Liska, Strategies to reduce oxygen inhibition in photoinduced polymerization. Chem. Rev. **114**, 557–589 (2014)
15. S.C. Ligon-Auer, M. Schwentenwein, C. Gorsche, J. Stampfl, R. Liska, Toughening of photocurable polymer networks: A review. Polym. Chem. **7**, 257–286 (2015)
16. S.C. Ligon, R. Liska, J. Stampfl, M. Gurr, R. Mülhaupt, Polymers for 3D printing and customized additive manufacturing. Chem. Rev. **117**, 10212–10290 (2017)
17. G. Moad, E. Rizzardo, S.H. Thang, Radical addition–fragmentation chemistry in polymer synthesis. Polymer **49**, 1079–1131 (2008)
18. A. Vitale, J.T. Cabral, Frontal conversion and uniformity in 3D printing by photopolymerisation. Materials **9**, 760 (2016)
19. T. Billiet, M. Vandenhaute, J. Schelfhout, S. Van Vlierberghe, P. Dubruel, A review of trends and limitations in hydrogel-rapid prototyping for tissue engineering. Biomaterials **33**, 6020–6041 (2012)
20. M. Pagac et al., A review of vat photopolymerization technology: Materials, applications, challenges, and future trends of 3D printing. Polymers **13**, 598 (2021)
21. Z. Zhao, X. Tian, X. Song, Engineering materials with light: Recent progress in digital light processing based 3D printing. J. Mater. Chem. C **8**, 13896–13917 (2020)
22. J.R. Tumbleston et al., Continuous liquid interface production of 3D objects. Science **347**, 1349–1352 (2015)
23. A.R. Johnson et al., Single-step fabrication of computationally designed microneedles by continuous liquid Interface production. PLoS One **11**, e0162518 (2016)
24. A. Bagheri, J. Jin, Photopolymerization in 3D printing. ACS Appl. Polym. Mater. **1**, 593–611 (2019)
25. E.J. Murphy, R.E. Ansel, J.J. Krajewski, Investment casting utilizing patterns produced by stereolithography, US4844144A. (1989)
26. C.W. Hull, Method for production of three-dimensional objects by stereolithography, US4929402A. (1990)
27. B. Steyrer, B. Busetti, G. Harakály, R. Liska, J. Stampfl, Hot lithography vs. room temperature DLP 3D-printing of a dimethacrylate. Addit. Manuf. **21**, 209–214 (2018)
28. G. Peer et al., Photopolymerization of cyclopolymerizable monomers and their application in hot lithography. Macromolecules **51**, 9344–9353 (2018)
29. X. Wang, M. Jiang, Z. Zhou, J. Gou, D. Hui, 3D printing of polymer matrix composites: A review and prospective. Compos. Part B Eng. **110**, 442–458 (2017)
30. H. Wu et al., Recent developments in polymers/polymer nanocomposites for additive manufacturing. Prog. Mater. Sci. **111**, 100638 (2020)
31. S.C. Ligon, R. Liska, J. Stampfl, M. Gurr, R. Muelhaupt, Polymers for 3D printing and customized additive manufacturing. Chem. Rev. **117**, 10212–10290 (2017)
32. N. Travitzky et al., Additive manufacturing of ceramic-based materials. Adv. Eng. Mater. **16**, 729–754 (2014)

33. T. Erps et al., Accelerated discovery of 3D printing materials using data-driven multiobjective optimization. Sci. Adv. (2021). https://doi.org/10.1126/sciadv.abf7435
34. E.M. Maines, M.K. Porwal, C.J. Ellison, T.M. Reineke, Sustainable advances in SLA/DLP 3D printing materials and processes. Green Chem. **23**, 6863–6897 (2021)
35. N. Corrigan, J. Yeow, P. Judzewitsch, J. Xu, C. Boyer, Seeing the light: Advancing materials chemistry through photopolymerization. Angew. Chem. Int. Ed. **58**, 5170–5189 (2019)
36. L.J. Tan, W. Zhu, K. Zhou, Recent Progress on polymer materials for additive manufacturing. Adv. Funct. Mater. **30**, 2003062 (2020)
37. C. Mendes-Felipe, J. Oliveira, I. Etxebarria, J. Luis Vilas-Vilela, S. Lanceros-Mendez, State-of-the-art and future challenges of UV curable polymer-based smart materials for printing technologies. Adv. Mater. Technol. **4**, 1800618 (2019)
38. H.N. Chia, B.M. Wu, Recent advances in 3D printing of biomaterials. J. Biol. Eng. **9**, 4 (2015)
39. D. Ahn, L.M. Stevens, K. Zhou, Z.A. Page, Rapid high-resolution visible light 3D printing. ACS Cent. Sci. **6**, 1555–1563 (2020)
40. X. Kuang et al., Advances in 4D printing: Materials and applications. Adv. Funct. Mater. **29**, 1805290 (2019)
41. M. Rafiee, R.D. Farahani, D. Therriault, Multi-material 3D and 4D printing: A survey. Adv. Sci. **7**, 1902307 (2020)
42. A. Andreu et al., 4D printing materials for vat photopolymerization. Addit. Manuf. **44**, 102024 (2021)
43. H.K. Balakrishnan et al., 3D printing: An alternative microfabrication approach with unprecedented opportunities in design. Anal. Chem. **93**, 350–366 (2021)
44. W.L. Ng et al., Vat polymerization-based bioprinting-process, materials, applications and regulatory challenges. Biofabrication **12**, 022001 (2020)

Chapter 3
3D Micro- and Nanostructuring by Two-Photon Polymerization

Ayman El-Tamer, Maria Surnina, Ulf Hinze, and Boris N. Chichkov

Abstract Additive manufacturing (AM) processes have become a resource-efficient and excellent tool for the easy fabrication of complex components from a wide range of materials. Among these AM processes, two-photon polymerization represents one of the most flexible and high-resolution processes, as it enables the full three-dimensional fabrication of complex structures based on CAD models with a resolution of less than 100 nm. The 2PP process is based on the principle of direct laser writing, which uses the nonlinear two-photon absorption at the focus of a femtosecond laser beam to induce a highly localized polymerization of the photosensitive material. Through computer-controlled three-dimensional guidance of the focus, complex structures can be generated directly in the volume of the material; thus, layer-by-layer fabrication, as in many other methods, is not required.

Due to these properties, 2PP opens up new possibilities in the development of novel and miniaturized devices for different applications, so that it is successfully applied in various research areas today. In this chapter, we would like to introduce both the principle of 2PP and the main application areas. In this context, we will highlight the three largest application areas, namely, optics, microfluidics, and biomedicine, and present interesting results that should give the reader a deep insight.

Keywords Nanotechnology · Two-photon polymerization · Additive manufacturing · Microstructures · Femtosecond laser

A. El-Tamer (✉) · M. Surnina
Laser nanoFab GmbH, Hannover, Germany
e-mail: a.el-tamer@lasernanofab.de

U. Hinze
Institute of Quantum Optics, Leibniz University Hannover, Hannover, Germany

Laser nanoFab GmbH, Hannover, Germany

B. N. Chichkov
Institute of Quantum Optics, Leibniz University Hannover, Hannover, Germany

S. L. Marasso, M. Cocuzza (eds.), *High Resolution Manufacturing from 2D to 3D/4D Printing*, https://doi.org/10.1007/978-3-031-13779-2_3

3.1 Introduction

The development of precise additive manufacturing processes has led to enormous progress in micro- and nanotechnology in recent decades. An important contribution to this has been made by two-photon polymerization (2PP), which is one of the most precise and versatile microtechnological 3D manufacturing processes.

2PP is an additive manufacturing process that can be classified in the group of 3D lithography processes and goes back to a work by Maruo, Nakamura, and Kawata from 1997 [1]. It differs from the well-known UV lithography processes by the application of short-pulsed laser radiation in the visible to near-infrared range and by the exploitation of nonlinear effects, namely, two-photon absorption.

With 2PP, 3D structures are created by direct laser writing within the photosensitive material. In this process, a photochemical reaction limited to the focal volume is initiated in the focus of the femtosecond laser beam by two-photon absorption, which solidifies the photo material by polymerization. By computer-controlled three-dimensional movement of the focus through the material, complex three-dimensional geometries can be created in the volume of the transparent photoresist; structural resolutions down to sub-100 nm have been demonstrated [2]. Compared to the typical lithography processes, a strict layered construction can be avoided in this way, allowing greater design freedom (see Fig. 3.1). The high resolution and full three-dimensional access during fabrication are unique features of this technology.

Due to its compatibility with many materials from conventional photolithographic processes, 2PP benefited early on from a wide range of available materials, enabling it to open up a broad spectrum of application areas in a relatively short time. Typical applications of 2PP are characterized by the need for high structure resolution and great structuring flexibility, with structure sizes ranging from a few micrometers to a few centimeters. Typical application areas today therefore include micro-optics, micromechanics, microfluidics, microelectronics, medicine, and biology.

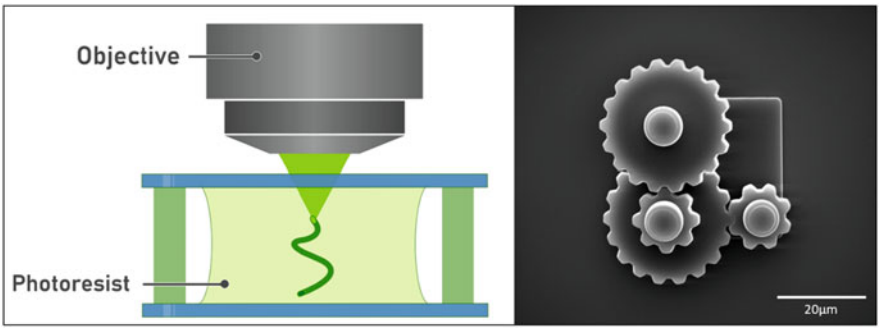

Fig. 3.1 (Left) Illustration of the three-dimensional direct writing process in the volume of the photosensitive material. (Right) SEM image of a micro gearbox produced by 2PP in one step

3.2 Principle of Two-Photon Polymerization

As the name two-photon polymerization implies, the 2PP process is based on a light-induced polymerization reaction that cross-links the photosensitive material used in the exposed area. The polymerization reaction is a radical polymerization with the typical reaction steps of initiation, propagation, and termination.

Photoresists often consist of a mixture of multifunctional monomers to which a small concentration of a photoinitiator is added. In the initiation step, the photoresist is irradiated by laser radiation. As a result of photon absorption, the initiator molecules are homolytically cleaved into free radicals, which act as starters of the radical polymerization reaction. The free radicals are highly reactive and react with the functional groups of the monomer molecules within a short time, thus producing chain radicals that grow in the propagation step by reacting with other monomer molecules until the chain reaction is interrupted in the termination step by disproportionation reactions or combination. In this way, the exposed photoresist is cross-linked and thereby transformed from the liquid state into the solid and insoluble state, which is known as a polymer (see Fig. 3.2).

In the 2PP process, this polymerization reaction is selectively initiated in the volume of the photoresist, which differs significantly from the UV lithography processes. This difference can be explained by the excitation process of the photoinitiator, which, compared to the UV lithography processes, is not based on single-photon absorption but on two-photon absorption.

In the single-photon absorption process, for example (see Fig. 3.3, top left), the energy required for the transition of the photoinitiator molecule from the ground state S_0 to the excited state S_1 is achieved by the absorption of a single photon $h\nu_{UV}$ whose energy corresponds to the energy gap between the two states. The absorption rate therefore depends linearly on the light intensity. For this reason, even low light intensities are sufficient to excite enough photoinitiator molecules to generate radicals, which then initiate the polymerization reaction. Exposure of the photoresist thus leads to polymerization, which spreads from the light entry point

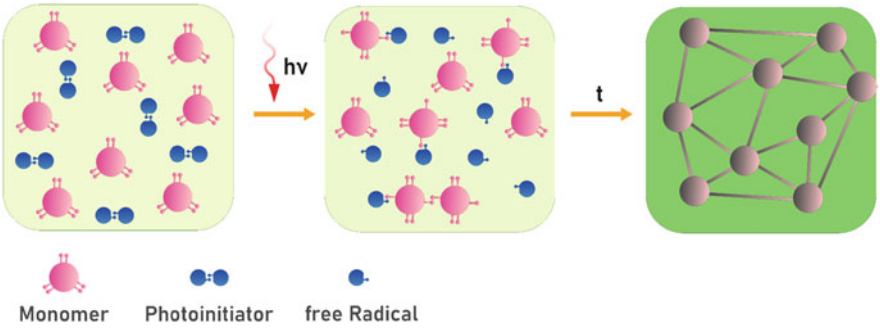

Fig. 3.2 Schematic illustration of the radical polymerization reaction

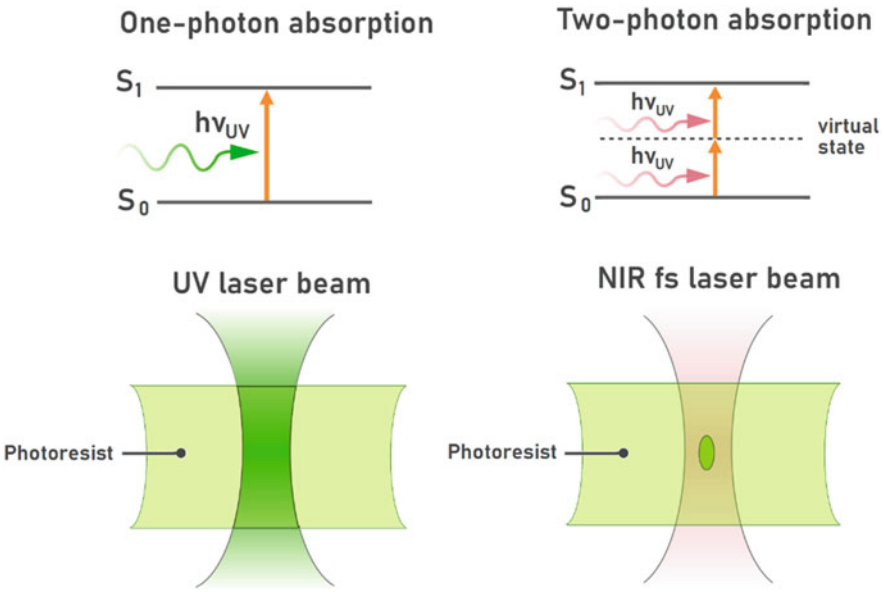

Fig. 3.3 Schematic illustration of the one-photon absorption (left) and the two-photon absorption (right) and their effect on the excitation processes

into the photoresist in the direction of light propagation, thereby curing the entire exposed photoresist after a short time (see Fig. 3.3, bottom left). In this case, three-dimensional structuring (UV lithography process) can only be achieved by building up layers, i.e., by sequentially exposing thin layers of the photoresist.

In contrast to this, two-photon absorption is a nonlinear light-matter interaction process in which two photons $h\nu_{IR}$ participate jointly in the absorption process, whose energies correspond in sum to the energy gap between the ground state S_0 and the excited state S_1 (see Fig. 3.3, top right) [3]. The two-photon absorption can be described by a virtual intermediate state with a lifetime of only a few femtoseconds. The absorption of the two photons must therefore occur almost simultaneously to enable the transition. The absorption rate is thus nonlinear and depends proportionally on the square of the light intensity. For this reason, the transition requires very high light intensities, which are only achieved in the waist of the focused ultrashort pulse laser beam. The initiation process can even be limited to a partial volume of the waist by suitable selection of the laser intensity, so that the polymerization is also limited to this subvolume (Fig. 3.3, bottom right). In this way, it is possible to structure with 2PP by direct laser writing with high spatial resolution within the light-sensitive material. A stringent layering process, as with conventional UV lithography methods, is therefore not necessary, which makes the structuring process very precise and flexible.

The structural resolution in the 2PP process is primarily determined by the microscope objective used and depends directly on its numerical aperture (NA).

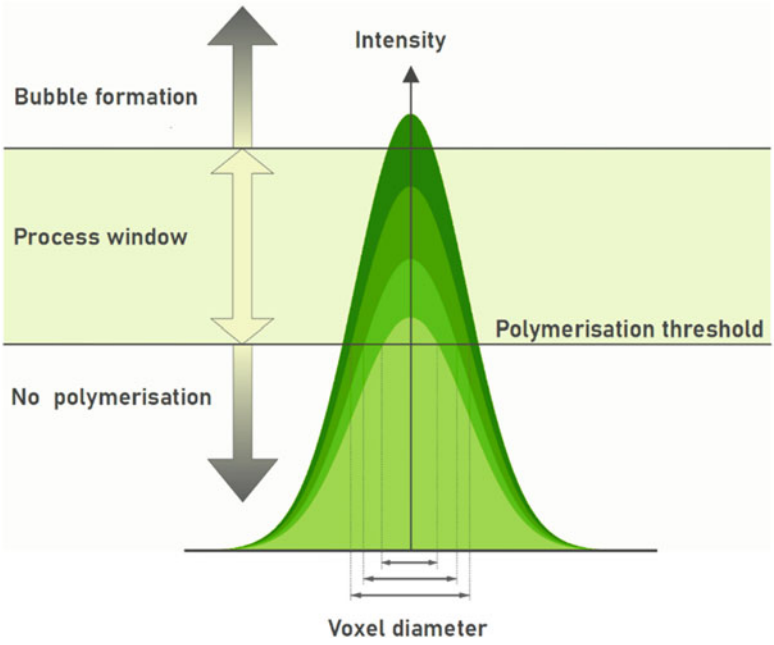

Fig. 3.4 Structure resolution as a function of the light intensity at the focus of the laser beam

The larger the NA, the higher the achievable structural resolution in the process. In contrast to the resolution of UV lithography processes, however, the structural resolution is not diffraction-limited, as it is also influenced by the light-material interaction in the process. In order to take this behavior into account, it is therefore often described by an intensity threshold model, which is based on two light intensity thresholds (see Fig. 3.4). These depend on the material used and define the limits for the process window of polymerization. The lower threshold describes the lowest possible light intensity at which polymerization begins, while the upper threshold indicates the light intensity at which the material begins to burn or the formation of bubbles occurs.

By assuming an approximately Gaussian intensity distribution in the waist of the focused laser beam, the structure resolution within the process window can be determined by the width of the intensity distribution at the height of the polymerization threshold. At a low light intensity, where only the peak of the intensity distribution exceeds the polymerization threshold, polymerization is also only induced in this small inner subregion of the focal volume, so that the structure resolution is below the diffraction limit. If the light intensity is now increased, the width of the intensity distribution increases, so that the polymerized volume also increases in size. This behavior applies to both the lateral and the axial structure resolution. The polymerized material volume in the focus is expanded in the lateral

and axial direction and has the shape of an ellipsoid, which is called a voxel (volume pixel) in analogy to the pixel.

According to this simplified model, unlimited structure resolution would be conceivable. However, this is limited by the material stability at low light intensities, because the degree of cross-linking of the polymers is reduced in this case, so that the structures thus created collapse or cannot withstand the subsequent process steps.

3.3 2PP Manufacturing Process

In 2PP, different sample configurations are used today, which are optimally chosen depending on the application and the viscosity of the resist used. For low-viscosity photoresists, the material is usually filled between two thin cover glasses which are separated by spacers (see Fig. 3.5a). For high-viscosity photoresists, on the other hand, it is sufficient to apply a drop of the material to a glass substrate (see Fig. 3.5b). For particularly tall structures or applications where the 2PP structure needs to be integrated into an existing sample, methods such as dip-in or wider objective working range (WOW-2PP) are also popular (see Fig. 3.5c), where the lens is dipped into the liquid photoresist to create the structure at a specific location [4, 5].

In order to build the structure, the 3D model of the desired structure is converted into movement coordinates by the control software and provided with laser switching positions. For this purpose, the model is divided into layers of defined thickness and each individual layer is further divided into individual paths with a defined path spacing. During the structuring process, the laser focus is moved in the sample along these predefined trajectories to build up the structure in the volume (see Fig. 3.6). After the structuring process, the unexposed photoresist is removed from the polymerized structures in a development process using a suitable solvent.

3.4 2PP Setup

The technical capabilities of a 2PP system are essentially determined by the optical system and the positioning systems used. The first necessary prerequisite to enable two-photon polymerization is the supply of the required light intensities for two-photon absorption. This therefore necessitates the use of pulsed laser systems, so that femtosecond lasers are usually used in 2PP, which emit pulsed radiation with a pulse length of a few 10 fs to a few 100 fs at a repetition rate in the MHz range. The advantage of this short-pulsed laser radiation is the large peak pulse intensity with simultaneously small pulse energy. The peak pulse intensity in the focus reaches several 100 kW/cm^2 up to several TW/cm^2, while the pulse energy ranges only from nJ to μJ. Thus, the light intensities required for the 2PP process can be provided

without a high average energy input into the material. In practice, Ti-Sa lasers (800 nm) are often used; about two-thirds of the published papers are based on this type of laser. Currently, however, frequency-doubled erbium and ytterbium-doped fiber lasers (780 nm and 520 nm, respectively) are also increasingly being used.

In order to generate three-dimensional structures with 2PP, the resist and laser focus have to be moved relative to each other. In principle, this can be achieved either by moving the sample relative to the fixed laser beam with a positioning system (see Fig. 3.7a), by deflecting the laser beam with a galvanometer laser scanner (see Fig. 3.7b) or by a combination of both methods (see Fig. 3.7c). All concepts have different advantages and disadvantages and are widely used today.

Galvanometer laser scanners are usually used when particularly fast beam deflection is required. Due to the low mass of the small deflection mirrors, a very dynamic beam deflection is possible, so that high writing speeds can be achieved. A disadvantage of using galvanometer scanners, however, is the limited scanner field of view, which is also dependent on the focusing optics. The laser focus can therefore only be guided within this scanner field of view. Structures that are larger than the scanner field of view must therefore be created using a stitching method (Fig. 3.7b). This means that the structure must be assembled piece by piece by creating a section and then moving it out of the field of view so that another section can be connected. This usually results in visible connection points and stitching

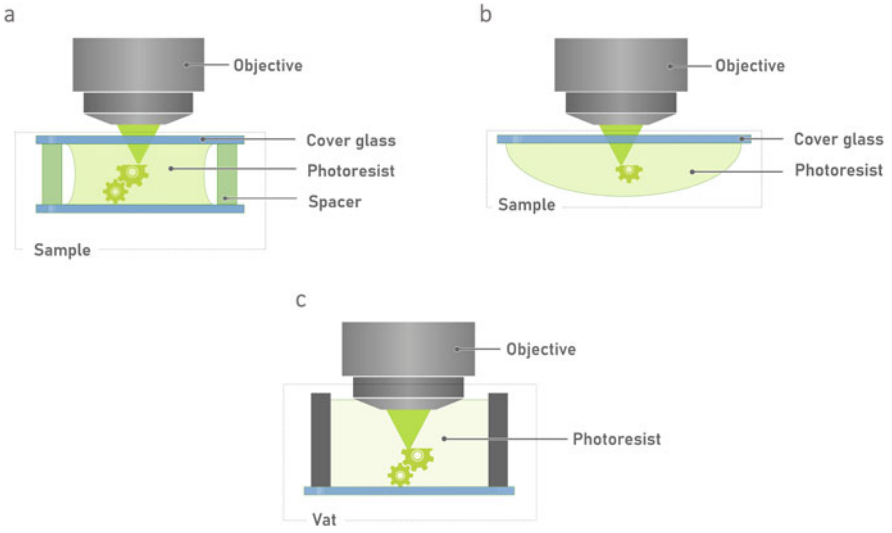

Fig. 3.5 Schematic illustration of the different sample configurations in 2PP. (**a**) Sandwich configuration: for low viscosity resists, the material is filled between two thin cover glasses and the structure is written in contact with the lower glass. (**b**) Drop configuration: for high viscosity resists, a drop is applied to a cover glass and the structure is written freely into the volume. (**c**) Vat configuration: the lens is dipped into the vat and the structure is written in contact with bottom of the vat

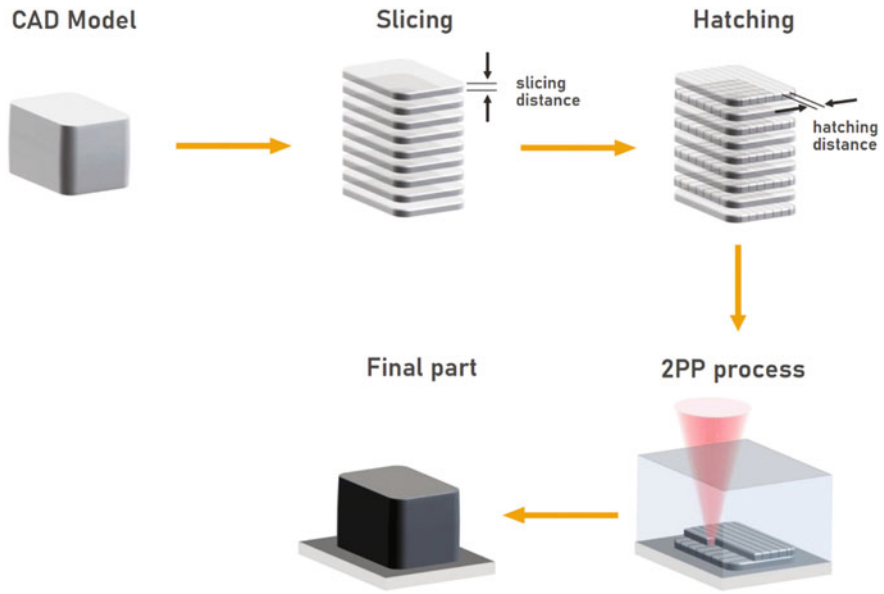

Fig. 3.6 Illustration of the individual process steps in 2PP manufacturing starting with model preparation through to the development process of the finished structure. (Adapted with permission from Springer Nature Customer Service Centre GmbH: Springer Interna-tional Publishing AG, 3D Mikro- und Nano-Strukturierung mittels Zwei-Photonen-Polymerisation by Ayman El-Tamer, Ulf Hinze, Boris N. Chichkov, Copyright 2017)

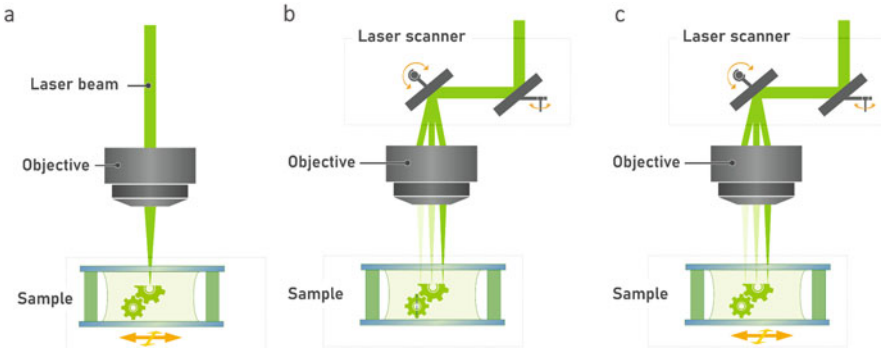

Fig. 3.7 Illustration of the different writing approaches in 2PP. (**a**) Static laser beam approach: writing is achieved by moving the sample relative to the static laser beam with an axis system. (**b**) Galvo scanner approach: writing is performed by moving the laser focus within the static sample with a galvanometer scanner. (**c**) Combined approach: writing is realized by synchronized movement of the scanner mirrors and axis system

errors. By using focusing optics specially designed for this processing concept (so-called F-theta lenses), the stitching errors can be reduced.

On the other hand, if it is important to avoid connection points or stitching errors during structuring, then alternatively the laser beam can be kept static and instead the sample can be moved against the laser beam with a positioning system (Fig. 3.7a). In this way, the laser focus can be guided within the travel range of the axis system without interruption, so that large structures are created without stitching. The disadvantage of this method, however, is the longer process time. The reason for this is the relatively large mass of the positioning axes, which cannot be accelerated as dynamically as the deflection mirrors in a scanner.

In order to exploit the advantages of these two methods, the movement of the scanner and axis system can be performed synchronously at the same time. Structuring is done with the scanner while the sample is simultaneously moved with the axis system (Fig. 3.7c). In this way, the structuring can be performed at high writing speed while reducing stitching errors and connection points. These are avoided in the direction of movement of the axes, so that they can only occur perpendicular to this direction of movement.

To meet the high precision and resolution requirements of the 2PP process, elaborately designed three-axis positioning systems are used that achieve a controlled positioning accuracy of better than 5 nm. The spectrum of positioning systems ranges from systems with air bearings and direct drives, which have travel ranges in the cm range and are scalable far beyond that, to very compact units with piezo drives that realize a travel range from 10 μm to several centimeters. The achievable writing speed of precise positioning systems is usually well below 1 m/s, with piezo systems usually up to a few cm/s.

For homogeneous processing of the material, it is important that the same laser energy is applied at every point in the photosensitive material. Therefore, the movements of the positioning system during the polymerization process should take place at a controlled, uniform speed. If complex three-dimensional path curves are to be traced, for example, to create the contours of lens-shaped elements, the positioning system should also have precise path control. Other elements of the optical system are used to control the properties of the laser beam. These include beam shaping, fast optical laser switches, and precise control of the laser energy delivered to the 2PP process.

In order to control which areas in the material are to be polymerized and which are not, it is necessary to be able to switch the laser beam on and off quickly and synchronously. The faster and more precisely this can be realized at the desired positions in the material, the more precisely a structure can be built and the higher the process speed can be scaled.

Based on this knowledge, a system can be optimized depending on the application, e.g., for the highest resolution, shortest process time, or specific processes and materials. However, in order to enable great flexibility in 2PP processing and thus make 2PP usable for a wide range of applications, a 2PP system must have different specifications than a system optimized for a specific application. For example, it is necessary for such a 2PP system to have an axis system with a large travel range that also has a particularly high positioning accuracy in order to achieve a large processing space. In this way, 2PP structures can also be integrated into

prefabricated components as part of integration processes without the processability being restricted by the size of the components.

A further specification that is of great importance for a wide range of applications is the possibility to use different lenses with different resolutions. While in 2PP the highest possible resolution is usually placed in front as an important criterion in the specifications, lower resolutions, on the other hand, are often hardly addressed. However, a low resolution is of great importance for applications where the size of the structure or the throughput at low resolution are of primary importance. This is because significantly larger structures can be created in a much shorter process time at lower resolutions. However, the possibility of using lenses with a smaller NA is not trivial and is associated with further technical requirements. First and foremost, there is the question of the maximum laser power available. In the case of low-power lasers, the necessary intensities can hardly be achieved with a small NA, so that the process has to be operated at very slow writing speeds or even comes to a complete standstill. In the case of large F-theta lenses, this is usually exacerbated by the fact that large working distances are sometimes required and, in addition, higher masses of the lenses have to be moved. For a flexible system, particularly powerful and precise axis systems with a large z-travel range must be combined with precise and fast scanner systems and powerful femtosecond lasers, which makes such 2PP systems significantly more complex and expensive.

One way in which such a system concept can be realized is described here using the M4D system type from the company Laser nanoFab GmbH (see Fig. 3.8). The system has an air-bearing high-performance nano-positioning axis system with a travel of more than 10 cm in each spatial direction, with a nm-positioning accuracy.

Fig. 3.8 View of a commercial 2PP system (M4D by Laser nanoFab GmbH)

In order to achieve very high writing speeds, the axis system is supplemented by a high-precision scanner system with two axes. This combination achieves a particularly large processing space, which is accessible for all structuring methods due to the five-axis principle. The 2PP system can be equipped with either one or two femtosecond lasers, with wavelengths of about 515 nm and 780 nm and powers starting at 500 mW. A wide range of objectives allows both low-resolution and high-resolution 2PP structuring processes to be operated. In addition, this type of system is equipped with the WOW-2PP process so that the focusing optics can also be immersed in the liquid resist.

3.5 Applications and Materials

Today, two-photon polymerization is established as an additive manufacturing process in research areas where high structural resolution and full three-dimensional processing are particularly important. Notable industrial applications are not recorded at the present time, mainly because of the long production times for large and high-resolution components. Typical applications of 2PP can be found in the fields of micro-optics, micromechanics, microfluidics, microelectronics, medicine, and biology. For this purpose, a wide range of commercially available materials with well-characterized properties are available today.

In this chapter, we would like to explore the benefits of 2PP in the fields of optics, fluidics, and biomedicine and present outstanding applications and results in these fields to give the reader a deep insight into 2PP and its applications.

3.5.1 Micro-optical Components

The increasing miniaturization and higher integration of optoelectronic components are reflected in our society in many technical areas. In optical technologies in particular, classical manufacturing processes such as diamond turning, electron beam lithography, selective chemical etching, grey tone lithography, and many other processes for the production of novel micro-optical components are increasingly reaching the limits of feasibility. For miniaturization and higher integration, highly developed optical designs are required, which in many cases far exceed the possibilities of classical technologies. For example, most processes are limited to a few standard geometries, they offer only limited possibilities for miniaturization, they do not allow the combination of several elements, or due to their low flexibility, they have limitations in the design of free-form surfaces. They are therefore limited in their ability to design and manufacture novel and powerful micro-optical components.

With the introduction of two-photon polymerization into the optical field, the simple production of two-dimensional and three-dimensional micro-optical

elements with highly transparent photoresists and a resolution down to the sub-100 nanometer range was made possible. This has not only boosted the ongoing trend towards miniaturization, it has also paved the way for the production of complex optical elements in the field of micro- and nano-optics. 2PP therefore contributes to far-reaching developments in many areas of optics. A large number of different micro- and nano-optical components have been successfully demonstrated in recent years. These include refractive free-form surfaces, optical waveguides, photonic crystals, diffractive elements as well as hybrid diffractive-refractive elements, and optical systems consisting of several components.

In the field of micro-optical elements, optics with free-form surfaces represent a special attraction for modern optics. Free-form optics offer an extraordinary freedom of design and are increasingly used as on-chip optics or in combination with fiber optics to create miniaturized and powerful optical systems with outstanding optical properties. Applications such as imaging, beam collimation, beam shaping, aberration correction, or polarization control are significantly enhanced by such free-form optics. In particular, free-form optics consisting of several lenses have significantly better imaging properties than comparable optics with spherical lenses and can substantially reduce aberrations when recording at large angles. However, their production on single-mode and multimode fibers with specific design goals is almost impossible with conventional manufacturing processes due to their small dimensions. 2PP therefore opens up new possibilities for the construction of new optical miniature instruments such as endoscopes, fiber imaging systems, and new illumination systems, whereby the time required from the design of the optical system through production and testing to the finished optical system can be limited to a few hours.

Different groups have presented the combination of free-form optics with single-mode and multimode fibers. Gissibl et al. presented, for example, various multi-lens objectives that were manufactured directly on the tips of single-mode fibers and on CMOS image sensors from IP-S (Nanoscribe GmbH) [6]. These multi-lens objectives consist of different free-form lens elements separated by an air gap and have a diameter of about 120 μm and a height of 100–200 μm (see Fig. 3.9a, b, and e). In a further publication, the same group also presented collimation optics (Fig. 3.9c), toric lenses, free-form surface optics for intensity beam shaping (see Fig. 3.9d), and chiral photonic crystals for circular polarization filtering that were aligned and built directly on the end facet of single-mode fibers from IP-Dip and IP-S (Nanoscribe GmbH) [7].

Bianchi et al. also demonstrated a parabolic reflector fabricated on the end facet of a multimode fiber made of a diacrylate monomer with a thioxanthone photoinitiator [8]. The design achieves a high numerical aperture and is not dependent on refraction. Thus, the focusing is not dependent on the refractive index of the immersion medium, which in turn realizes a fixed-focus position, both for laser focusing and for imaging in different materials.

A further field of application in micro-optics is represented by diffractive optical elements (DOEs) or combined diffractive-refractive optical elements. Such elements are used, for example, for wavefront shaping, phase matching, or polarization

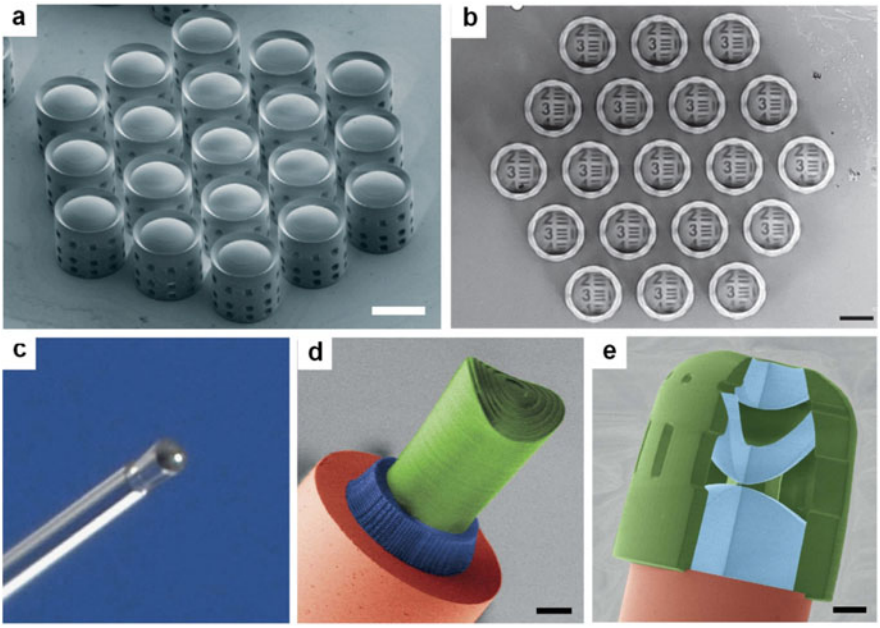

Fig. 3.9 (**a**) Scanning electron microscope image of the hexagonal lens arrangement. Each doublet lens system has a diameter of 120 μm and a height of 128 μm. Scale bar, 100 μm. (**b**) Image of a part of the USAF 1951 resolution test chart at a distance of 30 mm taken through a hexagonal lens arrangement. The image section consists of 640 × 480 pixels. Scale bar, 70 μm = 50 pixels. (Reprinted with permission from Springer Nature: Nature Photonics [6], Copyright 2016, advance online publication, 27 June 2016 (doi: 10.1038/NPHOTON)). (**c**) Macro photograph of a lens that collimates a Gaussian beam emerging from a single-mode fiber. (**d**) Colored scanning electron microscope image of a model device manufactured by three-dimensional direct laser writing. On top of the end facet of an optical fiber (red), a chiral photonic crystal structure (blue) for polarization control and a free-form lens with Fresnel zone plate (green) for beam shaping are placed. The optical components are fabricated by two different photoresists. Scale bar, 25 μm. (**e**) Colored scanning electron microscope image of a model device that consists of three free-form lenses (blue) and could be used on a fiber. Scale bar, 25 μm. (Reprinted from [7],licensed under CC BY 4.0, License at http://creativecommons.org/ licenses/by/4.0/)

control. In terms of miniaturization, diffractive optical elements and geometric optical phase elements offer enormous advantages over refractive optics because they can perform similar tasks with a significantly lower structure height. DOEs generate a spatial phase shift due to their surface profile and can therefore be used for focusing and beam shaping. The special feature of geometric optical phase elements is that they can impose any phase profile on an incident light field using purely geometric means. Optical elements made of dielectric materials, in particular, have great application potential due to their high transparency and long lifetime. However, their production has to date been realized with very cost-intensive nanofabrication processes such as electron beam lithography, focused ion milling and atomic layer deposition of dielectric layers, or with less flexible

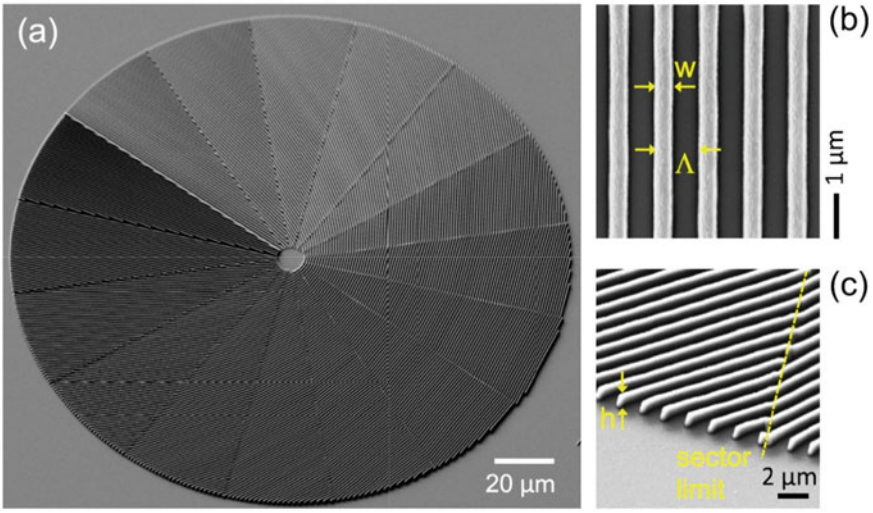

Fig. 3.10 (**a**) 45°-slanted SEM image of a 16-step 1/2 plate of diameter 200 µm. Note that surface charging alters the imaging contrast. (**b**) Top view SEM image of the local photopolymerized grating characterized by the filling factor $w/\Lambda \approx 0.3$. (**c**) SEM image at the rim of the element, where $h = 1$ µm is the height of the structure. (Reprinted from Ref. [9], with the permission from AIP Publishing)

processes such as diamond turning, grayscale, or mask lithography. Compared to these manufacturing processes, 2PP is a much more flexible process, which can be used much more cost-effectively, especially in the field of prototyping. 2PP also allows scaling of the components and is therefore not limited to microscopic flat optics.

In recent years, various groups worldwide have been working on the use of 2PP in this area. Wang et al. were able to successfully produce various geometric optical phase elements on the basis of the photoresist SZ2080 (Fig. 3.10) [9]. Gissibl et al. have also produced DOEs for the generation of different intensity patterns on glass fiber end facets using IP-Dip (Nanoscribe GmbH) [10], as in their work on refractive optics on glass fiber. Recently, the construction of binary and multilevel to continuous DOEs by means of 2PP, especially in combination with refractive optics, has received special attention. Binary or two-level DOEs can be used to generate any longitudinal intensity distribution that is of great importance for many laser technology applications. Osipov et al. and Pavelyev et al. have presented various DOEs in their work which can be used to generate, e.g., uniform longitudinal intensity distributions (axial light segment) [11], or bottle-shaped intensity distributions (light bottle) [12]. In these publications, they used the well-known materials mr-NIL 6000 from Micro Resist Technology GmbH and SU-8 from MicroChem Corp. However, binary DOEs have the disadvantage of reduced diffraction efficiency. For a higher diffraction efficiency, it is therefore

necessary to build DOEs from multilevel or continuous microreliefs, as impressively demonstrated by Pavelyev et al. and Yu et al. using the SU-8 photoresist [13, 14].

Combinations of diffractive and refractive optical elements have been considered particularly attractive for a long time, since they can combine the properties of diffractive and refractive optical elements in one optical component, thus enabling the construction of very powerful optical systems that cannot be realized with purely diffractive or refractive optics alone. Diffractive-refractive trifocal lenses are an important example of such an optical element. They are of great importance for medicine because multifocal intraocular lenses (IOLs) can be produced according to their principle. Trifocal intraocular lenses are of particular relevance for the therapy of patients suffering from cataract (clouding of the crystalline lens in the eye), as they offer as lens implants a good alternative to the natural eye lens, because in comparison to monofocal IOLs they enable the patient to see sharply at different distances after surgery. In 2012, Osipov et al. presented in their paper the construction of a trifocal lens consisting of a spherical glass lens and a DOE that was produced using SU-8 (Gersteltec Engineering Solutions). For this purpose they arranged both components in a small distance behind each other, so that two further focuses could be generated by the DOE in addition to the focus of the glass lens [15]. Based on this principle, Hinze et al. demonstrated in 2016 a trifocal lens consisting of a single element [16]. They combined a DOE made of mr-NIL 6000 (Micro Resist Technology GmbH) and an aspherical lens from OrmoStamp (Micro Resist Technology GmbH) by building the lens onto the back of the DOE using a molding process (Fig. 3.11). In this way, they were able to significantly reduce the process time during the fabrication of the diffractive-refractive trifocal lens, since only the relevant DOE had to be built with the aid of 2PP.

A further example of the beneficial use of diffractive optics comes from photovoltaics. In photovoltaics, fundamental loss mechanisms set an upper limit for the efficiency of photovoltaic (PV) cells. The efficiency of today's single-junction PV cells is well below 30%. The reason for this is the relatively narrow wavelength range in which the PV cell can efficiently convert photon energy into electrical energy. Single-junction PV cells consist of a semiconductor with a single defined bandgap, so that photons with energies smaller than this bandgap cannot be absorbed, while photons with energies larger than this bandgap lose their excess energy through heat dissipation. Possible solutions to increase the yield therefore aim to build multijunction solar cells from materials with different bandgaps in order to convert the entire light spectrum. However, such tandem or multijunction cells consist of several vertically arranged subcells, which are particularly cost-intensive and difficult to manufacture. Inspired by this problem, Xiao et al. presented an interesting solution for the production of cost-effective and highly efficient solar cells [17]. In their approach, they used 2PP to create a specially designed planar dispersive diffractive optical element from IP-Dip photoresist which serves as a structured surface of a novel PV cell to spectrally split the incident sunlight perpendicular to the direction of propagation. In this way, the spectrally separated light underneath the element can hit adjacent subcells, which are designed for the respective wavelength. This model makes it possible

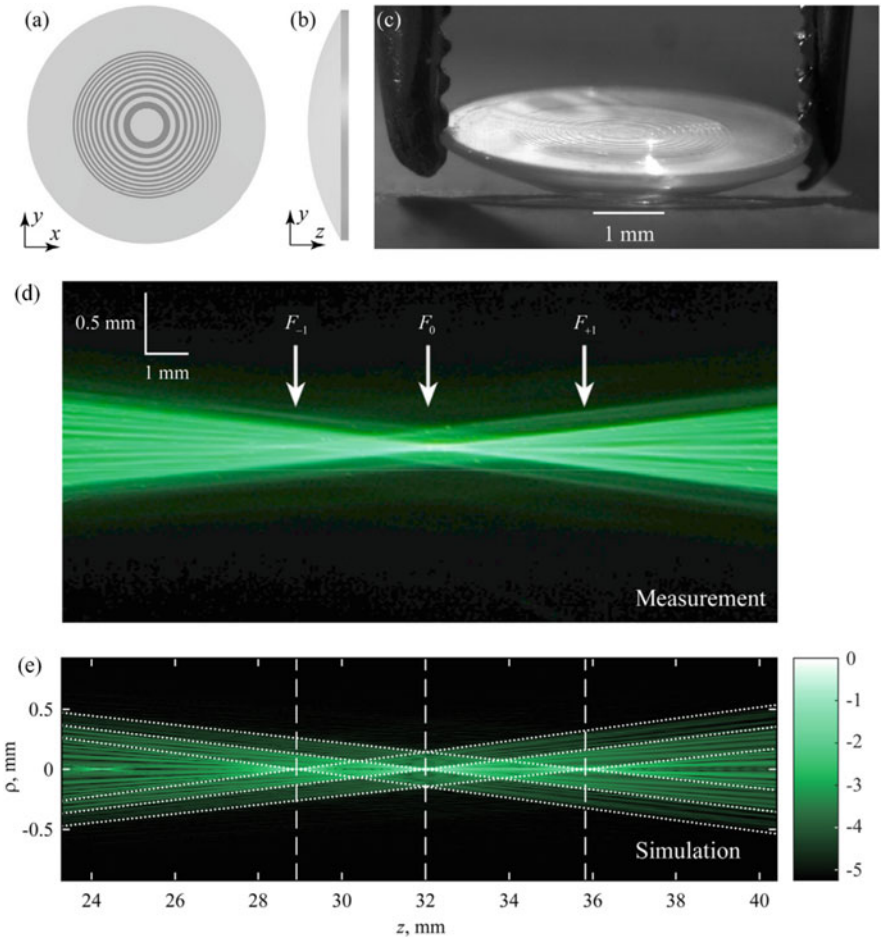

Fig. 3.11 Refractive lens and multifocal diffractive zone plate combined in one optical element: (**a**) schematic top view of the plane side of the plano-convex lens with the diffractive relief, (**b**) schematic side view of the lens, and (**c**) the photograph of the fabricated element held with tweezers. (**d**) Propagation of the probe after passing through the multifocal lens. The main focus F0 and the foci F−1 and F+1 generated by the lens element are indicated. The photo was post-processed for better print reproduction (condensed along optical axis, enhanced contrast) and (**e**) theoretically calculated distribution plotted with a logarithmic (base10) color map. Dashed lines indicate the positions of the foci, and dotted lines show the geometrical boundaries of the spherical beams converging to the designed foci. (Reprinted from Ref. [16], copyright 2016, with permission from Elsevier)

to produce highly efficient PV modules in a simple way, because the horizontal arrangement of different semiconductor materials is particularly easy and, above all, less expensive to implement than the layered arrangement (Fig. 3.12). The use of 2PP also gives special design freedom for designing and manufacturing planar

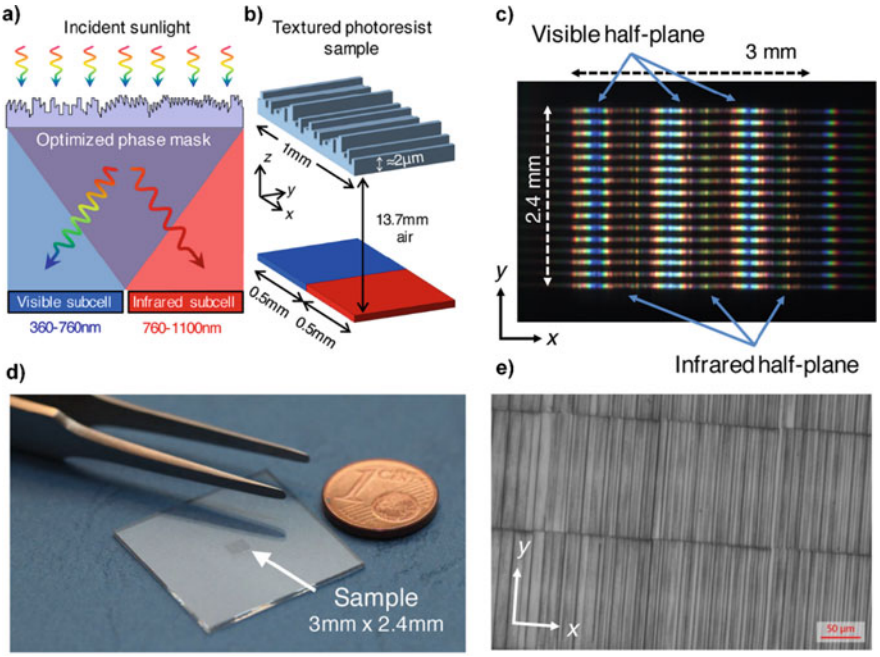

Fig. 3.12 (**a**) A thin diffractive phase mask element is designed to laterally split the solar spectrum into two spectral bands and direct each band to separate partitions in the far-field image. (**b**) Diagram of the optical structure designed in this work showing geometric parameters. (**c**) Visible CCD image of the sample in the far field, showing lateral splitting of the spectrum from three periods of the phase mask texture. (**d**) Photograph of the fabricated phase mask sample. (**e**) Scanning electron microscopy (SEM) image of a portion of the sample, showing 5-µm-wide strips of constant height. Dark horizontal lines mark the separation between stitched areas. (Reprinted with permission from Ref. [17]. Copyright 2016, American Chemical Society)

dispersive diffractive optics, which can be supplemented by molding processes for series production, e.g., to multiply the optics produced in a fast, simple, and cost-effective way. This example impressively shows how 2PP can also be used for large-scale industrial purposes.

Last but not least, in this chapter we would like to focus on a further very interesting area of 2PP application, namely, the production of waveguides or waveguide connections. Optical waveguides are becoming increasingly important in optical communication. This is due to the exponentially increasing data rates in information processing, which are continuously pushing electronic circuits to their physical limits in terms of bandwidth and spatial density. Approaches such as silicon photonics platforms are therefore regarded as one of the most promising options for enabling high data rates in the future. However, while the development of such silicon-on-insulator (SOIs) circuits is making enormous progress in the on-chip integration of complex photonic circuits, interchip connectivity still poses major challenges. The main reason for this are the two-dimensional manufacturing

processes used for manufacturing, such as electron beam lithography or UV lithography. The disadvantage of these technologies is that they do not provide satisfactory waveguide interconnect solutions for the development of complex photonic systems from different chips. While wire bonding is well established in the electronics industry as a technique for building electrical interconnections, photonic systems suffer from a lack of a comparable solution, since approaches for the construction of waveguide connections for large-scale industrial purposes have to offer similar possibilities in terms of flexibility and throughput as wire bonding.

In recent years, two-photon polymerization (2PP) has proven to be an extremely powerful tool for this application. Various publications have shown that 2PP is particularly suitable for the production of three-dimensional waveguides. This is because it combines three of the most significant properties for this application: 3D compatibility, great design flexibility, and submicron resolution. The question of light coupling is of great relevance for photonic applications, since for the operation of integrated photonic circuits, the lowest possible power losses during coupling are of elementary importance. Therefore, Lee et al. demonstrated a concept of vertically standing and curved waveguides which are suitable for coupling light that is incident perpendicular to the plane into planar waveguides and thus into photonic circuits or sensor arrangements [18]. The group investigated waveguides with different arc radii and diameters as well as different suspended splitter with defined splitting ratios (Figs. 3.13 and 3.14). They were able to fabricate them using IP-L (Nanoscribe GmbH) and show that coupling losses of only 1.5 dB are possible with their approach. This makes it clear that 2PP has the potential to solve these existing problems in the field of integrated photonic circuits.

The key approach for simple fiber coupling or interchip connectivity, however, was provided by the studies of Lindemann et al. With the help of 2PP, they succeeded for the first time in demonstrating photonic wire bonds (PWBs) that in many respects resemble wire bonds in electronics [19]. This technique made three-dimensional chip-to-chip connections possible, with which the group demonstrated a PWB connection between integrated SOI waveguides for the first time and was able to prove its function by experiments on data transmission. In their concept,

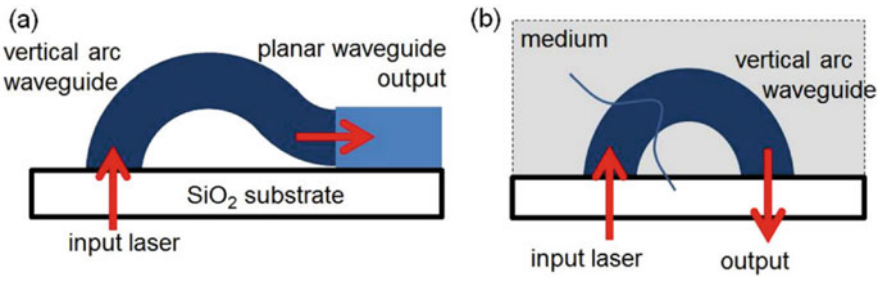

Fig. 3.13 Schematic design of vertical arc waveguides. (**a**) Vertical to inplane light coupling to planar waveguide circuits. (**b**) Evanescent-wave sensors for bio- and environmental sensing. (Reprinted from Ref. [18], with the permission from AIP Publishing)

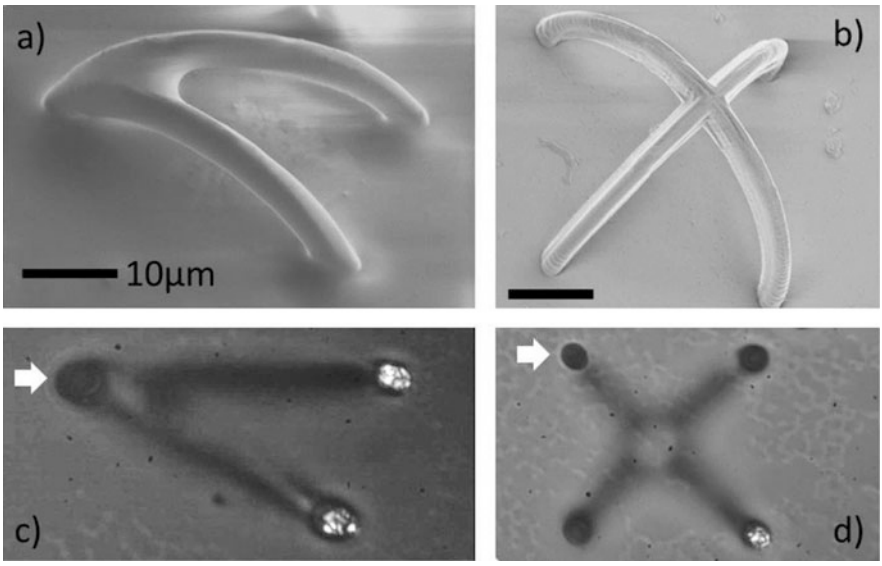

Fig. 3.14 (**a** and **c**) Three-way and (**b** and **d**) four-way splitters produced from intersecting vertical arc waveguides. Scale bars are 10 µm. (**c** and **d**) Input ports marked with white arrows, producing output beams as imaged. (Reprinted from Ref. [18], with permission from AIP Publishing)

integrated photonic subsystems and optical fiber ends are mounted on a carrier and embedded in the photoresist SU-8 2075 (MicroChem). After measuring the relative positions of the integrated waveguide facets, adapted PWB geometries are calculated and built using 2PP (Fig. 3.15). The unexposed resist is then removed in a development step and replaced by a low index material. In this way, no high-precision alignment of the components is necessary, which is of great importance for fully automated industrial production. In further work, the group also demonstrated connections between photonic chips with three-dimensional freeform photonic wire bonds that can transmit a wavelength division multiplexing (WDM) signal with 5.25 Tbit/s aggregate data rate without measurable signal degradation [20], as well as the highly efficient coupling between multicore fibers and planar photonic silicon circuits [21].

In a paper by Schumann et al., it was also shown that 2PP can not only be used for the construction of precise and low-loss waveguides, it can also be used to easily construct other three-dimensional photonic components, such as polarization-rotating components and optical resonators, and integrate them into photonic circuits using IP-Dip (Nanoscribe GmbH) photoresist (Fig. 3.16) [22]. This allows the full three-dimensionality to be introduced into the planar photonic circuits, thus enabling the realization of high-performance optical on-chip components of the next generation.

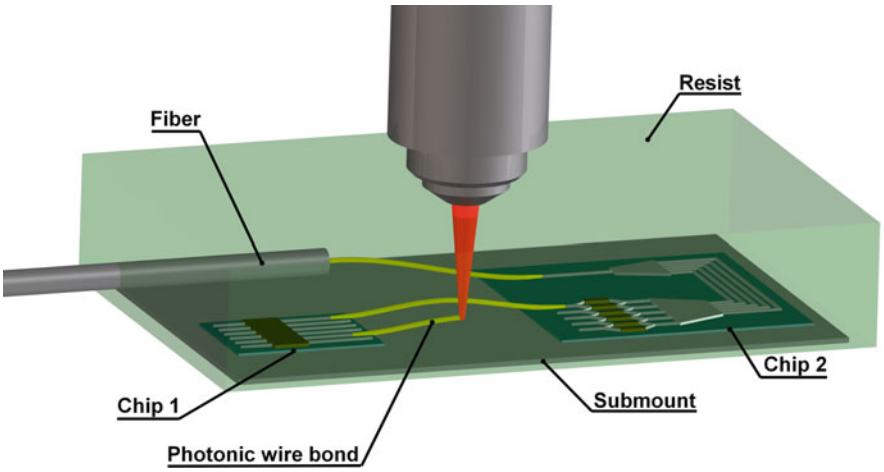

Fig. 3.15 Schematic illustration of a photonic multichip system based on photonic wire bonding: photonic chips (chip 1, chip 2) and optical fibers are mounted on a common submount and embedded into a photosensitive resist. Two-photon polymerization in the focus of a pulsed laser beam is then used to define three-dimensional freeform photonic wire bond (PWB) structures in the volume of the resist. (Reprinted with permission from Springer Nature Customer Service Centre GmbH: Springer International Publishing AG, Two-Photon Polymerization in Optics, Microfluidics, and Biomedicine by Ayman El-Tamer, Ulf Hinze, Boris N. Chichkov, Copyright 2020)

All of these studies have clearly shown that 2PP can play an important role in the field of integrated photonic circuits in order to eliminate existing limitations in the production of waveguide connections and light coupling.

3.5.2 Microfluidics

Microfluids differ considerably in their behavior from macroscopic fluids, because effects that are negligible in classical fluid mechanics can become dominant on the microscale. At low Reynolds numbers, for example, friction forces and capillary forces are more dominant than inertial forces or weight forces. This leads to a negligible gravitational force when transporting very small quantities of liquid and to laminar flows without significant turbulence. The mixing of microfluids is therefore only possible by diffusion or by technical means. Microfluidics is mainly represented by lab-on-a-chip (LOC) technology, which today plays an increasing role in the natural sciences, materials science, pharmacy, and medicine. For analyses in biomedicine, for example, LOC devices can be set up that combine several laboratory functions on a single chip. These offer a significant advantage over conventional analytical methods because they do not only reduce the sample volume, but also lead to major time and cost savings. In recent years, microfluidic

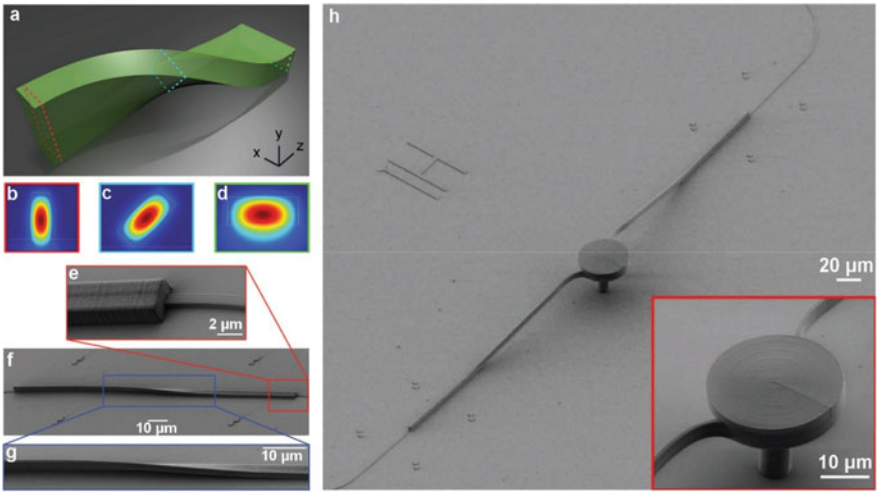

Fig. 3.16 Broadband polarization conversion. (**a**) Scheme showing the principle of operation of the mode evolution-based polarization rotator. As the cross section of the rotator is twisted, the mode is expected to rotate as well. (**b**–**d**) COMSOL FEM simulations of electric field mode profiles at the positions marked in (**a**). (**e**–**g**) SEM images of the fabricated polarization rotator connecting two facing tapered nanophotonic waveguides. FEM, finite element method; SEM, scanning electron microscope. (**h**) Disk SEM images of the fabricated bridge waveguide and disk resonator coupled to a nanophotonic silicon nitride circuit. *DLW* direct laser writing, *SEM* scanning electron microscope. (Reprinted with permission from Springer Nature Customer Service Centre GmbH: Springer International Publishing AG, Light: Science & Applications, [22], Copyright 2014)

systems have therefore become increasingly important in biomedical research and are now widely used in various fields such as synthesis, analysis, sensor technology, and catalysis.

Typical manufacturing processes for LOC chips comprise technologies such as photolithography in combination with etching processes, stereolithography, soft lithography, nanoimprint lithography, injection molding, laser ablation, or femtosecond laser-assisted wet etching of glass. While soft lithography has so far been the method of choice for small series production, the importance of additive manufacturing processes, such as 3D printing, is currently increasing. This is because 3D printing simplifies the production process and also delivers reproducible results, which is of particular interest for prototype construction. It also enables the production of complete microfluidic systems in a single step that does not require any further assembly steps.

Two-photon polymerization (2PP) is of elementary interest for the field of microfluidics due to its high flexibility and submicrometer resolution, especially with regard to the constantly growing trend towards miniaturization of components and the increasing integration of complex functions. Compared to other 3D printing processes, however, it does not represent an economical solution for the design of

large, low-resolution fluidic components. Its main field of application is therefore the fabrication and integration of small high-resolution fluidic components. The fabrication of integrated active and passive microscale components is of elementary importance for the development of novel microfluidic chips, as they extend the functional range of complex LOC systems and thus open up new fields of application.

Examples of such microfluidic structures can be found in various fields of research. In LOC technology, filters and mixers are among the most important functional devices. In particular, filters with predefined pore size have a large number of applications in the biological and biochemical fields, as they simplify the separation and sorting of fluid particles and are therefore of particular interest for analysis applications. Such filters can be used, for example, for isolating blood plasma, removing red and white blood cells, or sorting cells and particles according to different sizes. Today, different methods can be used for their production, whereby these methods differ in their 3D capabilities. Due to their inherent two-dimensional properties, for example, standard photolithographic methods can only be used to a limited extent for three-dimensional constructions. They can be used, for example, to produce filters from periodic structures, whereby the pore size can only be defined in two dimensions, namely, the distance between the structures in the plane. As a result, the filters have limited mechanical stability and the pore size for filtering nonspherical particles, such as red blood cells, must be smaller than the smallest dimension of the particles, which places high demands on the process resolution. In comparison, 2PP can be used to create three-dimensional filters that can be defined arbitrarily in all three dimensions, which leads to a higher density of the connection points due to the three-dimensional structure and thus to significantly higher mechanical stability. In addition, the required process resolution is smaller due to the fully adjustable pore size, since the pore size can be completely adapted to the shape of the particles that have to be filtered and is therefore not dependent on the smallest dimension of the particles.

There are some interesting publications on this subject today. Amato et al. have demonstrated the production and integration of a porous 3D filter into commercially available sealed microfluidic chips using SZ2080 [23]. The group used 2PP to construct the filter directly inside the microchannel. This has the advantage that microfluidic chips can be used that are commercially available and optimized for the target application. As a demonstrator, they produced a three-dimensional filter with a pore size of approximately 1 μm and tested it with a suspension of 3-μm polystyrene particles in a rhodamine-6G solution, according to the functional principle shown in Fig. 3.17. It could be shown that the filter is able to completely remove the particles from the fluorescent solution in continuous operation for a period of up to 25 min at which no clogging was observed during the entire operating period. The filter can even be cleaned by reversing the flow and reused several times. As an important application, the group performed a preliminary validation of the filter for plasma extraction from whole blood, demonstrating that the filter can also be used for softer particles such as red blood cells.

The separation and sorting of particles according to their size is also an important application in microfluidics. Perrucci et al. used stereolithography and 2PP for the

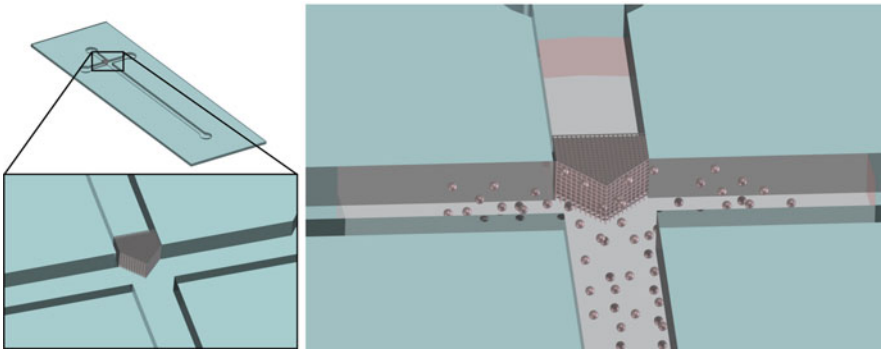

Fig. 3.17 (Left) Model of the microfluidic chip with integrated filter, as well as an enlarged view of the integrated filter. (Right) Functional principle of the filter in the microfluidic chip. (Reprinted with permission from Springer Nature Customer Service Centre GmbH: Springer International Publishing AG, Two-Photon Polymerization in Optics, Microfluidics, and Biomedicine by Ayman El-Tamer, Ulf Hinze, Boris N. Chichkov, Copyright 2020)

production of a microfluidic chip with integrated filter, whereby stereolithography was used for the construction of the microfluidic chip and 2PP for the construction of the integrated filter made of Femtobond (Laser nanoFab GmbH) [24]. For their experiments, a chip with one inlet and one outlet was produced and in a second step a suspended microfilter with a pore size of 4 μm was integrated into the inlet using 2PP (Fig. 3.18). Compared to a filter integrated in the channel, a filter in the inlet offers a significantly larger filter area and can therefore support a larger flow. To characterize the filter, fluorescent particles in a liquid were used and analyzed by fluorescence microscopy. As a result, the fluorescence tests showed that particles larger than 4 μm were stopped by the filter, while smaller particles could pass unhindered. The use of filters of this type is interesting for sorting particles by size, which is an important application in microfluidics.

A further important application in microfluidics is the production of mixers. The mixing of two liquids within the microfluidic channels poses a great challenge, since laminar flows usually develop in the microchannels due to the low Reynolds number, so that the liquids can hardly mix because of the missing turbulences. Natural mixing in microfluidics is usually based on molecular diffusion, which is insufficient for microfluidic applications. Therefore, great efforts are being made in LOC technology to integrate mixing devices into microfluidic chips in order to achieve a significantly better mixing efficiency. In general, a distinction is made between active and passive mixing devices, whereby the active devices are controlled externally, while the passive devices fulfil their function through their geometry. Passive devices are therefore of particular interest with regard to integration due to their low complexity and simple operation. However, they suffer from a lower mixing efficiency compared to active devices. For this reason, various recent publications have concentrated on the development of new passive concepts

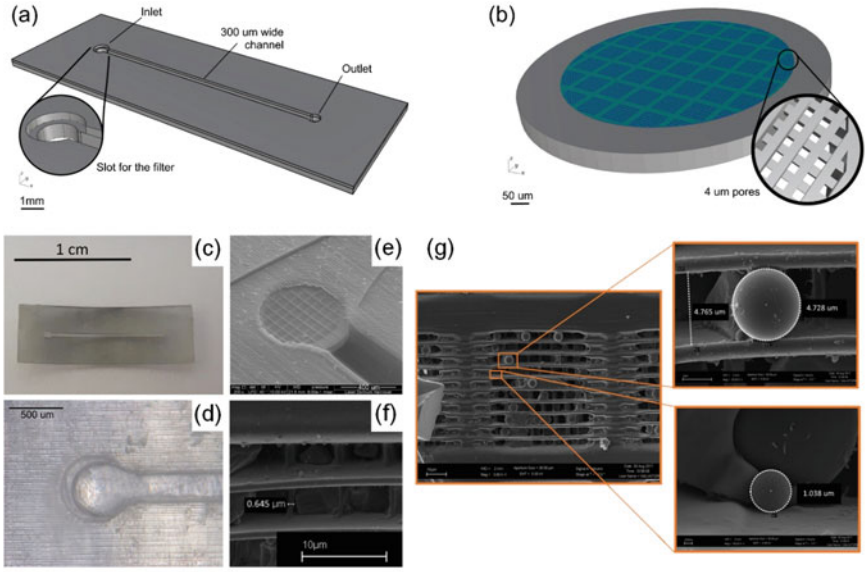

Fig. 3.18 (**a**) Microfluidic chip geometry. (**b**) Filter geometry: cyan and blue grids represent the filtrating structure, while the grey ring represents the support structure. (**c**–**f**) Images of the device at different manufacturing steps: (**c**) the microfluidic chip after post-curing, (**d**) detail of the filter slot inside the microfluidic inlet, (**e**) FESEM image of the filter integrated in the inlet, and (**f**) detail of the nanometric filter features. The visible debris inside the filter pores derive from filter handling during characterization. (**g**) FESEM images of the fluorescent particles in the filter. (Reprinted from [24], Copyright 2018, with permission from Elsevier)

with higher efficiency. In the following, we will discuss two interesting concepts of this kind.

Lim et al. presented an integrated passive three-dimensional micromixer, which they call crossing manifold micromixer (CMM) and that consists of a stack of crossing tube bundles fabricated from SU-8 3035 (MicroChem) [25]. Their concept is based on two mixers connected in series, the first horizontally and the second vertically. In this way, maximum mixing efficiency is ensured in a relatively short distance. In a numerical analysis, the group was able to show that a mixing rate of 90% can be achieved over a channel length of 250 µm if two mixers, each consisting of six layers of tubes, are installed in series. For the experimental analysis, two mixers were built up directly in a photolithographically produced microchannel using 2PP and the flow of ethanol was investigated by confocal microscopy using a fluorescent dye. By comparing the laminar flow properties of the experimental measurements with the numerical expectations, the expected efficiency could be confirmed. According to the same principle, Wu et al. produced a similar mixer using SU-8 2075 (MicroChem), which they extended by two additional filter elements (Fig. 3.19). This mixer is capable of mixing the liquid with an efficiency of 87% and filtering it at the same time [26].

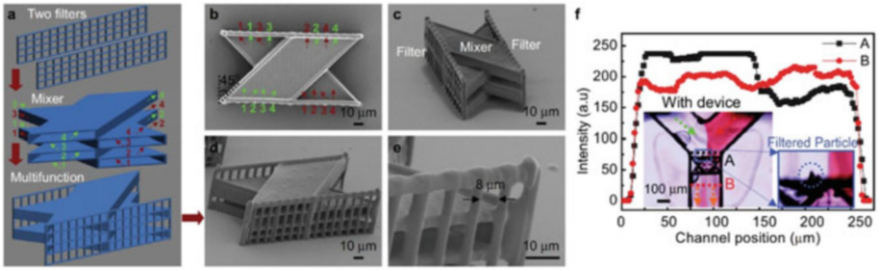

Fig. 3.19 Design, fabrication, performance, and application of a 3D ship-in-a-bottle biochip integrated with multifunctions. (**a**) Schematic design principle of a novel multifunctional filter-mixer device in which two filters were formed at the inlet and outlet of a passive-type mixer. (**b**) Top view SEM image of the fabricated multifunctional device and its mixing mechanism. (**c–e**) 30°, 45° tilted view, and magnified SEM images observed from different directions clearly showing the two filters and four-layer microstructures of the mixer. (**f**) Mixing efficiency in the microchannel with integrated mixing device. The curves represent the grayscale intensity extracted from the optical microscopic images to quantitatively investigate the mixing efficiency. The mixing efficiency can reach as high as 87% within a short distance (only one time for the channel width). (Reprinted from [26], copyright 2014. Laser Photonics Rev. published by Wiley-VCH Verlag GmbH & Co. KGaA Weinheim)

A further interesting passive concept was introduced by Liu et al. in 2014. In their paper, the group presented a three-dimensional micromixer with propeller blades, which is manufactured directly in the microchannel using Photomer 3015 (Henkel Inc.) (Fig. 3.20) [27]. The propeller blades are designed to disturb the laminar flow in three dimensions and thus achieve a high mixing rate. In the experiments, different blade shapes were compared, whereby it was shown that the screw-shaped propeller generates additional streamlines in the Z-direction and thus increases the mixing efficiency. As a result, it could be shown that a single-screw propeller can achieve a mixing rate of 80%. This was additionally verified by a COMSOL simulation.

3.5.3 Biomedical Applications

Biomedicine has become one of the most important applications of two-photon polymerization (2PP). The advantages of 2PP, such as the ability to process various biocompatible materials and the fact that it is a purely optical process that enables noncontact fabrication directly from CAD design, make it interesting for various biomedical applications. One of its most important applications today is the development of scaffolds in the field of tissue engineering. However, it is also increasingly used for the rapid prototyping of medically relevant structures and the construction of microstructured implants.

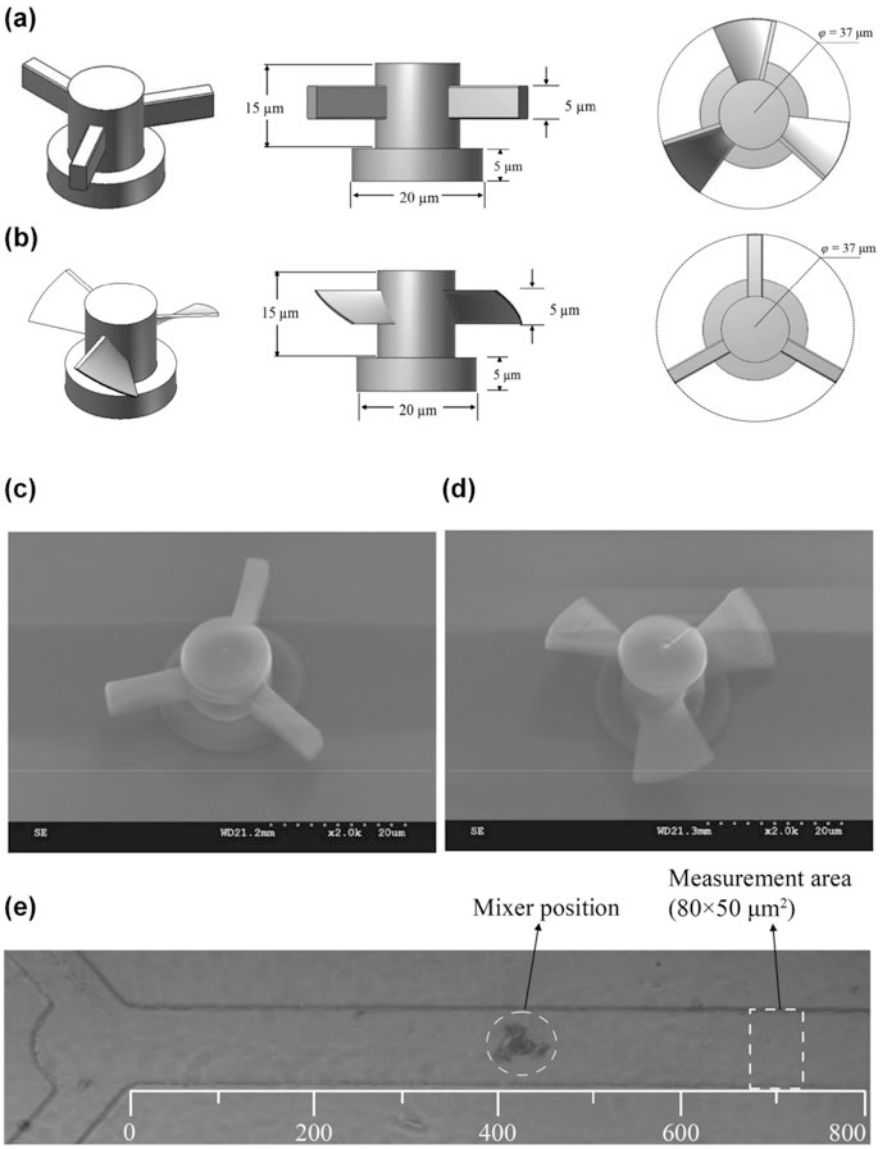

Fig. 3.20 Dimensions of micromixers: (**a**) flat and (**b**) screw-shaped blades. (**c**–**d**) SEM images of the 3D propellers: (**c**) flat and (**d**) screw-shaped blades. (**e**) Mixer position and measurement area in the Y-shaped microchannel. (Reprinted from Ref. [27], with permission from MYU Tokyo)

The in vitro production of living tissue is one of the challenging tasks in tissue engineering (TE) and is of great importance for the research and understanding of the complex biological processes in organisms. As is already known today, the morphology and differentiation of cells in a physiological 3D environment differ

considerably from cells in 2D tissue cultures. Therefore, the development of a specific tissue type in an artificial environment poses a particular challenge because it is controlled in natural tissue by the native extracellular matrix. As a natural three-dimensional scaffold, this matrix possesses mechanical and chemical properties that are typical for the tissue and influence the adhesion, migration, proliferation, and differentiation of the cells in a special way that is characteristic for each specific tissue. The investigation of these necessary properties and their transfer to artificial three-dimensional scaffold structures is therefore the subject of current research, with the aim of producing artificial scaffold structures that resemble the natural extracellular matrix in the most important properties. This forms the basis for specific in vitro tissue construction and tissue regeneration [28–31].

Koroleva et al., for example, produced defined scaffolds from polylactic acid (PLA) and examined them with regard to their suitability for the formation of neuronal tissue, which is of great importance for repairing nerve injuries [32]. In another study, they produced scaffolds with different pore sizes from a Zr-Si organic-inorganic hybrid polymer and investigated the influence of pore size on the formation of bone tissue [33] (Fig. 3.21a). The same hybrid material was also used by Timashev et al. in 2016 to produce scaffolds that were studied in a primary culture of embryonic mouse neurons (Fig. 3.21b) [34]. They were able to show that dissociated hippocampal cells adhere to the scaffolds, produce neurites, and prolong and differentiate into adult neurons. Käpylä et al. investigated the effect of different porosity values of scaffolds on the adhesion and proliferation of human fat stem cells by using scaffolds with precisely tuned scaffold parameters made of Ormocomp (Micro Resist Technology GmbH) [35].

In recent years, remarkable progress has also been made in the field of hydrogels. Hydrogels offer particular advantages for TE applications as they can mimic the basic three-dimensional biological, chemical, and mechanical properties of native tissue and are therefore ideal as a material for building scaffolds. In general, hydrogels cannot be structured three-dimensionally, which limits their use in scaffold production. The development of novel structurable hydrogels is therefore of great interest for tissue engineering. Several years ago, Kufelt et al. succeeded in developing novel cross-linkable hydrogels based on hyaluronic acid and chitosan, which can be structured with the help of 2PP and additionally demonstrate the construction of defined scaffolds from these hydrogels (Fig. 3.21c, d) [36, 37]. Accardo et al. also demonstrated the advantages of hydrogels and produced free-standing scaffolds based on a PEGDA hydrogel and used them for the investigation of three-dimensional neuronal cell cultures [38].

Currently, the use of degradable materials for the production of scaffolds is increasing significantly because degradable scaffolds are of great interest for tissue engineering and regenerative medicine since they dissolve during tissue formation and therefore do not remain as foreign bodies in the newly formed tissue. A few years ago, Felfel et al. were able to demonstrate the construction of defined three-dimensional degradable scaffolds with adjustable degradation profiles made of poly(D,L-lactide-co-ε-caprolactone) copolymer with different lactic acid (LA) and ε-caprolactone (CL) ratios [39]. The great advantage of a material of this type

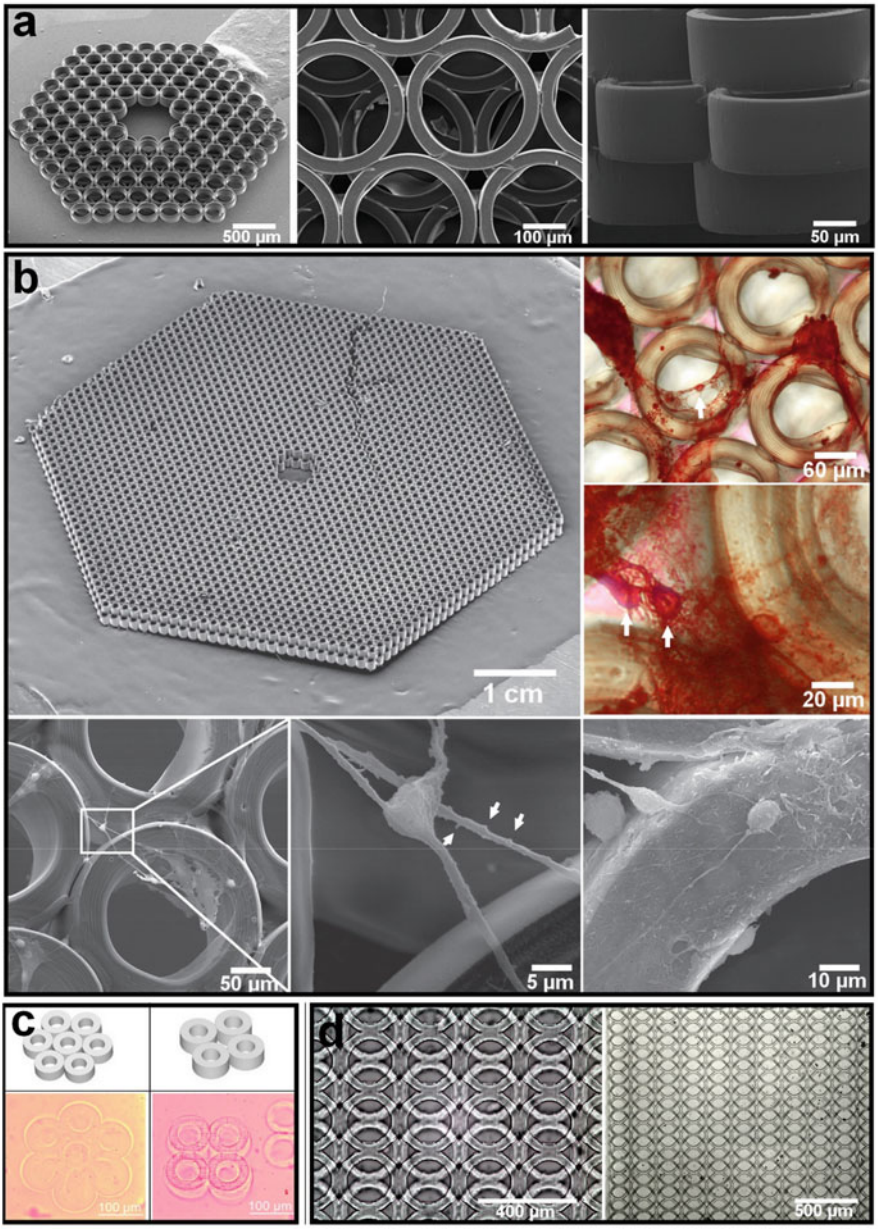

Fig. 3.21 (**a**) SEM images of 2PP-fabricated Zr-Si inorganic-organic hybrid scaffold with a pore size of 250 µm. (Reprinted from Ref. [33], licensed under CC BY 4.0, License at http://creativecommons.org/licenses/by/4.0/). (**b**) Representative images of Zr-Si scaffolds produced by 2PP and hippocampal cells grown on the Zr-Si scaffold. Arrows indicate the formation of spines on neuronal dendrites. (Reprinted from Ref. [34], licensed under CC BY 3.0, License at https://creativecommons.org/licenses/by/3.0/). (**c**) Microscopic images of 2PP-manufactured hyaluronic acid (HAGM) scaffold geometries: one-layered ring-like structures according to the applied CAD models. (Reprinted with permission from Ref. [36]. Copyright (2014) American Chemical Society). (**d**) Optical microscope images of ringlike microstructures fabricated from photosensitive chitosan hydrogel using two-photon polymerization. (Reprinted from Ref. [37], Copyright 2015, with permission from Elsevier)

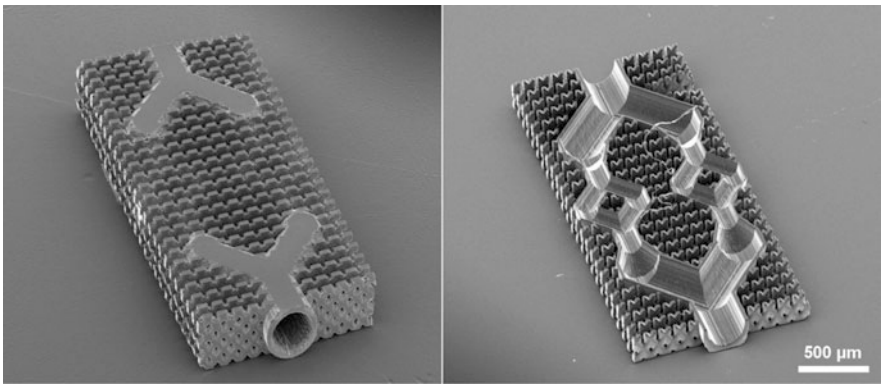

Fig. 3.22 (Left) Microfluidic model of a blood vessel system and (right) horizontal section through the structure. (Reprinted with permission from Springer Nature Customer Service Centre GmbH: Springer International Publishing AG, 3D Mikro- und Nano-Strukturierung mittels Zwei-Photonen-Polymerisation by Ayman El-Tamer, Ulf Hinze, Boris N. Chichkov, Copyright 2017)

is that it can be adjusted to the development time of a certain tissue type and thus remains in the tissue for the ideal duration. This is of particular importance for the development of tissue for implantation and for in vivo examinations.

An interesting paper on the in vivo use of scaffolds was presented by Mačiulaitis et al. in 2015. In a preclinical study, the group demonstrated the successful in vivo use of scaffolds from the organic-inorganic hybrid material SZ2080 by implanting scaffolds into a rabbit organism for up to 6 months and then histologically examining them [40].

A further challenge in tissue engineering is the in vitro construction of thick tissue models, as the cells in the depth of the tissue cannot be sufficiently perfused. In natural tissue, this is achieved by microvessels or capillaries that ensure the exchange of fluids, nutrients, electrolytes, hormones, and other substances between blood and tissue. For a successful formation of thick tissue layers, similar synthetic microvessels have to be produced for tissue engineering and integrated into the cell culture. Due to the small capillary dimensions, which are usually less than 10 micrometers in diameter, it is only possible to produce them using a high-precision technology with a process resolution of less than 1 µm.

This necessary vascularization for the in vitro generation of tissue constructions was taken up a few years ago by Professor Chichkov's research group. The group presented an interesting solution based on 2PP, which is derived from a simplified model of a microvascular system with the typical branches of small vessels. The developed vascular system was additionally enveloped by a scaffold-like structure to enable three-dimensional tissue formation in cell culture (Fig. 3.22). The structure was manufactured from the biocompatible polymer FemtoBond (Laser nanoFab GmbH) with a minimum structure size of less than 5 µm. In contrast, the use of conventional 3D printing methods would not be possible in this case due to their limited resolution.

The papers mentioned are only a small selection of a large number of publications on 2PP in the field of tissue engineering. This shows how strongly 2PP has established itself as an outstanding tool in this field over the last decade. In the future it can be assumed with great certainty that 2PP will continue to contribute to far-reaching developments in this field.

3.6 Conclusion

Two-photon polymerization (2PP) is a laser-based additive manufacturing process that enables the contactless manufacturing of complex three-dimensional polymer-based structures from predefined CAD models and with a structural resolution of less than 100 nm. It relies on a nonlinear two-photon absorption that initiates the polymerization process at the focus of the laser beam. In this way, the desired structure can be created in the volume of the photoresist by direct laser writing, which offers a particularly simple method for the three-dimensional production of complex and high-resolution structures.

Over the past 10 years, two-photon polymerization (2PP) has proven to be an outstanding high-resolution and flexible additive manufacturing process for the production of complex 3D structures and has enabled the development of novel and miniaturized components in various research areas. In optics, its application led to a significant development in the fabrication of two- and three-dimensional optical elements with highly transparent photoresists, further reinforcing the ongoing trend towards miniaturization and paving the way for the fabrication of complex optical elements in micro- and nano-optics. In recent years, it has successfully been used to demonstrate various micro- and nano-optical components, including refractive free-form surfaces, optical waveguides, photonic crystals, diffractive elements, hybrid diffractive-refractive elements, and multicomponent optical systems. In addition, 2PP has established itself as an exciting tool for the fabrication of waveguides and waveguide connections, enabling the development of complex photonic circuits in research.

In the field of microfluidics, two-photon polymerization has set new standards in the miniaturization of fluidic components and the integration of components with complex functions due to its high flexibility and submicrometer resolution, thus enabling the development of novel lab-on-a-chip systems. With its help, various microfluidic components such as mixers, filters, or flow meters as well as complex optofluidic components such as sensitive refractometers have been demonstrated.

Biomedicine, which today is one of the main areas of application of 2PP, has benefited in particular in recent years from the wide range of biocompatible materials that can be processed using 2PP. As a result, the ability was provided to create complex biological structures, which is of elementary importance for various biomedical applications. In this way, 2PP enabled the production of novel scaffolds from different biocompatible materials for tissue engineering.

This development makes clear that the relevance of additive manufacturing processes in various areas of research and industry will continue to increase significantly in the future. Due to the increasing complexity of future devices, miniaturization will also gain in importance, which will make 2PP an important tool for industrial applications. It is therefore to be expected that 2PP will grow out of the laboratory scale in order to establish itself in industry.

Acknowledgments The authors would like to thank funding from the European Union's Horizon 2020 research and innovation program under grant agreement no. 951890 (Platforma), Bundesministerium für Wirtschaft und Energie (ZIM KK5366201 KL 1), Federal Ministry of Education and Research with RESPONSE "Partnership for Innovation in Implant Technology", and the Deutsche Forschungsgemeinschaft (DFG, German Research Foundation) under Germany's Excellence Strategy – EXC-2123 QuantumFrontiers – 390837967.

References

1. S. Maruo, S. Kawata, Two-photon-absorbed photopolymerization for three-dimensional microfabrication (1997). https://doi.org/10.1109/memsys.1997.581794
2. V.F. Paz et al., Development of functional sub-100 nm structures with 3D two-photon polymerization technique and optical methods for characterization. J. Laser Appl. **24**(4), 042004 (2012). https://doi.org/10.2351/1.4712151
3. M. Göppert-Mayer, Über Elementarakte mit zwei Quantensprüngen. Ann. Phys. (1931). https://doi.org/10.1002/andp.19314010303
4. T. Bückmann et al., Tailored 3D mechanical metamaterials made by dip-in direct-laser-writing optical lithography. Adv. Mater. **24**(20), 2710–2714 (2012). https://doi.org/10.1002/adma.201200584
5. K. Obata, A. El-Tamer, L. Koch, U. Hinze, B.N. Chichkov, High-aspect 3D two-photon polymerization structuring with widened objective working range (WOW-2PP). Light Sci. Appl. **2**(DECEMBER), 8–11 (2013). https://doi.org/10.1038/lsa.2013.72
6. T. Gissibl, S. Thiele, A. Herkommer, H. Giessen, Two-photon direct laser writing of ultracompact multi-lens objectives. Nat. Photonics **10**(8), 554–560 (2016). https://doi.org/10.1038/nphoton.2016.121
7. T. Gissibl, S. Thiele, A. Herkommer, H. Giessen, Sub-micrometre accurate free-form optics by three-dimensional printing on single-mode fibres. Nat. Commun. **7**, 1–9 (2016). https://doi.org/10.1038/ncomms11763
8. S. Bianchi, V.P. Rajamanickam, L. Ferrara, E. Di Fabrizio, C. Liberale, R. Di Leonardo, Focusing and imaging with increased numerical apertures through multimode fibers with micro-fabricated optics. Opt. Lett. **38**(23), 4935 (2013). https://doi.org/10.1364/ol.38.004935
9. X. Wang, A.A. Kuchmizhak, E. Brasselet, S. Juodkazis, Dielectric geometric phase optical elements fabricated by femtosecond direct laser writing in photoresists. Appl. Phys. Lett. **110**(18) (2017). https://doi.org/10.1063/1.4982602
10. T. Gissibl, M. Schmid, H. Giessen, Spatial beam intensity shaping using phase masks on single-mode optical fibers fabricated by femtosecond direct laser writing. Optica **3**(4), 448 (2016). https://doi.org/10.1364/optica.3.000448
11. V. Osipov, V. Pavelyev, D. Kachalov, A. Žukauskas, B. Chichkov, Realization of binary radial diffractive optical elements by two-photon polymerization technique. Opt. Express **18**(25), 25808 (2010). https://doi.org/10.1364/oe.18.025808
12. V. Pavelyev et al., Diffractive optical elements for the formation of 'light bottle' intensity distributions. Appl. Opt. **51**(18), 4215–4218 (2012). https://doi.org/10.1364/AO.51.004215

13. V. Pavelyev, V. Osipov, D. Kachalov, B. Chichkov, Diffractive optical elements with radial four-level microrelief fabricated by two-photon polymerization. Opt. Commun. **286**(1), 368–371 (2013). https://doi.org/10.1016/j.optcom.2012.07.116
14. Y.-H. Yu, Z.-N. Tian, T. Jiang, L.-G. Niu, B.-R. Gao, Fabrication of large-scale multilevel phase-type Fresnel zone plate arrays by femtosecond laser direct writing. Opt. Commun. **362**, 69–72 (2016). https://doi.org/10.1016/j.optcom.2015.08.039
15. V. Osipov, L.L. Doskolovich, E.A. Bezus, W. Cheng, A. Gaidukeviciute, B. Chichkov, Fabrication of three-focal diffractive lenses by two-photon polymerization technique. Appl. Phys. A Mater. Sci. Process. **107**(3), 525–529 (2012). https://doi.org/10.1007/s00339-012-6903-9
16. U. Hinze et al., Additive manufacturing of a trifocal diffractive-refractive lens. Opt. Commun. **372**, 235–240 (2016). https://doi.org/10.1016/j.optcom.2016.04.029
17. T.P. Xiao et al., Diffractive spectral-splitting optical element designed by adjoint-based electromagnetic optimization and fabricated by femtosecond 3D direct laser writing. ACS Photonics **3**(5), 886–894 (2016). https://doi.org/10.1021/acsphotonics.6b00066
18. C.W. Lee, S. Pagliara, U. Keyser, J.J. Baumberg, Perpendicular coupling to in-plane photonics using arc waveguides fabricated via two-photon polymerization. Appl. Phys. Lett. **100**(17), 2012–2015 (2012). https://doi.org/10.1063/1.4704358
19. N. Lindenmann et al., Photonic waveguide bonds – A novel concept for chip-to-chip interconnects. Opt. InfoBase Conf. Pap., 9–11 (2011). https://doi.org/10.1364/ofc.2011.pdpc1
20. N. Lindenmann et al., Photonic wire bonding: a novel concept for chip-scale interconnects. Opt. Express **20**(16), 17667 (2012). https://doi.org/10.1364/oe.20.017667
21. N. Lindenmann et al., Connecting silicon photonic circuits to multicore fibers by photonic wire bonding. J. Lightwave Technol. **33**(4), 755–760 (2015). https://doi.org/10.1109/JLT.2014.2373051
22. M. Schumann, T. Bückmann, N. Gruhler, M. Wegener, W. Pernice, Hybrid 2D-3D optical devices for integrated optics by direct laser writing. Light Sci. Appl. **3**(December 2013), 1–9 (2014). https://doi.org/10.1038/lsa.2014.56
23. L. Amato, Y. Gu, N. Bellini, S.M. Eaton, G. Cerullo, R. Osellame, Integrated three-dimensional filter separates nanoscale from microscale elements in a microfluidic chip. Lab Chip **12**(6), 1135–1142 (2012). https://doi.org/10.1039/c2lc21116e
24. F. Perrucci et al., Optimization of a suspended two photon polymerized microfluidic filtration system. Microelectron. Eng. **195**, 95–100 (2018). https://doi.org/10.1016/j.mee.2018.04.001
25. T.W. Lim et al., Three-dimensionally crossing manifold micro-mixer for fast mixing in a short channel length. Lab Chip **11**(1), 100–103 (2011). https://doi.org/10.1039/c005325m
26. D. Wu, S.Z. Wu, J. Xu, L.G. Niu, K. Midorikawa, K. Sugioka, Hybrid femtosecond laser microfabrication to achieve true 3D glass/polymer composite biochips with multiscale features and high performance: The concept of ship-in-a-bottle biochip. Laser Photonics Rev. **8**(3), 458–467 (2014). https://doi.org/10.1002/lpor.201400005
27. Y.J. Liu et al., Three-dimensional passive micromixer fabricated by two-photon polymerization for microfluidic mixing. Sensors Mater. **26**(2), 39–44 (2014). https://doi.org/10.18494/sam.2014.939
28. I.A. Paun et al., Laser-direct writing by two-photon polymerization of 3D honeycomb-like structures for bone regeneration. Biofabrication **10**(2) (2018). https://doi.org/10.1088/1758-5090/aaa718
29. J.A. Crowe et al., Development of two-photon polymerised scaffolds for optical interrogation and neurite guidance of human iPSC-derived cortical neuronal networks. Lab Chip **20**(10), 1792–1806 (2020). https://doi.org/10.1039/C9LC01209E
30. A. Koroleva et al., In vitro development of human iPSC-derived functional neuronal networks on laser-fabricated 3D scaffolds. ACS Appl. Mater. Interfaces **13**(7), 7839–7853 (2021). https://doi.org/10.1021/acsami.0c16616
31. A. El-Tamer et al., Development of in vitro 3D brain models on laser fabricated scaffolds. Trans. Addit. Manuf. Meets Med. **3**(1), 532–532 (2021). https://doi.org/10.18416/AMMM.2021.2109532

32. A. Koroleva et al., Two-photon polymerization-generated and micromolding-replicated 3D scaffolds for peripheral neural tissue engineering applications. Biofabrication **4**(2) (2012). https://doi.org/10.1088/1758-5082/4/2/025005
33. A. Koroleva et al., Osteogenic differentiation of human mesenchymal stem cells in 3-D Zr-Si organic-inorganic scaffolds produced by two-photon polymerization technique. PLoS One **10**(2), 1–18 (2015). https://doi.org/10.1371/journal.pone.0118164
34. P.S. Timashev et al., 3D in vitro platform produced by two-photon polymerization for the analysis of neural network formation and function. Biomed. Phys. Eng. Express **2**(3) (2016). https://doi.org/10.1088/2057-1976/2/3/035001
35. E. Käpylä et al., Direct laser writing and geometrical analysis of scaffolds with designed pore architecture for three-dimensional cell culturing. J. Micromech. Microeng. **22**(11) (2012). https://doi.org/10.1088/0960-1317/22/11/115016
36. O. Kufelt, A. El-Tamer, C. Sehring, S. Schlie-Wolter, B.N. Chichkov, Hyaluronic acid based materials for scaffolding via two-photon polymerization. Biomacromolecules **15**(2), 650–659 (2014). https://doi.org/10.1021/bm401712q
37. O. Kufelt, A. El-Tamer, C. Sehring, M. Meißner, S. Schlie-Wolter, B.N. Chichkov, Water-soluble photopolymerizable chitosan hydrogels for biofabrication via two-photon polymerization. Acta Biomater. **18**, 186–195 (2015). https://doi.org/10.1016/j.actbio.2015.02.025
38. A. Accardo, M.C. Blatché, R. Courson, I. Loubinoux, C. Vieu, L. Malaquin, Two-photon lithography and microscopy of 3D hydrogel scaffolds for neuronal cell growth. Biomed. Phys. Eng. Express **4**(2) (2018). https://doi.org/10.1088/2057-1976/aaab93
39. R.M. Felfel et al., In vitro degradation and mechanical properties of PLA-PCL copolymer unit cell scaffolds generated by two-photon polymerization. Biomed. Mater. **11**(1) (2016). https://doi.org/10.1088/1748-6041/11/1/015011
40. J. Mačiulaitis et al., Preclinical study of SZ2080 material 3D microstructured scaffolds for cartilage tissue engineering made by femtosecond direct laser writing lithography. Biofabrication **7**(1), 015015 (2015). https://doi.org/10.1088/1758-5090/7/1/015015

Chapter 4
Powder Bed Fusion

C. Badini and E. Padovano

Abstract This chapter presents the available powder bed fusion technologies for the processing of polymers. Selective laser sintering (SLS) is the most commonly used technique; the process involves the deposition of a powder layer and the use of a laser to selectively melt the region of interest. The 3D object is therefore produced with a layer-by-layer strategy. The increasing interest of both scientific and industrial communities for this technique has promoted its development, which nowadays is involved for the production of functional prototypes and a small series of components. An alternative and emerging technique is multi-jet fusion (MJF); differently from selective laser sintering, MJF uses an infrared (IR) radiation to promote the melting of thermoplastic polymers. Both these processes will be discussed in terms of required processing conditions, available materials and all the processing aspects which can influence the properties of the final component. Conclusively, some alternative technologies including selective mask sintering (SMS), high-speed sintering (HSS) and selective inhibition sintering (SIS) will be presented.

Keywords Additive manufacturing · Powder bed fusion technologies · Polymer powders

4.1 Introduction

The powder bed fusion (PBF) process is one of the most popular techniques associated with additive manufacturing. According to ISO/ASTM 52900 [1], PBF includes any technology in which a source of thermal energy is used to selectively fuse a region of a powder bed.

C. Badini · E. Padovano (✉)
Department of Applied Science and Technology, Politecnico di Torino, Torino, Italy
e-mail: claudio.badini@polito.it; elisa.padovano@polito.it

S. L. Marasso, M. Cocuzza (eds.), *High Resolution Manufacturing from 2D to 3D/4D Printing*, https://doi.org/10.1007/978-3-031-13779-2_4

Historically, the first process that shows comparable characteristics with respect to the modern PBF technique was proposed by Pierre Ciraud in 1971 [2]. He described a process where particles were used to form a powder layer onto a matrix; then a laser, an electron or a plasma beam locally heated the particles leading to the consolidation of a continuous layer. In 1979 Ross Housholder firstly described a powder laser sintering process in a patent [3]; however, only in 1997 Carl Deckard, while he was at the University of Texas, filed two patents inherent to the description of the method and the first modern PBF apparatus for the fabrication of parts through the deposition and the selective sintering of subsequent powder layers [4, 5]. Starting from this early system, the evolution of this technology was continuous, and nowadays, powder bed fusion technology, with particular reference to selective laser sintering, represents one of the most used and widespread 3D printing technology worldwide.

The available polymer-PBF (p-PBF) technologies are selective laser sintering (SLS), which is the most common and investigated from both scientific and industrial communities, multi-jet fusion (MJF) and some alternative PBF techniques specifically designed to increase the process productivity. These last techniques are defined as line-wise and layer-wise PBF processes, respectively, and they mainly include selective mask sintering (SMS), high-speed sintering (HSS) and selective inhibition sintering (SIS) techniques.

All PBF processes can be identified by three main steps (powder recoating, energy input followed by coalescence and cooling of the system), as described in the following:

– The *powder recoating* refers to the process of spreading a fixed amount of powder particles to obtain a smooth and homogeneous powder layer. This step plays a fundamental role because it greatly influences both the quality of the deposited layer and the properties of the printed part. Wang et al. [6] underlined that the recoating step affects the density and the homogeneity of the layer of the powder; moreover, this initial stage also influences the force which is applied to the underlying solidified part. All these factors contribute to the success and the performance of the building process in terms of build speed, dimensional accuracy and part properties.

  The deposition of subsequent powder layers occurs using a recoater that generally shows two main geometries: a blade or a roller. Because of the importance of this step, many researchers investigated the interaction between the recoater and the powder as a function of the recoater shape.

  Parteli et al. [7] focused the attention on the use of a roller for the SLS process and developed a model which describes the transport of particles using this coating device. The results show that the surface roughness and the packing characteristic of the powder layer is greatly influenced by the process speed.

  According to Haeri et al. [8], the use of a roller allows obtaining a higher-quality powder layer with respect to that produced by a blade. This can be explained by considering the higher contact area of a roller if compared to a blade; the roller promotes the progressive rearrangement of particles during

the deposition step forming a homogeneous and uniform powder layer. On the contrary, the slender shape of the blade leads to a limited interaction with the particles inducing a dragging effect; as a consequence, a rough powder layer forms. These considerations induced Haeri [9] to further investigate this issue. A later study evidenced that the optimization of the blade geometry profile in terms of width, height and shape can significantly improve the powder bed quality.

Once the region of interest belonging to a single layer is scanned, the powder bed is lowered by a height corresponding to one-layer thickness and a new powder layer is deposited.

– *Energy input* is the thermal source required to induce the fusion of powder particles in a selected area on the powder bed. The most common thermal sources for commercial PBF systems are lasers, able to provide a precise delivery of coherent energy. Through a proper mirror system, it is in fact possible to focus the laser beam on a single powder layer with a high spatial resolution. On the base of the nature of the material to be processed, different lasers can be used. In fact, polymers and metal powders show a significantly different absorption spectrum, and moreover, they require significantly different amounts of energy to melt; therefore, different laser sources are required.

  As an alternative, nonlaser thermal sources can be adopted such as the high-power electron beam, which is used for the additively processing of metal powders through the so-called "electron beam melting (EBM)" technology. The use of this kind of thermal source involves an equipment which is significantly different with respect to a laser sintering machine. Another nonlaser thermal source is used in multi-jet fusion technique, where an infrared light selectively heats the region of the powder layer containing a previously dispersed heat-conducting liquid.
– Coalescence and cooling are the two mechanisms that lead to the consolidation of a single layer and the formation of a bonding with the previously scanned layer. The particle coalescence involves that two or more particles form sintering necks and bond together, thanks to the reduction of their free energy [10]. In polymer-PBF, this mechanism is mainly induced by the temperature increase occurring after the exposure to the energy source and the viscous motion. Then, the polymer solidifies as a consequence of heat loss, and the system cools firstly down to the temperature of the powder bed and then to the room temperature reached when the object is built.

  According to Sillani et al. [11], two of the main factors influencing the coalescence phase are associated with the rheological behaviour of the powder materials to be processed by PBF, namely, the viscosity and the surface tension.

4.2 Selective Laser Sintering (SLS)

As previously mentioned, selective laser sintering was the first commercialized PBF process. Once the patent application was filed, Deckard and some of his colleagues

founded the company Nova Automation, which was later renamed as DTM Corporation. It developed, manufactured and put into the market rapid prototyping and manufacturing SLS systems. Although SLS was originally developed for research purposes, the launch of Sinterstation 2000 by DTM in 1993 represented the first example of 3D printer designed for industrial use.

In 2001, DTM Corporation was acquired from 3D Systems Inc., which nowadays represents one of the reference points for additive manufacturing field. These emerging technologies have attracted a growing interest not only from the scientific community, but also of the industrial ones. Therefore, in addition to the activities of the American DTM Corporation, new companies progressively born worldwide and started commercializing PBF systems such as EOS GmbH. Although the latter initially focused on stereolithography process and 3D scanning systems, afterwards it extended its interest in the PBF process and named it as "laser sintering".

Moreover, thanks to the great versatility of this technology, in a few years the selective laser sintering approach, which was originally developed to produce polymer components, was extended to the processing of both metals and ceramics.

Selective laser sintering allows obtaining parts with high dimensional accuracy (higher with respect to other AM techniques such as fused deposition modelling), high productivity and good mechanical properties. The possibility to produce both pure polymeric and composite parts with complex geometry without the need of using neither supports nor moulds increases the potential applications of SLS at industrial scale. Nowadays, SLS represents a cost-effective alternative for the production of functional prototypes and small series with respect to both other AM technologies (such as fused deposition modelling or stereolithography) and conventional ones such as injection moulding [12].

The progressive development of AM technologies with the aim to move from the fabrication of prototypes to the production of end-use components inevitably increases the requirements in terms of the quality of the printed parts. Therefore, the physical, thermal and mechanical properties of AM components have to withstand operational requirements which are comparable to those of parts that are obtained by traditional manufacturing techniques [13].

In recent years, the great efforts and financial resources invested in the development of SLS technology allowed achieving numerous advancements in terms of the SLS equipment (improvements of used laser system, heating source able to provide high stability of temperature within the building camera during the entire process, recoater system), SLS process (investigation of all involved physical aspects and optimization of process parameters) and characterization of starting material properties. All these issues led to an improvement of SLS performance. However, this technology has not yet achieved the same maturity of conventional thermoplastic manufacturing processes. This is mainly due to limited consistency and reliability of the process that has a great effect on the quality of the final parts [14]. In fact, the residual porosity and the quality of the interfaces between layers, which are intrinsically associated with the AM process but not involved in conventional ones, lead to an anisotropy of the mechanical properties of the resultant parts [15, 16]. In addition, the possible thermal distortion can lead to curling and

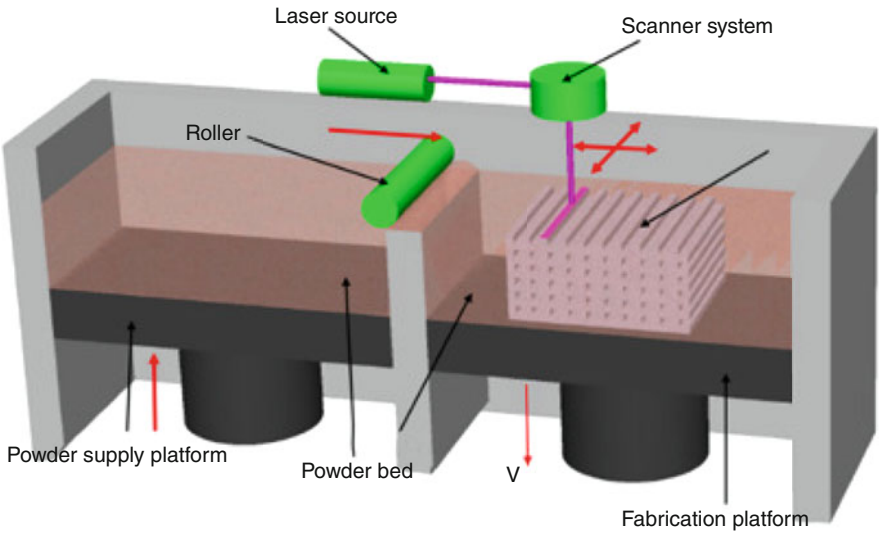

Fig. 4.1 Scheme of the SLS equipment. (Reprinted with permission from Ref. [18])

warping of fabricated parts [17]. Therefore, to obtain components which can satisfy the requirements imposed by the industrial world and to widen the SLS application scale, this technology needs to be further investigated and improved.

The following section will describe the main steps that characterize the SLS process as well as the very complex phenomena involved.

4.2.1 SLS Process Technology

The SLS process can be described as the layer-by-layer repetition of three main stages, namely, warm-up, building and cooling steps. Figure 4.1 illustrates the SLS apparatus and its main components.

The warm-up stage is characterized by a preheating of the system up to a defined temperature, referred as powder bed temperature (Tb), which is selected on the base of the powder to be processed and is maintained during the whole process. Generally, it is set in a range between 40 and 90 °C or higher with respect to the material glass transition temperature [19] . The choice of this temperature is crucial because it allows decreasing the amount of energy required to melt the powder when a laser scans a layer. At the same time, it must ensure that a homogeneous and uniform powder layer can be obtained during the recoating. In fact, temperature greatly influences the physical properties of the powder and therefore its flowability during the spreading steps.

It is generally accepted that during the SLS process, the temperature of the powder bed needs to lie between the onset of the crystallization temperature and the onset of the melting one, which can be referred as "processing window" or "sintering window".

The energy required to increase the temperature of the system to reach an isothermal condition is usually achieved by using continuous IR lamps and/or resistance heaters placed onto the powder bed.

The building step is the most structured phase of the process because it includes the powder recoating, the laser energy input and the interaction of this heating source with the polymer powder to achieve its melting and conclusively the material consolidation.

Firstly, a uniform and controlled-thickness layer of polymer powder is deposited onto the building platform using a blade or a roller. Then, a CO_2 laser placed just above the powder bed selectively scans the powder surface to induce the melting of polymer particles constituting the area of interest. In fact, by means of a scanning mirror system and based on a previously set computer-controlled model, the laser beam moves across the powder layer, providing a selected region of the powder bed the extra energy required to locally melt the polymer grains.

After the laser exposure, the molten powder coalesces at a temperature which is close to the polymer melting point; then, the material solidifies upon cooling reaching the bed temperature. During this process, in addition to the increase of the part height of a value corresponding to a layer, the bonding between previously scanned layers is ensured.

When the laser beam heats and melts the polymer grains, these melted grains coalesce and densify. The main driving forces for coalescence and solidification are the viscous flow of the polymer melt and the loss of heat within the powder bed [20].

Zhao et al. [21] described the sintering behaviour of two equal size polymer particles using three consecutive, but significantly overlapped, phenomena. Firstly, sintering necks form between particles and progressively grow. The second stage involves the network of channels along the grain edges. In fact, due to the shrinkage of these channels, the grains grow to reach, in the third phase, the formation of larger spherical particles. In the literature, a large number of models that concern the simulation of sintering process can be found. One of the first one was proposed by Frenkel et al. [22], who described the coalescence speed which occurs by viscous flow. This study evidenced that there are two material properties that greatly influence the coalescence step, namely, the surface tension and the viscosity. However, this model adequately represented only the first stages of polymer sintering. Pokluda et al. [23] proposed a modified version of Frenkel's model which aims to extend its validity throughout the whole process, but using a limited number of parameters. This last model is based on the equilibrium between the surface tension and the viscous dissipation, considering other possible operating forces as not significant. However, it was found that these models did not fit well the sintering of polymers because they did not include a complete evaluation of their rheological viscoelastic behaviour.

Therefore, further studies elaborated models which take into consideration the importance of these rheological properties such as the viscosity that can significantly vary as a function of the temperature, shear rate and time.

The model proposed by Bellehumeur et al. [24], in fact, combined Frenkel's approach with Maxwell's equation; the latter introduced the polymer viscoelastic behaviour in the description of the sintering process. The validation of this approach through experimental results confirmed the great influence that viscous elastic properties have on polymer particles.

Once the fabrication of 3D objects is completed as a result of the repetition of the recoating and building stages, the sintered part is cooled from the bed temperature to the room temperature. This cooling is generally performed in homogeneous conditions in order to avoid the development of residual stresses within the material [22, 25].

After that, the unmelt powder is removed from the powder cake and the final component is recovered.

4.2.2 Materials for SLS

Carl Deckard, creator of the SLS technology, did not focus the attention only on the development and commercialization of the SLS process and apparatus, but he considered essential the development of materials suitable to be processed with this technology. For this reason, in 2012 he co-founded Structure Polymers, a company with the objective of developing advanced materials for powder fusion technologies.

The rapid evolution of selective laser sintering and the increasing interest in this technology for potential applications at industrial scale make the development of new raw powders that can be processed by SLS necessary, in addition to the optimization of the process itself. In fact, it is worth noting that the majority of published studies focused their attention on the optimization of process parameters in order to obtain full dense parts with enhanced mechanical properties or on the study of the variation of mechanical performances of 3D objects as a function of their building orientation [16, 22, 25, 26]. Nevertheless, the key role of the starting material and related quality has been recognized as essential for maximizing the performance of both the SLS process and resultant printed samples [27–30].

Theoretically speaking, any polymer in the form of a powder can be processed by selective laser sintering if its interaction with a laser beam results in the absorption of an energy amount high enough to cause the full or partial melting of the material [12]. However, some limitations must be considered because some properties of starting powders strongly influence the success of the SLS process.

According to Schmid et al. [31], some of the most important requirements for a material which make it suitable to be processed by SLS are thermal properties, optical properties, viscosity and surface tension and particle shape and distribution.

4.2.2.1 Thermal Properties

The SLS process involves the heating of the powder bed at a non-ambient temperature. Then, an energy source in the form of a laser beam provides the extra amount of energy able to melt the polymer particles. Finally, the sintered powders belonging to one layer cool down to the powder bed temperature, while a bond with the previous scanned layer forms. In a process which is so greatly influenced by temperature variations and thermal phenomena, the understanding of the thermal behaviour of the starting material during the whole process is fundamental. Therefore, a strict control of operational temperature is required. For semi-crystalline polymers, which are the most used for SLS, the processing temperature has to be fixed in a range between the onset of crystallization and melting point. This thermal range is referred to as "sintering window" and it should be as wide as possible: if the operational temperature is too close to the crystallization one, this latter can be induced when the cooling rate is slow. A premature crystallization can cause the curling or warpage of the parts.

Moreover, thermal conditions which characterize the building chamber during the SLS process should be investigated. However, only few studies can be found in the literature on this issue.

4.2.2.2 Optical Properties

The interaction between the laser beam and the powder particles is one of the key steps of the SLS process. This interaction occurs in a very short time, during which the polymer must absorb a sufficient amount of energy to be melted. Generally, SLS systems are equipped with a CO_2 laser: the choice of this energy source is justified by considering the high absorption of polymers at the wavelength of 10.6 μm, typical of CO_2 lasers. In fact, most polymers are aliphatic compounds containing functional groups that are easily excited in the infrared region, and therefore, they are able to absorb a high fraction of this radiation.

4.2.2.3 Viscosity and Surface Tension

The key role of these two properties was originally evidenced by Frenkel et al. [22]: a low melt viscosity and a high surface tension are in fact important to promote a successful coalescence of particles. According to Sillani et al. [11], the polymer melt should have a low value of zero shear viscosity to obtain the full coalescence in the short time expected for the process. Contrary with respect to other processing techniques such as injection moulding, SLS does not involve an additional compacting during the building process; therefore, a low melt viscosity at low shear stress condition is essential [31].

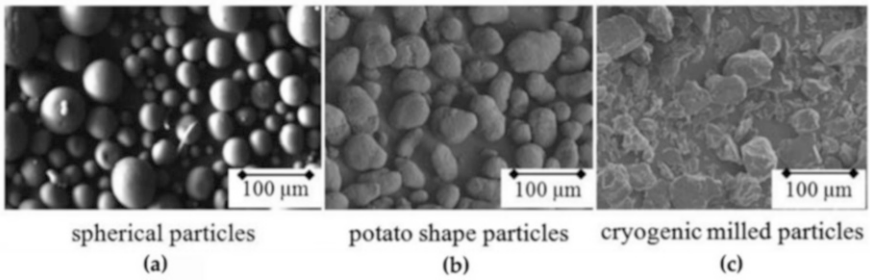

Fig. 4.2 (**a**) Spherical particles obtained by co-extrusion, (**b**) potato-shaped particles obtained by precipitation from ethanol solution and (**c**) irregular particles obtained by cryogenic milling process. (Reprinted with permission from Ref. [32])

4.2.2.4 Particle Shape and Distribution

The evaluation of both particle shape and size distribution constitutes a standard practice when a new powdered system is going to be processed by SLS. The key role of these two powder properties is due to their impact on the flow behaviour of the powders. In fact, polymer particles must be characterized by a proper geometry and dimensional distribution, which allow a free flow of particles when they are deposited by the recoater, and the formation of a thin and homogeneous layer. Moreover, their size has to be suitable to be easily melt when laser beam is applied.

Polymer powder systems can be produced through different production processes, which strongly influence their shape. There are mainly three particle geometries that can be obtained as shown in Fig. 4.2 [29, 32]. Spherical particles (Fig. 4.2a) can be generated by a co-extrusion process of a mixture of soluble and non-soluble materials. Secondly, particles with the so-called potato shape (Fig. 4.2b) are produced through the precipitation process; this geometry is the most common for the polyamide 12 (PA12) powders, the most widely used commercial material for SLS. The third possibility involves a shape which is very different with respect to the previously listed ones: cryogenically milled particles (Fig. 4.2c) are in fact characterized by a random and very irregular geometry.

The investigations of many researchers agree that spherical particles are the most suitable for the SLS process because they allow obtaining a powder bed showing the highest density and homogeneity [12].

In addition to a spherical geometry, the achievement of a powder bed with good quality is obtained by controlling the dimensional distribution of the particle size, taking into consideration that generally the thickness of a deposited powder layer is in the range from 100 to 150 μm. Based on the various studies in the literature, however, there are several dimensional ranges that can be considered as suitable for the SLS process.

Wang et al. [33] reported that the optimum particle size distribution (PSD) is in the range between 45 and 90 μm, and a narrow distribution is more advisable. A

wider range is considered by Chung et al. [34]: on the base of the results obtained in this study, PSD should be slightly smaller with respect to the layer thickness. For this reason, particles with a size from a minimum of 10 μm to a maximum of 150 μm are preferred. However, when using powder with a wide size distribution, the optimization of process parameters requires particular attention [35]. A third approach is used by Schmid et al. [29], who identified as optimal for SLS the powders showing a particle size distribution in the range from 20 to 80 μm. Powder systems characterized by a too high fraction of very fine particles show low flow properties, which lead to a low-quality powder bed.

The above discussed requirements for SLS powders are quite challenging; this is the main cause of the limited number of materials nowadays available to be processed by this technology. Among polymers, only thermoplastic materials can be considered; on the contrary, thermosetting ones are not suitable because they cannot by melted by the interaction with a laser beam. Moreover, thermoplastic powders can be recycled in subsequent SLS jobs, preventing the material waste.

Thermoplastic can be distinguished between amorphous and semi-crystalline ones, which show very different thermal behaviours caused by a different structure and organization of chain molecules.

The main amorphous materials that can be processed via selective laser sintering include polycarbonate (PC), polystyrene (PS) and styrene-acrylonitrile copolymer.

Thanks to the good mechanical properties and its relatively low cost, PC is used in many applications. Denucci [36] was one of the first researchers who produced patterns of investment casting via SLS. It was found that this approach offers numerous advantages when compared to some components produced with more conventional materials such as wax. For this reason, the fabrication of these patterns is nowadays realized mainly using PC. As for other amorphous materials, the thermal behaviour of PC as a function of the thermal conditions involved during SLS required a detailed investigation. Many studies were therefore focused on the development of thermal models describing the SLS process of PC [37–39]. Berzins et al. [39] demonstrated that the variation of material thermal properties as a function of both the temperature and the position of a scanned layer, which is progressively far from the platform as the process evolves, is fundamental to effectively predict the heat transfer during sintering.

Moreover, the potential use of PC to fabricate functional components in addition to prototypes makes the optimization of process parameters to obtain printed parts with good mechanical properties necessary [40].

The investigation of additional amorphous polymers such as polystyrene (PS), high-impact polystyrene (HIPS) and styrene-acrylonitrile copolymer was performed using two different approaches, similar to those previously described, which respectively involve the simulation of sintering mechanism as a function of SLS thermal conditions and the optimization of process parameters to maximize the properties of printed parts [41–44].

However, the literature reveals that SLS processing of amorphous thermoplastics generally leads to parts with very low relative density and therefore poor mechanical properties; on the contrary, components fabricated starting from semi-crystalline

polymers exhibit higher relative density and enhanced mechanical performances. As previously discussed, this is mainly due to the organization of macromolecules.

Nowadays, thermoplastic semi-crystalline materials are the most used powder systems for SLS, and among them, polyamide 12 was surely the most widely commercialized powder because it can satisfy all the requirements for SLS powders.

From a processability point of view, PA12 shows a wide temperature range between the melting and crystallization onset (detected during heating and cooling, respectively). As previously mentioned, it is generally accepted from the scientific community that for semi-crystalline materials, the powder bed temperature should lie between the sintering window [45], which should in turn be as large as possible. In addition, it was found that the interaction of the CO_2 laser with PA12 involves a reflection of only 5–6% of the incoming laser energy and therefore a high absorption coefficient [46]. The good thermal properties and high absorption of infrared radiation, in addition to a proper rheological behaviour [47–49], make PA12 well suitable for SLS. Numerous studies report that the optimization of process parameters leads to obtain PA12 dense parts with high mechanical properties. Caulfield et al. [50] investigated the impact of energy density variation (which is a function of the process parameters) obtained by varying the laser power on both the physical and mechanical properties of PA12 specimens. By increasing the energy density, it is possible to obtain parts with a higher density and consequently with enhanced tensile strength and Young modulus. A similar relationship between mechanical performances and provided energy density was observed by Starr et al. [51], who reported an enhancement of tensile properties as a function of increased energy density until a plateau value is reached. On the other hand, according to Vasquez et al. [52], too much high energy density causes a decrement of mechanical performance probably due to the onset of material degradation, leading to the formation of bubbles and porosity within the obtained parts.

Many of them belong to the family of polyamides (such as PA6 and PA11 and their composites), which are generally used for engineering purposes, where a combination of good mechanical properties and thermal resistance is required. In this context, SLS engineering polymers can be used for replacing conventional materials, exploiting the competitive advantages associated with the lightness of components and the possibility of easily producing complex shapes or assemblies as a single component.

Recently, an increasing interest arose for the development of SLS high-performance polymers belonging to polyaryletherketone (PAEK) group, such as polyetheretherketone (PEEK) and polyetherketone PEK. They show a unique combination of mechanical properties and good chemical and high temperature resistance that guarantees a continuous use of these materials at high temperature (PEEK can be used for applications up to 260 °C).

Although the properties of PAEK are very appealing, some drawbacks limit their use such as the high cost, the required high temperature to be processed and the low resistance to UV light.

Other semi-crystalline commodity polymers include polypropylene (PP) and polyethylene (PE). Although these materials are traditionally used in a wide range

of application fields such as engineering, packaging and medical ones, the study of their processability by SLS requires further investigations. Goodridge et al. [53] successfully produced multilayer structures starting from ultra-high-density polyethylene (UHDPE) via SLS. However, the study revealed that the narrow sintering window of this material greatly limits its processability; the success of the process can be achieved only by strictly controlling the selection of a proper temperature bed, suitable to minimize the thermal gradient during the process. The investigation of these materials is mainly limited to research purposes and specific applications. Salmoria et al. [54] investigated the fabrication of high-density polyethylene (HDPE) scaffold structures that have a potential use in human tissue regeneration; their results show that structures with different porosity degrees can be obtained by varying the particle size of starting powders.

4.3 Multi-Jet Fusion

Multi-jet fusion (MJF) is an additive manufacturing technique which was patented by Hewlett-Packard Inc. (HP) in 2014 and introduced into the market 2 years later. This relative newcomer technology belongs to the PBF process family and gets its name from the inkjet heads that distribute multi-agents on a selected region of powder layer in order to promote particle melting. A so conceived printing process shows affinities with metal binder jetting technology, where a liquid binder agent is applied to each powder layer to promote the part consolidation. The use of inks aimed to enhance optical-to-thermal energy conversion to obtain an increased production volume and an improvement of both edge definition and surface finishing.

4.3.1 MJF Process Technology

The MJF system is constituted by three different units:

- The processing station where the powders are stored and mixed, and the final component is removed after the printing is completed.
- The build unit which is the core of the system because it includes the printing platform where the building process occurs. It is designed to be moved from the processing station to the printer block and vice versa. Here the MJF process occurs.
- The printer unit which is the system where the build unit is placed when a new job is going to start.

Like all AM technologies, the MJF process begins with the elaboration of a CAD model, which allows creating the component to be printed with a high design freedom.

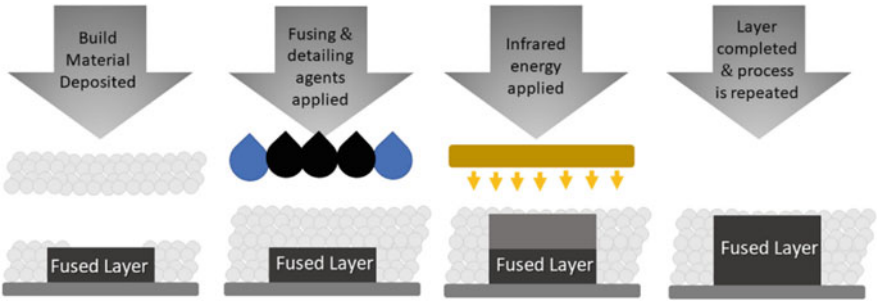

Fig. 4.3 Main steps involved in the multi-jet fusion process. (Reprinted with permission from Ref. [55])

As previously mentioned, the material cartridges are inserted into the processing station and then transferred to the build unit through a clean and automated process. When the build unit is placed into the printer, the multi-jet fusion process can start leading to the fabrication of 3D parts.

Similarly to the SLS process, a layer of powder is spread onto the powder bed, which is uniformly preheated under a heat lamp system placed over the building platform. However, unlike SLS, the melting of the polymer powder is not obtained after the laser scanning, but through the interaction between the powder impregnated with multi-agents and the infrared lamp. In fact, an inkjet head selectively distributes both the fusing and detailing agents on the powder layer (Fig. 4.3): the former is deposited in the selected regions where the particles have to be melted. On the contrary, the detailing agent is spread at their edges in order to prevent the sintering of the neighbour powder and therefore to delimit the 2D shape of the forming layer. The role of this additional agent is important because it allows obtaining a very high dimensional accuracy of the final part, which shows clean contours and very small details, and thus prevents inaccuracies in specific zones.

Then, an infrared heating source moves across the building platform and promotes the melting of regions where the fusing agent is applied. On the contrary, the areas where the detailing agent has been deposited remain as unmelt particles. In fact, the interaction between the powder filled with the fusing agent and the IR source promotes the heating and melting of particles. The liquid inks are known as a radiation-absorbing material; however, the chemical composition of these components is generally not reported in the literature because it is considered proprietary. The material recoating and the process involving both the distribution of multi-agents and the IR heating are carried out by two different heads which move parallel to the powder bed, but in a perpendicular direction, one with respect to the other; it allows the operator to optimize both processes as independent steps.

When the job ends, the build unit is removed from the printer and transferred into the processing station to let the powder cool down to room temperature. The operator carefully extracts the parts from the build unit and manually removes the remaining powder. The powder which is not involved in the MJF process can be

recovered to be used in next jobs providing reusability rates as high as possible. Generally, this unused powder is however mixed with fresh material and used for subsequent jobs.

The fabrication of functional polymeric parts through multi-jet fusion technology shows many advantages as follows:

- Low cost per part: multi-jet fusion has some of the lowest cost per part with respect to any other 3D printing technology; nevertheless, it is not as cheap as a fused deposition modelling 3D printer.
- Fast printing process: one of the main advantages of this technology is the possibility to produce high-density parts faster than via selective laser sintering. As underlined by Tey et al. [56], the planar fusion mode strategy involved during MJF allows to significantly reduce the layer processing time and therefore to increase the overall process production with respect to SLS, which uses a point-by-point time-consuming scanning mode. Xu et al. [57] estimated that MJF shows a printing speed almost ten times higher with respect to SLS.
- It is an environmentally friendly technology: generally, the materials processed by SLS show a reusability ratio of about 50%. On the contrary, powders that are not involved in the building of 3D objects can be recovered and stored in the processing station to be reused in subsequent jobs. According to HP [58], the reusability of MJF materials is not lower than 70% (reported value for PA12 reinforced with glass beads). The most used material, that is, PA12, shows a high reusability of 80%; reusability reaches a theoretical value of 100% for polypropylene. The production of a lower amount of wasted powder implies less environmental damage.
- Possibility to print coloured parts: generally, polymer AM technologies do not offer the possibility to obtain coloured parts or this possibility is strongly limited, such as in the case of stereolithography, which can print few colours. MJF offers a range of powders that allows the processing of parts in full colour, avoiding further post-processing treatments such as painting.
- Good aesthetic finishing: MJF allows obtaining both bulk component and lattice structures with a high level of details and good surface quality.
- MJF processes occur in open air: on the contrary, generally SLS is performed under an inert purge gas.

Although multi-jet fusion technology shows numerous previously mentioned advantages, some drawbacks need to be considered:

- Limited material availability: materials that can be process by MJF are essentially semi-crystalline thermoplastics (PA-based polymers and PP) and thermoplastic elastomers. Nowadays, the material palette includes less than 10 different powdered systems that can be processed by this technology.
- Very high cost for 3D equipment: it represents the biggest limit in using MJF technology because a high initial investment implies a long time before any benefit can be obtained.

4.3.2 Materials for MJF

When multi-jet fusion technology was developed and commercialized by HP, the only available material was polyamide 12 (PA12). It is the most widely investigated material for both the polymer powder fusion processes of SLS and MJF. As PA12 is a semi-crystalline polymer, when heated to melting temperature, the crystal domains go into molten state showing low melt viscosity. The proper fluidity allows filling the pores and thus results in a high density degree of printed parts.

In addition to this suitable thermal behaviour, PA12 shows good mechanical performance; chemical resistance to oil, greases and aliphatic hydrocarbons; and thermal resistance in addition to lightness that make it an ideal candidate for a wide range of applications.

Silani et al. [11] selected PA12 powder as a reference material to compare selective laser sintering and multi-jet fusion additive manufacturing technologies in terms of properties of both starting material and final component. The results show that the experimental conditions involved during SLS and MJF processes, respectively, can differently modify the properties of starting powders and therefore can influence their recyclability. In fact, for the MJF system, the movement of the IR lamp across each layer of powder is faster with respect to the scanning rate of the laser in the SLS process. The shorter exposure time for the MJF process reduces the modification of the polymer chain length, favouring the recyclability of powders. The comparison of mechanical properties of samples produced by the two technologies evidences some differences. In fact, the trend of mechanical property variation is different by considering the two processes. It is worth noting that samples built along the z direction (the specimen axis is parallel with respect to the building direction) show a lower tensile strength and elastic modulus when processed by SLS. This is due to the weaker interlayer bonding between adjacent layers achieved by this technology. On the contrary, the mechanical performance of z samples fabricated by MJF are higher; the use of a fusing agent in combination with IR radiation seems therefore to favour the interlayer adhesion leading to a final component with better isotropic properties.

The great efforts and huge investments that both scientific and industrial communities put into the development of new solutions made possible the enlargement of powdered materials that are available for MJF processing. Among them there are polyamide 12 reinforced with glass filler, polyamide 11 (PA11) and polypropylene (PP). However, the predominance of polyamide-based materials for MJF greatly limits the potential application fields of this technology. Therefore, two additional materials belonging to a different polymer family have been recently introduced into the market; they are thermoplastic polyurethane (TPU) and thermoplastic amide (TPA), two elastomeric polymers.

The use of glass fillers as reinforcement for thermoplastic material is common in many applications because it increases the load-bearing capability in the elastic deformation range [59]. A composite material constituted by glass beads added to the PA12 matrix was therefore developed for the MJF process.

O'Connor et al. [60] compared the properties of PA12 and PA12-GB processed by MJF. Although the two materials show similar chemical and thermal properties, basically associated with the common nature of the PA matrix, the mechanical performances of printed specimens are reported to vary. The incorporation of glass beads into the PA12 matrix leads to a significant increment of the elastic modulus (estimated around 85%), while both the tensile strength and elongation at break were found to decrease. The evaluation of flexural properties confirmed this trend. The authors attributed the obtained results to the poor adhesion between the glass spheres and the polymer matrix.

The higher stiffness of PA12-GB composites makes this material ideal for applications such as enclosures, housing and tooling. Moreover, a higher dimensional stability of composite was observed with respect to the pure matrix, which favours the fabrication of objects with a bigger size.

Another powdered system that can be processed by MJF is PA11, which also belongs to the polyamide family.

The interest for this material is due to its properties: it is a renewable material that comes from castor oil which shows excellent mechanical properties and good chemical resistance. The impact strength and the elongation at break, higher with respect to PA12, make PA11 ideal for applications such as prostheses, insoles and sports accessories.

As compared to PA12, a lower number of papers in the literature deal with PA11, and most of them are focused on the mechanical properties of obtained parts. Wei et al. [56] investigated the mechanical performances of this material in terms of tensile and flexural properties; moreover, the study evidenced a strong correlation between these properties and the porosity of the specimens. Lee et al. [61] examined the effect of building orientation on the mechanical behaviour of the material; also in this case, the role of porosity was considered. The mechanical behaviour of PA11 as a function of the powder refresh ratio was the object of interest of Pandelidi et al. [62].

Among semi-crystalline thermoplastic polymers, belonging to the polyolefin family, polypropylene (PP) is also available as a printing material for multi-jet fusion. Fused deposition modelling is the most commonly used processing technique for this material. However, its main limits are linked to the tendency of PP to warp during the FDM process and the poor adhesion of the filament with the building platform. However, PP can also be processed by selective laser sintering. Recently, the chemical and thermal properties of this material were found to be compatible with the MJF process. Although the peculiar layer processing approach of MJF technology should allow obtaining a more compact structure with a reduced anisotropy with respect to that observed for other AM technologies such as FDM, Safka et al. [58] found that both the impact and tensile properties of PP produced via MJF show a significant variation as a function of the building orientation of the sample.

In addition to biocompatibility, excellent chemical resistance and low moisture absorption, another interesting property of PP for MJF is associated with the theoretically 100% recyclability declared by HP [58] due to the high thermal

stability and the morphology of the PP starting powder. The experimental conditions involved in the MJF process do not show a significant impact on the properties of PP.

The versatility of this material allows it to be used in many application fields such as automotive, industrial and medical ones.

TPUs are linear segmented block copolymers showing hard and soft segments [63]. The former act as tie points serving as physical cross-links and reinforcing fillers; on the other hand, soft segments form an elastomer matrix and mainly give TPU its typical elastic behaviour. This structure is responsible for the peculiar characteristic of this material, which shows the mechanical properties of a vulcanized rubber and the processability of a thermoplastic polymer. However, a very broad range of properties can be obtained by tuning the composition of the block copolymers and therefore modifying the relative amount of the two segment fractions.

The high versatility of this material makes it attractive for many applications. Among them, the idea of using the peculiar properties of TPU creating highly customizable components with complex geometry encourages many researchers in investigating the processability of TPU by additive manufacturing techniques.

Before becoming available for MJF, the processing of TPU was possible through selective laser sintering [64–66] or fused deposition modelling (FDM starts from the material in the form of a filament, which is deposited using a layer-by-layer strategy until to the building of a 3D object is completed) [67–69]. These studies revealed that TPU can be processed through AM techniques. According to Verbelen et al. [70], the good flowability of powders, their low melt viscosities and low shrinkage upon hardening make TPU a suitable material for multi-jet fusion. On the contrary, some issues such as the porosity of obtained parts and the material degradation during the processing need to be further investigated and overcome.

Currently, very few papers can be found in the literature about the processing of TPU through multi-jet fusion technology. Wei et al. [56] focused the attention on this material by investigating both the properties of starting powders and those of printed specimens. Material anisotropy can be observed from the evaluation of both flexural and tensile properties. Results show that tensile strength and elongation at break are lower for Z samples with respect to X and Y ones. However, the trend is different when flexural properties are determined: flexural strength is higher for samples built with the Z orientation with respect to X specimens. This is probably due to the different impacts that porosity has on flexural and tensile properties.

Another elastomeric polymer which can be processed by MJF is the thermoplastic amide (TPA) provided by Evonik. Its flexibility, very low density and good mechanical resistance at low temperatures can be exploited in specific applications such as winter sports equipment, car interiors and fluid system applications.

To the authors' knowledge, no paper can be found in the literature regarding the characterization of TPA-based specimens.

4.4 Alternative p-PBF Technologies: Line-Wise and Layer-Wise Processes

It is well known that powder bed fusion processes offer the highest flexibility degree among AM technologies, justifying their increasingly wide diffusion in many application fields. However, many of these techniques involve the use of expensive laser systems working with a point-by-point scanning strategy, which is a time-consuming approach. From this consideration, an innovative idea of developing a way to fuse "lines" or even "layers" of polymer powder at once was born. The main advantage is associated with the dramatic decrease of processing time making these alternative solutions very interesting for industrial applications.

Gibson et al. [71] report three main processes which were developed to satisfy the previously cited necessity that are selective mask sintering (SMS), high-speed sintering (HSS) and selective inhibition sintering (SIS) processes. The common approach of these systems is the use of infrared energy to promote the fusion of selected areas belonging to each layer. On the contrary, the main difference is associated with the way it is used to distinguish the areas that need to be molten from the other zones.

Figure 4.4 illustrates the different approaches of these alternative PBF systems.

Speed Part, a company from Sweden, developed a process called selective mask sintering, whose central feature is the sintering of the whole powder layer at one time. For each layer, an IR radiation is applied to the region of interest which is selected by a digitally printed optical mask. Layer by layer the shape of the photomask changes as a function of the component slicing. This approach is much faster (layer processing time is estimated to be 5–10 s) and cost-effective (the cost of an IR lamp is significantly lower than a laser and galvanometer) with respect to other PBF technologies such as selective laser sintering.

According to Hermann et al. [72], the high speed of the SMS process makes it suitable for all the steps constituting the product life cycle of a polymer part: from the first prototypes, through the production of components and finally to the "spare parts on demand". The first material processed by SMS was a nylon reinforced with a glass filler.

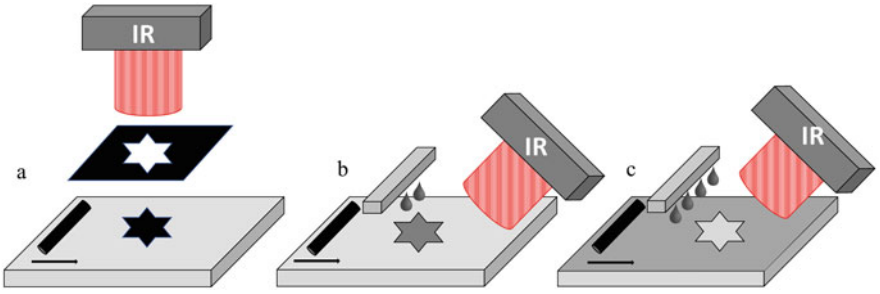

Fig. 4.4 Scheme of (**a**) selective mask sintering, (**b**) high-speed sintering and (**c**) selective inhibition sintering techniques

Later, another company, namely, Sintermask Technologies AB, focused its attention on this technology and introduced into the market the first commercially available SMS machine.

One of the drawbacks of this technology is that the powder needs to absorb and sinter or melt when the IR lamp passes through the powder bed, which involves a very short time. To satisfy this requirement, the powder is generally grey or black; this strongly limits the palette of available colours.

Loughborough University and Sheffield University, both in England, developed another layer-wise process, namely, high-speed sintering (HSS), that was then commercialized by Factum.

HSS applied a dark liquid ink onto the surface of a PA-based powder, which is usually white. The so impregnated areas represent the cross section that will be sintered when an IR radiation scans across the powder bed. The chemical composition of the ink allows the absorption of IR radiation. In fact, when the infrared heater irradiates the bed surface, only the regions where the ink is deposited are able to absorb enough energy to sinter. On the contrary, the remaining powder is not involved in the process.

After the sintering completion, the material need not cool down at a temperature lower than its crystallization point in order to avoid the development of residual stresses which cause warping and failure of the object under construction. As discussed for SLS, processable materials need to show a wide gap between melting and crystallization temperature.

According to Ellis et al. [73], the mechanical properties of PA-based samples can be improved by tuning the absorption spectrum of the radiation-absorbing ink and the emission spectrum: greater overlap of these spectra leads to a more efficient energy transfer. This should enhance the quality of obtained parts and therefore improve their mechanical properties. The results evidence that a variation of IR radiation exposure time doubles the elongation at break obtained by processing the same material by SLS.

The third alternative approach is the selective inhibition sintering (SIS) process which was developed at the University of Southern California. In this case, the used approach is opposite with respect to the HSS system: in fact, an inhibitor is deposited onto the powder regions where the sinter should be avoided when the IR lamp moves across the powder layer. The function of the inhibitor agent is therefore to avoid the sintering of selected areas. Instead of using a chemical product that inevitably contaminates the powders and makes their recyclability difficult, some attempts were pursued using a movable plate hindering the regions that have not been sintered.

According to Asiabanpour et al. [74], the main advantages of this technique include low cost, high processing speed (with a required time of a few seconds to sinter one layer) and the good quality of parts in terms of dimensional accuracy and surface quality.

The mechanical properties of 3D objects fabricated by SIS mainly depend on the sintering mechanism occurring during the process [75].

4.5 Conclusions

In recent years, as far as the processing of polymers concern, various additive manufacturing technologies have grown and rapidly evolved. Among them, powder bed fusion has enabled the production of highly customized, geometrically complex and high-precision parts that are not technically feasible through conventional manufacturing techniques. PBF includes different processes which share the same basic principles: they make use of a heat source to consolidate three-dimensional objects starting from the polymer in the form of a powder, which is homogeneously deposited on a building platform using a layer-by-layer strategy. The two main and investigated polymer-PBF technologies differ in the heat source that is applied to consolidate the powder layer: selective laser sintering (SLS), as suggested by the name itself, works with a laser; on the other hand, infrared lamp is used in multi-jet fusion (MJF).

SLS was the first commercialized PBF technique, and nowadays, it is also the most popular and widespread one; however, MJF represents a competitive alternative thanks to the improved process productivity it can reach. Both these technologies have been described in terms of process conditions and available materials.

Moreover, some additional p-PBF processes were introduced as alternative solutions for industrial applications because they allow to significantly decrease the processing time. These are selective mask sintering (SMS), high-speed sintering (HSS) and selective inhibition sintering (SIS) processes: they use an infrared radiation as heat source, but they adopt different strategies to distinguish the areas to be selectively molten with respect to the others.

References

1. ISO/ASTM 52900:2015, Additive manufacturing – General principles – Terminology. Available at https://www.iso.org/obp/ui/#iso:std:iso-astm:52900:ed-1:v1:en (2015)
2. D.L. Bourell, J. Beaman, C.L. Ming, D.W. Rosen, A brief history of additive manufacturing and the 2009 roadmap for additive manufacturing: Looking back and looking ahead, in *US – Turkey Workshop on Rapid Technologies*, (2009)
3. R.F. Housholder, Process Molding **4**(12), 0–5 (1979)
4. C. R. Deckard, Method for producing parts by selective laser sintering (1990)
5. C. R. Deckard, Apparatus for producing parts by selective laser sintering (19):14 (1997)
6. L. Wang, A. Yu, E. Li, H. Shen, Z. Zhou, Effects of spreader geometry on powder spreading process in powder bed additive manufacturing. Powder Technol. **384**, 211–222 (2021)
7. E.J.R. Parteli, T. Pöschel, Particle-based simulation of powder application in additive manufacturing. Powder Technol. **288**, 96–102 (2016)
8. S. Haeri, Y. Wang, O. Ghita, J. Sun, Discrete element simulation and experimental study of powder spreading process in additive manufacturing. Powder Technol. **306**, 45–54 (2017)
9. S. Haeri, Optimisation of blade type spreaders for powder bed preparation in additive manufacturing using DEM simulations. Powder Technol. **321**, 94–104 (2017)

10. J.K. Mackenzie, R. Shuttleworth, A phenomenological theory of sintering. Prooc. Phys. Sect. B **62**, 833 (1949)
11. F. Sillani, R.G. Kleijnen, M. Vetterli, M. Schmid, K. Wegener, Selective laser sintering and multi jet fusion: Process-induced modification of the raw materials and analyses of parts performance. Addit. Manuf. **27**(February), 32–41 (2019)
12. R.D. Goodridge, C.J. Tuck, R.J.M. Hague, Laser sintering of polyamides and other polymers. Prog. Mater. Sci. **57**(2), 229–267 (2012)
13. I. Campbell, D. Bourell, I. Gibson, Additive manufacturing: Rapid prototyping comes of age. Rapid Prototyp. J. **18**(4), 255–258 (2012)
14. D.L. Bourell, T.J. Watt, D.K. Leigh, B. Fulcher, Performance limitations in polymer laser sintering. Phys. Procedia **56**(C), 147–156 (2014)
15. A. Mokrane, M. Boutaous, S. Xin, Process of selective laser sintering of polymer powders: Modeling, simulation, and validation. C. R. – Mec. **346**(11), 1087–1103 (2018)
16. S. Dupin, O. Lame, C. Barrès, J.Y. Charmeau, Microstructural origin of physical and mechanical properties of polyamide 12 processed by laser sintering. Eur. Polym. J. **48**(9), 1611–1621 (2012)
17. S.P. Soe, Quantitative analysis on SLS part curling using EOS P700 machine. J. Mater. Process. Technol. **212**(11), 2433–2442 (2012)
18. X. Wang, M. Jiang, Z. Zhou, J. Gou, D. Hui, 3D printing of polymer matrix composites: A review and prospective. Compos. Part B Eng. **110**, 442–458 (2017)
19. G. Lumay, F. Francqui, C. Detrembleur, N. Vandewalle, Influence of temperature on the packing dynamics of polymer powders. Adv. Powder Technol. **31**(10), 4428–4435 (2020)
20. M. Kontopoulou, J. Vlachopoulos, Melting and densification of thermoplastic powders. Polym. Eng. Sci. **41**(2 SPEC. ISS), 155–169 (2001)
21. M. Zhao, D. Drummer, K. Wudy, M. Drexler, Sintering study of polyamide 12 particles for selective laser melting. Int. J. Recent Contrib. Eng. Sci. IT **3**(1), 28 (2015)
22. C.A. Chatham, T.E. Long, C.B. Williams, A review of the process physics and material screening methods for polymer powder bed fusion additive manufacturing. Prog. Polym. Sci. **93**, 68–95 (2019)
23. O. Pokluda, C.T. Bellehumeur, J. Vlachopoulos, Modification of Frenkel's model for sintering. AICHE J. **43**(12), 3253–3256 (1997)
24. C.T. Bellehumeur, M. Kontopoulou, J. Vlachopoulos, The role of viscoelasticity in polymer sintering. Rheol. Acta **37**(3), 270–278 (1998)
25. R. Brighenti, M.P. Cosma, L. Marsavina, A. Spagnoli, M. Terzano, Laser-based additively manufactured polymers: A review on processes and mechanical models. J. Mater. Sci. **56**(2), 961–998 (2021)
26. C. Badini, E. Padovano, V.G. Lambertini, Preferred orientation of chopped fibers in polymer-based composites processed by selective laser sintering and fused deposition modeling: Effects on mechanical properties. J. Appl. Polym. Sci. (November 2019), 1–12 (2020)
27. A. Amado, M. Schmid, G. Levy, K. Wegener, Advances in SLS powder characterization, in *Proceedings of the 22th Solid Freeform Fabrication Symposium, Austin, Texas*, vol. 12, (2011), pp. 438–452
28. J. Clayton, D. Millington-Smith, B. Armstrong, The application of powder rheology in additive manufacturing. JOM **67**(3), 544–548 (2015)
29. M. Schmid, A. Amado, K. Wegener, Polymer powders for selective laser sintering (SLS). AIP Conf. Proc. **1664**(1), 160009–170003 (2015)
30. M. Beltrán, Measurement science needs for real-time control of additive manufacturing powder bed fusion processes. Int. J. Prod. Res. (2015). https://doi.org/10.6028/NIST.IR.8036
31. M. Schmid, A. Amado, K. Wegener, Materials perspective of polymers for additive manufacturing with selective laser sintering. J. Mater. Res. **29**(17), 1824–1832 (2014)
32. M. Schmid, K. Wegener, Additive manufacturing: Polymers applicable for laser sintering (LS), in *Procedia Engineering*, (Elsevier Ltd, 2016)
33. G. Wang, P. Wang, Z. Zhen, W. Zhang, J. Ji, Preparation of PA12 microspheres with tunable morphology and size for use in SLS processing. Mater. Des. **87**, 656–662 (2015)

34. H. Chung, S. Das, Processing and properties of glass bead particulate-filled functionally graded Nylon-11 composites produced by selective laser sintering. Mater. Sci. Eng. A **437**(2), 226–234 (2006)
35. S. Kumar, Selective laser sintering/melting, in *Comprehensive Materials Processing*, (Elsevier, 2014), pp. 93–104
36. P.K. Denucci, New process creates prototypes-fast. Foundry Manag. Technol. **121**(11), 22–24 (1993)
37. J.D. Williams, C.R. Deckard, Emerald article: Advances in modeling the effects of selected parameters on the SLS process advances in modeling the effects of selected parameters on the SLS process. Group **4**(2), 90–100 (2011)
38. J.C. Nelson, S. Xue, J.W. Barlow, J.J. Beaman, H.L. Marcus, D.L. Bourell, Model of the selective laser sintering of bisphenol-A polycarbonate. Ind. Eng. Chem. Res. **32**(10), 2305–2317 (1993)
39. M. Berzins, T.H.C. Childs, G.R. Ryder, The selective laser sintering of polycarbonate. CIRP Ann. – Manuf. Technol. **45**(1), 187–190 (1996)
40. Y. Shi, J. Chen, Y. Wang, Z. Li, S. Huang, Study of the selective laser sintering of polycarbonate and postprocess for parts reinforcement. Proc. Inst. Mech. Eng. Pt. L J. Mater. Des. Appl. **221**(1), 37–42 (2007)
41. D. Strobbe, S. Dadbakhsh, L. Verbelen, P. Van Puyvelde, J.P. Kruth, Selective laser sintering of polystyrene: A single-layer approach. Plast. Rubber Compos. **47**(1), 2–8 (2018)
42. N. Mys, A. Verberckmoes, L. Cardon, Processing of syndiotactic polystyrene to microspheres for part manufacturing through selective laser sintering. Polymers (Basel) **8**(11), 1–16 (2016)
43. Z. Yang, H. Peng, W. Wang, T. Liu, Crystallization behavior of poly(ε-caprolactone)/layered double hydroxide nanocomposites. J. Appl. Polym. Sci. **116**(5), 2658–2667 (2010)
44. C. Yan, Y. Shi, J. Yang, J. Liu, Investigation into the selective laser sintering of styrene-acrylonitrile copolymer and postprocessing. Int. J. Adv. Manuf. Technol. **51**(9–12), 973–982 (2010)
45. F. Lupone, E. Padovano, M. Pietroluongo, S. Giudice, O. Ostrovskaya, C. Badini, Optimization of selective laser sintering process conditions using stable sintering region approach. Express Polym Lett **15**(2), 177–192 (2021)
46. T. Laumer, T. Stichel, K. Nagulin, M. Schmidt, Optical analysis of polymer powder materials for selective laser sintering. Polym. Test. **56**, 207–213 (2016)
47. S. Dadbakhsh, L. Verbelen, O. Verkinderen, D. Strobbe, P. Van Puyvelde, J.P. Kruth, Effect of PA12 powder reuse on coalescence behaviour and microstructure of SLS parts. Eur. Polym. J. **92**(December 2016), 250–262 (2017)
48. B. Haworth, N. Hopkinson, D. Hitt, X. Zhong, Shear viscosity measurements on Polyamide-12 polymers for laser sintering. Rapid Prototyp. J. **19**(1), 28–36 (2013)
49. H. Zarringhalam, N. Hopkinson, N.F. Kamperman, J.J. de Vlieger, Effects of processing on microstructure and properties of SLS nylon 12. Mater. Sci. Eng. A **435–436**, 172–180 (2006)
50. B. Caulfield, P.E. McHugh, S. Lohfeld, Dependence of mechanical properties of polyamide components on build parameters in the SLS process. J. Mater. Process. Technol. **182**(1–3), 477–488 (2007)
51. T.L. Starr, T.J. Gornet, J.S. Usher, The effect of process conditions on mechanical properties of laser-sintered nylon. Rapid Prototyp. J. **17**(6), 418–423 (2011)
52. M. Vasquez, B. Haworth, N. Hopkinson, Optimum sintering region for laser sintered Nylon-12. Proc. Inst. Mech. Eng. B J. Eng. Manuf. **225**(12, December), 2240–2248 (2011)
53. R.D. Goodridge, R.J.M. Hague, C.J. Tuck, An empirical study into laser sintering of ultra-high molecular weight polyethylene (UHMWPE). J. Mater. Process. Technol. **210**(1), 72–80 (2010)
54. G.V. Salmoria, C.H. Ahrens, P. Klauss, R.A. Paggi, R.G. Oliveira, A. Lago, Rapid manufacturing of polyethylene parts with controlled pore size gradients using selective laser sintering. Mater. Res. **10**(2), 211–214 (2007)
55. H.J. O'Connor, A.N. Dickson, D.P. Dowling, Evaluation of the mechanical performance of polymer parts fabricated using a production scale multi jet fusion printing process. Addit. Manuf. **22**(May), 381–387 (2018)

56. S.T. Wei, K. Zhou, C. Chao, A comprehensive investigation on 3D printing of polyamide 11 and thermoplastic polyurethane via multi jet fusion. Polymers (Basel) **13**(13), 2139 (2021)
57. Z. Xu, Y. Wang, D. Wu, K.P. Ananth, J. Bai, The process and performance comparison of polyamide 12 manufactured by multi jet fusion and selective laser sintering. J. Manuf. Process. **47**(October), 419–426 (2019)
58. HP, *HP 3D Printing Materials* (HP, 2020). Available at https://h20195.www2.hp.com/v2/getpdf.aspx/4AA7-1533ENA.pdf
59. W. Shen, C.Y. Tang, C.P. Tsui, L.H. Peng, Effects of two damage mechanisms on effective elastic properties of particulate composites. Compos. Sci. Technol. **62**(10–11), 1397–1406 (2002)
60. H.J. O'Connor, D.P. Dowling, Comparison between the properties of polyamide 12 and glass bead filled polyamide 12 using the multi jet fusion printing process. Addit. Manuf. **31**(January 2019), 100961 (2020)
61. K.P.M. Lee, C. Pandelidi, M. Kajtaz, Build orientation effects on mechanical properties and porosity of polyamide-11 fabricated via multi jet fusion. Addit. Manuf. **36**(August), 101533 (2020)
62. C. Pandelidi, K.P.M. Lee, M. Kajtaz, Effects of polyamide-11 powder refresh ratios in multi-jet fusion: A comparison of new and used powder. Addit. Manuf. **40**(February), 101933 (2021)
63. A. Frick, A. Rochman, Characterization of TPU-elastomers by thermal analysis (DSC). Polym. Test. **23**(4), 413–417 (2004)
64. S. Ziegelmeier, F. Wöllecke, C.J. Tuck, R.D. Goodridge, R.J.M. Hague, Aging behavior of thermoplastic elastomers in the laser sintering process. J. Mater. Res. **29**(17), 1841–1851 (2014)
65. G.M. Vasquez, C.E. Majewski, B. Haworth, N. Hopkinson, A targeted material selection process for polymers in laser sintering. Addit. Manuf. **1**(2014), 127–138 (2014)
66. K. Plummer, M. Vasquez, C. Majewski, N. Hopkinson, Study into the recyclability of a thermoplastic polyurethane powder for use in laser sintering. Proc. Inst. Mech. Eng. Pt. B J. Eng. Manufact. **226**(7), 1127–1135 (2012)
67. J. Leng, J. Wu, N. Chen, X. Xu, J. Zhang, The development of a conical screw-based extrusion deposition system and its application in fused deposition modeling with thermoplastic polyurethane. Rapid Prototyp. J. **26**(2), 409–417 (2020)
68. A. Haryńska, I. Gubanska, J. Kucinska-Lipka, H. Janik, Fabrication and characterization of flexible medical-grade TPU filament for fused deposition modeling 3DP technology. Polymers (Basel) **10**(12), 1304 (2018)
69. N.K. Martin, J. Domínguez-Robles, S.A. Stewart, V.A. Cornelius, Q.K. Anjani, E. Utomo, I. García-Romero, R.F. Donnelly, A. Margariti, D.A. Lamprou, E. Larrañeta, Fused deposition modelling for the development of drug loaded cardiovascular prosthesis. Int. J. Pharm. **595**(December 2020), 120243 (2021)
70. L. Verbelen, S. Dadbakhsh, M. Van den Eynde, D. Strobbe, J.P. Kruth, B. Goderis, P. Van Puyvelde, Analysis of the material properties involved in laser sintering of thermoplastic polyurethane. Addit. Manuf. **15**, 12–19 (2017)
71. I. Gibson, D. Rosen, S. Brent, *Additive Manufacturing Technologies. 3D Printing, Rapid Prototyping, and Direct Digital Manufacturing*, 2nd edn. (Springer, New York, 2015)
72. D.S. Hermann, R. Larson, Selective mask sintering for rapid production of parts, implemented by digital printing of optical toner masks, in *International Conference on Digital Printing Technologies*, (Society for Imaging Science and Technology, 2008)
73. A. Ellis, C.J. Noble, L. Hartley, C. Lestrange, N. Hopkinson, C. Majewski, Materials for high speed sintering. J. Mater. Res. **29**(17), 2080–2085 (2014)
74. B. Asiabanpour, B. Khoshnevis, K. Palmer, Advancements in the selective inhibition sintering process development. Virtual Phys. Prototyp. **1**(1), 43–52 (2006)
75. A. Ponnambalam, B. Esakki, C. Udayagiri, Investigation on multi-layer selective inhibition sintering process using finite element analysis. Mater. Today Proc. **4**(2), 2439–2444 (2017)

Chapter 5
Direct Writing: Inkjet and Aerosol-Jet Printing

Pasquale D'Angelo and Davide Vurro

Abstract The term additive manufacturing (AM) is used to denote the set of manufacturing techniques for the fabrication of 3D objects by means of layer-by-layer addition. AM is an emerging area of great interest both for basic research and the industrial sector.

It allows combining a marked versatility in terms of product design, with reduced cost for the materials and related consumption, also allowing an optimal adaptability to mass production manufacturing. The genesis and evolution of AM technologies is enclosed in a short time frame, since during the middle of the 1980s stereolithography emerged as a toll to produce 3D artifacts from templates made of resins. From then on, a great deal of interest in research laboratories has been raised by the bottom-up/top-down deposition of resins and, above all, non-contact writing implemented by liquid precursors, or inks.

The fast evolution of ink-based printing techniques in particular strongly impacts the reliability of 3D printed electronic devices fabricated on flexible substrates and wearable platforms. 3D printed electronics requires the use of innovative substrates, mainly based on polymeric compounds, endowed with specific properties, such as flexibility and/or conformability, and depending on the field of application, a biocompatible character is also often required. Printing techniques based on the use of inks require simple processes, low costs, reduced amounts of inks, reduced levels of waste, easy modification by a dedicated 3D modeling software (i.e., the computer-aided design, CAD, software) of the desired device geometry, and, finally, a large set of printable materials onto different substrates.

The combination between the above properties and the possibility of implementing a fast prototyping manufacturing of a large variety of artifacts makes printing techniques preferable with respect to photolithographic tools, in the context of both basic research and R&D laboratories.

P. D'Angelo (✉) · D. Vurro
Institute of Materials for Electronics and Magnetism-Italian National Research Council (IMEM-CNR), Parma, Italy
e-mail: pasquale.dangelo@imem.cnr.it

S. L. Marasso, M. Cocuzza (eds.), *High Resolution Manufacturing from 2D to 3D/4D Printing*, https://doi.org/10.1007/978-3-031-13779-2_5

The present chapter deals with the basic principles of inkjet and aerosol-jet printing, which are the most promising printing techniques for the rapid prototyping manufacturing of 3D printed electronics, shedding light onto both their main advantages and drawbacks and presenting some literature examples of electronic device application, with a special reference to bioelectronics.

Keywords Non-contact printing · Direct writing · Inkjet printing · Aerosol-jet printing · 3D printed electronics · Fast prototyping · Bioelectronics

5.1 Introduction

Printing techniques can be divided into two main classes according to the features of the printing mode of operation. They can hence be designated as contact and non-contact printing, depending on the different processes implementing the ink deposition [1].

The contact printing techniques are the most common ones and widespread used for the development of electronic and mechanical devices. This family of deposition methods of 3D shaped artifacts are based on the use of a pre-patterned mold in contact with a suitable substrate, and the features patterned on the mold define those of the manufactured object upon deposition of a given ink.

In particular, gravure printing [2], roll-to-roll [3, 4], transfer printing [5], and nanoimprinting [6] are the most known contact printing techniques.

Contact printing methods show some noticeable disadvantages in terms of material consumption and degree of flexibility shown by the preestablished patterns when contextualized to applications requiring a fast prototyping manufacturing.

Non-contact techniques compensate for the deficiencies showed by contact mode printing procedures. This mainly occurs thanks to the use of a CAD for the design of printing patterns, which allows the possibility of using a nozzle set at a fixed distance from the substrate for implementing the material deposition with a limited consumption. The non-contact mode also permits the deposition on non-flat substrates through the displacement of the sample plate [7–9].

A measure of the increasing interest by scientists that are familiar with the research methodology making use of printing techniques is given by the histogram reported in Fig. 5.1 (source Isi-WoS), describing the number of publications dealing with 3D printing techniques for applications in electronics in the last 25 years, where it is evident how a noticeable increment has taken place in the last decade.

3D printed electronics has currently gained a maturity level such as the 3D printed devices are ready to invade the market. The Report Code SE 2466, released on June 2020 by MarketsandMarkets, has predicted a market growth at a compound annual growth rate (CAGR) of 21.5% from 2020 to 2025, with an expected turnover of 20.7 billion USD by 2025 due to the Covid-19 impact on the market of printing technologies, applications, and materials in end-use industry [10].

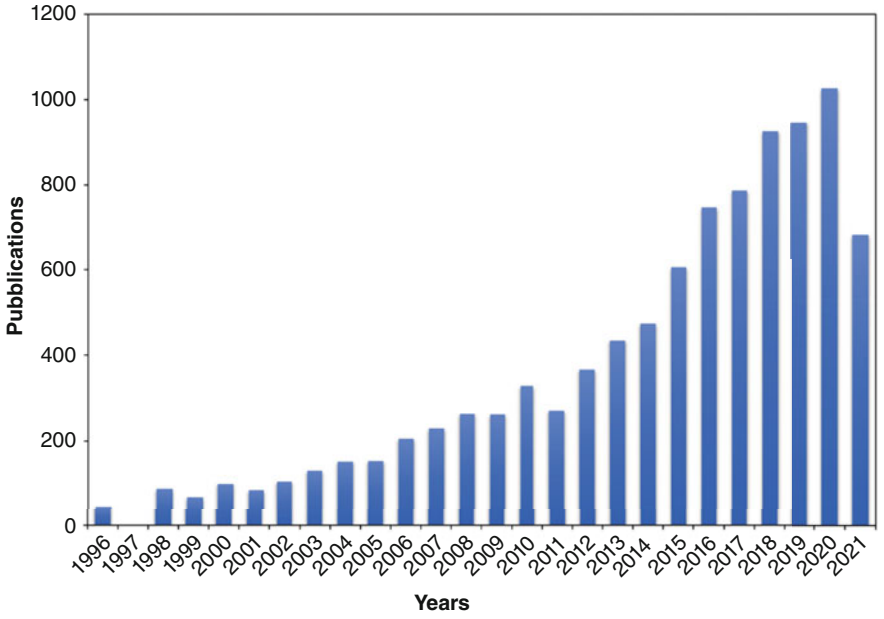

Fig. 5.1 Time evolution of scientific production dealing with 3D printing techniques for electronics. (Source: Web of Science, WoS)

5.2 Inkjet Printing

Currently, inkjet printers are everyday life tools accessible to everyone at a low cost. For this reason, among non-contact printing techniques, inkjet printing (IJP) has attracted the most attention of researchers to the point that it is surely the most mature and commonly used method, not only in the research field but also in terms of industrial output.

From the research point of view, a wide range of applications are based on the use of the IJP technique, ranging from the manufacturing of flexible electronics, via the implementation of electrodes/interconnections in integrated electronics and the manufacturing of active interfaces in electronic devices (such as transistors and/or photovoltaic modules), to the development of applications in the medical field, such as biosensors for the diagnosis of several diseases and electrodes for biosignaling.

The parallel development of basic research studies and production routes experimented in several R&D laboratories has made this kind of technology solid also in the context of mass production, guaranteeing a good yield in terms of low production cost/waste and high versatility in terms of design/flexibility of the features that are intended to be achieved.

5.2.1 IJP Operation Principle

The IJP is a non-contact printing technique classified as a direct writing (DW) method. It is based on the ejection of a fixed amount of a material (i.e., the ink, which is basically a solution or a dispersion of nanoparticles) through a nozzle. The ink impacts on a substrate (rigid or flexible) placed on a moving plate, replicating a CAD drawing of the desired pattern converted into a vector-based tool path driving a moving plate [7, 11].

The plate is heated with the aim of favoring the fast evaporation of the solvent in order to define the pattern features. A post-processing step is required in the case of conductive inks based on nanoparticles in order to promote a sintering of the ink aimed at promoting a coalescence of the conducting nanosystems and, as a result, to ensure the formation of a well-interconnected network inside the whole as-deposited pattern [12, 13].

IJP deposition systems exploit three different actuators for the generation of the ink flow. The actuators, in particular, differ each other for the physical principle they are based on. The most used actuators are the thermal, piezoelectric, and electrodynamic ones [1]. In all cases, ink generation is promoted by electronically driven physical mechanisms.

Thermal actuators promote the generation of ink-based drops by means of a thermal expansion of the ink, occurring once it is exposed to high temperatures. Thermal actuators are indeed incompatible with inks undertaking a thermal degradation [14]. Conversely, piezoelectric actuators implement the generation of ink-based droplets upon the mechanical deformation of the ink reservoir, which is promoted by the application of a bias voltage on the piezoelectric actuator in contact with the reservoir walls [15].

Electrodynamic-based actuators exploit the application of an electric field between a conducting nozzle and the substrate, thus implementing an electrically driven deposition of the ink [16].

Two operation modes can be carried out by IJP systems, namely, the continuous inkjet (CIJ) and the drop-on-demand (DoD) delivery of inks [17].

In the CIJ mode, a continuous ink flow is generated and driven towards the substrate. Inkjet printers equipped with a piezoelectric actuator implement a CIJ operation mode, whose basic principle is reported in Fig. 5.2. Once the ink reaches the nozzle, it forms a stream that tends to break up, generating some droplets with a mean diameter of 120 μm. These droplets tend to move randomly with a preferable direction along the z-axis. This phenomenon is known as Plateau–Rayleigh instability, a fluid-dynamic instability that is due to the action of the surface tension at the outlet of the nozzle. Surface tension, indeed, provokes a separation of the continuous stream in the form of small droplets insofar as, while the total volume per unit time is preserved, the size of the stream tends to reduce [17]. Under ideal conditions, the ink flow breaks up in such a way that the generated droplets are characterized by a drifting with a speed ranging from 10 to 20 m s^{-1}. Typically, a CIJ printhead is able to generate a rate of hundreds of thousands of

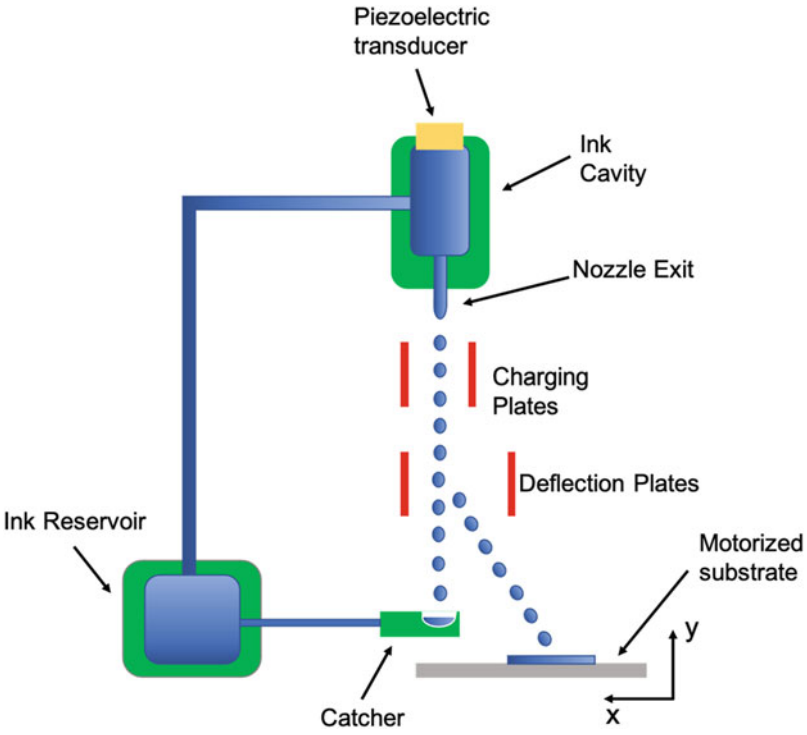

Fig. 5.2 Schematization of the operation mode of continuous inkjet printers

droplets per second, even if some of them will not ever reach the substrate. The pattern will be defined by droplets that, first, experience an electrostatic charging while passing through two parallel charging plates (at the nozzle outlet) that are driven by a voltage bias and, then, are deflected and hence directed towards the substrate placed on a moving plate, once they pass through a couple of voltage-biased deflection plates [18].

Uncharged droplets are collected by a catcher and then sent to a recycling system providing for a refilling of the ink reservoir.

While allowing the reduction of both ink consumption and waste, this recovery process is not always applicable to all the inks available for IJP systems; for instance, polymeric inks may undergo a degradation upon CIJ processes [19].

A typical CIJ system is compatible with inks showing a viscosity within the range of 2–10 cP and is able to generate cylindrical ink streams with a diameter of 60 μm, travelling at a speed that, as already mentioned, ranges from 10 to 20 cm s^{-1} [17].

Inkjet systems based on a DoD operation mode do not exploit a continuous ink stream at the nozzle output but, conversely, allow generating droplets only when it is needed.

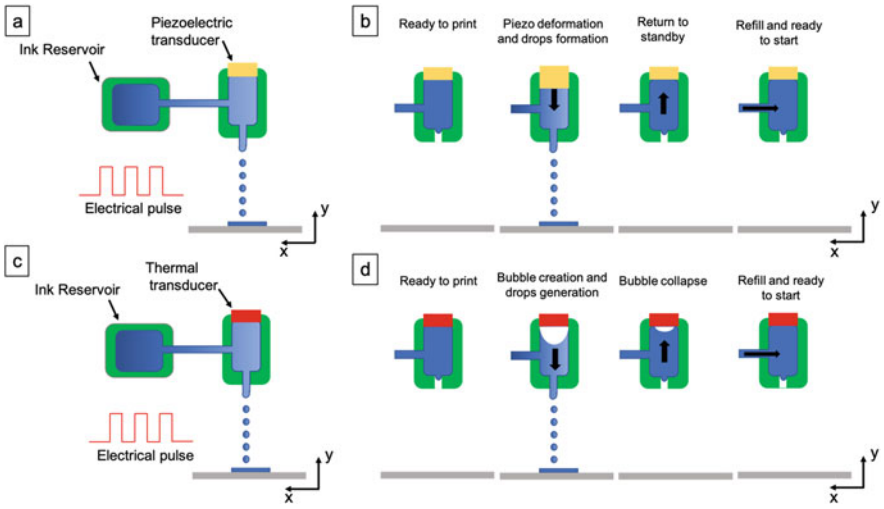

Fig. 5.3 DoD operation mode based on the use of a piezoelectric transducer is reported in panel (**a**); the related drop generation principle is reported in (**b**). In panel (**c**) the use of a thermal transducer in DoD systems is reported, together with the related drop generation principle (panel **d**)

DoD printheads are based on an ink reservoir directly connected to a cavity equipped with an actuator, which is accordingly filled by a small amount of the ink to be deposited (Fig. 5.3a, c).

The formation of droplets is hence carried out by a stimulus applied to the actuator, mainly electrical, and the deposition occurs directly on the substrate. In this way, a DoD apparatus allows maintaining low levels of ink consumption/waste without the need for a recycling system.

Two versions of a prototypical DoD system are available, differing on the type of actuator they are based on, i.e., a piezoelectric or a thermal actuator. As reported in Fig. 5.3d, for DoD printers with a thermal actuator, an electrical pulse activates a heater acting on the ink contained in the cavity [20]. The ink solvent evaporates, thus generating a steam bubble that pushes the ink out of the nozzle. The following bubble bursting favors the cavity refilling.

The use of DoD systems with thermal actuators is typical of commercial inkjet printers commonly used in home environment or office. It just requires opportune specifications for inks, which must be based on highly volatile solvents and non-thermolabile materials.

DoD printers exploiting a piezoelectric actuator are indeed common in the industrial and research fields. As reported in Fig. 5.3b, in this case a deformation of the piezoelectric actuator upon application of an electric pulse induces the ink outflow at the nozzle outlet, while the relaxation of the same piezoelectric element allows the cavity refilling [21]. Piezoelectric actuator-based printers provide less stringent limitations in terms of ink features. IJP systems operating under DoD mode

are compatible with inks characterized by a wider viscosity interval, i.e., ranging between 10 and 100 cP, compared to that of CIJ systems. Typical ink streams characterized by a mean droplet size having a diameter of 50 μm are generated by DoD systems, while the stream speed at the nozzle outlet ranges between 5 and 10 m s^{-1} [17]. Both CIJ and DoD allow a process resolution higher than 20 μm depending, for instance, on the applied voltage at the actuator and the speed of the moving plate.

The features of inkjet-printed patterns depend on several factors, but the ones weighting the most in determining the characteristics of a final product by a IJP process are the chemical nature of the used inks, in terms of both the solvents they are based on and their composition and their physical properties. Clearly, some modelization developed within the domain of fluid mechanics theory can be used to describe the features of the stream and, accordingly, of the entire printing process. As a matter of fact, the quality of IJP processes depends on the physical properties of an ink in terms of viscosity and surface tension, which are crucial for determining the quality level of the printed patterns. In fact, viscosity and surface tension of a liquid ink rule the formation and the shape of generated droplets, respectively.

The Ohnesorge number (*Oh*) provides the expression (Eq. 5.1) determining the relationship between these physical quantities and accounts for the liquid viscosity during the formation of droplets. It is expressed in terms of two dimensionless quantities, i.e., the Reynolds (Re, Eq. 5.2) and the Weber (*We*, Eq. 5.3.) numbers, as:

$$Oh = \frac{\sqrt{We}}{\mathrm{Re}} = \frac{\eta}{\sqrt{\rho D_N \sigma}} \tag{5.1}$$

$$\mathrm{Re} = \frac{\rho V D_N}{\eta} \tag{5.2}$$

$$We = \frac{\rho V^2 D_N}{\sigma} \tag{5.3}$$

where η, ρ, and σ are the ink viscosity, density, and surface tension, respectively, while D_N denotes the diameter of the nozzle.

Re is defined as the ratio of inertial to viscous shear forces and gives a quantitative measure of the features of a fluid flow in a round-shaped pipe. In particular, it is used to distinguish a laminar flow (occurring at Re < 2100, according to the API 13D recommendations) from a turbulent one. Indeed, We is defined as the ratio between the kinetic energy (causing a deformation of ink droplets) and the forces resulting from the surface tension realizing the cohesion of the same droplets travelling with a flow rate characterized by a given velocity *V* [17].

Low *Oh* values mean that viscous surface tension effects dominate during the droplet formation process and the droplet stability is then favored. Conversely, high Oh values provide a condition in which a viscous dissipation dominates the droplet formation, hence affecting the proper generation of the same droplets. Theoretically, a correct ink deposition by an inkjet printer can only take place if Oh ranges between 0.1 and 1, or if its reciprocal value 1/Oh, denoted as Z number, ranges from 1 to 10 [22]. If $Z < 1$, the low ink density causes the formation of polydispersed droplets in terms of size and volume, while Z values higher than 10 are related to highly dense inks, and the droplet formation is even forbidden in this case.

As mentioned above, the inkjet deposition process is also influenced by the chemical composition of printable inks. Inks are, in fact, solutions or dispersions of nanocomposite materials in a solvent mixture, where each solvent composing the mixture is characterized by an own evaporation rate. A wrong mixture of solvents adversely affects the quality features of printed patterns. The most evident drawback of a wrong mixture of solvents is the coffee ring effect (CRE), a pattern instability due to a nonuniform evaporation of solvents leading to printed patterns with an uneven profile. The printed lines are accordingly characterized by a thin core and a thicker edge (Fig. 5.4a) [23, 24].

Several strategies have been proposed to overcome this concern. For instance, it has been demonstrated that the use of surfactants reduces the CRE [25]. Furthermore, also the use of organic solvents (ethylene glycol), providing for high homogeneity in colloidal inks [26], and the use of alcohol mixtures containing n-butanol [27], providing an homogeneous distribution of nanoparticles inside the ink droplets, are efficient strategies to reduce the CRE.

Finally, a reduced CRE takes place by controlling the migration of nanoparticles (and, more in general, of nanosystems composing the ink) to the contact lines upon controlling the drying conditions of solvents. Hence, highly volatile solvents are preferred in order to induce a faster drying of the ink at the substrate interface [28].

5.2.2 Application of the IJP Technique for 3D Printed Bioelectronics

During the last decade, the IJP technique has had a strong impact on the development of printed artifacts in the context of electronic device application, both for research purposes and in terms of mass production aims. In particular, the scientific production dealing with 3D printed electronics witnesses a massive use of this technique in several kinds of applications, starting from the basic metallic interconnections up to the development of actual devices. For instance, photovoltaic modules [29–34], electrical components [35–38], pressure and temperature sensors [39–42], and organic thin-film transistors (OTFTs) [43–45] have been manufactured by IJP technology.

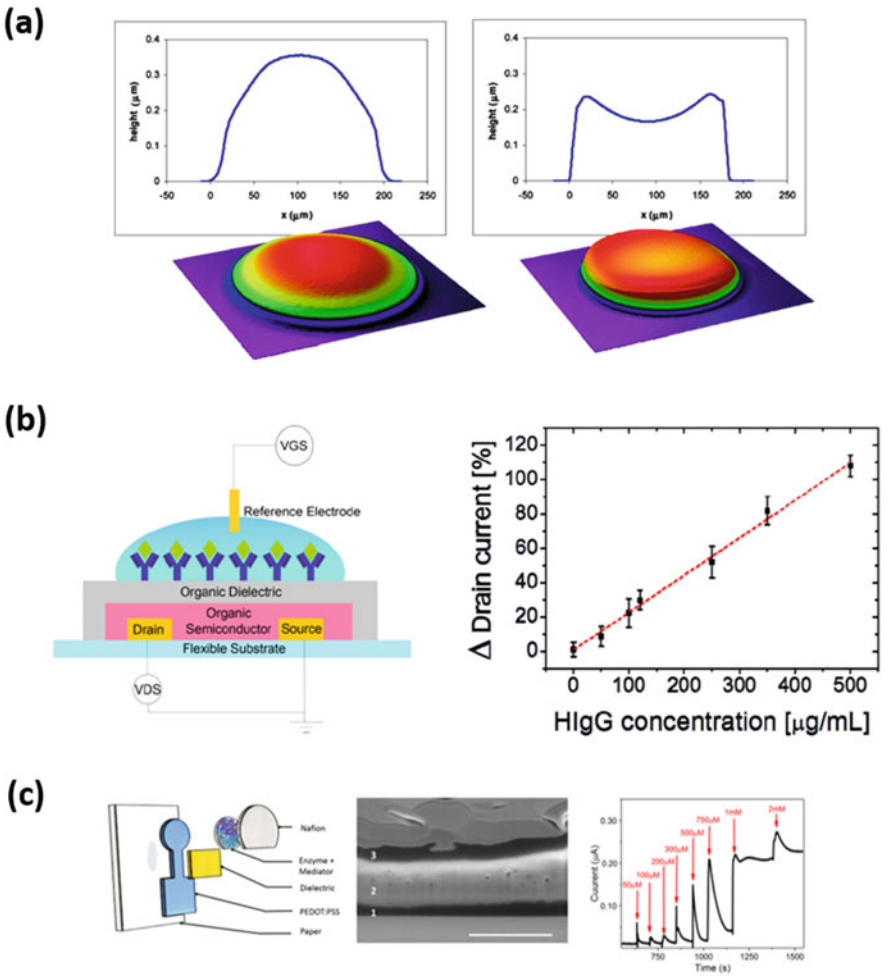

Fig. 5.4 The left side of panel (**a**) shows the schematization of an inkjet-printed pixel with a correct profile, while the schematization of an ill-defined pixel due to the coffee ring effect is depicted in the right side of panel (**a**) (Reprinted with permission from [23] copyright 2008 American Chemical Society); IgG detection by a full printed OTFT is reported in panel (**b**). The left panel shows a schematic of the inkjet-printed BioFET with a CYTOP top gate dielectric functionalized for HIgG detection, while the right side shows the device calibration curve (linear dependence of the percentage variation of the channel current as a function of the HIgG concentration). (Reprinted with permission from [53]); (**c**) schematics of an all-printed PEDOT/PSS-based biosensor on a paper substrate comprising a dielectric (yellow layer), a biological coating made of an electron mediator and an enzyme (GOx), and a nafion capping layer. A SEM micrograph image of the stacking layers and the current vs. time response at different glucose concentrations in saliva samples are reported too. (Reprinted under Creative Commons Attribution License from CC BY [54])

This technique is versatile in terms of allowed materials and patterned line features, being also compatible with different kinds of substrates. In this respect, it has attracted the interest for the production of wearable devices requiring the use of flexible and conformable supports [40, 46].

A great deal of interest in IJP has been addressed to the production of wearable and flexible biosensing platforms such as OTFTs [47]; ion to electron transducing systems known as organic electrochemical transistors (OECTs) [48]; various electrodes for biosignaling [49, 50], also made of conducting polymers and implemented on tattoos [51]; and skin-attachable sensors [52].

Biosensors require suitable characteristics determined by different conditioning factors for proper working in terms of sensitivity, stability, and reliability when operated for the detection of bioanalytes (transistors) or for the recording of physiologic signals such as electrocardiograms (ECG) and the electroencephalograms (EEG). In particular, IJP based on DoD systems is preferable for research purposes aimed at fulfilling the right requirements of stability/reliability. This is because such systems allow obtaining a better control of the deposited patterns and permit to extend the range of materials that can be printed. As a consequence, the use of DoD printers gives the possibility of testing more stable and reproducible conducting inks and resilient protecting inks, while allowing at the same time the production of fully printed devices. This is basically due to the fact that inks made of both organic and inorganic materials have allowed the deposition of almost all the layers and interfaces comprising a device.

Noteworthy examples of efficient and stable devices for biosensing, with different interfaces or completely fabricated by IJP, include the fabrication of BioFETs, which are top gate OTFT with functionalized polymeric gates for immunosensing, exploited for human immunoglobulin (HIgG) detection based on the functionalization of a top insulating layer with an antigen–antibody approach [53] and a fully inkjet-printed glucose sensor on commercial glossy paper [54]. The first device is made (from the bottom to the top) of a flexible (PEN) substrate, Au source and drain electrodes (44 Ω/square sheet resistance), and an active layer (the channel, made of an amorphous organic semiconductor ink, the p-type SP400–1750), all these layers being deposited by an IJP technique. The device has been completed by a spin-coated top insulator, a perfluoropolymer known as CYTOP functionalized by the antibody, through an amino-functionalization by APTES for the immobilization of human immunoglobulin (HIgG), and a liquid electrolyte with a reference electrode. The field-effect-type mode of operation is then influenced by a capacitive coupling (dependent on the concentration of the analyte in PBS) and the effective gate dielectric. The percentage variation of the device channel current variation shows a linear increase as a function of the HIgG concentration, providing a limit of detection (LoD, i.e., the lowest concentration of a substance that a sensor can reliably detect) of 5.71 $\mu g\ mL^{-1}$, with good device reproducibility upon repeated measurements and selectivity assessed by comparing the response with that of a nonspecific antigen, i.e., the goat IgG (Fig. 5.4b).

The second device is a long-term stable analytical biosensor following the logic of immunosensors, i.e., electrochemical biosensing platforms, commonly known as

screen-printed electrodes (SPEs) due to the standard screen printing process used for their fabrication, exploiting a functionalization for implementing biorecognition elements. It is made of inkjet-printed components on a paper substrate, namely, three electrodes (acting as working, counter-, and reference electrodes) made of a well-known polymer used in several device applications due to its high conductivity and electrochemical properties, i.e., the poly(3,4 ethylenedioxythiophene)/polystyrene sulfonate (PEDOT:PSS). Successive layers made of a dielectric material (SunTronic EMD6415), a biological coating comprising an electron mediator and the enzyme (glucose oxidase, GOx), and a nafion film acting as encapsulation layer, have been printed on the PEDOT:PSS working electrode. The normalized response from current vs. time curves has shown that the sensor is able to detect glucose concentrations in saliva within a physiologically relevant range (Fig. 5.4c), with a stability of the device response evaluated over a period of 1 month after the device fabrication and its storage in ambient conditions.

Recently, biosensors based on the OECT architecture/operation have also gained the attention of the scientific community, and 3D printing methods based on IJP technology have been considered for device manufacturing. One of the pioneering works dealing with OECT biosensing regards an all-PEDOT:PSS device used for the selective detection of dopamine in ascorbic and uric acids with a LoD of 6 μM [55]. The detection has been implemented by evaluating changes into the device transconductance parameter (which quantifies the attitude of the ion-to-electron transduction by an OECT) assessed on its turn from the transistor characteristics in the presence of the dopamine analyte and the interfering species.

The IJP technique has also been used in combination with other printing methods to define immunosensors based on the SPE concept. For instance, very recently an immunosensor for the detection of HT-2 mycotoxin has been developed by fabricating electrical connections by the screen printing technique and the graphene oxide (GO)-based working microelectrode by an inkjet printer [56]. The GO electrode has been accordingly functionalized by the antiHT-2 antibody upon exploiting the presence of residual carboxylic groups on the GO layer. The biosensor allowed a detection of HT-2 in a biological matrix made of fetal bovine serum with a LoD of 1.6 ng ml^{-1}.

Another interesting biotechnological application of the IJP technique regards its combination with the microneedle technology. Microneedles are attractive for advanced transdermal drug delivery applications, so that patches equipped with microneedles loaded using some drugs are the subject of a growing research activity. IJP technology is mainly used to promote the coating of microneedle-based systems in a more efficient and nondisruptive way compared to the usual dip-coating approaches. A work by Uddin et al. [57] shows the coverage by an inkjet printing approach of stainless-steel microneedles (50 μm in diameter), fabricated by an infrared laser, with three anticancer agents, i.e., 5-fluororacil, curcumin, and cisplatin, and a hydrophilic graft copolymer (Soluplus) assisting the drug delivery for insoluble drugs. The needle coverage efficiency has been found to be dependent on the process parameters (i.e., the applied voltage and the duration of the electric pulse acting on the actuator) and geometrical factors (i.e., the nozzle diameter),

and the successful drug release has been also shown by in vitro tests on abdominal pigskin [57]. Ross et al. have shown the same approach by Uddin and co-workers to cover stainless steel microneedles (10 μm thick) with insulin polymeric layers, where several polymeric materials have been used with a dual function, that is, to promote a homogeneous insulin-loaded coverage and to act as a protecting layer for the drug [58].

5.3 Aerosol-Jet Printing

The aerosol-jet printing (AJP) technique is an innovative manufacturing protocol for the implementation of in-line, all-printed devices. AJP can be considered as a finer evolution of IJP, both techniques being based on the deposition of ink droplets forming a stream that is directed towards a substrate placed at a given distance from the outlet of a nozzle, even if the AJP deposition process is inherently different from that of IJP. In fact, AJP is ruled by an aerodynamic printing principle where an aerosol mist made of aerosolized droplets, with different diameters (from 1 to 5 μm) and composed by nanosystems with a size ranging from 10 to 700 nm, are transported by a nitrogen gas flow or even by compressed air [59]. AJP is however characterized by a higher definition with respect to that achievable by IJP, having a line resolution of about 8 μm [60]. AJP allows the deposition of a larger set of materials, characterized by a viscosity ranging between 1 and 1000 cP [59]. Typical working distances of 3–5 mm between the nozzle and the substrate also promote the AJP as a suitable printing tool for implementing the fabrication processes on rough substrates, even allowing the printing on 3D substrates and circuit design in the vertical stacking.

As a non-contact, DW technique, AJP basically allows reproducing the same applications obtained by IJP, and even if this printing technique is still less mature than IJP, it is currently stealing the spotlight to the latter because, under a technological point of view, the set of the objective advantages allowed by AJP promotes its better industrial scalability and confers to it a marked attitude for in-line mass production of disparate artifacts.

5.3.1 AJP Operation Principle

The process scheme of an AJP system is conceptually the same as an IJP in so far as aerosol-jet printers' components implement the generation of an aerosol-based stream by an atomizer and its deposition on a substrate, placed on a moving plate, by a deposition head (DH) equipped with a nozzle. The only conceptual difference is that AJP systems foresee a further intermediate step between the generation of an aerosol-based ink and its deposition, namely, a transport and confinement of the aerosol mist in a pipeline by means of two opportune nitrogen flows, the carrier gas

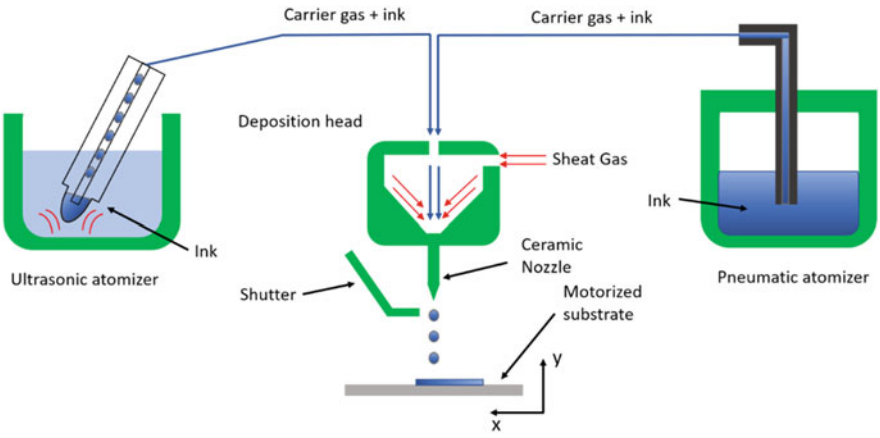

Fig. 5.5 Schematization of an aerosol-jet printer operation mode; both UA (left side) and PA (right side) atomizer are reported

flow (CGF) and the sheath gas flow (ShGF). The ShGF promotes the enhancement of the aerosol-based stream velocity within the pipeline and forces the aerosolized droplets along the ideal central axis of the stream, collimating it and limiting the nonnegligible spreading of droplets that would tend to deviate from the streamline.

The basic scheme of an aerosol-jet printer is reported in Fig. 5.5. Two kinds of atomizers implement the aerosol formation in AJP systems, the ultrasonic (UA) and the pneumatic (PA) atomizer. While UAs are compatible with low-density inks, with a viscosity between 1 and 10 cP, PAs are used to deposit inks with a viscosity higher than 10 cP, up to 1000 cP, the latter having a viscosity comparable to that of glycerin. This means that the ink loading by a compositional percentage of the functional nanosystems can be pushed up to 70%. Hence, in this extreme case a high conductivity for conducting inks can be reached even by a single-pass deposition process.

UAs are made of a glass ink reservoir contained in a chamber partially filled by some water surrounding it. The ink reservoir typically requires a filling by 2 mL of the desired ink.

In UAs, an ultrasonic wave is exploited to create an aerosol from a surface acoustic wave. Generated droplets are expected to follow a log-normal distribution mass and size distribution [61]. During the aerosol generation, heavier droplets tend to precipitate and recombine, so that only lightweight droplets are captured by the CGF, directed towards the DH by passing through the mist tube and ejected from the nozzle in the form of a continuous stream.

PAs are made of a plastic jar containing the ink reservoir (requiring a filling by a higher ink volume of 20 mL) and a metallic cylinder. The aerosol formation is ruled by the application of a high-pressure gas flow on the ink, collected by the cylinder cavity and directed towards a mist tube. The latter collimates the generated aerosol inside a filter known as virtual impactor, whose function consists of selecting the

smaller aerosol droplets which are removed by an exhaust. The as-treated aerosol is then directed towards the DH.

The DH (Fig. 5.5) is made of a focusing chamber in which CGF and ShGF flow in a way that their combination provides for a coaxial configuration focusing the ink stream within the nozzle, which is made of a ceramic material and has typical diameters ranging between 100 and 300 μm. Loss processes take place in the DH, due to collisions between some droplets and the inner walls of the same DH. Nevertheless, the sheath flow is expected to limit the nozzle clogging, which typically strongly affects the printing process by inkjet printers. It is worth mentioning that, depending on the nature of the ink, clogging issues may also affect the printing process by AJP systems.

The substrate collecting the ink stream is placed on a motorized deposition plate controlled by a 2D (and in some printer models by a 3D) motion control system whose movement is controlled by a software converting the CAD design into a vector-based tool path. The plate speed affects the thickness of a printed line in such a way that the higher the plate speed, the thinner the lines obtained for a given printer setup in terms of ShGF and CGF. The plate temperature is crucial in determining the final quality features of the printing process. In commercial printers it can be set in a temperature range from room temperature to 120 °C with the aim of controlling the evaporation rate of the solvent and the related drying process of the ink impacting with the substrate.

Although this technology is less mature than the IJP one, literature offers some interesting insights for a proper understanding of the physics behind the AJP process. In our opinion, the work by E.B. Secor [62] furnishes a guideline for a broader audience approaching the AJP technology, giving a general overview of the printing process. The concepts expressed in this work are based on general principles and are contextualized to commercially available printers. The latter aspect is quite relevant as, despite the general character of basic operation principles, the features of printed artifacts inherently depend on the printer geometry.

As far as the properties of the generated aerosol stream is concerned, AJP systems would ideally operate under a laminar flow condition, in the subsonic regime. In fact, the typical size of a nozzle outlet (hundreds of micrometers) and the magnitude of both ShGF (20–300 ccm) and CGF (20–40 ccm) rates allowed and typically used by actual printers qualitatively indicate that the flow velocity (expressed as $4(\mathrm{ShG} + \mathrm{CG}) / \pi \mathrm{D_N}2$, where $\mathrm{D_N}$ is the nozzle diameter) varies between some tens of $\mathrm{m \cdot s^{-1}}$ to about 200 $\mathrm{m \cdot s^{-1}}$. In addition, the Reynolds number (expressed as $4\rho(\mathrm{ShG} + \mathrm{CG}) / \pi\mu \mathrm{D_S}$, where ρ and μ are the nitrogen density and dynamic viscosity, respectively, and D_S is the stream diameter) for a typical *AJ* printer is <2500, indeed corresponding to a laminar flow regime [63]. The aerosol stream collimation [62] may be used to quantitatively define the line width (*LW*) in the case of laminar flow conditions for a nozzle with a given diameter D_N, whereas *LW* can be expressed as follows [64]:

$$LW = D_N \sqrt{1 - \sqrt{\frac{FR}{1 + FR}}} \tag{5.4}$$

Here, *FR* is the focus ratio, defined as the ratio between the sheath and carrier gas flow rates. *FR* defines the features of a line regardless of the ink properties (nature, size distribution, solvents). Equation 5.4 predicts that the line width decreases upon increasing the *FR* parameter, in agreement with the phenomenology and the modelization behind the stream confinement described in ref. [65].

This equation well describes the behavior of PEDOT:PSS printed lines, except for the case of nozzles with larger diameters at the lowest integer value of FR (i.e., $FR = 1$), where the observed deviations have been ascribed to the overspray (OS) phenomenology [64].

OS is a typical printing instability by AJP systems consisting of an ill-defined profile for printed lines caused by a deposition of individual droplets, or clusters made of a limited number of coalesced droplets, out of the line profile [65].

The overspray phenomenology has been widely investigated in a large set of works, mainly dealing with prototypical inks made of metallic (silver) nanosystems [66, 67], even if the OS phenomenology has been extended to other materials of interest in bioelectronics and biotechnologies, such as PEDOT:PSS [64] and biological inks [68], respectively.

Actually, the scheme adopted to describe an aerosol-jet printer as a system operating under ideal laminar flow conditions does not take into consideration that real AJP systems are, on contrast, nonideal. In fact, real AJ printers implement a droplet formation characterized by a nonuniform size distribution. This is because of turbulences causing a deviation of small droplets from the coaxial aerosol stream. Hence, a strategy to reduce OS provides for the use of nozzles with larger diameters. In fact, the larger is the nozzle's diameter, the weaker are turbulences at the nozzle exit and the less pronounced is the overspray effect. OS is also due to a drying of external droplets at the nozzle exit induced by the sheath gas flow and no more collimated under the effect of the same ShGF, due to a reduction of their volume/mass and a consequent reduced inertia under the gas flow action. Such drying effect is sometimes overcome by adding small amounts of less volatile cosolvents, such as ethylene glycol, in ink formulations [69].

5.3.2 *Application of the AJP Technique for 3D Printed Bioelectronics*

AJP compatibility with a large set of inks and the versatility of this technique in terms of allowed deposition routes for the implementation of 2D and 3D structures have opened the way towards the development of disparate applications in the field of 3D printed electronics. For instance, some examples of applications based on AJP regard the implementation of conformal structures following the profile of curved

substrates [70] or even actual 3D structures such as micro-pillars [70] and antennas [70]. Also conductive traces for the implementation of vertical interconnections manufactured by exploiting the positioning of the DH along the z-axis, which is allowed by some models of aerosol-jet printers [71], have been manufactured by this technique.

Literature reported not only interconnections for integrated electronics [72, 73], but also electronic components, such as resistors or capacitors made of silver traces as electrical pads and PEDOT/PSS or SU-8 photoresist as conducting and dielectric materials, respectively [74].

3D printed electronic devices manufactured by means of AJP systems include several examples of all-printed organic solar cells (OSC) [75] and photodiodes [76]; flexible OTFTs made of carbon-based materials, such as single-walled carbon nanotubes (SWCNTs) [77] and reduced graphene oxide [78]; and electrolyte-gated transistors, based on organic semiconductors such as poly(3-hexylthiophene) (P3HT) [79] and oxides, such as indium tin oxide thin-film transistors showing a high mobility of 10 $cm^2V^{-1}s^{-1}$ and a 2D insulator–metal transition [80]. Several examples of ion-gel organic transistors are reported in literature. Xia et al. demonstrated an all-organic ion-gel-gated P3HT transistor and related integrated circuits (inverters). The device was fully printed on a flexible poly(ethylene naphthalate) substrate, with source, drain, and gate electrodes made of PEDOT/PSS and an ion gel gate electrode based on an ink made of a mixture of the ionic liquid 1-ethyl-3-methylimidazolium bis(trifluoromethylsulfonyl)imide (EMIM-TFSI) and the poly(styrene-b-methylmethacrylate-b-styrene) (PS-PMMA-PS) block copolymer. The gate allowed obtaining a low-voltage operation (below 2 V), a high output conductance (>2 mS mm^{-1}), a low threshold voltage (<1 V), and high inverter switching frequencies (1–10 kHz) [81].

More recently, Li et al., demonstrated a printed SWCNT-based TFT with a transparent, mechanically flexible, and thermally stable polyfluorinated electrolyte (PFE), acting as a high-capacitance gate dielectric. The air-stable ambipolar response was also supported by a low subthreshold swing (<0.15 V dec^{-1}) and a high on–off ratio (<10^5) under low-voltage operation [82].

The AJP technique has found wide use in biotechnologies and the pioneering work dealing with the use of this technology, due to Marquez et al., concerns precisely the printing of different biomaterials, such as enzymes, cells, and proteins [83]. They showed, for instance, the deposition of 3T3 mouse fibroblast cells on 2D substrates, validating their viability upon dedicated analysis, and the manufacturing of fibronectin protein micropatterns. DNA strands, whose integrity was tested prior, during, and after the deposition using agarose gel electrophoresis, were deposited by Grunwald et al., showing that only depositions by PAs guarantee the integrity of the as-deposited DNA layers [84].

These works opened the way towards the use of aerosol-based printing techniques for biotechnology-relevant applications concerning, for instance, the deposition of cell cultures on scaffolds for tissue regeneration, as well as the possibility of implementing all-printed biosensors based on biocompatible, flexible/conform organic materials and requiring specific biofunctionalization protocols for the

interfaces comprising the device (and, in case, also implemented by printing techniques).

Despite the large set of literature production concerning the AJP fabrication of electronic devices and related circuit integration strategies, as well as optical devices and tools for energy conversion, the attention towards biosensing platforms is a field of quite recent development. A description concerning research routes on different solutions for biosensing applications such as electronic, electrochemical, and optical diagnostic tools fabricated by AJP is hereinafter provided.

Aerosol-jet-printed OECT platforms for the selective detection of bioanalytes have just recently emerged [64] and exploited to detect glucose in an artificial sweat buffer, using a standard enzymatic functionalization (by GOx) of both printed and sputtered platinum gate electrodes [85], and delta-9-tetrahydrocannabinol in synthetic saliva buffer, using a bare platinum wire as gate electrode [86].

More in general, biosensors based on electrochemical concepts have shown a noticeable potential towards the detection of different bioanalytes for the diagnosis of several diseases. Recent works deal with biosensors based on the SPE concept for the detection of cytokines. Inflammatory cytokines are small proteins whose presence in supraphysiologic concentration is associated with a variety of inflammatory or autoimmune diseases. Their popularity has peremptorily grown during the SARS-CoV-2 pandemic since they are reliable markers for this infection, especially interleukin IL-6 and IL-10. In fact, the COVID-19 infection is accompanied by the so-called cytokine-storm reaction, i.e., an increase of levels of circulating pro-inflammatory cytokines.

Cantù et al. proposed an all-printed electrochemical biosensor for the detection of interleukin-8 [87]. The device has been manufactured by depositing silver traces used to connect the carbon-based working and counter electrodes and the Ag/AgCl reference electrode to a potentiostat and a protecting layer made of a photocurable dielectric, the NOA 81, which is passivated upon exposure under UV radiation. The hydrophobic NOA 81 circular profile also acted as a well to confine the solution containing the analyte onto the electrode region. All layers were fabricated using a PA and the working electrode was functionalized by anti-IL-8 antibodies prior to incubate some IL-8-based solution with the aim of promoting the antigen–antibody conjugation. The sensor, characterized by means of anodic stripping voltammetry, showed a LoD of 2.1 ng ml^{-1}, further reduced to 0.3 ng ml^{-1} upon decoration of the working electrode with multiwall carbon nanotubes (MWCNTs) prior to perform the antibody functionalization.

A recent work by Parate and coworkers [88] shows a graphene-based immunosensor for the detection of two cytokines, i.e., the interferon gamma (IFN-γ) and the interleukin 10 (IL-10), by exploiting an interdigitated electrode (IDE) configuration. They prepared a graphene-based ink compatible with AJP by dispersing a graphene–nitrocellulose powder in ethyl lactate/dibutyl phthalate cosolvent solution (Fig. 5.6a). The antibody anchoring has been promoted by exploiting the presence of carboxyl functional groups and a standard protocol using N-(3-dimethylaminopropyl) -N′-ethylcarbodiimide (EDC) and N-hydroxysuccinimide (NHS) in 2-(N-morpholino)ethanesulfonic acid (MES) buffer

solution. The antigen (IFN-γ or IL-10) has been successively incubated to promote its conjugation with the antibody, taking care of blocking the unfunctionalized portion of the IDE surface by a mixture of Tween-20, fish gelatin, and bovine serum albumin (BSA). Such procedure is aimed at preventing the nonspecific detection of interfering substances present in the test solution, which is made of the antigens to be detected (at different concentrations) and bovine minced implant serum acting as physiological medium (Fig. 5.6b). Electrochemical impedance spectroscopy (EIS) in the presence of a standard redox probe (ferro−/ferricyanide in PBS electrolyte) has been used as a characterization tool capable of monitoring the influence of antigen coverage on charge transfer mechanism efficiency. Using an equivalent circuit model applied to the acquired Nyquist plots, the percentage variation of the charge transfer resistance (Rct) with respect to that of blank measurements (EIS for nonconjugated electrodes) has been assessed and set as the sensing parameter (calibration curve: ΔR_{ch} vs. analyte concentration). The assessed LoDs for IFN-γ and IL-10 detection are 25 and 46 pg/mL, respectively, upon a rapid response time (33 min) regime of sensing operation (Fig. 5.6c).

Aerosol-jet capabilities are evident from examples showing how this technique can give, for instance, a further boost for microneedle technology. While IJP is suitable for covering microneedles by drugs, AJP allows in principle an in-line process involving all the fabrication steps required for the manufacturing of a microneedle system. In this respect, microsystems such as microelectrode arrays (MEAs) have been already demonstrated to be achievable by an AJP-based approach. A work by Zips et al. shows, for example, how the combination of AJP and IJP may assist the fabrication of MEAs starting from PEDOT:PSS–MWCNT ink formulation. The system is made of microneedles, with a mean diameter of 10 μm and a mean height of 33 μm, onto a polyethylene naphthalate (PEN) dielectric substrate. Their main characteristics, tested by electrochemical measurements, consist of a capacitance of 242 ± 70 nF and an impedance of 128 ± 22 kΩ at 1 KHz, being also stable in aqueous electrolytes and capable of recording extracellular signals from cardiomyocyte-like HL-1 cells [89].

5.4 Conclusions

Non-contact DW methods represent a current paradigm for the manufacturing of 3D printed tools, with a particular tendency at favoring the implementation of 3D printed electronic devices. In this respect, two ink-based deposition techniques, i.e., the IJP and the AJP, are suitable to promote rapid prototyping methods of fabrication with a strong impact on the end-use industry. This is because the related deposition systems are user-friendly, quick in their operation, and, above all, suitable for the in-line production of devices from liquid precursors, with the further possibility to be integrated in assembly lines and the attitude to be used for complementing already existing mass production methods. On the one hand, even if such methods are more (IJP) or less (AJP) mature to be considered as the future of modern industry, their

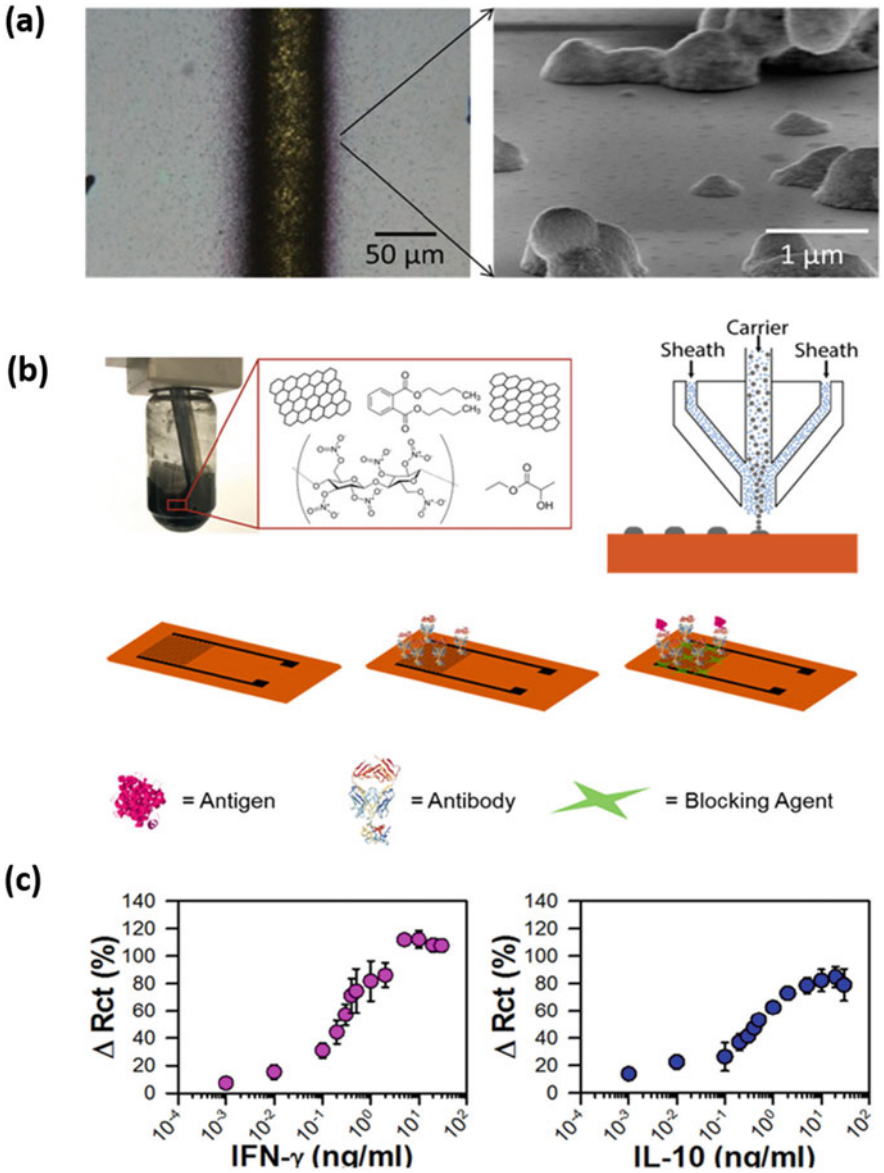

Fig. 5.6 SEM image (right side of panel (**a**)) showing an aerosol-jet-printed silver line with an ill-defined profile and magnified micrograph (left side of panel (**a**)) showing a comprehensive picture of the overspray phenomenology. (Reprinted with permission from [65], copyright 2013, American Chemical Society); (**b**) AJP-compatible ink formulation (top part of panel (**b**)), schematic picture of the all-printed graphene-based IDE biosensor on a polyimide substrate and related biofunctionalization protocol (bottom part of panel (**b**)), comprising the IL-10 and/or INF-γ antibody anchoring, the related antigen conjugation, and the final functionalization by the blocking agent based on a mixture among BSA, fish gelatin, and Tween-20, aimed at passivating the exposed surface of the graphene electrode after the antigen–antibody functionalization steps; panel (**c**) shows the IDE biosensor response consisting of the percentage variation of Rct, calculated from EIS analysis, for different IFN-γ (left side of panel (**c**)) and IL-10 (right side of panel (**c**)) concentrations, and related error bars calculated as standard deviation of the mean for three different devices at any antibody concentration. (Reprinted with permission from [88], copyright 2020, American Chemical Society)

massive use in R&D and, above all, in research laboratories is increasing day by day.

The physics behind IJP has been so far deeply understood, while AJP, which is a finer version of IJP that gives the possibility of both exploring a wider set of inks and allowing more complex 3D processes, is still investigated under the point of view of basic research approaches. Nevertheless, both techniques have been demonstrated to be suitable for implementing in a fast way the same electronic products obtained with standard techniques, such as lithographic pathways, also giving the possibility of implementing a fast circuit integration. Even if device performances require a refining of deposition methods, intrinsically limited by the nature of the basic principles (i.e., generation of ink streams) and precursors (inks that, for instance, do not allow an atom by atom assembly), organic electronics and bioelectronics have benefited from the introduction of such techniques. Several kinds of devices have been demonstrated, with performance comparable to that of devices obtained by standard methods and also based on organics and liquid precursor conductors and dielectrics. In addition, such methods are also compatible with the deposition of biological matrices/materials, paving the way towards the implementation of bioelectronic devices and biotechnological tools. Among several branches of science, medicine has surely drawn on promising solutions from these methods. In particular, biosensors for the diagnosis of several diseases, electrodes for biosignaling, and the study of cell physiology, but also tools for therapy by the controlled release of drugs, have been demonstrated by bench tests (performed also in physiologic ambient (such as biological fluids) and applied for validating their suitability for in vivo analysis.

References

1. S. Khan, L. Lorenzelli, R.S. Dahiya, Technologies for printing sensors and electronics over large flexible substrates: A review. IEEE Sensors J. **15**, 3164–3185 (2015). https://doi.org/10.1109/JSEN.2014.2375203
2. J.H. Noh, I. Kim, S.H. Park, et al., A study on the enhancement of printing location accuracy in a roll-to-roll gravure offset printing system. Int. J. Adv. Manuf. Technol. **68**, 1147–1153 (2013). https://doi.org/10.1007/s00170-013-4907-z
3. R.R. Søndergaard, M. Hösel, F.C. Krebs, Roll-to-roll fabrication of large area functional organic materials. J. Polym. Sci. Part B Polym. Phys. **51**, 16–34 (2013)
4. R. Søndergaard, M. Hösel, D. Angmo, et al., Roll-to-roll fabrication of polymer solar cells. Mater. Today **15**, 36–49 (2012)
5. A. Carlson, A.M. Bowen, Y. Huang, et al., Transfer printing techniques for materials assembly and micro/nanodevice fabrication. Adv. Mater. **24**, 5284–5318 (2012)
6. N. Kooy, K. Mohamed, L.T. Pin, O.S. Guan, A review of roll-to-roll nanoimprint lithography. Nanoscale Res. Lett. **9**, 1–13 (2014). https://doi.org/10.1186/1556-276X-9-320
7. M. Singh, H.M. Haverinen, P. Dhagat, G.E. Jabbour, Inkjet printing-process and its applications. Adv. Mater. **22**, 673–685 (2010). https://doi.org/10.1002/adma.200901141
8. T.K. Saha, T.N. Knaus, A. Khosla, P.K. Sekhar, Investigation of printing properties on paper substrate. J. Electrochem. Soc. **165**, B3163–B3167 (2018). https://doi.org/10.1149/2.0211808jes

9. H. Zhang, S.K. Moon, T.H. Ngo, 3D printed electronics of non-contact ink writing techniques: Status and promise. Int. J. Precis Eng. Manuf. Technol. **1–14** (2019). https://doi.org/10.1007/s40684-019-00139-9
10. Inverter Market Size Share and Trends forecast to 2025 | MarketsandMarkets™. https://www.marketsandmarkets.com/Market-Reports/printed-electronics-market-197.html. Accessed 14 Oct 2021
11. L. Nayak, S. Mohanty, S.K. Nayak, A. Ramadoss, A review on inkjet printing of nanoparticle ink for flexible electronics. J. Mater. Chem. C **7**, 8771–8795 (2019). https://doi.org/10.1039/c9tc01630a
12. T. Seifert, E. Sowade, F. Roscher, et al., Additive manufacturing technologies compared: Morphology of deposits of silver ink using inkjet and aerosol jet printing. Ind. Eng. Chem. Res. **54**, 769–779 (2015). https://doi.org/10.1021/ie503636c
13. B. Polzinger, F. Schoen, V. Matic, et al., UV-sintering of inkjet-printed conductive silver tracks, in *Proceedings of the IEEE Conference on Nanotechnology*, (IEEE, 2011), pp. 201–204
14. T.C. Gomes, R.F. De Oliveira, C.J.L. Constantino, et al., Thermal inkjet printing of copper tetrasulfonated phthalocyanine (CuTsPc) as a semiconducting layer on flexible MIS capacitors. Mater. Res. **17**, 1466–1473 (2014)
15. Y. Brauniger, S. Lochmann, J. Grothe, et al., Piezoelectric inkjet printing of Nanoporous carbons for micro-supercapacitor devices. ACS Appl. Energy. Mater. **4**, 1560–1567 (2021). https://doi.org/10.1021/acsaem.0c02745
16. S.Y. Kim, K. Kim, Y.H. Hwang, et al., High-resolution electrohydrodynamic inkjet printing of stretchable metal oxide semiconductor transistors with high performance. Nanoscale **8**, 17113–17121 (2016). https://doi.org/10.1039/c6nr05577j
17. K.K.B. Hon, L. Li, I.M. Hutchings, Direct writing technology-advances and developments. CIRP Ann. Manuf. Technol. **57**, 601–620 (2008). https://doi.org/10.1016/j.cirp.2008.09.006
18. B.-J. de Gans, P.C. Duineveld, U.S. Schubert, Inkjet printing of polymers: State of the art and future developments. Adv. Mater. **16**, 203–213 (2004). https://doi.org/10.1002/ADMA.200300385
19. J.S.R. Wheeler, S.W. Reynolds, S. Lancaster, et al., Polymer degradation during continuous ink-jet printing. Polym. Degrad. Stab. **105**, 116–121 (2014). https://doi.org/10.1016/j.polymdegradstab.2014.04.007
20. X. Cui, T. Boland, D.D. D'Lima, M.K. Lotz, Thermal inkjet printing in tissue engineering and regenerative medicine. Recent Pat. Drug Deliv. Formul. **6**, 149–155 (2012). https://doi.org/10.2174/187221112800672949
21. C. O'Mahony, A. Bocchino, M.J. Haslinger, et al., Piezoelectric inkjet coating of injection moulded, reservoir-tipped microneedle arrays for transdermal delivery. J. Micromech. Microeng. **29**, 085004 (2019). https://doi.org/10.1088/1361-6439/ab222b
22. N. Reis, C. Ainsley, B. Derby, Ink-jet delivery of particle suspensions by piezoelectric droplet ejectors. J. Appl. Phys. **97**, 94903 (2005). https://doi.org/10.1063/1.1888026
23. D. Soltman, V. Subramanian, Inkjet-printed line morphologies and temperature control of the coffee ring effect. Langmuir **24**, 2224–2231 (2008). https://doi.org/10.1021/la7026847
24. P. He, B. Derby, Controlling coffee ring formation during drying of inkjet printed 2D inks. Adv. Mater. Interfaces **4**, 1700944 (2017). https://doi.org/10.1002/admi.201700944
25. T. Kajiya, W. Kobayashi, T. Okuzono, M. Doi, Controlling the drying and film formation processes of polymer solution droplets with addition of small amount of surfactants. J. Phys. Chem. B **113**, 15460–15466 (2009). https://doi.org/10.1021/jp9077757
26. L. Wang, J. Wang, Y. Huang, et al., Inkjet printed colloidal photonic crystal microdot with fast response induced by hydrophobic transition of poly(N-isopropyl acrylamide). J. Mater. Chem. **22**, 21405–21411 (2012). https://doi.org/10.1039/c2jm33411a
27. G. Hu, L. Yang, Z. Yang, et al., A general ink formulation of 2D crystals for wafer-scale inkjet printing. Sci. Adv. **6** (2020). https://doi.org/10.1126/sciadv.aba5029
28. M. Majumder, C.S. Rendall, J.A. Eukel, et al., Overcoming the "coffee-stain" effect by compositional Marangoni-flow-assisted drop-drying. J. Phys. Chem. B **116**, 6536–6542 (2012). https://doi.org/10.1021/jp3009628

29. V. Gevaerts, A. Biezemans, H. Mannetje, et al., Inkjet printing assisted monolithic interconnection of CIGS using shunt-free laser scribing, in *Conference Record of the IEEE Photovoltaic Specialists Conference*, (Institute of Electrical and Electronics Engineers Inc., 2020), pp. 1779–1781
30. M. Buffiere, K. Ali, E. Fares, et al., Inkjet-printed compact TiO_2 electron transport layer for perovskite solar cells. Energ. Technol. **8**, 2000330 (2020). https://doi.org/10.1002/ente.202000330
31. D. Corzo, K. Almasabi, E. Bihar, et al., Digital inkjet printing of high-efficiency large-area nonfullerene organic solar cells. Adv. Mater. Technol. **4**, 1900040 (2019). https://doi.org/10.1002/admt.201900040
32. F. Mathies, H. Eggers, B.S. Richards, et al., Inkjet-printed triple cation perovskite solar cells. ACS Appl. Energy Mater. **1**, 1834–1839 (2018). https://doi.org/10.1021/acsaem.8b00222
33. X. Peng, J. Yuan, S. Shen, et al., Perovskite and organic solar cells fabricated by inkjet printing: Progress and prospects. Adv. Funct. Mater. **27**, 1703704 (2017)
34. M. Chen, A. Iyer, R. Opila, Developing inkjet printed PEDOT/PSS films for solar cells, in *Conference Record of the IEEE Photovoltaic Specialists Conference*, (Institute of Electrical and Electronics Engineers Inc., 2019), pp. 443–446
35. C.L. Cho, H.L. Kao, Y.H. Wu, et al., Fully inkjet-printed dual-mode ring Bandpass filter using a cross-bridge structure embedded with a metal-insulator-metal capacitor. IEEE Trans. Compon. Packag. Manuf. Technol. **8**, 1869–1875 (2018). https://doi.org/10.1109/TCPMT.2018.2856855
36. W. Sun, Q. Zhao, F. Qiao, et al., An 8b 0.8kS/s configurable VCO-based ADC using oxide TFTs with Inkjet printing interconnection, in *Proceedings – IEEE International Symposium on Circuits and Systems*, (Institute of Electrical and Electronics Engineers Inc, 2017)
37. H.L. Kao, C.L. Cho, Fully inkjet-printed three-dimensional bandpass filter on liquid crystal polymer substrate, in *Proceedings – Electronic Components and Technology Conference*, (Institute of Electrical and Electronics Engineers Inc, 2018), pp. 2218–2222
38. B.J. Kang, C.K. Lee, J.H. Oh, All-inkjet-printed electrical components and circuit fabrication on a plastic substrate. Microelectron. Eng. **97**, 251–254 (2012). https://doi.org/10.1016/j.mee.2012.03.032
39. X. Wu, Y. Khan, J. Ting, et al., Large-area fabrication of high-performance flexible and wearable pressure sensors. Adv. Electron. Mater. **6**, 1901310 (2020). https://doi.org/10.1002/aelm.201901310
40. B.A. Kuzubasoglu, E. Sayar, S.K. Bahadir, Inkjet-printed CNT/PEDOT:PSS temperature sensor on a textile substrate for wearable intelligent systems. IEEE Sensors J. **21**, 13090–13097 (2021). https://doi.org/10.1109/JSEN.2021.3070073
41. S.L. Swisher, M.C. Lin, A. Liao, et al., Impedance sensing device enables early detection of pressure ulcers in vivo. Nat. Commun. **6**, 1–10 (2015). https://doi.org/10.1038/ncomms7575
42. C. Xu, Y. Yang, W. Gao, Skin-interfaced sensors in digital medicine: From materials to applications. Matter **2**, 1414–1445 (2020)
43. G. Mattana, A. Loi, M. Woytasik, et al., Inkjet-printing: A new fabrication technology for organic transistors. Adv. Mater. Technol. **2**, 1700063 (2017)
44. J. Kwon, Y. Takeda, K. Fukuda, et al., Three-dimensional, inkjet-printed organic transistors and integrated circuits with 100% yield, high uniformity, and long-term stability. ACS Nano **10**, 10324–10330 (2016). https://doi.org/10.1021/acsnano.6b06041
45. J.A. Lim, J.H. Kim, L. Qiu, et al., Inkjet-printed single-droplet organic transistors based on semiconductor nanowires embedded in insulating polymers. Adv. Funct. Mater. **20**, 3292–3297 (2010). https://doi.org/10.1002/adfm.201000528
46. B. Ju, I. Kim, B.M. Li, et al., Inkjet printed textile force sensitive resistors for wearable and healthcare devices. Adv. Healthc. Mater. **10**, 2100893 (2021). https://doi.org/10.1002/ADHM.202100893
47. D.H. Lee, H.S. Cho, D. Han, et al., Highly selective organic transistor biosensor with inkjet printed graphene oxide support systemf. J. Mater. Chem. B **5**, 3580–3585 (2017). https://doi.org/10.1039/c6tb03357a

48. Y. Li, N. Wang, A. Yang, et al., Biomimicking stretchable organic electrochemical transistor. Adv. Electron. Mater. **5**, 1900566 (2019). https://doi.org/10.1002/aelm.201900566
49. E. Bihar, T. Roberts, M. Saadaoui, et al., Inkjet-printed PEDOT:PSS electrodes on paper for electrocardiography. Adv. Healthc. Mater. **6**, 1601167 (2017). https://doi.org/10.1002/adhm.201601167
50. J.C. Batchelor, A.J. Casson, Inkjet printed ECG electrodes for long term biosignal monitoring in personalized and ubiquitous healthcare, in *Proceedings of the Annual International Conference of the IEEE Engineering in Medicine and Biology Society, EMBS*, (Institute of Electrical and Electronics Engineers Inc, 2015), pp. 4013–4016
51. L.M. Ferrari, U. Ismailov, J.M. Badier, et al., Conducting polymer tattoo electrodes in clinical electro- and magneto-encephalography. npj Flex. Electron. **4**, 1–9 (2020). https://doi.org/10.1038/s41528-020-0067-z
52. S. Ali, S. Khan, A. Bermak, Inkjet-printed human body temperature sensor for wearable electronics. IEEE Access **7**, 163981–163987 (2019). https://doi.org/10.1109/ACCESS.2019.2949335
53. C. Martínez-Domingo, S. Conti, A. de la Escosura-Muñiz, et al., Organic-based field effect transistors for protein detection fabricated by inkjet-printing. Org. Electron. **84**, 105794 (2020). https://doi.org/10.1016/j.orgel.2020.105794
54. E. Bihar, S. Wustoni, A.M. Pappa, et al., A fully inkjet-printed disposable glucose sensor on paper. npj Flex. Electron. **2**, 1–8 (2018). https://doi.org/10.1038/s41528-018-0044-y
55. I. Gualandi, D. Tonelli, F. Mariani, et al., Selective detection of dopamine with an all PEDOT:PSS organic electrochemical transistor. Sci. Rep. **6**, 1–10 (2016). https://doi.org/10.1038/srep35419
56. J. Kudr, L. Zhao, E.P. Nguyen, et al., Inkjet-printed electrochemically reduced graphene oxide microelectrode as a platform for HT-2 mycotoxin immunoenzymatic biosensing. Biosens. Bioelectron. **156**, 956–5663 (2020). https://doi.org/10.1016/j.bios.2020.112109
57. M.J. Uddin, N. Scoutaris, P. Klepetsanis, et al., Inkjet printing of transdermal microneedles for the delivery of anticancer agents. Int. J. Pharm. **494**, 593–602 (2015). https://doi.org/10.1016/j.ijpharm.2015.01.038
58. S. Ross, N. Scoutaris, D. Lamprou, et al., Inkjet printing of insulin microneedles for transdermal delivery. Drug Deliv. Transl. Res. **54**(5), 451–461 (2015). https://doi.org/10.1007/S13346-015-0251-1
59. T. Seifert, M. Baum, F. Roscher, et al., Aerosol jet printing of Nano particle based electrical Chip interconnects, in *Materials Today: Proceedings*, (Elsevier, 2015), pp. 4262–4271
60. J. Navratil, A. Hamacek, J. Reboun, R. Soukup, Perspective methods of creating conductive paths by Aerosol Jet Printing technology. Proc. Int. Spring Semin. Electron. Technol. **2015**, 36–39 (2015). https://doi.org/10.1109/ISSE.2015.7247957
61. S. Kooij, A. Astefanei, G.L. Corthals, D. Bonn, Size distributions of droplets produced by ultrasonic nebulizers. Sci. Rep. **9** (2019). https://doi.org/10.1038/s41598-019-42599-8
62. E.B. Secor, Principles of aerosol jet printing. Flex. Print. Electron. **3**, 035002 (2018). https://doi.org/10.1088/2058-8585/aace28
63. G. Chen, Y. Gu, H. Tsang, et al., The effect of droplet sizes on overspray in aerosol-jet printing. Adv. Eng. Mater. **20**, 1701084 (2018). https://doi.org/10.1002/adem.201701084
64. G. Tarabella, D. Vurro, S. Lai, et al., Aerosol jet printing of PEDOT:PSS for large area flexible electronics. Flex. Print. Electron. **5**, 014005 (2020). https://doi.org/10.1088/2058-8585/ab61c4
65. A. Mahajan, C.D. Frisbie, L.F. Francis, Optimization of aerosol jet printing for high-resolution, high-aspect ratio silver lines. ACS Appl. Mater. Interfaces **5**, 4856–4864 (2013). https://doi.org/10.1021/am400606y
66. C. Goth, S. Putzo, J. Franke, Aerosol Jet printing on rapid prototyping materials for fine pitch electronic applications, in *Proceedings – Electronic Components and Technology Conference*, (IEEE, 2011), pp. 1211–1216
67. M. Smith, Y.S. Choi, C. Boughey, S. Kar-Narayan, Controlling and assessing the quality of aerosol jet printed features for large area and flexible electronics. Flex. Print. Electron. **2**, 015004 (2017). https://doi.org/10.1088/2058-8585/aa5af9

68. N.X. Williams, N. Watson, D.Y. Joh, et al., Aerosol jet printing of biological inks by ultrasonic delivery. Biofabrication **12**, 025004 (2020). https://doi.org/10.1088/1758-5090/ab5cf5
69. E.B. Secor, Guided ink and process design for aerosol jet printing based on annular drying effects. Flex. Print. Electron. **3**, 035007 (2018). https://doi.org/10.1088/2058-8585/aadffd
70. J.A. Paulsen, M. Renn, K. Christenson, R. Plourde, Printing conformal electronics on 3D structures with aerosol jet technology, in *FIIW 2012 – 2012 Future of Instrumentation International Workshop Proceedings*, (2012), pp. 47–50
71. Z. Zhan, L. Yu, J. Wei, et al., Application of Aerosol Jet technology in through-via interconnection for MEMS wafer-level packaging. Microsyst. Technol. **21**, 451–455 (2014). https://doi.org/10.1007/s00542-014-2107-x
72. S. Padovani, S. Sinesi, S. Priante, et al., New method for head-up display realization by mean of chip on board and aerosol jet process, in *Electronics System Integration Technology Conference, ESTC 2010 - Proceedings*, (IEEE, 2010), pp. 1–3
73. A. Mette, P.L. Richter, M. Hörteis, S.W. Glunz, Metal aerosol jet printing for solar cell metallization. Prog. Photovolt. Res. Appl. **15**, 621–627 (2007). https://doi.org/10.1002/pip.759
74. A.A. Gupta, A. Bolduc, S.G. Cloutier, R. Izquierdo, Aerosol Jet Printing for printed electronics rapid prototyping. Proc. IEEE Int. Symp. Circuits Syst. **2016**, 866–869 (2016). https://doi.org/10.1109/ISCAS.2016.7527378
75. P. Yang, T. Zhai, B. Yu, et al., Toward all aerosol printing of high-efficiency organic solar cells using environmentally friendly solvents in ambient air. J. Mater. Chem. A **9**, 17198–17210 (2021). https://doi.org/10.1039/d1ta02890a
76. R. Eckstein, T. Rödlmeier, T. Glaser, et al., Aerosol-jet printed flexible organic photodiodes: Semi-transparent, color neutral, and highly efficient. Adv. Electron. Mater. **1**, 1500101 (2015). https://doi.org/10.1002/aelm.201500101
77. C.S. Jones, X. Lu, M. Renn, et al., Aerosol-jet-printed, high-speed, flexible thin-film transistor made using single-walled carbon nanotube solution. Microelectron. Eng. **87**, 434–437 (2010). https://doi.org/10.1016/j.mee.2009.05.034
78. R. Liu, F. Shen, H. Ding, et al., All-carbon-based field effect transistors fabricated by aerosol jet printing on flexible substrates. J. Micromech. Microeng. **23**, 065027 (2013). https://doi.org/10.1088/0960-1317/23/6/065027
79. F. Zare Bidoky, W.J. Hyun, D. Song, C.D. Frisbie, Printed, 1 V electrolyte-gated transistors based on poly(3-hexylthiophene) operating at >10 kHz on plastic. Appl. Phys. Lett. **113**, 053301 (2018). https://doi.org/10.1063/1.5025475
80. W. Xie, X. Zhang, C. Leighton, C.D. Frisbie, 2D insulator–metal transition in aerosol-jet-printed electrolyte-gated indium oxide thin film transistors. Adv. Electron. Mater. **3**, 1600369 (2017). https://doi.org/10.1002/aelm.201600369
81. Y. Xia, W. Zhang, M. Ha, et al., Printed sub-2 V Gel-electrolyte-gated polymer transistors and circuits. Adv. Funct. Mater. **20**, 587–594 (2010). https://doi.org/10.1002/adfm.200901845
82. H. Li, Y. Tang, W. Guo, et al., Polyfluorinated electrolyte for fully printed carbon nanotube electronics. Adv. Funct. Mater. **26**, 6914–6920 (2016). https://doi.org/10.1002/adfm.201601605
83. G.J. Marquez, M.J. Renn, W.D. Miller, Aerosol-based direct-write of biological materials for biomedical applications, in *Materials Research Society Symposium – Proceedings*, (Cambridge University Press, 2002), pp. 343–349
84. I. Grunwald, E. Groth, I. Wirth, et al., Surface biofunctionalization and production of miniaturized sensor structures using aerosol printing technologies. Biofabrication **2**, 014106 (2010). https://doi.org/10.1088/1758-5082/2/1/014106
85. J. Fan, A.A. Forero Pico, M. Gupta, A functionalization study of aerosol jet printed organic electrochemical transistors (OECTs) for glucose detection. Mater. Adv. (2021). https://doi.org/10.1039/d1ma00479d
86. D. Majak, J. Fan, S. Kang, M. Gupta, Delta-9-tetrahydrocannabinol (Δ9-THC) sensing using an aerosol jet printed organic electrochemical transistor (OECT). J. Mater. Chem. B **9**, 2107–2117 (2021). https://doi.org/10.1039/d0tb02951c

87. E. Cantù, S. Tonello, G. Abate, et al., Aerosol jet printed 3D electrochemical sensors for protein detection. Sensors (Switzerland) **18**, 3719 (2018). https://doi.org/10.3390/s18113719
88. K. Parate, S.V. Rangnekar, D. Jing, et al., Aerosol-jet-printed graphene Immunosensor for label-free cytokine monitoring in serum. ACS Appl. Mater. Interfaces **12**, 8592–8603 (2020). https://doi.org/10.1021/acsami.9b22183
89. S. Zips, L. Grob, P. Rinklin, et al., Fully printed μ-needle electrode Array from conductive polymer ink for bioelectronic applications. ACS Appl. Mater. Interfaces **11**, 32778–32786 (2019). https://doi.org/10.1021/ACSAMI.9B11774

Chapter 6
Volumetric 3D Printing

Valentina Bertana and Monica Periolatto

Abstract Volumetric 3D printing can be defined as the technology which is the fastest to convert the idea of an object into a 3D version of the same. Indeed, through a continuous floodlighting of a photosensitive resin, the conversion from liquid to solid occurs under the observers' eyes within few seconds time. The first volumetric 3D printing process was designed taking inspiration from holography, which consists of the representation of 3D images on a bidimensional plane from a light interference pattern. Later, the introduction of computed axial lithography furtherly enhanced the printing times. Nonetheless, the rotary motion of the resin vat combined with the projection of the longitudinal object sections at different azimuthal angles allowed to achieve the additive manufacturing of more complex geometries with respect to holographic 3D printing. In the last years, a new volumetric technique was reported, namely, the xolography process. Also in this case, the resin vat moves with respect to the light sources (in this case, there are two). Different from computed axial lithography, the resin vat does not rotate but rather moves linearly with a speed based on the frame rate used for the stack of layers' projection. The present chapter aims to give a comprehensive overview of a relatively recent 3D printing technology, completed with a description of feasible materials for volumetric additive manufacturing.

Keywords 3D printing · Volumetric printing · Holography printing · Computed axial lithography · Xolography · Radical polymerization · Photoinitiators · Dual-color photoinitiators · Photoinhibitors · Biofabrication

V. Bertana (✉) · M. Periolatto
Department of Applied Science and Technology (DISAT), Politecnico di Torino, Turin, Italy
e-mail: valentina.bertana@polito.it

S. L. Marasso, M. Cocuzza (eds.), *High Resolution Manufacturing from 2D to 3D/4D Printing*, https://doi.org/10.1007/978-3-031-13779-2_6

6.1 Introduction

Since 1986, when Charles W. Hull claimed the invention of an apparatus for the production of 3D objects [1], a tremendous progress has been observed in the field of additive manufacturing (AM). Stereolithography (SL), which C.W. Hull reported in his patent, and later Paul F. Jacobs accurately described [2], paved the way for the light-triggered fabrication of prototypes. Even if nowadays a plethora of AM applications exist and new ones are continuously introduced, there are still issues to be solved. As regards light-based manufacturing, the two most relevant ones are the relative slow build rates and the so-called layering artifacts. The latter is referred to the typical uneven stepped surfaces which characterizes most of the layer-by-layer built objects. When volumetric 3D printing was introduced, both issues have been overcome.

Different from 3D printing as most of us know, volumetric 3D printing consists of the fabrication of objects not following the layer-by-layer strategy but rather a multi-angle approach. Indeed, no platform moving inside a resin vat is employed, but the resin is directly polymerized by light beams inside the vat, which must be transparent to the polymerizing wavelengths provided.

Volumetric 3D printing is a relatively young technology, which embraces three distinct printing strategies. Thus, holographic 3D printing, tomographic 3D printing, and xolography are defined. Even if they are based on different optical principles, they share common basics. Firstly, the light beams triggering the resin polymerization must be optimized to carry the right amount of energy dose, in the right place. Polymerization occurs within the whole resin volume, not in the restricted space defined by the layer; therefore, a precise confinement of the polymerization sites is required to avoid deformed 3D printed objects. Secondly, the presence of inhibitors is needed to ensure a nonlinear polymerization behavior with a threshold-dependent response. Indeed, in the radical photo-induced polymerization, the cross-linking is governed by the presence of inhibiting species; the most common one is molecular oxygen. During the initial printing phase, light triggers the generation of radicals, which are rapidly deactivated by oxygen (or by other inhibitors). This step is crucial for an almost total oxygen depletion at the printing site, before the actual polymerization reaction starts [3].

Actually, the optimization of light energy dose and resin formulation is shared also with other additive manufacturing processes in order to reach the best resolution the 3D printer can have. In particular, as regards laser-based technologies applied to liquid polymeric blends, the overall printing accuracy strictly depends on the resolution achieved in two main directions. Therefore, lateral and axial resolutions are distinguished: lateral resolution indicates the minimum resolvable distance on the xy plane (the image plane), while axial resolution is defined in depth (along the optical axis). Abbe and Rayleigh criteria applied to incoherent light are commonly recognized for determining lateral and axial resolutions, respectively. In the case of coherent light, these criteria were revised to provide more accurate results. Thus, axial and lateral resolutions for laser-based system are reported in Equations 6.1 and 6.2 [4]:

$$R_{\text{lateral}} = 0.82\frac{\lambda}{\text{NA}} \tag{6.1}$$

$$R_{\text{axial}} = \frac{2\lambda}{\text{NA}^2} \tag{6.2}$$

λ is the laser wavelength and NA the numerical aperture of the optical system. From these equations, it is clear that optical systems always suffer from a worse axial resolution than lateral resolution. For this reason, the superimposition of beams in volumetric 3D printing must be accurately studied in order to compensate the limitations due to axial resolution.

In the following sections, an overview of the three volumetric printing strategies is presented. Finally, an insight on the employed materials is reported.

6.2 Holographic Volumetric 3D Printing

Holographic volumetric 3D printing is probably the first volumetric approach reported in literature. If researchers had the possibility to investigate such additive manufacturing strategy, it was thanks to the work of Professor Dennis Gabor. Gabor was the first to theorize holography as a technique to record and reproduce three-dimensional images on two-dimensional supports, pointing out that the physics behind holography allows to store image information in a compact way [5].

Holography is allowed by the wave nature of light: it is based on the creation of a hologram, a planar pattern generated by the interference of light beams. In the simplest configuration, a coherent beam passes through a beam splitting mirror. One of the resulting beams illuminates the object to record and then diffracts from it, while the other one, also called reference beam, directly goes to the hologram plane. The diffracted and reference beam interfere, generating an interference pattern which is recorded on a glass plate coated with a transparent photographic emulsion (see Fig. 6.1). Irradiating the hologram with the same coherent beam, a 3D image identical to the recorded object is projected [5].

With the same principle, holographic 3D printing consists of the replica of a 3D geometry by multiple-beam interference. Different from holographic lithography, holographic 3D printing allowed the researchers to go beyond the patterning of structures which have one dimension order of magnitudes smaller than the other two. Indeed, holographic lithography products are characterized by symmetry and repetition of structures at a sub-micrometric scale. Such structures come from the 3D interference patterns of multiple laser beams. Finely tuning propagation direction, intensity, polarization, and phases of each coherent laser beam, it is possible to obtain large-volume structures, such as photonic crystals. Photonic crystals are materials in which the dielectric constant is periodically modulated by tuning the empty/void distribution (i.e., polymerizing certain amount of dielectric resist). An optical setup for multiple-beam holographic lithography can involve

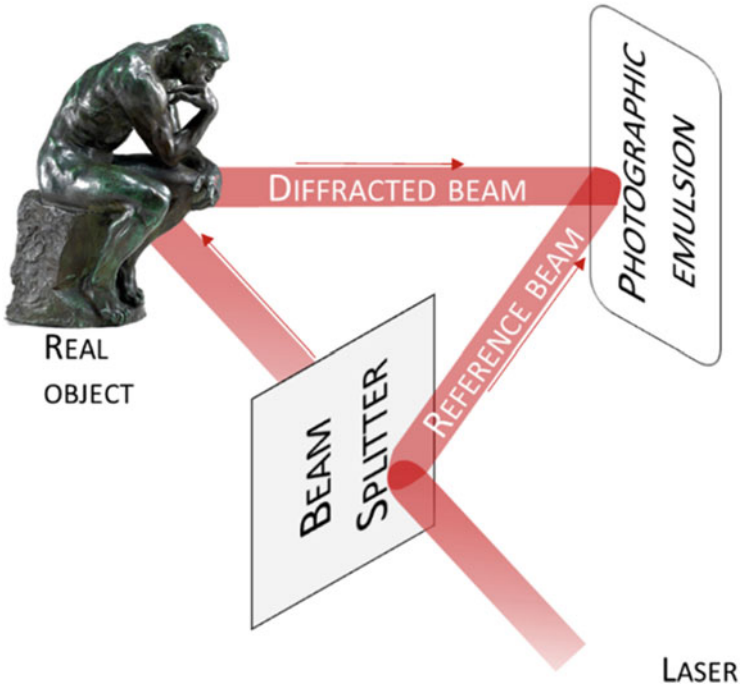

Fig. 6.1 A schematic representation of a simple holography setup. A laser beam is split and the two resulting beams interfere on the hologram plane. The hologram is recorded by a photographic emulsion

multiple bulk elements, such as half-wave plates and polarizing beam splitter [6]. However, researchers have also studied the use of refractive or diffractive optical elements which significantly simplify the whole setup. For example, Lin et al. [7] claimed the use of a single diffractive optical element and a single laser exposure for the fabrication of three-dimensional photonic crystals. The single diffractive optical element consists of a glass slide patterned with four gratings. When five separate beams, generating from an aperture array traversed by one single laser beam, pass through the single diffractive optical element, a diffraction pattern comes out. The intensity profile can be estimated; thus iso-intensity surfaces can be predicted. Such surfaces reflect the amount of material which will be polymerized and thus the distribution of dielectric material inside each unit cell. The generation of different 3D geometries comes from the phase shift of one of the five beams by the action of a rotation element. The diffraction pattern is then directed into a photoresist volume, typically some tens of microns thick. Here, the exposed resist part is rendered insoluble, while the unexposed part is washed away as in a typical planar lithography process. Also Ohlinger et al. [8] reported the use of such setup for holographic printing (see Fig. 6.2).

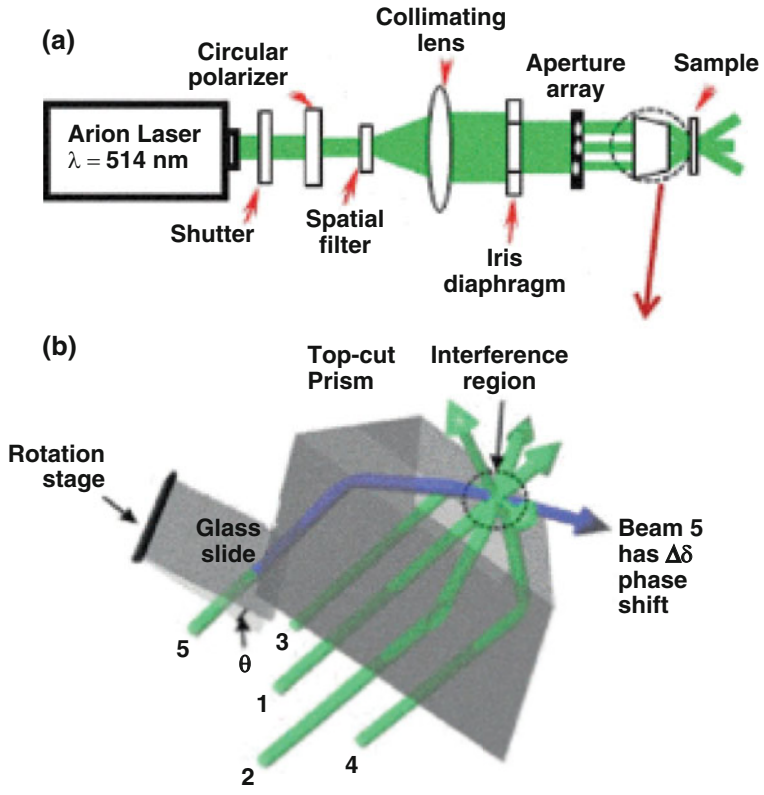

Fig. 6.2 Holographic lithography. (**a**) Experimental setup of the five beam holographic fabrications. (**b**) Scheme of the five beam interferences. The phase delay is introduced by the glass slide mounted on the rotational element. (Reprinted with permission from Ref. [8])

The patterning with a single laser and a single diffractive device integrating three gratings was more recently employed also by Liu et al. for fabricating nanobowtie arrays over large areas, as reported in Fig. 6.3 [9].

The first described holographic 3D printer setup dates to 2017 in the work of Shusteff et al. [10]. Three orthogonal beams intersect each other to create the image inside the liquid resin container. The beams come from the partitioning of a single holographically generated image by means of two 45° tilted mirrors. A schematic of the optical setup is reported in Fig. 6.4.

Figure 6.4 shows a block diagram of the holographic 3D printer setup. Its main components are the coherent light source (a visible laser emitting at 532 nm), a set of lenses defining the optical path, and a phase-only spatial light modulator (SLM). The latter is crucial for the projection of the computer-generated hologram (CGH). Indeed, in holographic 3D printing, the hologram is not impressed on a photosensitive substrate upon the interaction of a diffracted and reference beam. Instead, the hologram of the object to be 3D printed is numerically generated

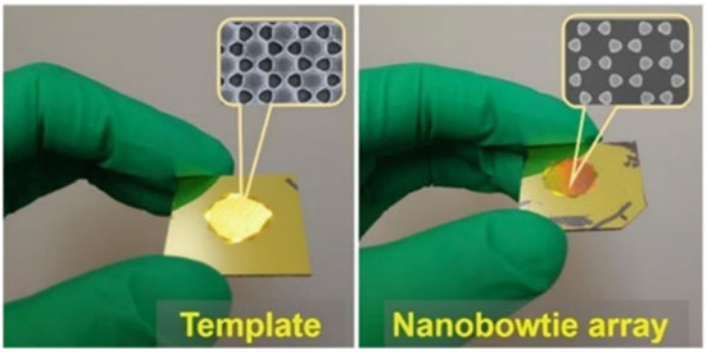

Fig. 6.3 Plasmonic nanobowtie structures fabricated by holographic lithography. (Reprinted with permission from Ref. [9])

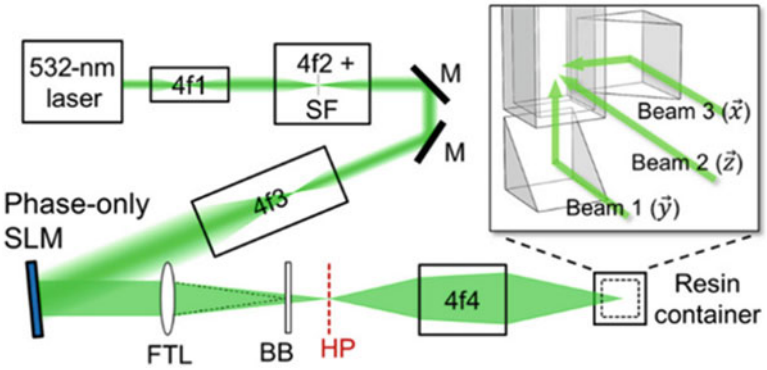

Fig. 6.4 Holographic volumetric 3D printing. Schematic of the setup: "4f" are lens pairs, "M" are mirrors, "SLM" is a spatial light modulator, "FTL" is a Fourier transform lens, "BB" is a beam block, and "HP" is the hologram plane. (Reprinted under the Creative Commons CC BY [11])

by extrapolating the phase information from the image itself. A digital image is composed of units, namely, the pixels. If in the spatial domain each pixel is characterized by an intensity value, in the frequency domain, an image is seen as a fluctuating pattern deriving from pixel intensity fluctuation along x and y directions. Often, such fluctuating patterns come from the combination of different sine waves having the right amplitude and phase. By Fourier transforming an image, thus translating it in the frequency domain, magnitude and phase information can be obtained. Phase is of particular interest for holographic 3D printing, since it stores the position information of the features composing the image. From a practical point of view, Fourier transforming an image means directing a coherent light beam toward the image to be replicated, placed at a specific distance before a proper lens, namely, a Fourier transform lens. The scattering of light interacting with the image passes through the lens and produces the Fourier transform pattern of the image at

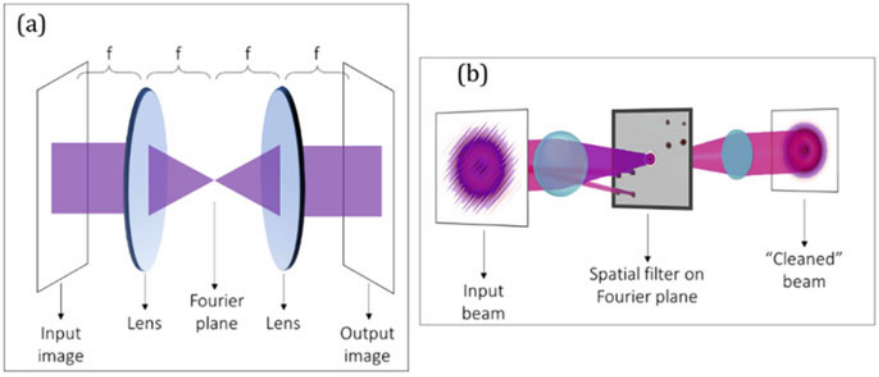

Fig. 6.5 Light beam Fourier transform. (**a**) Simplified structure of a typical "f system," where "f" is the lens' focal length. (**b**) Beam filtering with spatial filter; the components outside the pinhole are blocked and only the low-frequency signal is transmitted

the Fourier plane. If the so-obtained light pattern is directed through another Fourier lens, the interference draws the image at a fixed distance from the lens itself, at the image plane (see Fig. 6.5a). Such optical setup is commonly called "4f system" and can be used also for image relaying (extending the focal distance) and beam expansion. In both cases, a spatial filter such as a pinhole could be placed at the Fourier plane to filter unwanted frequencies, thus enhancing output beam quality (Fig. 6.5b).

In the case of holographic 3D printing, the Fourier transform of the image is not obtained by illuminating an object with a coherent light but rather creating the same diffraction effect by phase retarding an incident light beam. In particular, the phase shifting can be obtained along x and y directions at discrete pixel steps by employing a spatial light modulator. SLM consists of a liquid crystal screen in which each pixel has two electrodes enclosing the crystals itself. The phase shifting occurs when a voltage is applied across the pixel, thus changing the crystal orientation and therefore the pixel refractive index. The phase pattern displayed by the SLM is also referred to as computer-generated hologram. When it goes through a Fourier transform lens (FTL), the intensity pattern which will define the object shape is obtained.

Before interacting with the resin, the intensity pattern is divided in three components in the holographic 3D printer setup: a frontal one and other two guided by two mirrors, one at the bottom and one on the right of the resin vat. Only the volume illuminated by the three beams will have enough energy to polymerize.

The reported technology allows to print structures without providing supporting elements. This is of great benefit both in terms of post-processing, which is reduced to part rinsing, and in terms of mechanical stability. Indeed, especially for soft materials such as hydrogels, the removal of supports would be detrimental. Moreover, the steadiness of liquid resin during printing reduces the shear forces on the growing object due to recoating and platform movements inside the resin

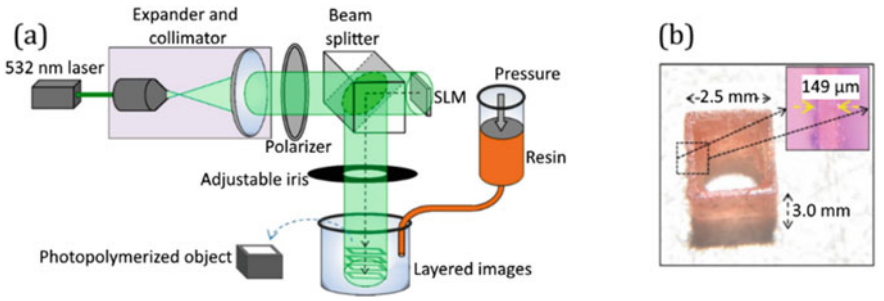

Fig. 6.6 Holographic printing. (**a**) Schematic apparatus and (**b**) printed object as reported from Lee et al. (Reprinted under the Creative Commons CC BY [12])

vat (as in stereolithography). As regards the printing accuracy and final resolution, it depends on the diffraction limit of the optical system. In the work of Shusteff et al. [10], they claim a minimum resolvable distance of 20–50 μm. However, the system resolution is strongly affected by oxygen diffusivity inside the resin. Indeed, if the time for starting resin gelation and then polymerization of a certain thickness is comparable to the time oxygen takes to diffuse inside the same thickness, the resin will not polymerize, and a deeper light intensity will be needed. Moreover, a computational effort is required to produce compensated beams to project inside the resin. Indeed, light absorption is a nonlinear phenomenon; thus, an attenuation and absorption model based on the Lambert-Beer law is introduced in order to generate intensity-modulated beams (having a gradient) to direct inside the resin volume and induce a homogeneous polymerization.

Similarly, Lee et al. proposed a 3D printing system based on the generation of CGH displayed by a SLM [12], as schematically reported in Fig. 6.6. However, in this case, polymerization occurs layer by layer. Indeed, the CGH is divided into sub-CGHs, representing the phase patterns of object's 2D layers. While the sub-CGHs are sequentially displayed, fresh unpolymerized resin is injected in the vat with a flowrate adjusted according to the exposure time (and the optical power) needed.

The introduction of holographic 3D printing has opened new possibilities in the field of additive manufacturing, overcoming lot of issues connected to support printing and layering artifacts. However, many aspects still need to be investigated to enhance the final resolution and the complexity of objects to be 3D printed.

6.3 Tomographic 3DPrinting and Computed Axial Lithography (CAL)

Immediately after the advent of holographic 3D printing, researchers worked on a new system, similar concept, which could improve the single shot stereolithography. In 2017, Kelly et al. introduced the computed axial lithography (CAL) [13]. It

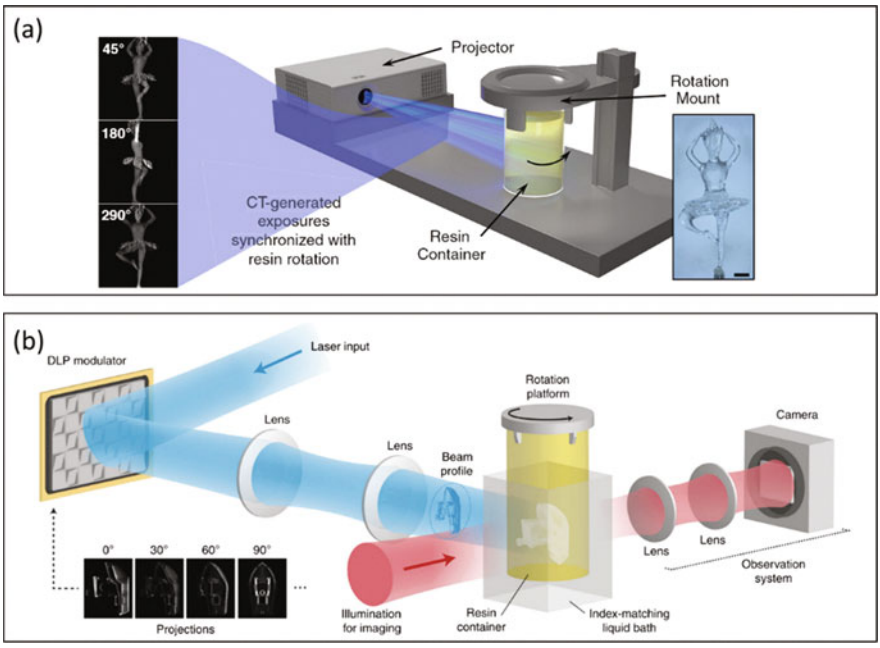

Fig. 6.7 Computed axial lithography (CAL). (**a**) A typical CAL setup. (Reprinted with permission from Ref. [15]). Scale bar 2 mm. (**b**) The CAL correction strategy proposed by Loterie. (Reprinted under the Creative Commons CC BY [16])

could be said that CAL technology was born from the application of computed tomographic (CT) imaging to stereolithography. The working principle behind CAL is very similar to a medical technique called intensity-modulated radiation therapy (IMRT). IMRT is employed to deliver controlled and focused doses of radiation only to malignant tumors, without affecting the surrounding organs. In the same way, CAL proposes to project the shape to be polymerized by different azimuthal angles directly in the resin vat.

A new system was designed. In this case, different from the holographic 3D printing, the resin vat rotates at a well-defined rate during printing. A video projector, typically a digital light processing (DLP) one, is employed to output the computed intensity light profiles inducing polymerization. Thus, a dynamic light field is projected according to the azimuthal angle and the rotation speed of the resin vat [14], as schematically shown in Fig. 6.7a. For CAL, the geometry of the object to be 3D printed is processed to obtain light intensity patterns. After a first discretization along z-axis (defined as "voxelization" in [17]), the layer image is converted in a binary image, where 0 stays for no material and 1 for polymerized material. Then, for each layer, the Radon transform is performed, obtaining the so-called sinogram. The sinogram is a sum of sinusoidal waves which describes the 2D layer as it would be seen from an intensity detector rotating all around the layer.

Then, back-projecting the inverse of the Radon transform, the projection of the object at different angles is obtained. Often, this back projection requires filtering operations in order to obtain sharper light intensity patterns and enhance the overall printing results. Even if the light projection interests the whole build volume, only certain areas, which are subjected to multiple angle exposure, will polymerize.

Some researchers have evidenced that, during printing, it can happen that not all the volume to be polymerized uniformly reticulates. This results in uneven effects which need to be corrected. Loterie et al. [16] have proposed a quite simple but efficient way to solve this issue. They placed a camera orthogonally to the polymerizing light beam (see Fig. 6.7b). This camera captures the polymerization of the model at specific time points. After the first part is printed, the camera images can be analyzed and the light intensity profile adjusted accordingly. Thus, from the second print, the exposure time remains the same while the dose is spatially adjusted to simultaneously polymerize the whole object. Chung Li et al. [18] claimed that this strategy recognizes solidification only until a voxel is darkened at all angles: this can introduce inaccuracies which are not correctly compensated in case of voxels which are transparent at some views. Therefore, they reported a way for real-time correction of the polymerization process exploiting Schlieren imaging. Introduced by Töpler in the second half of the nineteenth century, Schlieren imaging is an optical filtering technique applied at the focal plane of a light beam (Fourier plane) which outputs light intensity variations according to refractive index inhomogeneities. Thus, the change in refractive index consequent to resin polymerization can be detected both in time and space. By comparing object reconstruction based on refractive index variation and object mesh, computational adjustment allows to correct in real-time imprecision in CAL process.

The possibility to illuminate the sample from different azimuthal angles with a single beam makes CAL a feasible strategy to 3D print structure with higher complexity degree than holographic 3D printing. In their work, Kelly et al. managed to replicate “The Thinker” sculpture by A. Rodin and a dental model. Another example of complex structure was reported by Loterie et al. [19] which replicated a mouse pulmonary artery model.

CAL allows to print objects in very short times if compared to stereolithography, for example. Macroscopic parts were printed in less than 5 min. The light intensity range goes from 0.1 to 3 mW/cm^2.

Also in this case, the liquid resin movement is not required; thus, very thick materials or fragile polymers can be 3D printed without affecting the final results. Gelatin methacrylate (GelMA) is a hydrogel material commonly employed in the biomedical field for resembling the cells’ natural environment. Kelly and co-workers [13] effectively managed to additively manufacture 3D highly flexible structures employing CAL with GelMA. At the same time, Bernal et al. [19] reported the fabrication of cell laden structures. Thanks to the short printing time, CAL represents a perfect choice for printing materials similar to GelMA containing living cells. Indeed, in standard bioprinting (viz., extrusion-based, stereolithography, digital light projection printing, and melt electrowriting), one of the main constraints is the residence time of cells inside cartridges. This commonly means a high stress

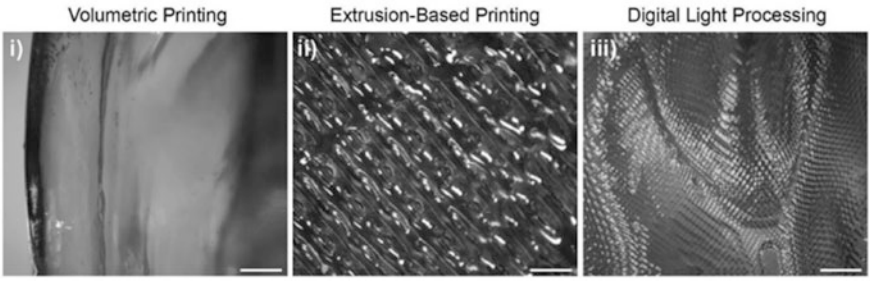

Fig. 6.8 Surface feature comparison between printing technologies: (i) volumetric printing, (ii) extrusion-based printing, and (iii) digital light processing (scale bars = 500 μm). (Reprinted with permission from Ref. [19])

for cells and low viability after printing due to the absence of an optimal culture environment during the process itself. Exploiting CAL, Bernal managed to print a human auricle model with cells inside. Further experiments revealed an 85% cell viability after printing and a successive increase in cells' metabolism, indicating their good health. The printing of such structures was also enhanced by using the so-called gelRESIN: this polymeric material can be subjected to thermo-reversible gelation. Therefore, when the printing occurs, the gelRESIN is in a gel state showing different advantages, first of all, the possibility to print suspended structures without movement-induced blurring; moreover, the cells' sedimentation is avoided, leading to uniformly distributed cells' volume.

Figure 6.8 perfectly demonstrates the possibility to print structures with high surface smoothness. In layer-by-layer printing, this would not be possible, since in one of the three directions, the effect of discrete slicing is always visible. For these interesting properties, Zhang et al. [20] have highlighted the possibility to use CAL for the 3D printing of the transparent cornea directly with the right material to be then implanted.

6.4 Xolography

Probably the most recent technique, xolography, is also defined as "dual-color volumetric printing." The printing process involves the simultaneous presence of two light beams at different wavelengths: a first one which activates the photoinitiator and a second one which initiates the polymerization reaction. The system proposed by Stefan Hecht group [21] comprises a resin vat and two separate light sources. The first one creates a thin sheet of light inside the resin vat. Orthogonally, a digital light projector (DLP) screens the layer image on the same plane where the sheet of light is shown in Fig. 6.9a. The resin container is moved relatively to the sheet of light along the growing direction of the object (commonly labeled as z-axis). Since

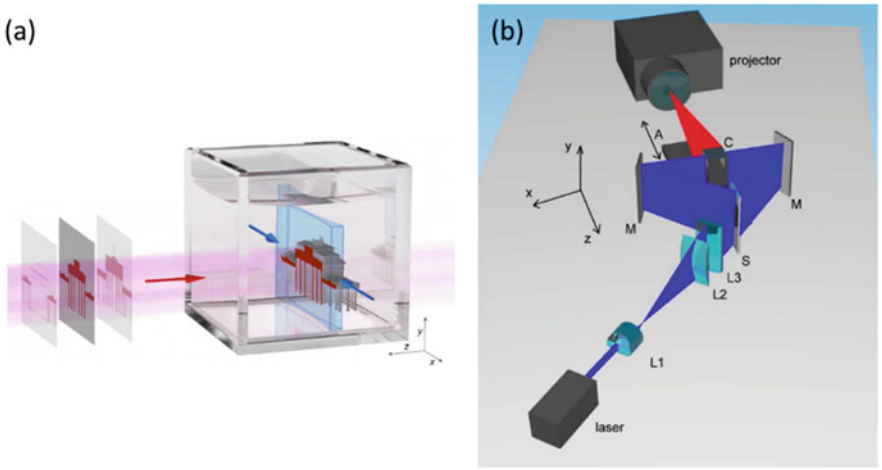

Fig. 6.9 Xylographic 3D printing technology. (**a**) Rendered illustration of the printing process: in blue, the activating beam, and in red, the initiating one. (**b**) Schematic of the printing setup, including the lenses (L1, L2, and L3), the beam splitter S, and the two mirrors M. (Reprinted with permission from Ref. [21])

the polymerization is triggered only when the two light sources act, each voxel is polymerized only once. In this way, the resolution along z-axis is well determined, and common stereolithography overcuring along z-axis is avoided.

The optical path and the printing setup proposed by Hecht are reported in Fig. 6.9b. The light sheet comes from a 375 nm continuous-wave laser. L1 lens is placed at the output of the laser and makes the beam diverge, and then L2 and L3 lenses collimate the diverging beam. At this stage, the light sheet is ready to be used for the polymerization purposes. However, according to the Beer-Lambert-Bouguer law, light attenuation goes with penetration depth. Especially for larger resin containers, the risk of nonuniform light sheet along the whole container section exists. Therefore, the light sheet coming from L3 is divided by a beam splitter ("S" in Fig. 6.9b) and directed toward two mirrors M facing each other with the resin vat between them. In this way, all the volume width is irradiated uniformly. As schematically reported in Fig. 6.9a, the sheet of light inside the resin vat is characterized by a beam waist, narrower in the middle and expanding toward the edges. A theoretical analysis was carried on by the authors to optimize the beam waist according to the volume width and obtaining a negligible variation of sheet thickness all along the vat.

Once the light sheet illuminates the part of the resin volume, the object slices are projected thanks to a modified DLP which achieves a pixel resolution of 21 μm × 21 μm. The overall resolution is approximately 25 μm in xy plane and 50 μm along z, about ten times higher than previously known macroscopic volumetric printing processes.

As previously mentioned, the optical setup for obvious reasons is fixed on the table; the object grows thanks to the vat movement. A servo-driven linear stage running at 25 μm steps is mounted to perform such linear shifting. The object's 3D model is divided in slices, and the sequence of slices is converted in a black and white movie. Then, the movie is projected; its frame rate is equal to v/r, where v is the speed of the resin vat and r the slice thickness. With xolography, the polymerization rate is estimated in 55 mm^3/s. To better understand how powerful this technology is, it suffices to say that common light-based 3D printers have growing rates of 500 mm/h, and two-photon polymerization (TPP), which is considered as the first example of volumetric printing, grows objects at roughly 10 mm^3/h [22].

A lot of improvements are foreseen for xolography technology, for example, the printing time. By increasing laser power and adding photoinitiators with faster thermal relaxation time, the printing speed can further increase. The higher the printing speed is, the easier to print suspended parts becomes. Moreover, the projection of grayscale or colored movies could lead to the modulation of cross-linking degree, useful for the 4D printing of materials (i.e., 3D printing of functionalized structures or structures able to change their shape).

6.5 Materials for Volumetric 3D Printing

An accurate resin formulation is as important as a precise optical alignment in volumetric 3D printing setup. Some properties exist which are required for printable resins, to ensure a final result with good optical, surface, and mechanical properties and a good resolution even for objects with complex geometries.

When dealing with light-based 3D printing, the first requirement surely is the photosensitivity of the liquid material that must be rapidly cured by the laser-generated images flashed into. The process should take short time, typically less than 10 s, and it is accomplished through balancing laser intensity, wavelength, and irradiation time and also adding to the resin suitable photoinitiators or sensitizers [23].

The first challenge is that light must penetrate the resin, while the solution remains tractable. The resin transparency and the amount of photoinitiator added to the formulation are crucial for this purpose. In particular, volumetric 3D printing method requires that the light patterns propagate through the whole diameter or width of the build volume. Resin composition (monomers/oligomers and photoinitiator) strongly influences an accurate object reconstruction. In other words, when designing a resin composition for volumetric printing, the initiator concentration must be low enough for the light to penetrate through the whole volume but also high enough to allow the resin to polymerize. According to the absorption coefficient of the photoinitiator for the illumination wavelength, its concentration should be adjusted so that the optical attenuation length is longer than the width of the printed

objects. In addition, resins should have a strong reactivity and low absorption to obtain well-defined final objects [17, 19].

A maximum photoinitiator concentration can be found, letting 90% of the light penetrate the curing solution, enhancing the process efficiency. Further increasing the amount of photoinitiator will result in a fast curing of the resin, but with the adverse effect of dulling the solution, hindering the light crossing. A dye can also be added to the formulation, to block undesired wavelengths and tune component opacity [14].

Among photoinitiators, Regehly and colleagues [21] report molecules known as dual-color photoinitiators (DCPIs), realized by integrating a benzophenone type II photoinitiator into a spiropyran photoswitch. These photoswitchable photoinitiators are used for xolography, a dual-color technique inducing local polymerization inside a confined monomer volume, upon linear excitation by intersecting light beams of different wavelengths. The first light wavelength is chosen to excite DCPI dissolved in the resin by cleaving a molecular ring in the backbone of the molecule; this reaction occurs only within the sheet of light. A second beam of light projects an image of a slice of the object to be 3D printed into the plane of the light sheet. The wavelength of the second beam is different from that of the first and causes any excited DCPI molecules to initiate polymerization of the resin, solidifying the slice. The resin volume is then moved with respect to the position of the light sheet, which is fixed. This changes the position of the light sheet in the resin, so the activation and initiation processes can begin again at a new position, thereby building up the object slice by slice. The authors demonstrated the effectiveness of their technique by printing a ball trapped as a loose object in a spherical cage, which was 8 millimeters in diameter. Using conventional layer-by-layer 3D printing, the ball would have needed to be printed with supports connecting it to the cage, and they would have been difficult to remove afterward [21, 22].

The next requirement, for volumetric 3D printable materials, is the stiffness in the printed volume, to allow the removal of the unpolymerized solution at the end of the process. After exposure, the structure must be got rid of uncured material by solvent rinsing, sometimes combined with moderate heating to liquefy or reduce the viscosity of the uncured material.

Chain reactions are responsible of it, due to cross-linking of polymer chains; if not enough initiator is added to the solution, these reactions slow down and some parts of the final printed object can be jelly like. To overcome this issue, a post-curing of the printed object can be useful, both by UV light or by a thermal treatment; anyway, the amount of light during 3D printing and the chemistry of polymeric chain propagation should be proper to confer a certain stiffness to the printed object in all its parts, enhancing material properties.

The main property influencing the rheology of the system is the viscosity of the resin. Layer-based photopolymer printing technologies typically impose a maximum viscosity limit on the prepolymer mixture to allow the resin to reflow between the printing of subsequent layers. To meet this major design constraint, photopolymer formulations are often blended with reactive diluent monomers to

reduce the resin viscosity. This process can adversely affect the properties of the resulting solid material [14, 21].

In the volumetric 3D printing process, more viscous materials can be used because the flow of the material is not required during printing. Since the process is layer-less and does not involve any relative motion between the resin and the printed part, it has positive implications for mechanically isotropic part strength. Viscous resins, with better material properties, can be printed in such way; some examples are tougher materials like acrylics or silicone. These can cure without any distortion of the printed parts, unlike by other conventional methods, where simply the act of moving the part with respect to the resin would lead to distortion. Moreover, all features within the parts are formed at the same time, so they do not show any surface issue [13].

The lack of relative motion and hydrodynamic stresses also broadens the range of materials that can be printed. Exceptionally high-viscosity materials, with viscosity higher than 100,000 cP versus 3000/4000 cP required for a typical layer-by-layer printing resin, and even solid gels were printed, which would be impossible in layer-based processes. High accessible viscosities mean that resins do not need to be diluted, so the final material properties are not compromised [24]. High-viscosity precursors also limit molecular diffusion-induced blurring. Noteworthy, such viscous resins are not prone to other printing methods, such as layer by layer.

Furthermore, extra-soft materials, such as hydrogels, can be wholly fabricated, which would otherwise be damaged or destroyed by fluid motion, and even cyanate esters, which are very temperature-sensitive, can be directly patterned in this manner.

The choice of a prepolymer mixture rather than monomers increases the density of the formulation, limiting the difference between solid and liquid resins. The result is that sedimentation is restrained, without any detrimental effect on the printing quality, and free-radical diffusion during the printing process is limited, therefore reducing proximity effect.

Moreover, 3D printing of elastomeric materials, such as silicone, is relevant for biomedical applications such as soft medical devices, like tissue-like vasculature models for surgery or rubberlike vents in hearing aids. Unfortunately, the printing of a structure that is extremely complex, with hollow parts, such as an artery, needs support structures in some shape or form, and the post-processing necessary to remove them is a problem, especially if the structure is fragile. It limits the design freedom and makes casting, additive manufacturing, or stereolithography not suitable for the application [16]. Volumetric 3D printing overcomes the limitations of previous methods. Highly viscous materials provide comprehensive support for objects being printed, so there is no need to incorporate dedicated solid supporting structures, large overhanging features, as there often is layer-based processing. The self-supporting nature of the process enables delicate structures to be fabricated in soft, highly compliant materials such as hydrogels. Complex silicone-based hollow structures, with channels as small as 1.8 mm for a pulmonary model, were quickly printed without any support struts. Even in this case a post-curing process was necessary to reduce the object tackiness. Loterie et al. [17] investigated three resin

formulations based on dipentaerythritol pentaacrylate, aliphatic urethane diacrylate, and a mixture of silicone-based prepolymers, mainly PDMS (polydimethylsiloxane), with viscosity ranging from 10,000 to 15,000 cP. Small arteries, with the smallest achieved diameter of 1.4 mm, and an extremely soft printed structure were successfully printed in just 30 s for acrylates and 15 s for silicones, without any solid supporting struts. The tensile properties of printed materials span from plastic to elastomeric, with modulus from 356 MPa to 280 kPa, obtained with the silicone-based formulation in presence of a thiol cross-linker. A post-curing of the silicone part in a mixture of thiol cross-linker and photoinitiator, for 5 min at 100 mW/cm^2, was required to increase hardness and stability of the object. The final material is suitable to produce surgical models that mimic the mechanical properties of biological tissues, due to its compliance, biocompatibility, and durability [17].

For acrylates or silicones, free radicals are generated by light activation and then rapidly quenched and deactivated by oxygen, during the initial inhibition phase of printing. Since the material begins to cross-link at a given position within the volume, oxygen must be sufficiently depleted locally. The nonlinear response of the material, necessary for volumetric 3D printing, is due to the oxygen inhibition process, which sets a critical dose threshold. After the resin is exposed from all angles, it can be observed the full 3D object overcoming inhibition simultaneously and materializing, within the volume. For material chemistries not inhibited by oxygen, a dose-response nonlinearity can be obtained by adding other inhibiting molecules to the resin [10, 14].

Van der Laan [25] examined butyl nitrite as a UV-active photoinhibitor of blue light-induced polymerization and explored its use to confine in depth the polymerized region in a volume of methacrylate resin. By employing two perpendicular irradiation patterns at blue and near-UV wavelengths to independently affect either polymerization initiation or inhibition, respectively, they enable 3D photopolymerization patterning in bulk resin, thereby complementing emergent approaches to volumetric 3D printing.

Nitrites, both inorganic and organic, are known to be inhibitors or retarders of free-radical chain-growth polymerization. Whereas inorganic nitrite salts can react with water to form nitric oxide and nitrous oxide species, organic nitrites reportedly require activation to effect polymerization inhibition, generally requiring low concentrations (from 0.0001% wt. to 0.1% wt.) to be effective.

Butyl nitrite was identified as an effective methacrylate photoinhibitor, where the polymerization rates for resin formulations exposed exclusively to blue light are significantly higher than those formulations concurrently exposed to both blue and near-UV lights. The effectiveness of butyl nitrite as a photoinhibitor is strongly monomer-dependent, and its inclusion can lead to reduced polymerization rates, without activation.

The potential for the photopolymerization of butyl nitrite-formulated resins to be spatially confined using concurrent blue and near-UV irradiation was investigated. Consequently, the regions irradiated exclusively with blue light cured rapidly to afford cross-linked, insoluble polymer, while the polymerization in the regions exposed to both blue and near-UV lights proceeded sufficiently slowly such that,

after irradiation cessation, they remained liquid and were readily washed away with solvent. Through this antiparallel, concurrent irradiation scheme, photopolymerization was successfully inhibited, such that the resin remained liquid through a thickness of up to 5 mm.

Moreover, photoinhibition of free-radical chain-growth photopolymerization via butyl nitrite photolysis can be rapidly switched on and off by cycling the incident near-UV light. The inhibiting radicals are in fact rapidly consumed in the absence of butyl nitrite photolysis, affording prompt photopolymerization rate recovery after cessation of near-UV exposure.

The concurrent activation of butyl nitrite as a photoinhibitor under near-UV irradiation and camphorquinone as a photoinitiator under blue irradiation can also result in a volumetric photopolymerization patterning. Thus, nonparallel, concurrent irradiation of formulated resin with both initiating and inhibiting wavelengths enables the fabrication of more complex, 3D objects in a single exposure. This allows for rapid, single-exposure fabrication of more complex, otherwise unattainable structures [25].

In a recent paper, Shusteff [23] reported a highly tunable strategy for volumetric 3D printing of a new thiol-ene photoresin.

Thiol-enes are polymers formed through the polymerization between a thiol and an alkene to form a thioether. They have drawn significant attention in recent years owing to the high degree of control and tunability over the reaction, yielding polymers with excellent mechanical properties. Thiol-ene materials are attractive because they have well-ordered polymer networks, allowing for a much wider variety of mechanical performances, from stiff and strong to soft and stretchy.

A critical issue is that thiol-ene cross-linking chemistry does not have the threshold response needed for volumetric 3D printing to work, because the oxygen inhibition in radical-initiated thiol-ene reactions is negligible. Since thiol-ene polymerization is not inhibited by oxygen, even in this case, a chemical inhibitor, 2,2,6,6-tetramethyl-1-piperidinyloxy or TEMPO, was added to the formulation, to enhance the thiol-ene cross-linking chemistry creating the required nonlinear threshold behavior.

In this way, thiol-ene resin follows a nonlinear response to the curing illumination, meaning the material has an energy threshold that allows a high control on the polymerization reaction that forms the hardened polymer. A quantitative ability to design the resin response to absorbed optical energy by measuring the gelation threshold, and incorporating it during the build, was shown. Regions that are not irradiated with the right amount of energy will remain liquid and can be poured away afterward. Furthermore, by modulating the content of initiator and inhibitor, the reaction kinetics can be greatly controlled.

By adjusting the relative monomer composition within thiol-ene resins, the modulus and toughness of printed objects can be varied by over two orders of magnitude (0.12–421 MPa, 0.50–36 $mJ \cdot m^{-3}$), and the ultimate strain changed by over one order of magnitude, from 36.1% to 293%.

These thiol-ene materials can find application as functional biological scaffolds, as the unreacted thiols can also be used for surface functionalization. Useful

applications can be found in medical and dental markets, where patient-specific geometries are important, as well as in creating artificial tissues and organ models from soft hydrogels [23].

Hydrogels, a 3D network of molecules composed of hydrophilic polymer chains, can be designed into any shape, size, or form and have the ability to absorb up to a thousand times their dry weight in a water-rich environment.

Hydrogels have been the material of choice for researchers focusing on biological applications such as organs, tissues, scaffolds, and other 3D structures, microfluidics for point-of-care applications, soft robotic structures for large deformations/drug encapsulations, and drug delivery. A 3D volumetric printing method was used to create a hydrogel ear [26].

Hydrogels are formed by cross-linking of polymer chains in an aqueous medium through various mechanisms such as physical entanglement, ionic interaction, and chemical cross-linking. Physical entanglement or physical gelation mostly depends on the intrinsic properties of the polymers, and therefore, the ability to control the microenvironment is limited. However, these gelation processes do not require the complex chemical modification to the chains, and also these processes are generally reversible. In contrast to the physical approach, chemical approach always requires controlled process conditions, but these controllable and precise cross-linking procedures are beneficial to develop a more accurate and hierarchically complex microenvironment.

Hydrogel plays a vital role in cell-laden 3D bioprinting, whereas those hydrogels mimic the physical and biochemical characteristics of native extracellular matrix (ECM). The complex microenvironment of the ECM does not replicate from the traditional static microenvironment of the hydrogel, but the evolution of the 3D bioprinting facilitates to accommodate the dynamic modulation and spatial heterogeneity of the hydrogel system.

The most used hydrogel-based polymers in the 3D printing techniques are alginate-, gelatin-, and poly(ethylene glycol) (PEG)-based materials. The properties of interest, due to the main biological and clinical application, are biocompatibility, immunocompatibility, mass transport, biodegradability, target microenvironment, mechanical properties, and effect of cross-linking reaction to the cell viability [27].

An optical-tomography-inspired printing approach, based on visible light projection, was developed to generate cell-laden tissue constructs with high viability (>85%) from gelatin-based photoresponsive hydrogels. Free-form architectures, difficult to reproduce with conventional printing, were obtained, including anatomically correct trabecular bone models with embedded angiogenic sprouts and meniscal grafts.

Moreover, free-floating structures are generated, as demonstrated by printing functional hydrogel-based ball-and-cage fluidic valves.

Several photoresponsive hydrogels have shown remarkable compatibility for cell encapsulation. As a cell-friendly bioresin for volumetric printing, a formulation based on gelatin methacryloyl dissolved in phosphate-buffered saline, with lithium phenyl-2,4,6-trimethylbenzoyl-phosphinate as photoinitiator for the free-radical polymerization of the methacryloyl moieties, was investigated by Bernal

[19]. With this approach, complex, free-form structures could be generated within seconds, from a volume of cell-laden hydrogels. The photoinitiator exhibits a superior quantum efficiency and molar extinction coefficient at visible wavelength ($\varepsilon = 50\ M^{-1}\ cm^{-1}$ at 405 nm), compared with other initiators used so far for the volumetric printing of noncell-compatible resins.

Interestingly, the photoinitiator concentration required to produce well-defined printed structures was only 0.037% wt., a value considerably lower than commonly used in previously reported additive bioprinting studies. This reduces the potential toxicity risks that are correlated with high concentrations of this photoinitiator.

The freedom of design provided by volumetric bioprinting approaches permits the production of hydrogel-based actuators through the direct fabrication of movable or articulating parts. With the adoption of volumetric bioprinting in the field of biofabrication, several future developments can be expected. There is virtually no limitation on the use of different photopolymers, and several photoresponsive natural or synthetic hydrogels could be optimized for this process, including but not limited to materials based on hyaluronan, PEG (polyethylene glycol), alginate, or decellularized ECM or even stimuli-responsive biomaterials for remote stimulation of the construct or controlled patterning of bioactive molecules [19].

6.6 Conclusion

In conclusion, volumetric 3D printing widens the field of photopolymers for additive manufacturing by allowing the use of higher-viscosity materials. It can thus enable printing of materials that are otherwise difficult or slow to 3D print because of their high viscosity in the precursor form. Example materials include those with high stiffness and thermal resistivity, along with silicones.

With all the benefits, this new method has some limitations including restrictions on part resolution and types of geometries that can be fabricated. Extremely complex structures would require lots of intersecting laser beams and would limit the process.

Moreover, currently the major limitation of xolography is the volume that can be printed: it is restricted by the distance the light beams can penetrate into the resin. Because the method requires the resin volume to be moved, objects with large dimensions in the direction of movement will take proportionally more time to build up than shorter ones. And although the reported chemistry enables high-resolution printing, it also limits the materials that can be used for xolography.

As with any new research area, the challenges are many. Further work is needed to thoroughly understand the resolution limits of the process and to improve its accuracy, which is dependent both on the optics and the photochemistry.

In particular, expanding material options for 3D printing technologies will pave the way for better control and complexity in 3D-printed materials.

Volumetric bioprinting permits the creation of geometrically complex, centimeter-scale constructs at an unprecedented printing velocity, opening new avenues for upscaling the production of hydrogel-based constructs and for their

application in tissue engineering, regenerative medicine, and soft robotics. Anyway, new developments are necessary to enable the creation of large, clinically relevant biofabricated grafts, with potential application for regenerative medicine in humans, produced with a high-speed scalable process.

Next steps pertaining to the technology should introduce the potential for printing multiple materials within the same process, as this will be important to further mimic the heterogeneous composition of living tissues. For example, multimaterial volumetric printing could be used to address the zonal architecture of certain tissues such as cartilage or menisci, create cell and material gradients, replicate biological interfaces, introduce vascularization in a single step, or even co-print mechanically strong polymers to reinforce the cell-laden bioprinted hydrogels.

Although this technology is definitely an exciting development, further engineering and polymer chemistry need to be completed in order to improve the resin properties, so more stable and performing structures can be fabricated.

References

1. C.W. Hull, Apparatus for production of three-dimensional objects by stereolithography (1986). https://doi.org/10.1145/634067.634234
2. P.F. Jacobs, Fundamentals of stereolithography: Solid freeform fabrication proceedings (1992). https://doi.org/10.1017/CBO9781107415324.004, pp. 196–211
3. A.K. O'Brien, C.N. Bowman, Impact of oxygen on photopolymerization kinetics and polymer structure. Macromolecules **39**, 2501–2506 (2006). https://doi.org/10.1021/ma051863l
4. T. Latychevskaia, Lateral and axial resolution criteria in incoherent and coherent optics and holography, near- and far-field regimes. Appl. Opt. **58**, 3597 (2019). https://doi.org/10.1364/ao.58.003597
5. D. Gabor, Holography, 1948–1971. Science **177**(1972), 299–313 (1979). https://doi.org/10.1126/science.177.4046.299
6. M. Campbell, D.N. Sharp, M.T. Harrison, R.G. Denning, A.J. Turberfield, Fabrication of photonic crystals for the visible spectrum by holographic lithography. Nature **404**, 53–56 (2000). https://doi.org/10.1038/35003523
7. Y. Lin, A. Harb, K. Lozano, D. Xu, K.P. Chen, Five beam holographic lithography for simultaneous fabrication of three dimensional photonic crystal templates and line defects using phase tunable diffractive optical element. Opt. Express **17**, 16625 (2009). https://doi.org/10.1364/OE.17.016625
8. K. Ohlinger, F. Torres, Y. Lin, K. Lozano, D. Xu, K.P. Chen, Photonic crystals with defect structures fabricated through a combination of holographic lithography and two-photon lithography. J. Appl. Phys. **108**, 073113 (2010). https://doi.org/10.1063/1.3493119
9. B. Liu, C. Zhan, X. Yao, S. Yan, B. Ren, Nanobowtie arrays with tunable materials and geometries fabricated by holographic lithography. Nanoscale **12**, 21401–21408 (2020). https://doi.org/10.1039/D0NR05546H
10. M. Shusteff, A.E.M. Browar, B.E. Kelly, J. Henriksson, T.H. Weisgraber, R.M. Panas, N.X. Fang, C.M. Spadaccini, One-step volumetric additive manufacturing of complex polymer structures. Sci. Adv. **3** (2017). https://doi.org/10.1126/sciadv.aao5496
11. J. Huang, Q. Qin, J. Wang, A review of stereolithography: Processes and systems. Processes **8**, 1138 (2020). https://doi.org/10.3390/PR8091138
12. C.-F. Lee, W.-F. Hsu, T.-H. Yang, R.-J. Chung, Three-dimensional (3D) printing implemented by computer-generated holograms for generation of 3D layered images in optical near field. Photonics **8**, 286 (2021). https://doi.org/10.3390/photonics8070286

13. B. Kelly, I. Bhattacharya, M. Shusteff, R.M. Panas, H.K. Taylor, C.M. Spadaccini, Computed Axial Lithography (CAL): Toward single step 3D printing of arbitrary geometries (2017)
14. B.E. Kelly, I. Bhattacharya, H. Heidari, M. Shusteff, C.M. Spadaccini, H.K. Taylor, Volumetric additive manufacturing via tomographic reconstruction. Science **363**(2019), 1075–1079 (1979). https://doi.org/10.1126/science.aau7114
15. Y. Shou, Thiol-ene materials promote volumetric 3D printing. MRS Bull. **46**, 12 (2021). https://doi.org/10.1002/adma.202003376
16. D. Loterie, P. Delrot, C. Moser, High-resolution tomographic volumetric additive manufacturing. Nat. Commun. **11**, 852 (2020). https://doi.org/10.1038/s41467-020-14630-4
17. D. Loterie, P. Delrot, C. Moser, Volumetric 3D printing of elastomers by tomographic back-projections (2018). 10.13140/RG.2.2.20027.46889
18. C. Chung Li, J. Toombs, H. Taylor, Tomographic color Schlieren refractive index mapping for computed axial lithography, in *Symposium on computational fabrication, ACM*, (New York, 2020), pp. 1–7. https://doi.org/10.1145/3424630.3425421
19. P.N. Bernal, P. Delrot, D. Loterie, Y. Li, J. Malda, C. Moser, R. Levato, Volumetric bioprinting of complex living-tissue constructs within seconds. Adv. Mater. **31**, 1904209 (2019). https://doi.org/10.1002/ADMA.201904209
20. B. Zhang, L. Gao, Q. Xue, Z. Cui, L. Ma, H. Yang, Strengths, weaknesses, and applications of computational axial lithography in tissue engineering. Bio-Design Manuf. **3**, 5–6 (2020). https://doi.org/10.1007/s42242-020-00057-9
21. M. Regehly, Y. Garmshausen, M. Reuter, N.F. König, E. Israel, D.P. Kelly, C.-Y. Chou, K. Koch, B. Asfari, S. Hecht, Xolography for linear volumetric 3D printing. Nature **588**, 620–624 (2020). https://doi.org/10.1038/s41586-020-3029-7
22. C. Darkes-Burkey, R.F. Shepherd, High-resolution 3D printing in seconds. Nature **588**, 594–595 (2020). https://doi.org/10.1038/d41586-020-03543-3
23. C.C. Cook, E.J. Fong, J.J. Schwartz, D.H. Porcincula, A.C. Kaczmarek, J.S. Oakdale, B.D. Moran, K.M. Champley, C.M. Rackson, A. Muralidharan, R.R. McLeod, M. Shusteff, Highly tunable thiol-ene photoresins for volumetric additive manufacturing. Adv. Mater. **32**, 2003376 (2020). https://doi.org/10.1002/adma.202003376
24. H. Taylor, H. Heidari, C.C. Li, J. Toombs, S.M. Luk, 3D printing challenges and new concepts for production of complex objects, in *3D printing for energy applications*, (Wiley, 2021), pp. 153–180. https://doi.org/10.1002/9781119560807.ch7
25. H.L. van der Laan, M.A. Burns, T.F. Scott, Volumetric photopolymerization confinement through dual-wavelength photoinitiation and photoinhibition. ACS Macro Lett. **8**, 899–904 (2019). https://doi.org/10.1021/acsmacrolett.9b00412
26. I. Karakurt, L. Lin, 3D printing technologies: Techniques, materials, and post-processing. Curr. Opin. Chem. Eng. **28**, 134–143 (2020). https://doi.org/10.1016/j.coche.2020.04.001
27. J.M. Unagolla, A.C. Jayasuriya, Hydrogel-based 3D bioprinting: A comprehensive review on cell-laden hydrogels, bioink formulations, and future perspectives. Appl. Mater. Today **18**, 100479 (2020). https://doi.org/10.1016/j.apmt.2019.100479

Part II
Impact on Different Research Fields and Case Studies

Chapter 7
Biomedical Applications

Ignazio Roppolo, Annalisa Chiappone, Alessandro Chiadò, Gianluca Palmara, and Francesca Frascella

Abstract In recent years, 3D printing technology has become a sufficiently mature technique to allow not only the production of objects starting from a design modeling but also a possible customization through the introduction of functionality by the end user. This rapid prototyping technique represents a very promising technology for device fabrication with different application fields (e.g., biological, environmental, food, aerospace), offering advantages over traditional manufacturing methods.

Moreover, the 3D printing archetype has introduced novel opportunities for the realization of smart devices, where the added value lies in their intrinsic functionality. In fact, 3D-printed functional materials can transform their structure in response to specific stimuli (e.g., temperature, pH, light radiation, etc.), adding to the printed object interesting properties to take advantage of. Recently, this paradigm has been explored and expanded by researcher's/engineer's community with the aim of realizing 3D printable objects that present exploitable chemical functionalities.

In this chapter, functional 3D objects for bio-applications have been reported, combining 3D printing technology with an accurate material engineering. The result is a single step 3D-printed object with intrinsic chemical functionalities that could be exploited to produce immunoassay-based and/or enzymatically active devices for biosensing purposes and precision medicine.

Keywords 3D printing · Functionality · Biosensors · Biorecognition · Biocatalysis · Precision medicine

I. Roppolo · A. Chiadò · G. Palmara · F. Frascella (✉)
Department of Applied Science and Technology – DISAT, Politecnico di Torino, Torino, Italy
e-mail: francesca.frascella@polito.it

A. Chiappone
Department of Chemical and Geological Sciences, Università di Cagliari, Cittadella delle Scienze, Monserrato, Italy

S. L. Marasso, M. Cocuzza (eds.), *High Resolution Manufacturing from 2D to 3D/4D Printing*, https://doi.org/10.1007/978-3-031-13779-2_7

7.1 Introduction

The rapid evolution of 3D printing technology in the last 20 years demonstrated that this technique has the potential to revolutionize the manufacturing processes in many industrial fields such as automotive, aerospace and aviation, medicine, and healthcare, as well as to be disruptive in academia [1]. 3D printing, or alternatively mentioned as additive manufacturing (AM), is an umbrella term that comprehends a wide set of technologies, which has in common the ability to produce 3D objects starting from digital objects designed by computer-aided design (CAD) software or 3D scanners. These models are then generally transformed in STL files (which acronym stays for standard tessellation language or standard triangle language), which are used by the 3D printer, after a slicing of the file in cross-sections, to define the controlled deposition of material layer by layer, until the complete fabrication of the object. One of the main advantages of 3D printing consists of the fast and relatively cheap fabrication of prototypes, avoiding tooling and time-consuming post processing. Furthermore, compared to conventional subtractive manufacturing processes, it allows higher personalization and the fabrication of more complex geometries [2]. Nowadays, 3D printing is mainly employed in manufacturing of small series where the primary goal is to obtain nearly finished products, because it allows faster modification and optimization of parts compared to high-volume production [3]. For example, nanocomposite polymeric materials are often employed in 3D printing to improve the mechanical properties of the final object [4]. Moreover, the use of engineered materials in 3D printing is exploited to fabricate objects with additional properties, enhancing their functionalities adding another grade of complexity to the structural or chemical properties. Those functional materials are typically studied to provide new intrinsic properties to the components, either with or without external stimuli; from this aroused the concept of 4D printing, as further development of 3D printing [5, 6]. Under the umbrella term "4D printed" are considered all the 3D-printed objects that can undergo shape-shifting in response to an external stimulus, for example, pressure, temperature, magnetic fields, or light [5–7]. Similarly, some authors proposed to use the same paradigm to objects that possess intrinsic biochemical functionalities [6]. In this frame, active devices for biotechnological applications have been reported, exploiting functional 3D objects with biorecognition and/or catalytic capabilities.

In this chapter, different types of devices fabricated by 3D printing technology exploited to perform bioanalytical analysis will be presented, focusing on the materials' design to achieve those smart objects exploiting intrinsic and/or tunable functionalities. In fact, 3D printing field showed increasing attention to bio-applications, most of all in tissue engineering and regenerative medicine [8, 9] or in the rapid prototyping and fabrication of components for biomedical purposes [10–13]. Recently, the field of fabrication of 3D-printed constructs for tissue engineering and regenerative medicine has been comprehensively reviewed [14–17]. Instead, this chapter aims to evidence the relationship between material design and the presence of (bio)chemical functionalities in 3D-printed devices, which will be

listed in different bio-applications such as biorecognition, biocatalysis, flexible and wearable sensors, and precision medicine. Before, to deepen those aspects, the working principles of the most common 3D printing methods will be presented, describing advantages and limitations. At last, future perspectives of the most novel trends in this advanced field will be discussed.

7.2 Additive Manufacturing (AM) Techniques for Biomedical Applications

On the market, several 3D printing techniques to process polymeric materials are present; nevertheless, those can be classified in three main categories, based on the underlying mechanism: the extrusion-based methods, the powder-based methods, and at last the light-induced methods (i.e., based on photopolymerization) [18–20]. Obviously, every 3D printing process presents its advantages and disadvantages if compared with the others. When a type of printing process is chosen, it must be taken into account the specific application as well as the materials to be used and the resolution requested [21]. Coming back to the specific of the techniques, those are usually defined as follows:

- Extrusion-based methods: AM process in which material is spread by means of a nozzle or a printing head [18].
- Powder-based methods: AM process in which powders are locally softened/melted by a controlled heating [20].
- Photopolymerization (light-induced) methods: AM process in which liquid monomer is rapidly solidified by light irradiation [21].

Each of these categories contains different equipment types, which may differ for construction approaches or material deposition. The most common are summarized in Table 7.1.

In the following paragraphs, the most diffused 3D printing methods used to fabricate objects with built-in (bio)chemical functionalities for biotechnological applications will be briefly introduced.

7.2.1 Additive Manufacturing: Extrusion-Based Methods

7.2.1.1 Fused Filament Fabrication

Fused filament fabrication (FFF) is the most diffused and acknowledged 3D printing method, also commonly known with the name FDM™ (fused deposition modeling), trademarked from Stratasys. At the present, FFF 3D printers are largely present in day-by-day experience, from big industries to houses for DIY modeling. Those 3D printers are employed in a wide range of applications, thanks to the large platelet of

Table 7.1 Categories of additive manufacturing processes, materials, and advantages vs. limitations

Additive manufacturing	Main techniques	Materials	Pro	Cons
Extrusion	Fused filament formation (FFF)	Thermoplastics	Multi-material, versatile, and low cost	Limited resolution Post processing
	Direct ink writing (DIW)	Plastics, food, and living cells	Versatile	Limited resolution
	Bioprinters	Chemical and physical gels and living cells	Specifically designed for bio-applications	Limited resolution
Powder bed	Selective laser sintering (SLS)	Thermoplastics	High mechanical properties No need of supports	Low resolution Limited range of printable materials
Photopolymerization	Stereolithography (SLA) Digital light processing (DLP), Continuous liquid interface polymerization (CLIP) Volume additive manufacturing (VAM)	Photopolymers	High range of printable materials High resolution	Single material
	Two-photon polymerization (TPP)	Photopolymers	Extremely high resolution	Low yield of production Expensive
	Photopolymer jetting (inkjet/Polyjet)	Photopolymers	Simple, multi-material	Limited range of printable materials

commercially available materials, to the large range of printing dimensions, and to their user-friendly and affordability [22]. Nowadays, when one thinks to 3D printing, FFF is the first technique to which the most refers to [23].

Feeding materials for an FFF 3D printer are wires or filaments, which are softened/melted and extruded through a heated nozzle, depositing the material on the build platform accordingly to the STL file. The softened filament solidifies cooling down, allowing the fabrication of the object in a layer-by-layer fashion [18].

Only thermoplastic polymeric materials (i.e., not cross-linked macromolecules) can be available for FFF because they must be softened; both amorphous (e.g., polystyrene, polycarbonate, ABS – acrylonitrile butadiene styrene) and crystalline (e.g., PLA, polylactic acid; PEEK, polyetheretherketone; nylon) materials can be processed [24].

The printing resolution belongs to the dimension of the extruding head, as well as by rheological issues (viscosity, temperature, speed of printing, etc.). Considering the 3D printers now available on the market, the highest declared resolution is about 10 μm, but for most of the equipment, it is about 50 μm. On the other hand, even layer thickness (i.e., slicing of the virtual file) is directly related to the dimension of the extruded filament, so the build rate decreases increasing the resolution, involving a suitable trade-off must [25].

One of the limits of FFF is in the extent of available geometries that could be printed, in particular regarding the hanging parts or large voids. In this case, the fabrication is necessary to use supports, often using a second material, which must be removed afterward with mechanical or chemical approaches.

Regarding the characteristics of the printed objects, interlayer adhesion, which belongs on many factors including the temperature of extrusion, the heat transfer of the material, the temperature of the build platform, and the geometry of the object, can be an issue. Poor adhesion weakens the object, leading to low mechanical properties and possible delamination. At last, the presence of porosity and defects decreases the mechanical performances and ultimately brings to failure [23].

Besides, FFF presents several advantages when compared to other 3D printing techniques. The most exploited one is to print multiple material in the same part (multi-material printing). This is achieved by using multiple nozzles, each one with a different filament: this enables a topological control of the chemical and physical properties of the part [26, 27]. Furthermore, FFF is the most common choice for rapid prototyping and hobby because of the low costs, the ease of use, and the absence of hazardous raw materials. At the present stage, there is an almost infinite range of FFF 3D printers available on the market, which cover a broad range of materials, printing dimensions, and of course prices (from few hundreds of € to hundreds of thousands of € for a single equipment) [28].

7.2.1.2 Direct Ink Writing

Another extrusion-based 3D printing technique is direct ink writing (DIW). Different from FFF, DIW 3D printer extrudes pastes or, in general, viscous liquids,

so materials are already in a liquid form. The viscous inks can be different but typically are constituted of solutions made of polymers in desired solvents (which can be either water or organic solvents), oligomers (i.e., macromolecules with a certain molecular weight) with suitable viscosity, or pastes that contain inorganic fillers bounded with a certain amount of plasticizing macromolecules [29].

A motorized screw and a pressure pump are usually employed to control the extrusion rate, which must be controlled to achieve a uniform extrusion of the paste through the nozzles. Similar to FFF technique, once extruded, the ink is deposited on the build platform, following the relative digital file. In case the extruded material does not have sufficient thixotropic properties to be self-standing and thus to form, layer by layer, the desired object, a rapid change of physical state (i.e., solidification) is used to perform the 3D printing process [30]. Several approaches can be employed; among the most common can be mentioned: rapid solvent evaporation [31], thermal-induced cross-linking [32], chemical-induced cross-linking [33], photo-induced cross-linking [34], and rapid phase transition [35]. There are also other examples since this 3D printing technique is in rapid evolution, for instance, a new DIW approach called "immersion precipitating 3D printing" recently has been introduced. By this method, a polymeric solution is extruded in a non-solvent and rapidly precipitate [36]. This technique allows to produce highly porous polymers, and it demonstrated to be suitable for many polymers in 3D printing.

The main advantages of DIW are its low cost and the compatibility with an extremely wide range of materials, also customizable by the user, together with an extremely flexible approach; also, DIW allows very high resolutions (<10 μm). The main issues in DIW are instead related to the control of the rheological properties of the inks, which is compulsory to obtain homogeneous extrusion and desired precision. Moreover, the rate of solidification must be set according to the printing process, since the fast change of physical state may cause nozzle clogging or bad adhesion between layers, while a slow change can bring to poor mechanical properties and lose of the geometries of the 3D-printed part. At last, operating even with organic solvents, DIW is generally more hazardous than FFF [29].

DIW is used to print different class of materials, not only polymers but also ceramics, colloids, and even wood. In case DIW is applied to soft and biological matter, this technique is known as bioprinting, which will be described more in details in the next paragraph.

7.2.1.3 Bioprinters

Generally speaking, the term "bioprinting" refers to a plethora of laboratory technologies which aims at fabricating biological constructs, primarily to reproduce living tissues [37]. Among the bioprinting equipment, it is worth to mention laser-assisted 3D printers, stereolithography (SLA)-based, pressure-assisted, or droplet-based [38].

This means that bioprinting can be classified in more than one category of the 3D printing techniques (Table 7.1). Nevertheless, the most developed one is the pressure-assisted (extrusion), and the term "bioprinter" is generally used for commercially available equipment able to extrude inks/gels/pastes through a motorized syringe and containing cells. Some of the most diffused commercial brands are EnvisionTEC; Organovo, Inc.; CELLINK; and Rokit Healthcare, Inc.

As all the extrusion-based techniques, bioprinting involves the selective deposition in a layer-by-layer fashion of cyto-compatible materials directly laden with living cells. Extrusion can be pneumatic, piston, or screw-driven, according to the producer. Usually the bioink is a gel, which means that melting or softening is not encompassed in the process even if, according to the equipment employed and to the material specifications, heating or refrigeration can be considered both to the material and on the build plate [39]. Furthermore, even modification of syringes enabled the production of more complex constructs such as embedded printing [40], coaxial printing [41], or in situ cross-linking [42].

Droplet-based bioprinting (DBB) is as well a very common method, even if it could be mostly considered a deposition technique rather than an extrusion-based. In fact, this involves droplet generation and deposition in a continuous or on-demand manner employing a different driving force such as electrical, thermal, or acoustic. Furthermore, DBB allows the printing of proteins or cells encapsulated in droplets, which was also exploited for co-patterning with gel-based scaffold materials. As ink-based technology, DBB is characterized by medium/high resolution (<10 μm in some case) and suitable for high-throughput applications, due to high printing speed. Conversely, the development of real 3D constructs (build on z-axis) is time consuming and not favored [37].

Regarding the printable materials, the primary interest is to print gels able to mimic the extracellular matrix, to aid cells' colonization. Gels can be both natural (e.g., collagen, gelatin, alginate, chitosan) and synthetic (e.g., poly(N-isopropylacrylamide), PEG-based, etc.), or blends of the two [43].

Regarding the applications, as mentioned, the first goal is to embed cells or other biological matter in order to artificially build controlled environments [44]. This can lead to innovative biomedical and pharmaceutical studies, developing artificial organs or tissues, that can be either scaffold-based or scaffold-free, fabricating organ-on-a-chip devices [45], and even reproducing patients' tissues, enabling a new approach to in vivo-like studies [37]. Being specifically developed for bio-matter, bioprinting allows the 3D shape of materials that cannot be processed with other technologies, gathered with the bio-field requirements. The possibility to impart 3D structuration to biomaterial, with controlled morphology, can improve the cell growth remarkably improving the results obtained in conventional bidimensional cell culture [37]. As drawback, the resolution is usually relatively low due to intrinsic material characteristics, and the suitable materials are limited by viscosity and biocompatibility [43].

7.2.2 Additive Manufacturing: Photopolymerization-Based Methods

Photopolymerization-based 3D printing techniques use light as a stimulus enabling the printing mechanism [22]. In fact, all the technologies encompassed in this category use light to produce solid objects through a fast transition from liquid to solid material, by light-induced polymerization mechanism. Many different light curing technologies have been developed and will be described in the following paragraphs [46].

Vat printing techniques are the most diffused light-induced 3D technologies. Again, vat 3D printing includes different methods, but in all of those, the liquid printable photocurable material is placed in a vat during printing procedure; stereolithography (SLA) and digital light processing (DLP) are in this context the two more common technologies. Both are based on the spatially controlled solidification of a liquid resin upon a selective exposure to light, even if performed with different approaches [47]. SLA is historically the first additive manufacturing technology, developed and patented by Charles Hull in the 1980s [48]. In SLA equipment, a laser light source scan point by point the surface of the photocurable resins contained in a vat, inducing controlled photopolymerization and solidification. The process is the repeated layer by layer, moving downward or upward the build platform along the z-axis, according to the printer configuration [22]. DLP is somehow an evolution of SLA. In DLP, the light source (typically a LED centered at 365 nm or 405 nm) illuminates a digital micro-mirror device (DMD), which shine all in one the designed pattern on the bottom of the vat containing the light-sensitive resin. The light source is usually placed below the vat, and in some equipment, the LED/DMD illuminating system is replaced by a LCD screen. In any case, the bottom of the vat must be transparent, and the printing direction is usually bottom-up along the z-axis [22]. A more recent evolution of the DLP technology is the continuous liquid interface polymerization (CLIP) [49] 3D printing, which shortens the printing times exploiting oxygen-induced-free radical polymerization inhibition to avoid the adhesion of the photocured layer to the bottom of the vat. This allows the development of a continuous process in z direction, which is peculiar of this technique. In the latest years, a further light-induced technology named volumetric additive manufacturing (VAM) [50] has been also proposed. Different from the other 3D printing technologies, this technique is not layer by layer but implies the selective light-induced solidification within a contained volume, exploiting the superimposition of patterned optical waves from multiple beams, enabling thus the direct generation of 3D geometries. The best performing light-induced techniques named so far can achieve resolutions at the micrometric scale [22]. Regarding materials in light-based 3D printing, the most common are low molecular weight (meth)acrylate monomers (e.g., polyethylene glycol(meth)acrylate, 1,6-hexanediol diacrylate, bisphenol-A-ethoxylate diacrylate, pentaerythritol tri−/tetra-acrylate). In any case, commercial resins are not detailed mixtures of monomers, formulated to fulfill the desired characteristics together with high printing speed and resolution.

A detailed list of the more commonly used materials can be found in literature [22, 46, 51]. Out of acrylate-based formulations, also thiol-ene/yne and epoxy monomers are employed [24]. To activate the photopolymerization mechanism, the presence of a proper photoinitiator is also necessary, in which range of reactivity should match the wavelength of the 3D printer. Eventually dyes can be also used to improve the printing resolution [22].

On the market, many SLA and DLP equipment are now present, which encompass a large range of dimension and costs, from big industrial 3D printers to cheap desktop ones. While a very important application still remains modeling/hobby and prototyping [52], SLA and DLP equipment are largely used in jewelry [53] and dentistry, due to their high precision and the possibility to create shapes not achievable with other 3D printing technologies [54]. In the academia, they are as well very used, with many reports which span over a broad range of applications such as microfluidics [55], electronics, or sensing [56, 57]. DLP has been used as bioprinting technique, employing an apparatus with light source with low energy coupled with sterilization tools. This demonstrated suitable for the printing of cytocompatible scaffolds embedding living cells [5].

As mentioned, the high resolution that can be achieved is the most important advantage of the light-based techniques, together with the accuracy and the smooth surface obtained. Furthermore, functional molecules or fillers can be easily incorporated in the polymer due to the fact that starting materials are liquid, allowing highly versatility in the development of 3D objects embedding intrinsic functionalities [58]. On the other hand, the main limitation is related to the use of single materials, at least on x-y plane.

7.2.2.1 Two-Photon Polymerization

The 3D printing technology with the highest resolution is two-photon polymerization (TPP), which is based on a nonlinear two-photon absorption process [59]. In TPP, the material reservoir is just a drop of liquid photocurable formulation. Different than other light-induced technologies, here the polymerization mechanism begins when two photons, usually with wavelength in the near-infrared spectrum, are absorbed simultaneously by the photoinitiator, generating the reactive species. This can occur only in a very limited spot (voxel) in which the light source, a femtosecond pulse laser, is focused. This also means that TPP can polymerize the material in any point of the drop, without the need of supports. Out of the focal point, the polymerization does not take place; therefore, the light pass through the material without inducing polymerization. TPP allows to create 3D structures with resolution at the nanometric scale (<100 nm), even if obviously it cannot be used for big object to the prolonged printing times [60]. Also in this case, the materials used are usually (meth)acrylate resins [61].

TPP was proposed for various biological applications such as tissue engineering [62] and medical sensors [63], as well as in other fields such as micromachining or photonics [64, 65]. As mentioned, the main advantage of TPP is the high resolution

that can be reached, while as main drawbacks, there are the very low yield of production and the limitation of the dimensions of the printed objects [61].

7.2.2.2 Photopolymer Jetting

Photopolymer jetting (InkJet/PolyJet) is another light-based technique in which the resin is injected from a printing head to create a two-dimensional pattern. Somehow is like standard inkjet but the drops are thicker and more viscous, enabling a rapid fabrication of a 3D object. After the deposition of every layer, light is provided to solidify the material. Having multiple printing head, it is also easy to fabricate multi-material objects [66].

This technology uses commercial photopolymer resins with precise viscosities. The complex technology required by this equipment leads to nearly complete industrial development, with the most of the marked occupied by Stratasys (PolyJet), which materials are proprietary [67].

With PolyJet, it is possible to produce objects with good resolution with a good variety of commercial materials; nevertheless, the mechanical and functional properties that can be reached are still limited [68, 69].

7.3 3D-Printed Functional Materials for Bio-applications

7.3.1 Biorecognition and Intrinsic Functionality

Biosensors are devices with analytical capabilities that can be used in different applications (i.e., diagnostics, food industry, environmental monitoring) for the specific recognition of different analytes, mostly proteins and small molecules [70]. In this context, 3D printing demonstrated to be effective in the manufacturing biosensing devices, showing several advantages for the fabrication of point-of-care (POC) platforms, devices able to perform testing directly without the support of laboratory equipment [71]. 3D printing has the potentialities to improve the biorecognition and the overall performances (e.g., enhanced sensitivity) when combined with other established recognition techniques, as well as to facilitate the immobilization of the biorecognition elements, as reported in the following.

7.3.1.1 Improved Biorecognition

The synergistic effect of 3D printing together with other techniques may lead to advancements in biotechnological applications, in this case sensing. Gomez and coworkers developed a molecular imprinted polymer (MIP) formulation for TPP [72], selecting N-carbobenzyloxy-L-phenylalanine as model template for the MIP

synthesis. This was done because the fluorescent analogue dansyl-L-phenylalanine is commercially available and allows an easy quantification of the binding properties of the MIP. As a proof of concept, an array of 20 × 60 μm cantilever sensors with embedded MIPs was fabricated (Fig. 7.1a). Incubating the array with the analyte, a reversible shift of the resonant frequency of the sensors was obtained (Fig. 7.1b), enabling the measurement of relative variations of about one order of magnitude more than other commercial micro gravimetric equipment, such as quartz crystal microbalance.

De Middeleer and coworkers used a similar approach to developed 3D-printed solid-phase extraction (SPE) sorbent for mycotoxin analysis [73]. The authors synthesized a MIP using metergoline as a model template for ergot alkaloid recognition and immobilized the artificial receptors on 3D cylindrical poly-ε-caprolactone (PCL) scaffolds, printed by melt extrusion. The functional analysis demonstrated that by employing 3D-printed MIP-based scaffolds, a robust analytical method for multi-mycotoxin testing was developed.

Another system helpful in the recognition of toxins was proposed by Gou et al. In this work, the authors designed a hydrogel matrix embedding functional polydiacetylene nanoparticles, which were exploited both for sensing and detoxification purposes [74]. The functional nanoparticles were synthesized with alkenyl groups on their surface and then chemically immobilized in a 3D poly(ethylene glycol) diacrylate (PEGDA) hydrogel printed using the DLP photopolymerization technique, mimicking a liver structure (Fig. 7.2c, d). After the incubation of this bioinspired device with 50 μg/mL of the toxin dispersed in murine red blood cells, the specific recognition of a pore-forming toxin was demonstrated: thanks to its large specific surface area, the functional 3D hydrogels captured and removed 100% of the toxin, demonstrating thus also a remarkable detoxification efficiency.

Those strategies were not only used to enhance the biorecognition for sensing purposes, but also in separation technology, for instance, chromatography. This technology allows to directly prepare the stationary phase rapidly and without further chemical modifications. In this context, Macdonald et al. reported the fabrication of 3D-printed polymeric thin-layer chromatography (TLC) platforms which were successfully applied for separating various dyes, proteins, and conjugates without any additional surface functionalization [75].

These devices were produced by PolyJet printing employing the commercial resin VeroClear RGD810. With a similar approach, Parker and coworkers reported a 3D-printed microfluidic device incorporating immunoaffinity monoliths for the extraction of preterm birth (PTB) biomarkers [76]. In this case, a glycidyl methacrylate monolith was fabricated in the channel of a 3D-printed device fabricated by stereolithography; the monolith was used as anchoring point for antibodies against the PTB to be detected in human serum matrix. At last, Belka et al. proposed alternative methods for solid-phase extraction of fabricating sorbents with a scabbard-like shape by FFF using LAY-FOMM60, to be used for the analysis of steroids in human plasma [77].

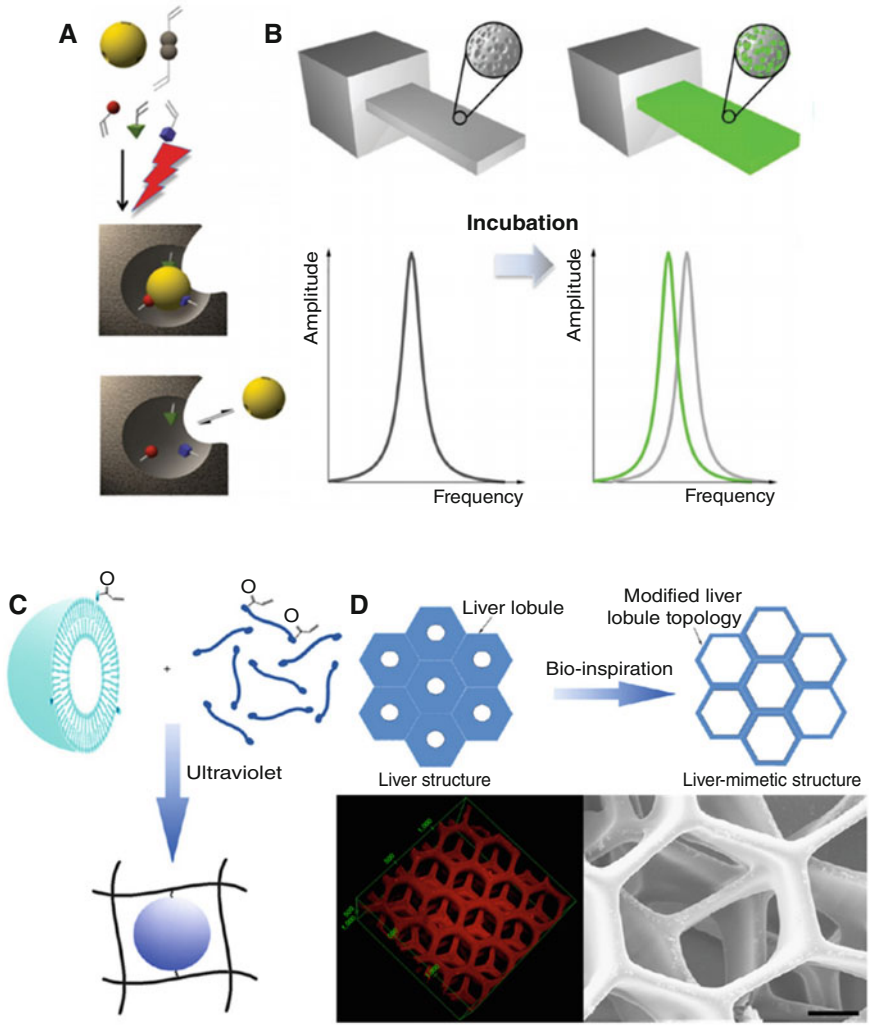

Fig. 7.1 (**a**) Steps of the photo-assisted MIP fabrication. (**b**) MIP cantilever fabricated by TPS and schematics of the sensing principle (Adapted from Ref. [72] with the permission from the Wiley-VCH Verlag). (**c**) Integration of nanoparticles in a photocured PEGDA hydrogel. (**d**) Liver-mimetic microstructure used as detoxifier (top) and its 3D structure measured by laser confocal microscopy and scanning electron microscope (scale bar 50 μm). (Adapted from Ref. [74] with the permission from the Springer Nature)

7.3.1.2 Improved Immobilization

One of the key aspects to successfully obtain a performing sensing layer during the development of biosensors is the controlled and stable immobilization of biorecognition elements [78].

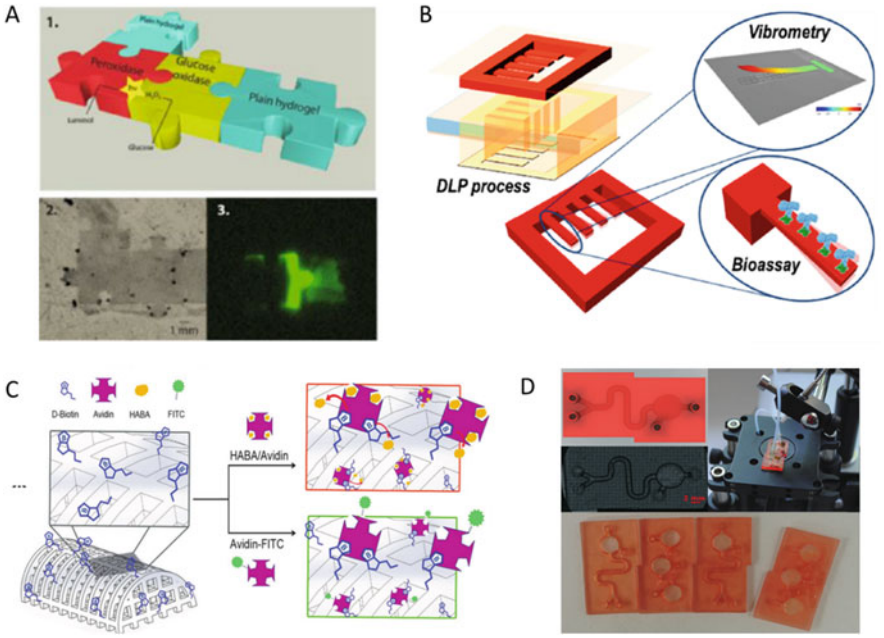

Fig. 7.2 (**a**) Puzzle-shaped 3D-printed PEGDA hydrogels entrapping horseradish peroxidase and glucose oxidase: (1) CAD of the 3D-printed objects and (2) imaging of the printed objects. (3) Chemiluminescent measurements (3 min) in the presence of 100 mM glucose and 220 μM luminol in Veronal buffer 30 mM and KCl 30 mM (Adapted from Ref. [81] Copyright 2016 American Chemical Society). (**b**) Workflow of the fabrication of 3D-printed microcantilever arrays and their vibrational characterization (Adapted from Ref. [82] Copyright 2017 American Chemical Society). (**c**) Schematic of the colorimetric- and fluorescence-based binding assays grafting biotin on 3D-printed microstructures (Reprinted from Ref. [83] with the permission from the WILEY-VCH Verlag). (**d**) CAD, microscope images, and picture of the 3D-printed microfluidic modular LOCs. (Adapted from Ref. [86] with the permission from the Royal Society of Chemistry)

Often, the surface functionalization is the most time-consuming procedure in the fabrication of biosensors [79, 80]; this leads many efforts to the development of 3D-printed objects that could be employed directly or with very limited (bio)chemical modification.

For instance, Mandon and coworkers produced functional 3D-printed objects entrapping biomolecules during the polymerization step [81]. For instance, they chose puzzle shapes as a proof of concept of more complex structures such as a multiplex biosensing layer. The PEGDA-based hydrogel was 3D printed using DLP, fabricating puzzle pieces containing different enzymes (Fig. 7.2a). Once fit together, glucose was used to observe the sequential activity of the two enzymes. Indeed, it was exploited as substrate by the glucose oxidase, producing hydrogen peroxide, which was subsequently used as substrate by the horseradish peroxidase to produce chemiluminescence in the presence of luminol.

Similarly, Stassi et al. fabricated 3D-printed functional microcantilever platform in a one-step process with DLP, which was later used for mass detection [82].

This biosensor was built adding acrylic acid to the bisphenol A ethoxylate diacrylate (BEDA) in a photocurable formulation, introducing a controlled amount of carboxyl groups in the polymeric matrix, which then were exploited as anchoring points for the immobilization of biorecognition elements. The proof of concept was then tested by immunoassays performed on the surface of the microcantilevers (Fig. 7.2b).

Another example of bioactive 3D scaffolds integrated into a monolithic lab-on-chip (LOC) was reported by Credi and coworkers by a stereolithography printing process [83]. In this work, the authors designed a biotin-conjugated UV-curable resin, which was used to produce scaffolds with features smaller than 100 μm and with pore size of 400 μm. HABA (4-hydroxyazobenzene-2-carboxylic acid)/avidin molecules were then employed as a standard biotin binding assay to detect biotin on the surface of the 3D-printed structures. Afterward, the biotinylated scaffolds were integrated in a microfluidic reactor, fluxing the HABA/avidin solution to perform real-time analyses (Fig. 7.2c).

Aronsson and coworkers reported the development of a hybrid peptide-polymer hydrogel, which combines covalent cross-linking with supramolecular interactions, to tune the mechanical properties as well as the biochemical functionalities [84]. The authors used bicyclo[6.1.0]nonyne-modified hyaluronic acid together with an eight-arm PEG bearing terminal azide groups, to take advantage of the click reaction between the alkyne and azide, thus achieving covalent cross-linking. Furthermore, a helix-loop-helix polypeptide able to dimerize into helix bundles was also tethered to the hyaluronic acid backbone: this polypeptide was used to change the cross-linking density and to impart desired mechanical properties to the printed components. At last, biotin conjugation into the polypeptide loop was used to immobilize a streptavidin-AP (alkaline phosphatase), monitoring its activity by using a chromogenic probe.

Intrinsic functionalities embedded in 3D-printed objects were also studied to upgrade well-established techniques, such as enzyme-linked immunosorbent assay (ELISA). This is considered the gold standard for the detection of many analytes, because of its remarkable sensitivity and sensibility [10]. Furthermore, being very versatile (e.g., an antibody can be produced against a wide range of target analytes) and its moderate price, ELISA is often applied in the food analysis to detect traces of contaminants and of pathogens. Conversely, the strict protocol requirements (need for laboratory equipment, protocol optimization related to target analyte, and the use of commercial polystyrene labware) hardly allow to reach the flexibility required to perform analyses outside of clinical or research environments [11].

3D printing technology has been recently investigated to solve these drawbacks, enabling the possibility to implement the ELISA tool in open-field applications. For example, centrifugal microfluidic devices were fabricated using ABS (acrylonitrile butadiene styrene) by PolyJet 3D printing, driven by a mini-centrifuge and employed to perform an ELISA, as reported by Ukita and coworkers [85, 87]. In this study, the colorimetric reaction was evaluated both by means of a

plate reader and a smartphone, showing comparable results. In this framework, Chiadò et al. reported the DLP fabrication of polymeric microfluidic devices, which were then used to detect biomarkers involved in angiogenesis [86]. The authors fabricated modular LOCs with embedded chemical groups which were exploited to immobilize biorecognition elements, thus producing biosensors which implement an immunoassay as detection method. Carboxylic moieties were introduced by adding acrylic acid in three different photocurable monomers that were compared in terms of physicochemical properties and protein grafting capabilities. A formulation with BEDA and 10% wt of acrylic acid was proved to be the best-performing material among all the tested ones, and it was used for the fabrication of a sensing platform composed of a microfluidic channel and an incubation well. The functional polymer was printed only in desired areas, to confine the active material to specific points, increasing the sensitivity and reducing the nonspecific binding on other parts of the LOC (Fig. 7.2d). A sandwich immunoassay and a portable fiber optic spectrometer were used to evaluate the optical density for the detection of vascular endothelial growth factor and angiopoietin-2.

Another kind of sought-after improvement in ELISA-based bioassays is to increase its sensitivity. This was achieved by increasing the available surface area, as demonstrated by Singh and coworkers. They introduced a so-called 3D well, a hollow cylinder-like structure made of ABS fabricated by FFF 3D printing, to study the serological diagnosis of infectious diseases [87, 88]. After the printing process, the surface modification was conducted by chemical etching to show hydrophilic properties, achieving effective protein binding capability, which resulted in higher sensitivity than standard 96-well ELISA toward rubella virus and measles virus (2.25- and 3-folds, respectively).

7.3.1.3 Improved Functionality

The use of composite and nanocomposite materials has always been one common strategy to improve the objects' properties. This can also be applied to the 3D printing field [21] where the addition of fillers into the printable matrices has led to the production of three-dimensional objects with enhanced electrical [89], mechanical [90], or functional [7, 91, 92] properties.

The use of conductive fillers in polymeric matrices (e.g., graphene/PLA or graphene/ABS) has been proposed for the production of 3D-printed electrochemical biosensors [93]. In these devices, oxidoreductase enzymes, coupled with conductive electrodes, are able to transduce the biochemical interactions into a readable electronic signal [94].

Graphene-PLA composite filaments were used to print, by means of an FFF equipment, 3D working electrodes of an amperometric biosensor for glucose monitoring in blood plasma using glucose oxidase (GOx) and ferrocene-carboxylic acid as a mediator [95], with a simultaneous determination of uric acid and nitrite. In this case, the COOH groups exposed on the surface of the 3D-printed graphene-PLA were used to immobilize the GOx enzyme that was then cross-linked with

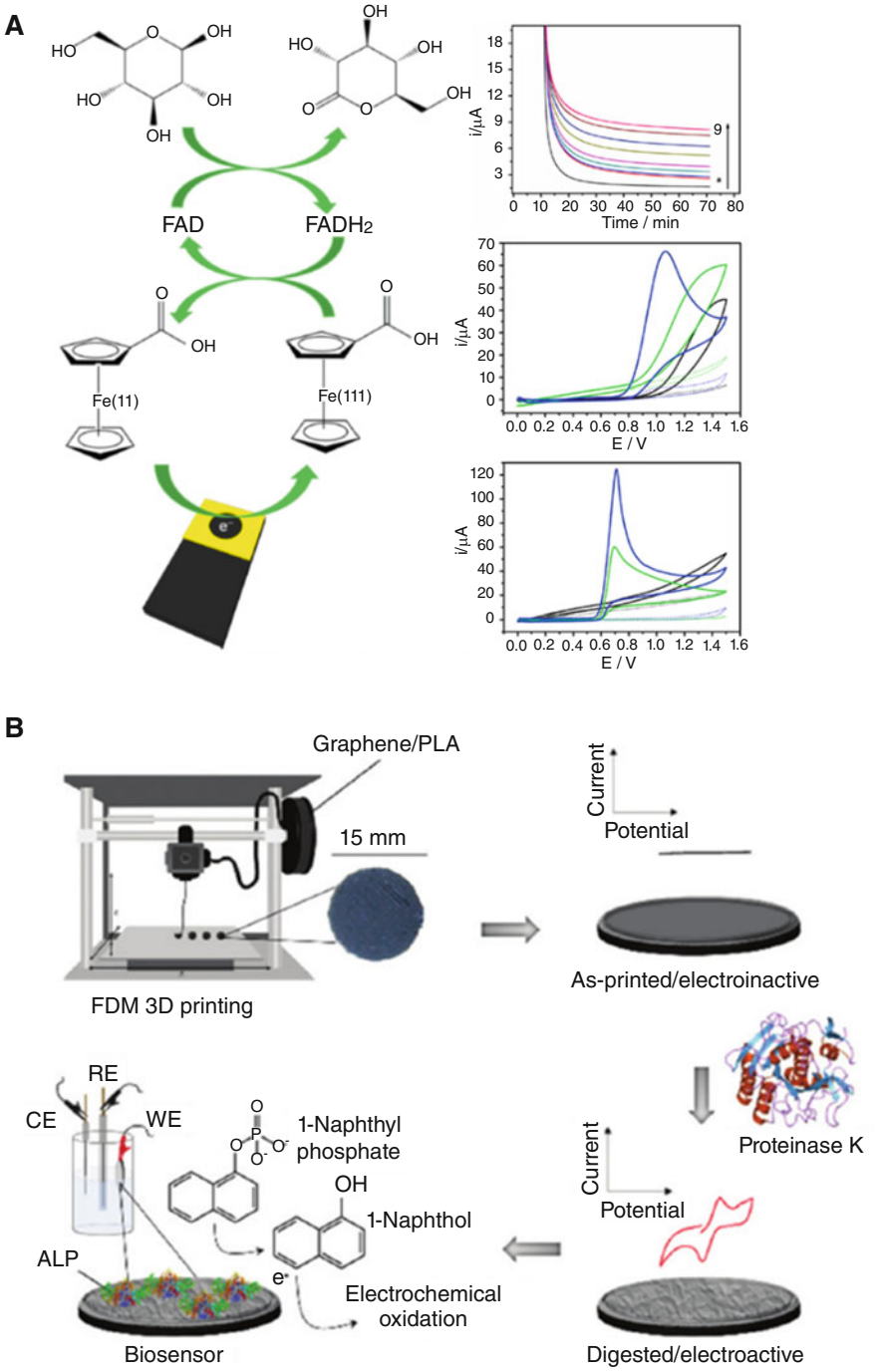

Fig. 7.3 (continued)

glutaraldehyde (Fig. 7.3a). The reported results showed a satisfactory detection of glucose at levels commonly found in blood samples: the chronoamperometric measurements gave a linear response for increasing concentrations of glucose with a limit of detection (LOD) of 15 μmol/L and LODs of 0.02 and 0.03 μmol/L for uric acid and nitrite, respectively.

3D-printed graphene-PLA electrodes were also proposed by Manzanares-Palenzuela et al. for the detection of 1-naphthol in contaminated wastewaters by cyclic voltammetry (CV) [96]. The device exploited the controlled degradation of PLA by using proteinase K, to activate the surface and achieve the controlled patterning of the 3D-printed surfaces to be used as working electrodes. Indeed, the as-printed surfaces are electrochemically irresponsive toward the ferro−/ferricyanide redox pair, whereas the proteinase K-mediated PLA hydrolysis exposes the embedded electroactive graphene and enhances the overall conductivity of the 3D-printed material and switches on the biosensors. On this activated surface, alkaline phosphatase was immobilized by adsorption to detect 1-naphthyl phosphate in solution (Fig. 7.3b). More recently, a new biosensor exploiting 3D-printed electrodes made of graphene-PLA was proposed by the same group [97].

This work described a 3D-printed electrochemical enzyme-based biosensor with a third-generation scheme of detection. The sensor did not need mediators because of the fast electron transfer between the redox enzyme and the electrode. The graphene-PLA 3D-printed electrodes were immersed in dimethylformamide or underwent the application of a constant potential to be electrochemically activated to enhance their conductivity. Two different configurations were evaluated for the detection of hydrogen peroxide: in one case, horseradish peroxidase (HRP) was directly immobilized onto the electrode surface, and in the second case, HRP was immobilized on the surface of the electrode previously decorated with gold nanoparticles. Both the configurations gave promising results from chronoamperometric measurements at different H_2O_2 concentrations with a LOD of 11.1 μM and 9.1 μM.

Fig. 7.3 (continued) (**a**) Scheme of the two steps of redox reactions exploited by the graphene-PLA composite biosensor to convert glucose into gluconolactone by using glucose oxidase and ferrocene-carboxylic acid. Insets: amperometric measurements of glucose (0–6.3 mmol/L) (top), cyclic voltammograms for 1.0 mmol/L uric acid (middle), and 1.0 mmol/L nitrite (bottom) recorded on the "as-printed" G-PLA electrode (black), after mechanical polishing (green) and solvent-treated after polishing (blue). Dashed lines correspond to the respective blanks (Reprinted from Ref. [95] with the permission from the WILEY-VCH Verlag). (**b**) Workflow of the fabrication steps of a 3D-printed graphene-PLA biosensor fabrication: the electrode is printed by FDM, and then the proteinase K-mediated PLA hydrolysis activates the surface, by exposing the electroactive graphene, because the as-printed electrodes are electrochemically irresponsive toward the ferro/ferricyanide redox pair. The immobilization of alkaline phosphatase allows the 1-naphthyl phosphate detection. (Reprinted from Ref. [96] with the permission from the Royal Society of Chemistry)

7.3.2 Flexible-Wearable Biosensors

A good part of the actually produced bioanalytical devices could envisage a great improvement if transformed into flexible-wearable electrochemical biosensor [98]. Above all, when applications in small metabolite monitoring are considered (e.g., glucose, lactose, or choline), medical devices using noninvasive approaches are requested. The possibility to make them wearable would represent a step forward in their development. To make this possible, the first requirement is flexibility that nowadays can be obtained by using smart textiles and stretchable electronics [99], often obtained by 3D printing with the subsequent addition of CNTs (carbon nanotubes), graphene, or metal nanoparticles [87].

The most suitable 3D printing technology to produce flexible electrodes and devices is DIW; this technique allows the design and patterning of highly precise enzyme-based POC (point-of-care) systems presenting uniform surface and few defects [100].

One example of DIW-printed flexible sensor was proposed by Dong and coworkers [101]. They produced a flexible amperometric lactate sensor based on a three-electrode configuration. A silver nanoparticle-based ink was extruded via DIW on a flexible polyethylene terephthalate (PET) substrate. A sulfonated fluoropolymer-copolymer, Nafion, was coated on the working electrode followed by the immobilization of the enzyme lactate oxidase. An oxidation peak at 0.25 V was revealed by CV (capacitance-voltage) measurements conducted at different lactate concentrations, and the amperometric biosensor gave a linear response as the lactate concentration increased from 0 to 15 mM.

Another example was given by Nesaei et al. that produced a flexible glucose biosensor [102]. A commercial carbon ink was modified with Prussian blue as electron transfer mediator, and in parallel, a GOx enzyme solution combined with tetraethoxysilane and hydroxypropyl cellulose to obtain a sol-gel printable ink was prepared. Both inks were 3D printed using DIW method (Fig. 7.4a). The chronoamperometric data revealed a linear oxidation current in the range of glucose concentration between 100 and 1000 mM; it was estimated a sensitivity of 17.5 nA/mM and a LOD of 6.9 mM.

Pu and colleagues used a rotating inkjet printing apparatus to obtain a micropatterning on a nonplanar surface to produce an implantable flexible enzyme-electrode sensor for continuous glucose monitoring [103]. A polyether ether ketone (PEEK) cylinder modified with silane agents was used as depositing substrate; a silver ink was used for the deposition of the counter and reference electrodes, while the working electrode was produced with a 3D multilayered nanostructure alternating the deposition of different inks containing gold nanoparticles, reduced graphene oxide (rGO), and Pt nanoparticles (PtNPs). The GOx enzyme was then printed onto the working electrode and covered by drop casting with Nafion to improve its biocompatibility and stability. The biosensor resulted capable to detect concentrations of glucose up to 570 mg/dL; this value results suitable for the detection in physiological conditions.

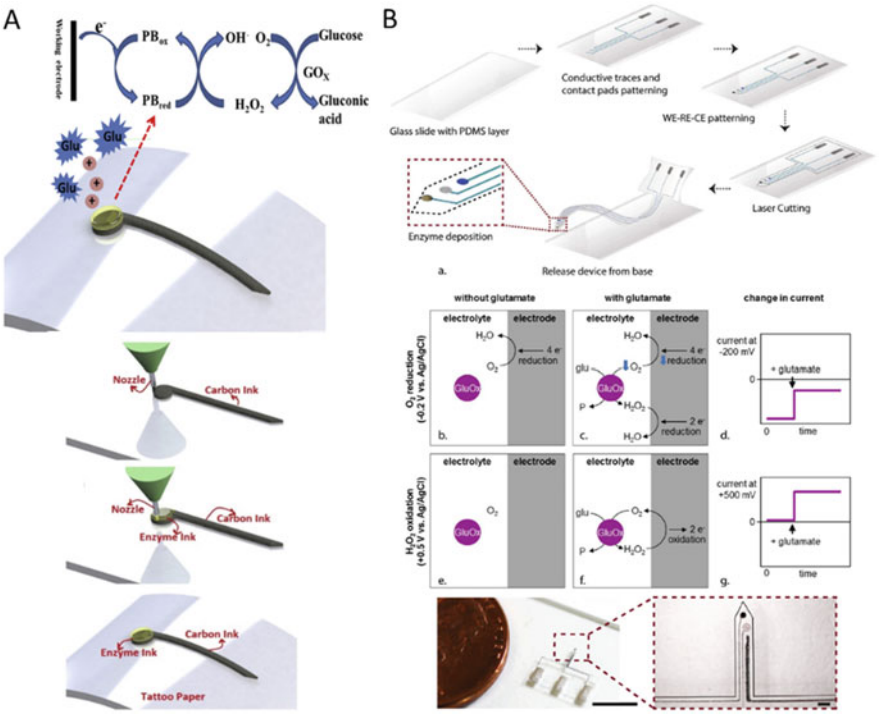

Fig. 7.4 (**a**) Workflow of the fabrication of the printed electrode by using a direct ink writing and an enzyme as printing materials on a flexible substrate (top); working principle of glucose sensing (Reprinted from Ref. [102] with the permission from the Elsevier B.V.) (**b**) Fabrication process of the PtNP-nanocomposite-based glutamate biosensor on a PDMS (polydimethylsiloxane) substrate (top); working principle of the biosensor (middle); picture of the micro-glutamate biosensor on PDMS substrate (scale bars: 5 mm and 200 μm). (Reprinted from Ref. [104] with the permission from the Elsevier B.V.)

An implantable amperometric biosensor for the evaluation of glutamate release from the spinal cord of a rat was also proposed in literature exploiting a similar approach [104].

A flexible silicone rubber (Ecoflex™) was mixed to conductive poly(3,4-ethylenedioxythiophene) polystyrene sulfonate (PEDOT:PSS), multiwalled carbon nanotubes, and platinum NPs for the production of the printable ink that was deposited by DIW on a flexible polymer substrate. Glutamate oxidase (GluOx) was used as sensing enzyme and immobilized on the electrodes with glutaraldehyde. This enzyme consumes O_2 to generate H_2O_2 that can be used for the amperometric evaluation of glutamate concentrations (Fig. 7.4b). It was observed that imposing a potential of 0.5 V vs. Ag/AgCl reference electrode, H_2O_2 is oxidized by the PtNPs, generating a current proportional to the concentration of glutamate, while at −0.2 V, the O_2 is reduced, generating a cathodic current that decreases when the enzyme consumes the oxygen in the presence of glutamate. Also, this system showed a

linear response in the range of 1–800 μM and a LOD of 0.5 μM when operated at 0.5 V and between 10 and 600 μM with a LOD of 0.2 μM when operated at −0.2 V.

The large number of printable biocompatible (nano)composites proposed for the production of scaffolds for tissue engineering and regenerative medicine [4] has opened the possibility to merge their properties with the versatility of the DIW technique leading to the production of flexible biosensors applied to the monitoring of cell culture metabolites. One example was given by Nolan et al. that produced a flexible biosensor array for the simultaneous monitoring of glucose, lactate, and glutamate from human astrocytes [105]. The active ink for the electrodes was formulated using PEDOT:PSS (poly(3,4-ethylenedioxythiophene) polystyrene sulfonate), silicone, activated carbon, and Pt microparticles. The immobilized enzymes glucose, lactate, and glutamate oxidases made the biosensor array selective toward the analytes of interest from astrocyte cultures at 37 °C. It was also demonstrated that the biosensor array can be printed onto different substrates such as cell culture plates, sheets of flexible laminates, and glass slides. Neuronal electrophysiology was also studied using a flexible biosensor exploiting a biocompatible graphene-based platform by Guo and coworkers [34]. The graphene ink was ink-jetted on a Kapton substrate where N27 neurons were cultured; the biocompatibility was assessed as cell survival after 72 h (85%).

7.3.3 Biocatalysis

In the previous sections, the different applications of enzyme-based biosensors and wearable electronics have been discussed. Enzyme-based devices demonstrated considerable capability in monitoring specific biomarkers in body fluids (e.g., sweat, saliva, tears, etc.) and in revealing environmental pollutants [106–109].

In the following paragraphs, biocatalytical devices will be discussed discerning pure enzymatical systems from bioreactors used for energy harvesting or for fine chemical synthesis.

7.3.3.1 Enzyme-Based Systems

Enzymes present catalytic activity and selectivity that can also be exploited for the development of analytical 3D-printed devices for biocatalysis. As it will be explained in the following paragraph, enzymes have been directly embedded in the printable material or immobilized on confined parts of the 3D-printed structures. Both strategies present some advantages and drawbacks.

Biosensors were built by 3D printing hydrogels embedding enzymes to obtain bioactive constructs with biomimetic capabilities [110]. PEGDA hydrogels were printed in the presence of alkaline phosphatase and thrombin as enzymes; AP catalyzes the formation and precipitation of calcium phosphate while thrombin

the formation of fibrin. The two enzymes co-immobilized into a bioinspired 3D object (mimicking bone tissue) led first to the calcification of the structure and subsequently to the covering of this last with a fibrin network, also able to entangle living cells. Despite the easiness and rapidity of the process, one of the main drawbacks of the direct incorporation of the enzymes in the printable materials are the preservation of the catalytic activity and the low long-term stability of the biomolecules.

Different studies were conducted, aiming to overcome these problems. One example is the work developed at the Karlsruhe Institute of Technology [111] where the stability problem was faced by testing different viscosity-enhancing additives. Polyxanthan, hectorite, and silica nanoparticles were tested to obtain stable PEGDA-based formulation embedding β-galactosidase (β-Gal). While polyxanthan and hectorite did not allow the formation of a mechanically stable 3D object, silica NPs allowed the production of good structures; nevertheless, the enzyme activity resulted to be only 10% compared to the free enzyme in solution, due to mass transfer limitations.

As an alternative, Wegner et al. [112] proposed a water-in-oil internal phase emulsion (HIPE)-encapsulating β-Gal as bioink for the 3D printing of scaffolds containing enzyme-loaded hydrogels. In this case, the new material showed a remarkable printability, with the possibility to print complex 3D geometries without the need of support structures. Also, the activity assays were performed on 3D-printed cylindrical-shaped constructs, evaluating the conversion of 2-nitrophenyl β-D-galactopyranoside (ONPG) to 2-nitrophenol (ONP) by spectrophotometry.

Original solutions were also reported trying to arrange low-cost and user-friendly apparatus, able to allow the 3D printing of enzyme-encapsulating materials for the realization of automated high-throughput screenings. As an example, Radtke et al. [113] implemented a common FFF printer for the encapsulation of active enzyme into hydrogels. As a proof of concept, PEGDA-based hydrogels, containing β-Gal, were again tested. In this case, a "mold-and-fill" procedure was followed in which a sacrificial ink was firstly used for the printing of hollow cylinders in a 48-wells plate, and then the space between the well rim and the printed cylinder was filled with liquid precursor of the PEGDA hydrogel containing β-Gal that was subsequently polymerized using a UV diode. The sacrificial structures could then be washed away at low temperature to obtain hollow structures with a height of 8 mm and a thickness of 1.6 mm. The catalytic activity of the enzyme was evaluated at different pH values by monitoring the formation of ONP from the substrate with a spectrophotometer.

A different flow bioreactor for the in vivo monitoring of glucose and lactate in the extracellular compartment of the rat brain was also printed by FFF by Su and colleagues [114]. An ABS flow reactor with two parallel reaction chambers, presenting a specific design aimed at enhancing the mixing effect and increasing the surface area, was built (Fig. 7.5a). The GOx enzyme was then immobilized onto the exposed surface in the inner part of the chambers, after its activation with glutaraldehyde; in the meantime, lactate oxidase was directly immobilized without the need for further modifications, thanks to the hydrophobic interactions with the styrene moieties of the ABS structure. The bioreactor was connected to a micro

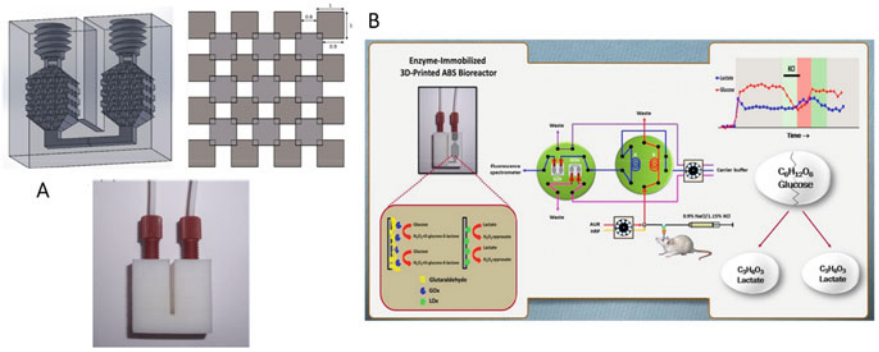

Fig. 7.5 (**a**) CAD drawings of the flow reactor, next to a layer of ordered cuboids in the reaction chamber. Below is a photograph of the printed reactor. (**b**) Scheme of the system for in vivo monitoring of the concentrations of rat brain's extracellular glucose and lactate. (Adapted from Ref. [114] Copyright 2016 American Chemical Society)

dialysis sampling probe and a spectrofluorometer. Aiming to evaluate the presence of glucose and lactate, the extracellular rat brain micro dialysate was mixed with HRP- and a H_2O_2-sensitive fluorogenic substrate. In this way, during the flux, HRP could recognize the H_2O_2 generated by the oxidation of glucose/lactate giving a fluorescence signal, thanks to its catalytic activity. The LOD of this detection system was assessed at 60 μM for glucose and 59 μM for lactate (Fig. 7.5b).

7.3.3.2 3D-Printed Bioreactors

Among the possible evolutions of 3D-printed materials embedding biocatalyst, the development of continuous-flow bioreactors for chemical synthesis or energy harvesting can surely be foreseen. The integration of enzymes that can provide high regio- and stereoselectivity, coupled with the enhanced 3D design, can become a point of innovation [115].

For this purpose, the deep understanding of the enzymes' behavior, including kinetics, stability, and immobilization strategies, is mandatory for the correct development of performing devices that can operate in continuous processes [116].

Starting with energy bio-applications, in most of the proposed case studies, the researchers proceed with the design and printing of the device with a subsequent functionalization and immobilization with the desired enzyme to obtain the required functionality. One example is the work proposed by Rewatkar and Goel. Here the researchers developed enzymatic biofuel cells (BFC) using a dual-extruder FFF 3D printer [117]. The BFC was designed as a Y-shaped microfluidic device in which the microchannels were produced with a simple PLA filament, while the electrodes were built from a conductive graphene/PLA composite (Fig. 7.5a). The graphene/PLA electrodes underwent an activation procedure in DMF [93] and were then modified by the immobilization of two enzymes: GOx was used on

the bioanode, while laccase was chosen for the biocathode. The performed tests revealed that the device presented an open circuit potential of 0.425 V and maximum peak power density of 4.15 $\mu W/cm^2$ at a current density of 13.36 $\mu A/cm^2$.

3D printing technology can also allow the design of reactors in which separated reactions can take place building up sequences of multistep biocatalytic reactions assuring the best reaction conditions for each step and avoiding unwanted side reactions or product inhibition.

Maier et al. produced 3D flow-reactor cartridges [118] by the FFF 3D printing of agarose-based enzyme-integrated hydrogels. As explained in the previous paragraphs, FFF requires relatively high processing temperatures to allow the deposition of the filament and the adhesion between layers; this can result problematic when enzymes must be embedded into the filament. For this reason, thermostable enzymes were chosen by Maier and coworkers, or other enzymes were modified by protein engineering methods to make them stable at the needed temperature. Firstly, agarose bioinks were prepared embedding an esterase (EstII) or an alcohol dehydrogenase (ADH) from the thermophilic microorganism *Alicyclobacillus acidocaldarius*; this ink was used to produce different structures. As proof of concept, the catalytic activity of the embedded enzymes was tested following two processes: in one case, the EstII activity was followed by immersing the loaded hydrogel in a solution containing 5(6)-carboxyfluorescein dihexyl ester as fluorogenic substrate and monitoring its de-esterification; in the meanwhile, ADH activity was assessed evaluating the catalyzed reduction of isobutyraldehyde to yield isobutanol.

The results showed that the catalytic activity of the two enzymes was not damaged by the deposition procedure that took place at 60 °C. As further step, a different enzyme, ketoisovalerate decarboxylase (KIVD) from the mesophilic organism *Lactococcus lactis*, was also modified by computational methods, random mutagenesis, and screening of a clone library to obtain thermostable variant suitable for the application in FFF printing. The selected mutation of the enzyme was embedded into the cartridge of a flow reactor aiming to get the ketoisovalerate conversion into isobutyraldehyde.

Exploiting the same concept, a 3D-printed enzyme-loaded agarose hydrogel was used to build part of a modular flow reactor for the production of a chemoenzymatic reaction cascade [119].

Phenacrylate decarboxylase from *Enterobacter* sp. was chosen as enzyme for the first reaction step of the reactor to catalyze the formation of 4-vinylphenol from *p*-coumaric acid; subsequently, a palladium-catalyzed Heck reaction promoted the coupling with iodobenzene for the formation of 4-hydroxystilbene showing the possibility to obtain cascade reactions. Despite the intriguing approach, the total yield of the reaction was relatively low (15%) (Fig. 7.6b).

A step further in the production of multi-reaction flow bioreactor is represented by the possibility of combining different enzymes in sequential reaction chambers, obtaining a real cascade bioreactor. This was reported by Franzreb group [120]. A reactor chamber (13×13 mm^2) was firstly built by PolyJet 3D printing using a polypropylene photopolymer and loaded with PEGDA-based hydrogels embedding three different enzymes that were printed with an extrusion-based machine (Fig.

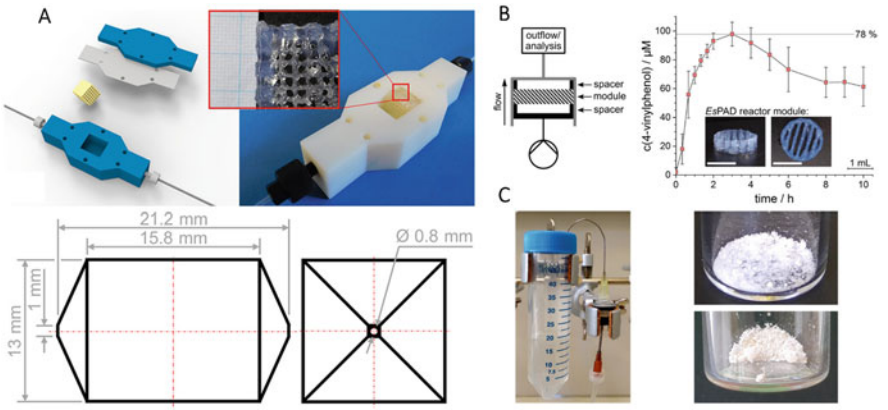

Fig. 7.6 (**a**) Reactor assembly, where the hydrogel structure is inserted in the reactor housing with connection to the fluidic system (Adapted from Ref. [120]). (**b**) Schematic setup of the flow reactor for flow experiments with one reactor module, next to a conversion of p-coumaric acid in a biocatalytic flow setup (Inset: 3D-printed reactor modules prior to assembly into the reactor). (**c**) Flow reactor setup of one out of four parallel reactors to produce 4-vinylphenol. The flow reactor next to the 50 mL collection tube is perfused with substrate solution by a syringe pump. On the right, the purified 4-vinylphenol (top) and, after subsequent Heck coupling, the purified 4-hydroxystilbene (bottom) are obtained as white crystals. (Adapted from Ref. [119] with the permission from the John Wiley and Sons)

7.6a). β-Galactosidase from *Aspergillus oryzae* (β-Gal), benzoylformate decarboxylase from *Pseudomonas putida* (BFD), and ADH from *Lactobacillus brevis* were chosen as enzymes. The first one allowed the selective hydrolysis of 2-nitrophenyl-β-D-galactopyranoside to 2-nitrophenol and galactose, while BFD and ADH were combined in a two-step reaction: firstly, BFD catalyzed the production of the intermediate (S)-2-hydroxy-1-phenyl-propanone by the carboligation of benzaldehyde and acetaldehyde; and then, the intermediate was further reduced to the product (1S,2S)-1-phenylpropane-1,2-diol by ADH. Finally, ADH was used for the enantioselective reduction of acetophenone to (R)-phenylethanol.

7.3.4 Precision Medicine

Patient-centered healthcare will represent the future of medicine, and for this reason, it has caught the attention of researcher operating in different biomedical sectors. Indeed, the possibility to provide customized treatments based on biological, physical, and medical differences of each individual is a challenging task that will greatly improve the success of medical treatments [121]; among the different possibilities, the patient-designed optimization of the dosage of a drug or medication has recently been considered. In this frame, 3D printing has been proposed for

the fabrication of tablets with customized dosage, multiple active pharmaceutical ingredients, and release profile [122].

7.3.4.1 Smart Tablets

Enteric, coated tablets were produced exploiting a dual-nozzle single step FFF 3D printing process [123]. The smart tablets were designed with a core-shell structure where the outer part, gastric-resistant, was produced with a methacrylic acid copolymer, presenting pH-dependent properties, while the inner structure was made of polyvinylpyrrolidone, using theophylline as a model drug. Budesonide and sodium diclofenac were also tested as drugs embedded in the core part, displaying a pH-sensitive drug release rate (Fig. 7.7a).

Fully customizable 3D-printed drug tablets were also proposed by Tan et al. [124]. Disc- and capsule-shaped tablets were produced using an extrusion-based 3D printer; the tables consisted of two surface-deteriorating matrices, one of those was incorporating the drug.

A biodegradable coating was deposited on the surface of the tablet excluding one side that was then directly exposed to the surrounding medium when in use. In this way, a precise control of the drug release profile over time could be achieved. The free surface, not loaded with the drug, was printed with different shaped cavities and used as a mold for the deposition of the drug-loaded matrix in order to provide a specifically designed release profile to the tablet. Paracetamol, phenylephrine hydrochloride, and diphenhydramine hydrochloride were tested as drugs demonstrating the possibility to achieve controlled release profiles. In the end, the customized and simultaneous release of two drugs, each with its own unique release profile, was also demonstrated (Fig. 7.7b).

Smart tablets have also been engineered aiming to achieve a better control over opioid abuse. Ong and coworkers fabricated tramadol tablets with alcohol-resistant and abuse-deterrent properties by direct powder extrusion 3D printing [125]. Hydroxypropyl cellulose was mixed with D-mannitol used as plasticizer, and tramadol hydrochloride was chosen as the active ingredient; polyethylene oxide was then added to the printable formulation as abuse-deterrent agent. The printed tablets demonstrated an abusive limitation potential of 13% when used with an intravenous route and of 70% with a nasal route, without alterations of the release profile in the presence of alcohol.

7.4 Conclusion

To summarize, in this chapter, the recent advances concerning 3D-printed devices with built-in (bio)chemical functionalities have been described, with particular emphasis on those exploitable to produce bioassay or enzyme-based objects for biotechnological applications. New potentials have been so demonstrated in several

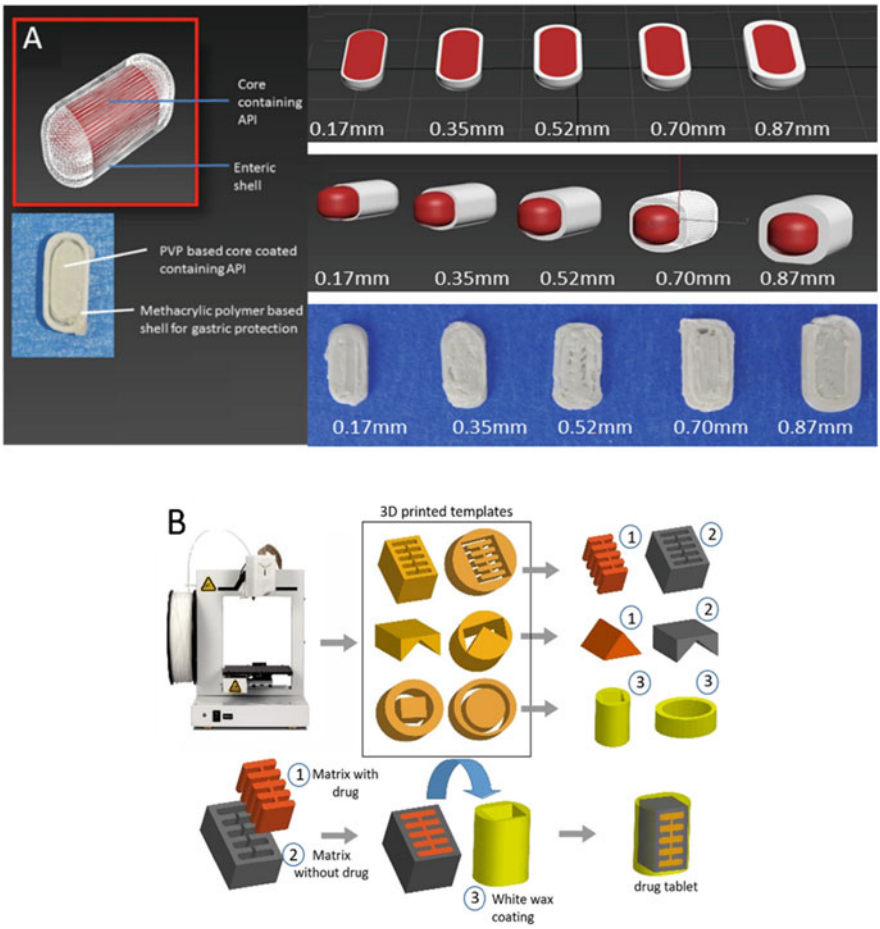

Fig. 7.7 (**a**) Schematic of shell-core designs with increasing shell thicknesses (0.17, 0.35, 0.52, 0.70, and 0.87 mm) and images of 30% completed shell-core designs with theophylline core and increasing shell thickness (Adapted from Ref. [123] with the permission from the Springer Nature). (**b**) Schematic of fabrication of the fully customizable drug tablet via 3D printing. (1) The matrix that contains the drug, (2) the matrix that does not contain the drug, and (3) the outer coating of white wax. Below is the process of fabricating the components via the molds and assembling the individual components into the drug tablet. (Reprinted from Ref. [124] with the permission from the Elsevier B.V.)

bio-application fields, such as biosensing or catalysis even in view of a broader implementation of precision medicine. The combination of functional materials with 3D printing generates different advantages, such as the rapid and versatile fabrication of items with fine-tuned materials, whose functionalities are designed taking in consideration the final use. This is mostly true in the development of bioanalytical LOC, which involve a careful blend of material and microfluidic design, trying to

improve recognition, immobilization, and stability of the biosensing elements. For instance, concerning immobilization, the entrapment of biological molecules in the whole polymeric matrix, or in selected parts of the object, can be obtained without any complex process, thanks to the layer-by-layer process.

In a nutshell, the structural and functional design of new devices is then expanded by the integration of both approaches, considering the benefits those techniques can offer when employed separately. Moreover, this strategy can be helpful also to improve the performance of routine methods in research laboratories, as reported for the well-known ELISA test. Nevertheless, even if different advantages can be listed out, some important challenges need to be resolved [126].

First of all, the physical and chemical properties of the materials should match with the printing mechanism. Therefore, a lot of work should be addressed to enhance the printability of materials containing the biomolecules responsible for the biochemical functionality of the object. Catalytical or biorecognition properties should be retained. At the same time, stability and processability should be preserved as well. Photopolymerization- or extrusion-based 3D printers, among the most exploited techniques, need harsh conditions such as high temperature or generate radical species, which are poorly compatible with the presence of antibodies, enzymes, nucleic acid probes, etc. Therefore, an effort to enhance the biocompatibility is awaited, in terms of stability (e.g., retained biological activity), or to cut mass transfer limitations off and keep the functions of the biomolecules. It must be noted that these aspects involve both the development of materials (e.g., novel photoinitiators) and biomolecule engineering (e.g., thermostability).

A secondary point is that on the market, there are specifically designed 3D printers for bio-application, the so-called bioprinter, but these are still costly and not intended for assembly production. In this view, any attempt such as the biomaker [113] reported above is welcomed.

At the same time, a further development can entail the combination of different 3D printing techniques in the same machine. Indeed, each technique shows its pros and cons. Then, the merging of various strategies may lead to multi-material objects with complexity tailored according to the final use. In this framework, well-established nanomaterials, already exploited in the conventional fabrication of bioanalytical devices, such as quantum dots or photonic crystals, have been only recently joined with 3D printing, giving rise to brand new technologies [127–129], or are still waiting for their integration with additive manufacturing. Finally, 3D printing offers the opportunity to get insights from the interaction between biology and material science, so that synergistic improvements are expected to foster fast and relevant unexplored advances in bio-applications.

References

1. N. Shahrubudin, T.C. Lee, R. Ramlan, An overview on 3D printing technology: Technological, materials, and applications. Procedia Manuf. **35**, 1286–1296 (2019). https://doi.org/10.1016/j.promfg.2019.06.089

2. Q. Yan, H. Dong, J. Su, J. Han, B. Song, Q. Wei, Y. Shi, A review of 3D printing technology for medical applications. Engineering **4**, 729–742 (2018). https://doi.org/10.1016/j.eng.2018.07.021
3. D.A. Kai, E.P. de Lima, M.W. Machado Cunico, S.E.G. da Costa, Additive manufacturing: A new paradigm for manufacturing. Proc. 2016 Ind. Syst. Eng. Res. Conf. ISERC **2016**, 452–457 (2016)
4. M. Hassan, K. Dave, R. Chandrawati, F. Dehghani, V.G. Gomes, 3D printing of biopolymer nanocomposites for tissue engineering: Nanomaterials, processing and structure-function relation. Eur. Polym. J. **121**, 109340 (2019). https://doi.org/10.1016/j.eurpolymj.2019.109340
5. X. Kuang, D.J. Roach, J. Wu, C.M. Hamel, Z. Ding, T. Wang, M.L. Dunn, H.J. Qi, Advances in 4D printing: Materials and applications. Adv. Funct. Mater. **29**, 1–23 (2019). https://doi.org/10.1002/adfm.201805290
6. C.A. Mandon, L.J. Blum, C.A. Marquette, Adding biomolecular recognition capability to 3D printed objects: 4D printing. Procedia Technol. **27**, 1–2 (2017). https://doi.org/10.1016/j.protcy.2017.04.001
7. S. Lantean, G. Barrera, C.F. Pirri, P. Tiberto, M. Sangermano, I. Roppolo, G. Rizza, 3D printing of magnetoresponsive polymeric materials with tunable mechanical and magnetic properties by digital light processing. Adv. Mater. Technol. **4**, 1–10 (2019). https://doi.org/10.1002/admt.201900505
8. S. Joshi, K.C.K. Rawat, V. Rajamohan, A.T. Mathew, K. Koziol, V. Kumar Thakur, A.S.S. Balan, 4D printing of materials for the future: Opportunities and challenges. Appl. Mater. Today **18**, 100490 (2020). https://doi.org/10.1016/j.apmt.2019.100490
9. M. Nadgorny, A. Ameli, Functional polymers and nanocomposites for 3D printing of smart structures and devices. ACS Appl. Mater. Interfaces **10**, 17489–17507 (2018). https://doi.org/10.1021/acsami.8b01786
10. H.N. Chan, M.J.A. Tan, H. Wu, Point-of-care testing: Applications of 3D printing. Lab Chip **17**, 2713–2739 (2017). https://doi.org/10.1039/c7lc00397h
11. C.K. Dixit, K. Kadimisetty, J. Rusling, 3D-printed miniaturized fluidic tools in chemistry and biology. TrAC – Trends Anal. Chem. **106**, 37–52 (2018). https://doi.org/10.1016/j.trac.2018.06.013
12. T. Han, S. Kundu, A. Nag, Y. Xu, 3D printed sensors for biomedical applications: A review. Sensors (Switzerland) **19** (2019). https://doi.org/10.3390/s19071706
13. J.F. Rusling, Developing microfluidic sensing devices using 3D printing. ACS Sensors **3**, 522–526 (2018). https://doi.org/10.1021/acssensors.8b00079
14. E. Dogan, A. Bhusal, B. Cecen, A.K. Miri, 3D printing metamaterials towards tissue engineering. Appl. Mater. Today **20** (2020). https://doi.org/10.1016/j.apmt.2020.100752
15. T. Genova, I. Roato, M. Carossa, C. Motta, D. Cavagnetto, F. Mussano, Advances on bone substitutes through 3d bioprinting. Int. J. Mol. Sci. **21**, 1–28 (2020). https://doi.org/10.3390/ijms21197012
16. J. He, B. Zhang, Z. Li, M. Mao, J. Li, K. Han, D. Li, High-resolution electrohydrodynamic bioprinting: A new biofabrication strategy for biomimetic micro/nanoscale architectures and living tissue constructs. Biofabrication **12** (2020). https://doi.org/10.1088/1758-5090/aba1fa
17. J. Li, C. Wu, P.K. Chu, M. Gelinsky, 3D printing of hydrogels: Rational design strategies and emerging biomedical applications. Mater. Sci. Eng. R. Rep. **140**, 100543 (2020). https://doi.org/10.1016/j.mser.2020.100543
18. C. Duty, C. Ajinjeru, V. Kishore, B. Compton, N. Hmeidat, X. Chen, P. Liu, A.A. Hassen, J. Lindahl, V. Kunc, What makes a material printable? A viscoelastic model for extrusion-based 3D printing of polymers. J. Manuf. Process. **35**, 526–537 (2018). https://doi.org/10.1016/j.jmapro.2018.08.008
19. S.A.M. Tofail, E.P. Koumoulos, A. Bandyopadhyay, S. Bose, L. O'Donoghue, C. Charitidis, Additive manufacturing: Scientific and technological challenges, market uptake and opportunities. Mater. Today **21**, 22–37 (2018). https://doi.org/10.1016/j.mattod.2017.07.001

20. S. Yuan, F. Shen, C.K. Chua, K. Zhou, Polymeric composites for powder-based additive manufacturing: Materials and applications. Prog. Polym. Sci. **91**, 141–168 (2019). https://doi.org/10.1016/j.progpolymsci.2018.11.001
21. X. Wang, M. Jiang, Z. Zhou, J. Gou, D. Hui, 3D printing of polymer matrix composites: A review and prospective. Compos. Part B Eng. **110**, 442–458 (2017). https://doi.org/10.1016/j.compositesb.2016.11.034
22. A. Bagheri, J. Jin, Photopolymerization in 3D printing. ACS Appl. Polym. Mater. **1**, 593–611 (2019). https://doi.org/10.1021/acsapm.8b00165
23. D. Popescu, A. Zapciu, C. Amza, F. Baciu, R. Marinescu, FDM process parameters influence over the mechanical properties of polymer specimens: A review. Polym. Test. **69**, 157–166 (2018). https://doi.org/10.1016/j.polymertesting.2018.05.020
24. M. Dzemko, B. Engelmann, J. Hartmann, J. Schmitt, Toward shifted production strategies through additive manufacturing: A technology and market review for changing value chains. Procedia CIRP **86**, 228–233 (2020). https://doi.org/10.1016/j.procir.2020.01.029
25. M. Harris, J. Potgieter, R. Archer, K.M. Arif, Effect of material and process specific factors on the strength of printed parts in fused filament fabrication: A review of recent developments. Materials (Basel) **12** (2019). https://doi.org/10.3390/ma12101664
26. F. Fenollosa, J.R. Gomà, I. Buj-Corral, A.T. Otero, J. Minguella-Canela, R. Uceda, A. Valls, M. Ayats, Foreseeing new multi-material FFF-additive manufacturing concepts meeting mimicking requirements with living tissues. Procedia Manuf. **41**, 1063–1070 (2019). https://doi.org/10.1016/j.promfg.2019.10.034
27. L.R. Lopes, A.F. Silva, O.S. Carneiro, Multi-material 3D printing: The relevance of materials affinity on the boundary interface performance. Addit. Manuf. **23**, 45–52 (2018). https://doi.org/10.1016/j.addma.2018.06.027
28. E. Cuan-Urquizo, E. Barocio, V. Tejada-Ortigoza, R.B. Pipes, C.A. Rodriguez, A. Roman-Flores, Characterization of the mechanical properties of FFF structures and materials: A review on the experimental, computational and theoretical approaches. Materials (Basel) **16** (2019). https://doi.org/10.3390/ma12060895
29. S.C. Daminabo, S. Goel, S.A. Grammatikos, H.Y. Nezhad, V.K. Thakur, Fused deposition modeling-based additive manufacturing (3D printing): Techniques for polymer material systems. Mater. Today Chem. **16**, 100248 (2020). https://doi.org/10.1016/j.mtchem.2020.100248
30. L. Li, Q. Lin, M. Tang, A.J.E. Duncan, C. Ke, Advanced polymer designs for direct-ink-write 3D printing. Chem. – A Eur. J. **25**, 10768–10781 (2019). https://doi.org/10.1002/chem.201900975
31. M.O. Aydogdu, B. Mutlu, M. Kurt, A.T. Inan, S.E. Kuruca, G. Erdemir, Y.M. Sahin, N. Ekren, F.N. Oktar, O. Gunduz, Developments of 3D polycaprolactone/beta-tricalcium phosphate/collagen scaffolds for hard tissue engineering. J. Aust. Ceram. Soc. **55**, 849–855 (2019). https://doi.org/10.1007/s41779-018-00299-y
32. Z. Ji, D. Jiang, X. Zhang, Y. Guo, X. Wang, Facile photo and thermal two-stage curing for high-performance 3D printing of poly(dimethylsiloxane). Macromol. Rapid Commun. **41**, 1–8 (2020). https://doi.org/10.1002/marc.202000064
33. M.A. Skylar-Scott, J. Mueller, C.W. Visser, J.A. Lewis, Voxelated soft matter via multimaterial multinozzle 3D printing. Nature **575**, 330–335 (2019). https://doi.org/10.1038/s41586-019-1736-8
34. Y. Guo, J. Xu, C. Yan, Y. Chen, X. Zhang, X. Jia, Y. Liu, X. Wang, F. Zhou, Direct ink writing of high performance architectured polyimides with low dimensional shrinkage. Adv. Eng. Mater. **21**, 1–8 (2019). https://doi.org/10.1002/adem.201801314
35. T. Mohan, A. Dobaj Štiglic, M. Beaumont, J. Konnerth, F. Gürer, D. Makuc, U. Maver, L. Gradišnik, J. Plavec, R. Kargl, K. Stana Kleinschek, Generic method for designing self-standing and dual porous 3D bioscaffolds from cellulosic nanomaterials for tissue engineering applications. ACS Appl. Bio Mater. **3**, 1197–1209 (2020). https://doi.org/10.1021/acsabm.9b01099

36. R. Karyappa, A. Ohno, M. Hashimoto, Immersion precipitation 3D printing (ip3DP). Mater. Horizons **6**, 1834–1844 (2019)
37. W. Sun, B. Starly, A.C. Daly, J.A. Burdick, J. Groll, G. Skeldon, W. Shu, Y. Sakai, M. Shinohara, M. Nishikawa, J. Jang, D.W. Cho, M. Nie, S. Takeuchi, S. Ostrovidov, A. Khademhosseini, R.D. Kamm, V. Mironov, L. Moroni, I.T. Ozbolat, The bioprinting roadmap. Biofabrication **12** (2020). https://doi.org/10.1088/1758-5090/ab5158
38. I. Matai, G. Kaur, A. Seyedsalehi, A. McClinton, C.T. Laurencin, Progress in 3D bioprinting technology for tissue/organ regenerative engineering. Biomaterials **226**, 119536 (2020). https://doi.org/10.1016/j.biomaterials.2019.119536
39. I.T. Ozbolat, M. Hospodiuk, Current advances and future perspectives in extrusion-based bioprinting. Biomaterials **76**, 321–343 (2016). https://doi.org/10.1016/j.biomaterials.2015.10.076
40. T. Bhattacharjee, S.M. Zehnder, K.G. Rowe, S. Jain, R.M. Nixon, W.G. Sawyer, T.E. Angelini, Writing in the granular gel medium. Sci. Adv. **1**, 4–10 (2015). https://doi.org/10.1126/sciadv.1500655
41. W. Liu, Z. Zhong, N. Hu, Y. Zhou, L. Maggio, A.K. Miri, A. Fragasso, X. Jin, A. Khademhosseini, Y.S. Zhang, Coaxial extrusion bioprinting of 3D microfibrous constructs with cell-favorable gelatin methacryloyl microenvironments. Biofabrication **10** (2018). https://doi.org/10.1088/1758-5090/aa9d44
42. J.H. Galarraga, M.Y. Kwon, J.A. Burdick, 3D bioprinting via an in situ crosslinking technique towards engineering cartilage tissue. Sci. Rep. **9**, 1–12 (2019). https://doi.org/10.1038/s41598-019-56117-3
43. M. Mobaraki, M. Ghaffari, A. Yazdanpanah, Y. Luo, D.K. Mills, Bioinks and bioprinting: A focused review. Bioprinting **18**, e00080 (2020). https://doi.org/10.1016/j.bprint.2020.e00080
44. R.R. Jose, M.J. Rodriguez, T.A. Dixon, F. Omenetto, D.L. Kaplan, Evolution of bioinks and additive manufacturing technologies for 3D bioprinting. ACS Biomater Sci. Eng. **2**, 1662–1678 (2016). https://doi.org/10.1021/acsbiomaterials.6b00088
45. A.K. Miri, E. Mostafavi, D. Khorsandi, S.K. Hu, M. Malpica, A. Khademhosseini, Bioprinters for organs-on-chips. Biofabrication **11** (2019). https://doi.org/10.1088/1758-5090/ab2798
46. S.C. Ligon, R. Liska, J. Stampfl, M. Gurr, R. Mülhaupt, Polymers for 3D printing and customized additive manufacturing. Chem. Rev. **117**, 10212–10290 (2017). https://doi.org/10.1021/acs.chemrev.7b00074
47. L.Y. Zhou, J. Fu, Y. He, A review of 3D printing technologies for soft polymer materials. Adv. Funct. Mater. **2000187**, 1–38 (2020). https://doi.org/10.1002/adfm.202000187
48. Hull, C.W., Spence, S.T., Albert, D.J., Smalley, D.R., Harlow, R.A. Steinbaugh, P., Tarnoff, H.L., Nguyen, H.D., Lewis, C.W., Vorgitch, T.J., 1991. *Methods and Apparatus for Production of Three-Dimensional Objects by Stereolithography*
49. J.R. Tumbleston, D. Shirvanyants, N. Ermoshkin, R. Janusziewicz, A.R. Johnson, D. Kelly, K. Chen, R. Pinschmidt, J.P. Rolland, A. Ermoshkin, E.T. Samulski, J.M. DeSimone, Continuous liquid interface production of 3D objects. Science (80-.) **347**, 1349–1352 (2015). https://doi.org/10.1126/science.aaa2397
50. M. Shusteff, A.E.M. Browar, B.E. Kelly, J. Henriksson, T.H. Weisgraber, R.M. Panas, N.X. Fang, C.M. Spadaccini, One-step volumetric additive manufacturing of complex polymer structures. Sci. Adv. **3** (2017). https://doi.org/10.1126/sciadv.aao5496
51. J. Zhang, P. Xiao, 3D printing of photopolymers. Polym. Chem. **9**, 1530–1540 (2018). https://doi.org/10.1039/c8py00157j
52. L.K. Fai, C.C. Kai, T.C. Hock, Microblasting characteristics of jewellery models built using stereolithography apparatus (SLA). Int. J. Adv. Manuf. Technol. **14**, 450–458 (1998)
53. M. Revilla-León, M. Sadeghpour, M. Özcan, An update on applications of 3D printing technologies used for processing polymers used in implant dentistry. Odontology **108**, 331–338 (2020). https://doi.org/10.1007/s10266-019-00441-7
54. B. Heidt, R. Rogosic, S. Bonni, J. Passariello-Jansen, D. Dimech, J.W. Lowdon, R. Arreguin-Campos, E. Steen Redeker, K. Eersels, H. Diliën, B. van Grinsven, T.J. Cleij, The liberalization of microfluidics: Form 2 benchtop 3D printing as an affordable alternative

to established manufacturing methods. Phys. Status Solid. Appl. Mater. Sci. **1900935**, 1–7 (2020). https://doi.org/10.1002/pssa.201900935
55. C. Liu, N. Huang, F. Xu, J. Tong, Z. Chen, X. Gui, Y. Fu, C. Lao, 3D printing technologies for flexible tactile sensors toward wearable electronics and electronic skin. Polymers (Basel) **10**, 1–31 (2018). https://doi.org/10.3390/polym10060629
56. M. Zarek, M. Layani, I. Cooperstein, E. Sachyani, D. Cohn, S. Magdassi, 3D printing of shape memory polymers for flexible electronic devices. Adv. Mater. **28**, 4449–4454 (2016)
57. K.S. Lim, J.H. Galarraga, X. Cui, G.C.J. Lindberg, J.A. Burdick, T.B.F. Woodfield, Fundamentals and applications of photo-cross-linking in bioprinting. Chem. Rev. (2020). https://doi.org/10.1021/acs.chemrev.9b00812
58. H. Quan, T. Zhang, H. Xu, S. Luo, J. Nie, X. Zhu, Photo-curing 3D printing technique and its challenges. Bioact. Mater. **5**, 110–115 (2020). https://doi.org/10.1016/j.bioactmat.2019.12.003
59. X. Zhou, Y. Hou, J. Lin, A review on the processing accuracy of two-photon polymerization. AIP Adv. **5** (2015). https://doi.org/10.1063/1.4916886
60. J.T. Fourkas, Fundamentals of two-photon fabrication, in *Three-Dimensional Microfabrication Using Two-Photon Polymerization*, (William Andrew Publishing, 2020), pp. 57–76
61. C.K. Ober, Materials systems for 2-photon lithography, in *Three-Dimensional Microfabrication Using Two-Photon Polymerization2*, (William Andrew Publishing, 2020), pp. 143–174
62. J. Song, C. Michas, C.S. Chen, A.E. White, M.W. Grinstaff, From simple to architecturally complex hydrogel scaffolds for cell and tissue engineering applications: Opportunities presented by two-photon polymerization. Adv. Healthc. Mater. **9**, 1–13 (2020). https://doi.org/10.1002/adhm.201901217
63. C.W. Ha, P. Prabhakaran, K.S. Lee, Versatile applications of three-dimensional objects fabricated by two-photon-initiated polymerization. MRS Commun. **9**, 53–66 (2019). https://doi.org/10.1557/mrc.2018.218
64. J. Li, P. Fejes, D. Lorenser, B.C. Quirk, P.B. Noble, R.W. Kirk, A. Orth, F.M. Wood, B.C. Gibson, D.D. Sampson, R.A. McLaughlin, Two-photon polymerisation 3D printed freeform micro-optics for optical coherence tomography fibre probes. Sci. Rep. **8**, 1–9 (2018). https://doi.org/10.1038/s41598-018-32407-0
65. S. Rodríguez, Redefining microfabrication of high-precision optics. PhotonicsViews **17**, 36–39 (2020). https://doi.org/10.1002/phvs.202000003
66. A.T. Gaynor, N.A. Meisel, C.B. Williams, J.K. Guest, Multiple-material topology optimization of compliant mechanisms created via Poly jet three-dimensional printing. J. Manuf. Sci. Eng. Trans. ASME **136**, 1–10 (2014). https://doi.org/10.1115/1.4028439
67. S. Tibbits, *4D Printing: Multi-Material Shape Change* (2014), pp. 421–433. https://doi.org/10.1142/9789811201493_0027
68. N.P. Macdonald, J.M. Cabot, P. Smejkal, R.M. Guijt, B. Paull, M.C. Breadmore, Comparing microfluidic performance of three-dimensional (3D) printing platforms. Anal. Chem. **89**, 3858–3866 (2017a). https://doi.org/10.1021/acs.analchem.7b00136
69. R.D. Sochol, E. Sweet, C.C. Glick, S. Venkatesh, A. Avetisyan, K.F. Ekman, A. Raulinaitis, A. Tsai, A. Wienkers, K. Korner, K. Hanson, A. Long, B.J. Hightower, G. Slatton, D.C. Burnett, T.L. Massey, K. Iwai, L.P. Lee, K.S.J. Pister, L. Lin, 3D printed microfluidic circuitry via multijet-based additive manufacturing. Lab Chip **16**, 668–678 (2016). https://doi.org/10.1039/c5lc01389e
70. M. Pohanka, Three-dimensional printing in analytical chemistry: Principles and applications. Anal. Lett. **49**, 2865–2882 (2016). https://doi.org/10.1080/00032719.2016.1166370
71. M. Belka, L. Konieczna, M. Okońska, M. Pyszka, S. Ulenberg, T. Bączek, Application of 3D-printed scabbard-like sorbent for sample preparation in bioanalysis expanded to 96-wellplate high-throughput format. Anal. Chim. Acta **1081**, 1–5 (2019). https://doi.org/10.1016/j.aca.2019.05.078
72. L.P.C. Gomez, A. Spangenberg, X.A. Ton, Y. Fuchs, F. Bokeloh, J.P. Malval, B. Tse Sum Bui, D. Thuau, C. Ayela, K. Haupt, O. Soppera, Rapid prototyping of chemical microsensors based on molecularly imprinted polymers synthesized by two-photon stereolithography. Adv. Mater. **28**, 5931–5937 (2016). https://doi.org/10.1002/adma.201600218

73. G. De Middeleer, P. Dubruel, S. De Saeger, Molecularly imprinted polymers immobilized on 3D printed scaffolds as novel solid phase extraction sorbent for metergoline. Anal. Chim. Acta **986**, 57–70 (2017). https://doi.org/10.1016/j.aca.2017.07.059
74. M. Gou, X. Qu, W. Zhu, M. Xiang, J. Yang, K. Zhang, Y. Wei, S. Chen, Bio-inspired detoxification using 3d-printed hydrogel nanocomposites. Nat. Commun. **5**, 1–9 (2014). https://doi.org/10.1038/ncomms4774
75. N.P. Macdonald, S.A. Currivan, L. Tedone, B. Paull, Direct production of microstructured surfaces for planar chromatography using 3D printing. Anal. Chem. **89**, 2457–2463 (2017b). https://doi.org/10.1021/acs.analchem.6b04546
76. E.K. Parker, A.V. Nielsen, M.J. Beauchamp, H.M. Almughamsi, J.B. Nielsen, M. Sonker, H. Gong, G.P. Nordin, A.T. Woolley, 3D printed microfluidic devices with immunoaffinity monoliths for extraction of preterm birth biomarkers. Anal. Bioanal. Chem. **411**, 5405–5413 (2019). https://doi.org/10.1007/s00216-018-1440-9
77. M. Belka, S. Ulenberg, T. Bączek, Fused deposition modeling enables the low-cost fabrication of porous, customized-shape sorbents for small-molecule extraction. Anal. Chem. **89**, 4373–4376 (2017). https://doi.org/10.1021/acs.analchem.6b04390
78. G. Palmara, F. Frascella, I. Roppolo, A. Chiappone, A. Chiadò, Functional 3D printing: Approaches and bioapplications. Biosens. Bioelectron. **175**, 112849 (2021). https://doi.org/10.1016/j.bios.2020.112849
79. R. Calmo, A. Chiadò, S. Fiorilli, C. Ricciardi, Advanced ELISA-like biosensing based on ultralarge-pore silica microbeads. ACS Appl. Bio Mater. **3**, 5787–5795 (2020). https://doi.org/10.1021/acsabm.0c00533
80. D. Sticker, R. Geczy, U.O. Häfeli, J.P. Kutter, Thiol-Ene based polymers as versatile materials for microfluidic devices for life sciences applications. ACS Appl. Mater. Interfaces **12**, 10080–10095 (2020). https://doi.org/10.1021/acsami.9b22050
81. C.A. Mandon, L.J. Blum, C.A. Marquette, Adding biomolecular recognition capability to 3D printed objects. Anal. Chem. **88**, 10767–10772 (2016). https://doi.org/10.1021/acs.analchem.6b03426
82. S. Stassi, E. Fantino, R. Calmo, A. Chiappone, M. Gillono, D. Scaiola, C.F. Pirri, C. Ricciardi, A. Chiadò, I. Roppolo, Polymeric 3D printed functional microcantilevers for biosensing applications. ACS Appl. Mater. Interfaces **9**, 19193–19201 (2017). https://doi.org/10.1021/acsami.7b04030
83. C. Credi, G. Griffini, M. Levi, S. Turri, Biotinylated photopolymers for 3D-printed unibody lab-on-a-chip optical platforms. Small **14**, 1–8 (2018). https://doi.org/10.1002/smll.201702831
84. C. Aronsson, M. Jury, S. Naeimipour, F.R. Boroojeni, J. Christoffersson, P. Lifwergren, C.F. Mandenius, R. Selegård, D. Aili, Dynamic peptide-folding mediated biofunctionalization and modulation of hydrogels for 4D bioprinting. Biofabrication **12** (2020). https://doi.org/10.1088/1758-5090/ab9490
85. Y. Ukita, Y. Utsumi, Y. Takamura, Direct digital manufacturing of a mini-centrifuge-driven centrifugal microfluidic device and demonstration of a smartphone-based colorimetric enzyme-linked immunosorbent assay. Anal. Methods **8**, 256–262 (2015). https://doi.org/10.1039/c5ay01969a
86. A. Chiadò, G. Palmara, A. Chiappone, C. Tanzanu, C.F. Pirri, I. Roppolo, F. Frascella, A modular 3D printed lab-on-a-chip for early cancer detection. Lab Chip **20**, 665–674 (2020). https://doi.org/10.1039/c9lc01108k
87. H. Singh, M. Shimojima, S. Fukushi, A. Le Van, M. Sugamata, M. Yang, Increased sensitivity of 3D-well enzymelinked immunosorbent assay (ELISA) for infectious disease detection using 3Dprinting fabrication technology. Biomed. Mater. Eng. **26**, S45–S53 (2015a). https://doi.org/10.3233/BME-151288
88. H. Singh, M. Shimojima, T. Shiratori, L. Van An, M. Sugamata, M. Yang, Application of 3D printing technology in increasing the diagnostic performance of enzyme-linked immunosorbent assay (ELISA) for infectious diseases. Sensors (Switzerland) **15**, 16503–16515 (2015b). https://doi.org/10.3390/s150716503

89. T. Distler, A.R. Boccaccini, 3D printing of electrically conductive hydrogels for tissue engineering and biosensors – A review. Acta Biomater. **101**, 1–13 (2020). https://doi.org/10.1016/j.actbio.2019.08.044
90. D. Lin, S. Jin, F. Zhang, C. Wang, Y. Wang, C. Zhou, G.J. Cheng, 3D stereolithography printing of graphene oxide reinforced complex architectures. Nanotechnology **26** (2015). https://doi.org/10.1088/0957-4484/26/43/434003
91. F. Frascella, G. González, P. Bosch, A. Angelini, A. Chiappone, M. Sangermano, C.F. Pirri, I. Roppolo, Three-dimensional printed photoluminescent polymeric waveguides. ACS Appl. Mater. Interfaces **10**, 39319–39326 (2018). https://doi.org/10.1021/acsami.8b16036
92. M. Gillono, I. Roppolo, F. Frascella, L. Scaltrito, C.F. Pirri, A. Chiappone, CO2 permeability control in 3D printed light responsive structures. Appl. Mater. Today **18**, 100470 (2020). https://doi.org/10.1016/j.apmt.2019.100470
93. C.L. Manzanares Palenzuela, M. Pumera, (Bio)analytical chemistry enabled by 3D printing: Sensors and biosensors. TrAC – Trends Anal. Chem. **103**, 110–118 (2018). https://doi.org/10.1016/j.trac.2018.03.016
94. J. Muñoz, M. Pumera, 3D-printed biosensors for electrochemical and optical applications. TrAC – Trends Anal. Chem. **128**, 115933 (2020). https://doi.org/10.1016/j.trac.2020.115933
95. R.M. Cardoso, P.R.L. Silva, A.P. Lima, D.P. Rocha, T.C. Oliveira, T.M. do Prado, E.L. Fava, O. Fatibello-Filho, E.M. Richter, R.A.A. Muñoz, 3D-printed graphene/polylactic acid electrode for bioanalysis: Biosensing of glucose and simultaneous determination of uric acid and nitrite in biological fluids. Sensors Actuators B Chem. **307**, 127621 (2020). https://doi.org/10.1016/j.snb.2019.127621
96. C.L. Manzanares-Palenzuela, S. Hermanova, Z. Sofer, M. Pumera, Proteinase-sculptured 3D-printed graphene/polylactic acid electrodes as potential biosensing platforms: Towards enzymatic modeling of 3D-printed structures. Nanoscale **11**, 12124–12131 (2019). https://doi.org/10.1039/c9nr02754h
97. A.M. López Marzo, C.C. Mayorga-Martinez, M. Pumera, 3D-printed graphene direct electron transfer enzyme biosensors. Biosens. Bioelectron. **151** (2020). https://doi.org/10.1016/j.bios.2019.111980
98. H. Lin, Y. Zhao, S. Lin, B. Wang, C. Yeung, X. Cheng, Z. Wang, T. Cai, W. Yu, K. King, J. Tan, K. Salahi, H. Hojaiji, S. Emaminejad, A rapid and low-cost fabrication and integration scheme to render 3D microfluidic architectures for wearable biofluid sampling, manipulation, and sensing. Lab Chip **19**, 2844–2853 (2019). https://doi.org/10.1039/c9lc00418a
99. H.C. Koydemir, A. Ozcan, Wearable, epidermal, and implantable sensors for biomedical applications. Annu. Rev. Anal. Chem. **11**, 1–20 (2018)
100. J.A. Lewis, Direct ink writing of 3D functional materials. Adv. Funct. Mater. **16**, 2193–2204 (2006). https://doi.org/10.1002/adfm.200600434
101. Y. Dong, X. Min, W.S. Kim, A 3-D-printed integrated PCB-based electrochemical sensor system. IEEE Sensors J. **18**, 2959–2966 (2018). https://doi.org/10.1109/JSEN.2018.2801459
102. S. Nesaei, Y. Song, Y. Wang, X. Ruan, D. Du, A. Gozen, Y. Lin, Micro additive manufacturing of glucose biosensors: A feasibility study. Anal. Chim. Acta **1043**, 142–149 (2018). https://doi.org/10.1016/j.aca.2018.09.012
103. Z. Pu, J. Tu, R. Han, X. Zhang, J. Wu, C. Fang, H. Wu, X. Zhang, H. Yu, D. Li, A flexible enzyme-electrode sensor with cylindrical working electrode modified with a 3D nanostructure for implantable continuous glucose monitoring. Lab Chip **18**, 3570–3577 (2018). https://doi.org/10.1039/c8lc00908b
104. T.N.H. Nguyen, J.K. Nolan, H. Park, S. Lam, M. Fattah, J.C. Page, H.E. Joe, M.B.G. Jun, H. Lee, S.J. Kim, R. Shi, H. Lee, Facile fabrication of flexible glutamate biosensor using direct writing of platinum nanoparticle-based nanocomposite ink. Biosens. Bioelectron. **131**, 257–266 (2019). https://doi.org/10.1016/j.bios.2019.01.051
105. J.K. Nolan, T.N.H. Nguyen, K.V.H. Le, L.E. DeLong, H. Lee, Simple fabrication of flexible biosensor arrays using direct writing for multianalyte measurement from human astrocytes. SLAS Technol. **25**, 33–46 (2019). https://doi.org/10.1177/2472630319888442

106. J. Kim, I. Jeerapan, J.R. Sempionatto, A. Barfidokht, R.K. Mishra, A.S. Campbell, L.J. Hubble, J. Wang, Wearable bioelectronics: Enzyme-based body-worn electronic devices. Acc. Chem. Res. **51**, 2820–2828 (2018). https://doi.org/10.1021/acs.accounts.8b00451
107. J. Kim, G. Valdés-Ramírez, A.J. Bandodkar, W. Jia, A.G. Martinez, R. Julian, P. Mercier, J. Wang, Non-invasive mouthguard biosensor for continuous salivary monitoring of metabolites. Analyst **139**, 1632–1636 (2014). https://doi.org/10.1039/c3an02359a
108. A. Martín, J. Kim, J.F. Kurniawan, J.R. Sempionatto, J.R. Moreto, G. Tang, A.S. Campbell, A. Shin, M.Y. Lee, X. Liu, J. Wang, Epidermal microfluidic electrochemical detection system: Enhanced sweat sampling and metabolite detection. ACS Sensors **2**, 1860–1868 (2017). https://doi.org/10.1021/acssensors.7b00729
109. R. Zou, S. Shan, L. Huang, Z. Chen, T. Lawson, M. Lin, L. Yan, Y. Liu, High-performance intraocular biosensors from chitosan-functionalized nitrogen-containing graphene for the detection of glucose. ACS Biomater Sci. Eng. **6**, 673–679 (2020). https://doi.org/10.1021/acsbiomaterials.9b01149
110. C.D. Devillard, C.A. Mandon, S.A. Lambert, L.J. Blum, C.A. Marquette, Bioinspired multi-activities 4D printing objects: A new approach toward complex tissue engineering. Biotechnol. J. **13**, 1–8 (2018). https://doi.org/10.1002/biot.201800098
111. B. Schmieg, J. Döbber, F. Kirschhöfer, M. Pohl, M. Franzreb, Advantages of hydrogel-based 3D-printed enzyme reactors and their limitations for biocatalysis. Front. Bioeng. Biotechnol. **6**, 1–12 (2019). https://doi.org/10.3389/fbioe.2018.00211
112. L. Wenger, C.P. Radtke, J. Göpper, M. Wörner, J. Hubbuch, 3D-printable and enzymatically active composite materials based on hydrogel-filled high internal phase emulsions. Front. Bioeng. Biotechnol. **8**, 1–17 (2020). https://doi.org/10.3389/fbioe.2020.00713
113. C.P. Radtke, N. Hillebrandt, J. Hubbuch, The biomaker: An entry-level bioprinting device for biotechnological applications. J. Chem. Technol. Biotechnol. **93**, 792–799 (2018a). https://doi.org/10.1002/jctb.5429
114. C.K. Su, S.C. Yen, T.W. Li, Y.C. Sun, Enzyme-immobilized 3D-printed reactors for online monitoring of rat brain extracellular glucose and lactate. Anal. Chem. **88**, 6265–6273 (2016). https://doi.org/10.1021/acs.analchem.6b00272
115. L. Tamborini, P. Fernandes, F. Paradisi, F. Molinari, Flow bioreactors as complementary tools for biocatalytic process intensification. Trends Biotechnol. **36**, 73–88 (2018). https://doi.org/10.1016/j.tibtech.2017.09.005
116. C. Zhao, N. Zhang, H. Zheng, Q. Zhu, M. Utsumi, Y. Yang, Effective and long-term continuous bio-hydrogen production by optimizing fixed-bed material in the bioreactor. Process Biochem. **83**, 55–63 (2019). https://doi.org/10.1016/j.procbio.2019.04.021
117. C.P. Radtke, N. Hillebrandt, J. Hubbuch, The biomaker: An entry-level bioprinting device for biotechnological applications. J. Chem. Technol. Biotechnol. **93**, 792–799 (2018b). https://doi.org/10.1002/jctb.5429
118. M. Maier, C.P. Radtke, J. Hubbuch, C.M. Niemeyer, K.S. Rabe, On-demand production of flow-reactor cartridges by 3D printing of thermostable enzymes. Angew. Chem. Int. Ed. **57**, 5539–5543 (2018). https://doi.org/10.1002/anie.201711072
119. M. Peng, E. Mittmann, L. Wenger, J. Hubbuch, M.K.M. Engqvist, C.M. Niemeyer, K.S. Rabe, 3D-printed phenacrylate decarboxylase flow reactors for the chemoenzymatic synthesis of 4-Hydroxystilbene. Chem. – A Eur. J. **25**, 15998–16001 (2019). https://doi.org/10.1002/chem.201904206
120. B. Schmieg, A. Schimek, M. Franzreb, Development and performance of a 3D-printable poly(ethylene glycol) diacrylate hydrogel suitable for enzyme entrapment and long-term biocatalytic applications. Eng. Life Sci. **18**, 659–667 (2018). https://doi.org/10.1002/elsc.201800030
121. A. Awad, S.J. Trenfield, S. Gaisford, A.W. Basit, 3D printed medicines: A new branch of digital healthcare. Int. J. Pharm. **548**, 586–596 (2018). https://doi.org/10.1016/j.ijpharm.2018.07.024
122. M.A. Alhnan, T.C. Okwuosa, M. Sadia, K.W. Wan, W. Ahmed, B. Arafat, Emergence of 3D printed dosage forms: Opportunities and challenges. Pharm. Res. **33**, 1817–1832 (2016). https://doi.org/10.1007/s11095-016-1933-1

123. T.C. Okwuosa, B.C. Pereira, B. Arafat, M. Cieszynska, A. Isreb, M.A. Alhnan, Fabricating a shell-core delayed release tablet using dual FDM 3D printing for patient-centred therapy. Pharm. Res. **34**, 427–437 (2017). https://doi.org/10.1007/s11095-016-2073-3
124. Y.J.N. Tan, W.P. Yong, J.S. Kochhar, J. Khanolkar, X. Yao, Y. Sun, C.K. Ao, S. Soh, On-demand fully customizable drug tablets via 3D printing technology for personalized medicine. J. Control. Release **322**, 42–52 (2020). https://doi.org/10.1016/j.jconrel.2020.02.046
125. J.J. Ong, A. Awad, A. Martorana, S. Gaisford, E. Stoyanov, A.W. Basit, A. Goyanes, 3D printed opioid medicines with alcohol-resistant and abuse-deterrent properties. Int. J. Pharm. **579**, 119169 (2020). https://doi.org/10.1016/j.ijpharm.2020.119169
126. G. Palmara, A. Chiadò, R. Calmo, C. Ricciardi, Succinic anhydride functionalized microcantilevers for protein immobilization and quantification. Anal. Bioanal. Chem. **408**, 7917–7926 (2016). https://doi.org/10.1007/s00216-016-9920-2
127. J. Bae, S. Lee, J. Ahn, J.H. Kim, M. Wajahat, W.S. Chang, S.Y. Yoon, J.T. Kim, S.K. Seol, J. Pyo, 3D-printed quantum dot nanopixels. ACS Nano **14**, 10993–11001 (2020). https://doi.org/10.1021/acsnano.0c04075
128. C.D. Brubaker, T.M. Frecker, J.R. McBride, K.R. Reid, G.K. Jennings, S.J. Rosenthal, D.E. Adams, Incorporation of fluorescent quantum dots for 3D printing and additive manufacturing applications. J. Mater. Chem. C **6**, 7584–7593 (2018). https://doi.org/10.1039/c8tc02024h
129. Y. Liu, H. Wang, J. Ho, R.C. Ng, R.J.H. Ng, V.H. Hall-Chen, E.H.H. Koay, Z. Dong, H. Liu, C.W. Qiu, J.R. Greer, J.K.W. Yang, Structural color three-dimensional printing by shrinking photonic crystals. Nat. Commun. **10** (2019). https://doi.org/10.1038/s41467-019-12360-w

Chapter 8
Electronic Applications

Matteo Manachino, Gianluca Melis, Stefano Stassi, Sergio Ferrero, and Luciano Scaltrito

Abstract In the last years, additive manufacturing technologies have been widely implemented in the production of electronic components. The possibility of incorporating electronic functionalities in complex-shaped devices together with the multimaterial and multilayered fabrication capability has brought to the realization by 3D printing approaches of passive elements such as resistors, capacitors, and conductive traces, active elements like transistors and LEDs (light-emitting diodes), and also multiple examples of sensors and actuators. Compared to traditional production, 3D printing electronics resulted as one of the most promising technologies for producing parts in a more effective and efficient manner.

Here, we review the state of the art related to the research activity in fabricating *electronic passive elements* and *active elements*. We also focus on 3D printed *sensors* and *actuators*, discussing both the physical working principles and the application fields of the different components.

Keywords Sensors · Actuator · Transistors · Electronic passive elements · Antennas · LED

8.1 Introduction

Additive manufacturing of electronic components was born as a prototyping technology of complex-shaped parts, not suitable to incorporate electronic functionalities. Nowadays, new 3D printing processes have been redesigned to target electronic systems, through the automatic placement of electronic components and embedded traces and vias, although without reaching an equal level of surface finish and reliability compared to traditional manufactured boards (printed circuit boards, PCBs). Improvements in the process standardization and the reliability of printed

M. Manachino · G. Melis · S. Stassi (✉) · S. Ferrero · L. Scaltrito
Dipartimento di Scienza Applicata e Tecnologia, Politecnico di Torino, Torino, Italy
e-mail: stefano.stassi@polito.it

S. L. Marasso, M. Cocuzza (eds.), *High Resolution Manufacturing from 2D to 3D/4D Printing*, https://doi.org/10.1007/978-3-031-13779-2_8

electronic systems are the goals of the continuous research, further empowered by material innovation focused at improving the printability of the medium while optimizing the electrical characteristics. Future challenges in 3D printed electronics involve the programming of a 3D CAD (computer-aided design) software capable of exploiting the third dimension in components' placement and routing [1].

Multimaterial and multilayered 3D printing technologies will increase production speed and complexity of flexible and high-performance electronic devices, such as resistors, capacitors, inductors and RF (radio frequency) filters [2, 3], 3D antennas, transistors, and sensors by in-process printing. This is the reason why 3D printing electronics, compared to traditional manufacturing, is one of the most promising technologies to produce parts in a more effective and efficient approach due to time and chemical wastage reduction [4].

Although fused deposition modeling (FDM) is the most exploited technique, researchers have experimented other approaches to print conductive material, such as stereolithography (SLA) or digital light processing (DLP) and digital light writing (DLW). The latter has been employed in a two-photon printer to fabricate a 3D structure of a polymer/gold composite [5]. Light-based technologies have been further exploited in the last years, due to their multimaterial and complex geometry processing capabilities [6].

The chapter has been organized in five sections. After a brief introduction, the first section describes the state of the art related to the research activity in fabricating *passive elements* such as traces and contacts, resistors, capacitors, and inductors; the second section is dedicated to the *active elements* like transistors, batteries, and LEDs. The third and the fourth sections deal with *sensors* and *actuators*, based on different physical principles. Finally, several *innovative applications* of 3D printed electronic components have been reported.

8.2 Passive Elements

Nanoparticles and polymer/nanoparticle composites have been exploited in 3D printing researches across the years as to produce complex structures made of metals, organic/inorganic semiconducting materials, and insulating matrices as presented by Kong et al. [7]. Carbon-based materials, graphene oxide (GO), and GO-based polymer composites represent one of the last frontiers of the research due to high thermal and electrical conductivity, biocompatibility, and mechanical strength [8]. Many other materials have been employed in the 3D printing process: ZrO_2 [9], SiC [10], ZnO [11], SiO_2 [12], etc.

It is noticeable the increasing interest in 3D-molded interconnect devices (3D-MID) which allows to additively manufacture complex geometries partially exploiting the out-of-plane building direction [13] (Fig. 8.1).

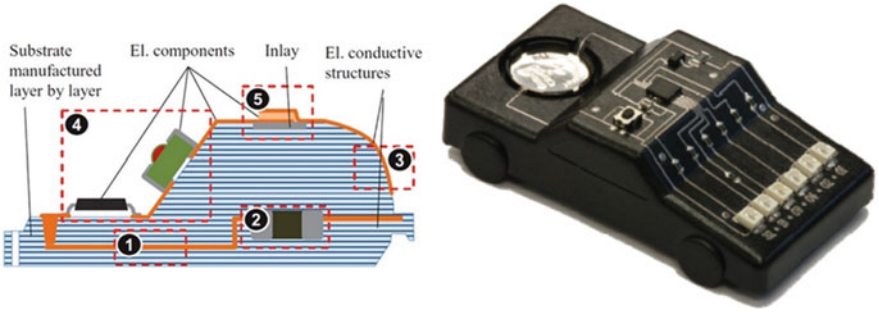

Fig. 8.1 (Left) Scheme of 3D-MID device and demonstrator. (1) Trace, (2) substrate embedded component, (3) 3D circuit trace, (4) SMD component, and (5) printed circuit component inlay embedded. Reprinted from Ref. [13], Copyright (2014), with permission from Elsevier. (Right) Image of 3D-MID device. Reprinted under the Creative Commons CC BY from Ref. [14]

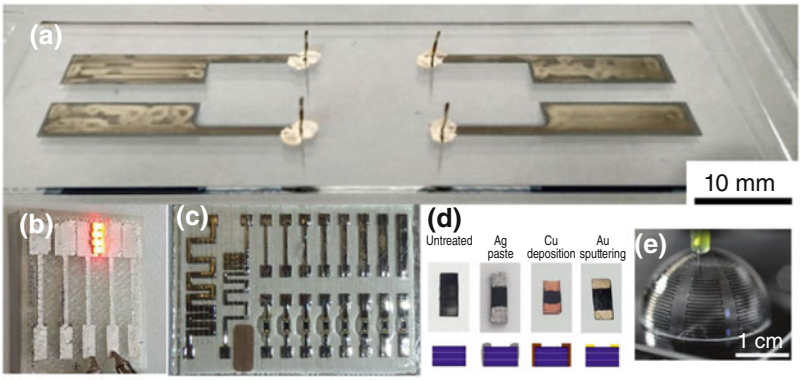

Fig. 8.2 (**a**) Inkjet printed and sintered silver pillars on bottom electrodes. Reprinted under the Creative Commons CC BY from Ref. [18]; (**b**) silver ink traces and pads of silver nano-powder paste on polylactic acid (PLA), Copyright 2021, Wiley. Reproduced with permission from Ref. [19]; (**c**) inkjet structure for JEDEC testing. Reprinted from Ref. [24], Copyright (2018), with permission from Elsevier; (**d**) PEGDA:PEDOT (poly(3,4-ethylenedioxythiophene):poly(styrenesulfonate) 3D printed polymer composite contacting: not contacted and contacted through silver paste, copper electrodeposition, and gold sputtering. Reprinted from Ref. [26]; (**e**) trace printing on spherical surface, Copyright 2011, Wiley. Reproduced with permission from Ref. [27]

8.2.1 Traces and Contacts

Aerosol jet [15], inkjet [16], and extrusion [17] are some of the most exploited techniques to 3D printed conductive traces, especially the second which uses inks (Fig. 8.2a) [18] containing nano-sized metal particles to produce vertical interconnects, although SLA and FDM are preferred in case of noncontact 3D printing of resin mixtures.

It would be advisable to consider, for further development of 3D printed electronics, complex machines capable to integrate the contact fabrication process. Researchers are moving toward this direction [19] setting up hybrid 3D printing techniques based on FDM/LDW (laser deposition welding) and selective laser sintering (SLS) to fabricate a finished electronic device in a unique printing/sintering additive process.

Based on the final trace conductivity, the boundary conditions (such as sintering methods of silver inks (Fig. 8.2b)), and the substrate, inkjet printers may be considered as a primary printing method to produce directly in the building process traces and contacts, with conductivities varying in the range of 0.1–30 $S \cdot \mu m^{-1}$. This variability is due to different substrates, which can affect the final adhesion, but mostly due to the processing and post-processing techniques such as dispensing the ink, even with multiple piezo-printheads, and sintering [19] or curing [20] it by laser, inkjet printing and furnace [21] post-processing or depositing the ink, and letting it dry with hot air [22].

Robustness and reliability of 3D printed traces, pads, and components [23, 24] must be assured to develop commercial devices fulfilling Joint Electron Device Engineering Council (JEDEC) testing requirements [25], as in Fig. 8.2c. Since in the layer-by-layer 3D printing process (e.g., SLA/LDW), the curing step is performed before the subsequent printing layer, the mechanical forces generated in the photopolymerization can lead the material to shrink during the printing stage, influencing its reliability and even causing failures, due to warpage.

The capability to incorporate metal contacts efficiently into a 3D printed sensor embedded in an electronic circuit is critical for the design and manufacturing of new bespoke devices. In this view, several metallizations have been tested on 3D printed conductive resin composites (Fig. 8.2d) [26] such as gold sputtering, silver paste deposition, and copper electroplating, although only the latter has been proven to assure the quality standards and repeatability typical of a commercial grade device. It is mandatory to evaluate contact and noncontact 3D printing technologies [4] focusing on the final functionality of the device, considering the working principle of each printing process.

8.2.2 Resistors

Most of the 3D printed resistors are functionalized to act as sensors or actuators, even if in this paragraph, only the fabrication of the 3D printed element will be evidenced, as a passive element.

New design has been suggested to 3D printed resistive actuators (Fig. 8.3a, b) capable of deforming upon heating [28], acting a reversible deformation to repeat the actuation resulting in a 4D printing technology [29]. New possibilities have been opened up in the field of printed resistors by direct in-process printing of 3D microfluidic channels (Fig. 8.3c), successively filled with liquid metal paste to

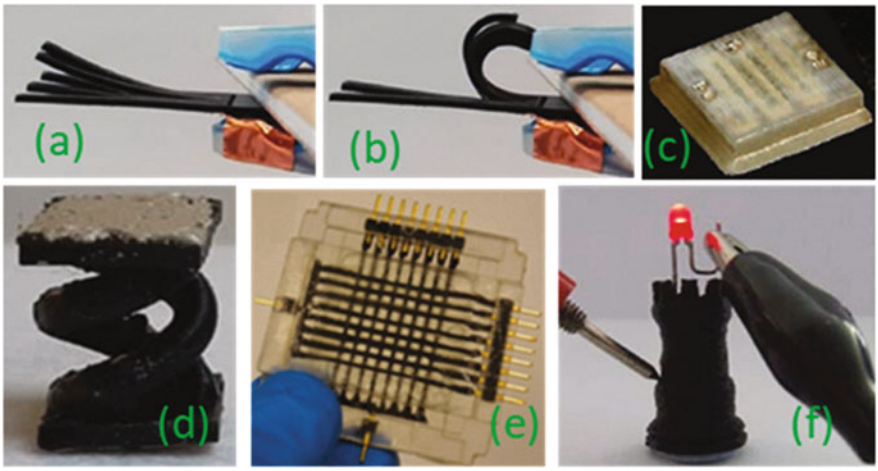

Fig. 8.3 (**a**, **b**) 3D printed resistive actuator deformed upon heating. Reprinted under the Creative Commons CC BY from Ref. [28]; (**c**) 3D printed resistor through solder paste filling and postcuring. Reprinted under the Creative Commons CC BY from Ref. [30]; (**d**) 3D printed PEGDA:PEDOT chemical vapor transducer. Reprinted under the Creative Commons CC BY from Ref. [31]; (**e**) 3D printed touch sensor. Reprinted under the Creative Commons CC BY from Ref. [37]; (**f**) 3D printed CB chess tower as resistive LED conditioning. Reprinted under the Creative Commons CC BY from Ref. [40]

fabricate precise embedded components, while benefiting from the metal adoption to create also external contacts [30].

In the field of conductive resins, it is noticeable, as reported in Fig. 8.3d, a 3D printed double helicoidal structure made of PEGDA:PEDOT [31], with a PEDOT content above the percolation threshold, exploited as acetone vapor transducer [32] due to the interaction of the polymeric resistive network with the gas phase [33]. The reduction of the material conductivity is attributed to the conformation variation of PEDOT chains, interacting with acetone molecules [34, 35]. This device is a proof of concept of how 3D printed resistors may be exploited in developing innovative long-term gas monitoring devices.

Multiwall carbon nanotubes (MWCNTs) [36] mixed with an elastomeric matrix have been employed to produce a flexible tactile sensor by SLA based on piezoresistive signal transduction [37] (Fig. 8.3e), even though the use of MWCNTs alone was shown to be insufficient to produce extremely sensitive strain sensors, despite their outstanding stretchability [38].

Loaded carbon black (CB) carnomorphs [39] (i.e., cheap composite conductive material) have been also studied and printed via FDM/FFF (fused filament fabrication) process. SEM studies demonstrated a sufficiently homogeneity in the CB dispersion at the nanoscale to form a resistive percolation network. A 3D structure has been tested in the form of a chess tower to act as resistive conditioning circuit for a LED (Fig. 8.3f) [40].

In 4D printing technology, smart materials are programmed through the combination of the classical 3D printing process and materials capable of varying their shape in response to an external stimulus. A further demonstrator has been presented by Chen et al. [29] who 3D printed via FDM and CB/PLA composite material with both sensing and actuating properties. The thermal behavior, described as a PTC/NTC resistor, respectively, at low/high temperature, coupled with the mechanical deformation induced by temperature variation, allows to exploit it as an actuator [41, 42].

McGhee et al. [43] demonstrated how commercially available conductive filaments [1] CB/graphene dispersed in PLA may be 3D printed (i.e., extruded) and exploited as a strain sensor, since they have been found to be piezoresistive, to create a force-sensing resistor placed in a Wheatstone bridge.

8.2.3 Capacitors

Abdallah et al. showed the 3D printing of a capacitive fluid level sensor using FFF and a PLA/graphite filament [44]. The sensor is composed of two interdigitated printed components and is capable of detecting changes in the system capacitance in order to determine the liquid level, as shown in Fig. 8.4a. The presence of fluid between the printed capacitor electrodes alters the dielectric constant of the two-phase medium between the plates, thus altering the capacitor's capacitance. The results indicated that there was a significant connection between the capacitance measured and the liquid level inside the sensor's fingers [45].

Further developments of 3D printed fluid level sensors have been contributed by Ozioko et al. [46] who fabricated a tilt sensor. Capacitive sensors were 3D printed and placed at the four corners of a cross-shaped channel and were used to provide object orientation through the capacitive fluid level measurement concept. The tilt range of one of the 3D printed interdigitated capacitive sensors was enhanced by increasing the channel's fluid capacity. This was accomplished by vertically embedding the interdigitated capacitive sensor inside a 3D printed substrate. The manufactured tilt sensor may be included into a robotic hand (Fig. 8.4b) or other intelligent items to detect their orientation as needed.

3D printed embedded capacitors can be produced, as previously reported on resistors, by 3D printing two separate cavities, as parallel plates, and successively filling them of liquid metal paste (Fig. 8.4c) [30].

Zhou et al. [47] experimented a high-efficiency and cheap technique to 3D print stretchable and flexible supercapacitors. They printed electrodes of reduced GO/CNTs/conducting polymer, while a polymeric hydrogel has been used as electrolyte to fabricate a solid-state supercapacitor, as in Fig. 8.4d. 4D printed supercapacitors retained their efficiency even under large mechanical deformations.

Beyond the 3D printing of single capacitors, a 3D printed micron-sized supercapacitive electrode by two-photon polymerization of a conductive PEGDA/EDOT

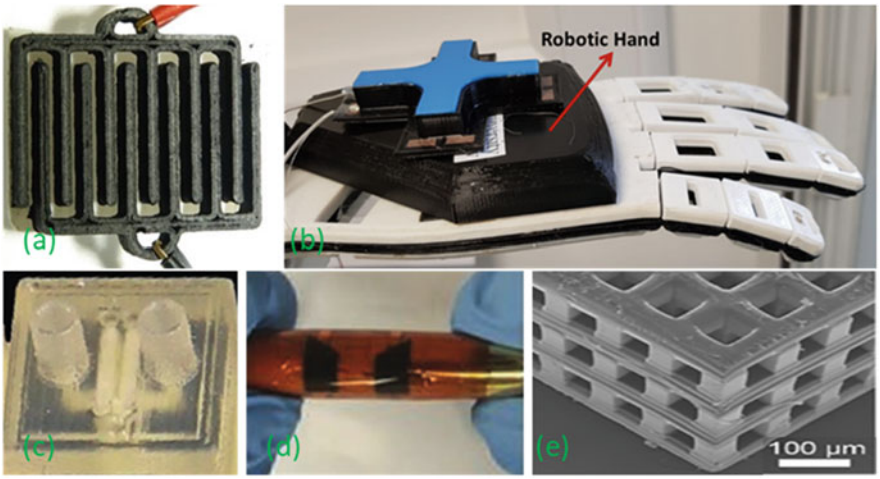

Fig. 8.4 (**a**) PLA/graphite capacitor. Reprinted under the Creative Commons CC BY from Ref. [44]; (**b**) 3D printed tilt sensor setup on a robotic hand. Reprinted under the Creative Commons CC BY from Ref. [46]; (**c**) 3D printed resistors through solder paste filling and postcuring. Reprinted under the Creative Commons CC BY from Ref. [30]; (**d**) RGO-CNT-PEDOT flexible supercapacitor, Copyright 2020, Wiley. Reproduced with permission Ref. [47]; (**e**) SEM image of 3D printed electrode for a micro-supercapacitor. Reprinted under the Creative Commons CC BY from Ref. [48]

(17 wt.% EDOT) resin isolated through an oxidative layer fabricated in the post-processing with a ferric chloride hexahydrate bath was also reported [48].

8.2.4 Inductors

3D printed embedded inductors can be fabricated, as previously reported, by injecting metal paste in a 3D printed microfluidic channel (Fig. 8.5a) that has the shape of a spiral coil [30].

Interesting advances have been reported in the field of 3D printing inductors, power coils, and transformers. As soon as multimaterial co-printing became no more prohibitive, it has been demonstrated by Lazarus et al. [49] that in multistage 3D printing process, it is possible to include magnetic core material as ferrofluids with the purpose of increasing the inductance and the coupling factor. Microfluidic channels were 3D printed (Fig. 8.5b) through a high-resolution 3D micro-stereolithographic printing technique, to fabricate a toroidal structure, successively filled in with liquid gallium alloy. The electrical performances were tested, and it was demonstrated that the ferrofluid inclusion (Fig. 8.5c) led to a significant increment in the electrical inductive properties such as in the inductance values and quality factor.

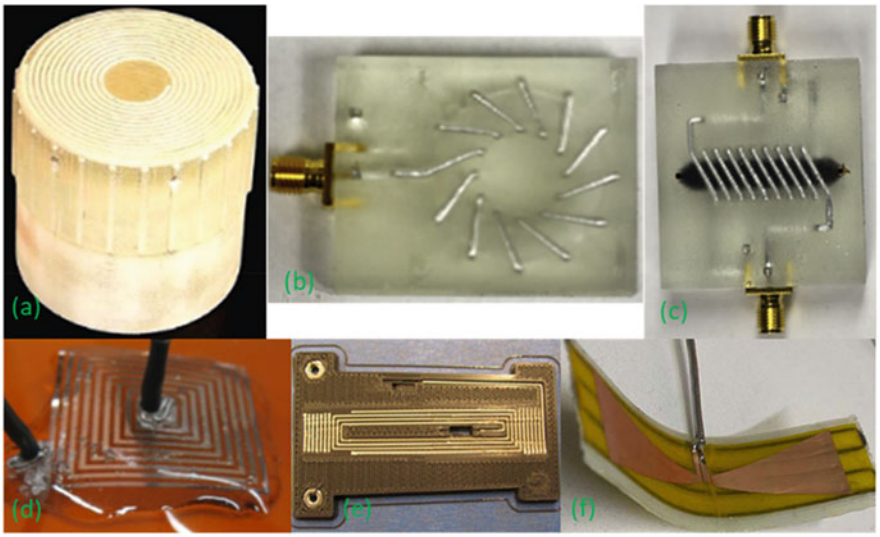

Fig. 8.5 (**a**) Solenoid-shaped inductor. Reprinted under the Creative Commons CC BY from Ref. [30]; (**b**) 3D printed metal windings of a toroid with 12 turns; (**c**) 3D printed metal windings of a solenoid with nine turns around the magnetic ferrofluid core. Reprinted from Ref. [49], Copyright (2019), with permission from Elsevier; (**d**) 3D printed planar inductor with contacts; (**e**) 3D printed metal/insulator wireless charge transfer. Reprinted under the Creative Commons CC BY from Ref. [50]; (**f**) deformable and stretchable antenna. Reprinted under the Creative Commons CC BY from Ref. [51]

Inkjet printing has extensively been used to print planar inductors, as reported in Fig. 8.5d on a Kapton substrate, for instance, exploited in the final application as an eddy current positioning transducer, although it is remarkable the reproducibility offered by this technology [52].

Commercially available 3D printers [53] for electronics offer more standardized multimaterial FDM 3D printing process [54], by using PLA and silver paste, respectively, as insulating and conductive materials. The final inductor, reported in Fig. 8.5e, has been printed on a multilevel geometry, taking advantage by the slicing operation, to produce a 3D inductor in which windings have more complex and curvilinear shape [50].

Further investigating advantages of 3D printing inductors, the focus should be moved onto antennas. In Fig. 8.5f, a 3D printed thermodeformable bowtie antenna is reported. This particular 4D printed device ensures reconfigurable RF tuning properties to the final application, due to the thermal control of the carbon fiber composite substrate [51].

8.3 Active Elements

In electronics, an active component is an element capable of supplying electrical energy to a circuit. They are components capable of providing a power gain; they inject power into the circuit and can control the flow of current (or energy) within it. This category of components includes several examples such as transistors, diodes, light-emitting diodes (LEDs), batteries, integrated circuits, silicon-controlled rectifiers, and operational amplifiers.

The world of mass electronics has led to the development of standard manufacturing processes for these components, in order to guarantee efficient supplies both technically and economically. However, in this field, there is a lot of research on the possibility of using additive manufacturing techniques to produce nonstandard active components, the production of which with traditional processes would not be allowed or would be expensive. In fact, AM (amplitude modulation) techniques make it possible to investigate new products, guaranteeing flexibility in the process and in the design.

This section presents the most significant research of active electronic devices developed with AM methods, evaluating manufacturing methods and future challenges. Transistors, LEDs, and batteries will be discussed.

8.3.1 Transistors

A transistor is an electronic semiconductor device that allows the control of an output signal by an input signal. Transistors are devices controlled both in closing and in opening, generally they have three terminals: source, drain, and gate electrodes. There are different types depending on the various applications (e.g., BJT (bipolar junction transistor), MOSFET (metal-oxide semiconductor field-effect transistor), and IGBT (insulated gate bipolar transistor)). The performances of a transistor are linked to several parameters such as carrier mobility, threshold voltage, and on/off ratio.

In a field-effect transistor (FET), current conduction occurs at the two ends (called “source” and “drain”) of a semiconductor layer called “channel”; the current flowing between the source and the drain is proportional to the gate control voltage, so that the FET can be considered a transconductance amplifier. The metal-oxide semiconductor field-effect transistors (MOSFETs) are a variant of the FETs.

Traditional manufacturing methods for transistors involve flexographic printing, gravure printing, and offset lithography because these techniques, with their high printing speed, are suitable for mass production [55]. At the research level, different AM techniques have been used to produce transistors, such as inkjet printing and aerosol jet printing. The paradigm is therefore different from industrial production; in fact with AM techniques, there is greater freedom to try and experiment with new materials or set of materials for substrates or different dielectrics [56]. These

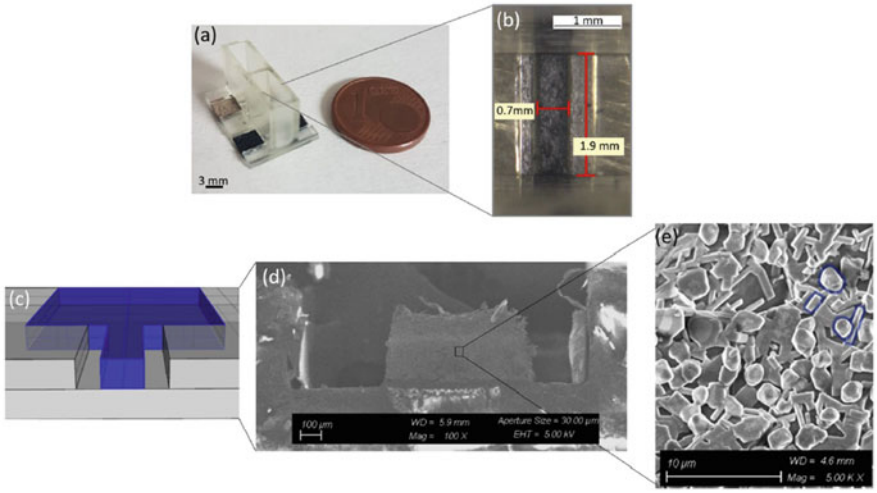

Fig. 8.6 3D printed OECT. (**a**) Image of device after printing and (**b**) microscope image of the 700 µm-wide channel; (**c**) scheme view of the 700 µm-wide channel geometry; (**d**) FESEM image of the channel and (**e**) of the PEGDA:PEDOT polymerized resin in which the PEDOT particles are highlighted in blue. (Reprinted under the Creative Commons CC BY from Ref. [59])

techniques show various advantages on which research is focused: first of all, they allow avoiding material waste; they also allow great flexibility in the design of the devices, guaranteeing different possibilities of customization.

Rother et al. [57], using aerosol jet printing of polymer-sorted (6,5) semiconducting carbon nanotubes with a toluene/terpineol solvent mixture, demonstrated the construction of an ambipolar FET. They obtained a device with high on/off ratios at low operating voltages. Another example of aerosol jet printing is reported in Kim et al. [58], in which the production of an electrolyte-gated transistors (EGTs) based on the polymer semiconductor poly(3-hexylthiophene) (P3HT) is described. They obtained on/off current ratios of 10^6, off currents of $<10^{-10}$ A ($<10^{-6}$ A cm^{-2}), saturation hole mobilities of 1.3 cm^2 V^{-1} s^{-1}, threshold voltages of −0.3 V, and subthreshold swings of 70 mV decade^{-1}.

Another AM technique used in this field is stereolithography. As a matter of fact, Bertana et al. [59] demonstrated an organic electrochemical transistor (OECT) using a composite resin of PEDOT:PSS and PEGDA. The device is shown in Fig. 8.6a and subsequently. The OECT, built for dopamine detection, showed a good sensitivity of 0.41 V/dec.

Despite these examples, the most used AM technique in this sector is certainly inkjet printing. The benefits of this technique are linked to the possibility to dispense only the required amount of material, without generating waste. Furthermore, it is characterized by a highly selective patterning nature [60]. Inkjet printing does not need a mask as traditional processes, so it allows easy customization.

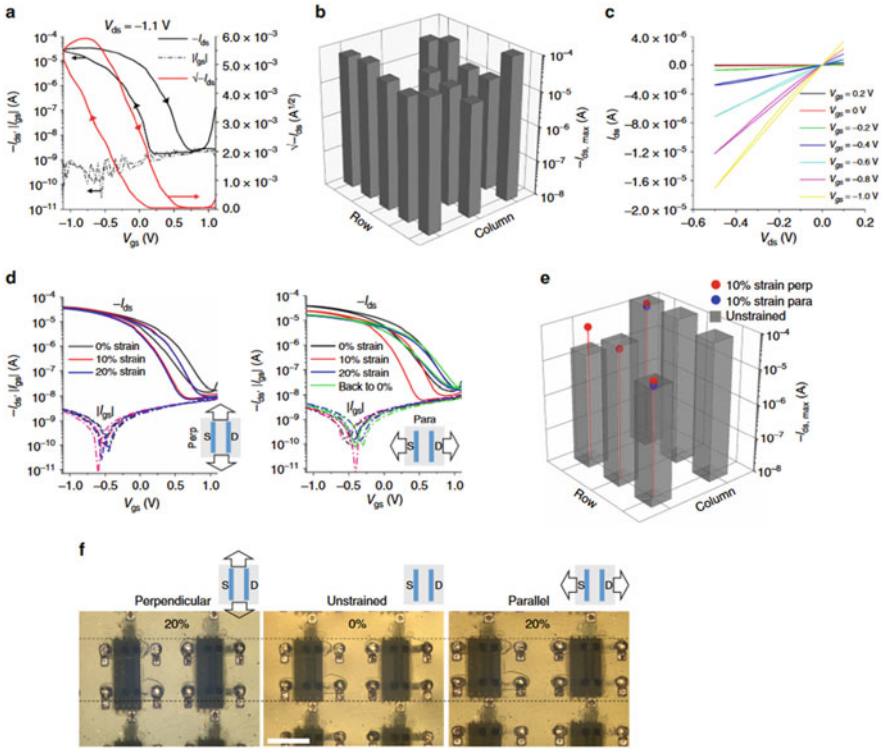

Fig. 8.7 (**a**–**e**) Electrical characterization of the printed FET; (**f**) some optical microscope images of the transistors stretched at 20% strain along the two main directions (perpendicular and parallel). (Reprinted under the Creative Commons CC BY from Ref. [62])

Ready et al. [61] printed a FET using an inkjet printing technique based on organic semiconductors, nano-metals, and polymer dielectrics. Using inkjet printing of polymers and CNT, Molina-Lopez et al. [62] produced stretchable transistor arrays with mobilities of 30 cm2 V − 1 s − 1 (Fig. 8.7).

Kim et al. [63] demonstrated the production of a single-crystalline organic thin-film transistor (TFT) using inkjet printing. The transfer characteristic of the TFT is shown in Fig. 8.8a, b. The device shows extracted field-effect mobility of 0.6 $cm^2\ V^{-1}\ s^{-1}$ with on/off current ratio of $10^5 \sim 10^6$ and subthreshold slope of 0.4∼0.9 V $decade^{-1}$.

Exploiting inkjet printing, Sirringhaus et al. [64] demonstrated a complete transistor circuit based on solution-processed polymer conductors, insulators, and self-organizing semiconductors. The device has a mobility of 0.02 $cm^2\ V^{-1}\ s^{-1}$ with on/off current ratio of 10^5.

A particular example of MOSFET produced by inkjet printing at room temperature is presented by Dasgupta et al. [65]. Their device has a field-effect mobility of 0.8 $cm^2\ V^{-1}\ s^{-1}$.

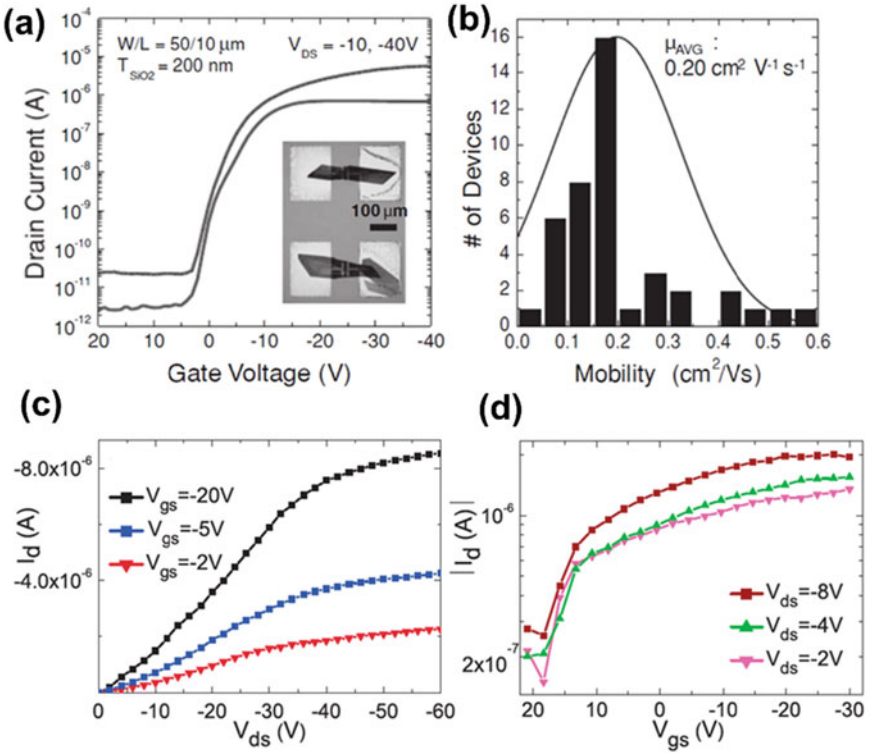

Fig. 8.8 (**a**) Transfer characteristic ($\log(I_D)$– V_{GS}) of a single-crystal TIPS (triisopropylsilylethynyl-substituted)-pentacene TFT fabricated with surface-patterned channel region (image in the inset with scale bar 100 µm). (**b**) Statistic data of field-effect mobility from 42 TFT devices. Reprinted from Ref. [63], Copyright (2012), with permission from John Wiley and Sons. (**c**) Output and (**d**) transfer characteristic of the inkjet printed graphene-based TFT. Reprinted with permission from Ref. [69]. Copyright 2012 American Chemical Society

Basiricò et al. [66] reported the fabrication of two kinds of organic transistors on transparent, flexible plastic substrate using inkjet printing. The devices, an organic thin-film transistor (OTFT) and an organic electrochemical transistor (OECT), used PEDOT:PSS as conductive ink and were assembled on polyethylene terephthalate (PET) substrate. They reported hole's mobility up to 7.8×10^{-3} cm^2 V^{-1} s^{-1} and Ion/Ioff ratio up to 10^4 for p-type device and electron mobility up to 3.7×10^{-3} cm^2 V^{-1} s^{-1} and Ion/Ioff up to 10^3 for n-type device.

A very promising research field for the inkjet printing technique concerns the use of graphene-based inks [67]. Carey et al. [68] demonstrated the production of FETs with graphene and hexagonal boron nitride (h-BN) inks. The devices achieved an average field-effect mobility of 150 ± 18 cm^2 V^{-1} s^{-1} when printed in a coplanar structure on PET and 91 ± 29 cm^2 V^{-1} s^{-1} on polyester textile. Torrisi et al. [69] produced thin-film transistors with graphene-based ink on Si/SiO_2 and borosilicate

glass substrates. The graphene-based ink was produced by liquid-phase exfoliation of graphite in N-methylpyrrolidone. Their devices, contacted with chromium/gold source and drain pads, had mobilities up to ~95 $cm^2\ V^{-1}\ s^{-1}$. In Fig. 8.8c, d, the output characteristics measured at $V_{gs} = 2$, 5, and 20 V and transfer characteristics measured at room conditions at different drain voltages ($V_{ds} = 2$, 4, and 8 V) are shown.

Inkjet printing is therefore enjoying great success in laboratory research as it shows excellent results and offers significant advantages. There are still several requirements to be met in order to bring the technology to an industrial level. Remarkable developments are reported on the improvement of soluble materials (conductive, insulating, and semiconductor inks), of the electrical performance, and of the device yield.

However, significant breakthrough is still needed to match the performance of transistors produced with conventional deposition or photolithography methods [70].

8.3.2 Batteries

A battery is a device that converts chemical energy into electrical energy through a redox reaction. Batteries are typically composed of the following elements: a positive electrode, a negative electrode, a liquid electrolyte, and polymer-based separators. There are different types of batteries depending on the materials used inside: alkaline, lithium, lithium polymer, nickel-cadmium, nickel-metal hydride, and zinc-carbon. Differences in construction may also relate to the final shape of the device; there are cylinder, coin, or rectangular batteries.

Blade coating is the most used industrial process to fabricate batteries [71]. Actually industrial batteries are not suitable for futuristic applications, like wearable or embedded electronics. Additive manufacturing offers an important opportunity to develop new kinds of batteries and allows researching new materials, new shapes, and new packaging. Pang et al. [72] reported some advantages that AM techniques can offer: they allow complex structures, they offer a precise control of electrodes' shape and thickness, they are easy to operate, and they offer the possibility to directly integrate the batteries in other structures.

Several AM techniques are used in order to fabricate batteries, for example, inkjet printing, direct ink writing, fused deposition modeling, and aerosol jet printing.

Using inkjet printing of silicon nanoparticles, Lawes et al. [73] demonstrated the fabrication of silicon anodes for lithium-ion (Li-ion) batteries. In the formulation of the inks, they used silicon nanoparticles and carbon black, and they tried different polymer binders (PEDOT:PSS, PVP, CMC, and sodium alginate), always with a ratio, respectively, of 2:2:1 by weight. The formulation with PEDOT:PSS offered the best performances. The device shows good performances with a capacity of >1700 mAh g^{-1} for 100 cycles and good stability over 1000 operational cycles. A 3D inkjet printed lithium-ion battery based on $LiMn_{0.21}Fe_{0.79}PO_4$@C (LMFP)

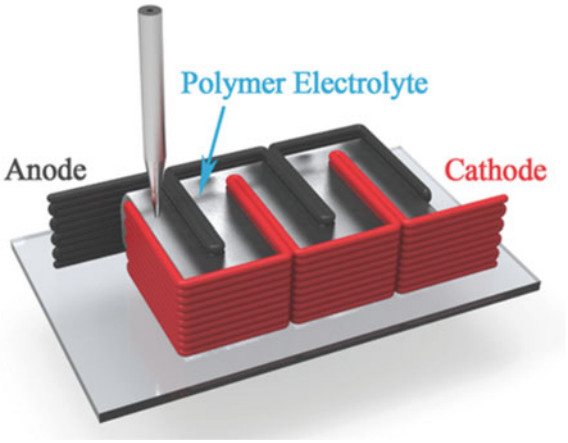

Fig. 8.9 Deposition for the lithium-ion battery. (Reprinted from Ref. [75], Copyright (2016), with permission from John Wiley and Sons)

nanocrystal cathodes was demonstrated by Hu et al. [74]. Their ink was composed of carbon black, LMFP, and PVDF (polyvinylidene difluoride) dissolved in in N-methylpyrrolidone (NMP). The device had excellent electrochemical performance: a capacity of 108.45 mAh g^{-1} at 100 C and a reversible capacity of 150.21 mAh g^{-1} at 10 C after 1000 cycles. Fu et al. [75] demonstrated a lithium-ion battery (Fig. 8.9) using direct ink writing to pattern their graphene oxide ink for electrodes. For the electrolyte, they used an ink composed of a mixture of poly(vinylidenefluoride)-co-hexafluoropropylene (PVDFco-HFP) and the Al_2O_3 nanoparticles.

Another AM technique used to print batteries is aerosol jet printing (AJP). Saleh et al. [76] fabricated a hierarchically porous lattice electrode through AJP of silver nanoparticles in order to enhance the electrolyte transport through the electrode volume and to increase the available surface area for electrochemical reaction. This structure showed excellent mechanical robustness; as a matter of fact, the morphology remained stable after 40 cycles.

Other research opportunities for batteries are offered by FDM technology. Reyes et al. [77] produced via FDM printing anode, cathode, and separator lithium-ion coin batteries. They used PLA infused with a mixture of ethyl methyl carbonate, propylene carbonate, and $LiClO_4$, and they obtained an ionic conductivity 0.085 mS cm^{-1}. C.W. Foster et al. [78] demonstrated graphene/PLA electrodes for Li-ion batteries using FDM printing.

From the given examples, it can be deduced how different AM techniques can be used depending on the optimization objectives that are pursued. In fact, in order to build an efficient energy storage device, it is necessary to consider that each device has its own criticalities such as the hierarchical assembly of the components or particularities on electrodes, separators, and electrolytes. For example, Gulzar et al. [79] underlined that a big amount of capacitive charge storage material is useful if the printed material is sufficiently electrically conductive and mass loading within the feed material prior to printing is considered.

In addition to the criticalities of the devices, it is necessary to consider those of the AM techniques; in fact, each printing method has a unique way of printing an object using specific feed material. For each application, the choice of the best coupling between the device to be printed and the printing technique must be carefully considered.

However, as in the case of transistors, despite the unexceptionable advantages that AM techniques can offer and are expected to offer in the future, currently, they do not yet represent an industry standard. More research is required to meet the power, energy, packaging, interconnect, form factor, and cost requirements of traditional technology.

8.3.3 LEDs

A light-emitting diode (LED) is an electronic device capable of converting electrical input into light emissions. From the physical point of view, an LED is a chip of semiconductor material doped with impurities to form a positive-negative (P-N) junction: the positive pole is called anode, while the negative one is called cathode.

A typical structure of an LED has three layers, of which two electrodes (anode and cathode) and an electroluminescent material are placed between them. There are different declinations of LED technology, such as organic light-emitting diodes (OLEDs) or quantum dot light-emitting diodes (QLEDs).

Traditionally, these devices are fabricated using classical techniques, for example, spin coating. However, AM techniques can represent a great opportunity for the development of various types of LEDs, as they allow to experiment with new shapes and new materials. The most used technique is certainly inkjet printing.

As far as LEDs are concerned, the inkjet technique involved studies on the types of inks or on the types of substrates. An example of the first case is proposed by Bao et al. [80] who developed a $CsPbBr_3/Cs_4PbBr_6$ ink in order to print mini-LED arrays. The device emitted strong green light at 525 nm. Some research has been developed also on the substrate to print on. As a matter of fact, an interesting example is represented by the research of Gu et al. [81] who inkjet printed perovskite inks into the liquid polydimethylsiloxane (PDMS) precursor.

Kong et al. [82] demonstrated a five-layer QLED with pure and tunable color emission properties on a curvilinear surface like a contact lens. Figure 8.10 shows the CAD model (a), the printed version (c – insert), and the characteristics of current density vs voltage. In order to improve the performances, they studied the layer thickness and uniformity and the ink formulations, and they used an inert printing environment. The device can emit light with a brightness of 100 cd m^{-2} at 4.5 V.

Liu et al. [83] demonstrated a QLED with a low turn-on voltage of 2.0 V, a luminance of 12,100 cd m^{-2} at the voltage of 12 V, and a maximum current efficiency of 4.44 cd A^{-1} at the luminance of 1974 cd m^{-2}. They built the device by inkjet printing poly(N,N′-bis-4-butylphenyl-N,N'bisphenyl)benzidine (poly-TPD) layer and mixed solvents of decane and cyclohexylbenzene. Xiang et al. [84]

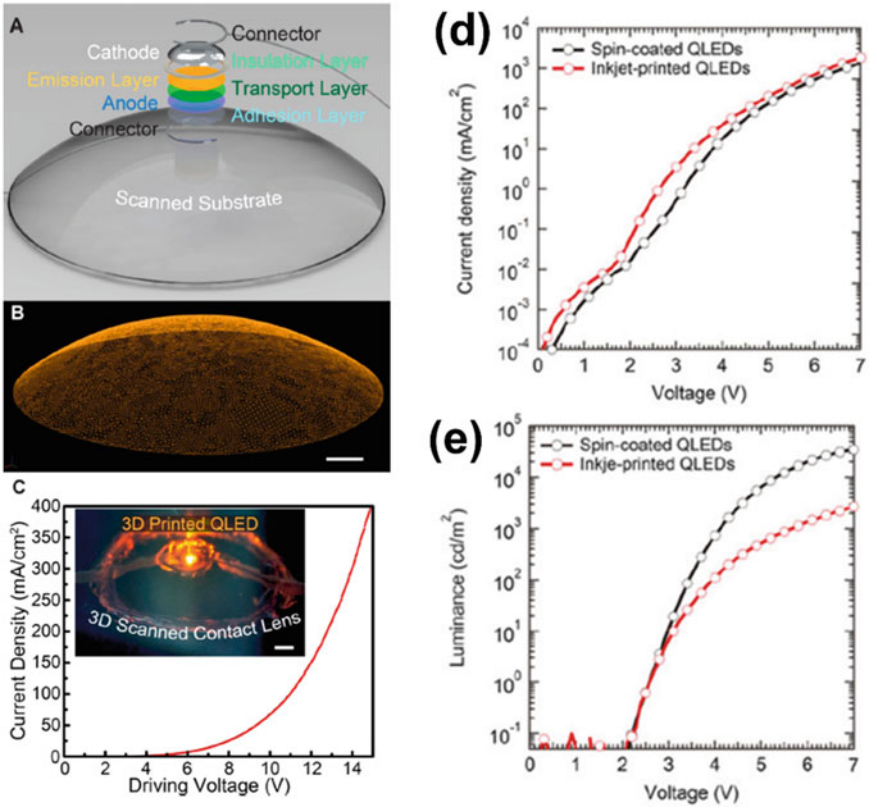

Fig. 8.10 (**a**) Scheme of 3D printed QD-LED on a 3D-scanned curvilinear substrate. (**b**) A 3D model of a contact lens. (**c**) Current density vs voltage of the 3D printed QD-LED on top of the scanned contact lens (electroluminescent image in the inset). Reprinted with permission from Ref. [82]. Copyright 2014 American Chemical Society. (**d**) Current density vs voltage characteristic comparison between spin-coated and inkjet printed QLEDs; (**e**) luminance vs voltage characteristic comparison between spin-coated and inkjet printed QLEDs. Reprinted from Ref. [85], Copyright (2016), with permission from John Wiley and Sons

reported a QLED with an external quantum efficiency over 16% and half lifetime of more than 1,721,000 h.

Han et al. [85] compared the performance of a QLED obtained through inkjet printing with one made with spin coating. The results, shown in Fig. 8.10d, e, point out that the current density of the inkjet version QLED is bigger than the spin coating version that is motivated by the ink composition. For what concerns the luminance, the situation is the opposite.

Yang et al. [86] reported a QLED display that emitted green light at a maximum luminance of 3000 cd m^{-2} at a peak current efficiency of 2.8 cd A^{-1}.

Another important kind of LEDs is the OLEDs. The traditional manufacturing process of these devices involves the thermal sublimation of organic materials in an

ultrahigh vacuum environment onto transparent substrates [87], but that process is time consuming, so also in this case, inkjet printing can be an important option to innovate. As a matter of fact, several examples can be reported also in this case [88, 89].

8.4 Sensors

The current improvements in technology and device connectivity brought the sensors to have a significant role in many different aspects of human life. This growing role has requested the possibility of fabricating sensors with complex geometries, and different functionalities are fully conformable to the substrate to be mounted on. Additive manufacturing technologies have attracted enormous attention for their ability to directly realize complex functional objects with a simple, low-cost, and free shape creation approach. Depending on the functional material used in the printing, the device can transduce physical quantities such as deformation, force, temperature, and chemical quantities related to the presence of liquid or gas species, ions, or biomolecules into an electrical signal. Because of the possibility to fabricate highly complex-shaped devices, sensors realized with additive manufacturing techniques have been mostly implemented for wearable health monitoring (body motion and temperature, heart and respiration rate, blood pressure, etc.). In addition, printed sensors have found applications even in automotive, chemical, and food industries as well as for environmental monitoring. In the following sections, four different classes of sensors fabricated with additive manufacturing technologies are described with a focus on the physical transduction mechanism implemented.

8.4.1 Mechanical Sensors

This class of sensors is related to the detection of mechanical parameters such as strain, pressure, force, and displacement. Several examples of strain gauges and tactile sensors have been fabricated with 2D printing technologies like inkjet and different 3D printing approaches to detect deformations. The great advantage with respect to standard strain gauges, mostly limited to work on flat surfaces because of their limited mechanical coupling, is the possibility to directly fabricate the final device on each type of complex-shaped device or to create sensors with conformable shapes and high deformability. Additive manufacturing strain gauges are mainly fabricated exploiting piezoresistive effect as transduction mechanism. Piezoresistive devices experience an electrical resistance variation when a strain is applied, due to geometrical or resistivity variation. Devices fabricated with inkjet technology are prepared with conductive inks composed of carbon-based nanoparticles such carbon black (CB), carbon nanotubes (CNTs), or graphene sheets, metallic nanoparticles

(mainly silver), or even conductive polymer (PEDOT) [40, 90–93]. 3D piezoresistive sensors are fabricated with conductive polymers, composites of thermoplastic polymers, and conductive fillers or conductive hydrogels [94] working as sensitive materials, often in combination (multimaterial printing) with insulating polymers used as packaging and support [95]. An interesting example of sensors printed with a combination of materials with different conductivities was presented by Guo and co-workers [96]. They presented a multimaterial and multiscale tactile sensor fabricated with direct ink writing (DIW) where bare silicone elastomer ink was used for the insulating and base layer, while top and bottom electrodes were printed with an ink composed of silicone and silver nanoparticles (Ag NPs) in a concentration above percolation threshold to ensure a good conductivity. The sensing layer was printed in a spring shape with a silicone/Ag NP composite ink in a ratio suitable to enhance the piezoresistive properties. The final device (Fig. 8.11a) showed the capabilities of detecting and differentiating human movements, including pulse monitoring and finger motions. An alternative approach was proposed by Agarwala et al. who fabricated by DLP approach a polymeric structure with empty microchannels in the core [97]. The microchannels were then filled with Ag NP ink acting as sensing element [98]. The printed sensor resulted sensible to normal (orthogonal to channels) and in-plane (parallel to channels) deformation with a gauge factor of 50 and maximum elongation of 18%.

Another class of printed strain sensors is based on the capacitive transduction mechanism. In this case, the device is composed of two electrodes separated by a dielectric medium. If the device is composed of flexible materials, an applied strain or force causes a geometry variation and thus a change in the sensor capacitive value. Capacitive tactile sensors show high sensitivity and low power consumption but are susceptible to interference from surrounding objects on their internal electric field [99]. Additive manufacturing technique is widely used in capacitive mechanical sensors to fabricate the electrical conductors (example in Fig. 8.11b) [100, 101], the dielectric layer [40], or both the components [102, 103]. An example was shown by Saari and co-workers who combined fiber encapsulation additive manufacturing and thermoplastic elastomer additive manufacturing to create a capacitive force sensor [104]. The final device was composed of two rigid 3D printed frames with embedded conductive wires in a spiral pattern and a soft elastomer spacer working as dielectric that can compress under applied force.

Other two transduction mechanisms used in mechanical sensors are piezoelectricity and triboelectricity. Both the physical mechanisms are highly sensitive and responsive to external stimuli, but they can be used only for sensing of dynamic strain or stress. Since an electrical potential is generated under applied stress, these kinds of sensors do not need external power to be interrogated and can be used as self-powered devices.

Piezoelectric materials generate electric charges on their faces (thus also an electrical potential) in response to an applied stress, but because of leakage current in piezoelectric sensors, the measurement of static deformation would be altered. Most of piezoelectric materials are ceramic, which results in challenging printing, but additive manufacturing techniques can exploit the piezoelectric functionality

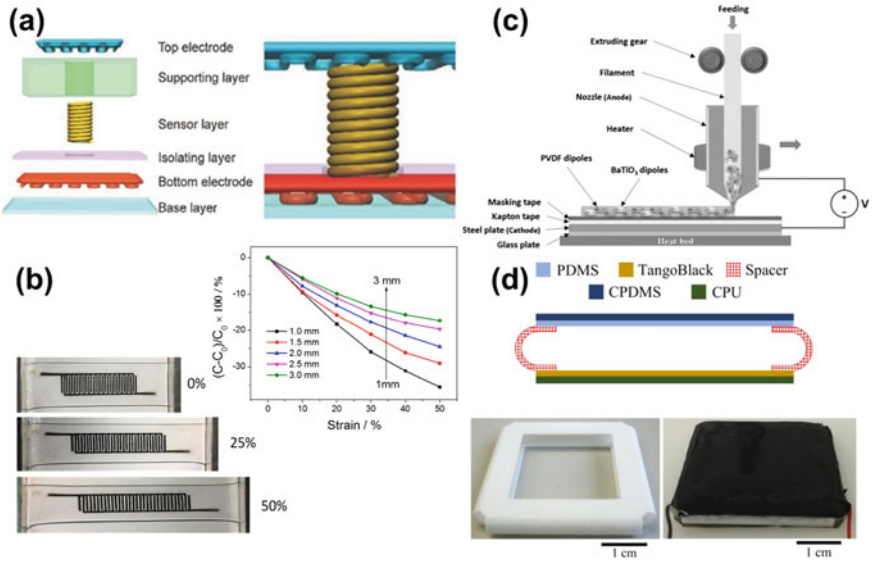

Fig. 8.11 (**a**) Scheme of the piezoresistive tactile sensors fabricated using a multimaterial DIW approach with a sensing layer designed in a spring shape. Reprinted from Ref. [96], Copyright (2017), with permission from John Wiley and Sons. (**b**) Images of capacitive sensors fabricated with CNT/Ecoflex printable ink under different tensile deformations. In the inset, the relative capacitance variation as a function of relative strain is reported. Reproduced from Ref. [101], with permission from the ©2018 IOP Publishing Ltd. All rights reserved. (**c**) Scheme of the electric poling-assisted additive manufacturing (EPAM) process used for the fabrication of PVDF/$BaTiO_3$ composite piezoelectric sensors. Reprinted from Ref. [108], Copyright (2017), with permission from John Wiley and Sons. (**d**) Scheme and image of a triboelectric tactile sensor where additive manufacturing technology was used to print both the two functional triboelectric layers and the spring structure used as spacer. Reprinted from Ref. [111], Copyright (2018), with permission from Elsevier

of some polymers, like polyvinylidene fluoride (PVDF) or its copolymer PVDF-TrFe [105–107] or organic-inorganic composites containing piezoelectric ceramic nanoparticles like PZT, $BaTiO_3$ [108, 109], and boron nitride [110]. A piezoelectric material, to work in a direct mode (which generates charges under mechanical deformation) as requested for a sensor, needs a poling step which aligns the dipoles to obtain the best response. This step is time consuming and needs the application of high electric field and temperature to the material. A great advantage of the additive manufacturing technology of piezoelectric materials is the possibility of poling the material directly during the printing step, applying an electrical potential between the substrate and the printing head. Kim and co-workers demonstrated that by electric poling-assisted additive manufacturing (EPAM) process (Fig. 8.11c), a combination of FDM printing and electrical poling process is possible to 3D printed PVDF/$BaTiO_3$ composite piezoelectric sensors with a PVDF β-phase (i.e., piezoelectric phase) content above 50% in a single fabrication step [108]. The

printed device showed the generation of electrical current under a periodic applied compression demonstrating its applicability as pressure sensor.

Triboelectric sensors are composed of two materials with different triboelectric polarities. The exploitation of these phenomena is recent, but it has already been widely implemented for sensing and energy harvesting applications. When the two layers touch under mechanical deformation, the friction induces a charge generation and thus an electrical potential. Since the charge generation happens only in the touch and release moment, these devices cannot sense a static stress. Triboelectric devices do not need any poling step, but only the correct choice of material pair, which represents an advantage with respect to piezoelectric sensors. One of the first examples of triboelectric sensors was proposed by Haque et al. where they 3D printed both the two functional triboelectric layers and the spring structure used as spacer (Fig. 8.11d) [111]. The device generates 1.2 mW peak power under hand tapping whereas 62.9 μW under finger tapping.

8.4.2 Temperature and Humidity Sensors

Nowadays, local temperature sensing finds many applications in wearable health monitoring, as well as industrial and environmental applications. Most of temperature sensors show a dependency also on humidity as well. This sensitivity represents an advantage for fabricating multifunctional sensors but requires a proper calibration to separate the contribution for both physical quantities [112]. Several inks for 3D printing technology have been implemented for a variety of capacitive or piezoresistive multifunctional sensing applications. Temperature causes a physical dimension variation of the dielectric layer or insulating matrix in composite-based devices, while humidity alters the intrinsic conductivity of the sensing materials adding water molecules on the sensor surface or bulk [113]. An interesting example of multifunctional sensing platform was presented by Quintero et al. based on inkjet printed fabrication on flexible polymeric substrates [114]. Using different printing inks, the multisensing platform was provided with four independent and calibrated sensors, a capacitive humidity detector, one resistive sensor for temperature sensing, and two other resistive-based gas sensors for ammonia detection. Another example of decoupling physical sensing quantities was presented by Chen and co-workers [115]. They printed, by FDM approach, a self-sensing actuator made of nanocarbon black/polylactic acid composites. Measuring actuator electrical resistance, they were able to decouple thermal and strain variations based on the different response time.

8.4.3 Chemical and Gas Sensors

The printing of conductive polymers or materials such as polyaniline (PANI), CNTs, graphene oxide, and metal nanoparticles has been widely used in chemical sensing as these materials readily absorb molecules into their surface or interior causing a change in their electrical or electrochemical responses [93, 94, 116]. Most of these resistive or capacitive sensors are sensitive to multiple gases, and thus they need to tailor their sensitivity and selectivity responses for different analyte compounds. Therefore, above the conductive layer, a functionalization step is performed, or an additional membrane or coating is printed to be sensitive to the gas that needs to be detected [117, 118]. An example of 3D printed gas sensor for ammonia detection was presented by Zhou et al. [119]. Firstly, they printed a 3D body-centered periodical mullite structure to ensure a high surface to volume ratio. The device surface was then modified with a polyaniline (PANI) network decorated with Ag nanoparticles (Fig. 8.12a). PANI worked as sensing layer since ammonia molecules can react with the polymer by withdrawing protons, leading to the localization of polarons and increasing the electrical resistance (Fig. 8.12b). Additionally, silver nanoparticles increase the active sites for ammonia molecules adsorption, increasing the sensitivity of the device to concentrations of 10 ppm.

8.4.4 Flow Sensors

Flow sensors for air or liquid motion detection find several implementations in different application fields. Different physical mechanisms are used as transduction method in flow sensors. Leigh and co-workers presented an impeller flow sensor fabricated by multimaterial FDM printing technology based on magnetic field sensing [120]. The main structure of the sensor was printed with polymeric material and then covered with several layers of magnetite composite (Fig. 8.12c, d). Magnetic fluctuations due to paddle rotation induced by flow velocity are detected using a Hall effect sensor.

Another interesting example was proposed by Adamski et al. who fabricated a 3D printed flowmeter based on Venturi effect [121]. In this work, 3D printing technology was used to fabricate the structure of flowmeter composed of fluidic channel in the micrometer range, while sensing was performed with commercial MEMS (microelectromechanical system) pressure sensors. The device was able to measure flow velocity in the 0–1.4 mL/s range.

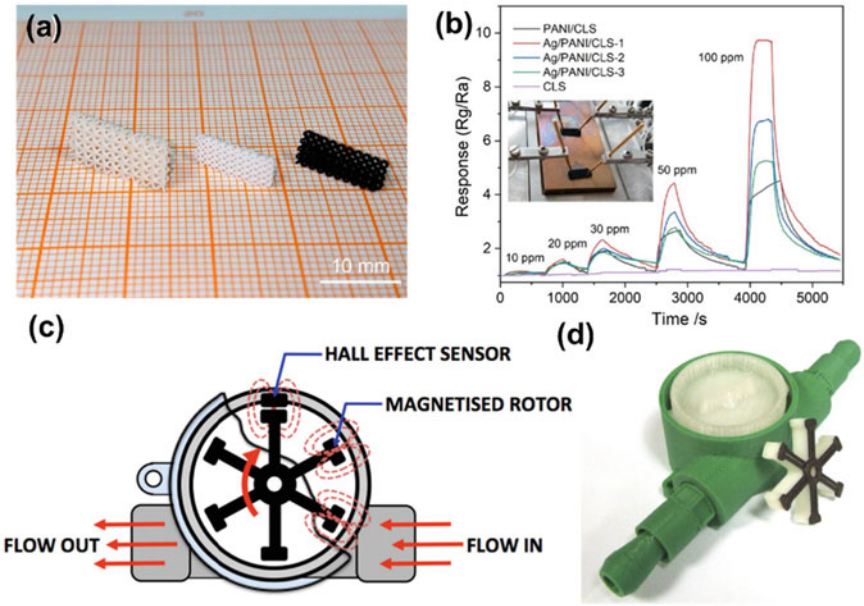

Fig. 8.12 (**a**) Image of the 3D printed body-centered periodical mullite structures before/after pyrolysis and a gas sensor after the deposition of Ag/PANI layer. (**b**) Resistance variation of gas sensors prepared with different sensing layers when exposed to different concentrations of ammonia gas. Reprinted from Ref. [119], Copyright (2020), with permission from Elsevier. (**c**, **d**) Working scheme and image of the 3D printed magnetic flow sensor and impeller. Reproduced from Ref. [120], with permission from the ©2014 IOP Publishing Ltd. All rights reserved

8.5 Actuators

MEMS (microelectromechanical systems) are gaining popularity in modern technological applications. From medical to measuring technologies and microfluidics to the Internet of Things (IoT), they have a wide range of applications. MEMS components are exploited as actuators in various applications, including smartphones and autonomous-driving cars. In comparison to pure microelectronics, MEMS actuator production is less standardized. The method of 3D printing might be one way to overcome this challenge. While the state of art of 3D printing technologies and materials is inadequate for MEMS manufacturing, special applications of 3D printed MEMS actuators lead to the fabrication of novel structures through a faster and cheaper manufacturing process [122, 123]. Different 3D printing technologies are exploited in order to evaluate the printing capability of the process related to the actuator requirements such as FDM with a minimum resolution of 200 μm [124]; SLA with a variable resolution of in the range of 30–70 μm [125]; 3D inkjet, whose reported minimum printed dimension is 28 μm [4]; and two-photon polymerization

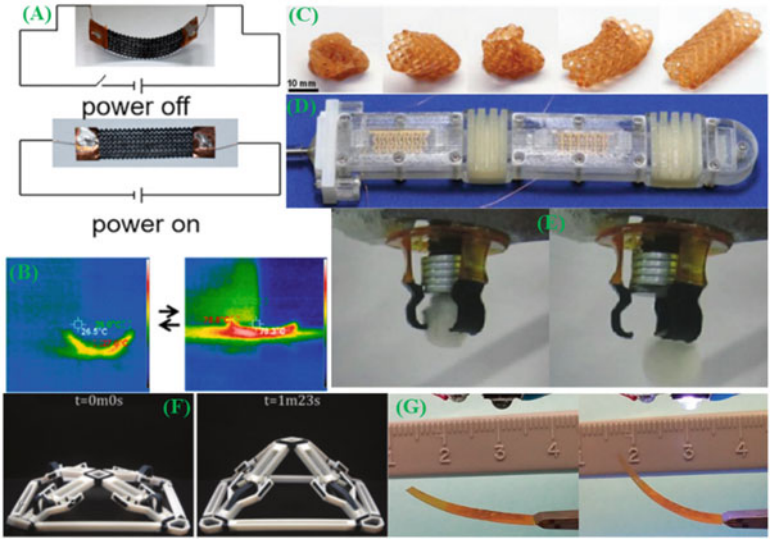

Fig. 8.13 (**a**) Electrically heated deformed actuator and cooled restoring. (**b**) Thermal image of infrared camera showing the heating and cooling processes. Reprinted from Ref. [128], Copyright (2021), with permission from Elsevier. (**c**) Shape memory of 3D printed cardiovascular stent deformations. Reprinted from Ref. [129], Copyright (2015), with permission from John Wiley and Sons. (**d**) Finger assembly of 3D printed electro-actuated micropumps. Reprinted from Ref. [130], Copyright (2017), with permission from Elsevier; (**e**) 3D printed magnetically actuated gripper. Reprinted from Ref. [131], Copyright (2017), with permission from John Wiley and Sons. (**f**) Temperature programmable 3D printed shape memory strips assembly. Reprinted under the Creative Commons CC BY from Ref. [132]; (**g**) UV photoactivated 3D printed actuator. Reprinted with permission from Ref. [133]. Copyright 2018 American Chemical Society

(TPP), which exhibits the best resolution, compared to previous technologies, in the range of 0.28–1.5 μm [126].

3D printing techniques allow for the fabrication of both surface-patterned materials and 3D devices defined as a static structure. While exploiting active materials, the fourth dimension is added to the device resulting in time-dependent shape morphing as a result of a proper conditioning signal, enabling 4D printing [127].

In Fig. 8.13, different 3D printed actuators are reported, which will be described on the base of the actuation principle of each device.

8.5.1 Thermally Conditioned Actuators

4D printing also includes effects of irreversible deformations caused by high-temperature-induced thermoplasticity, enabling the extension of the actuator linearity response range. Zhao et al. [28] proved that the alternate conditioning of

the two-layer structure caused the accumulation of thermoplastic deformations producing a substantial displacement, defined as ratcheting. Finally, they were able to design a 3D printed actuator capable of producing a large displacement if electrically heated, which could be exploited as a bendable framework, whose actuation can be reversed, so a 4D printed system.

As reported in Fig. 8.13c, Zarek et al. [132] 3D printed through high-resolution SLA shape memory oligomers and through DLP liquid resins. The 3D printed cardiovascular stent contained macro-methacrylate, conferring to the object shape memory capability, that is the primary principle in soft robotic applications. When this behavior is induced by a thermal flux, it is due to the physical and chemical molecular cross-linking that fixes the 3D shape. The capability of controlling the alternation of the molecular bonds upon thermal flux confers the time-morphing of the device.

Chen et al. [130] exploited the viscoelasticity of a strip with shape memory properties, to 3D print a programmable actuator able to deform upon thermal flux, considering the polymer preheated above the glass transition temperature. The reversibility of the deformation occurred below this temperature causing the mechanical relaxation of the assembled structure and defining a moving mechanism that is bistable (Fig. 8.13f).

8.5.2 Piezo/Electrically Activated Actuators

Wang et al. [128] 3D printed through FDM a multimaterial device composed of a paper bottom layer and a top graphene/PLA layer (Fig. 8.13a). This object worked as actuator, whose deformation was reversible and controlled by a voltage source, and it was designed with a corrugated geometry. The 4D structure was able of deforming upon the heat dissipation due to the voltage conditioning, generated by the mismatch of the expansion coefficients of the two layers. Heat dissipation due to the cooling effect let the object to assume the initial shape, due to the shape memory effect (Fig. 8.13b).

Both electrical activation and thermal activation are the most common energization forms for 3D printed actuators; in fact different devices were fabricated based on the primer principle [123]. Lee et al. [28] developed through FDM an electrical switching device made of PLA/PVA with excellent electrical and mechanical properties, which can be classified as MEMS. Han et al. [130], as showed in Fig. 8.13d, assembled multiple 3D printed soft and hard polymers with embedded micropumps to electrically activate the motion of a conjugate fluid enabling the electro-hydraulic control of the assembled device, which was a mimicking of the human finger motion in the mm-scale positioning.

Xie et al. [135] 3D printed a scissor-like piezoelectric extension tactile actuator, based on a vibrational transduction system. The scissor geometry was able to

amplify the vibration amplitude, increasing the signal to noise ratio. Based on the piezoelectric actuation, many nm-positioning systems were developed, such as the one reported by Fiaz et al. [136], who 3D printed a classical cantilever structure by E-beam melting of a Ti-6Al-4 V alloy micro-sized powder, and they proved its usage as a rapid and precise stage placement.

8.5.3 Optically Triggered Actuators

Hagaman et al. [133] fabricated a dual-layer structure composed of a Kapton passive layer and a 3D printed layer of photoactive poly-siloxane-based compound, which was referred to as P1 or P2 active material based on the composition. The displacement principle was the cis-trans isomerization due to UV or blue light irradiation, respectively, for P1 and P2. As reported in Fig. 8.13g, the light irradiation caused a change in the shape of the structure leading to the photo-actuation of the 3D printed device. The exhibited morphing was reversible and fast for both structures. Although in P1-based device the bending angle was larger, in the P2-based device, the photo-induced mechanical stress was greater, leading to the conclusion to exploit the latter as a photo-induced stress mechanical displacement transducer.

Lu et al. [137] managed to 3D print by syringe a functionalized liquid crystalline elastomer. This material exhibited excellent shape changing properties, due to transient UV exposure, with stable and long-lasting deformation due to disassociation of isomers. In the end, the mechanical relaxation process was accomplished by thermal treatment. This configures it as a light-programmable actuator.

8.5.4 Magnetic-Driven Actuators

Regarding magnetic actuated devices, Ji et al. [131] investigated a multimaterial 3D printing technique to print directly through DLP a mixture of ferrous-ferric oxidated NPs with photo-resin. Fe_3O_4 particles conferred to the photopolymerized soft material magnetic properties enabling the co-printing of paramagnetic or diamagnetic resins. In Fig. 8.13e, the assembly of the 3D printed, magnetic-controlled actuator capable of bearing and transporting objects upon magnetic actuation is reported.

Bernasconi et al. [138] fabricated through SLA 3D printing and metal electroplating a cantilever based on magnetic metals, and they were able to measure and model the relation between the mechanical deflection and the magnetic field.

8.6 Innovative Applications

Additive manufacturing represents an important choice for the development of novel electronic applications. Many technologies, like FDM, SLA, SLS, and inkjet, are used depending on the characteristics of various materials or applications.

In this paragraph, a review of electronic applications developed using AM techniques is presented. The fields of interest are robotics, wearable, and communications.

8.6.1 Robotics

In the field of robotics, there are several examples of how additive manufacturing techniques can have several advantages over traditional techniques. First of all, the greater freedom of achievable geometries makes AM techniques the most suitable for particular and high-added value applications. In addition, these techniques also facilitate a trend related to 4D printing of intelligent materials. The definition of 4D printing refers to "the change of shape, property, and functionality from a 3D printed structure response to time or external stimulus" [139]. The physical mechanisms that trigger the change in materials are, for example, heat and the presence of water or light or the change in pH. This section will explore soft tactile sensors and actuators.

Soft tactile sensors (STSs) are a new kind of wearable electronic devices which provide the possibility of mechanical signal interaction between the human/machine and the surrounding environments [140].

In the field of robotics, tactile sensors represent an important option for the development of electronic skins. In fact, their use allows transforming mechanical signals (e.g., forces, torsions, vibrations, and pressures) into electrical signals.

To replicate the functionality of the human skin, the requirements of wearable tactile sensors include [141] the following:

- Flexibility, bendability, and stretchability in order to be wearable and skin-attachable on arbitrarily surface shapes.
- High sensitivity and high repeatability of the signal/measure.
- Good linear input-output characteristics.
- Fast response to dynamic loads.

The functioning of the STS is based on different physical principles, and a general classification can concern three main classes of devices: piezoelectric, capacitive, and piezoresistive [99].

Usually, a tactile sensor requires several parts: a sensing element, flexible electrodes, a flexible substrate, and a device packaging. All these parts can be fabricated using AM techniques. As a matter of fact, scientific research has concentrated in recent years on the development of innovative components that comply with the aforementioned constraints. In particular, the most evident

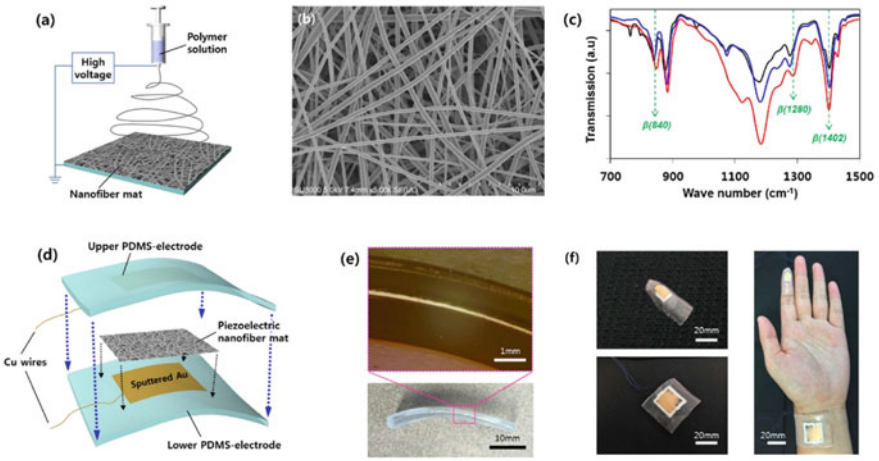

Fig. 8.14 (**a**) Scheme of electrospinning process to build multilayer structure, (**b**) SEM image of fiber mat, (**c**) infrared spectra of electrospun fiber mat, and (**d**) scheme of tactile sensor configuration. (**e**) Image and cross-section of 3D printed sensor. (**f**) Image of the printed sensor in different operative configurations. (Reproduced from Ref. [106], with permission from the ©2017 IOP Publishing Ltd. All rights reserved)

results have been obtained in the search for new materials to develop the sensing element or new processes suitable for various needs.

An important example in the field of tactile sensors is represented by Lee et al., [106]. They developed a skin-conformal flexible tactile sensor, based on human surfaces, with elastomeric sheets integrated with a piezoelectric nanofiber mat. They built the layers in polydimethylsiloxane (PDMS) using 3D printed molds of the various parts of the body of interest (fingers of the hand or wrist) as shown in Fig. 8.14. They managed to obtain a device with similar performance to flat sensors in terms of signal sensitivity and linearity between input and output.

Another example of innovative tactile sensors is the research of Zhang et al. [142]. They demonstrated a fingertip-shape tactile sensor using a piezoelectric composite functionalized with 0.2 wt% boron nitride nanotubes (BNNTs). This device allows haptic sensing through a robotic hand, and it can detect spatial distribution of forces on surfaces. The device reaches a high relative sensitivity of 120 mV/kPa wt% over a broad press region.

An interesting method called embedded 3D printing (e-3DP) to produce strain sensors with elastomeric matrices was developed by Muth et al. [143]. This method involves the composition of a viscoelastic ink, which acts as a resistive sensitive element, inside an elastomeric liquid which acts as a matrix. They demonstrated the method developing several strain sensors with different geometries (e.g., different fingers).

In addition to sensors, it is interesting to evaluate the opportunities offered by AM techniques with regard to actuators in the field of robotics. The actuator can

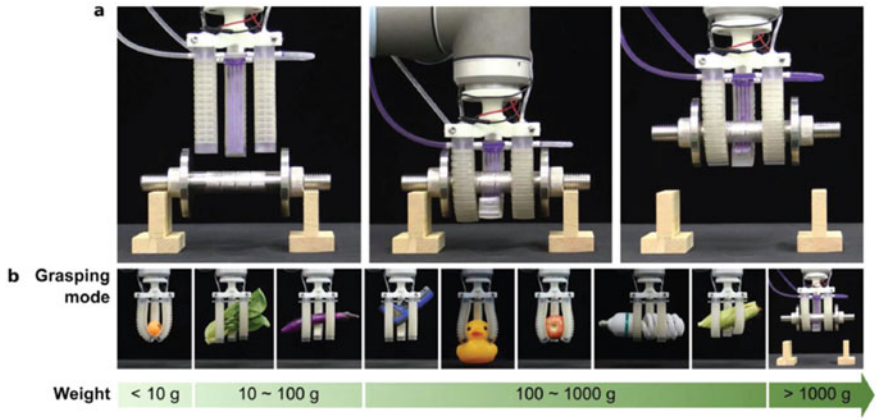

Fig. 8.15 Gripper equipped with three actuators. (Reprinted from Ref. [144], Copyright (2019), with permission from John Wiley and Sons)

be defined as a transducer capable of transforming a signal from a physical domain (typically of the electrical type) into an equivalent quantity belonging to another domain (e.g., mechanical, hydraulic, thermal, etc.). Depending on the physical principle of transduction mechanism, there are different types of actuators: electric, electrostatic, electromagnetic, thermal, and hydraulic. The actuators can be built according to 3D or 4D printing techniques.

Zhang et al. [144] demonstrated a fast-response stiffness-tunable (FRST) soft actuator via multimaterial 3D printing. They built a robotic gripper with three thermal FRST that can grasp and lift objects of several shapes (Fig. 8.15). The maximum load of the device is 1.5 kg.

4D printing is also an important solution for the development of soft actuators for robotics. Wang et al. [29] demonstrated a 4D printed system with mechanical claws, capable of understanding the shapes of objects and to adapt accordingly. The actuator is composed of a bilayer structure of graphene polylactic acid (GPLA) filaments printed on copy paper.

López-Valdeolivas et al. [145] reported the 4D printing of liquid crystalline elastomer (LCE) structures. Thanks to the optimization of the orientation of the FDM printing process, they managed to obtain a control of the actuator response based on external physical stimuli (heat, light, pH, or moisture). Their fabrication process involves an extrusion of the material and the following deposition of tracks with various shapes. These shapes are then subjected to UV photoexposure.

This soft material is an important choice for the actuators because it has important morphing properties. Actuators based on liquid crystal elastomers are used also in Saed et al. [146]. In this paper, the authors used direct ink writing to pattern the 3D structures.

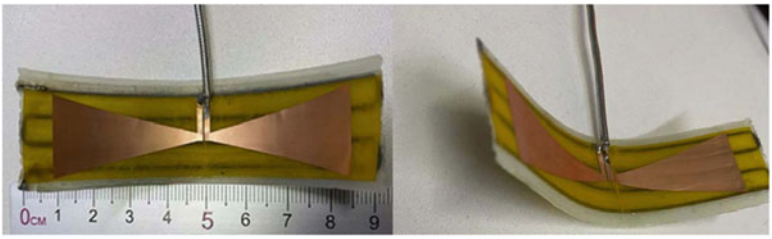

Fig. 8.16 Printed antenna on flexible substrate. (Reprinted under the Creative Commons CC BY from Ref. [147])

8.6.2 Communications

AM techniques can also be exploited for electronic printing in the field of communication. There are several applications in this sector, such as the printing of deformable and shape-changing antennas and RFID (radio frequency identification) sensors.

In the field of antenna printing, 4D printing represents an innovative solution as it allows the creation of devices capable of changing the shape according to the required situations. This allows a great flexibility for final applications. The structural and reversible deformations of the antenna shapes allow new functions, such as the remote control of bending and twisting to reconfigure the antenna according to a specific spectrum.

Wu et al. [147] built a thermo-deformable bow tie antenna using 4D printing. They printed the antenna on the surface of a nylon composite material with carbon fiber that can cause thermal deformation (Fig. 8.16). This paper shows a low-cost way to print antenna capable of changing performance. As a matter of fact, a deformable antenna allows changes in the pattern and frequency to achieve the maximum gain change within a specific range.

Another example of low-cost 3D/4D printed flexible antenna is present in Bito et al. [148]. They built numerous antennas on substrates like paper or polymer (e.g., LCO) via inkjet. This method allows a strong cost reduction.

In addition to antennas, AM techniques can be implemented in many other applications in the communication fields. A sector that is generating a lot of interest at the research level is certainly the printing of RFID sensors. In this context, several aspects must be evaluated according to the various applications. First of all, a first criterion concerns the compatibility between the deposited material and the substrate. Furthermore, the electrical characteristics of the substrate, like relative permittivity or dielectric, must be evaluated over different frequencies and temperatures. In several cases, the most used method is the printing, on paper substrates, of nanoparticles of silver inks. Silver is a good choice for these applications due to its good conductance and low oxidation. Yang et al. [149] studied the silver inks for inkjet application. For what concerns the substrate, paper is a

desirable choice, because it is a low-cost material with high diffusion. Furthermore, paper has an organic nature that allows an easy recycling process.

RFID tags from printed electronics have several applications in different fields, from communication to healthcare, as demonstrated in Sharif et al. [150]. In Kim et al. [151], a good example of printed electronics with silver inks on paper substrate is shown. They reported the printing of RFID tags and RFID-enabled sensors utilizing carbon nanotubes (CNTs). Lakafosis et al. [152] demonstrated the fabrication of RFID tags and wireless sensors via inkjet printing. The developed system on paper was tested on a wide range of frequencies from LF/DC to ultrahigh frequency (UHF) and super high frequency (SHF). Other examples of printed electronics on paper are described in Kim et al. [153], for instance, passive/active electronics, antennas, and scavenging devices.

RFID tags are manufactured also with other techniques, like FDM. Terranova et al. [154] created a RFID tag using PLA filaments with FDM. The tag was metallized on the top and bottom surfaces to confine the electromagnetic field within the cylinder shape.

In addition to RFID tags, another example of application is represented by NFC tags. Balliu et al. [155] used the laser sintering of silver nanoparticle inks that were inkjet printed on paper, to fabricate a NFC tag. Their work focused on the particular use of lasers and to the attention to not burn the substrate by the intense irradiation.

8.6.3 Wearable

In the field of electronics, AM techniques offer many opportunities for innovative applications also in the wearable sector. This generic term indicates all those applications that involve devices in contact with the skin. Consequently, all the devices in this section must guarantee certain performances from the point of view of compatibility with the human skin, such as nontoxicity. A fundamental feature for wearable devices is the presence of flexible supports to best fit on the human surface. Obviously, flexibility requirement concerns not only the physical support but also the printed electronic device.

The applications offered by AM techniques have involved a lot of research in the most diverse applications. In this section, we will present wearable applications related to the demonstration of strain sensors, pressure sensors, supercapacitors, nanogenerators, energy harvesting devices, and energy storage.

Rim et al. [156] reported several examples of wearable strain sensor applications, with devices mounted on different parts of the body, like the hand, the knee, or the neck. There are also formulations that include a mix of sensors; in fact, Gao et al. [157] demonstrated a dual 3D printed strain and pressure sensor. All these sensors show excellent performances: they measure large strain (>20%), they have large gauge factor (>10), and they have fast response time (<30 ms) as demonstrated by Zhang et al. [158].

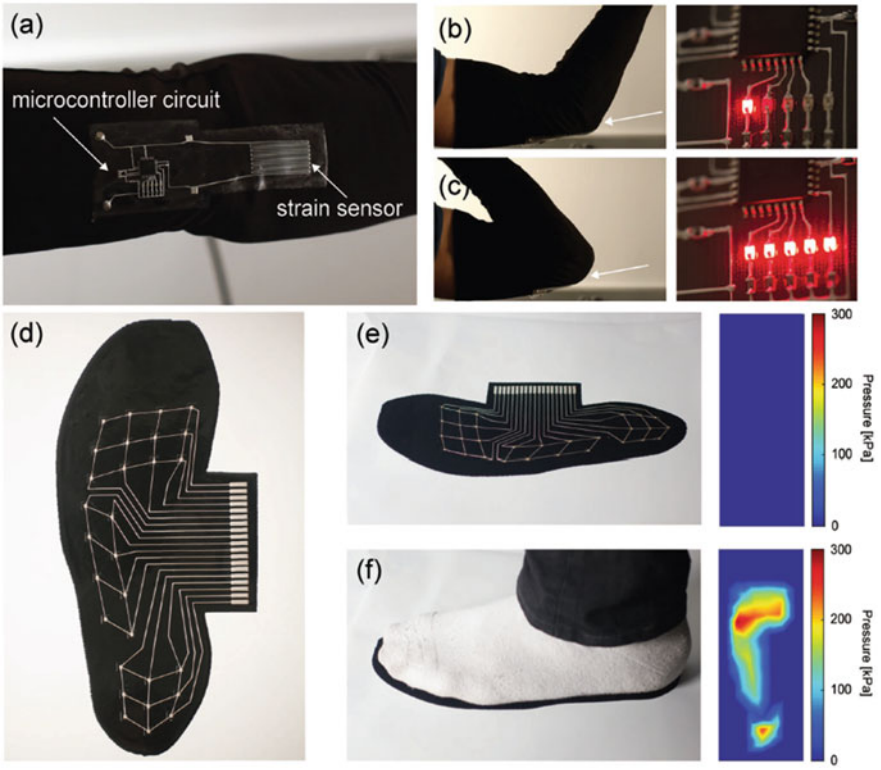

Fig. 8.17 wearable strain sensor. (Reprinted from Ref. [160], Copyright (2017), with permission from John Wiley and Sons)

An example of research on the flexibility of sensor holders is shown in Wang et al. [159]. They used a 3D printed hydrogel film with conductive tape to fabricate the resistive strain sensor.

Valentine et al. [160] demonstrated a sensor integrated on a shoe insole (Fig. 8.17). Their system involves the use of direct ink writing on a black-doped thermoplastic polyurethane (TPU) matrix and the deposition of conductive traces in AgTPU for the sensing part. During walking, the sensor can detect the plantar pressure profile of the person.

The sector of wearable applications includes numerous examples of tools designed to monitor certain aspects of human health [161]. There are applications of 3D printed devices related to glucose sensors [162], electrolyte monitoring systems [163], and glutamate detection systems [164]. Obviously, all these devices in the healthcare sector can have feedback in terms of daily activity but above all sports activity [165].

All applications of wearable devices require an energy supply to work. Also in this case, the various AM techniques provide interesting solutions; in fact, there are

several researches that demonstrated, through additive techniques, the realization of energy harvesting, energy storage, and energy generation tools.

Xu et al. [166] reported the fabrication, with ink deposition techniques, of energy harvesting devices such as solar cells, thermoelectric nanogenerators (TEGs), and piezoelectric/triboelectric nanogenerators (PENGs/TENGs) for wearable applications. In this field, considerable research has been reported through the deposition of CNTs. The main techniques used to print CNTs are material extrusion, vat polymerization, powder bed fusion, and material jetting [167]. For the energy storage wearable applications, we can cite many 3D printed CNT-based supercapacitors, like the ones demonstrated in [168] or in [169].

8.7 Conclusion

3D printing technologies provide a great degree of customization of products and the feasibility to fabricate a wide spectrum of electrical components from passive elements such as resistors, capacitors, and inductors to active elements like transistors or LED, as well as several kinds of sensors and actuators.

The concept of directly 3D printing fundamental electronic components, including conductive and isolating regions, in order to overcome the concept of flatness in printed circuit boards and enable the development of 3D electronics is the starting point to enable 4D printing, which is capable of fabricating thermally or optically configurable time-varying property components.

The possibility to directly realize with additive manufacturing technology complex objects directly composed of functional materials allows the realization of traditional sensors with a fast and simple approach and opens the way to the fabrication of new types of sensor devices with geometry and functionality impossible to reach with classical semiconductor technology.

Soft material-based 3D printed actuators allow a programmable and smooth motion with the possibility to fabricate complex structures with low cost, targeted to the newest and promising technologies, providing numerous advantages with respect to the rigid structure of traditional actuators, with low power consumption and weight. Soft actuators may be driven by heat fluxes, electric or magnetic fields, and light sources in opposition to the mechatronic conditioning of traditional actuators.

The availability of cheap, reliable, and functional materials is a prerequisite to the customization of goods integrating electrical components to exploit the potential of 3D printing in biomedical, automotive, and avionic industrial applications.

References

1. E. Macdonald et al., 3D printing for the rapid prototyping of structural electronics. IEEE Access **2**, 234–242 (2014). https://doi.org/10.1109/ACCESS.2014.2311810
2. P.F. Flowers, C. Reyes, S. Ye, M.J. Kim, B.J. Wiley, 3D printing electronic components and circuits with conductive thermoplastic filament. Addit. Manuf. **18**, 156–163 (2017). https://doi.org/10.1016/j.addma.2017.10.002
3. Y. Xie et al., Microwave metamaterials made by fused deposition 3D printing of a highly conductive copper-based filament. Appl. Phys. Lett. **110**(18), 181903 (2017). https://doi.org/10.1063/1.4982718
4. G.L. Goh, H. Zhang, T.H. Chong, W.Y. Yeong, 3D printing of multilayered and multimaterial electronics: A review. Adv. Electron. Mater., 2100445 (2021). https://doi.org/10.1002/aelm.202100445
5. E. Blasco et al., Fabrication of conductive 3D gold-containing microstructures via direct laser writing. Adv. Mater. **28**(18), 3592–3595 (2016). https://doi.org/10.1002/adma.201506126
6. D.K. Patel, A.H. Sakhaei, M. Layani, B. Zhang, Q. Ge, S. Magdassi, Highly stretchable and UV curable elastomers for digital light processing based 3D printing. Adv. Mater. **29**(15), 1606000 (2017). https://doi.org/10.1002/adma.201606000
7. Y.L. Kong et al., 3D printed quantum dot light-emitting diodes. Nano Lett. **14**(12), 7017–7023 (2014). https://doi.org/10.1021/nl5033292
8. S. Sayyar, S. Gambhir, J. Chung, D.L. Officer, G.G. Wallace, 3D printable conducting hydrogels containing chemically converted graphene. Nanoscale **9**(5), 2038–2050 (2017). https://doi.org/10.1039/C6NR07516A
9. Y. Li, B. Chen, Z. Zhang, R. Han, Self-consistent mean-field theory of the XXZ ferrimagnetic spin chain with single-ion anisotropy. Phys. B Condens. Matter **456**, 16–20 (2015). https://doi.org/10.1016/j.physb.2014.08.013
10. K. Cai et al., Geometrically complex silicon carbide structures fabricated by robocasting. J. Am. Ceram. Soc. **95**(8), 2660–2666 (2012). https://doi.org/10.1111/j.1551-2916.2012.05276.x
11. C.R. Tubío, F. Guitián, A. Gil, Fabrication of ZnO periodic structures by 3D printing. J. Eur. Ceram. Soc. **36**(14), 3409–3415 (2016). https://doi.org/10.1016/j.jeurceramsoc.2016.05.025
12. J.E. Smay, J. Cesarano, J.A. Lewis, Colloidal inks for directed assembly of 3-D periodic structures. Langmuir **18**(14), 5429–5437 (2002). https://doi.org/10.1021/la0257135
13. J. Hoerber, J. Glasschroeder, M. Pfeffer, J. Schilp, M. Zaeh, J. Franke, Approaches for additive manufacturing of 3D electronic applications. Procedia CIRP **17**, 806–811 (2014). https://doi.org/10.1016/j.procir.2014.01.090
14. B. Lu, H. Lan, H. Liu, Additive manufacturing frontier: 3D printing electronics. Opto-Electron. Adv. **1**(1), 170004–170004 (2018). https://doi.org/10.29026/oea.2018.170004
15. M. Hedges, A.B. Marin, M. Hedges, *3D Aerosol Jet® Printing – Adding Electronics Functionality to RP/RM*, p. 5
16. T.H.J. van Osch, J. Perelaer, A.W.M. de Laat, U.S. Schubert, Inkjet printing of narrow conductive tracks on untreated polymeric substrates. Adv. Mater. **20**(2), 343–345 (2008). https://doi.org/10.1002/adma.200701876
17. K.B. Perez, C.B. Williams, Combining additive manufacturing and direct write for inte-grated electronics—A review, in *International Solid Freeform Fabrication Symposium, Austin (TX)*, (2013)
18. E. Sowade, M. Polomoshnov, A. Willert, R.R. Baumann, Toward 3D-printed electronics: Inkjet-printed vertical metal wire interconnects and screen-printed batteries. Adv. Eng. Mater. **21**(10), 1900568 (2019). https://doi.org/10.1002/adem.201900568
19. B. Wałpuski, M. Słoma, Additive manufacturing of electronics from silver Nanopowders sintered on 3D printed low-temperature substrates. Adv. Eng. Mater. **23**(4), 2001085 (2021). https://doi.org/10.1002/adem.202001085

20. P. Costa, J. Nunes-Pereira, C.R. Tubio, J.R. Dios, S. Lanceros-Mendez, Chapter 9: High deformation multifunctional composites: materials, processes, and applications, in *Advanced Lightweight Multifunctional Materials*, ed. by P. Costa, C. M. Costa, S. Lanceros-Mendez, (Woodhead Publishing, 2021), pp. 317–350. https://doi.org/10.1016/B978-0-12-818501-8.00008-1
21. K.S. Bhat, R. Ahmad, Y. Wang, Y.-B. Hahn, Low-temperature sintering of highly conductive silver ink for flexible electronics. J. Mater. Chem. C **4**(36), 8522–8527 (2016). https://doi.org/10.1039/C6TC02751B
22. L. Polavarapu, K.K. Manga, H.D. Cao, K.P. Loh, Q.-H. Xu, Preparation of conductive silver films at mild temperatures for printable organic electronics. Scopus, Consultato: Ottobre 13, 2021. [Online]. Disponibile su: https://scholarbank.nus.edu.sg/handle/10635/53104 (2011)
23. T. Tilford, S. Stoyanov, J. Braun, J.C. Janhsen, M.K. Patel, C. Bailey, Comparative reliability of inkjet-printed electronics packaging. IEEE Trans. Compon. Packag. Manuf. Technol. **11**(2), 351–362 (2021). https://doi.org/10.1109/TCPMT.2021.3049952
24. T. Tilford et al., Design, manufacture and test for reliable 3D printed electronics packaging. Microelectron. Reliab. **85**, 109–117 (2018). https://doi.org/10.1016/j.microrel.2018.04.008
25. Home | JEDEC. https://www.jedec.org/
26. V. Bertana et al., 3D printed active objects based on the promising PEDOT: PSS resin: Investigation of their integration inside an electronic circuit. Int. J. Eng. Res. Technol. **13**, 462 (2020). https://doi.org/10.37624/IJERT/13.3.2020.462-469
27. J.J. Adams et al., Conformal printing of electrically small antennas on three-dimensional surfaces. Adv. Mater. **23**(11), 1335–1340 (2011). https://doi.org/10.1002/adma.201003734
28. S.-C. Zhao, M. Maas, K. Jansen, M. van Hecke, 3D printed actuators: Reversibility, relaxation, and ratcheting. Adv. Funct. Mater. **29**, 8 (2019)
29. Y. Wang, X. Li, 4D printing reversible actuator with strain self-sensing function via structural design. Compos. Part B **211**, 108644 (2021). https://doi.org/10.1016/j.compositesb.2021.108644
30. S.-Y. Wu, C. Yang, W. Hsu, L. Lin, 3D-printed microelectronics for integrated circuitry and passive wireless sensors. Microsyst. Nanoeng. **1**(1), 15013 (2015). https://doi.org/10.1038/micronano.2015.13
31. G. Scordo et al., Effect of volatile organic compounds adsorption on 3D-printed PEGDA:PEDOT for Long-term monitoring devices. Nanomaterials **11, 1**(1) (2021). https://doi.org/10.3390/nano11010094
32. C. Dincer et al., Disposable sensors in diagnostics, food, and environmental monitoring. Adv. Mater. **31**(30), 1806739 (2019). https://doi.org/10.1002/adma.201806739
33. M.F. Farooqui, M.A. Karimi, K.N. Salama, A. Shamim, 3D-printed disposable wireless sensors with integrated microelectronics for large area environmental monitoring. Adv. Mater. Technol. **2**(8), 1700051 (2017). https://doi.org/10.1002/admt.201700051
34. A.S. Alshammari, M.R. Alenezi, K.T. Lai, S.R.P. Silva, Inkjet printing of polymer functionalized CNT gas sensor with enhanced sensing properties. Mater. Lett. **189**, 299–302 (2017). https://doi.org/10.1016/j.matlet.2016.11.033
35. M.F. Mabrook, C. Pearson, M.C. Petty, Inkjet-printed polymer films for the detection of organic vapors. IEEE Sensors J. **6**(6), 1435–1444 (2006). https://doi.org/10.1109/JSEN.2006.884168
36. M. Vatani, Y. Lu, E.D. Engeberg, J.-W. Choi, Combined 3D printing technologies and material for fabrication of tactile sensors. Int. J. Precis. Eng. Manuf. **16**(7), 1375–1383 (2015). https://doi.org/10.1007/s12541-015-0181-3
37. C. Liu et al., 3D printing Technologies for Flexible Tactile Sensors toward wearable electronics and electronic skin. Polymers **10**(6), 629 (2018). https://doi.org/10.3390/polym10060629
38. J.Y. Kim et al., 3D printable composite dough for stretchable, ultrasensitive and body-patchable strain sensors. Nanoscale **9**(31), 11035–11046 (2017). https://doi.org/10.1039/c7nr01865g

39. S.H. Foulger, Electrical properties of composites in the vicinity of the percolation threshold. J. Appl. Polym. Sci. **72**(12), 1573–1582 (1999). https://doi.org/10.1002/(SICI)1097-4628(19990620)72:12<1573::AID-APP10>3.0.CO;2-6
40. S.J. Leigh, R.J. Bradley, C.P. Purssell, D.R. Billson, D.A. Hutchins, A simple, low-cost conductive composite material for 3D printing of electronic sensors. PLoS One **7**(11), e49365 (2012). https://doi.org/10.1371/journal.pone.0049365
41. M.C. Lonergan, E.J. Severin, B.J. Doleman, S.A. Beaber, R.H. Grubbs, N.S. Lewis, Array-based vapor sensing using chemically sensitive, carbon black−polymer resistors. Chem. Mater. **8**(9), 2298–2312 (1996). https://doi.org/10.1021/cm960036j
42. M. Sumita, K. Sakata, S. Asai, K. Miyasaka, H. Nakagawa, Dispersion of fillers and the electrical conductivity of polymer blends filled with carbon black. Polym. Bull. **25**(2), 265–271 (1991). https://doi.org/10.1007/BF00310802
43. J.R. McGhee, M. Sinclair, D.J. Southee, K.G.U. Wijayantha, Strain sensing characteristics of 3D-printed conductive plastics. Electron. Lett. **54**(9), 570–572 (2018). https://doi.org/10.1049/el.2018.0363
44. A. Abdallah, M. Pauritsch, C. Gasser, F. Stangl, M. Primas, U. Traussnigg, 3D printed capacitive fluid level sensor. Proceedings **2**(13), 861 (2018). https://doi.org/10.3390/proceedings2130861
45. A.Y. Chen, E. Pegg, A. Chen, Z. Jin, G.X. Gu, 4D printing of electroactive materials. Adv. Intell. Syst., 2100019 (2021). https://doi.org/10.1002/aisy.202100019
46. O. Ozioko, H. Nassar, R. Dahiya, 3D printed interdigitated capacitor based tilt sensor. IEEE Sensors J., 1–1 (2021). https://doi.org/10.1109/JSEN.2021.3058949
47. Y. Zhou, C.B. Parker, P. Joshi, A.K. Naskar, J.T. Glass, C. Cao, 4D printing of stretchable supercapacitors via hybrid composite materials. Adv. Mater. Technol. **6**(1), 2001055 (2021). https://doi.org/10.1002/admt.202001055
48. K. Kurselis, R. Kiyan, V.N. Bagratashvili, V.K. Popov, B.N. Chichkov, 3D fabrication of all-polymer conductive microstructures by two photon polymerization. Opt. Express **21**, 31029–31035 (2013). https://doi.org/10.1364/OE.21.031029
49. N. Lazarus, S.S. Bedair, G.L. Smith, Creating 3D printed magnetic devices with ferrofluids and liquid metals. Addit. Manuf. **26**, 15–21 (2019). https://doi.org/10.1016/j.addma.2018.12.012
50. T. Hou et al., Design of 3D wireless power transfer system based on 3D printed electronics. IEEE Access **7**, 94793–94805 (2019). https://doi.org/10.1109/ACCESS.2019.2928948
51. L. Wu et al., Deformable bowtie antenna realized by 4D printing. Electronics **10**(15), 1792 (2021). https://doi.org/10.3390/electronics10151792
52. N. Jeranče, N. Bednar, G. Stojanović, An ink-jet printed Eddy current position sensor. Sensors **13**(4), 5205–5219 (2013). https://doi.org/10.3390/s130405205
53. Multi-Material 3D Printing Ups The Comfort For Hush Puppies Shoes "Fabbaloo". https://www.fabbaloo.com/news/multi-material-3d-printing-ups-the-comfort-for-hush-puppies-shoes
54. D. Cadman, S. Zhang, Y. Vardaxoglou, Fused deposition modelling for microwave circuits & antennas, in *2016 International Symposium on Antennas and Propagation (ISAP)*, (2016), pp. 418–419
55. N. Saengchairat, T. Tran, C.-K. Chua, A review: Additive manufacturing for active electronic components. Virtual Phys. Prototyp. **12**, 1–16 (2016). https://doi.org/10.1080/17452759.2016.1253181
56. A. Espera, J.R. Dizon, Q. Chen, R. Advincula, 3D-printing and advanced manufacturing for electronics. Prog. Addit. Manuf. **4**, 245–267 (2019). https://doi.org/10.1007/s40964-019-00077-7
57. M. Rother, M. Brohmann, S. Yang, S. Grimm, S. Schießl, A. Graf, J. Zaumseil, Aerosol-jet printing of polymer-sorted (6,5) carbon nanotubes for field-effect transistors with high reproducibility. Adv. Electron. Mater. **3**, 1700080 (2017). https://doi.org/10.1002/aelm.201700080
58. S. Kim, K. Hong, K. Lee, C. Frisbie, Performance and stability of aerosol-jet-printed electrolyte-gated transistors based on poly(3-hexylthiophene). ACS Appl. Mater. Interfaces **5** (2013). https://doi.org/10.1021/am401200y

59. V. Bertana, G. Scordo, M. Parmeggiani, L. Scaltrito, S. Ferrero, M. Gomez, M. Cocuzza, D. Vurro, P. D'Angelo, S. Iannotta, C. Pirri, S. Marasso, Rapid prototyping of 3D organic electrochemical transistors by composite photocurable resin. Sci. Rep. **10** (2020). https://doi.org/10.1038/s41598-020-70365-8
60. J. Stringer, T.M. Althagafi, C. Tse, D. Ta, J. Shephard, E. Esenturk, C. Connaughton, T. Wasley, J. Li, R. Kay, P. Smith, Integration of additive manufacturing and inkjet printed electronics: A potential route to parts with embedded multifunctionality. Manuf. Rev. **3**, 12 (2016). https://doi.org/10.1051/mfreview/2016011
61. S. Ready, A. Arias, S. Sambandan, Ink jet printing devices and circuits. In: *Materials Research Society Fall Meeting*, Boston, MA, (2009)
62. F. Molina-Lopez, T. Gao, U. Kraft, C. Zhu, T. Öhlund, R. Pfattner, V. Feig, Y. Kim, S. Wang, Y. Yun, Z. Bao, Inkjet-printed stretchable and low voltage synaptic transistor array. Nat. Commun. **10** (2019). https://doi.org/10.1038/s41467-019-10569-3
63. Y.-H. Kim, B. Yoo, J. Anthony, S. Park, Controlled deposition of a high-performance small-molecule organic single-crystal transistor Array by direct ink-jet printing. Adv. Mater. (Deerfield Beach, Fla.). **24**, 497–502 (2012). https://doi.org/10.1002/adma.201103032
64. H. Sirringhaus, T. Kawase, R. Friend, T. Shimoda, M. Inbasekaran, W. Wu, E. Woo, High-resolution inkjet printing of all-polymer transistor circuits. Science (New York, N.Y.) **290**, 2123–2126 (2001). https://doi.org/10.1126/science.290.5499.2123
65. S. Dasgupta, R. Kruk, N. Mechau, H. Hahn, Inkjet printed, high mobility inorganic-oxide field effect transistors processed at room temperature. ACS Nano **5**, 9628–9638 (2011). https://doi.org/10.1021/nn202992v
66. L. Basiricò, P. Cosseddu, B. Fraboni, A. Bonfiglio, Inkjet printing of transparent, flexible, organic transistors. Thin Solid Films (2011). https://doi.org/10.1016/j.tsf.2011.04.188
67. 2D materials hold key to printing wearable electronics. Nano Today **18**, 4–5., ISSN 1748-0132 (2018). https://doi.org/10.1016/j.nantod.2017.12.004
68. T. Carey, S. Cacovich, G. Divitini, J. Rentals, A. Mansouri, J. Kim, C. Wang, C. Ducati, R. Sordan, F. Torrisi, Fully inkjet-printed two-dimensional material field-effect heterojunctions for wearable and textile electronics. Nat. Commun. **8** (2017). https://doi.org/10.1038/s41467-017-01210-2
69. F. Torrisi, T. Hasan, W. Wu, Z. Sun, A. Lombardo, T. Kulmala, G.-W. Hsieh, S. Jung, F. Bonaccorso, P. Paul, D. Chu, A. Ferrari, Inkjet-printed graphene electronics. ACS Nano **6**, 2992–3006 (2012). https://doi.org/10.1021/nn2044609
70. S. Chung, K. Cho, T. Lee, Recent Progress in inkjet-printed thin-film transistors. Adv. Sci. **6**, 1801445 (2019). https://doi.org/10.1002/advs.201801445
71. C. Cobb, C. Ho, Additive manufacturing: Rethinking battery design. Interface Mag. **25**, 75–78 (2016). https://doi.org/10.1149/2.F08161if
72. Y. Pang, Y. Cao, Y. Chu, M. Liu, K. Snyder, D. MacKenzie, C. Cao, Additive manufacturing of batteries. Adv. Funct. Mater. **30**, 1906244 (2019). https://doi.org/10.1002/adfm.201906244
73. S. Lawes, Q. Sun, A. Lushington, B. Xiao, Y. Liu, X. Sun, Inkjet-printed silicon as high performance anodes for Li-ion batteries. Nano Energy **36** (2017). https://doi.org/10.1016/j.nanoen.2017.04.041
74. J. Hu, Y. Jiang, S. Cui, Y. Duan, T. Liu, H. Guo, L. Lin, Y. Lin, J. Zheng, K. Amine, F. Pan, 3D-printed cathodes of LiMn1−xFexPO4 nanocrystals achieve both ultrahigh rate and high capacity for advanced lithium-ion battery. Adv. Energy Mater. **6**, 1600856 (2016). https://doi.org/10.1002/aenm.201600856
75. K. Fu, Y. Wang, C. Yan, Y. Yao, Y. Chen, J. Dai, S. Lacey, Y. Wang, J. Wan, T. Li, Z. Wang, Y. Xu, L. Hu, Graphene oxide-based electrode inks for 3D-printed lithium-ion batteries. Adv. Mater. **28**, 2587–2594 (2016). https://doi.org/10.1002/adma.201505391
76. M. Saleh, J. Li, J. Park, R. Panat, 3D printed hierarchically-porous microlattice electrode materials for exceptionally high specific capacity and areal capacity lithium ion batteries. Addit. Manuf. **23** (2018). https://doi.org/10.1016/j.addma.2018.07.006
77. C. Reyes, R. Somogyi, S. Niu, M.A. Cruz, F. Yang, M.J. Catenacci, C.P. Rhodes, B.J. Wiley, Three-dimensional printing of a complete lithium ion battery with fused filament fabrication. ACS Appl. Energy Mater. **1**(10), 5268–5279 (2018)

78. C.W. Foster, M.P. Down, Y. Zhang, X. Ji, S.J. Rowley-Neale, G.C. Smith, P.J. Kelly, C.E. Banks, 3D printed graphene based energy storage devices. Sci. Rep. **7**, 42233 (2017)
79. U. Gulzar, C. Glynn, C. O'Dwyer, Additive manufacturing for energy storage: Methods, designs and material selection for customizable 3D printed batteries and supercapacitors. Curr. Opin. Electrochem. **20** (2020). https://doi.org/10.1016/j.coelec.2020.02.009
80. Z. Bao, J.-W. Luo, Y.-S. Wang, T.-C. Hu, S.-Y. Tsai, Y.-T. Tsai, H.-C. Wang, F.-H. Chen, Y.-C. Lee, T.-L. Tsai, R.-J. Chung, R.-S. Liu, Microfluidic synthesis of CsPbBr3/Cs4PbBr6 nanocrystals for inkjet printing of mini-LEDs. Chem. Eng. J. **426**, 130849 (2021). https://doi.org/10.1016/j.cej.2021.130849
81. Z. Gu, Z. Huang, X. Hu, Y. Wang, L. Li, M. Li, Y. Song, In-situ inkjet printing of perovskite single-crystal array embedded PDMS film for wearable light-emitting devices. ACS Appl. Mater. Interfaces **12**, 22157–22162 (2020). https://doi.org/10.1021/acsami.0c04131
82. Y. Kong, I. Tamargo, H. Kim, B. Johnson, M. Gupta, T.-W. Koh, H.-A. Chin, D. Steingart, B. Rand, M. McAlpine, 3D printed quantum dot light-emitting diodes. Nano Lett. **14** (2014). https://doi.org/10.1021/nl5033292
83. Y. Liu, X. Zhongwei, C. Zheng, T. Guo, X. Xie, L. Qian, D. Fu, X. Yan, Efficient all-solution processed quantum dot light emitting diodes based on inkjet printing technique. ACS Appl. Mater. Interfaces **9** (2017). https://doi.org/10.1021/acsami.7b05381
84. C. Xiang, L. Wu, Z. Lu, M. Li, Y. Wen, Y. Yang, W. Liu, T. Zhang, W. Cao, S.-W. Tsang, B. Shan, X. Yan, L. Qian, High efficiency and stability of ink-jet printed quantum dot light emitting diodes. Nat. Commun. **11** (2020). https://doi.org/10.1038/s41467-020-15481-9
85. J. Han, D. Ko, M. Park, J. Roh, H. Jung, Y. Lee, Y. Kwon, J. Sohn, W. Bae, B.D. Chin, C. Lee, Toward high-resolution, inkjet-printed, quantum dot light-emitting diodes for next-generation displays. J. Soc. Inf. Disp. **24** (2016). https://doi.org/10.1002/jsid.467
86. P. Yang, L. Zhang, D. Kang, R. Strahl, T. Kraus, High-resolution inkjet printing of quantum dot light-emitting microdiode arrays. Adv. Opt. Mater. **8**, 1901429 (2019). https://doi.org/10.1002/adom.201901429
87. S.-C. Chang, J. Liu, J. Bharathan, Y. Yang, J. Onohara, J. Kido, Multicolor organic light-emitting diodes processed by hybrid inkjet printing. Adv. Mater. **11**, 734–737 (1999). https://doi.org/10.1002/(SICI)1521-4095(199906)11:93.0.CO;2-D
88. H. Gorter, M. Coenen, M.W.L. Slaats, M. Ren, W. Lu, C.J. Kuijpers, P. Groen, Toward inkjet printing of small molecule organic light emitting diodes. Thin Solid Films **532**, 11–15 (2013). https://doi.org/10.1016/j.tsf.2013.01.041
89. T. Hebner, C. Wu, D. Marcy, M. Lu, J. Sturm, Ink-jet printing of doped polymers for organic light emitting devices. Appl. Phys. Lett. **72**, 519–521 (1998). https://doi.org/10.1063/1.120807
90. V. Correia, C. Caparros, C. Casellas, L. Francesch, J.G. Rocha, S. Lanceros-Mendez, Development of inkjet printed strain sensors. Smart Mater. Struct. **22**(10), 105028 (2013). https://doi.org/10.1088/0964-1726/22/10/105028
91. J. Bito et al., Inkjet-/3D-/4D-printed autonomous wearable RF modules for biomonitoring, positioning and sensing applications, Anaheim, California, United States. Proc. SPIE – Int. Soc. Opt. Eng., 101940Z (2017). https://doi.org/10.1117/12.2262795
92. G. Cummins, M.P.Y. Desmulliez, Inkjet printing of conductive materials: A review. Circuit World **38**(4), 193–213 (2012). https://doi.org/10.1108/03056121211280413
93. S. Kim et al., Inkjet-printed antennas, sensors and circuits on paper substrate. IET Microwaves Antennas Propag. **7**(10), 858–868 (2013). https://doi.org/10.1049/iet-map.2012.0685
94. S. Liu, L. Li, Ultrastretchable and self-healing double-network hydrogel for 3D printing and strain sensor. ACS Appl. Mater. Interfaces **9**(31), 26429–26437 (2017). https://doi.org/10.1021/acsami.7b07445
95. J.T. Muth et al., Embedded 3D printing of strain sensors within highly stretchable elastomers. Adv. Mater. **26**(36), 6307–6312 (2014). https://doi.org/10.1002/adma.201400334
96. S.-Z. Guo, K. Qiu, F. Meng, S.H. Park, M.C. McAlpine, 3D printed stretchable tactile sensors. Adv. Mater. **29**(27), 1701218 (2017). https://doi.org/10.1002/adma.201701218

97. S. Agarwala et al., Development of bendable strain sensor with embedded microchannels using 3D printing. Sensors Actuators A Phys. **263**, 593–599 (2017). https://doi.org/10.1016/j.sna.2017.07.025
98. Y.-L. Park, B.-R. Chen, R.J. Wood, Design and fabrication of soft artificial skin using embedded microchannels and liquid conductors. IEEE Sensors J. **12**(8), 2711–2718 (2012). https://doi.org/10.1109/JSEN.2012.2200790
99. Y. Tang, B. Dai, B. Su, Y. Shi, Recent advances of 4D printing technologies toward soft tactile sensors. Front. Mater. **8**, 658046 (2021). https://doi.org/10.3389/fmats.2021.658046
100. D.B. Krkljes, G.M. Stojanovic, An ink-jet printed capacitive sensor for angular position/velocity measurements. Adv. Electr. Comp. Eng. **16**(4), 77–82 (2016). https://doi.org/10.4316/AECE.2016.04012
101. K. Li, H. Wei, W. Liu, H. Meng, P. Zhang, C. Yan, 3D printed stretchable capacitive sensors for highly sensitive tactile and electrochemical sensing. Nanotechnology **29**(18), 185501 (2018). https://doi.org/10.1088/1361-6528/aaafa5
102. L.-M. Faller, W. Granig, M. Krivec, A. Abram, H. Zangl, Rapid prototyping of force/pressure sensors using 3D- and inkjet-printing. J. Micromech. Microeng. **28**(10), 104002 (2018). https://doi.org/10.1088/1361-6439/aaadf4
103. A. Frutiger et al., Capacitive soft strain sensors via multicore-Shell fiber printing. Adv. Mater. **27**(15), 2440–2446 (2015). https://doi.org/10.1002/adma.201500072
104. M. Saari, B. Xia, B. Cox, P.S. Krueger, A.L. Cohen, E. Richer, Fabrication and analysis of a composite 3D printed capacitive force sensor. 3D Print. Addit. Manuf. **3**(3), 136–141 (2016). https://doi.org/10.1089/3dp.2016.0021
105. H. Kim, F. Torres, Y. Wu, D. Villagran, Y. Lin, T.-L. Tseng, Integrated 3D printing and corona poling process of PVDF piezoelectric films for pressure sensor application. Smart Mater. Struct. **26**(8), 085027 (2017). https://doi.org/10.1088/1361-665X/aa738e
106. H.B. Lee, Y.W. Kim, J. Yoon, N.K. Lee, S.-H. Park, 3D customized and flexible tactile sensor using a piezoelectric nanofiber mat and sandwich-molded elastomer sheets. Smart Mater. Struct. **26**(4), 045032 (2017). https://doi.org/10.1088/1361-665X/aa64ca
107. M.B. Kirkpatrick, J.A. Tarbutton, T. Le, C. Lee, Characterization of 3D printed piezoelectric sensors: Determination of d33 piezoelectric coefficient for 3D printed polyvinylidene fluoride sensors, in *2016 IEEE Sensors, Orlando, FL, USA*, (2016), pp. 1–3. https://doi.org/10.1109/ICSENS.2016.7808876
108. H. Kim, F. Torres, D. Villagran, C. Stewart, Y. Lin, T.B. Tseng, 3D printing of $BaTiO_3$/PVDF composites with electric in situ poling for pressure sensor applications. Macromol. Mater. Eng. **302**(11), 1700229 (2017). https://doi.org/10.1002/mame.201700229
109. X. Zhou, K. Parida, O. Halevi, S. Magdassi, P.S. Lee, All 3D printed stretchable piezoelectric Nanogenerator for self-powered sensor application. Sensors **20**(23), 6748 (2020). https://doi.org/10.3390/s20236748
110. J. Zhang et al., 3D printed piezoelectric BNNTs nanocomposites with tunable interface and microarchitectures for self-powered conformal sensors. Nano Energy **77**, 105300 (2020). https://doi.org/10.1016/j.nanoen.2020.105300
111. R.I. Haque, O. Chandran, S. Lani, D. Briand, Self-powered triboelectric touch sensor made of 3D printed materials. Nano Energy **52**, 54–62 (2018). https://doi.org/10.1016/j.nanoen.2018.07.038
112. Z. Lei, Q. Wang, P. Wu, A multifunctional skin-like sensor based on a 3D printed thermo-responsive hydrogel. Mater. Horiz. **4**(4), 694–700 (2017). https://doi.org/10.1039/C7MH00262A
113. S. Ali, A. Hassan, G. Hassan, J. Bae, C.H. Lee, All-printed humidity sensor based on graphene/methyl-red composite with high sensitivity. Carbon **105**, 23–32 (2016). https://doi.org/10.1016/j.carbon.2016.04.013
114. A.V. Quintero et al., Smart RFID label with a printed multisensor platform for environmental monitoring. Flex. Print. Electron. **1**(2), 025003 (2016). https://doi.org/10.1088/2058-8585/1/2/025003

115. D. Chen et al., 4D printing strain self-sensing and temperature self-sensing integrated sensor–actuator with bioinspired gradient gaps. Adv. Sci. **7**(13), 2000584 (2020). https://doi.org/10.1002/advs.202000584
116. T. Pandhi, A. Chandnani, H. Subbaraman, D. Estrada, A review of inkjet printed graphene and carbon nanotubes based gas sensors. Sensors **20**(19), 5642 (2020). https://doi.org/10.3390/s20195642
117. J. Dai et al., Printed gas sensors. Chem. Soc. Rev. **49**(6), 1756–1789 (2020). https://doi.org/10.1039/C9CS00459A
118. S. Stassi et al., Polymeric 3D printed functional microcantilevers for biosensing applications. ACS Appl. Mater. Interfaces **9**(22), 19193–19201 (2017). https://doi.org/10.1021/acsami.7b04030
119. S. Zhou, H. Mei, M. Lu, L. Cheng, 3D printed and structurally strengthened ammonia sensor. Compos. A: Appl. Sci. Manuf. **139**, 106100 (2020). https://doi.org/10.1016/j.compositesa.2020.106100
120. S.J. Leigh, C.P. Purssell, D.R. Billson, D.A. Hutchins, Using a magnetite/thermoplastic composite in 3D printing of direct replacements for commercially available flow sensors. Smart Mater. Struct. **23**(9), 095039 (2014). https://doi.org/10.1088/0964-1726/23/9/095039
121. K. Adamski, B. Kawa, R. Walczak, 3D printed flowmeter based on Venturi effect with integrated pressure sensors. Proceedings **2**(13), 1509 (2018). https://doi.org/10.3390/proceedings2131509
122. T. Blachowicz, A. Ehrmann, 3D printed MEMS technology—Recent developments and applications. Micromachines **11**(4), 434 (2020). https://doi.org/10.3390/mi11040434
123. L. Moroni, J.R. de Wijn, C.A. van Blitterswijk, 3D fiber-deposited scaffolds for tissue engineering: Influence of pores geometry and architecture on dynamic mechanical properties. Biomaterials **27**(7), 974–985 (2006). https://doi.org/10.1016/j.biomaterials.2005.07.023
124. Z. Wang, R. Abdulla, B. Parker, R. Samanipour, S. Ghosh, K. Kim, A simple and high-resolution stereolithography-based 3D bioprinting system using visible light crosslinkable bioinks. Biofabrication **7**(4), 045009 (2015). https://doi.org/10.1088/1758-5090/7/4/045009
125. J. Malda et al., 25th anniversary article: Engineering hydrogels for biofabrication. Adv. Mater. **25**(36), 5011–5028 (2013). https://doi.org/10.1002/adma.201302042
126. M. Straub, M. Gu, Near-infrared photonic crystals with higher-order bandgaps generated by two-photon photopolymerization. Opt. Lett. **27**(20), 1824–1826 (2002). https://doi.org/10.1364/OL.27.001824
127. M. López-Valdeolivas, D. Liu, D.J. Broer, C. Sánchez-Somolinos, 4D printed actuators with soft-robotic functions. Macromol. Rapid Commun. **39**(5), 1700710 (2018). https://doi.org/10.1002/marc.201700710
128. Y. Wang, X. Li, 4D printing reversible actuator with strain self-sensing function via structural design. Compos. Part B Eng. **211**, 108644 (2021). https://doi.org/10.1016/j.compositesb.2021.108644
129. M. Zarek, M. Layani, I. Cooperstein, E. Sachyani, D. Cohn, S. Magdassi, 3D printing of shape memory polymers for flexible electronic devices. Adv. Mater. **28**(22), 4449–4454 (2016). https://doi.org/10.1002/adma.201503132
130. D. Han, H. Gu, J. Kim, S. Yokota, A bio-inspired 3D-printed hybrid finger with integrated ECF (electro-conjugate fluid) micropumps. Sens. Actuators A Phys. **257**, 47–57 (2017). https://doi.org/10.1016/j.sna.2017.02.002
131. Z. Ji, C. Yan, B. Yu, X. Wang, F. Zhou, Multimaterials 3D printing for free assembly manufacturing of magnetic driving soft actuator. Adv. Mater. Interfaces **4**(22), 1700629 (2017). https://doi.org/10.1002/admi.201700629
132. T. Chen, K. Shea, An autonomous programmable actuator and shape reconfigurable structures using Bistability and shape memory polymers. 3D Print. Addit. Manuf. **5**(2), 91–101 (2018). https://doi.org/10.1089/3dp.2017.0118
133. D.E. Hagaman, S. Leist, J. Zhou, H.-F. Ji, Photoactivated polymeric bilayer actuators fabricated via 3D printing. ACS Appl. Mater. Interfaces **10**(32), 27308–27315 (2018). https://doi.org/10.1021/acsami.8b08503

134. Y. Lee et al., Three-dimensionally printed micro-electromechanical switches. ACS Appl. Mater. Interfaces **10**(18), 15841–15846 (2018). https://doi.org/10.1021/acsami.8b01455
135. X. Xie, Y. Zaitsev, L.F. Velásquez-García, S.J. Teller, C. Livermore, Scalable, MEMS-enabled, vibrational tactile actuators for high resolution tactile displays. J. Micromech. Microeng. **24**(12), 125014 (2014). https://doi.org/10.1088/0960-1317/24/12/125014
136. H.S. Fiaz, C.R. Settle, K. Hoshino, Metal additive manufacturing for microelectromechanical systems: Titanium alloy (Ti-6Al-4V)-based nanopositioning flexure fabricated by electron beam melting. Sens. Actuators Phys. **249**, 284–293 (2016). https://doi.org/10.1016/j.sna.2016.08.029
137. X. Lu et al., 4D-printing of Photoswitchable actuators. Angew. Chem. Int. Ed. **60**(10), 5536–5543 (2021). https://doi.org/10.1002/anie.202012618
138. R. Bernasconi, C. Credi, M. Tironi, M. Levi, L. Magagnin, Electroless metallization of stereolithographic Photocurable resins for 3D printing of functional microdevices. J. Electrochem. Soc. **164**(5), B3059 (2017). https://doi.org/10.1149/2.0081705jes
139. W.E.N. Yintang, Z. Shuquan, H.E. Jiankang, Z. Qingliang, L. Bo, W.E.N. Shifeng, et al., Four-dimensional printing – The additive manufacturing technology of intelligent components. J. Mechan. Eng. **56**, 1–25 (2020). https://doi.org/10.3901/jme.2020.15.001
140. R.L. Truby, J.A. Lewis, Printing soft matter in three dimensions. Nature **540**, 371–378 (2016). https://doi.org/10.1038/nature21003
141. C. Liu, N. Huang, F. Xu, J. Tong, Z. Chen, X. Gui, Y. Fu, C. Lao, 3D printing Technologies for Flexible Tactile Sensors toward wearable electronics and electronic skin. Polymers **10**, 629 (2018). https://doi.org/10.3390/polym10060629
142. J. Zhang, S. Ye, L. Honglei, X. Chen, X. Chen, B. Li, W. Tang, Q. Meng, P. Ding, H. Tian, X. Li, Y. Zhang, P. Xu, J. Shao, 3D printed piezoelectric BNNTs nanocomposites with tunable interface and microarchitectures for self-powered conformal sensors. Nano Energy **77**, 105300 (2020). https://doi.org/10.1016/j.nanoen.2020.105300
143. J. Muth, D. Vogt, R. Truby, Y. Mengüç, D. Kolesky, R. Wood, J. Lewis, 3D printing: Embedded 3D printing of strain sensors within highly stretchable elastomers (Adv. Mater. 36/2014). Adv. Mater. (Deerfield Beach, Fla.) **26**, 6307–6312 (2014). https://doi.org/10.1002/adma.201400334
144. Y.-F. Zhang, N. Zhang, H. Hingorani, N. Ding, D. Wang, C. Yuan, B. Zhang, G. Gu, Q. Ge, Fast-response, stiffness-tunable soft actuator by hybrid multimaterial 3D printing. Adv. Funct. Mater. **29** (2019). https://doi.org/10.1002/adfm.201806698
145. M. López-Valdeolivas, D. Liu, D. Broer, S. Somolinos, Carlos., 4D printed actuators with soft-robotic functions. Macromol. Rapid Commun. **39** (2017). https://doi.org/10.1002/marc.201700710
146. M. Saed, C. Ambulo, H. Kim, R. De, V. Raval, K. Searles, D. Siddiqui, J.M. Cue, M. Stefan, M. Shankar, T. Ware, Molecularly-engineered, 4D-printed liquid crystal elastomer actuators. Adv. Funct. Mater. **29**, 1806412 (2018). https://doi.org/10.1002/adfm.201806412
147. L. Wu, J. Huang, M. Zhai, B. Sun, H. Chang, S. Huang, H. Liu, Deformable bowtie antenna realized by 4D printing. Electronics **10**, 1792 (2021). https://doi.org/10.3390/electronics10151792
148. J. Bito, R.A. Bahr, J. Hester, J. Kimionis, A. Nauroze, W. Su, B. Tehrani, M. Tentzeris, Inkjet-/3D-/4D-printed autonomous wearable RF modules for biomonitoring. Position. Sens. Appl. **101940Z** (2017). https://doi.org/10.1117/12.2262795
149. L. Yang, A. Rida, R. Vyas, M.M. Tentzeris, RFID tag and RF structures on a paper substrate using inkjet-printing technology. IEEE Trans. Microw. Theory Tech. **55**, 2894–2901 (2007)
150. A. Sharif, J. Ouyang, Y. Yan, A. Raza, M.A. Imran, Q.H. Abbasi, Low-cost inkjet-printed RFID tag antenna Design for Remote Healthcare Applications. IEEE J. Electromagn. RF Microw. Med. Biol. **3**, 261–268 (2019)
151. S. Kim, Inkjet-printed electronics on paper for RF identification (RFID) and sensing. Electronics **9**, 1636 (2020). https://doi.org/10.3390/electronics9101636
152. V. Lakafosis, H. Lee, G. Shaker, L. Yang, G. Orecchini, A. Traille, M. Tentzeris, L. Roselli, Inkjet printed, self powered, wireless sensors for environmental, gas, and authentication-based sensing. IEEE Sensors J. **11**, 3139–3152 (2011). https://doi.org/10.1109/JSEN.2011.2166996

153. S. Kim, B. Cook, T. Le, J. Cooper, H. Lee, V. Lakafosis, R. Vyas, R. Moro, M. Bozzi, A. Georgiadis, A. Collado, M. Tentzeris, Inkjet-printed antennas, sensors and circuits on paper substrate. IET Microwaves Antennas Propag. **7**, 858–868 (2013). https://doi.org/10.1049/iet-map.2012.0685
154. S. Terranova, F. Costa, G. Manara, S. Genovesi, Three-dimensional Chipless RFID tags: Fabrication through additive manufacturing. Sensors **20**, 4740 (2020). https://doi.org/10.3390/s20174740
155. E. Balliu, H. Andersson, M. Engholm, T. Öhlund, H.-E. Nilsson, H. Olin, Selective laser sintering of inkjet-printed silver nanoparticle inks on paper substrates to achieve highly conductive patterns. Sci. Rep. **8**, 10408 (2018). https://doi.org/10.1038/s41598-018-28684-4
156. Y.S. Rim, S.-H. Bae, H. Chen, N. Marco, Y. Yang, Recent Progress in materials and devices toward printable and flexible sensors. Adv. Mater. **28**, 4415–4440 (2016). https://doi.org/10.1002/adma.201505118
157. Y. Gao, G. Yu, T. Shu, Y. Chen, Y. Wenzhen, Y. Liu, J. Long, W. Xiong, F.-Z. Xuan, 3D-printed coaxial fibers for integrated wearable sensor skin. Adv. Mater. Technol. **4**, 1900504 (2019). https://doi.org/10.1002/admt.201900504
158. Y. Zhang, G. Shi, J. Qin, S. Lowe, S. Zhang, H. Zhao, Z.,.Y. Lin, Recent Progress of direct ink writing of electronic components for advanced wearable devices. ACS Appl. Electron. Mater. **1** (2019). https://doi.org/10.1021/acsaelm.9b00428
159. J. Wang, Y. Liu, S. Su, J. Wei, S.E. Rahman, F. Ning, G. Christopher, W. Cong, J. Qiu, Ultrasensitive wearable strain sensors of 3D printing tough and conductive hydrogels. Polymers **11**, 1873 (2019). https://doi.org/10.3390/polym11111873
160. A. Valentine, T. Busbee, J. Boley, J. Raney, A. Chortos, A. Kotikian, J. Berrigan, M. Durstock, J. Lewis, Hybrid 3D printing of soft electronics. Adv. Mater. **29**, 1703817 (2017). https://doi.org/10.1002/adma.201703817
161. A. Kalkal, S. Kumar, P. Kumar, R. Pradhan, M. Willander, G. Packirisamy, S. Kumar, B. Malhotra, Recent advances in 3D printing technologies for wearable (bio)sensors. Addit. Manuf. **46**, 102088 (2021). https://doi.org/10.1016/j.addma.2021.102088
162. S. Nesaei, Y. Song, Y. Wang, X. Ruan, D. Du, A. Gozen, Y. Lin, Micro additive manufacturing of glucose biosensors: A feasibility study. Anal. Chim. Acta **1043** (2018). https://doi.org/10.1016/j.aca.2018.09.012
163. T. Kim, Q. Yi, E. Hoang, R. Esfandyarpour, Bioelectronic wearables: A 3D printed wearable bioelectronic patch for multi-sensing and in situ sweat electrolyte monitoring (Adv. Mater. Technol. 4/2021). Adv. Mater. Technol **6**, 2170022 (2021). https://doi.org/10.1002/admt.202170022
164. T.N.H. Nguyen, J.K. Nolan, H. Park, S. Lam, M. Fattah, J.C. Page, H.-E. Joe, M.B.G. Jun, H. Lee, S.J. Kim, R. Shi, H. Lee, Facile fabrication of flexible glutamate biosensor using direct writing of platinum nanoparticle-based nanocomposite ink. Biosens. Bioelectron. **131**, 257–266 (2019)
165. D.R. Seshadri, R.T. Li, J.E. Voos, J.R. Rowbottom, C.M. Alfes, C.A. Zorman, C.K. Drummond, Wearable sensors for monitoring the physiological and biochemical profile of the athlete. npj Digit Med. **2**(1), 72 (2019)
166. S. Xu, W. Wu, Ink-based additive Nanomanufacturing of functional materials for human-integrated smart wearables. Adv. Intell. Syst. **2** (2020). https://doi.org/10.1002/aisy.202000117
167. G.L. Goh, S. Agarwala, W.Y. Yeong, Directed and on-demand alignment of carbon nanotube: A review toward 3D printing of electronics. Adv. Mater. Interfaces **6**, 1801318 (2019). https://doi.org/10.1002/admi.201801318
168. P. Chen, H. Chen, J. Qiu, C. Zhou, Inkjet printing of single-walled carbon nanotube/RuO2 nanowire supercapacitors on cloth fabrics and flexible substrates. Nano Res. **3**, 594–603 (2010). https://doi.org/10.1007/s12274-010-0020-x
169. B. Chen, Y. Jiang, X. Tang, Y. Pan, S. Hu, Fully-packaged carbon nanotube supercapacitors by direct ink writing on flexible substrates. ACS Appl. Mater. Interfaces **9**, 28433–28440 (2017). https://doi.org/10.1021/acsami.7b06804

Chapter 9
Energy Storage Applications

Pietro Zaccagnini and Andrea Lamberti

Abstract Additive manufacturing techniques can be exploited to produce effective energy storage devices such as batteries and supercapacitors. Direct ink writing, fused melt deposit, and selective laser sintering techniques are exploited for these purposes. Between them, direct ink writing is the most explored. These fabrication processes allow the production of either 2D or 3D devices with remarkable performances, in some cases. In the following, supercapacitors' and batteries' properties and figures of merit will be recalled briefly, and a description of the recent advances in additive manufacturing approaches to energy storage device production will be given.

Keywords Energy storage devices · Batteries · Supercapacitor · Flexible devices · 3D printing · 2D devices

9.1 Introduction

Nowadays, energy issues and environmental problems are two of the most crucial points to deal with. In 2018, less than 15% of the sources of the total energy supply were renewable. Being so addicted to coal, oil, and natural gas led to the emission of 33.513 Mt. of CO_2 in that year [1].

The negative effects of the bad management of energy policy have reached a point where they can no longer be ignored. In the last 50 years, the CO_2 emissions due to fuel combustion increased progressively [1]. Nowadays, the overwhelming majority of the world's total energy supply comes from not renewable sources: oil, coal, and natural gas. On top of that, the future perspectives are exceptionally bleak

P. Zaccagnini (✉) · A. Lamberti
Politecnico di Torino, Dipartimento di Scienza Applicata e Tecnologia (DISAT), Torino, Italy

Istituto Italiano di Tecnologia, Center for Sustainable Future Technologies, Torino, Italy
e-mail: pietro.zaccagnini@polito.it

S. L. Marasso, M. Cocuzza (eds.), *High Resolution Manufacturing from 2D to 3D/4D Printing*, https://doi.org/10.1007/978-3-031-13779-2_9

also because of the recent exponential industrial growth of countries such as China and India, destined to become two of the strongest world's economic powers [2]. The situation is critical and requires a different approach than the one adopted until now, to avoid arriving at a point of no return.

The EU takes the energy issue to the heart and sets up a strategy for which it will be feasible to drastically cut greenhouse gas emissions to 80–95% by 2050 [2]. To do that, it is necessary to reach a secure, competitive, and decarbonized energy system 30 years after going through an unprecedented revolution strongly focused on the new renewable energy sources.

Energy storage technologies have undergone a dramatic spur in the last decays in parallel to energy harvesting techniques. It is evident that besides generating energy, it is of utmost importance to be able to store it safely and stably. Among these energy storage systems, a key role is played by the rechargeable batteries and the so-called supercapacitors (SCs), also known as ultracapacitors or electrochemical capacitors.

9.1.1 Supercapacitors

Supercapacitors (SCs) are a particular type of electrochemical device. SCs have filled the "gap" left by previous energy storage technologies. They have features that are intermediate between standard electrolytic capacitors and batteries. More in detail, SCs can store energy with a density that is 10–100 times greater than the standard capacitor but smaller compared to battery energy density. On the other hand, SCs can provide a lot of energy in a short time (high power density), unlike batteries, but of course, their power density is not so high as the standard capacitors. To show this in a graphical way, a Ragone chart, which plots power density vs. energy density for different storage technologies, is reported in Fig. 9.1.

Supercapacitors are, in general, made up of the following elements: two electrodes that should be properly engineered to maximize the specific surface area (SSA) of the active materials on them and their functional characters, key parameters that are related to the number of charges on the electrode surface, increasing the overall capacitance of the device; separator, a solid material whose function is to prevent a short circuit between the electrodes and to keep the electrolyte phase containing the ions; and the electrolyte phase itself engineered according to the active material's needs to exploit the material's specific capacitances.

According to the charge storage mechanism, SCs can be divided into three categories: electrical double-layer capacitors (EDLCs), pseudocapacitors (exploiting fast redox reaction), and hybrid capacitors (a combination of the previous two types or Li-ion capacitors). These working principles are schematically explained in Fig. 9.2, in which also dielectric capacitors are reported to better appreciate the differences.

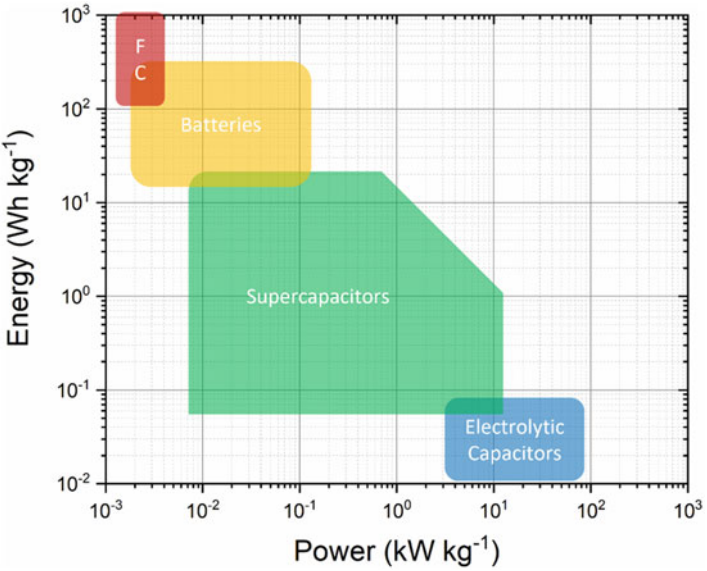

Fig. 9.1 Ragone plot showing the energy density vs. power density plot of different energy storage technologies. Fuel cells are noted as FC

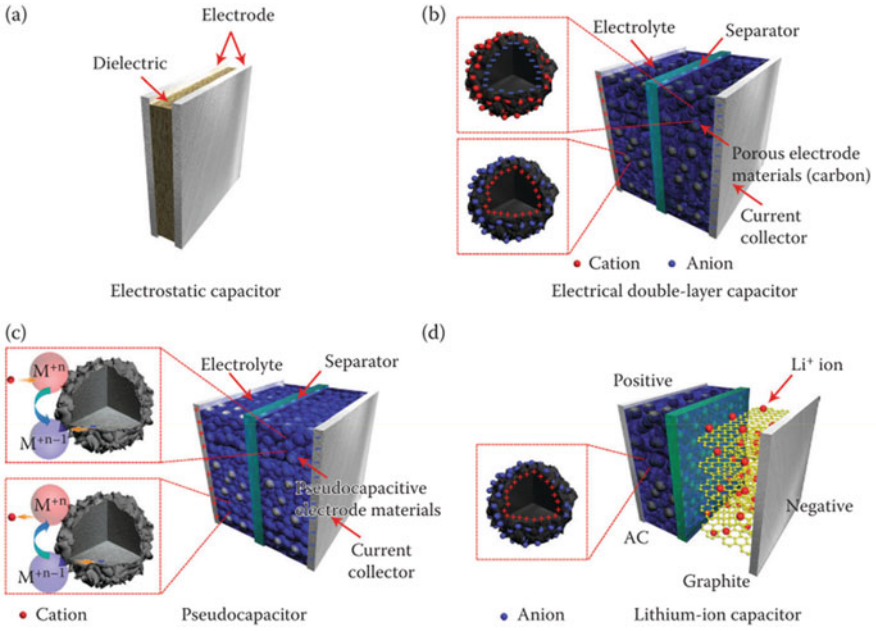

Fig. 9.2 Typical capacitor's architectures: (**a**) electrostatic capacitor and (**b**) an electrical double-layer capacitor, in (**c**) an exemplary pseudocapacitor while in (**d**) a Li-ion capacitor. (Reproduced from Ref. [3] with permission from the Royal Society of Chemistry)

EDL represents the fundamental charge storage mechanism of supercapacitors: by biasing two electrodes immersed into an electrolyte, ions of the opposite charge from the electrolyte build up at the electrode/electrolyte interface to achieve electroneutrality. In this process, no charge transfer is present between the electrode and the electrolyte. On the other hand, when reversible and fast faradaic reactions occur at those interfaces, pseudocapacity is used as a charge accumulation mechanism.

9.1.2 Batteries

Rechargeable batteries belong to the so-called secondary batteries family with higher energy density than the primary (not rechargeable) ones. Among all, lithium-ion batteries (LIBs) are one of the greatest successes of modern electrochemistry of materials. Their science and technology have been extensively reported in reviews [4–7] and dedicated books [8, 9].

A commercial LIB does not contain lithium metal: it comprises a negative electrode (generally, graphitic carbon) and a positive electrode (generally, layered lithium metal oxides such as $LiCoO_2$) both capable of reversibly intercalating Li^+ ions, these being separated by a solvent-based lithium-ion-conducting electrolyte (generally, a separator diaphragm soaked in mixed ethylene – diethyl carbonate solution of $LiPF_6$).

The working principle of a secondary Li-ion battery is schematically explained in Fig. 9.3.

In general, both the electrodes of a lithium-ion battery have a structure capable of lithium storage. Rather than the traditional redox galvanic action, Li-ion secondary cell chemistry depends on an “intercalation/de-intercalation” mechanism.

The active materials for Li-based batteries must be both electronic and ionic conductors to allow their correct operation, because low electronic conductivity or low mobility of Li^+ would limit the current flow and, consequently, the power

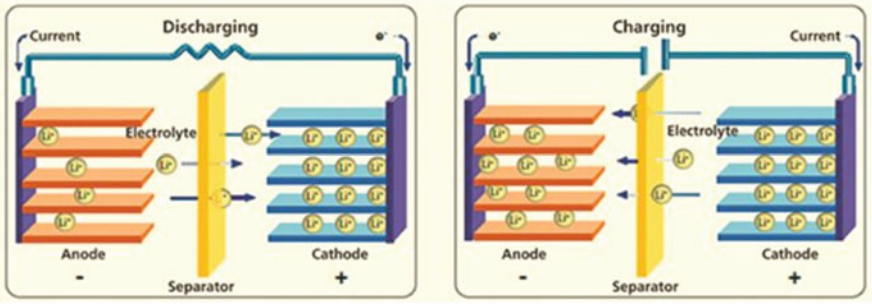

Fig. 9.3 Schematic representation of the working mechanism of Li-ion batteries. (Reprinted under the Creative Commons CC BY from Ref. [10])

delivered by the device. Thus, it is important to fabricate nanostructured electrode materials that provide high surface area and short diffusion paths for ionic transport and electronic conduction. Moreover, nanoscale materials can better tolerate the typical volume changes and structural evolution upon Li-ion insertion/deinsertion, which greatly affect the cycle/service life of LIBs.

9.2 2D and 3D Printing of Micro-supercapacitors

9.2.1 Supercapacitors' Electrochemical Characterizations

In this section, a brief overview of the standard electrochemical characterization techniques concerning supercapacitors is given. Some figures of merit will be provided to facilitate the reading of the cited literature.

Cyclic Voltammetry (CV)
CV is a potentiostatic technique in which a voltage is let vary between two limits at fixed sweep velocity. Herein, by potentiostatic, it is meant any procedure under voltage control and measured current. The main characterization parameter is the scan rate, ν, which influences the electrochemical response. The higher the scan rate, the lower could be the recorded capacitive hysteresis because of the resistive behavior of the device under test, as depicted in Fig. 9.4. Ideally, a capacitance shall not be a function of the scanning velocity, but in electrochemical systems, this happens regardless of the nature of the electrochemical interface because the ion's

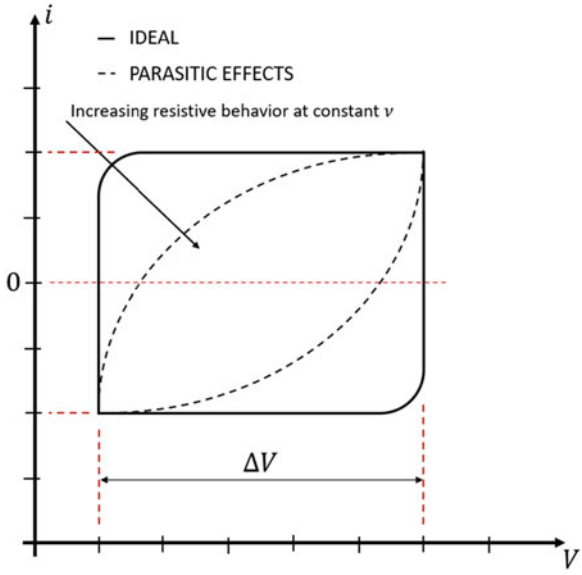

Fig. 9.4 CV plot of a supercapacitor. In black, the ideal profile, in dashed parasitic effects in the system

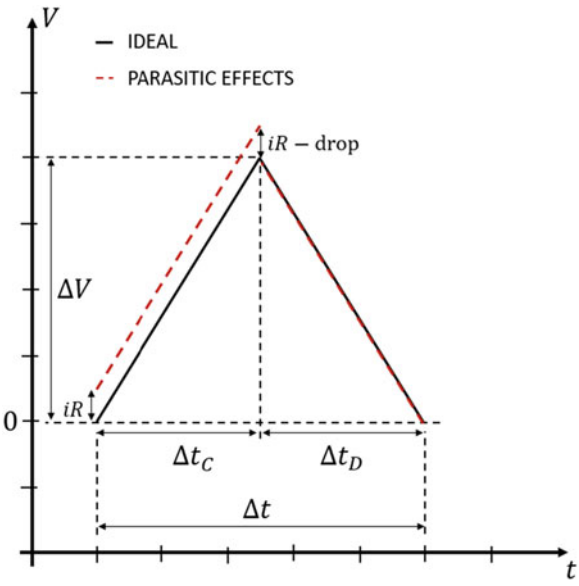

Fig. 9.5 GCD plot of a supercapacitor. In black, the ideal profile, in dashed red parasitic effects in the system

mobility in solution does not occur at all the frequencies of the applied varying electric fields.

Galvanostatic Charge and Discharge (GCD)

GCD is a galvanostatic technique (i.e., current is controlled, voltage is measured) in which a constant current is left flowing in charging and discharging fashion. In the case of capacitive systems, a linear voltage variation is expected as a response, as depicted in Fig. 9.5. Ohmic losses are responsible for voltage drops addressed as iR-drop. These types of tests are the most exploited ones to characterize supercapacitors, especially at the industrial level. Several information can be derived from the different current rates like specific capacitance and capacitance retention, energy, and coulombic efficiencies. From the energy and power data evaluated during these experiments, it is possible to represent the device performance in the Ragone plot in the energy vs. power representation. A close set of formulas can be used for such calculations with any type of supercapacitor tested. If one evaluates exactly energy and charge,

$$E = \int_{\Delta t} i(t)v(t)\,dt$$

$$Q = \int_{\Delta t} i(t)\,dt$$

where $v(t)$ and $i(t)$ are the voltage and current signals, respectively. If the evaluations are carried out in the semi-periods Δt of charge and discharge, then charging and discharging quantities are available for the evaluation of the coulombic and energetic efficiencies:

$$\eta_C = \frac{Q_d}{Q_c}$$

$$\eta_E = \frac{E_d}{E_c}$$

Both parameters are good estimators for device quality, as reported also in Ref [11].

With the calculated energy and capacity, capacitance can be evaluated, especially with discharge quantities via the relation:

$$C_d = \frac{1}{2}\frac{Q^2}{E}$$

Finally, the average discharge power can be calculated according to

$$P = \frac{E_d}{\Delta t_d}$$

Electrochemical Impedance Spectroscopy (EIS)

EIS is a powerful tool to access device or interfacial properties in electrochemical systems. This technique allows probing the cell impedance frequency by frequency resulting in a broad frequency evaluation of the impedance spectra. Several representations of the impedance spectra can be adopted to compare the results, but the Nyquist plot is one of the most straightforward allowing easy reading of the spectra. A typical Nyquist plot of an electrochemical capacitor system is depicted in Fig. 9.6, readapted from Ref [12]. It has not been excluded that some variations to the ideal profile not shown in Fig. 9.6 can be attributed to the micro- and nanostructured features of the active materials as shown in the simulations of Cooper et al., where the effects of only porous structures are considered [13]. Important parameters such as the real part's boundary values, namely, the equivalent series resistance (ESR) and the internal resistance (IR), can be directly evaluated, and the cell capacitance can be calculated from the imaginary part. Quantification of ohmic contributions to the real part of the impedance is important to minimize energy losses during device operation, hence maximizing the energetic efficiency.

The possible opening of a semicircle at the high frequencies in the Nyquist plot can be attributed to nonuniform electrodes as described by Dsoke et al. in Ref. [14]. Since this kind of contribution can be minimized by operating on the fabrication procedures, attention shall be paid to the fabrication of the electrodes.

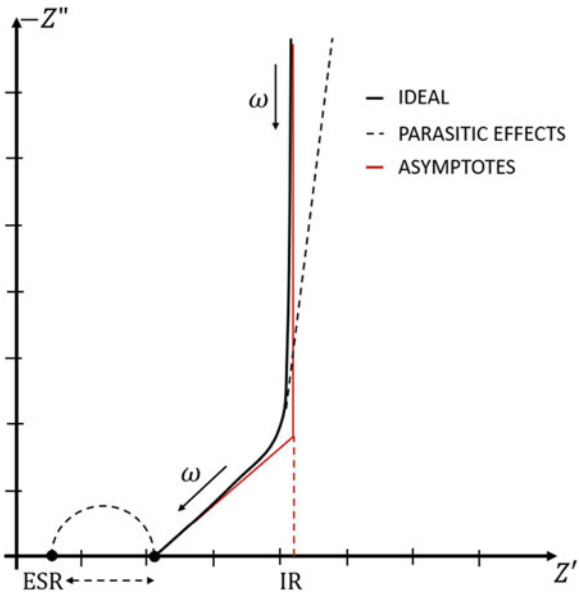

Fig. 9.6 Nyquist plot of a supercapacitor reproduced based on [12]. In black, the ideal profile, in dashed parasitic effects in the system, and in red the asymptotes

9.2.2 EDLC Materials

Idrees et al. demonstrated a direct ink writing (DIW) 3D printed EDLC device printed using Hyrel3D 30 M printer equipped with an extrusion head [15]. In this work, the activated carbon (AC) was the main active material, synthesized from a starch source. The activated material was thoroughly washed and then used to prepare inks for the 3D printing process. The weight percentage of the AC in the ink was 35% as the maximum observed printable limit. The electrolyte was 3D printed too, and the final device was characterized by a stacked configuration with metal current collectors. The rated electrochemical performances were 328.9 mF cm^{-2}, or 3.5 F g^{-1}, in polyvinyl alcohol (PVA) H_3PO_4 at 1.0 V with energy and power densities of 0.484 Wh kg^{-1} and 15.01 W kg^{-1}, respectively. In a cyclability test, the device retained 90% of its initial capacitance after 500 cycles.

In the field of selective laser sintering (SLS) processes, in 2014, it was demonstrated that polymers converted into carbon materials under laser radiation have features like graphene [16]. The material was named laser-induced graphene (LIG). During the photothermal process, the polymer breaks his bonds rearranging in a carbon structure. Successively, it was demonstrated that by tuning the laser parameters, it is possible to tune the morphology as shown in Fig. 9.9c) [17]. The technique allows to process materials with unique features from this point of view such as ion exchange properties and compatibility with the laser conversion process. This was the case of the work of Lamberti et al., in which sulphonated polyether ether ketone (SPEEK) was exploited as substrate for LIG production and as ion exchange membrane for the solid electrolyte. A picture of the LIG electrodes obtained on SPEEK is reported in Fig. 9.7d) [18].

In a recent work of Reina et al. [19], a 2D LIG device obtained via a SLS process was decorated with AC particles to boost the EDLC capacitance of LIG. In this case, LIG was exploited as current collector, mainly. An AC slurry diluted into dimethyl sulfoxide (DMSO) together with carbon blacks (CB) and polyvinylidene fluoride (PVdF) as binder led to a remarkable increase in performances. The diluted mixture was vacuum infiltrated in the LIG matrix compatible with the AC and CB particles. In order to ease the process, LIG wettability was increased, thanks to nitric acid activation favoring infiltration [19].

Carbon nanotubes (CNTs) were also demonstrated to be 3D printable in DIW setups. N-dodecyl sulfate surfactant was used to stabilize the CNT suspension in water-based ink. Interdigitated devices were printed together with a gel electrolyte composed of PVA-LiCl. A flexible micro-supercapacitor (MSC) was fabricated by printing over a Kapton substrate. The MSC rated 15.34 F cm^{-3} at 1.0 V voltage window with ESR of 100 Ω. Volumetric energetic quantities were rated 2 mWh cm^{-3} and 10 W cm^{-3}. Concerning cycling stability, the device retained 95.6% initial capacitance after 5000 cycles at 1.32 A cm^{-3} [20].

9.2.3 Redox-Active Materials: 2D-3D Pseudocapacitors

Redox-active materials like metal oxides (MOs) or conducting polymers (CPs) can show voltage to charge characteristics typical of capacitive systems, hence giving rise to pseudocapacitance. Charge storage mechanisms in these two classes of materials are different: in MOs, changes in oxidation state of transition metal atoms are responsible for accumulation while in CP polymer's doping is the liable phenomenon for charging and discharging. In both cases, active material conductivity is of fundamental role in favoring the storage process. In conductive polymers, for example, as the material gets doped, conductivity increases since the band structure approaches the semimetallic phase [21].

In the case of MOs, the charging process is related to a surface abundance of reaction sites, having a coverage θ. It is assumed that the equilibrium redox potential linearly increases with θ giving rise to a capacitor response [22]. With respect to batteries then, no clear peak will be identified in the current-voltage characteristics but a rectangular symmetric curve. In literature, some models related to storage caused by defect states in the bandgap of MOs are reported also [23]. In CPs, the doping levels due to oxidant and reductant species are less than unit per monomer [24].

2D materials like reduced graphene oxide (rGO), MXene, and metal dichalcogenides can show pseudocapacitive behavior such as intercalation pseudocapacitance, that is, ion insertion in the crystallographic planes of 2D materials, like lithium-ion in graphite batteries. This phenomenon, differently from batteries, happens with faster kinetic and does not produce any phase change in the material [25].

In 2D-3D manufacturing, electrochemical supercapacitors based on pseudocapacitive materials have been demonstrated either in 2D or 3D architecture. Direct ink writing (DIW), laser scribing techniques, and fused deposition modeling (FDM) are used to pattern electrodes or current collectors directly, in some cases, 3D scaffolds; interdigitated structures are fabricated, as observed in Fig. 9.9, and stacked with or covered by polymer electrolyte to make all-solid-state devices.

Metal oxides and intercalation materials are the most preferred because of the good trade-off between theoretical-specific capacitance, electrochemical performance, and costs. Polymers are mainly limited by the low specific capacitances. Most of the literature are focused on the development of MnO_2-based technologies because of its appealing characteristics as shown in Fig. 9.8. Usually, they are exploited as decoration of conductive substrates in order to improve performances, as shown in the micrographs of Fig. 9.9.

In 2015, a selective laser sintering (SLS) process was implemented to build 2D devices based on manganese dioxide, MnO_2, and ferric hydroxide, FeOOH [28]. The laser tool was a Universal X-660 laser cutter platform, based on a CO_2 laser. In this case, laser radiation was used to convert a polymeric substrate into conductive material named laser-induced graphene (LIG). This conductive phase, in this occasion, was exploited as high surface area current collector where active pseudocapacitive materials were deposited. The device architecture is reported in Fig. 9.7b). In the case of MnO_2, the material was electrodeposited from a 0.01 M $Mn(CH_3COO)_2$ aqueous solution. Electron micrographs are reported in Fig. 9.9a). In the other case, also FeOOH was electrodeposited from a pH-adjusted electrodeposition bath containing $FeCl_3$. Starting thicknesses were close to 30 μm for the LIG current collector, and after the electrodeposition, the overall thicknesses were not above 150 μm letting these kinds of devices being considered 2D. Despite the lower specific capacitance of MnO_2, this family of devices showed the best performances in this work, with an outstanding areal capacitance of 934 mF cm^{-2} if compared to the hybrid device FeOOH – MnO_2 with 21.9 mF cm^{-2}. However, in the second case, higher power densities were achieved: 11.8 mW cm^{-2} in the case of the asymmetric device, while 2.33 mW cm^{-2} in the other case. The electrolyte was a gel polymer type consisting of LiCl in PVA matrix. Both devices showed a good capacitance retention greater than 80% upon cycling at constant current rates of 1 mA cm^{-2}.

In 2018, a direct ink writing (DIW) method was exploited to fabricate a 2D device. The active material was a hybrid configuration of vanadium pentoxide, V_2O_5, and vanadium nitrate, VN, quantum dots (VNQDs) as cathode and anode, respectively [27]. This was an example of all-3D printed 2D device by means of a Fisnar F4200n benchtop robot. A device picture is reported in Fig. 9.7c). Also the polymer electrolyte composed of LiCl-PVA was deposited via nozzle. The device showed c.a. 208 mF cm^{-2} at 1.6 V voltage window with fair high energy and power densities of 73.9 μWh cm^{-2} and 3.77 mW cm^{-2}, respectively. The device could retain 65% of its initial capacitance after 8000 cycles at a current density rate of 6 mA cm^{-2}.

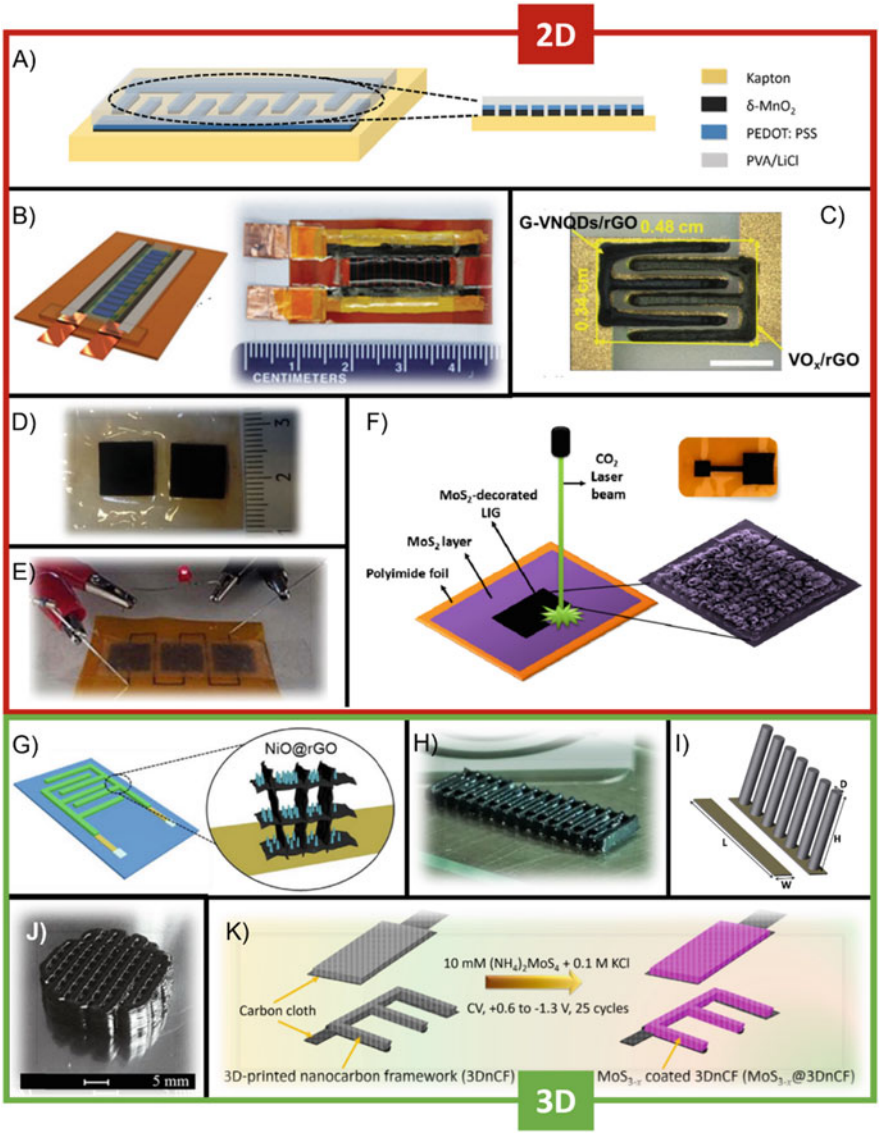

Fig. 9.7 Examples of electrode architecture in 2D and 3D printing technologies. 2D devices can be ink printed as in the cases of (**a**) δ-MnO_2 on polyimide [26] and (**c**) VNO-rGO composite [27]. In cases (**b**) and (**d–f**), laser was used to pattern current collectors, subsequently functionalized with pseudocapacitive materials (**b** and **f**), covered by ion exchange membrane (**d**) or used as EDLC electrodes directly (**e**) [17, 18, 28, 29]. 3D printed architectures of thicknesses greater than 0.5 mm. In cases (**g**) and (**k**), a carbon matrix was printed as support extension to the current collector and then functionalized [30, 31]. Whereas in cases (**h–j**), the active material was directly printed [32–34] (**j**) was reprinted (adapted) with permission from Ref. [34]. (Copyright 2018 American Chemical Society)

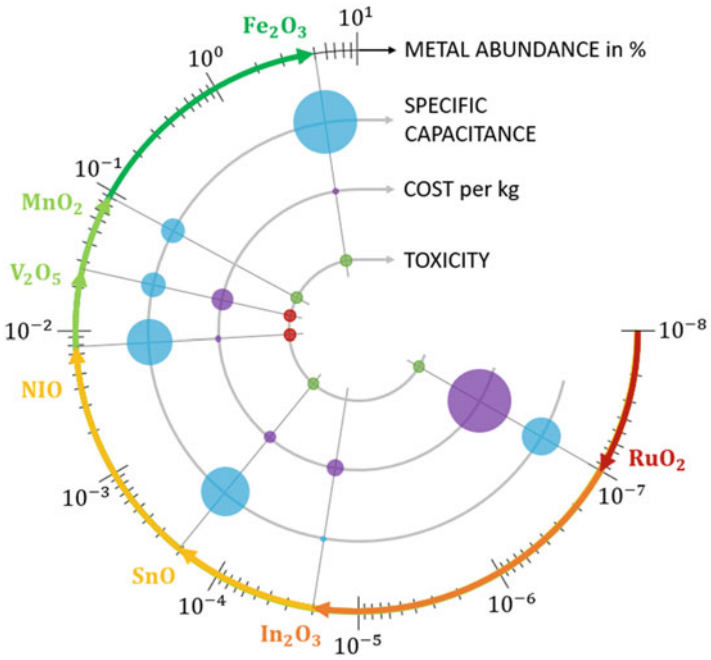

Fig. 9.8 Metal oxides in capacitive energy storage. Metal atom abundance, specific capacitances, costs, and toxicity are represented

In another work, Wang et al. demonstrated a type of current collector-free system based on the deposition of an ink composed of δ-MnO_2 dispersed in a 1:10 solution of propylene glycol:water carefully filtered in order to avoid nozzle clogging [26]. The printing tool was a Dimatix DMP-2800 inkjet printer (Fujifilm Dimatix) equipped with a 10 Pl cartridge, DMC-11610. The printed MO was then covered by inkjet printed PEDOT:PSS. The device is schematically reported in Fig. 9.7a), while an electron micrograph is reported in Fig. 9.9d). The symmetrical device was characterized in aqueous polymer gel electrolyte composed of LiCl in PVA matrix. The device behaved resistively because of the absence of the current collector, as the reported ESR was 7 kΩ. However, reasonable volumetric energy and power densities were rated, 0.2 mWh cm^{-3} and 18.0 mW cm^{-3}, respectively.

A DIW method was implemented to fabricate thick 3D scaffolds with high MnO_2 loading [35]. The 3D template was created with an ink of dispersed graphene oxide (GO) in a mixture of water and 5% hydroxypropyl methylcellulose, extruded by means of an air-powered fluid dispenser Ultimus V, EFD. The scaffold was then annealed at 1050 °C for 3 h with controlled heating and cooling rate of 2 °C min^{-1}. The burned structure resulted in good structural and electrical properties. The pseudocapacitive material was electrodeposited directly on the reduced graphene oxide scaffold. Micrographs of the obtained materials are reported in Fig. 9.9f). The device was tested in a 3 M LiCl solution in stacked configuration. The calculated specific capacitance was 0.55 F cm^{-2}, corresponding to 275 F g^{-1}.

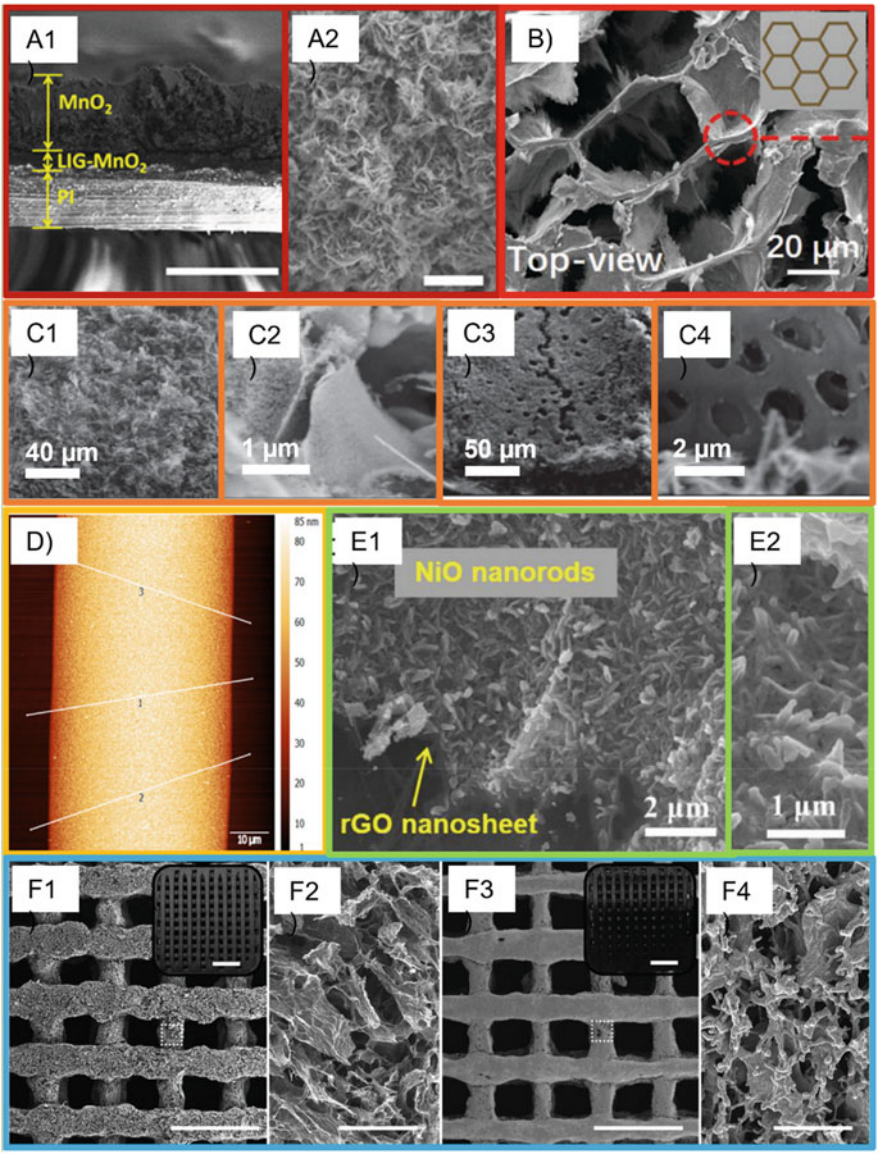

Fig. 9.9 Micrographs of the structural features of 3D printed materials. In (A1) and (A2) are side view and top view of LIG decorated with MnO_2 (the scale bar corresponds to 100 µm) [28]. In (B), the honeycomb structure of the composite material composed of Mxene, MnO_2 NWs, AgNWs, and C60 [36]. In (C1) and (C2), the sheet morphology of LIG, while in (C3) and (C4) the porous one [17]. In (D), an AFM image showing the thickness features of the 3D printed optimized δ-MnO_2 ink [26]. In (E1) and (E2), the rGO nanosheet covered by grown NiO [30]. In (F1–F4), 3D scaffold electron microscopies in the case of the graphene aerogel lattice, in (F1) and (F2), and of the 3D printed template electrodeposited with MnO_2, in (F3) and (F4). Scale bars are of 1 mm in (F1) and (F3) and of 40 µm in (F2) and (F4) [35]

In 2019, an Rgo 3D printed template was grown in an extrusion-based 3D printing system and subsequently subjected to an electrodeposition process of NiO from nickel nitrate [30]. After the deposition process, the device was calcinated at 300 °C for 2 h. The device was characterized in symmetrical configuration. The device architecture is depicted in Fig. 9.7g), while materials' micrographs are shown in Fig. 9.9e). An areal capacitance of 197.5 mF cm^{-2} was rated at voltage window of 1.0 V in a gel polymer electrolyte composed of PVA-1 M KOH. Stability tests showed a capacitance retention of 86.1% after 10,000 cycles carried out at 3 V s^{-1}.

In 2020, Li et al. showed a 3D printable electrode where the active material was titanium carbide Mxene, $Ti_3C_2T_x$, mixed with MnO_2 nanowires (NWs) and silver NWs, AgNWs. The material was printed by means of benchtop robot FiSNAR F7304N on a stretchable substrate, that is, PDMS [36]. A micrograph of the obtained material is reported in Fig. 9.9b). To guarantee good mechanical properties, the composite material was also provided with some C60 carbon black. The symmetrical device was rated with an areal capacitance of 216 mF cm^{-2} at 0.8 V of stability window in a polymer-based electrolyte consisting of PVA-KOH mixture. The energy density was 19.2 μWh cm^{-2}, while the power density reached an outstanding value of 58.3 mW cm^{-2}, properly due to the good electrical conductivity of MXene.

From a critical point of view, symmetrical characterizations are not always recommended. By considering the electrochemical processes occurring at the electrode's material, for example, it is possible to appreciate that some redox-active materials shall be preferentially used at anodes or cathodes. Materials like MnO_2 undergo simple reactions, like

$$MnO_2 + C^+ + e^- \rightleftharpoons MnOOC$$

being C^+ a proton or an alkali metal cation. In a SC cell, then, it would be preferred to exploit such material at anodes. Some other materials, like NiO, either in the oxide or hydroxide state, are more suitable at cathodes since the possible electrochemical reactions are

$$Ni(OH)_2 + OH^- \rightleftharpoons NiOOH + H_2O + e^-$$

$$NiO + OH^- \rightleftharpoons NiOOH + e^-$$

Some other materials, like iron oxide, can undergo several solid-state reactions according to the nature of the oxide itself [37], as can be observed by the following electrochemical reactions:

$$3FeO + H_2O \rightleftharpoons Fe_3O_4 + 2H^+ + 2e^-$$

$$2FeO + H_2O \rightleftharpoons Fe_2O_3 + 2H^+ + 2e^-$$

$$2FeO \cdot (x\ H_2O) + H_2O \rightleftharpoons Fe_2O_3 \cdot (y\ H_2O) + 2H^+ + 2e^-$$

$$2Fe_3O_4 + H_2O \rightleftharpoons 3Fe_2O_3 + 2H^+ + 2e^-$$

$$2Fe_3O_4 \cdot (x\ H_2O) + H_2O \rightleftharpoons 3Fe_2O_3 \cdot (y\ H_2O) + 2H^+ + 2e^-$$

Most of these reactions are pH dependent, hence implying a proper electrolyte design. Anodic and cathodic measurements must be performed to optimize the device performance.

Concerning the development of polymer-based devices, in 2011, polypyrrole (Ppy) was electrodeposited on a 3D-patterned device grown with a lithographic process [33]. SU8 of different thicknesses was spin coated on a SiO_2 substrate, UV cured, and developed to have current collector and lamellar structure of cylindrical pillars on the interdigitated current collectors, as illustrated in Fig. 9.7i). The whole structure was then pyrolyzed at 1000 °C for 1 h in a forming atmosphere composed of hydrastar mixture with 5% H_2. Ppy was then electrodeposited in a three-electrode setup by dispersing this monomer in a supported electrolyte of $LiClO_4$. The characterized device showed an areal capacitance of 78.35 mF cm^{-2} at 0.8 V of voltage window.

Polyaniline (PANI) was used in a 2D device configuration with LIG current collectors [28]. The device was characterized in PVA-H_2SO_4 gel electrolyte with 0.8 V voltage window. The device architecture is reported in Fig. 9.7b). The device rated an areal capacitance of 361 mF cm^{-2} with an energy density of 8.0 μWh cm^{-2} and maximum power density of 0.65 mW cm^{-2}. Concerning the cycling stability, the microsupercapacitor could retain 97% of its initial capacitance after 6000 cycles at 0.8 mA cm^{-2}.

Another PANI composite material was 3D printed in a DIW process in 2018 by Wang et al. [34]. PANI was obtained via polymerization reaction, and the ink was composed of NMP-water solvent mixture and printed via homemade tool. A 3D structure produced with the present material is reported in the picture of Fig. 9.7j). An interdigitated device was assembled and tested in a 0.8 V voltage window. The rated gravimetric capacitance was of 93 F g^{-1} with a very low ESR of 0.8 Ω. Concerning the device stability, the SC could retain 75% of the initial capacitance after 1000 cycles at 50 mA cm^{-2}.

2D Active Materials: 2D-3D Pseudocapacitors

Metal dichalcogenides, reduced graphene oxide, and recently synthesized MXene represent the state of the art of the most exploited and studied 2D materials for capacitive energy storage. In these materials, intercalation pseudocapacitance is the most common mechanism featuring ions entering the tunnels or layers of redox-active materials with a charge transfer and no crystallographic phase change.

The exceptional conductive properties of MXene let Yang et al. develop an ink for a DIW process based on MXene only. They demonstrated the possibility to get interdigitated devices without any current collector, as reported in Fig. 9.7h). One peculiar aspect of these types of materials is that, if compared with high-surface-area activated carbons, the specific capacitance is way larger although it has a reduced specific surface area. Indeed, in the work of Yang et al., they could get devices working at 2 F cm^{-2} in a gel polymer electrolyte of PVA-H_2SO_4 with voltage window of 0.6 V. Despite the resistive behavior (ESR 16.83 Ω), the device rated 2 mWh cm^{-2} and 6.5 mW cm^{-2}. Finally, it could cycle 10,000 cycles at 1 A g^{-1} retaining 90.4% of the initial capacitance [32].

Azhari et al. exploited the additive manufacturing equipment from the 3D Systems, Burlington, to print rGO-based electrodes decorated with palladium nanoparticles [38]. The stacked electrodes were measured 700 mF cm^{-2}, equivalent to 270 F g^{-1} in this case, in 1.0 V voltage window in 1 M H_2SO_4. Concerning the cycling stability, the SC retained 85% of its initial capacitance after 1000 cycles recorded at 3 A g^{-1}.

In another work of Zhu et al., a mixture of GO and graphene nanoplatelets (GNPs) was exploited to print capacitive electrodes. GNPs were used to improve the ink conductivity and were introduced together with some reactants used to induce gelation post printing, such as resorcinol and formaldehyde. Silica nanoparticles were used to improve the final rheological properties of the ink. A 3D scaffold was fabricated and tested in stacked configuration. The related performances were 85 F g^{-1} at 0.8 V in 3 M KOH, with a low ESR of 0.5 Ω. Gravimetric and volumetric energy densities were rated 0.14 mWh cm^{-3} and 0.26 Wh kg^{-1}, concerning power densities: 3 W cm^{-3} and 4 kW kg^{-1}. Moreover, the device could retain 95.5% of its initial specific capacitance after 10,000 cycles at 200 mV s^{-1} [39].

Clerici et al. reported the one-pot synthesis of MoS_2-decorated LIG. An MoS_2 dispersion was spin coated on the polyimide substrate and exposed to laser radiation. The conversion process was demonstrated resulting into LIG decoration with MoS_2. A representative process scheme is provided in Fig. 9.7f). The MSC was characterized in aqueous polymer electrolyte 1 M NaCl in a PVP matrix. The device was also shown to be able to directly store electrical energy coming from a harvesting source like a solar cell [29]. The overall performance was of 13 mF cm^{-2} at 1.0 V with 3.0 μWh cm^{-2} and 100 μW cm^{-2} as areal energies and power, respectively. Finally, the device retained 100% capacitance after 2000 at 10 mV s^{-1}.

A GO variation named reduced Holey GO was 3D printed via DIW procedure and functionalized with cobalt oxide, Co_3O_4. An interdigitated device was rated 241.3 mF cm^{-2} at 1.0 V in PVA-KOH gel polymer electrolyte [40]. The presented literature results, as well as many others, are summarized in Table 9.1.

Table 9.1 Summarized information and performances, concerning 2D/3D supercapacitor technologies

Process data			Electrical parameters							
Technique	Architecture	Material composition	Capacity capacitance	Voltage	Electrolyte	Resistance	Energy density	Power density	Retention – cy.# @ rate	References
DIW	Interdigitated 3D	MXene	2 F cm^{-2}	0.6 V	PVA-H_2SO_4	ESR 16.83 Ω	2 mWh cm^{-2}	6.5 mW cm^{-2}	90.4% – 10,000 @ 1 A g^{-1}	[32]
DIW	Interdigitated 2D	VOx-rGO VNQDs-rGO	207.9 mF cm^{-2}	1.6 V	PVA-LiCl	//	73.9 μWh cm^{-2}	3.77 mW cm^{-2}	65% – 8000 @ 6 mA cm^{-2}	[27]
DIW	Staked	Thermally reduced GO-Pd	700 mF cm^{-2} 270 F g^{-1}	1.0 V	1 M H_2SO_4	ESR 0.5 Ω			85% – 1000 @ 3 A g^{-1}	[38]
DIW	Interdigitated	CNT	15.34 F cm^{-3}	1.0 V	PVA-LiCl	ESR 100 Ω	2 mWh cm^{-3}	10 W cm^{-3}	95.6% – 5000 @ 1.32 A cm^{-3}	[20]
DIW	3D scaffold	Graphene aerogel – GO-SiO_2	85 F g^{-1}	0.8 V	3 M KOH	ESR 0.5 Ω	0.14 mWh cm^{-3} 0.26 Wh kg^{-1}	3 W cm^{-3} 4 kW kg^{-1}	95.5% – 10,000 @ 200 mV s^{-1}	[39]
DIW	3D scaffold	MnO_2	0.55 F cm^{-2} 275 F g^{-1}	0.8 V	3 M LiCl	ESR 1.2 Ω cm^2	0.4 mWh cm^{-2}	30 mW cm^{-2}	100% – 10,000 @ 20 mV s^{-1}	[35]
SLA	Interdigitated		0.206 mF cm^{-2}	1.0 V	PVA-$LiClO_4$	//	//	//	//	[41]
DIW	Interdigitated 3D	NiO	197.5 mF cm^{-2}	1.0 V	PVA-1 M KOH	ESR 1.4 Ω	//	//	86.1% – 10,000 @ 3 V s^{-1}	[30]

(continued)

Table 9.1 (continued)

Process data			Electrical parameters							
Technique	Architecture	Material composition	Capacity capacitance	Voltage	Electrolyte	Resistance	Energy density	Power density	Retention – cy.# @ rate	References
DIW	Interdigitated	rHGO	241.3 mF cm^{-2}	1.0 V	PVA-KOH	//	//	//	91% – 11,000 @ 10 mA cm^{-2}	[40]
SLS	Interdigitated 2D	LIG-MnO_2	934 mF cm^{-2} 93.4 F cm^{-3}	1.0 V	PVA-LiCl	//	32.4 μWh cm^{-2} 3.2 mWh cm^{-3}	2.33 mW cm^{-2} 298 mW cm^{-3}	82% – 6000 @ 1 mA cm^{-2}	[28]
		LIG-FeOOH-LIG-MnO_2	21.9 mF cm^{-2} 5.4 F cm^{-3}	1.8 V	PVA-LiCl	//	9.6 μWh cm^{-2} 2.4 mWh cm^{-3}	11.8 mW cm^{-2} 2.9 W cm^{-3}	84% – 2000 @ 1 mA cm^{-2}	
		LIG-PANI	361 mF cm^{-2} 47.5 F cm^{-3}	0.8 V	PVA-H_2SO_4	//	8.0 μWh cm^{-2} 1.1 mWh cm^{-3}	0.65 mW cm^{-2} 1.5 mW cm^{-3}	97% – 6000 @ 0.8 mA cm^{-2}	
	Staked	Polypyrrole on ITO	3.6 mF cm^{-2} 2.0 mF cm^{-2}	1.2 V 0.8 V	PVA-H_3PO_4 PEO-$LiCF_3SO_3$ + PEG	IR 1300 Ω cm^2 IR 1700 Ω cm^2	12 Wh kg^{-1} //	// //	30% – 1000 @ 10 mA cm^{-2} 90% – 1000 @ 10 mA cm^{-2}	[42]
		Polypyrrole on C	20.0 mF cm^{-2} 5.0 mF cm^{-2}	1.2 V 0.8 V	PVA-H_3PO_4 PEO-$LiCF_3SO_3$ + PEG	IR 500 Ω cm^2 IR 1860 Ω cm^2	// //	// //	60% – 1000 @ 10 mA cm^{-2} 79% – 1000 @ 10 mA cm^{-2}	
DIW	Interdigitated 3D	PPy/C-MEMS	78.35 mF cm^{-2}	0.8 V					57% – 1000 @ 20 mV s^{-1}	[33]

DIW	Interdigitated 2D	d-MnO_2-PEDOT:PSS	2.4 F cm^{-3}	0.8 V	PVA-LiCl	ESR 7 kΩ	0.2 mWh cm^{-3}	18.0 mW cm^{-3}	78% – 3600 @ 0.2 A cm^{-3}	[26]
DIW	Staked	Activated carbons	328.9 mF cm^{-2} 3.5 F g^{-1}	1.0 V	PVA H_3PO_4		0.484 Wh kg^{-1}	15.01 W kg^{-1}	90% – 500 @ NS	[15]
DIW	Interdigitated 3D	Sodium ascorbate-capped MXene	720.7 F cm^{-3}	1.0 V	PVA-H_2SO_4	ESR 20 Ω	120 mWh cm^{-3}	1.9 W cm^{-3}	94.7% – 4000 @ 1 A g^{-1}	[43]
DIW	3D scaffold	PANI-GO	93 F g^{-1}	0.8 V	1 M H_2SO_4	ESR 0.8 Ω	//	//	75% – 1000 @ 50 mA cm^{-2}	[34]
DIW	Interdigitated 2D	MXene MnO_2-NW ag-NW	216 mF cm^{-2}	0.8 V	PVA-KOH	ESR 15 Ω	19.2 μWh cm^{-2}	58.3 mW cm^{-2}	85% – 10,000 @ 200 mV s^{-1}	[36]
FDM	Interdigitated	AC MoSx	4.2 mF cm^{-2}	0.6 V	PVA-H_2SO_4	ESR 50 Ω	0.2 μWh cm^{-2}	100 μW cm^{-2}	90% – 10,000 @ 0.16 mA cm^{-2}	[44]
FDM	3D scaffold	MXene MoS_2-x	160 mF cm^{-2}	1.6 V	PVA-H_2SO_4	ESR 2.2 Ω	56.9 μWh cm^{-2}	6 mW cm^{-2}	92.8% – 25,000 @ 7.5 mA cm^{-2}	[31]
SLA	3D scaffold and staked	GO	13.1 F g^{-1} 57.55 mF cm^{-2} 259.9 F cm^{-3}	1.0 V	PVA-KOH	ESR 4 Ω	8 μWh cm^{-2} 36 μWh cm^{-3}	12.56 mW cm^{-2} 56.52 mW cm^{-2}	96% – 5000 @ 100 mV s^{-1}	[45]
SLA	Interdigitated 2D	MoS_2 – Decorated LIG	10 mF cm^{-2}	1.0 V	PVA 1 M NaCl	ESR 600 Ω	3 μWh cm^{-2}	2 mW cm^{-2}	100% – 2000 @ 0.25 mA cm^{-2}	[29]
SLA	Interdigitated 2D	AC – Decorated LIG	20.7 mF cm^{-2}	0.8 V	KCl 1 M		0.3 μWh cm^{-2}	200 μW cm^{-2}	90% – 420 h FT @ 0.8 V	[19]

9.3 2D and 3D Printing of Micro-batteries

9.3.1 Electrochemical Characterization of Batteries

Batteries are electrochemical energy storage devices in which chemical energy is converted into electrical one because of redox reaction. According to the chemical reversibility of the reactions occurring at both positive and negative electrodes, batteries are classified into primary and secondary. In primary batteries, there is no reversibility in the electrochemical processes; hence, devices are not rechargeable. Whereas in secondary battery technology, electrochemical processes are chemically reversible, the devices are hence rechargeable. Secondary batteries are most investigated also in the field of 3D energy storage devices and thus will be the main treated device category in this section.

Anodic and cathodic battery materials are divided into intercalation and conversion materials. Intercalation materials like graphite or transition metal dichalcogenides are those materials in which reversible insertion (or inclusion) of ionic species occurs between the planes of the layered structures. Conversion materials are divided into two categories according to the reaction type and are mainly based on transition metal compounds:

- Type A: $M_aX_b + (bc)Li^+ + (bc)e^- \leftrightharpoons aM^0 + bLi_cX$
- Type B: $X + aLi^+ + ae^- \leftrightharpoons Li_aX$

where M is the transition metal element and X the anionic species in the lattice matrix. The classes of these materials are transition metal oxides, fluorides, sulfides, phosphides, and nitrides. They possess higher theoretical capacity with respect to intercalation materials and sometimes lower costs. One peculiar aspect of conversion material can be the low volume expansion during electrochemical reaction, making them appealing for 3D printing of battery electrodes. In particular, lithium-titanium oxide (LTO) and lithium iron phosphate (LFP) show low to no volume expansion with 0% for LTO and 2.2% for LFP.

A graphical recap concerning battery materials was reported in the research review of Nitta et al. [46]. The two main images are reported in Figs. 9.10 and 9.11.

Cyclic Voltammetry (CV)

Battery materials are tested electrochemically in half cells vs. metallic lithium and lithium reference. Cyclic voltammetries, galvanostatic charge and discharge, and electrochemical impedance spectroscopy can be also well exploited to characterize battery materials. Because of the low reaction kinetics due to intrinsic materials' resistivities and consequent iR-drop effect, battery materials are tested at low time constants, that is, low scan rates or current rates, to get information and energy out of the chemically reversible reactions. In Fig. 9.12, the CV of a lithium cobalt oxide electrode is reported. In this voltammogram, oxidation and reduction peaks are visible. Electrochemical reversibility is achieved when the peaks distance is

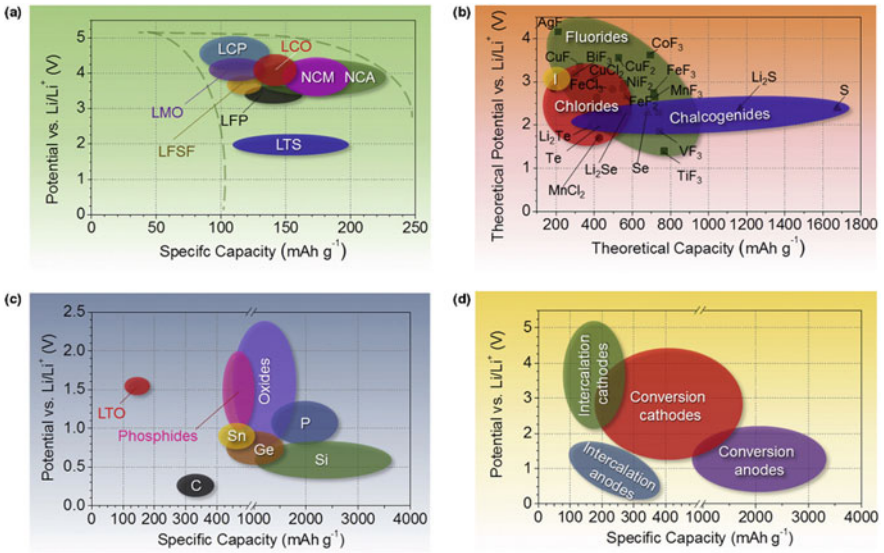

Fig. 9.10 Approximate range of average discharge potentials and specific capacity of some of the most common (**a**) intercalation-type cathodes (experimental), (**b**) conversion-type cathodes (theoretical), (**c**) conversion-type anodes (experimental), and (**d**) an overview of the average discharge potentials and specific capacities for all types of electrodes. (Reprinted under the Creative Commons CC BY NC ND from Ref. [46])

limited to less than 60 mV implying a situation in which the equilibrium reaction rate constant is high. For low constant rates, the reactions can be considered quasi-reversible or irreversible from an electrochemical point of view, affecting the so-called polarization parameter in battery. As mentioned above, iR-drop affects the actual oxidation and reduction potentials; therefore, the resistivities of the materials play a fundamental role in battery operation.

Galvanostatic Charge and Discharge (GCD)

Galvanostatic tests are run referring to the so-called C-rate. The C-rate is a measurement of the intensity at which batteries are charged and discharged relatively to their maximum capacity. Given a material of known specific capacity (e.g., mAh g^{-1}), by knowing the amount of material in the device, the current equivalent to the C-rate is calculated to provide a fixed discharge time. For example, 1C gives 1 h of discharge, 10C 6 min, and C/10 10 h. A representative image of a GCD plot is reported in Fig. 9.13. Here, it is clearer the concept of polarization effects mentioned before. $\Delta E = E_{ox} - E_{red}$ represents the thermodynamic hysteresis due to the electrochemical reversibility of the redox process. Kinetic polarization is due to the resistive effects, that is, the iR-drop. The more resistive the electrode, the more slopy the charging and discharging branches will become with increasing C-rate.

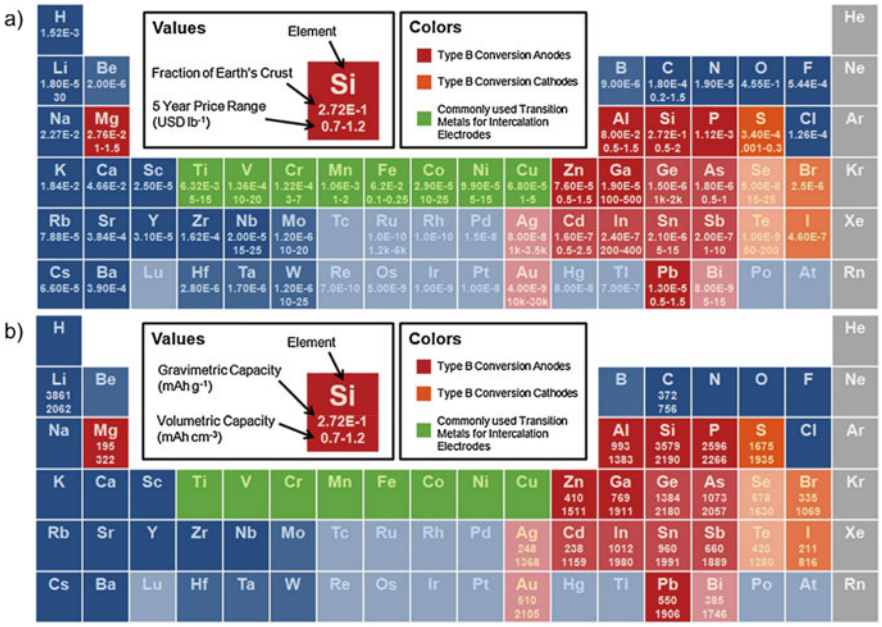

Fig. 9.11 (**a**) Availability and (**b**) capacities of elements that may host Li as electrodes. Elements with abundance (as fraction of Earth's crust) below 10^{-5} are slightly faded, and elements below 10^{-7} are faded further. Gravimetric and volumetric capacities are theoretical values calculated based on delithiated mass and lithiated volume. (Reprinted under the Creative Commons CC BY NC ND from Ref. [46])

All the previous considerations let bring to the conclusion that the more resistive the electrodes, the lower will be the energetic efficiency in batteries, being the electrodes themselves slightly energetically inefficient because of the thermodynamic limitations. To better appreciate this, let us recall that in the ideal case, the black dashed line of Fig. 9.13, the electrode energy content is $E = V\,Q$, which is the area under the potential profile cure. Further, while increasing the C-rate, capacity fading with respect to the theoretical value can be observed because of mass-transport limitation. The typical figure of merit is the further increased sloping near the potential limits.

From the energy and power data evaluated during these experiments, it is possible to represent the device performance in the Ragone plot in the energy vs. power representation, as in the case of supercapacitors. A close set of formulas are useful to be applied for such. If one evaluates exactly energy and charge, then

$$E = \int_{\Delta t} i(t)v(t)\,dt$$

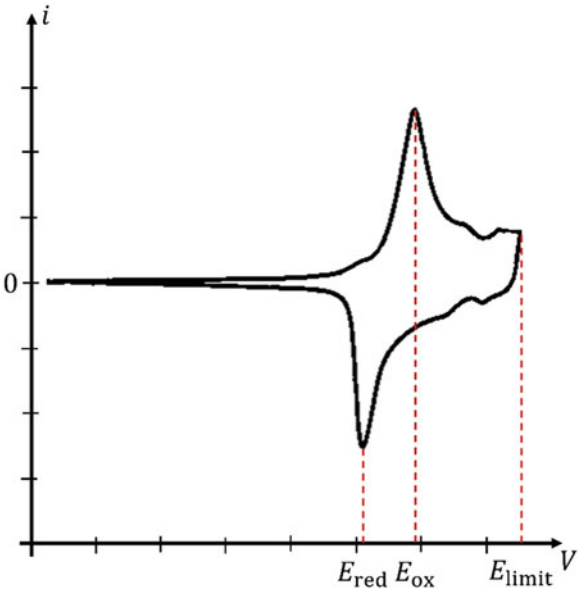

Fig. 9.12 CV plot of a LCO electrode in which oxidation and reduction reactions are clearly visible

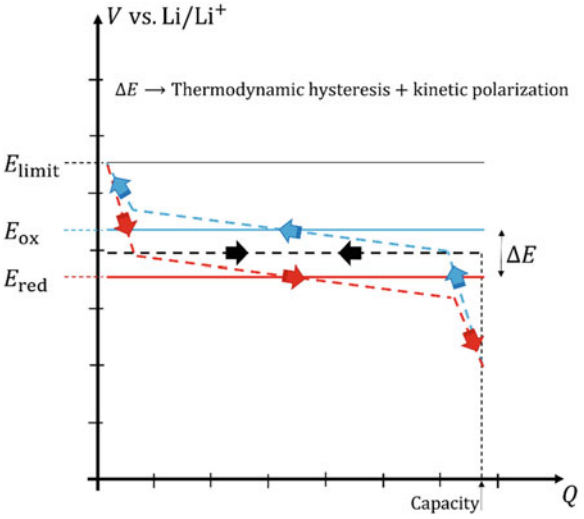

Fig. 9.13 Galvanostatic plot of a LCO electrode in V vs. Q scale. ΔE hysteresis is due to thermodynamic ($E_{ox} - E_{red}$) and kinetic polarization (iR-drop) reasons. The dashed black line represents an ideal behavior of a battery electrode; red and blue lines represent discharge and charge profiles, respectively. Continuous lines are ideal behaviors with only thermodynamic hysteresis effect, while dashed lines are more representative of a real behavior strongly influenced by iR-drop

$$Q = \int_{\Delta t} i(t)\, dt$$

where $v(t)$ and $i(t)$ are the voltage and current signals, respectively. If the evaluations are carried out in the semi-periods Δt of charge and discharge, then charging and discharging quantities are available for the evaluation of the coulombic and energetic efficiencies:

$$\eta_C = \frac{Q_d}{Q_c}$$

$$\eta_E = \frac{E_d}{E_c}$$

Finally, the average discharge power can be calculated according to

$$P = \frac{E_d}{\Delta t_d}$$

Electrochemical Impedance Spectroscopy (EIS)
EIS can be exploited to get information concerning the reaction speed and electrode uniformity [47, 48]. As reported in [47], the overall cell behavior is influenced by the single electrode reaction speed (time constants) as evidenced in the typical semicircle in the Nyquist plots. Studies can be carried on in half cells to study the single electrode materials or in full cell to evaluate the overall behavior. However, from the full cell, it is difficult to get information on the single electrodes. When the electrode processes are dominated by diffusion phenomena, it is possible to observe such behavior also in the low-frequency regime. Improper active material contacting on the current collector will cause an overall increase in the real part of the impedance reducing hence the kinetic properties of the final device. From this point of view, impedance spectroscopy confirms to be a powerful tool for insightful design of the electrodes. In Fig. 9.14, an exemplary Nyquist plot is reported. The two semicircles in bold line represent the electrode processes whose contribution to the overall resistance is $R_1 + R_2$. If the two time constants are of close values, the two semicircles overlap. The dashed semicircle can be attributed to parasitic effects introduced by the electrode fabrication process [48], as for the case of supercapacitors also. A diffusive behavior and consequent capacitive cell response might be also observed in battery impedance spectroscopy although the frequency range can result quite low to be properly appreciated. However, also in batteries, the limiting value of the real part defines the internal resistance (IR), which dictates the overall resistive response of the cell.

9.3.2 2D and 3D Printing of Secondary Batteries

Most of the literature on micro-batteries are focused on the coupling of mainly LFP or lithium manganese oxide (LMO) as cathode materials and LTO as anode material [49–55]. In most of these cases, DIW is the main adopted technique although some others like SLA and FDM were used. Concerning devices obtained with DIW method, all the works are focused on the printability of the inks which are

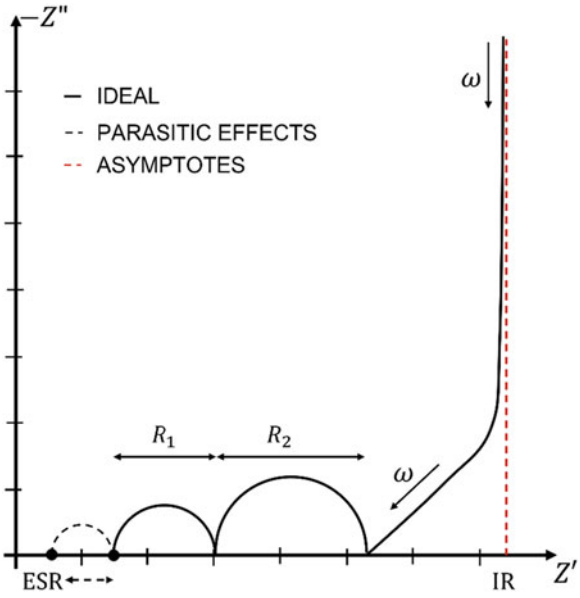

Fig. 9.14 Possible Nyquist plot of a battery device in which electrode reactions are clearly observable since the two time constants are much different. The dashed semicircle represents the effect of parasitic effects at electrode level due to nonuniform materials or issues at the current collector/active material interface

prepared with average apparent viscosity in the range of 10^5–10^6 Pa s at shear rate of 10^{-2} s^{-1}. Some of these works concern the preparation of the whole device like in the case of the process of Fig. 9.15a) and in the case of the device of Fig. 9.16a). Some works are focused only on the electrolyte preparation as depicted in the representation of Fig. 9.15b) [52, 56]. In this case, the slurry viscosity prior to printing the gel electrolyte composed of PVdF-alumina blend swollen in 1 M $LiPF_6$ in EC:DEC above the standard electrodes was 10^2 Pa s at 10^{-1} s^{-1}. Regardless, in this work, 3D printing technology has been proved to be a reliable method for the fabrication of batteries since the printed electrolyte performances were remarkable if compared with state-of-the-art separators. A process scheme is reported in Fig. 9.15b). The LFP electrode performance resulted unaltered in this half-cell experiment. In all the other DIW works based on the fabrication of devices, interdigitated structures were developed. LFP-LTO cells were assembled with open circuit voltages in the range of 1.5 V–1.8 V according to the potential difference between the standard electrode materials in lithium electrolyte environment. Remarkable results were obtained by the group of Lewis which demonstrated the possibility to fabricate micro-batteries with outstanding performance with additive manufacturing technologies. Indeed, in the case of commercial separator, the group demonstrated an LFP-LTO device with good cyclability and specific capacity below 5C, fair good capacity retention upon cycling (c.a. 75% after 100 cycles at 0.2 mA cm^{-2}), high coulombic and energetic efficiencies, and outstanding estimated self-discharge degree of discharge of 80% after 5 years. In all these works, it comes that a limitation of 3D technologies is given by the materials themselves. Not in all cases is possible to print very thick electrodes because of the materials' resistivities. After a limiting thickness,

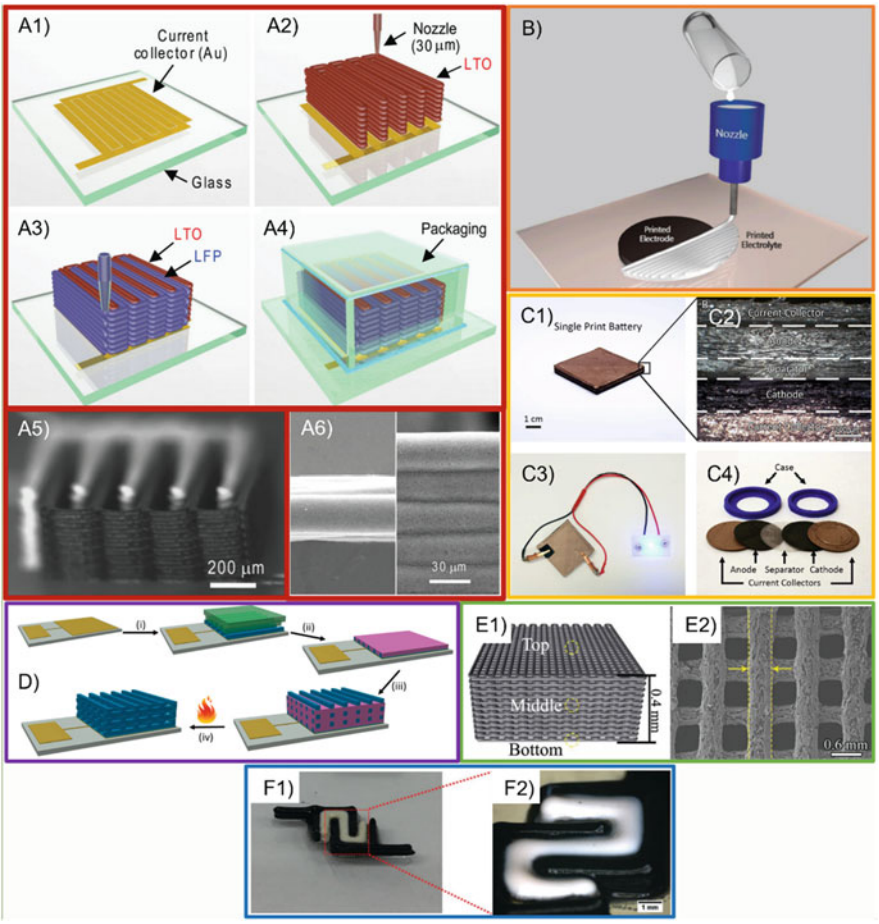

Fig. 9.15 In (**a**) 1, 2, 3, and 4 are representations of the interdigitated micro-battery fabrication and in 5 and 6 details of the printed electrodes layers [50]. In (**b**), a schematic representation of the DIW applied to print separators directly on standard electrodes [52]. In (**c**), 1 represents the stack, whose enlargement is depicted in 2. In 3, the working device while in 4 the 3D printed materials for device and coin cell packaging [53]. (**d**) Schematic illustration of the TiO_2 woodpile fabrication process [57]. In (**e**) 1 the Ni/rGO framework and in 2 a low magnification of the porous structure [58]. In (**f**) 1 a photograph of the micro-battery and in 2 a magnification of the 3D printed electrolyte [59]. (**c**) and (**d**) were reprinted (adapted) with permission from Ref. [53, 57]. (Copyright 2018 American Chemical Society)

electrode response does not follow the increasing trend of the electrode thickness and the specific capacitance fades. To solve this problem, attempts have been made by adding conductive particles such as Ketjenblack (KB) or rGO [49, 51, 55].

Packaging to preserve the electrochemical environment is the most difficult task for organic-based systems, but different solutions have been implemented with PDMS, PMMA, and Swagelok cells. Chen et al. exploited stereolithography as

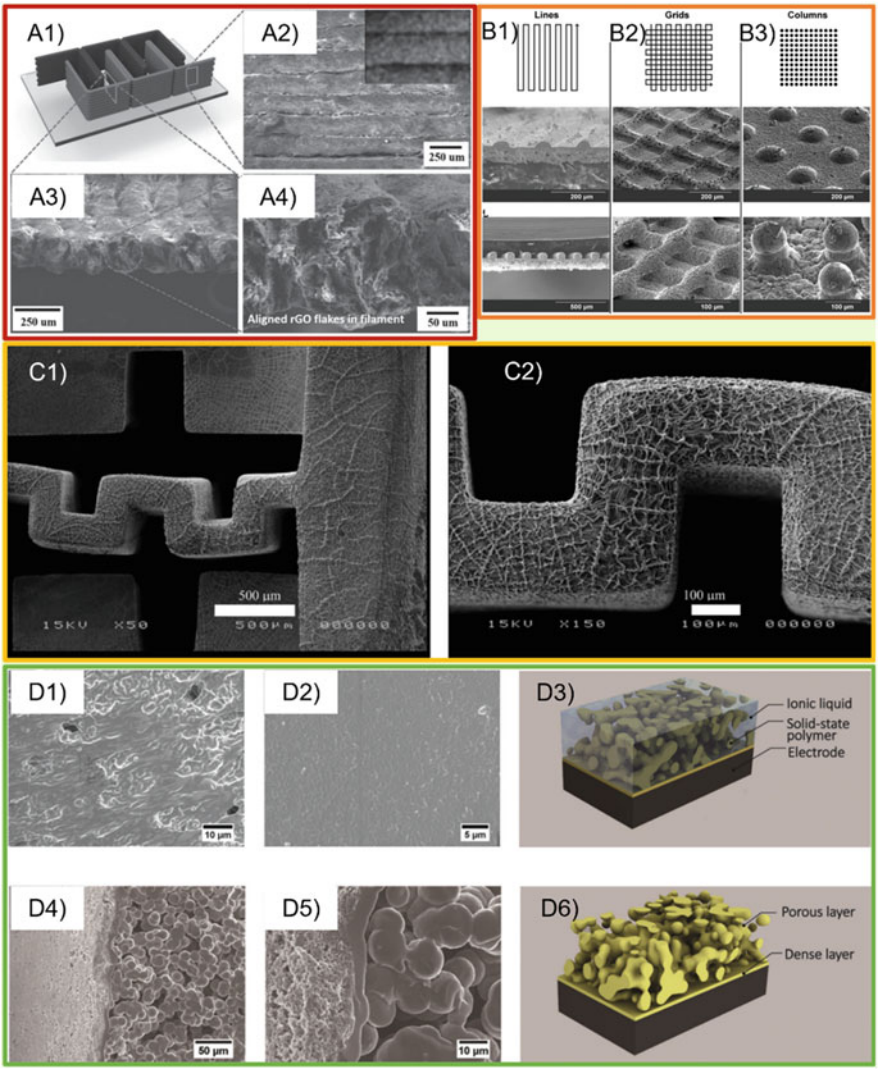

Fig. 9.16 In (**a**), 1 the device, in 2 it is possible to appreciate the layered structure, and in the inset, the element mapping of Fe to show the LFP distribution. In 3, a cross-section of the electrode's filaments and in 4 a further magnified electrode image [49]. In (**b**), 1, 2, and 3 groups are reported micrographs concerning lines, grids, and columns, obtained with different rheological properties of the inks [61]. In (**c**), 1 and 2 SEM pictures of the GPE [54]. In (**d**), the printed electrolyte. In 1 and 2, cross-section and surface of the printed system depicted in 3. In 4 and 5, images of the dense layer at the interface of the washed sample depicted in 6 [59]

low-cost and high-throughput method to fabricate a 3D micro-battery [54]. PEGDA was used as UV-curable resin to produce the gel polymer electrolyte (GPE) with the solvent 1 M $LiClO_4$ in ethylene carbonate:propylene carbonate (EC:PC) in 1:1 volume proportion; micrographs of the GPE are shown in Fig. 9.16c). The

GPE paste was exploited to produce the electrode's slurries also, consisting of combinations of LFP or LTO powders together with Super P CB. The inks were poured into molds and exposed to UV light for device assembling. A polyethylene oxide (PEO)-based GPE membrane alone was tested with standard electrodes in coin cell configuration with regular device operation. Afterward, the same material was employed for the 3D printed solid-state device. Electrochemical results for the whole SLA printed device were not good, but the authors claimed the possibility to have room for improvements. In the work of Reyes et al., FDM was employed to fully 3D print a lithium-ion battery exploiting PLA-based filaments. The filaments were produced by dissolving polymer pellets in solution together with the active materials. The authors successfully 3D printed electrodes, electrolyte, and coin cell package. Also in this case, the authors infused all the battery components with 1 M $LiClO_4$ in 1:1 volume parts of EMC/PLA. All the printed battery elements were 150 μm thick. In Fig. 9.15c), images of (1) the device, (2) micrographs of stacked layers, (3) demonstration of operability, and (4) a set of 3D printed elements for coin cell tests are reported [53]. In the recent years, FDM was also exploited to carry on studies on half-cell components of batteries. In 2018, Maurel and co-workers demonstrated for the first time a 3D printable graphite/PLA filament fore anode application in lithium-ion batteries. Filaments comprising PLA, graphite, and conductive additives were tested to find the best filament composition to be 3D printed. Remarkably, the theoretical capacity was almost reached with a 10% content of carbon black as conductive additive. The specific capacity was 200 mAh g^{-1} at C/20. Also in this case, thin films showed good rate capabilities while thicker ones a dramatic decrease in performance [60].

In 2019, a similar work was proposed by Foster and co-workers. They demonstrated the possibility to 3D print graphene/PLA composite with improved conductivity and specific capacity of 500 mAh g^{-1} at 40 mA g^{-1}. They showed that with a chemical treatment, the electrode porosity increases because of an increased surface area [62]. Concerning solid-state electrolytes, Mcowen et al. reported the fabrication of $Li_7La_3Zr_2O_{12}$ (LLZ) 3D solid-state electrolyte device. This electrolyte is known to be able to work with LFP LCO electrodes, and it is stable against lithium metal. Indeed, in this report, the working in a Li|LLZ|Li symmetrical cell to test the material stability was only demonstrated. The authors also reported the possibility to get different shapes of the solid electrolyte, by changing rheological properties. Results are shown in Fig. 9.16b) [61].

In the work of Cheng et al., DIW of hybrid solid-state electrolyte is reported. In this work, the authors focused on the 3D printing of electrolytes and compared the effects of casting or printing the electrolyte ink, composed of PVDF-co-HFP with TiO_2 nanoparticles with lithium bis(trifluoromethyl sulfone) imide, LiTFSI, mixed with [PYR13] [TFSI]. In Fig. 9.15f), a picture of the printed device is shown. They observed no differences in capacity retention, but half cells with MnO_2 as active material showed increased specific capacity. The printing method was at high temperatures such as 120 °C. The temperature treatment prevents the shrinkage and loss of structural integrity. Also, they showed that a very dense layer at the boundary between the deposited is beneficial in terms of interfacial resistance reduction, as

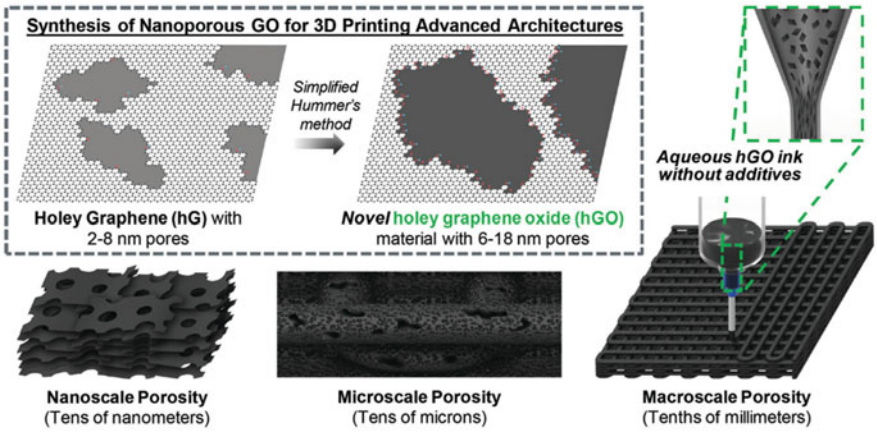

Fig. 9.17 Schematic representation of the processes used to synthesize hGO, a highly porous 2D nanomaterial, as well as create an aqueous and additive-free 3D printable hGO ink for extruding complex 3D architectures with hierarchical porosity (macroscale → nanoscale). Nanomaterial [63]

shown in Fig. 9.16d). Coulombic efficiency was kept high at 98.6% for 100 cycles [59].

A similar work concerning the characterization of transition metal oxides with no lithium in the original matrix was carried on by Li and co-workers on titania. 3D printed electrodes via DIW were obtained on gold current collectors, as depicted in the process scheme of Fig. 9.15d). The material showed a capacity of 250.9 mAh g^{-1} in half-cell configuration. Comparisons were made between a 2D woodpile structure and a control film sample. Interestingly, the group obtained better behavior in terms of rate capabilities with respect to the control film [57].

The following examples concern the application of 3D printing technology to Li-air batteries. In the first case, Lacey et al. reported the fabrication of a cathode material suitable for Li-O_2 application. They exploited rGO obtained via oxidation and activation of commercial graphene powder to prepare the ink which was printed without any other additive in a self-standing mesh. After the chemical activation, the electrode was showing trimodal porosity, that is, distributed from the microporosity range to micrometric features. A schematic representation of the process is reported in Fig. 9.17. The material was referred to as holey rGO (hGO). The discharge capacitance was around 14 mAh cm^{-2} at 2.7 V discharge [63].

In another work, Qiao and co-workers combined 3D printing with thermal shock synthesis to produce ultrathick cathodes composed of Ni/rGO framework for Li-CO_2 batteries. The woodpile electrode was printed with GO and subsequently reduced. The thermal shock was carried on at 1900 K for less than 1 s. Nanometric particles of Ni were attached then to the rGO matrix [58]. The presented literature results, as well as many others, are summarized in Table 9.2.

Table 9.2 Summarized information and performances, concerning 2D/3D battery technologies

Process data			Electrical parameters							
Technique	Architecture	Material composition	Capacity at C-rate	Voltage	Electrolyte	Resistance	Energy density	Power density	Retention – cy.# @ rate	References
DIW		SnO_2 quantum dots	991.6 mAh g^{-1}		1 M LiPF6 EC:DEC					[64]
DIW	Interdigitated 3D	GO-LTO LFP	91 mAh g^{-1}		1 M LiPF6 EC:DEC					[49]
DIW	Interdigitated 3D	LTO-LFP	1.5 mAh cm^{-2} 1C	1.8 V			2.7 mWh cm^{-2}	2.7 mW cm^{-2}	90% – 30 @ ##	[50]
DIW	Interdigitated 3D	$LiMn_{(1-x)}Fe_xPO_4$	161.4 mAh g^{-1}	4.1–3.4 V	1 M LiPF6 EC:DEC				90% – 1000 @ 10C	[51]
DIW	Interdigitated	LTO-LFP	154 mAh g^{-1} @ 0.2C	4.1–3.4 V	3D printed PVDF-Al2O3 1 M LiPF6 1:1 EC:DEC				100% – 100 @ 0.2C	[52]
DIW	Interdigitated	α-MnO_2	110 mAh g^{-1} @ 16 mA g^{-1}	4.0–1.5 V	PVDF-co-HFP TiO_2 LiTFSI [PYR13][TFSI]				98.6% – 100 @ 16 mA g^{-1}	[59]
DIW	3D scaffold and staked	GO-Ni Li-CO_2	14.6 mAh cm^{-2} 8911 mAh g^{-1}	4.0–2.7 V	1 M LiTFSI in TEG DME DMSO					[58]
FDM	3D scaffold and staked	Graphene/PLA half cell	500 mAh g^{-1} @ 40 mA g^{-1}		1 M LiPF6 EC:DMC					[62]
FDM	3D scaffold and staked	Graphene/PLA half cell	200 mAh g^{-1} @ C/20		1 M LiPF6 EC:DEC					[60]

FDM	3D scaffold	LMO-LTO	3.91 mAh cm^{-3}	3.0–2.0 V	PLA 1 M $LiClO_4$ 1:1 PC:DMC		0.14 Wh L^{-1}	0.83 W L^{-1}		[53]
SLA	3D scaffold	Au|LAGP|Au Li|LAGP|Li			$Li_{1.4}Al_{0.4}Ge_{1.6}(PO_4)_3$	ESR 7 kΩ IR > 100 kΩ				[56]
SLA	Interdigitated micro-battery	LFP-LTO	1.4 μAh cm^{-2}	1.5 V	PEO 1 M $LiClO_4$ 1:1 PC:DMC					[54]
DIW	Stacked	LFP-LTO 1.0 mm	4.45 mAh cm^{-2} @ 0.12 mA cm^{-2}	1.8 V	PVP 1 M LiTFSI in PC					[55]
DIW	Stacked	Li|LLZ|Li			$Li_7La_3Zr_2O_{12}$ (LLZ)					[61]
DIW	3D scaffold and staked	rGO from natural graphite	3.1 mAh cm^{-2} 600 mAh g^{-1} @ 0.1 mA cm^{-2}	2.7 V	1 M LiTFSI in DMSO					[63]
		rGO from Vor-X graphene	10.5 mAh cm^{-2} 2471 mAh g^{-1} @ 0.1 mA cm^{-2}	2.7 V	1 M LiTFSI in DMSO					
DIW	3D scaffold	TiO_2 – Half cell	250.9 mAh g^{-1} @ 1.5 C	3.0–1.0 V	1 M $LiClO_4$ 1:1 EC:DMC					[57]

9.4 Conclusion

Additive manufacturing technologies have been widely explored up to present days to demonstrate the possibility to fabricate miniaturized energy storage devices. 2D and 3D architectures, interdigitated or stacked, were proposed as main configurations. The fabrication techniques allow electrodes and cell design flexibility. Direct ink writing is the most exploited technique as well as laser writing processes. Despite the good characterizations of both starting materials like inks and final products, the literature is missing a proper reporting in electrochemical performances of the energy storage devices. The computation of the specific quantities must be properly reported. Power capabilities and energy densities shall be reported in specific quantities in Watts and Watt-hour specifications, respectively. In this way, comparison among literature products results straightforward. Moreover, research in this field shall focus on the production and optimization of low resistance electrode technologies to improve the energetic performances of the final energy storage devices.

References

1. IEA Key, Key world energy statistics 2020. Int. Energy Agency **33**, 4649 (2020). https://webstore.iea.org/download/direct/4035%0A, http://data.iea.org/payment/products/103-world-energy-statistics-and-balances-2018-edition-coming-soon.aspx%0A, https://www.oecd-ilibrary.org/energy/key-world-energy-statistics-2020_295f00f5-en
2. G.H. Oettinger, Energy roadmap 2050. Policy (2012). https://doi.org/10.2833/10759
3. J. Zhang, C. Zhong, Y. Deng, W. Hu, J. Qiao, L. Zhang, A review of electrolyte materials and compositions for electrochemical supercapacitors. Chem. Soc. Rev. **44**, 7484–7539 (2015). https://doi.org/10.1039/c5cs00303b
4. Y. Wang, B. Liu, Q. Li, S. Cartmell, S. Ferrara, Z.D. Deng, J. Xiao, Lithium and lithium ion batteries for applications in microelectronic devices: A review. J. Power Sources **286**, 330–345 (2015). https://doi.org/10.1016/j.jpowsour.2015.03.164
5. J.P. Rivera-Barrera, N. Muñoz-Galeano, H.O. Sarmiento-Maldonado, SoC estimation for lithium-ion batteries: Review and future challenges. Electronics **6**, 102 (2017). https://doi.org/10.3390/electronics6040102
6. Y. Chen, Y. Kang, Y. Zhao, L. Wang, J. Liu, Y. Li, Z. Liang, X. He, X. Li, N. Tavajohi, B. Li, A review of lithium-ion battery safety concerns: The issues, strategies, and testing standards. J. Energy Chem. **59**, 83–99 (2021). https://doi.org/10.1016/j.jechem.2020.10.017
7. Y. Yang, E.G. Okonkwo, G. Huang, S. Xu, W. Sun, Y. He, On the sustainability of lithium ion battery industry – A review and perspective. Energy Storage Mater. **36**, 186–212 (2021). https://doi.org/10.1016/j.ensm.2020.12.019
8. G. Zhou, *Next-Generation High Performance Lithium–Sulfur Batteries* (2017), http://www.springer.com/series/8790
9. W. Zhou, X. Liu, K. Zhou, J. Jia, *Nanomaterials in Advanced Batteries and Supercapacitors* (Springer, Cham, 2016). https://doi.org/10.1007/978-3-319-26082-2
10. N. Chawla, N. Bharti, S. Singh, Recent advances in non-flammable electrolytes for safer lithium-ion batteries. Batteries **1**, 1–26 (2019). https://doi.org/10.3390/batteries5010019
11. P. Zaccagnini, A. Lamberti, A perspective on laser-induced graphene for micro-supercapacitor application. Appl. Phys. Lett. **120**, 100501 (2022). https://doi.org/10.1063/5.0078707

12. B.E. Conway, *Electrochemical Supercapacitors* (Springer US, Boston, 1999). https://doi.org/10.1007/978-1-4757-3058-6_10
13. S.J. Cooper, A. Bertei, D.P. Finegan, N.P. Brandon, Simulated impedance of diffusion in porous media. Electrochim. Acta **251**, 681–689 (2017). https://doi.org/10.1016/j.electacta.2017.07.152
14. S. Dsoke, X. Tian, C. Täubert, S. Schlüter, M. Wohlfahrt-Mehrens, Strategies to reduce the resistance sources on electrochemical double layer capacitor electrodes. J. Power Sources **238**, 422–429 (2013). https://doi.org/10.1016/j.jpowsour.2013.04.031
15. M. Idrees, S. Ahmed, Z. Mohammed, N.S. Korivi, V. Rangari, 3D printed supercapacitor using porous carbon derived from packaging waste. Addit. Manuf. **36**, 101525 (2020). https://doi.org/10.1016/j.addma.2020.101525
16. J. Lin, Z. Peng, Y. Liu, F. Ruiz-Zepeda, R. Ye, E.L.G. Samuel, M.J. Yacaman, B.I. Yakobson, J.M. Tour, Laser-induced porous graphene films from commercial polymers. Nat. Commun. **5**, 1–8 (2014). https://doi.org/10.1038/ncomms6714
17. A. Lamberti, F. Perrucci, M. Caprioli, New insights on laser-induced graphene electrodes for flexible supercapacitors: Tunable morphology and physical properties. Nanotechnology **28**, 174002 (2017). https://doi.org/10.1088/1361-6528/aa6615
18. A. Lamberti, M. Serrapede, G. Ferraro, M. Fontana, F. Perrucci, S. Bianco, A. Chiolerio, S. Bocchini, All-SPEEK flexible supercapacitor exploiting laser-induced graphenization. 2D Materials **4**, 035012 (2017). https://doi.org/10.1088/2053-1583/aa790e
19. M. Reina, A. Scalia, G. Auxilia, M. Fontana, F. Bella, S. Ferrero, A. Lamberti, Boosting electric double layer capacitance in laser-induced graphene-based supercapacitors. Adv. Sustain. Syst. **6** (2022). https://doi.org/10.1002/adsu.202100228
20. B. Chen, Y. Jiang, X. Tang, Y. Pan, S. Hu, Fully packaged carbon nanotube supercapacitors by direct ink writing on flexible substrates. ACS Appl. Mater. Interfaces **9**, 28433–28440 (2017). https://doi.org/10.1021/acsami.7b06804
21. A.M. Bryan, L.M. Santino, Y. Lu, S. Acharya, J.M. D'Arcy, Conducting polymers for Pseudocapacitive energy storage. Chem. Mater. **28**, 5989–5998 (2016). https://doi.org/10.1021/acs.chemmater.6b01762
22. V. Augustyn, P. Simon, B. Dunn, Pseudocapacitive oxide materials for high-rate electrochemical energy storage. Energy Environ. Sci. **7**, 1597–1614 (2014). https://doi.org/10.1039/c3ee44164d
23. M.J. Young, A.M. Holder, S.M. George, C.B. Musgrave, Charge storage in cation incorporated α-MnO_2. Chem. Mater. **27**, 1172–1180 (2015). https://doi.org/10.1021/cm503544e
24. G.A. Snook, P. Kao, A.S. Best, Conducting-polymer-based supercapacitor devices and electrodes. J. Power Sources **196**, 1–12 (2011). https://doi.org/10.1016/j.jpowsour.2010.06.084
25. Y. Liu, S.P. Jiang, Z. Shao, Intercalation pseudocapacitance in electrochemical energy storage: Recent advances in fundamental understanding and materials development. Mater. Today Adv. **7**, 100072 (2020). https://doi.org/10.1016/j.mtadv.2020.100072
26. Y. Wang, Y.Z. Zhang, D. Dubbink, J.E. ten Elshof, Inkjet printing of δ-MnO_2 nanosheets for flexible solid-state micro-supercapacitor. Nano Energy **49**, 481–488 (2018). https://doi.org/10.1016/j.nanoen.2018.05.002
27. K. Shen, J. Ding, S. Yang, 3D printing quasi-solid-state asymmetric micro-supercapacitors with ultrahigh areal energy density. Adv. Energy Mater. **8** (2018). https://doi.org/10.1002/aenm.201800408
28. Y. Ji, L. Li, R. Ye, N.D. Kim, Y. Li, Y. Yang, H. Fei, G. Ruan, Q. Zhong, Z. Peng, J.M. Tour, J. Zhang, C. Gao, High-performance Pseudocapacitive microsupercapacitors from laser-induced graphene. Adv. Mater. **28**, 838–845 (2015). https://doi.org/10.1002/adma.201503333
29. F. Clerici, M. Fontana, S. Bianco, M. Serrapede, F. Perrucci, S. Ferrero, E. Tresso, A. Lamberti, In situ MoS2 decoration of laser-induced graphene as flexible supercapacitor electrodes. ACS Appl. Mater. Interfaces **8**, 10459–10465 (2016). https://doi.org/10.1021/acsami.6b00808
30. T. Wang, L. Li, X. Tian, H. Jin, K. Tang, S. Hou, H. Zhou, X. Yu, 3D-printed interdigitated graphene framework as superior support of metal oxide nanostructures for remarkable micro-pseudocapacitors. Electrochim. Acta **319**, 245–252 (2019). https://doi.org/10.1016/j.electacta.2019.06.163

31. K. Ghosh, M. Pumera, MXene and MoS3−x coated 3D-printed hybrid electrode for solid-state asymmetric supercapacitor. Small Methods **5** (2021). https://doi.org/10.1002/smtd.202100451
32. W. Yang, J. Yang, J.J. Byun, F.P. Moissinac, J. Xu, S.J. Haigh, M. Domingos, M.A. Bissett, R.A.W. Dryfe, S. Barg, 3D printing of freestanding MXene architectures for current-collector-free supercapacitors. Adv. Mater. **31** (2019). https://doi.org/10.1002/adma.201902725
33. M. Beidaghi, C. Wang, Micro-supercapacitors based on three dimensional interdigital polypyrrole/C-MEMS electrodes. Electrochim. Acta **56**, 9508–9514 (2011). https://doi.org/10.1016/j.electacta.2011.08.054
34. Z. Wang, Q. Zhang, S. Long, Y. Luo, P. Yu, Z. Tan, J. Bai, B. Qu, Y. Yang, J. Shi, H. Zhou, Z.Y. Xiao, W. Hong, H. Bai, Three-dimensional printing of polyaniline/reduced graphene oxide composite for high-performance planar supercapacitor. ACS Appl. Mater. Interfaces **10**, 10437–10444 (2018). https://doi.org/10.1021/acsami.7b19635
35. B. Yao, S. Chandrasekaran, J. Zhang, W. Xiao, F. Qian, C. Zhu, E.B. Duoss, C.M. Spadaccini, M.A. Worsley, Y. Li, Efficient 3D printed Pseudocapacitive electrodes with ultrahigh MnO2 loading. Joule **3**, 459–470 (2019). https://doi.org/10.1016/j.joule.2018.09.020
36. X. Li, H. Li, X. Fan, X. Shi, J. Liang, 3D-printed stretchable micro-supercapacitor with remarkable areal performance. Adv. Energy Mater. **10** (2020). https://doi.org/10.1002/aenm.201903794
37. M. Alexandreli, C.B. Brocchi, D.M. Soares, W.G. Nunes, B.G. Freitas, F.E.R. de Oliveira, L.E.C.A. Schiavo, A.C. Peterlevitz, L.M. da Silva, H. Zanin, Pseudocapacitive behaviour of iron oxides supported on carbon nanofibers as a composite electrode material for aqueous-based supercapacitors. J. Energy Storage **42**, 103052 (2021). https://doi.org/10.1016/j.est.2021.103052
38. A. Azhari, E. Marzbanrad, D. Yilman, E. Toyserkani, M.A. Pope, Binder-jet powder-bed additive manufacturing (3D printing) of thick graphene-based electrodes. Carbon **119**, 257–266 (2017). https://doi.org/10.1016/j.carbon.2017.04.028
39. C. Zhu, T. Liu, F. Qian, T.Y.J. Han, E.B. Duoss, J.D. Kuntz, C.M. Spadaccini, M.A. Worsley, Y. Li, Supercapacitors based on three-dimensional hierarchical graphene aerogels with periodic macropores. Nano Lett. **16**, 3448–3456 (2016). https://doi.org/10.1021/acs.nanolett.5b04965
40. X. Tian, K. Tang, H. Jin, T. Wang, X. Liu, W. Yang, Z. Zou, S. Hou, K. Zhou, Boosting capacitive charge storage of 3D-printed micro-pseudocapacitors via rational holey graphene engineering. Carbon **155**, 562–569 (2019). https://doi.org/10.1016/j.carbon.2019.08.089
41. S.H. Park, M. Kaur, D. Yun, W.S. Kim, Hierarchically designed electron paths in 3D printed energy storage devices. Langmuir **34**, 10897–10904 (2018). https://doi.org/10.1021/acs.langmuir.8b02404
42. S.A. Hashmi, R.J. Latham, R.G. Linford, W.S. Schlindwein, Conducting polymer-based electrochemical redox supercapacitors using proton and lithium ion conducting polymer electrolytes. Polym. Int. **47**, 28–33 (1998). https://doi.org/10.1002/(SICI)1097-0126(199809)47:1<28::AID-PI3>3.0.CO;2-C
43. C.W. Wu, B. Unnikrishnan, I.W.P. Chen, S.G. Harroun, H.T. Chang, C.C. Huang, Excellent oxidation resistive MXene aqueous ink for micro-supercapacitor application. Energy Storage Mater. **25**, 563–571 (2020). https://doi.org/10.1016/j.ensm.2019.09.026
44. K. Ghosh, M. Pumera, Free-standing electrochemically coated MoS: Xbased 3D-printed nanocarbon electrode for solid-state supercapacitor application. Nanoscale **13**, 5744–5756 (2021). https://doi.org/10.1039/d0nr06479c
45. J. Xue, L. Gao, X. Hu, K. Cao, W. Zhou, W. Wang, Y. Lu, Stereolithographic 3D printing-based hierarchically cellular lattices for high-performance quasi-solid supercapacitor. Nano-Micro Lett. **11**, 1–13 (2019). https://doi.org/10.1007/s40820-019-0280-2
46. N. Nitta, F. Wu, J.T. Lee, G. Yushin, Li-ion battery materials: Present and future. Mater. Today **18**, 252–264 (2015). https://doi.org/10.1016/j.mattod.2014.10.040
47. L.A. Middlemiss, A.J.R. Rennie, R. Sayers, A.R. West, Characterisation of batteries by electrochemical impedance spectroscopy. Energy Rep. **6**, 232–241 (2020). https://doi.org/10.1016/j.egyr.2020.03.029

48. H.L. Pan, Y.S. Hu, H. Li, L.Q. Chen, Significant effect of electron transfer between current collector and active material on high rate performance of $Li_4Ti_5O_{12}$. Chin. Phys. B. **20**, 1–5 (2011). https://doi.org/10.1088/1674-1056/20/11/118202
49. K. Fu, Y. Wang, C. Yan, Y. Yao, Y. Chen, J. Dai, S. Lacey, Y. Wang, J. Wan, T. Li, Z. Wang, Y. Xu, L. Hu, Graphene oxide-based electrode inks for 3D-printed lithium-ion batteries. Adv. Mater. **28**, 2587–2594 (2016). https://doi.org/10.1002/adma.201505391
50. K. Sun, T. Wei, B.Y. Ahn, J.Y. Seo, S.J. Dillon, J.A. Lewis, 3D printing of interdigitated Li-ion microbattery architectures. Adv. Mater. **25**, 1–5 (2013). https://doi.org/10.1002/adma.201301036
51. J. Hu, Y. Jiang, S. Cui, Y. Duan, H. Guo, L. Lin, Y. Lin, J. Zheng, F. Pan, J. Hu, Y. Jiang, S. Cui, Y. Duan, T. Liu, H. Guo, L. Lin, Y. Lin, J. Zheng, K. Amine, F. Pan, 3D-printed cathodes of LiMn 1-x Fe x PO 4 nanocrystals achieve both ultrahigh rate and high capacity for advanced lithium-ion battery. Adv. Energy Mater. (2016). https://doi.org/10.1002/aenm.201600856
52. A.J. Blake, R.R. Kohlmeyer, J.O. Hardin, E.A. Carmona, B. Maruyama, J.D. Berrigan, H. Huang, M.F. Durstock, 3D printable ceramic – Polymer electrolytes for flexible high-performance Li-ion batteries with enhanced thermal stability. Laser Phy. Rev. **6**, 1–10 (2017). https://doi.org/10.1002/aenm.201602920
53. C. Reyes, R. Somogyi, S. Niu, M.A. Cruz, F. Yang, M.J. Catenacci, C.P. Rhodes, B.J. Wiley, 3D printing a complete lithium ion battery with fused filament fabrication. ACS Appl. Energy Mater. **1**, 5268–5279 (2018). https://doi.org/10.1021/acsaem.8b00885
54. Q. Chen, R. Xu, Z. He, K. Zhao, L. Pan, Printing 3D gel polymer electrolyte in lithium-ion microbattery using Stereolithography. J. Electrochem. Soc. **164**, 1852–1857 (2017). https://doi.org/10.1149/2.0651709jes
55. T. Wei, B.Y. Ahn, J. Grotto, J.A. Lewis, 3D printing of customized Li-ion batteries with thick electrodes. Adv. Mater. **30**, 1703027 (2018). https://doi.org/10.1002/adma.201703027
56. J. Kasemchainan, C. Kuss, D.E.J. Armstrong, D. Cai, R.J. Wallace, F.H. Richter, H.J. Thijssen, P.G. Bruce, Environmental science ceramic and polymer microchannels for all-solid-state batteries. Energy Environ. Sci. **11**, 185–201 (2018). https://doi.org/10.1039/C7EE02723K
57. W. Li, Y. Zhou, I.R. Howell, Y. Gai, A.R. Naik, S. Li, K.R. Carter, J.J. Watkins, Direct imprinting of scalable, high-performance woodpile electrodes for three-dimensional lithium-ion Nanobatteries. ACS Appl. Mater. Interfaces (2018). https://doi.org/10.1021/acsami.7b14649
58. Y. Qiao, Y. Liu, C. Chen, H. Xie, Y. Yao, S. He, W. Ping, 3D-printed graphene oxide framework with thermal shock synthesized nanoparticles for Li-CO 2 batteries. Adv. Funct. Mater. **28**, 1805899 (2018). https://doi.org/10.1002/adfm.201805899
59. M. Cheng, Y. Jiang, W. Yao, Y. Yuan, R. Deivanayagam, T. Foroozan, Z. Huang, B. Song, R. Rojaee, T. Shokuhfar, Y. Pan, J. Lu, R. Shahbazian-yassar, Elevated-temperature 3D printing of hybrid solid-state electrolyte for Li-ion batteries. Adv. Funct. Mater. **28**, 1800615 (2018). https://doi.org/10.1002/adma.201800615
60. A. Maurel, M. Courty, B. Fleutot, H. Tortajada, M. Armand, S. Grugeon, S. Panier, L. Dupont, Highly loaded graphite-PLA composite based filaments for lithium-ion battery 3D-printing. ECS Meet. Abstr. (2018). https://doi.org/10.1021/acs.chemmater.8b02062
61. D.W. Mcowen, S. Xu, Y. Gong, Y. Wen, G.L. Godbey, J.E. Gritton, T.R. Hamann, J. Dai, G.T. Hitz, L. Hu, E.D. Wachsman, 3D-printing electrolytes for solid-state batteries. Adv. Mater. **30**, 1707132 (2018). https://doi.org/10.1002/adma.201707132
62. C.W. Foster, G. Zou, Y. Jiang, M.P. Down, Next-generation additive manufacturing: Tailorable graphene/Polylactic (acid) filaments allow the fabrication of 3D printable porous anodes for utilisation within Lithium-ion batteries. Batteries Supercaps, 1–7 (2019). https://doi.org/10.1002/batt.201800148
63. S.D. Lacey, D.J. Kirsch, Y. Li, J.T. Morgenstern, B.C. Zarket, Y. Yao, J. Dai, L.Q. Garcia, B. Liu, T. Gao, S. Xu, S.R. Raghavan, J.W. Connell, Y. Lin, L. Hu, Extrusion-based 3D printing of hierarchically porous advanced battery electrodes. Adv. Mater. **30**, 1705651 (2018). https://doi.org/10.1002/adma.201705651
64. C. Zhang, K. Shen, B. Li, S. Li, S. Yang, Continuously 3D printed quantum dot-based electrodes for lithium storage with ultrahigh capacities. J. Mater. Chem. A **6**, 19960–19966 (2018). https://doi.org/10.1039/c8ta08559e

Chapter 10
Photonic Applications: Impact on "Dielectric Laser Acceleration" and Other Case Studies

Costantino De Angelis, Andrea Locatelli, Giorgio S. Mauro, Rita Rizzoli, Gino Sorbello, and Giuseppe Torrisi

Abstract High precision manufacturing is playing a fundamental role in Photonics to enable innovation in several disciplines ranging from optical communications to imaging, healthcare and security. Printing has a potential huge impact on the manufacturing of photonic crystals (PCs). The concept of PCs and photonic band gap materials has opened a new era allowing the realization of advanced nanomaterials for photonics. This chapter mainly describes the impact of High-Resolution Manufacturing techniques on the conception of new bulk materials and on their application as dielectric laser-driven accelerators. The light flow control enabled by PCs represents a unique possibility to reach high energies in compact accelerator structures. Examples of PC structures, having different geometries and accelerating properties, are discussed, illustrating their fabrication process. Recent developments of high-resolution printing of complex photonic devices for other applications are also mentioned.

C. De Angelis · A. Locatelli
Dipartimento di Ingegneria dell'Informazione, Università degli Studi di Brescia, Brescia, Italy
e-mail: costantino.deangelis@unibs.it; andrea.locatelli@unibs.it

G. S. Mauro
Istituto Nazionale di Fisica Nucleare—Laboratori Nazionali del Sud, Catania, Italy
e-mail: mauro@lns.infn.it

R. Rizzoli
IMM-Consiglio Nazionale delle Ricerche, Bologna, Italy
e-mail: rizzoli@bo.imm.cnr.it

G. Sorbello
Dipartimento di Ingegneria Elettrica Elettronica ed Informatica, Università di Catania, Catania, Italy

Istituto Nazionale di Fisica Nucleare—Laboratori Nazionali del Sud, Catania, Italy
e-mail: gino.sorbello@unict.it

G. Torrisi (✉)
Istituto Nazionale di Fisica Nucleare—Laboratori Nazionali del Sud, Catania, Italy
e-mail: giuseppe.torrisi@lns.infn.it

S. L. Marasso, M. Cocuzza (eds.), *High Resolution Manufacturing from 2D to 3D/4D Printing*, https://doi.org/10.1007/978-3-031-13779-2_10

Keywords Direct laser writing · Dielectric laser accelerators · Photonic crystals · Woodpile · Linear accelerator

10.1 Introduction

High-resolution printing can enable the fabrication of complex 3D geometries down to a wavelength-scale periodic arrangement of atoms and molecules, thus opening the way to a complete control of the electromagnetic fields inside such periodic structures.

Advances in material science and physics allowed us to use metals to confine radio-frequency and microwaves in certain region of space in order to transfer power and information, with several applications in telecommunications and other disciplines. In the field of communication systems, a larger operating frequency is connected to increased speed of information transmission and a miniaturization of the devices. However, at higher frequencies, metals are lossy and lose most of their useful properties; for this reason, at infrared and optical wavelengths, metals are often replaced by (low-loss) dielectrics. This is the case of optical communication systems where optical fibers, which simply guide light by total internal reflection, have revolutionized the telecom industry allowing wideband optical communications in solid core fibers and devices. However, properties of optical fibers are limited and governed the characteristics by of the glass. For example, standard fibers require a solid core with limitations related to non-linearity of materials and to the maximum power that can be carried.

One important difference between standard metallic waveguides, which cannot be scaled at optical wavelengths, and optical fibers is the presence of a solid core in the latter. In many applications, the presence of a solid core has a limited impact, but in the case of particle acceleration this prevents the flow of particles to be manipulated and accelerated.

Sub-wavelength printing, allowing the control of periodic arrangements of different materials, can introduce better control of the properties of the materials, and this adds new possibilities for confinement and manipulation of electromagnetic waves. The periodic arrangement can be scaled with the operating wavelength, and the results are independent from the selected scale. However, this approach becomes particularly interesting at optical and infrared frequencies since it allows metals to be replaced with dielectrics. It is possible to engineer periodic patterns that forbid electromagnetic propagation by reflecting light waves over a defined range of frequencies allowing light to propagate only along prescribed paths. A fine control of material properties prevents light to propagate in certain directions at precise frequency bands and opens the way to advanced light manipulation, beyond the microwave regime, at optical wavelengths in hollow core structures very similar to metallic waveguides: in other words, it is possible to confine electromagnetic waves in vacuum, and not only in region with high refractive index.

The possibility to confine electromagnetic fields in a hollow core structure has many advantages; for example, hollow core fibers can handle high power without experiencing non-linear effects. Regardless of the possibility of managing high powers, it is essential to have a hollow core structure for particle accelerators. For this reason, high-resolution printing of periodic structures and photonic crystals concepts are naturally applied to particle accelerators.

A photonic crystal (PC) is an optical structure arranged in a periodic geometry, which induces a periodic change of the refractive index, affecting the propagation of light. A PC can confine optical electromagnetic modes inside well-defined photonic frequency band gaps [1]. Thanks to this property, the energy of charged particles moving along the waveguide can be increased if an appropriate transverse magnetic (TM, with a longitudinal electric field component) mode can propagate inside the defect of a PC lattice. All-dielectric (typically, silicon-based) guided-mode structures can be used for particle laser acceleration [2–4] in different configurations:

- Photonic band gap (PBG) fiber structures [5]
- 2D planar structures [6]
- 3D structures such as the "woodpile" geometry [3, 7, 8]

The interest for dielectric laser-driven accelerators (DLAs) is increasing due to their compactness, which is due to an operating wavelength reduced by almost 5 orders of magnitude when working in the visible or near infrared, the availability of efficient tabletop lasers, and the higher acceleration gradient (up to GV/m) with respect to conventional RF metallic linear accelerators (LINACs). Moreover, a main advantage is represented by the maturity of the technology for the fabrication of DLA structures. It is worth noting that some suitable nanofabrication processes will be described in this chapter. As a brief summary, the 2D structures can be obtained by using photolithography and reactive ion etching (RIE) techniques. Fabrication of 3D photonic crystals can follow different approaches: multilayer lithography [9], Deep UV Photolithography [7], wafer fusion [10], stacking [11], Two-Photon Lithography [12], Direct Laser Writing (DLW) [8] combined with silicon double inversion [13], transferring and stacking of pre-patterned, free-standing silicon membranes [14], and others [15]. For instance, the devices described in [16] were fabricated by an electron-beam lithography tool.

In particular, the DLW Two-Photon Polymerization (TPP) technique is inherently three-dimensional [17, 18], in contrast to the 2.5D layer-by-layer approaches which are limited in the number of achievable layers [7, 19] since stacking of many layers is challenging. The fabrication of Si-based PCs by employing high-resolution 3D printing requires to use complicated techniques [8, 13]. Polymeric structures with the desired dimensions can be manufactured by Stereolithography (SL), with dimensions in the range from hundreds of micrometers to tens of millimeters, or by the DLW technique, which is able to reach resolutions of tens of nanometers. Then, the template is substituted with polysilicon (poly-Si) or amorphous silicon by using the Si double-inversion process. This method exploits standard Si microelectronics technologies for deposition and etching of low-temperature Si oxide (LTO), TEOS,

poly-Si, Si_3N_4 thin films, the Low-Pressure Chemical Vapour Deposition (LPCVD) technique, based on thermal decomposition of proper precursor gases at low pressure, modified Spin-on-Glass (SOG) deposition at room temperature, and RIE of various materials such as polymers, SiO_2 and Si. The described approach is not limited by the number of layers, and however, the resulting oval-shaped silicon rods and round-edge channels affect the refractive index of the structure.

The challenge of expanding the frontiers of high-resolution 3D printing technology is to enable the direct 3D printing of materials and structures with the desired functionalities. The direct printing of a 3D dielectric PC structure, avoiding other complicated processes, will require the development of innovative functional polymerizable dielectric materials, such as those containing a high percentage of dielectric nanoparticles. Moreover, another very interesting rapid prototyping method is the laser-induced direct-write layer-by-layer deposition from the gas phase, which is a local Chemical Vapour Deposition technique induced by a focused laser. This technique was applied to the fabrication of PBG microstructures many years ago [20] and is similar to the layer-by-layer rapid prototyping, with the advantage of directly creating the final structure and the disadvantage of being very challenging.

10.2 Hollow Core Devices for Particle Acceleration

The electrical breakdown in metals limits the highest electric field that can be safely used in conventional particle accelerators. Standard particle accelerators consist of metal cavities driven by high-power microwaves and typically operate with accelerating fields up to 10–30 MV/m. Charged particle devices based upon conventional radio-frequency (RF) technology are often large and expensive due to accelerator length and total stored energy needed to accelerate particles to high energy. Size and cost reduction are required for many applications. Frequency scaling leads to a natural reduction of the accelerator size. Because of the high power loss in metals at optical frequencies, dielectrics are the only viable candidates for confinement of electromagnetic energy in such schemes [2]. With their high damage threshold, dielectric laser accelerators allow to achieve accelerating gradients up to the GV/m, which are 1 or 2 orders of magnitude higher than the ones obtainable with metallic structures.

Among the dielectric structures employable for particle acceleration, geometries characterized by a full 3D band gap, such as the woodpile structure, are of particular interest [1, 3]. By removing some dielectric material from the periodic structure (introducing a so called ‘defect’), it is indeed possible to trap a specific mode inside the device. For particle acceleration purposes, the defect is typically a hollow-core channel (a waveguide or a cavity) and the trapped, guided mode can be either a launch Transverse Electric (TE-like) mode or a Transverse Magnetic (TM-like) accelerating mode, in a similar fashion with respect to what happens in classical metallic RF LINACs.

In the following, two examples of hollow-core devices for particle acceleration will be presented: a 2D triangular lattice in a dielectric slab and a 3D woodpile hollow-core waveguide.

10.2.1 2D Photonic Crystal Device: The Slab with Periodic Arrangement of Holes

Photonic crystal slabs, also called planar photonic crystals, are planar 'two-dimensional' structures only if their extension in the vertical z direction is infinite. Real devices possess a finite thickness in the vertical z-direction and can only mimic the functionalities of a 2D z-invariant structure.

However, 2D structures can be considered for specific applications and more in general for preliminary studies [21].

In order to introduce gradual complexity, we first report on 2D structures. Examples of two-dimensional photonic crystals, which are periodic in two directions and homogeneous in the third one, are lattices of periodically arranged dielectric columns in air [1] or holes in a dielectric substrate; in both cases, these arrangements can be fabricated by printing (i.e. with additive manufacturing) or in the latter case by drilling holes in a dielectric slab. In case of hole dimensions in the micrometer or submicrometer range, drilling can be performed by combining lithographic techniques (photo, deep-UV or e-beam lithography) with etching of the dielectric material by wet or dry etching (RIE/DRIE). We focus on a triangular lattice of air columns, since it can be shown that this structure has a complete band gap [1], i.e. the periodic arrangement forbids the electromagnetic propagation by reflecting light waves over a defined range of frequencies. By introducing a suitable linear defect in the perfectly periodic photonic crystal we can confine the electromagnetic waves.

As a matter of fact, defects in photonic crystal slabs can be used to form waveguides and cavities. With such building blocks, many interesting devices have been experimentally realized using standard lithographic techniques. However, this ease of fabrication comes at a price: careful design is required to minimize losses [1]. In Fig. 10.1, an example of 2D accelerating structure is shown. The structure, presented in [6, 22], is a directional coupler formed by two adjacent vacuum waveguides realized in an alumina PC quasi-2D structure. In order to have an efficient energy exchange between the two waveguides, the linear defects have been designed and tuned so that the interacting modes have the same propagation constant. This 2D PC is based on a triangular lattice of periodically arranged vacuum holes for which the lattice constant d (i.e. the distance between the centers of two adjacent holes) is chosen in such a way to have a band gap around the working frequency. The defect size has been chosen in order to synchronize the accelerating mode with the particle beam. Notice that the accelerating and the launch waveguide have been called WG1 and WG2, respectively.

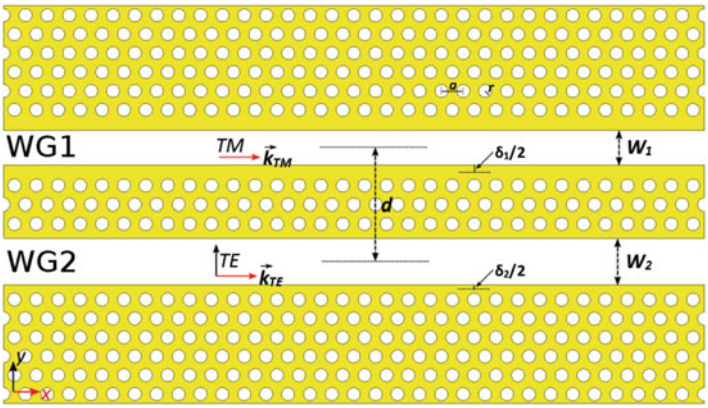

Fig. 10.1 Geometry of a 2D PC coupler consisting of vacuum holes in alumina. TE wave is launched from the WG2 waveguide and coupled to the TM mode in waveguide WG1 (reprinted with permission from [6])

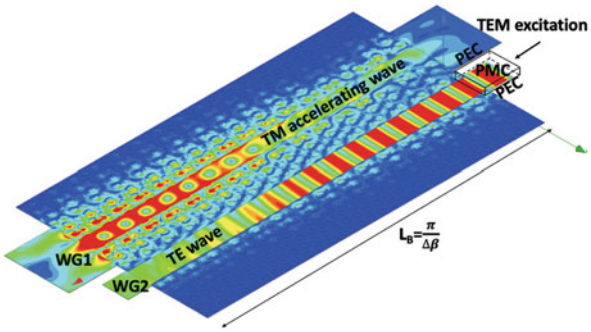

Fig. 10.2 3D model of the simulated 2D directional coupler based on a triangular lattice. The telecom waveguide, named WG2, is characterized by a TE_{10}-like mode that, after a beating period, becomes a TM-like mode into the accelerating waveguide, named WG1. The latter has a dominant field component along the waveguide axis and is thus suitable for particle acceleration (reprinted with permission from [6])

This dielectric coupler has been tuned with the supercell method considering an infinite periodic two-channel waveguide and then has been truncated at the appropriate beat length and validated through the use of full-wave electromagnetic simulators, from which the electric field, visible in Fig. 10.2, has been computed.

WG1 has a strong longitudinal electric field component (the accelerating mode), as it allows the propagation of a TM-like mode suitable for accelerating particles, similarly to a standard metallic LINAC. The field in the larger waveguide WG2 has a strong transverse electric field component similar to the classic TE_{10} mode or Gaussian mode, denoted as telecom mode: notice that it is necessary to exploit this mode for the excitation of the structure because a TM-like mode cannot be easily

coupled with a standard telecom laser Gaussian mode or the TEM mode of a parallel plate metallic waveguide since the overlap integral with such mode would be zero.

As pointed before, the structure is wavelength independent and the design can be scaled at any working frequency by imposing the correct lattice constant d, provided that the relative dielectric constant does not change, i.e. the material used for the actual fabrication can be replaced and chosen with the same dielectric constant at the operating frequency. For example, by employing alumina as material ($\epsilon_r = 9.7$), the fundamental, wavelength-normalized, structure dimensions are $d = 0.2445\lambda$, $r = 0.07336\lambda$, $\delta_1 = 0.08943\lambda$ and $\delta_2 = 0.0246\lambda$.

10.2.2 3D Photonic Crystal Device: The Woodpile Structure

The previous study of a 2D accelerating structure has the limit of confining the accelerating mode only in two dimensions; for this reason, the use of full 3D PCs, having a complete band gap in all the three dimensions is preferable when one wants to employ this technology for dielectric laser accelerators. The main advantages in the use of a 3D photonic crystal are the capacity to control the field in all the three directions and the possibility to employ standard TEM-like waveguides for launching the field inside the accelerating waveguide. In particular, for the purpose of particle acceleration, here we will focus on a 3D PC in a *woodpile* configuration. It consists in a "pile" of rectangular bricks, with a cross section $w \times h$, that are stacked as shown in Fig. 10.3. Bricks in each layer of the pile are rotated by 90° with respect to the bricks in the previous one, and thus the resulting total structure is composed of several layers with brick axes alternatively aligned along x or z. The distance between the centers of two adjacent bricks of the same layer is the lattice constant, d.

From Fig. 10.3, it is clear that high-resolution 3D printing is an enabling technology for woodpile fabrication and this observation is even more valid in

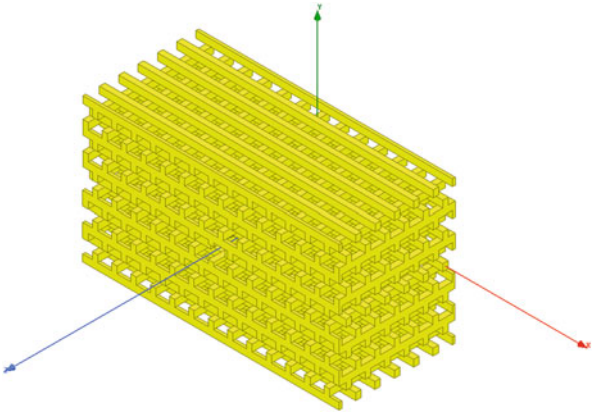

Fig. 10.3 Woodpile PC structure

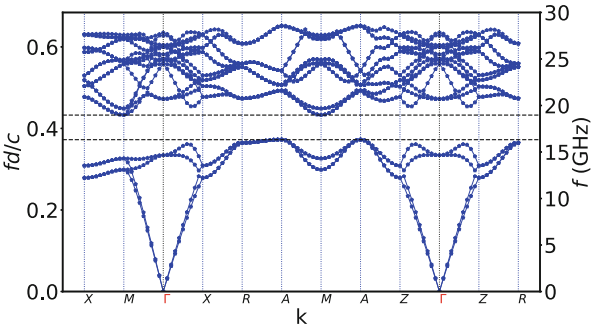

Fig. 10.4 Example of calculated band diagram for a woodpile structure. The plot shows the frequency (or normalized frequency) versus the wave number in the first Brillouin zone. A band gap centered at normalized frequency $f_{\text{norm}} = 0.4$ is also visible (reprinted with permission from [23])

presence of defect channels and channel intersections. This is particularly true when the structure needs to operate at the wavelength selected for dielectric laser acceleration technology, which is around 1550 nm. Considering silicon as the material of choice ($\epsilon_r = 11$), the wavelength-normalized dimensions are $w = 0.1213\lambda$, $h = 0.152\lambda$ and $d = 0.43\lambda$. Very well-defined structures were fabricated by using multilayer lithography and LPCVD deposition of poly-Si, but the approach is costly, time consuming and limited in the achievable number of layers. Vice versa, the technology combining DLW 3D printing with the silicon double inversion processes, as described in the introduction, is quite promising for the fabrication of woodpile structures. For the periodic structure, in order to evaluate the frequency band gap, the photonic band structure of the modes must be determined. It is essentially a plot of the mode frequency versus the wave number along one (or several) 'paths' followed inside the structure. Let n stand for a particular mode, so that we can identify any mode through a unique label (k, n). We call n the band number. If n is a continuous variable, the different bands correspond to different lines with a specific frequency behavior, and we obtain the so-called band structure (or dispersion relation) for the considered PC crystal. As said, the band structure will consist of a continuum of mode bands and of frequency gaps in which the electromagnetic propagation is forbidden, as shown in Fig. 10.4. By using this property, under particular conditions, the periodic structure can support a complete band gap, impenetrable to the electromagnetic field, and can confine and guide electromagnetic fields. In particular, once the configuration that presents the largest band gap has been found, a 'defect' can be created by removing some material from the structure. This defect can support an electromagnetic mode that can be guided along the structure to form a dielectric waveguide or trapped inside to form a resonant cavity. In particular, for particle acceleration, and in analogy with the standard metallic accelerating structures, we are especially interested in modes with a dominant electric field along the direction of the travelling particles, such as the TM_{01}-like accelerating mode, or in modes suitable for coupling the electromagnetic field inside the accelerating structure, such as the TE_{10}-like mode usually employed in waveguide couplers or mode converters.

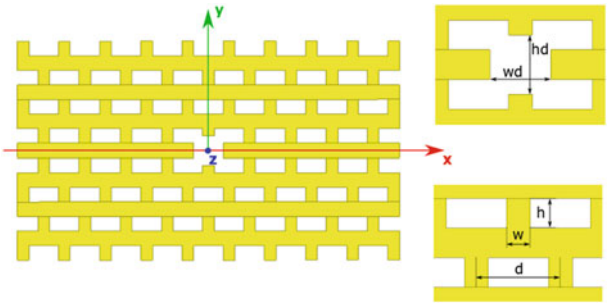

Fig. 10.5 Woodpile waveguide. (Top right) detail of the central defect (front view) with dimensions $w_d \times h_d$; the structure is made symmetric in the vertical direction (xz symmetry plane) for reducing the transverse components; (bottom right) fundamental structure dimensions. (Reprinted with permission from [24])

10.2.2.1 Hollow-Core Woodpile Waveguides

As a first example, a hollow-core woodpile waveguide supporting a TE_{10}-like mode is presented [3, 24, 25]. Figure 10.5 shows a structure front view where a $w_d \times h_d$ central defect has been introduced. As shown, the structure has also been modified in order to be symmetric with respect to the xz plane in order to reduce the transverse components of the mode. The waveguide operates at the wavelength of 1550 nm, and the corresponding lattice constant is $d = 645$ nm. The woodpile brick dimensions are equal to $w = 182$ nm and $h = 228$ nm. The infinite z-periodic guiding structure can be studied with the supercell method, starting from the woodpile primitive cell. The electric field components of the guided TE_{10}-like mode are shown in Fig. 10.6, plotted along the hollow-core channel of length $4d = 2.58\,\mu$m for an input power equal to 1 W. Moreover, Fig. 10.7 shows the electric field vector along the hollow-core axis. The mode profile here depicted strongly resembles the TE_{10} fundamental mode of metallic rectangular waveguides.

As a second hollow-core dielectric woodpile waveguide example, we report a structure that supports a TM_{01}-like mode, operating at the wavelength of 1550 nm. The structure has the same lattice constant, rod dimensions and length of the previously presented TE_{10}-like waveguide, but this time the central hollow-core defect has been tuned in order to support a mode with a strong longitudinal component, thus suitable for particle acceleration along the hollow channel. Figures 10.8 and 10.9 show, respectively, the electric field components module along the TM_{01}-like waveguide hollow-core channel and the electric field vector along the hollow-core axis.

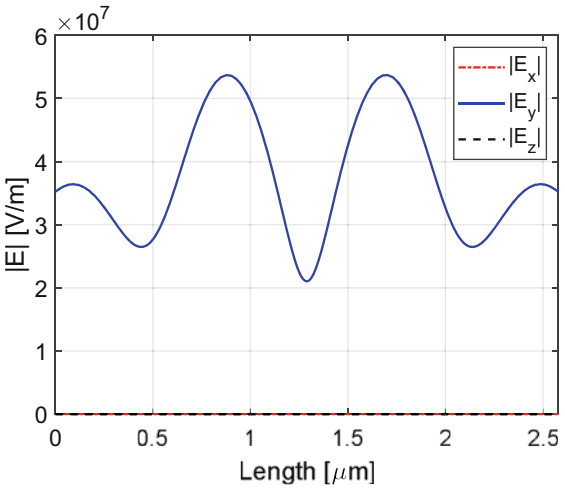

Fig. 10.6 Electric field components module along the structure hollow-core channel of length $4d = 2.58\,\mu\text{m}$. It can be seen that $|E_y|$ has a larger amplitude with respect to the other two components, as in the case of the TE_{10}-like mode (see reference system of Fig. 10.5)

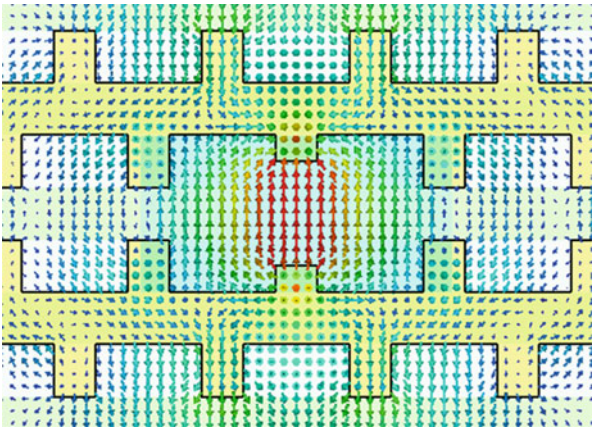

Fig. 10.7 Electric field vector along a slice in the xy plane

10.2.2.2 Hollow-Core Woodpile Coupler

In this section, a woodpile hollow-core side-coupler (or mode launcher-converter) design is presented [26]. The travelling wave structure, operating at the wavelength of 1550 nm ($f_0 \simeq 193.6\,\text{THz}$), is specifically designed for electron acceleration and is depicted in Fig. 10.10. Figure 10.11 displays the operation principle of the device: the laser power, propagating according to the Transverse Electric TE_{10}-like mode, is injected into a waveguide (or optical fiber) which splits into two branches arriving to the mode converter section. Here, the waves arriving from the two input waveguides are converted into the fundamental accelerating TM_{01}-like mode, which propagates along the hollow-core central waveguide (beam channel), accelerating the particle bunch along its interaction length. When the wave reaches the end of the accelerating waveguide, it is back-converted into two waves which are picked up by

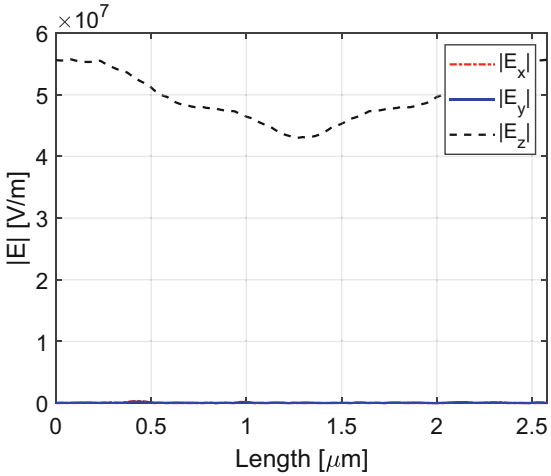

Fig. 10.8 Magnitude of the electric field components along the structure hollow-core channel of length $4d = 2.58\,\mu\text{m}$. It can be seen that $|E_z|$ has a larger amplitude with respect to the other two components, as in the case of the TM_{01}-like mode

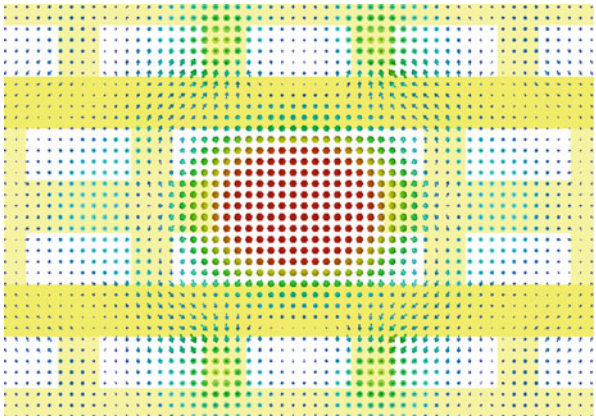

Fig. 10.9 Electric field vector along a slice in the xy plane

a second mode converter and driven out of the structure. This mode launcher design finds strong analogies with the travelling wave ones used for metallic RF LINACs where the input coupler is realized by a slot that connects the launch waveguide and the first accelerating cell [27].

The band diagram of the woodpile structure is calculated through the use of the MIT Photonic Bands (MPB) software [28]. In order to obtain the maximum band gap, the normalized brick dimensions $w = 0.2\sqrt{2}/d$ and $h = 0.25\sqrt{2}/d$ have been used. The band gap can be centered at the desired working frequency by choosing the lattice constant d through the expression $f_{[\text{THz}]} \approx f_{\text{norm}} c/d$. By choosing $d = 645\,\text{nm}$, a band gap centered at around 193 THz is obtained. The fundamental woodpile dimensions are $w = 182\,\text{nm}$ and $h = 228\,\text{nm}$. The accelerating waveguide, whose projected band structure is visible in Fig. 10.12, has been tuned in order to support a confined TM_{01}-like mode and has dimensions $w_d = 752\,\text{nm}$ and $h_d = 684\,\text{nm}$. Figure 10.13 shows the electric field components

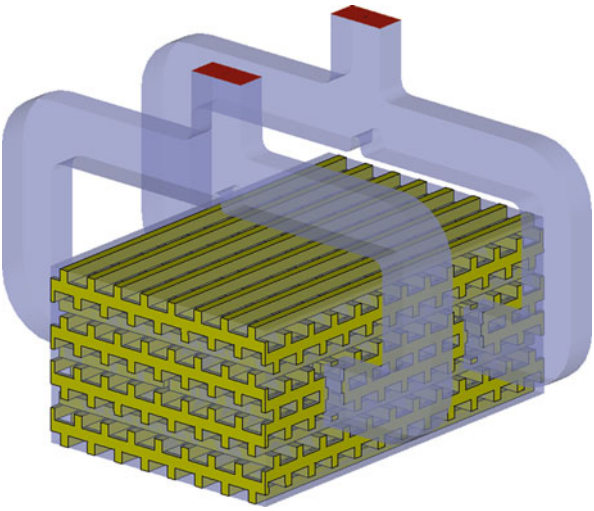

Fig. 10.10 3D model of the presented woodpile coupler with the input and output waveguides. (Reprinted from [26])

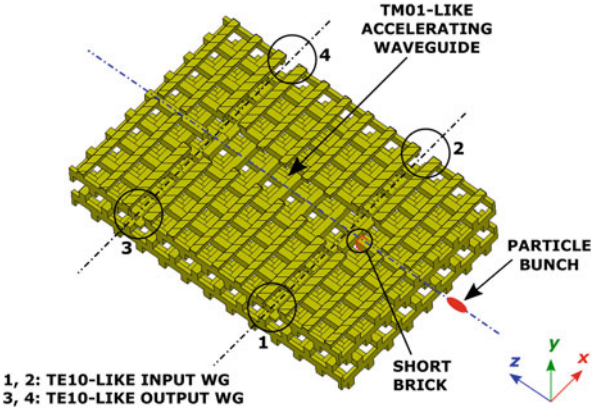

Fig. 10.11 Structure slice in the xz plane. It is composed of a mode converter (from TE10-like to TM01-like mode) and an accelerating waveguide. One of the two bricks composing the short wall of the mode converter is also highlighted. (Reprinted from [26])

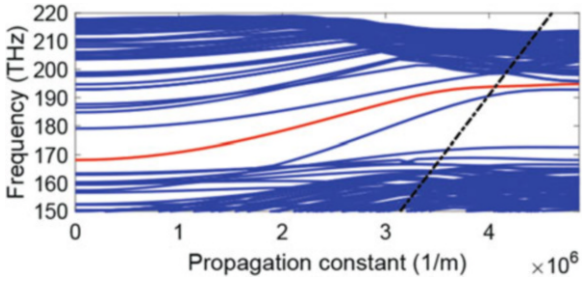

Fig. 10.12 Projected band diagram along the accelerating hollow-core waveguide axis (z axis). The light line (black dash-dotted curve) intercepts the guided TM_{01}-like mode at the frequency of 193.6 THz. (Reprinted from [26])

along the structure axis for an accelerating waveguide length $3d = 1935$ nm and an input power of 500 W: the field presents a strong longitudinal component $|E_z|$, while the transverse components, $|E_x|$ and $|E_y|$, are almost equal to zero, as in the case of a TM_{01}-like mode.

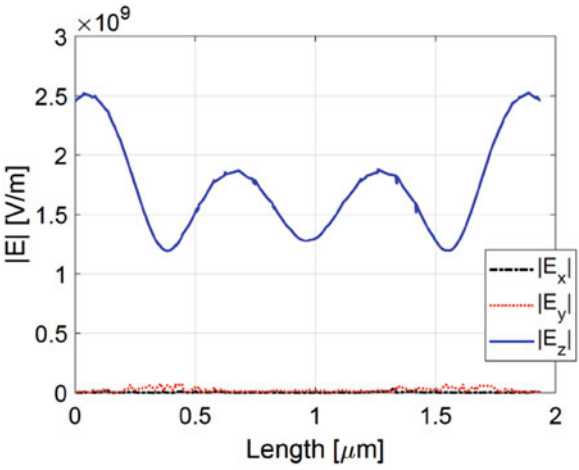

Fig. 10.13 Electric field components along the accelerating waveguide axis, at $f_0 = 193.66\,\text{THz}$, for a length of $3d = 1935\,\text{nm}$. (Reprinted from [26])

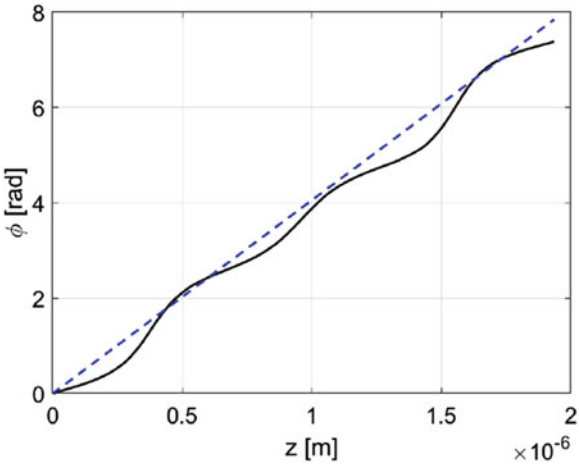

Fig. 10.14 Phase plot of the guided TM_{01}-like mode longitudinal (accelerating) component $|E_z|$ (black line) vs. $k_z = \frac{\omega}{c}$ (blue dashed line), at $f_0 = 193.66\,\text{THz}$ along the entire accelerating waveguide length. It is clear that the guided mode travels at the speed of light, thus the structure is suitable for relativistic electron acceleration. (Reprinted from [26])

Last but not least, in Fig. 10.14, it can be seen that the TM_{01}-like mode is characterized by a phase velocity which is equal to the speed of light at the operating frequency and along the accelerating hollow-core waveguide, enabling the presented travelling wave structure for relativistic electron acceleration.

10.2.3 Dielectric DC-Break Devices

In the previous section, we focused on an application that requires to employ optical frequencies and hollow-core driving structures, i.e. DLAs. These devices can represent a "killer application" for 3D-printed hollow-core electromagnetic band

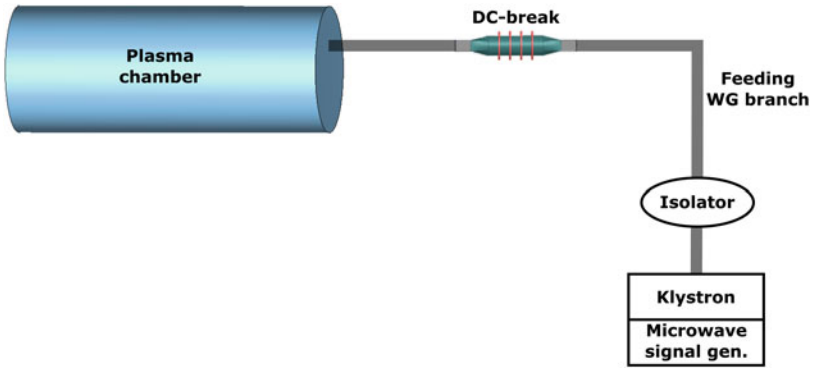

Fig. 10.15 Schematic of an ion source comprising the RF feeding line. In order to insulate the high-voltage plasma chamber from microwave amplifier located at ground, a DC-break device able to break the DC-path and to efficiently transfer RF power (usually up to 1 kW) has to be inserted along the RF path

gap devices since conventional solid-core waveguide structures do not allow the particle flow.

The dielectric nature of the woodpile guide suggests also another application where this time the use of dielectrics is necessary to sustain high voltages, while efficiently transferring high RF power with a guided wave solution. In this case, standard metallic waveguides are inappropriate since they do not provide DC insulation. Here, we discuss this alternative application of the hollow-core waveguides with particular emphasis on the ion sources setups. Ion sources are a critical component of all particle accelerators: they create the initial beam that is accelerated by the rest of the machine. The ion sources plasma chambers are placed at high voltage (usually up to 50 kV [29, 30]) to allow the beam extraction. In order to insulate the high-voltage plasma chamber from the microwave amplifier located at ground, a device (called hereinafter *DC-break*) able to break the DC-path and to efficiently transfer RF power (usually up to 1 kW) has to be inserted in the RF feeding line, as seen in Fig. 10.15, where a schematic view of the ion source is depicted. Beside the DC insulation requirement, the design of a waveguide DC-break [31] needs to guarantee low reflection and negligible radiation losses of the transmitted RF power from the ground RF generator to the high-voltage source. The previously presented and realized hollow-core waveguides, properly scaled to the ion source operating frequency, are able to fulfill the insulation requirement and low RF losses which are typically required in these setups and so could be employed as DC-break devices placed along the RF feeding line of microwave ion sources. As an example of application of DC-break devices in microwave ion sources, Fig. 10.15 shows a classical ion source setup: the microwave signal (in this case operating at 18 GHz) is generated through a signal generator and amplified by the Klystron in order to reach the desired power value. Then, it is guided to the microwave ion source plasma chamber through a metallic waveguide feeding line, which is a stand-

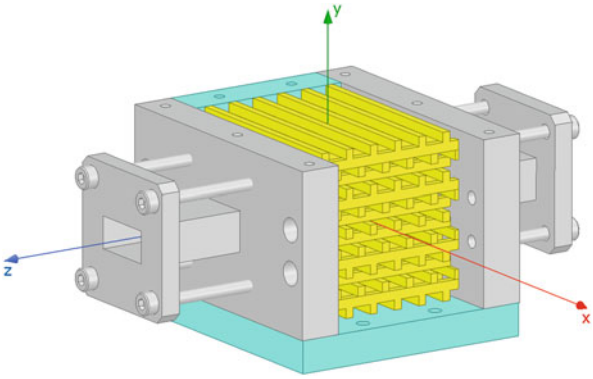

Fig. 10.16 Woodpile DC-break structure including metallic WR62 waveguides, front and back metallic flanges as well as top, bottom, right and left side plexiglass enclosure (light blue domains, only two of the four regions are shown. (Reprinted with permission from [32])

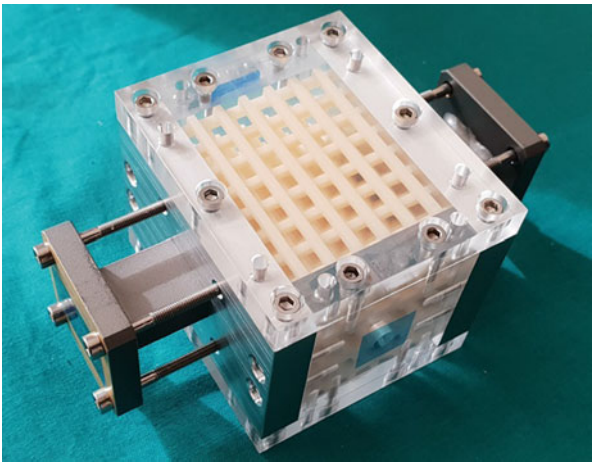

Fig. 10.17 Dielectric woodpile DC-break prototype. (Reprinted with permission from [23])

ard metallic WR62 waveguide in the case at hand. The DC-break device is placed along the feeding line, before entering the high-voltage plasma chamber. Usually, the DC-break devices are composed of a metallic wave-guiding body interlinked with rings of dielectric. Instead, the presented structure is composed of a dielectric woodpile waveguide, made of alumina and rescaled to operate at the frequency of 18 GHz [23]. In order to feed the structure, a simple metallic waveguide-to-woodpile transition is proposed, as seen in Fig. 10.16: two standard WR62 metallic waveguides, mounted over two large flat metallic flanges, are juxtaposed to the dielectric woodpile waveguide at both the input and output interfaces. The hollow-core woodpile waveguide, whose length has been set to 40 mm in order to ensure insulation up to 40 kV (a typical value for ion source setups), is tuned in the way to maximize the microwave transmission from input to output waveguides. Figure 10.17 shows the realized alumina prototype, while in Fig. 10.18 the woodpile DC-break and a standard metallic one are shown side by side. Among the advantages that come from employing the dielectric woodpile device, it is worth noticing the

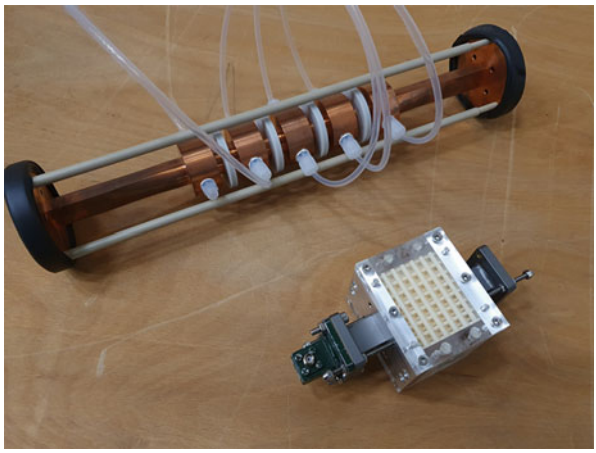

Fig. 10.18 Comparison between a metallic DC-break and the dielectric woodpile structure. (Reprinted with permission from [23])

overall compactness of this novel solution and the absence of voltage divider and cooling setup, the latter two complicating the device fabrication.

The advantages of 3D-printing for realizing the woodpile structure are evident for this latter application. Figure 10.19 shows the layers forming a woodpile coupler with linear defects designed for 3D printing fabrication.

10.3 Other Applications

10.3.1 Other Applications in Photonics

In [33], the authors report for the first time the fabrication of a microstructured optical fiber with a dispersion profile that, according to calculations, is near-zero and flat, with three zero dispersion wavelengths in the mid-IR. Simulations of multimode supercontinuum generation were performed using a simplified technique. Strong agreement between experiments and simulations were observed using this approach. The capability of tailoring dispersion profile is one of the most important features of microstructured optical fibers (MOFs). A fiber with flat and near-zero dispersion profile was designed for the purpose of generating a supercontinuum (SC) with large bandwidth and high coherence. In [33], SC generation in a multimode fiber is explored using an intermediate approach that considers the supercontinuum generated by multiple modes but without using a multimode pulse propagation model. The fiber was fabricated in three steps: (1) preform and tube extrusion, (2) caning and (3) drawing. The preform was fabricated using the extrusion technique. The extruded preform is pulled down to 1 mm diameter cane on a fiber drawing tower and inserted into a 10 mm diameter tube with a 1 mm hole in the center. Finally, the cane and the tube are pulled together into the final fiber.

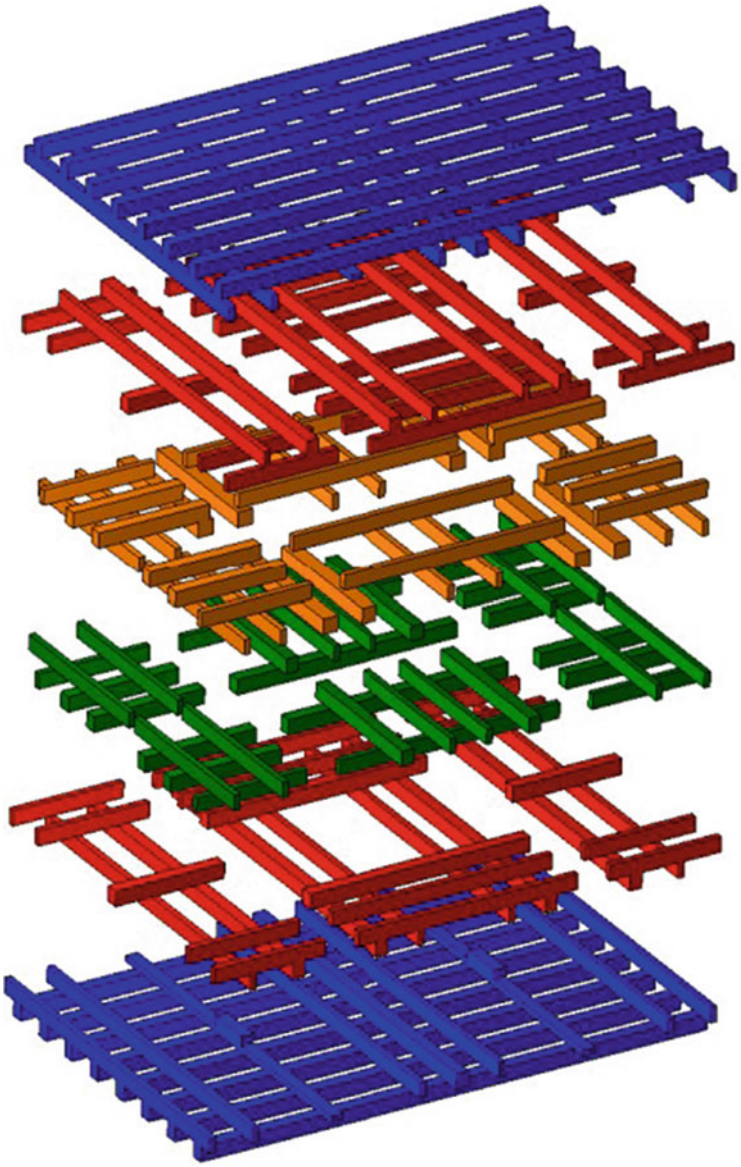

Fig. 10.19 Proposed 3D-printed version of the woodpile coupler

Photonic crystal fibers are characterized by a hollow channel that can be infiltrated with solutions of the biological compounds to be studied [34]. The fiber preform can in principle be prepared by 3D printing, and the size can be reduced to its final dimension by the fiber drawing process. In future applications, direct 3D printing can be envisaged. The 3D printing can in principle also be used to provide

a proper functionalization of the inner surface of the fiber in order to respond to a particular target as in [34].

Slow light has been one of the hot topics in the photonics community in the past decade, generating great interest both from a fundamental point of view and for its considerable potential for practical applications. Slow light photonic crystal waveguides, in particular, have played a major part and have been successfully employed for delaying optical signals and the enhancement of both linear and nonlinear devices. Photonic crystal cavities achieve similar effects to that of slow light waveguides, but over a reduced bandwidth. These cavities offer high quality factors in small interaction volumes, for the realization of optically and electrically pumped ultra-low threshold lasers and the enhancement of non-linear effects. To attain these exciting results, a robust repeatable fabrication technique must be developed. In [35], an in-depth look at fabrication protocol which employs electron-beam lithography for the definition of photonic crystal patterns and uses wet and dry etching techniques is presented.

10.3.2 Nanoantenna Printing

Nanoantennas are typically prepared by electron-beam lithography (EBL) and lift-off techniques [36]. This process allows for precise control of the nanostructure geometries but hampers direct and maskless large-area fabrication on reasonable time scales. In principle, state-of-the-art photo-lithography methods such as the ones used in the semiconductor industry today enable a fast production of decimeter-sized arrays of nanometer-sized and well-defined metal structures. However, mask fabrication for this process is expensive and not flexible, and low-cost access to such facilities is quite limited, particularly on a research level. In contrast to that, direct laser writing (DLW) as a two-photon absorption process allows to get a homogeneous and well-controlled fabrication of nanostructures over large areas at low costs. In this approach, a tightly focused spot of femtosecond laser light causes local polymerization in a polymer and thus enables the writing of arbitrarily shaped 3D structures, e.g. for perfect absorption, telecommunications and optical devices for integrated optics. In [36], direct laser writing lithography combined with argon ion etching can be used as a reliable method to prepare homogeneous large-area arrays of plasmonic nanoantennas for vibrational sensing in the mid-infrared range. Nanoantenna arrays with different longitudinal and transversal spacings were fabricated by exploiting the versatility of DLW with respect to the arrangement of nanostructures. Scientists already demonstrated the use of femtosecond direct laser writing lithography for a fast and homogeneous large-area fabrication of plasmonic nanoantennas on a substrate by creating a patterned polymer as an etch mask on a metal layer. Subsequent argon ion beam etching allows to get plasmonic nanoantennas with feature sizes below the diffraction limit of the laser light. They exhibit tunable high-quality plasmon resonances in the mid-infrared spectral range, which are ideally suited for surface-enhanced infrared absorption (SEIRA)

Fabrication techniques for optical nanoantennas include methods for thin-film deposition and patterning, growth of nanowires and chemical methods for synthesis of nanoparticles [37]. The properties of the materials depend strongly on wavelength, particularly close to a bandgap, and also depend on the fabrication method. A review of materials and fabrication methods for dielectric nanophotonics can be found in [38].

10.3.3 Nano-Composites: New Materials for Photonics

Complete photonic bandgaps (PBGs) in periodic PCs are only possible in materials with high refractive index. However, it has been shown that a complete PBG can be obtained in a low refractive index material by using highly symmetric photonic structures such as quasicrystals [39]. Photonic quasicrystals (PQCs) are artificial dielectric inhomogeneous media, where scattering centers are located in the vertices of a quasi-periodic structure. PQCs have neither true periodicity nor translational symmetry but have a quasi-periodicity that exhibits long-range order and orientational symmetry so that 2D PQCs may have high-order rotational and mirror symmetries not achievable by conventional PCs. Several studies about quasicrystals have demonstrated that, in general, most of the PQCs have wide complete band gaps and small threshold value of refractive index for opening a complete gap. Thus, they have the optimal conditions for forming a complete isotropic PBG even in soft materials like polymers. The possibility to exploit polymers and other soft materials is a very important point because of the advantages of using versatile cheap technologies to realize both large-area and high-quality structures. The fabrication of a complicated three-dimensional PQC was first experimentally demonstrated by using SL, a 3D printing technique. The structure had 12 fivefold, 15 threefold and 30 twofold symmetry axes, and the authors measured an effective quasi-spherical Brillouin zone. On the other hand, they were unable to find a complete bandgap opening [40]. 2D and 3D PQCs were fabricated following two types of approaches: (1) DLW, a TPP technique, or interference between multiple laser beams and (2) direct lithographic reproduction of a quasi-periodic pattern, using advanced techniques such as nanoimprint lithography or direct writing by EBL. Expanded applicability of photonic materials comes from the introduction of active functionality in them. For this purpose, semiconductor nanocrystals are a very promising material as an active medium in nanoparticle–polymer composites (nanocomposites). These nanostructured materials are generating interest in optoelectronics and photonics because of the absorption or emission properties of the semiconductor nanoparticles hosted in the nanocomposite. Colloidal semiconductor nanocrystals are a class of nano-materials with significant potential for serving as luminescent chromophores in applications ranging from lasers and optoelectronic devices to biological fluorescence tagging. An obvious advantage of such nanostructures over conventional chromophores is the remarkable spectral coverage for luminescence from the ultraviolet to the near infrared. In [41], a

two-dimensional (2D) active new designed PQC which consists of air rods in an organic/inorganic nanocomposite is proposed and experimentally demonstrated. The nanocomposite was prepared by incorporating CdSe/CdS core/shell nanorods (NR) into a polymer matrix. Scanning electron microscopy and far field diffraction are used to characterize the experimental structure, which was fabricated using direct-write electron-beam lithography (EBL). The e-beam is locally focused on the sample to expose selected regions of material homogenously along the depth of the substrate according to the calculated desired pattern.

10.4 Conclusions

This chapter investigates the recent developments in high precision fabrication techniques for the manufacturing of photonic crystals (PCs) and their impact on the "dielectric laser acceleration" application and other case studies. The advantages and the challenges of the DLW Two-Photon Polymerization (TPP) technique are described since it represents the most suitable approach for the direct 3D printing of all dielectric structures. Special design procedures—also in terms of materials and structures geometries—are given in order to obtain electromagnetic structures having the desired functionalities. In particular, all-dielectric (typically, silicon-based) guided-mode structures, which can be used for particle laser acceleration in different configurations (PBG fiber, 2D planar and 3D 'woodpile' structures), are investigated due to the growing interest for dielectric laser-driven accelerators (DLAs). The ability of photonic crystals of molding the flow of light could represent a breakthrough in this field since the approach has the potential to reduce the particle accelerator size of 3 orders of magnitude and at same time to achieve higher acceleration gradient (up to GV/m) with respect to conventional RF metallic Linear accelerators (LINACs). 3D printing techniques for the fabrication of optical nanoantennas and of photonic devices such as photonic quasicrystals by exploiting new nano-composite materials are also presented.

References

1. J.D. Joannopoulos, S.G. Johnson, J.N. Winn, R.D. Meade, *Photonic Crystals: Molding the Flow of Light*, 2nd edn. (2011)
2. R.J. England, R.J. Noble, K. Bane, D.H. Dowell, C.-K. Ng, J.E. Spencer, S. Tantawi, Z. Wu, R.L. Byer, E. Peralta, K. Soong, C.-M. Chang, B.Montazeri, S.J. Wolf, B. Cowan, J. Dawson, W. Gai, P. Hommelhoff, Y.-C. Huang, C. Jing, C. McGuinness, R.B. Palmer, B. Naranjo, J. Rosenzweig, G. Travish, A. Mizrahi, L. Schachter, C. Sears, G.R. Werner, R.B. Yoder, Dielectric laser accelerators. Rev. Mod. Phys. **86**, 1337–1389 (2014). https://link.aps.org/doi/10.1103/RevModPhys.86.1337

3. B.M. Cowan, Three-dimensional dielectric photonic crystal structures for laser-driven acceleration. ***Phys. Rev. Special Topics-Accel. Beams **11**(1), 011301 (2008)
4. R.H. Siemann, Energy efficiency of laser driven, structure based accelerators. Phys. Rev. ST Accel. Beams **7**, 061303 (2004). https://link.aps.org/doi/10.1103/PhysRevSTAB.7.061303
5. X.E. Lin, Photonic band gap fiber accelerator. Phys. Rev. ST Accel. Beams **4**, 051301 (2001). https://link.aps.org/doi/10.1103/PhysRevSTAB.4.051301
6. G. Torrisi, L. Celona, C. De Angelis, S. Gammino, A. Locatelli, D. Mascali, G. Mauro, G. Sorbello, Numerical study of photonic-crystal-based dielectric accelerators, in *10th Int. Particle Acc. Conf.(IPAC'19), Melbourne, Australia, 19–24 May 2019* (JACOW Publishing, Geneva, 2019), pp. 3653–3656
7. S.Y. Lin, J.G. Fleming, D.L. Hetherington, B.K. Smith, R. Biswas, K.M. Ho, M.M. Sigalas, W. Zurzycki, S.R. Kurtz, J. Bur, A three-dimensional photonic crystal operating at infrared wavelength. Nature **394**, 251–253 (1998)
8. I. Staude, C. McGuinness, A. Frölich, R.L. Byer, E. Colby, M. Wegener, Waveguides in three-dimensional photonic bandgap materials for particle-accelerator on a chip architectures. Opt. Express **20**(5), 5607–5612 (2012). http://www.osapublishing.org/oe/abstract.cfm?URI=oe-20-5-5607
9. S.G. Johnson, J.D. Joannopoulos, Three-dimensionally periodic dielectric layered structure with omnidirectional photonic band gap. Appl. Phys. Lett. **77**(22), 3490–3492 (2000). https://doi.org/10.1063/1.1328369
10. S. Noda, K. Tomoda, N. Yamamoto, A. Chutinan, Full three-dimensional photonic bandgap crystals at near-infrared wavelengths. Science **289**(5479), 604–606 (2000). https://www.science.org/doi/abs/10.1126/science.289.5479.604
11. K. Aoki, H.T. Miyazaki, H. Hirayama, K. Inoshita, T. Baba, N. Shinya, Y. Aoyagi, Three-dimensional photonic crystals for optical wavelengths assembled by micromanipulation. Appl. Phys. Lett. **81**(17), 3122–3124 (2002). https://doi.org/10.1063/1.1515117
12. B. Cumpston, S. Ananthavel, S. Barlow, D.L. Dyer, J.E. Ehrlich, L. Erskine, A.A. Heikal, S.M. Kuebler, I.-Y.S. Lee, D. McCord-Maughon, J. Qin, H. Röckel, M. Rumi, X.-L. Wu, S.R. Marder, J.W. Perry, Two-photon polymerization initiators for three-dimensional optical data storage and microfabrication. Nature **398**, 51–54 (1999)
13. I. Staude, M. Thiel, S. Essig, C. Wolff, K. Busch, G. von Freymann, M. Wegener, Fabrication and characterization of silicon woodpile photonic crystals with a complete bandgap at telecom wavelengths. Opt. Lett. **35**(7), 1094–1096 (2010). http://www.osapublishing.org/ol/abstract.cfm?URI=ol-35-7-1094
14. C. Lee, Z. Wu, Y. Xuan, R.J. England, M. Qi, Novel fabrication of 3d woodpile accelerator by silicon membrane stacking. AIP Conf. Proc. **1777**(1), 060005 (2016). https://aip.scitation.org/doi/abs/10.1063/1.4965634
15. S.G. Johnson, Fabrication of three-dimensional crystals: those clever experimentalists, in *From Lecture Series Photonic Crystals: Periodic Surprises in Electromagnetism*. http://ab-initio.mit.edu/photons/tutorial/
16. N.V. Sapra, K.Y. Yang, D. Vercruysse, K.J. Leedle, D.S. Black, R.J. England, L. Su, R. Trivedi, Y. Miao, O. Solgaard, R.L. Byer, J. Vukovic, On-chip integrated laser-driven particle accelerator. Science **367**(6473), 79–83 (2020)
17. M. Deubel, G. von Freymann, M. Wegener, S. Pereira, K. Busch, C.M. Soukouli, Direct laser writing of three-dimensional photonic-crystal templates for telecommunications. Nature **3**, 444–447 (2004)
18. N. Tétreault, G.G. von Freymann, M. Deubel, M. Hermatschweiler, F. Pérez-Willard, S. John, M. Wegener, G.A. Ozin, New route to three-dimensional photonic bandgap materials: silicon double inversion of polymer templates. Adv. Mater. **18**(4), 457–460 (2006). https://onlinelibrary.wiley.com/doi/abs/10.1002/adma.200501674
19. C. McGuinness, E. Colby, R. Byer, Accelerating electrons with lasers and photonic crystals. J. Mod. Opt. **56**(18–19), 2142–2147 (2009). https://doi.org/10.1080/09500340903318539

20. M.C. Wanke, O. Lehmann, K. Müller, Q. Wen, M. Stuke, Laser rapid prototyping of photonic band-gap microstructures. Science **275**(5304), 1284–1286 (1997). http://www.jstor.org/stable/2892386
21. B. Naranjo, A. Valloni, S. Putterman, J. Rosenzweig, Stable charged-particle acceleration and focusing in a laser accelerator using spatial harmonics. Phys. Rev. Lett. **109**(16), 164803 (2012)
22. A. Locatelli, G. Sorbello, G. Torrisi, L. Celona, C. De Angelis, Photonic crystal waveguides for particle acceleration, in *2017 Prog, Electromagnetic. Res. Symposium-Spring (PIERS)* (IEEE, Piscataway, 2017), pp. 1008–1013
23. G.S. Mauro et al., Fabrication and characterization of woodpile waveguides for microwave injection in ion sources. IEEE Trans. Microw. Theory Techn. **68**(5), 1621–1626 (2020)
24. G.S. Mauro, A. Locatelli, G. Torrisi, L. Celona, C. De Angelis, G. Sorbello, Woodpile EBG waveguide as a DC electrical break for microwave ion sources. Microwave Opt. Technol. Lett. **61**(3), 610–614 (2019)
25. G. Torrisi et al., Design and characterization of a silicon w-band woodpile photonic crystal waveguide. IEEE Microw. Wirel. Compon. Lett. **30**(4), 347–350 (2020)
26. G.S. Mauro et al., Numerical simulation and beam-dynamics study of a hollow-core woodpile coupler for dielectric laser accelerators, in *Proc. 12th Int. Particle Accelerator Conf. (IPAC'21)*. (JACoW Publishing, 2021), pp. 2022–2025. Paper TUPAB246. https://doi.org/10.18429/JACoW-IPAC2021-TUPAB246. https://jacow.org/ipac2021/papers/TUPAB246.pdf
27. G. Torrisi, G.S. Mauro, G. Sorbello, G. Castorina, L. Celona, L. Faillace, B. Spataro, and V. Dolgashev, RF design and experimental test of a quadrupole-free x-band TM01 mode launcher. URSI Radio Sci. Bull. **2020**(373), 22–27 (2020)
28. S.G. Johnson, MIT Photonics-Bands (MPB). http://ab-initio.mit.edu/photons/tutorial/
29. Y.-S. Cho, D.-I. Kim, H.-S. Kim, K.-T. Seol, H.-J. Kwon, Multi-layered waveguide DC electrical break for the PEFP microwave proton source. J. Korean Phys. Soc. **63**(11), 2085–2088 (2013). https://doi.org/10.3938/jkps.63.2085
30. T. Taylor, J.F. Mouris, An advanced high-current low-emittance DC microwave proton source. Nucl. Instrum. Methods Phys. Res. **336**(1–2), 1–5 (1993)
31. O. Leonardi, G. Torrisi, L.D. Donato, A. Locatelli, L. Celona, C.D. Angelis, G. Sorbello, Hollow-core electromagnetic band gap waveguide as DC-break for ion sources, in *2017 Progress in Electromagnetics Research Symposium—Spring (PIERS)* (2017), pp. 1014–1017
32. G.S. Mauro, A. Locatelli, G. Torrisi, A. Rovelli, L. Celona, C. De Angelis, G. Sorbello, S. Gammino, Hollow core dielectric EBG waveguide to feed microwave ion sources, in *2019 13th European Conference on Antennas and Propagation (EuCAP)* (2019), pp. 1–5
33. W.Q. Zhang, H. Ebendorff-Heidepriem, T.M. Monro, V. Shahraam Afshar, Fabrication and supercontinuum generation in dispersion flattened bismuth microstructured optical fiber. Opt. Express **19**(22), 21135–21144 (2011). http://www.osapublishing.org/oe/abstract.cfm?URI=oe-19-22-21135
34. F. Giovanardi, A. Cucinotta, A. Rozzi, R. Corradini, F. Benabid, L. Rosa, L. Vincetti, Hollow core inhibited coupling fibers for biological optical sensing. J. Lightwave Technol. **37**(11), 2598–2604 (2019)
35. C.P. Reardon, I.H. Rey, K. Welna, L. O'Faolain, T.F. Krauss, Fabrication and characterization of photonic crystal slow light waveguides and cavities. JoVE **69**, e50216
36. S. Bagheri, K. Weber, T. Gissibl, T. Weiss, F. Neubrech, H. Giessen, Fabrication of square-centimeter plasmonic nanoantenna arrays by femtosecond direct laser writing lithography: effects of collective excitations on SEIRA enhancement. ACS Photon. **2**(6), 779–786 (2015). https://doi.org/10.1021/acsphotonics.5b00141
37. M.R. Hasan, O.G. Hellesø, Dielectric optical nanoantennas. Nanotechnology **32**(20), 202001 (2021). https://doi.org/10.1088/1361-6528/abdceb
38. D.G. Baranov, D.A. Zuev, S.I. Lepeshov, O.V. Kotov, A.E. Krasnok, A.B. Evlyukhin, B.N. Chichkov, All-dielectric nanophotonics: the quest for better materials and fabrication techniques. Optica **4**(7), 814–825 (2017). http://www.osapublishing.org/optica/abstract.cfm?URI=optica-4-7-814

39. Z. Vardeny, A. Nahata, A. Agrawal, Optics of photonic quasicrystals. Nat. Photon. **7**, 177–187 (2013)
40. W. Man, M. Megens, P.J. Steinhardt, P.M. Chaikin, Experimental measurement of the photonic properties of icosahedral quasicrystals. Nature **436**(7053), 993–996 (2005)
41. L. Petti, M. Rippa, R. Capasso, M. Zanella, L. Manna, P. Mormile, CDSE/CDS nanorods-polymer nanocomposites patternable by e-beam lithography: a novel active 2d photonic quasicrystal simulated, designed, fabricated and characterized. AIP Conf. Proc. **1459**(1), 154–156 (2012)

Chapter 11
Future Prospective

Alberto Ballesio, Matteo Parmeggiani, Matteo Cocuzza, and Simone Luigi Marasso

Abstract The chapters of this book describe the lively world which is moving around additive manufacturing (AM) and 3D printing with a deep focus on the polymer-based techniques and related applications. In the last chapter, final considerations on the future prospective are critically discussed to favor a better understanding of the expected next big steps in the field.

Keywords 3D printing · Additive manufacturing · 4D printing · Micro printing

11.1 Future Prospective

This book provides a new insight on the most promising polymer-based technologies and applications for high-resolution additive manufacturing (AM) and 3D printing. As depicted by the chapters dedicated to the first part "Part I – Technologies and Materials" – there are some more mature technologies like vat photopolymerization, powder bed fusion, and inkjet printing, which have been already attractive for industrialization aims and found successful exploitations [1–3]. As major concern about these technologies, the limitations in terms of materials and resolution restrict the development of groundbreaking applications especially in the fields of micro- and opto-electronics as well as in miniaturized medical devices.

Two-photon polymerization (2PP), volumetric 3D printing, and aerosol jet printing are increasing rapidly their fields of application, mostly as enabling technologies. These technologies are able to provide amazing 3D structures, thanks to their extremely high resolution. For instance, the idea of directly printing a

A. Ballesio · M. Parmeggiani
Department of Applied Science and Technology (DISAT), Politecnico di Torino, Torino, Italy

M. Cocuzza · S. L. Marasso (✉)
Department of Applied Science and Technology (DISAT), Politecnico di Torino, Torino, Italy

CNR-IMEM, Parco Area delle Scienze, Parma, Italy
e-mail: simone.marasso@polito.it

S. L. Marasso, M. Cocuzza (eds.), *High Resolution Manufacturing from 2D to 3D/4D Printing*, https://doi.org/10.1007/978-3-031-13779-2_11

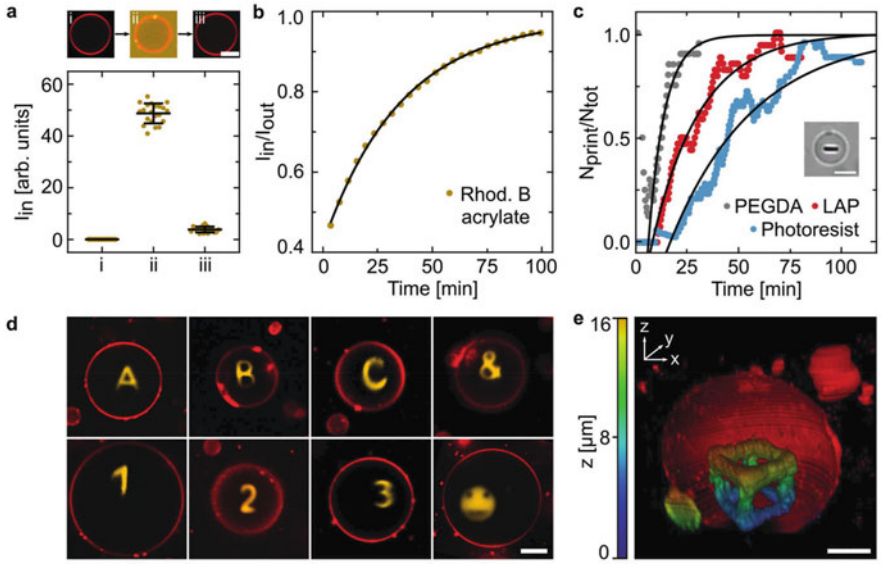

Fig. 11.1 Experimental panel of 2PP application for 3D printing inside cells: (**a**) giant unilamellar lipid vesicles confocal images before (I) and after mixing with the photoresist (II) and after diluting (II); (**b**) Ratio between inside and outside of the fluorescence intensity versus time; (**c**) Membrane permeability of PEGDA, LAP, and the complete photoresist; (**d**) Confocal images of 2D printed structures inside vesicles; (**e**) 3D printed cube inside the vesicle. (Reprinted under the Creative Commons CC BY license from Ref. [4])

3D structure inside a cell was definitively unthinkable before the advent of 2PP, while now, this has been successfully carried out [4] (Fig. 11.1). On the other hand, specific limitations can apply to the different techniques. As an example, in xolography, the volume that can be printed is restricted by the penetration depth of the light beam into the resin.

The major concern is the exploitation of these technologies outside the research laboratories, where they are limited to the researchers' specific case of studies. Limitations in terms of equipment costs, materials, and calibrations are the main barriers to their widespread diffusion and then to their applications at industrial scale.

A prospective progress of the presented techniques is related to the evolution of the so-called 4D printing. This new concept is based on the predictable behavior of the 3D printed objects, or of part of them, able to change their properties when exposed to specific conditions as the change in light, heat, humidity, or external magnetic field. This ability is related to responsive engineered materials, which may be hydrogels, liquid crystals, and composite materials. Possible applications of 4D printing in high-resolution AM are in the fields of optics, biomedicine, and micro-robotics [5]. Moreover, since the 3D laser lithography is the preferred technique, specific photoresists are used to obtain these responsive materials.

Another main topic in which future progresses are expected is related to the development of multi-material 3D printing. This technology allows obtaining a

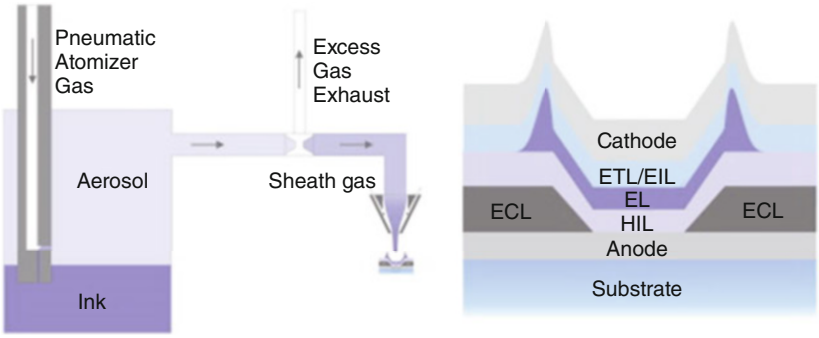

Fig. 11.2 Left: direct write aerosol jet printing system schematic. Right: the schematic representation of a top-emitting OLED architecture. (Reprinted with permission from Ref. [9])

complex 3D object made by different materials in a single printing process. The various materials are characterized by different properties and behaviors in order to add specific functionalities. These include mechanical, chemical, electrical, and optical functionalities which allow for a working device production, as, for example, transistors [6], energy storage devices [7], sensors, and soft robotic devices [8]. This challenge requires not only new materials and composites but also technological improvement for the printers. Jet technologies are the most technologically ready to achieve a multilayered multi-material printing for electronic components, while maintaining a good control and reasonable resolution (Fig. 11.2).

The improvements of the technologies involve not only the evolution of the printing hardware but should also be accompanied by further development of the design software. The standard software tools should include multi-materials and final device simulations to comply with real industrial design requirements. In fact, the use of the 3D model as initially designed can support the simulation development; meanwhile, more adequate software is needed to support the engineers to properly design the required 3D object with its functionalities and to simulate it. Nowadays, simple open-source slicer software can be used to compile the STL model and obtain a G file, or an equivalent one, and then load it in the printer. More complex tools are needed to obtain a complete virtual model also called digital twin of the part to be manufactured. In fact especially with the advent of Industry 4.0, the industrial practice is to use the digital twin approach to monitor all the production steps from the design to the machining and final release [10]. In this view, the virtual copy of the physical object provides a connection between the real and the virtual systems. This allows to gather, examine, and simulate data in the virtual model and then to improve the performance of the real object.

In the second part of this book dedicated to the "impact on different research fields and case studies," a selected number of applications in medicine and engineering are presented. The number of biomedical applications is growing very fast, and the added value of 3D printing in this context is considerable. Indeed, a customization of the prototypes and devices is commonly needed in order for them

to be applicable and compatible to the specific biological protocols and interactions with cells and tissue. For example, microfluidics that execute protocols for separation [11] are completely different with respect to the ones needed for cell cultures [12]. Furthermore, since 3D printing needs external energy to cure the resins and polymers, the risk for a poor biocompatibility is very high. To overcome this issue, new kinds of photo-initiators are investigated allowing for low-energy curing systems, avoiding the need for solvents, and improving biosafety for photopolymers [13, 14]. Other aspects related to the printing systems concern the apparatus cost and maintenance. Indeed, this kind of system requires strict conditions in order to not interfere with the cell cultures and biological protocols. Multi-material printing is considered a breakthrough also for biomedical applications, since it enables the printing and integration of different functionalities in the same object [15]. Moreover, it allows for higher level of complexity especially in microfluidic devices, where, for example, a tuning of the hydrophilic feature of the surface can be used to obtain the formation of oil/water/oil double emulsions [16].

In the last few years, 3D printed electronics attracted a growing interest from industries and researchers, thanks to its ability of delivering features and functionalities that would be impossible to accomplish by exploiting traditional fabrication techniques [17]. A wide spectrum of applications has been demonstrated, comprising both passive and active elements [18, 19]. The ability of fabricating fundamental electronic components in three dimensions, thus overcoming the flatness characterizing traditional circuit boards, is one of the requirements for 4D printing. A wide variety of different applications falls under this name, but from an electronic point of view, 4D printing is related to the fabrication of components with thermally, electronically, or optically configurable time-varying properties [20]. From this point of view, the direct fabrication of complex objects composed of functional materials will allow for the realization of novel devices with geometries and functionalities inaccessible with classical semiconductor technology [21]. Particularly promising are 3D printed actuators based on soft materials, characterized by lower power consumption and weight with respect to the rigid traditional structures [22, 23]. In the near future, the constant development of novel cheap, reliable, and functional materials is going to enable the customization of goods integrating electrical components, such as, for instance, wearable sensors [24]. Moreover, the increasing implementation of the Internet of Things (IoT) is accompanied by a growing need for portable, flexible, and wearable self-powered electronic systems. Also in this view, 3D printing provides the possibility of overcoming the limitations of traditional fabrication processes, especially concerning the implementation of novel micro-electrochemical energy storage devices (MEESDs) [25]. Additive manufacturing has indeed been widely explored to fabricate electrochemical energy storage systems with a plethora of different architectures and materials [26–28]. However, while detailed characterization of starting materials and final products is available in the literature, an important gap can be found concerning the proper reporting of electrochemical performances. Comparison between different works found in the literature may not be straightforward, with power capabilities and energy densities not always reported through specific and comparable figures of

merit. Future researches should indeed focus on a more detailed and precise electrochemical characterization of the devices, as well as on a more standardized way of presenting the results.

Regarding optics and photonics, AM technologies are broadening the possibilities for new designs and production rules. A continuous increase in the number of materials that can be used and of new fabrication methods, as well as better performances in spatial resolution, is constantly improving those fields.

Some challenges still need to be addressed and are fundamental for the future of this technology.

The first issue is the throughput, which needs to be improved in order to get out of laboratories and into factories. For this reason, many efforts are made for the development of better photoinitiators, lasers with a higher power, and systems with an increased scanning speed for multiphoton stereolithography (MP-STL) processes [29].

Another key challenge is the multiscale printing: photonic and optoelectronic systems need both components with macroscale size and parts with extremely tiny dimensions and feature sizes. So far, the best resolution is obtained with oil-immersed objectives with extremely short working distances, which are not compatible with macroscale fabrication. To solve that new AM techniques or a combination of AM techniques with in situ elements for both processing and sensing will be needed; another solution may be a shift toward continuous printing [29].

In photonics, the alternation of different materials is of paramount importance, so multimaterial processing is another branch that requires future efforts. While direct ink writing (DIW) is a first answer, inks with optoelectronic properties are still lacking [29].

Another aspect to further explore is the full exploitation of the third dimension: standard photonics have mostly planar configurations, so as to completely change the direction new design rules are required for both the devices and their interconnections [29].

References

1. Y. Dong et al., 4D printed hydrogels: Fabrication, materials, and applications. Adv. Mater. Technol. **5**, 2000034 (2020)
2. S. Nayar, S. Bhuminathan, W. Bhat, Rapid prototyping and stereolithography in dentistry. J. Pharm. Bioallied Sci. **7**, 218 (2015)
3. G. Scordo et al., A novel highly electrically conductive composite resin for stereolithography. Mater. Today Commun. **19**, 12–17 (2019)
4. T. Abele et al., Two-photon 3D laser printing inside synthetic cells. Adv. Mater. **34**, 2106709 (2022)
5. C.A. Spiegel et al., 4D printing at the microscale. Adv. Funct. Mater. **30**, 1907615 (2020)
6. V. Bertana et al., Rapid prototyping of 3D organic electrochemical transistors by composite photocurable resin. Sci. Rep. **10**, 1–11 (2020)

7. U. Gulzar, C. Glynn, C. O'Dwyer, Additive manufacturing for energy storage: Methods, designs and material selection for customizable 3D printed batteries and supercapacitors. Curr. Opin. Electrochem. **20**, 46–53 (2020)
8. X. Li et al., Multimaterial microfluidic 3D printing of textured composites with liquid inclusions. Adv. Sci. **6**, 1800730 (2019)
9. J.G. Tait et al., Uniform Aerosol Jet printed polymer lines with 30μm width for 140ppi resolution RGB organic light emitting diodes. Org. Electron. **22**, 40–43 (2015)
10. F. Pires, A. Cachada, J. Barbosa, A.P. Moreira, P. Leitao, Digital twin in industry 4.0: Technologies, applications and challenges, in *2019 IEEE 17th International Conference on Industrial Informatics (INDIN)*, (IEEE, 2019), pp. 721–726. https://doi.org/10.1109/INDIN41052.2019.8972134
11. F. Barbaresco, M. Cocuzza, C.F. Pirri, S.L. Marasso, Application of a micro free-flow electrophoresis 3D printed lab-on-a-Chip for micro-nanoparticles analysis. Nano **10**, 1277 (2020)
12. M.J. Lerman, J. Lembong, G. Gillen, J.P. Fisher, 3D printing in cell culture systems and medical applications. Appl. Phys. Rev. **5**, 041109 (2018)
13. Y. Liu et al., High-performance lignin-based water-soluble macromolecular Photoinitiator for the fabrication of hybrid hydrogel. ACS Sustain. Chem. Eng. **7**, 4004–4011 (2019)
14. A.A. Pawar et al., High-performance 3D printing of hydrogels by water-dispersible photoinitiator nanoparticles. Sci. Adv. **2**, e1501381 (2016)
15. F. Li, N.P. Macdonald, R.M. Guijt, M.C. Breadmore, Increasing the functionalities of 3D printed microchemical devices by single material, multimaterial, and print-pause-print 3D printing. Lab Chip **19**, 35–49 (2018)
16. M.J. Männel, N. Weigel, N. Hauck, T. Heida, J. Thiele, Combining hydrophilic and hydrophobic materials in 3D printing for fabricating microfluidic devices with spatial wettability. Adv. Mater. Technol. **6**, 2100094 (2021)
17. H.W. Tan, Y.Y.C. Choong, C.N. Kuo, H.Y. Low, C.K. Chua, 3D printed electronics: Processes, materials and future trends. Prog. Mater. Sci. **127**, 100945 (2022)
18. H.W. Tan, T. Tran, C.K. Chua, A review of printed passive electronic components through fully additive manufacturing methods. Virtual Phys. Prototyp. **11**, 271–288 (2016)
19. N. Saengchairat, T. Tran, C.-K. Chua, A review: Additive manufacturing for active electronic components. Virtual Phys. Prototyp. **12**, 31–46 (2017)
20. Y. Xia, Y. He, F. Zhang, Y. Liu, J. Leng, A review of shape memory polymers and composites: Mechanisms, materials, and applications. Adv. Mater. **33**, 2000713 (2021)
21. I.T. Garces, C. Ayranci, Active control of 4D prints: Towards 4D printed reliable actuators and sensors. Sensors Actuators A Phys. **301**, 111717 (2020)
22. A. Miriyev, K. Stack, H. Lipson, Soft material for soft actuators. Nat. Commun. **8**, 596 (2017)
23. G. Haghiashtiani, E. Habtour, S.-H. Park, F. Gardea, M.C. McAlpine, 3D printed electrically-driven soft actuators. Extreme Mech. Lett. **21**, 1–8 (2018)
24. J. Zhang et al., 3D printable, ultra-stretchable, self-healable, and self-adhesive dual cross-linked nanocomposite ionogels as ultra-durable strain sensors for motion detection and wearable human-machine interface. Chem. Eng. J. **431**, 133949 (2022)
25. W. Zhang et al., 3D printed micro-electrochemical energy storage devices: From design to integration. Adv. Funct. Mater. **31**, 2104909 (2021)
26. D.M. Soares et al., Additive manufacturing of electrochemical energy storage systems electrodes. Adv. Energy Sustain. Res. **2**, 2000111 (2021)
27. S. Zhang et al., 3D-printed wearable electrochemical energy devices. Adv. Funct. Mater. **32**, 2103092 (2022)
28. J. Yan et al., Direct-ink writing 3D printed energy storage devices: From material selectivity, design and optimization strategies to diverse applications. Mater. Today (2022). https://doi.org/10.1016/j.mattod.2022.03.014
29. A. Camposeo, L. Persano, M. Farsari, D. Pisignano, Additive manufacturing: Applications and directions in photonics and optoelectronics. Adv. Opt. Mater. **7**, 1800419 (2019)

Index

A
Actuator, 108, 110, 111, 115, 149, 192, 194–196, 210, 212–218, 222, 296
Additive manufacturing (AM), 4–7, 12, 13, 18, 19, 28, 30, 31, 38, 48, 57, 76, 77, 81, 84, 92, 95, 97, 132, 138, 145, 156–164, 191, 199, 203, 207–209, 216, 222, 248, 257, 264, 273, 293
Aerosol-jet printing, 106–124
Antennas, 120, 192, 198, 219, 220, 286, 287

B
Batteries, 192, 199, 203–205, 234, 236–237, 241, 252–263
Biocatalysis, 157, 174–178
Bioelectronics, 7, 112–116, 119–122, 124
Biofabrication, 149
Biorecognition, 115, 156, 164–171, 181
Biosensors, 107, 113–115, 120, 121, 123, 124, 164, 166–169, 171–174

C
Computed axial lithography (CAL), 138–141
Continuous liquid interface production (CLIP), 7, 19, 35–36, 158, 162

D
Dielectric laser accelerators, 270–288
Digital light processing (DLP), 19, 30, 33–35, 139, 141, 158, 162, 192
Direct laser writing (DLW), 50, 59, 76, 192, 271, 286, 287
Direct writing, 48, 106–124, 287
Dual-color photoinitiators (DCPIs), 144

E
Electronic passive elements, 192–198, 222
Energy storage devices, 204, 233–264, 295

F
Fast prototyping, 106
Femtosecond laser, 48, 52, 56, 57, 67, 286
Flexible devices, 114, 120, 172, 192
4D printing, 4–13, 143, 156, 194, 196, 198, 213, 214, 216, 218, 219, 222, 234–264, 294, 296
Functionality, 27, 156, 157, 163–171, 176, 179, 180, 194, 207, 208, 216, 222, 272, 273, 287, 288, 295, 296

H
Holography printing, 133, 134

I
Ink jet printing, 30, 107–116, 194, 198–203, 205, 207, 220, 293

L
Light-emitting diode (LED), 199, 205
Linear accelerator, 271, 288

S. L. Marasso, M. Cocuzza (eds.), *High Resolution Manufacturing from 2D to 3D/4D Printing*, https://doi.org/10.1007/978-3-031-13779-2

M
Micro structures, 71, 74, 166, 167, 272, 284

N
Nanotechnology, 4, 48
Non-contact printing, 106–108, 116

P
Photo curable resins, 5, 12, 40, 43, 162
Photoinhibitors, 146, 147
Photonic crystals (PC), 58, 59, 76, 133, 134, 181, 271, 273–281, 286, 288
Polymer powders, 86, 89, 93, 95, 98
Powder bed fusion (PBF) technologies, 5, 33, 81–100
Precision medicine, 157, 178–180
Printability, 5, 7, 11, 12, 175, 181, 192, 256

R
Radical polymerization, 22, 25, 40, 44, 49, 148, 162

S
Sensors, 58, 64, 67, 112, 114, 115, 121, 157, 163, 165, 171, 172, 192, 194–197, 207–212, 216, 217, 219–222, 295, 296
Stereo lithography (SL), 5, 19, 67–69, 84, 94, 132, 138–140, 142, 145, 158, 160, 165, 168, 200, 258, 271
Stereolithography apparatus (SLA), 5, 6, 19, 30–33, 158, 160, 162, 192, 194, 216, 249, 251, 263
Supercapacitors (SCs), 196, 197, 220, 222, 234–239, 242, 254, 256

T
3D models, 4, 7, 10, 11, 29, 52, 143, 206, 274, 280, 295
3D printed electronics, 106, 112–116, 119, 192, 296
3D printing, 4–13, 22, 23, 27, 29, 33, 35, 36, 39, 43, 67, 75, 82, 84, 94, 106, 107, 112–116, 119–122, 132–150, 156, 157, 159, 160, 162–181, 191–198, 200, 206–208, 210–218, 220–222, 234–264, 271, 272, 275, 276, 284–288, 294–296
Top-down approach, 5, 7–10, 13, 30, 31
Transistors, 107, 114, 115, 120, 192, 199–203, 205, 222, 295
2D devices, 242, 243, 247
Two-photon polymerization (2PP/TPP), 2, 5, 6, 10, 19, 30, 48–77, 143, 158, 163–164, 192, 196, 212, 271, 288, 293, 294

U
UV curing, 21

V
Vat photopolymerization, 4, 18–44
Volumetric printing, 132–150

W
Woodpile, 258, 261, 271–273, 275–285, 288

X
Xolography, 132, 141–150, 294